ANCHAM

ANALYTICAL CHEMISTRY

OCTOBER 15, 1994

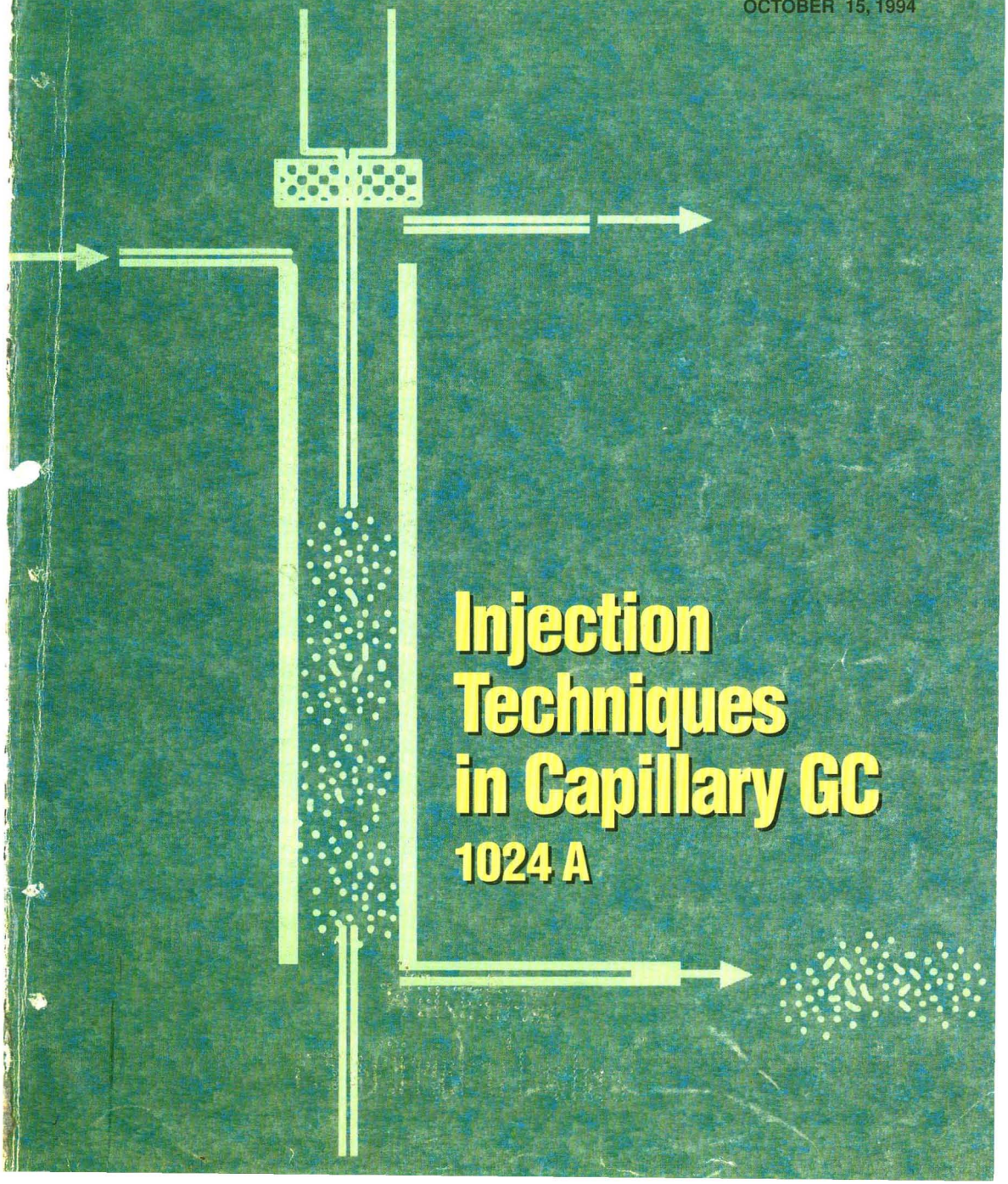

Injection Techniques in Capillary GC

1024 A

Looking for Spectra? Look to Aldrich.

Aldrich FT-IR Libraries... ...with SpecID *Plus* peak search software for Microsoft Windows

The Aldrich Library of FT-IR Spectra on CD-ROM includes more than 10,000 condensed-phase and 5,000 vapor-phase spectra. It is a valuable resource for schools and libraries. This database is also a practical tool for the Analytical Laboratory, Research and Development, and Quality Control Departments.

Identify unknown sample spectra...

- Select peak locations and intensities
- View reference spectra containing specified peaks and intensities
- Select additional peaks to narrow field of matches
- Export spectra to other Windows software for reports and presentations

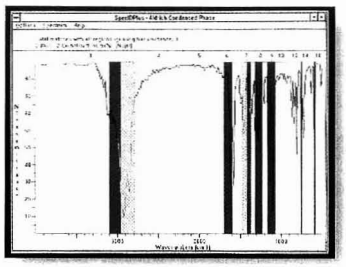

Spectra are visible on-screen and stored on the CD-ROM

Aldrich FT-IR Library Books... ...and SpecID peak search software for Microsoft Windows

This version of the SpecID peak search software has the same Windows interface for peak and intensity selection as SpecID *Plus*. In this version, unknown spectra are visually compared to reference spectra in the Aldrich FT-IR Library books.

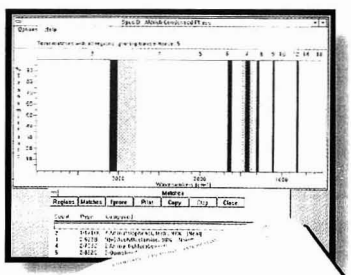

This search program references page, volume, and spectrum numbers in the Aldrich FT-IR Library books.

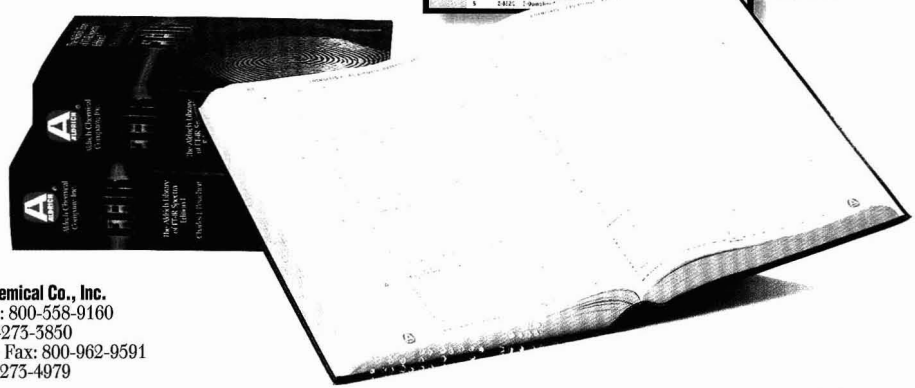

Aldrich Chemical Co., Inc.
Toll Free: 800-558-9160
Tel.: 414-273-3850
Toll Free Fax: 800-962-9591
Fax: 414-273-4979

SIGMA-ALDRICH™ Techware
FROM BENCHTOP TO BOOKSHELF

SIGMA-ALDRICH

More Information - Circle 7

Let's Face It: You Need a Better Solution for Validation Compliance.

Symmetry C_{18} and C_8

The New Standard for the Next Generation of HPLC Assays

Now with Symmetry™ HPLC columns from Waters, there's a new standard of performance to help you speed up validation of new drug assays. Our new column technology gives you unmatched peak symmetry for maximum sensitivity and accurate quantitation. It also gives you greater reproducibility for more confidence in the long-term compliance of your HPLC methods.

We Started Over So You Won't Have to

Starting over meant developing Symmetry silica from first principles—synthesizing new high purity silica particles from ultrapure reagents. It also meant improving every element of the manufacturing process—sizing and surface modifying the silica, precision machining and chemically cleaning the steel column tube and endfittings, plus packing and testing. This means every Symmetry column delivers the consistent performance you need to meet your system suitability requirements throughout the drug development process.

Set a New Standard for All Your HPLC Assays

The Symmetry standard—column after column, year after year, no matter who uses your methods or where they're used around the world. It's the new standard for all your HPLC assays.

Involved in new drug assay development? Call us now at **1-800-252-4752**.

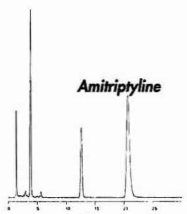

Amitriptyline (pKa 9), a challenging compound by anyone's definition, has an asymmetry measurement of 2.0 in a pH 7 mobile phase with no amine modifiers.

Symmetry columns are also available in convenient cartridge columns with reusable endfittings.

CIRCLE 1 ON READER SERVICE CARD

Waters and Symmetry are trademarks of Waters Corporation. © 1994 Waters Corporation.

Contents

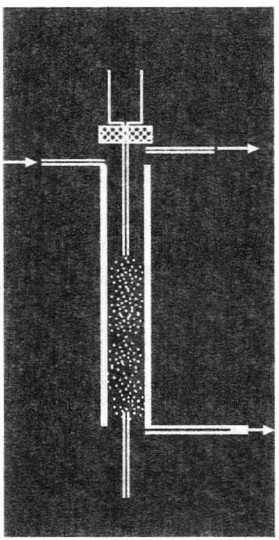

1009 A

1024 A

REPORT

1009 A
ON THE COVER. Injection techniques in capillary GC
Although capillary GC is more than 30 years old, injection techniques have not achieved the degree of reliability needed for routine analysis. Konrad Grob of the Kantonales Laborium Zürich (Switzerland) describes various injection techniques, reviews existing problems, and discusses promising ideas.

REPORT

1024 A
In vivo NMR of drugs
NMR spectroscopy and imaging are novel, noninvasive techniques for measuring the concentration, distribution, and pharmacokinetics of certain drugs in vivo in humans and animals. Richard A. Komoroski of the University of Arkansas for Medical Sciences discusses special considerations, multinuclear applications, and future prospects for this technique.

EDITOR: **ROYCE W. MURRAY**
University of North Carolina

ASSOCIATE EDITORS: **Catherine C. Fenselau,** University of Maryland Baltimore County, **William S. Hancock,** Hewlett Packard, **James W. Jorgenson,** University of North Carolina, **Robert A. Osteryoung,** North Carolina State University, **Edward S. Yeung,** Iowa State University/Ames Laboratory

Editorial Headquarters
Research section
Department of Chemistry
Venable and Kenan Laboratories
University of North Carolina
Chapel Hill, NC 27599-3290
Phone: 919-962-2541
Fax: 919-962-2542
E-mail: Murray @ uncvx1.oit.unc.edu

Editorial Headquarters
A-page section
1155 Sixteenth St., N.W.
Washington, DC 20036
Phone: 202-872-4570
Fax: 202-872-4574
E-mail: acx96 @ acs.org

Managing Editor: Mary Warner
Senior Editor: Louise Voress
Associate Editors: Grace K. Lee, Felicia Wach
Editorial Assistant: Deborah Noble
Contributing Editor: Marcia Vogel
Head, Graphics and Production: Leroy L. Corcoran
Division Art Director: Alan Kahan
Art Director: Peggy Corrigan
Designer: Michele Telschow
Production Editors: Kathleen Savory, Elizabeth Wood
Electronic Composition: Wanda R. Gordon

ANALYTICAL CHEMISTRY

OCTOBER 15, 1994
VOLUME 66 NUMBER 20

ANCHAM
66(20) 989 A–1042 A/3289–3552 (1994)
ISSN 0003-2700

Registered in U.S. Patent and Trademark Office
©Copyright 1994 by the American Chemical Society

DEPARTMENTS

997 A
In This Issue

1003 A
Analytical Currents

1006 A
News
DAC programs promote analytical chemistry. • 1994–95 DAC officers. • Janata receives Electrochemical Society award. • For Your Information.

1020 A
Software
HyperChem molecular modeling software will be helpful for individuals who do not have access to large computer-based molecular modeling systems, according to R. K. Gilpin. • David M. Haaland reviews Omnic, a Windows-based software package designed for mid- and near-IR spectral analyses. • Software released.

1034 A
Meetings
Conferences. • Call for Papers.

1035 A
Product Review
DTA heats up analysis. Bench and research chemists are relying on differential thermal analysis to help characterize a wide spectrum of materials ranging from glasses to ceramics to polymers to metals. We review the basic theory involved and compare six representative commercial DTA instruments.

1040 A
Information Express

RESEARCH

Accelerated Article

3289
Electrospray Mass Spectrometric Study of Protein–Ketone Equilibria in Solution
J.C.Y. Le Blanc, K.W.M. Siu, and Roger Guevremont*

Articles

3297
Gas-Phase Biosensor for Ethanol
*Kohji Mitsubayashi, Kenji Yokoyama, Toshifumi Takeuchi, and Isao Karube**

3303 ■
Interlaboratory Comparison of Autoradiographic DNA Profiling Measurements. 1. Data and Summary Statistics
James L. Mudd, F. Samuel Baechtel, David L. Duewer, Lloyd A. Currie, Dennis J. Reeder, Stefan D. Leigh, and Hung Kung Liu*

3318
Kinetic Method for the Quantitative Resolution of Structural Isomers Based on the Catalytic Properties of β-Cyclodextrin
*Ellen Tuanying Chen and Harry L. Pardue**

3323
Capillary Optical Sensors
*Bernhard H. Weigl and Otto S. Wolfbeis**

3328
Multicomponent Determination of Chlorinated Hydrocarbons Using a Reaction-Based Chemical Sensor. 1. Multivariate Calibration of Fujiwara Reaction Products
John M. Henshaw, Lloyd W. Burgess, Karl S. Booksh, and Bruce R. Kowalski*

continued on p. 993 A

Publications Division
Director: Robert H. Marks
Head, Special Publications: Anthony Durniak
Head, Journals: Charles R. Bertsch
Head, Publications Marketing: David Schulbaum

Journals Dept., Columbus, Ohio
Editorial Office Manager: Mary E. Scanlan
Journals Editing Manager: Kathleen E. Duffy
Associate Editor: Lorraine Gibb
Assistant Editor: Stephanie L. Mallon

Advisory Board: Phyllis Brown, Bruce Chase, Joseph G. Gordon, David M. Haaland, Joel M. Harris, Franz Hillenkamp, Kiyokatsu Jinno, Dennis C. Johnson, Richard A. Keller, Peter Kissinger, Gary E. Maciel, Scott M. McLuckey, Milos V. Novotny, Geraldine Richmond, Ralph Riggin James A. Yergey *Ex Officio:* Janet Osteryoung

A-page Advisory Panel: Frank V. Bright, Raymond E. Clement, Therese M. Cotton, Norman J. Dovichi, Royce C. Engstrom, Mary Ellen P. McNally, John W. Olesik, J. Michael Ramsey, Robert D. Voyksner

Copyright Permission: An individual may make a single reprographic copy of an article in this publication for personal use. Reprographic copying beyond that permitted by Section 107 or 108 of the U.S. Copyright Law is allowed, provided that the appropriate per-copy fee is paid through the Copyright Clearance Center, Inc., 222 Rosewood Dr., Danvers, MA 01923. For reprint permission, write Copyright Administrator, Publications Division, ACS, 1155 Sixteenth St., N.W., Washington, DC 20036.

BPA International Business Publication Membership Applied for August 1993.

Analytical Chemistry (ISSN 0003-2700) is published semimonthly by the American Chemical Society, 1155 Sixteenth St., N.W., Washington, DC 20036. Second-class postage paid at Washington, DC, and additional mailing offices. Postmaster: Send address changes to *Analytical Chemistry*, Member & Subscriber Services, P.O. Box 3337, Columbus, OH 43210.

Canadian GST Reg. No. R127571347.

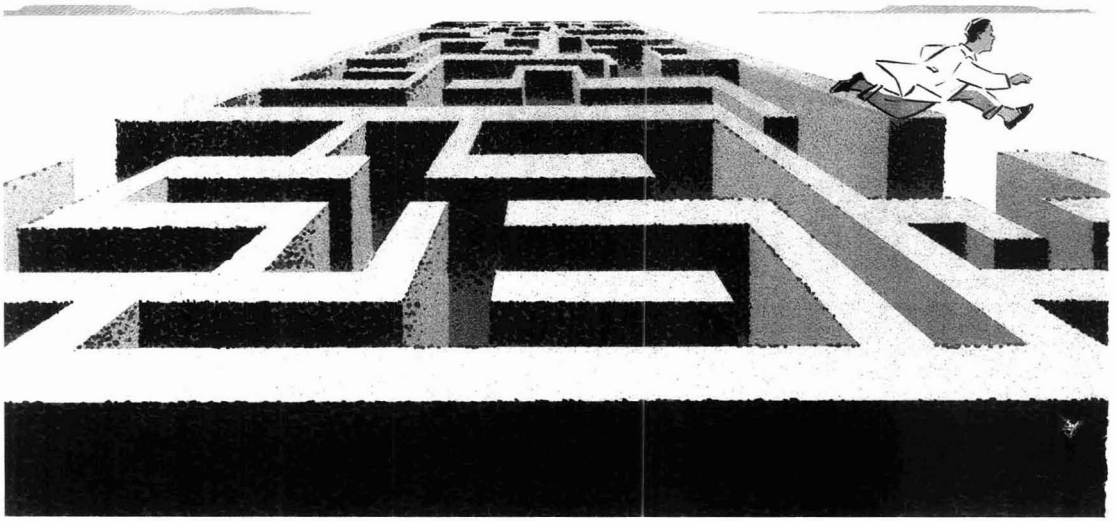

Developing a new SPE method? Let our tech support save you time and steps.

The next time you're developing a new Solid Phase Extraction (SPE) method, don't wander through a maze of chromatographic theory and vague instructions; call 1-800-JTBAKER.

Our technical support includes 150 step-by-step application notes, a comprehensive bibliography of published articles, and a 60-page technical guide. Best of all, you can count on us for friendly, expert advice when you hit a dead end with methods development or optimization.

You already know BAKERBOND spe columns and cartridges for their outstanding reproducibility. Now, call 1-800-JTBAKER or fax 908-859-9318 for free trouble-shooting or to receive our other valuable reference materials for SPE.

And leap your methods development mazes . . . in a single bound.

CERTIFIED ISO9000 PHILLIPSBURG NJ - 9001 JACKSON TN - 9002

J.T.Baker® *Right from the Start.®*

Right from the Start® is a trademark of J.T.Baker Inc. ©1994 J.T.Baker Inc.

CIRCLE 9 ON READER SERVICE CARD

Contents

3337
Multicomponent Determination of Chlorinated Hydrocarbons Using a Reaction-Based Chemical Sensor. 2. Chemical Speciation Using Multivariate Curve Resolution
*R. Tauler, A. K. Smilde, J. M. Henshaw, L. W. Burgess, and B. R. Kowalski**

3345
Multicomponent Determination of Chlorinated Hydrocarbons Using a Reaction-Based Chemical Sensor. 3. Medium-Rank Second-Order Calibration with Restricted Tucker Models
*A. K. Smilde, R. Tauler, J. M. Henshaw, L. W. Burgess, and B. R. Kowalski**

3352
Submersible, Osmotically Pumped Analyzers for Continuous Determination of Nitrate In Situ
Hans W. Jannasch Kenneth S. Johnson, and Carole M. Sakamoto*

3362
Raman Spectroscopy of Covalently Bonded Alkylsilane Layers on Thin Silica Films Immobilized on Silver Substrates
*Wade R. Thompson and Jeanne E. Pemberton**

3371
Monodisperse Dried Microparticulate Injector: A New Tool for Studying Fundamental Processes in Inductively Coupled Plasmas
John W. Olesik and Steven E. Hobbs*

3379
Surface-Enhanced Raman Gene Probes
T. Vo-Dinh, K. Houck, and D. L. Stokes*

3384
Free Radical Detector for Tropospheric Measurement Using Chemical Amplification
*Jia Hu and Donald H. Stedman**

3394
Electrospray Mass Spectrometric Analysis and Photocatalytic Degradation of Polyethoxylate Surfactants Used in Wool Scouring
Kim B. Sherrard, Philip J. Marriott, Malcolm J. McCormick, Ray Colton, and Geoff Smith*

3400
Low-Pressure Inductively Coupled Plasma Ion Source for Molecular and Atomic Mass Spectrometry
E. Hywel Evans, Warren Pretorius, Les Ebdon, and Steve Rowland*

3408
Chemical Electron-Transfer Reactions in Electrospray Mass Spectrometry: Effective Oxidation Potentials of Electron-Transfer Reagents in Methylene Chloride
Gary J. Van Berkel and Feimeng Zhou*

3416
Accumulation and Storage of Ionized Duplex DNA Molecules in a Quadrupole Ion Trap
*Mitchel J. Doktycz, Sohrab Habibi-Goudarzi, and Scott A. McLuckey**

3423
Matrix-Assisted Laser Desorption/Ionization Using an Active Perfluorosulfonated Ionomer Film Substrate
*Jian Bai, Yan-Hui Liu, Teresa C. Cain, and David M. Lubman**

3431
Chemical Characterization of Single Particles by Laser Ablation/Desorption in a Quadrupole Ion Trap Mass Spectrometer
John M. Dale, Mo Yang, William B. Whitten, and J. Michael Ramsey*

3436
Improvement in Detection Limits for the Determination of Paralytic Shellfish Poisoning Toxins in Shellfish Tissues Using Capillary Electrophoresis/Electrospray Mass Spectrometry and Discontinuous Buffer Systems
*S. J. Locke and P. Thibault**

3447
Postionization Chemical Separation: A Mass Spectrometric Technique for Isotopic Analysis of Mixtures
Karl K. Irikura, Edmund H. Fowles, and J. L. Beauchamp*

3449
Analytical Applications and Implications of Intramolecular Micelle-Mimetic Ionene Aggregates
Willie L. Hinze, Bernardo Moreno, Frank H. Quina, Yasuzo Suzuki, and Hong Wang*

continued on p. 995 A

Registered names and trademarks used in this publication, even without specific indication thereof, are not to be considered unprotected by law.

1994 subscription rates include air delivery outside the U.S., Canada, and Mexico. Canadian subscriptions are subject to 7% GST.

	Members	Nonmembers (personal)	Nonmembers (institutional)
U.S.	$ 37	$ 79	$ 481
Canada and Mexico	72	114	516
Europe	127	169	571
Other countries	154	196	598

Nonmember rates in Japan: Rates above do not apply to nonmember subscribers in Japan, who must enter subscription orders with Maruzen Company Ltd., 3–10. Nihonbashi 2-chome, Chuo-ku, Tokyo 103, Japan. Tel: (03) 272-7211.

For multi-year and other rates, call toll free 800-227-5558 in the U.S. and Canada; in the Washington, DC, metropolitan area and outside the U.S., call 202-872-4363; fax 202-872-4615.

Single issues, current year, $21.00 except review issue, $50.00, and LabGuide, $50.00; **back issues and volumes and microform editions** available by single volume or back issue collection. For information or to order, call the number listed for subscription orders by phone; or write the Microform & Back Issues Office at the Washington address.

Subscription orders by phone may be charged to VISA, MasterCard, or American Express. Call toll free 800-333-9511 in the continental U.S.; in the Washington, DC, metropolitan area and outside the continental U.S., call 202-872-8065. Mail orders for new and renewal subscriptions should be sent with payment to American Chemical Society, Department L-0011, Columbus, OH 43268-0011.

Changes of address must include both old and new addresses with ZIP code and a recent mailing label. Send all address changes to the ACS Columbus address. Please allow 6 weeks for change to become effective. **Claims for missing numbers** will not be allowed if loss was due to failure of notice of change of address to be received in the time specified; if claim is dated (a) North America—more than 90 days beyond issue date, (b) all other foreign—more than 180 days beyond issue date. Hard copy claims are handled at the ACS Columbus address.

ACS membership information: Lorraine Bowlin (202-872-4567)

Learn to Work Smarter . . .
Not Harder . . . with

American Chemical Society

Short Courses

Coming To:
Columbus, Ohio • October 27–28, 1994
St. Louis, Missouri • October 31–November 1, 1994
Boston, Massachusetts • December 1–2, 1994

Master Essential State-of-the-Art Skills in These Top-Rated Courses:

Capillary Gas Chromatography: Techniques and Problem Solving (Ext. 730)
Solve Your Day-to-Day Analysis Problems
Instructors: **Miles Novotny** and **Stuart P. Cram**

Chemical Engineering and Process Fundamentals for Chemists (Ext. 731)
Solve Your Process Problems by Learning Fundamental Chemical Engineering
Instructor: **Richard G. Griskey**

Interpretation of Mass Spectra (Ext. 732)
Enhance Your Ability to Analyze Samples Using Mass Spectrometry
Instructors: **O. David Sparkman** and **J. Throck Watson**

Statistical Analysis of Laboratory Data (Ext. 733)
Master the Fundamentals of Laboratory Data Treatment
Instructors: **Stanley N. Deming** and **Stephen L. Morgan**

Technical Writing Workshop (Ext. 734)
Improve Your Professional Writing Skills
Instructor: **Anne Eisenberg**

Receive Information Instantly By FAX!

Obtain information on any of these popular short courses with ACS's new FAX-on-demand service. Simply call (800) 366-CHEM and have your FAX number ready.

Then, follow the simple, step-by-step directions, entering the extension of your desired short course(s), which are listed to the right of the course. Within moments, you'll have complete details in hand—including course descriptions, dates, locations, registration forms, and hotel information.

To obtain information by mail, write or call:
American Chemical Society, 1155 Sixteenth Street, N.W., Washington, DC 20036.
Telephone: (800) 227-5558 (TOLL FREE) or (202) 872-4508.

3458
Selectivity in Micellar Reversed-Phase Liquid Chromatography: C-18 and C-8 Alkyl Bonded Phases
Barry K. Lavine, Sumar Hendayana, and Jonathan Tetreault*

3466
Modification of the Electrophoretic Mobility of Neutral and Charged Polysaccharides
*Morgan Stefansson and Milos Novotny**

3472
Microchip Capillary Electrophoresis with an Integrated Postcolumn Reactor
Stephen C. Jacobson, Lance B. Koutny, Roland Hergenröder, Alvin W. Moore, Jr., and J. Michael Ramsey

3477
Maltooligosaccharides as Chiral Selectors for the Separation of Pharmaceuticals by Capillary Electrophoresis
*Helena Soini, Morgan Stefansson, Marja-Liisa Riekkola, and Milos V. Novotny**

3485
Electroosmotic Pumping and Valveless Control of Fluid Flow within a Manifold of Capillaries on a Glass Chip
*Kurt Seiler, Zhonghui H. Fan, Karl Fluri, and D. Jed Harrison**

3492
Interpretation of the Retention Mechanism of Transition-Metal Cations in Ion Interaction Chromatography
Sergio Zappoli and Chiara Bottura*

Correspondence

3500
Subfemtomole Detection of Catecholamine with Interdigitated Carbon Microelectrodes in HPLC
Hisao Tabei, Masaya Takahashi, Satoshi Hoshino, Osamu Niwa, and Tsutomu Horiuchi*

3503
Comment on Wet Effluent Denuder Coupled Liquid/Ion Chromatography Systems: Annular and Parallel Plate Denuders
Franco De Santis

Technical Notes

3505
Determination and Characterization of Unreacted Hydroxyl Groups in a Cross-Linked Poly(ortho ester)
John D. Stong and Leonore C. Witchey-Lakshmanan*

3512
Analysis of Human Cerebrospinal Fluid by Capillary Electrophoresis with Laser-Induced Fluorescence Detection
Jonas Bergquist, S. Douglass Gilman, Andrew G. Ewing, and Rolf Ekman*

3519
Fabrication of Patterned Sensor Arrays with Aryl Azides on a Polymer-Coated Imaging Optical Fiber Bundle
*Karen S. Bronk and David R. Walt**

3521
Solvent Extraction of Radium with Crown Ether Carboxylic Acids
*M. K. Beklemishev, Sadik Elshani, and C. M. Wai**

3525
Diffusion Denuder Method for Sampling Vapor-Phase Nicotine in Mainstream Tobacco Smoke
David A. Lewis, Ian Colbeck, and Derek C. Mariner*

3528
Reactivation and Stability of Pyrolytic Carbon Film Electrodes on Macor Substrates
*Jill K. Clark, William A. Schilling, Charles A. Wijayawardhana, and Paula R. Melaragno**

3533
Performance of a Novel Silica T-Tube Interface for the AAS Detection of Arsenic and Selenium Compounds in HPLC Column Eluate
*Georges-Marie Momplaisir, Tian Lei, and William D. Marshall**

3540
Real-Time Measurement Capabilities Using Aerosol Time-of-Flight Mass Spectrometry
*T. Nordmeyer and K. A. Prather**

3543
Simple Fiber-Optic Interface for On-Line Supercritical Fluid Extraction Fourier Transform Infrared Spectrometry
Daniel L. Heglund, David C. Tilotta, Steven B. Hawthorne, and David J. Miller*

Author Index **3552**

Instructions for authors of AC Research and guidelines for the Instrumentation, Report, Analytical Approach, and A/C Interface features are published in the Jan. 1 issue, p. 185. Please consult these instructions prior to submitting a manuscript for consideration for publication.

Manuscripts for publication in AC Research (4 copies of text and illustrative material) should be submitted to the Editor at the University of North Carolina address. Please include a signed copyright status form; a copy of this document appears on p. 191 of the Jan. 1 issue. Manuscripts for publication in the A-page section should be submitted to the Washington editorial staff.

Supplementary material is noted in the table of contents with a ■. It is available as photocopy ($10.00 for up to 3 pages and $1.50 per page for additional pages, plus $2.00 for foreign postage) or as 24X microfiche ($10.00, plus $1.00 for foreign postage). Canadian residents should add 7% GST. See supplementary material notice at end of journal article for number of pages. Orders *must* state whether for photocopy or for microfiche and give complete title of article, names of authors, journal, issue date, and page numbers. Prepayment is required and prices are subject to change. Order from Microforms & Back Issues Office at the ACS Washington address.

The American Chemical Society and its editors assume no responsibility for the statements and opinions advanced by contributors. Views expressed in the editorials are those of the editors and do not necessarily represent the official position of the American Chemical Society.

The paper used in this publication meets the minimum requirements of American National Standard for Information Sciences—Permanence of Paper for Printed Library Materials, ANSI Z39.48-1984.

Journals Department
American Chemical Society
2540 Olentangy River Road
P.O. Box 3330
Columbus, OH 43210
614-447-3600, Ext. 3171
TELEX 6842086 Fax 614-447-3745

Member & Subscriber Services
American Chemical Society
P.O. Box 3337
Columbus, OH 43210
614-447-3776
800-333-9511

Advertising Office: Centcom Ltd., 1599 Post Road East, P.O. Box 231, Westport, CT 06881

Learn from Recognized Experts How to Work Smarter!

Register Today for One of These Results-Oriented Training Courses from the American Chemical Society

November 1994 • Somerset, New Jersey

in conjunction with the 1994 Eastern Analytical Symposium

Air Toxics Analysis by U.S. EPA Methods
Jerry Winberry and *Dr. R. Rasmussen*
Thursday-Friday, November 17-18, 1994

Analytical Methods for Proteins
Dr. Robert Copeland
Thursday-Friday, November 17-18, 1994

Chaos and Computers: New Trends in Laboratory Information and Management
Dr. Raymond Dessy
Wednesday, November 16, 1994

Chemical Engineering and Process Fundamentals for Chemists
Dr. Richard Griskey
Monday-Wednesday, November 14-16, 1994

Designing, Selling, and Leading the Small R&D Project
Augustus (Gus) Walker
Monday, November 14, 1994

Effective Management of Chemical Analysis Laboratories
Dr. Claude Lucchesi
Monday-Tuesday, November 14-15, 1994

Environmental Data Validation
William Purves
Monday-Tuesday, November 14-15, 1994

Gas Chromatography
Dr. Harold M. McNair
Monday-Tuesday, November 14-15, 1994

Interpretation of Infrared Spectra
Howard J. Sloane
Tuesday-Thursday, November 15-17, 1994

Interpretation of Mass Spectra
Dr. Jack T. Watson and
O. David Sparkman
Thursday-Friday, November 17-18, 1994

Keeping Your Company Profitable and Competitive: Customer Driven Quality and Statistical Process Control
Dr. Alan Riga
Monday, November 14, 1994

Laboratory Information Management Systems: From Problem Definition to System Evaluation
Dr. Gerst Gibbon and *Joseph Golden*
Wednesday, November 16, 1994

Quality Assurance Practices for the Environmental Laboratory
Steven Callio
Thursday-Friday, November 17-18, 1994

Solid Phase Extraction in Environmental and Clinical Chemistry
Dr. E. Michael Thurman, Margaret Mills, and *Lynn Jordan*
Thursday-Friday, November 17-18, 1994

Successful Selling in the Chemistry and Chemical Engineering Marketplace
O. David Sparkman
Tuesday-Wednesday, November 15-16, 1994

Technical Writing Workshop
Dr. Anne Eisenberg
Thursday-Friday, November 17-18, 1994

Thermal Analysis in Polymer Characterization
Dr. Edith Turi (Course Director),
Dr. Richard Chartoff, and *Harvey Bair*
Monday-Tuesday, November 14-15, 1994

For more information call (800) 227-5558 or (202) 872-4508. Or FAX or mail the coupon below.

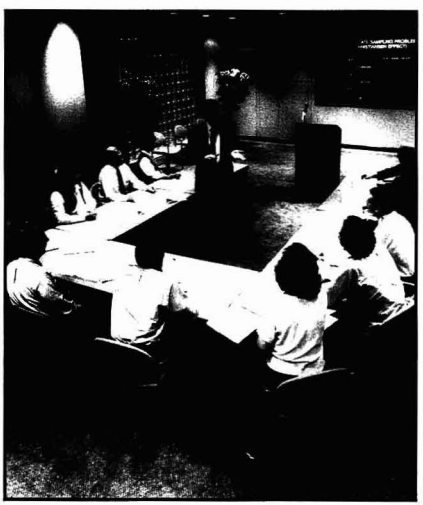

YES! Please send me a free catalog describing ACS Short Course sessions in conjunction with the November 1994 EAS in Somerset, New Jersey.

Name _____

Title _____

Organization _____

Address _____

City _____

State, Zip _____

FAX _____ Phone _____

Mail to: **American Chemical Society,** Dept. of Continuing Education, Meeting Code EAS94, 1155 Sixteenth Street, N.W., Washington, D.C. 20036

FAX to: (202) 872-6336

In This Issue

Brief introductions to the research articles in this issue

Accelerated Article

ESMS of protein–ketone equilibria in solution

Electrospray MS has generated significant interest in protein analysis. K.W.M. Siu and colleagues at the National Research Council of Canada demonstrate that ESMS can also be a powerful technique for the study of solution equilibria under conditions in which the measurement biases are minimized. They show that the ES mass spectra of basic protein solutions containing ketones exhibit ions that are attributable to protein–ketone adducts whose relative abundances correspond to the relative concentrations of these adducts in solution as controlled by reaction statistics. The reactions are applied to the measurement of the total number of free amino sites in proteins. (p. 3289)

DNA profiling study

The forensic use of DNA profiling methods is increasing, and DNA restriction fragment length polymorphism (RFLP) analysis is now recognized as valid. Dennis J. Reeder and colleagues of NIST and the FBI Academy report on the results obtained in an interlaboratory study sponsored by the Technical Working Group for DNA Analysis (TWGDAM). In the first of a three-part report, they present an overview of the TWGDAM-recommended RFLP general protocol and design of the studies; summary data and experimental details; various statistical and graphical summaries; graphical summaries of ancillary studies relevant to the TWGDAM data; an approximate allocation of various sources of measurement variance; and a determination of an interlaboratory measurement comparison "window," an expected RFLP measurement uncertainty estimate. (p. 3303)

A SERS look at DNA detection

Specific DNA sequences can be detected by using molecular biology techniques such as hybridization with complementary nucleic acid sequences or "gene probes" that have radioactive or fluorescent labels. However, the potential hazards associated with the use of radiolabels and the low spectral selectivity of fluorescent and chemiluminescent labels detract from their usefulness in situ. T. Vo-Dinh, K. Houck, and D. L. Stokes of Oak Ridge National Laboratory have used cresyl fast violet dye as a gene probe label for surface-enhanced Raman spectroscopy (SERS) of gene sequences. The method could be extended by using more than one SERS dye gene probe to label different specific sequences in a single assay. (p. 3379)

Diagnosing central nervous system disorders with CE

HPLC and ion-exchange chromatography are effective tools for the analysis of cerebrospinal fluid, but they can be time consuming and often require substantial sample pretreatment. Andrew E. Ewing and colleagues of Penn State University and Göteborg University (Sweden) suggest that CE with laser-induced fluorescence detection and precolumn derivatization with 3-(4-carboxybenzoyl)-2-quinolinecarboxaldehyde is well suited to this analysis. They analyze 10-μL samples of human cerebrospinal fluid from Alzheimer's patients and children with different neurological disorders and observe differences in amino acid levels among the patients and patient pools examined. (p. 3512)

Ethanol biosensor

Because continuous monitoring of ethanol in the gas phase has both human health and behavior-related applications, many types of gas sensors have been developed. Isao Karube and colleagues of the University of Tokyo (Japan) describe the construction of a gas-phase biosensor by using an immobilized alcohol oxidase (AOD) enzyme electrode and a reaction cell that has gas- and liquid-phase compartments separated by a diaphragm membrane. They evaluate two types of porous poly(tetrafluoroethylene) diaphragm membranes and use the sensor to measure gaseous ethanol over the concentration range from 0.358 to 1242 ppm. (p. 3297)

Dopamine by microbore HPLC and IDA microelectrodes

Microbore HPLC is an ideal mode of analysis for small-volume biological samples, particularly neurotransmitters, because low dispersion in the column increases the sensitivity. Carbon microelectrodes are well suited for microbore HPLC detection because of their high S/N and current density. Hisao Tabei and colleagues of Nippon Telephone and Telegraph (Japan) fabricate an interdigitated array microelectrode from the carbon film of pyrolyzed 3,4,9,10-perylenetetracarboxylic dianhydride on oxidized silicon wafers and use it in a microbore HPLC system. The detection limit for dopamine is 0.5 fmol. (p. 3500)

PCF electrodes on Macor substrates

Pyrolytic carbon film (PCF) electrodes based on Macor substrates should be well suited for construction of electrodes with unusual sizes and shapes because they display good charge transfer characteristics and because Macor can be machined with ordinary high-speed tools. Before these electrodes can be used routinely, however, researchers need to address two concerns: electrode activity over long periods of time and

film reactivation. Paula R. Melaragno and co-workers at Denison University report that electrode activity, estimated via cyclic voltammetry of ferricyanide, is virtually unchanged after 120 min in solution and that after 20 h in solution, the response decays by less than 40%. Electrodes deactivated by air exposure could be restored to good levels of performance via electrode anodization. (p. 3528)

Detecting toxic surfactants

Non-ionic surfactants are increasingly being used as effective and less harmful alternatives to their ionic equivalents for many industrial applications. Some of these surfactants are toxic, however, and must be degraded prior to disposal. Philip J. Marriott and co-workers at the Royal Melbourne Institute of Technology (Australia), La Trobe University (Australia), and the CSIRO Division of Wool Technology (Australia) use electrospray MS to identify the mixture of components in three non-ionic surfactants (nonylphenol ethoxylate, secondary alcohol ethoxylate, and primary alcohol ethoxylate) used in wool scouring. ESMS shows that the products of the photocatalytic decomposition of secondary alcohol ethoxylate are the same as those produced by collisionally activated decomposition. (p. 3394)

GC and low-pressure ICPMS join forces

The recently completed initial investigations of GC coupled to low-pressure ICPMS indicate that the combination is applicable to element-selective detection of organic compounds that are of environmental concern. E. Hywel Evans and colleagues of the University of Plymouth (U.K.) demonstrate that, by decreasing power and plasma gas flow, it is possible to sustain a helium plasma by using only the carrier gas from the gas chromatograph. In addition, by adjusting the plasma gas flow and forward power, it is possible to influence the degree of fragmentation of the inorganic species. Detection limits for several analytes are determined, and the mass spectra obtained are similar to those obtained with an electron impact ionization source. (p. 3400)

Determining oxidation potentials of transient species

Radical ions are typically not observed in electrospray MS because they are not formed by simple acid/base chemistry and because they are not stable in solution long enough. Gary J. Van Berkel and Feimeng Zhou of Oak Ridge National Laboratory use cyclic voltammetry, UV–vis absorption spectroscopy, and electrospray MS to study the mono- and di-cations produced by three model compounds in three different solvent–reagent systems. Knowledge of the solvent–reagent oxidation potentials and the electrochemical redox potentials of an analyte of interest allows a solvent–reagent system to be chosen to selectively ionize an analyte or range of analytes to a desired state for subsequent analysis by ESMS. (p. 3408)

Accumulating and storing ionized duplex DNA ions

Although it is difficult to prove conclusively that a gaseous ionized complex observed in a mass spectrometer originated as a specific complex in the condensed phase, strong and rapidly growing evidence suggests that this is the case. Scott A. McLuckey and colleagues of Oak Ridge National Laboratory describe their efforts to evaluate the possibility of injecting and storing ionized duplex DNA ions in a quadrupole ion trap for mass analysis and for determining what other types of information might be obtainable. Their results indicate that the ions are kinetically stable under the ion injection, storage, and mass analysis conditions of the quadrupole ion trap operated with a relatively high pressure of bath gas. (p. 3416)

Enhanced MALDI performance

Although matrix-assisted laser desorption/ionization (MALDI) has become a powerful tool in biological MS, its success depends heavily on the choice of UV-absorbing matrix material, and more than 30 different matrices have been identified for various classes of molecules. David M. Lubman and colleagues at the University of Michigan use a perfluorosulfonated ionomer film as an active substrate for MALDI MS detection of various macromolecules in chemical digests of proteins, protein profiling in milk and egg white samples, cell lysate analysis, and oligonucleotide detection. The improvement in detection and resolution by using this substrate compared with an inert stainless steel probe tip is demonstrated. (p. 3423)

Single particle analysis in a quadrupole ion trap

The characterization of particles has become increasingly important in materials science as new materials synthesis processes rely on microparticulate precursors, and particles in aerosols continue to play an important role in understanding environmental issues. John M. Dale and colleagues at Oak Ridge National Laboratory characterize single particles by laser desorption/ionization in a quadrupole ion trap mass spectrometer. Particles are introduced into the center of the space surrounded by the hyperbolic electrode surfaces of the mass spectrometer; ions are then desorbed or ablated from the surfaces of the particles with laser pulses from a Nd:YAG laser as the particles fall through the trap, and subsequently mass analyzed using the mass-selective instability mode of operation of the ion trap. A conservative detection limit of 0.7 fm per particle is determined for tetraphenylphosphonium bromide. (p. 3431)

Postponing separation

Typically, to distinguish different ions of the same mass, the elements are separated prior to mass spectrometric analysis. Karl K. Irikura, Edmund H. Fowles, and J. L. Beauchamp of the California Institute of Technology propose postponing the separation until after the sample is ionized and utilizing gas-phase ion chemistry for the difficult preparative work. They demonstrate this technique for the separation of $^{187}Re^+$ and $^{187}Os^+$ as well as $^{186}Os^+$ and $^{186}W^+$. (p. 3447)

Real-time aerosol analysis

Determining the size and chemical composition of individual aerosol particles in real time has been an elusive goal for aerosol researchers since the early 1970s. K. A. Prather and T. Nordmeyer of the University of California–Riverside combine aerodynamic particle sizing with TOFMS to determine the size and composition of a range of particle sizes. Both the complete mass spectrum and size information are obtained for ~ 200 single particles in 1 min by beginning with particle concentrations of 10^2–10^3 cm^{-3}. The total efficiency using aerosol TOFMS

is determined by the fraction of particles entering the particle interface that produce both mass spectra and size information. (p. 3540)

Safer shellfish with CZE

Detecting native paralytic shellfish poisoning (PSP) toxins has been difficult because of the highly polar nature of these compounds and the fact that they lack a useful chromophore that would permit sensitive UV absorption or fluoresence detection. Existing CZE methods are of limited practical value in monitoring toxins in shellfish extracts at concentrations close to the regulatory level. P. Thibault and S. J. Locke of the National Research Council of Canada report that the use of on-column sample preconcentration with capillary isotachophoresis and discontinuous buffer systems prior to CZE separation improves the concentration detection limit by 2 orders of magnitude over that obtainable by using conventional CZE. (p. 3436)

Building a better micelle

Despite the numerous successful applications of micellar media in analytical methodology, practical difficulties such as foam formation and problems in recovery and isolation of analytes from surfactant solutions have limited or diminished their usefulness in certain situations. Willie L. Hinze and co-workers of Wake Forest University detail the synthesis and some analytical applications of cationic polyelectrolytes of the [*x*,*y*]-ionene type, materials that retain the important fundamental features of micellar systems while circumventing many of the difficulties encountered with conventional surfactant micelles. These hydrophobic ionenes can form intramolecular aggregates and function as micelle-mimetic agents because they mimic the key properties of traditional surfactant micelles. (p. 3449)

Selecting surfactants for LC

Micellar LC involves the use of surfactants in the mobile phase, but surfactant adsorption onto the solid phase can affect the retention characteristics of the column. Barry Lavine, Sumar Hendayana, and Jonathan Tetreault of Clarkson University use a test mixture of five vanillin analogues and coumarin as probes for gauging the effect of surfactant type and concentration on retention and selectivity in a micellar RPLC system. From the chromatograms, they assign possible adsorption configurations for sodium dodecyl sulfate and cetyltrimethylammonium on C_{18} and C_8 stationary phases. (p. 3458)

Modifying electrophoretic mobility of neutral and charged polysaccharides

Glycoconjugate analysis has been simplified by the development of CZE methods for sensitive determination of oligosaccharides cleaved from glycoproteins as well as detection of fluorescently labeled polysaccharides. Milos Novotny and Morgan Stefansson of Indiana University demonstrate the use of buffer additives to either induce or reduce the electrophoretic mobility of polysaccharides during CZE. Difficult-to-analyze classes of polysaccharides, such as modified celluloses and heparins, are successfully determined using detergents and ion-pairing agents, respectively, as buffer additives. Migration models based on secondary thermodynamic equilibria are presented and evaluated for different polysaccharides. (p. 3466)

CE and postcolumn reactor on a microchip

Constructing a postcolumn reactor for capillary separations with extremely low volume connections to minimize band distortion has been difficult. J. Michael Ramsey and co-workers of Oak Ridge National Laboratory describe their approach to the problem: fabricating a first-generation postcolumn reactor for electrophoretic separations on a microchip. They investigate the broadening of the analyte band caused by conventional mechanisms, including injection plug length, detector observation length, and axial diffusion, and the added influence of combining the separation effluent and reagent stream of the fluorescent tag, *o*-phthaldialdehyde. The researchers also demonstrate the use of a gated injector that maintains the integrity of the analyte, buffer, and reagent streams. (p. 3472)

Maltooligosaccharides aid chiral separations

Although cyclodextrins have been quite effective as chiral selectors, occasionally these molecules fail to achieve the desired separation of enantiomers. Recently, linear maltooligosaccharides have been investigated as chiral selectors for pharmaceuticals. Building on the work of earlier researchers, Milos V. Novotny and colleagues of Indiana University investigate this obscure but useful type of host–guest complexation. They assess different maltodextrins for their capacity to separate enantiomers under various conditions by using CE. Optimized separations of simendan, ibuprofen, warfarin, and ketoprofen enantiomers as well as the determination of ibuprofen in serum are demonstrated. (p. 3477)

Fluid flow in a manifold of capillaries

A manifold of intersecting capillaries can be used to separate sample components by CE, with electroosmotic flow as the pumping mechanism. For practical use of electroosmotic pumping, it is necessary to understand the factors that control flow within the manifold. D. Jed Harrison and colleagues of the University of Alberta (Canada) discuss diffusional and convective mixing at the intersection of two channels containing different solutions. They demonstrate that judicious application of voltages to multiple channels can be used to control mixing and to direct the flow of solvent and sample. (p. 3485)

Interpreting retention behavior of transition-metal cations

Although chromatographic techniques are increasingly being used for determination of metals, the retention mechanism of metal separations on reversed-phase columns has not been fully elucidated. Sergio Zappoli and Chiara Bottura of the University of Bologna (Italy) investigate the retention behavior of heavy metals on a silica-based C_{18} column by using octanesulfonate as an ion interaction reagent and a mild organic complexing agent. A mathematical relationship is proposed to predict the retention factors of heavy metals under different elution conditions. (p. 3492)

Annular and parallel plate denuders revisited

Simon and Dasgupta recently described their observation that a high-efficiency wetted denuder with a parallel plate geometry exhibits supertheoretical collection efficiency (*Anal. Chem.* **1993**, *65*, 1134–39). Franco De Santis of CNR–Istituto Inquinamento Atmosferico (Italy) reports a correction to the expres-

sion that describes the diffusion-based collection efficiency. When the corrected formula is used, the efficiency of the parallel plate denuder is in agreement with the theoretical efficiency curve. (p. 3503)

Detecting unreacted hydroxyl groups

The chemical microstructure of cross-linked poly(ortho esters), which are used as bioerodible matrices for delivery of bioactive compounds, is important for correlating reaction conditions, stoichiometry, drug loading, physical properties, and in vivo performance with polymerization kinetics. John D. Stong and Leonore C. Witchey-Lakshmanan of Merck Research Laboratories describe an LC method for determining unreacted hydroxyl groups in a cross-linked poly(ortho ester). The method involves exhaustive derivatization of unreacted hydroxyl groups in the intact polymer followed by mild hydrolysis and gradient LC analysis. (p. 3505)

Solvent extraction of radium

Although numerous reports exist in the literature regarding crown ether extraction of alkaline earth metals, few of them involve radium. C. M. Wai, M. K. Beklemishev, and Sadik Elshani of the University of Idaho describe their evaluation of a series of 11 crown ether carboxylic acids with different hydrocarbon substituents for solvent extraction of radium in aqueous solutions. The extraction proceeds from alkaline media into chloroform solutions of the crown ethers, requires no specific counteranions, and is reversible with respect to pH. The researchers report that substitution of *tert*-butyl groups in the benzene rings of *sym*-dibenzo-16-crown-5-oxyacetic acid increases the lipophilicity of the macrocyclic compound and enhances the extraction efficiency for radium. (p. 3521)

Smoke stripper for nicotine determination

It has become important to determine the composition of tobacco smoke as public smoking laws are enacted and second-hand smoke policy issues are debated. Nicotine, which along with tar has been listed on cigarette packages since the early 1970s, is probably the compound of greatest concern because of its possible role in addiction. David A. Lewis, Ian Colbeck, and Derek C. Mariner at the University of Essex (U.K.) describe the fabrication and use of a sampling tube coated with oxalic acid to study the partitioning of nicotine between the vapor phase and smoke particulates. Cigarette smoke is pumped through the glass tube, and any nicotine in the vapor phase is adsorbed onto the walls of the tube. The walls are washed to extract the nicotine, and the extract is analyzed by GC. (p. 3525)

Fiber optics lift restrictors on SFE monitoring

Most SFE is performed off line, requiring depressurization to collect the extract. As a result, volatile components can be lost because the CO_2 stream flows faster after depressurization. Interfaces for SFE/IR spectroscopy share the same flow restrictor clogging problems encountered with off-line SFE or require expensive high-pressure flow cells. Daniel L. Heglund, David C. Tilotta, Steven B. Hawthorne, and David J. Miller of the University of North Dakota have developed a fiber-optic interface for SFE/FT-IR that consists of fiber-optic cables and a stainless steel "union cross" tube, which is inexpensive and rugged to 400 atm with a spectral window of 5000–800 cm^{-1}. They demonstrate low- to sub-part-per-million detection limits tal petroleum hydrocarbons in soil samples by using the interface for static on-line SFE/FT-IR. (p. 3543)

Kinetic quantification of isomers

Kinetic methods with spectrophotometric detection have been used to quantitate mixtures of heterogeneous compounds in competing reactions. However, few reactions have been found in which structural isomers of a single compound can compete with significantly different reaction rates. Ellen Tuanying Chen and Harry L. Pardue of Purdue University use β-cyclodextrin as a catalyst for the ester hydrolysis of *o*-, *p*-, and *m*-nitrophenyl acetate. The three isomers react with the cyclodextrin at different rates and are quantitated in two- or three-component mixtures by using curve-fitting methods. (p. 3318)

Skinny optodes

Dipping optical fibers in a chemically sensitive coating is one way to create an integrated sensor that can be immersed directly in a sample, but the coating thickness is often irregular and hard to control. Bernhard H. Weigl and Otto S. Wolfbeis of Karl Franzens University (Austria) have developed an alternative method to make integral optic sensors by using glass capillary tubes as a base. The tubes are coated internally with the chemical sensor cocktail by using a peristaltic pump and serve as optical detectors and sample cuvettes of defined volume. Weigl and Wolfbeis demonstrate the performance of the optodes for rapid reversible detection of CO_2. (p. 3323)

Chemometrics improves chlorinated hydrocarbon determination

The Fujiwara reaction is useful for quantitative and qualitative determinations of halogenated hydrocarbons in a variety of matrices. However, the lack of selectivity and the instability of the Fujiwara reaction has plagued researchers over the years. In this series of three papers, Bruce R. Kowalski, Lloyd W. Burgess, and colleagues of the University of Washington use partial least squares; generalized rank annihilation; trilinear decomposition; multivariate curve resolution; and medium-rank, second-order calibration to improve the data obtained from the spectroscopic analysis of mixtures of 1,1,1-trichloroethane, trichloroethylene, and chloroform exposed to the Fujiwara reagent. (pp. 3328, 3337, and 3345)

Monitoring nitrates in natural waters

Although electrochemical sensors have been developed to monitor dissolved compounds in natural waters, they can be difficult to use for long periods of time without cleaning and recalibration. Immersible wet-chemistry analyzers usually require electrical power for pumping. Hans W. Jannasch, Kenneth S. Johnson, and Carole M. Sakamoto of the Monterey Bay Aquarium Research Institute and Moss Landing Marine Laboratories describe the construction and performance of a continuous flow analyzer for nitrates that uses osmotic pumping to introduce ambient water, reagents, and calibration solutions into the reaction and detector chambers. The self-calibrating analyzer, which can operate for a month or more without operator intervention, shows a linear response from 0 to 20 μmol/L and has a 90% response time of ~ 30 min. (p. 3352)

A silver lining for silica gel structures

Surface-immobilized alkylsilanes are used in applications ranging from microsensor fabrication to chromatographic media, but these organically modified oxide surfaces are still not well characterized. Wade R. Thompson and Jeanne E. Pemberton of the University of Arizona describe the preparation of alkylsilane layers for surface-enhanced Raman spectroscopy. They use a smooth Ag surface modified with a thin layer of sol–gel silica, which serves as a model for RPLC silica gel. The silica layer is then modified with alkylsilanes of interest. (p. 3362)

Studying ICPs

The processes leading to ICP emission and MS signals can be affected by sample droplet size. John W. Olesik and Steven E. Hobbs of The Ohio State University study the spatially and temporally resolved ICP emission intensities produced when a stream of monodisperse sample droplets are introduced using the monodisperse dried microparticulate injector (MDMI). Vertical emission profiles obtained using the MDMI are compared with those obtained using a conventional nebulizer/spray chamber, and the relationship between vertical emission profiles and particle vaporization is discussed. (p. 3371)

Atmospheric free radicals

Free radicals play an important role in the chemistry of the atmosphere. However, because of their high reactivity and variability throughout the day, it is difficult to measure the concentration of free radicals. One approach is chemical amplification, in which each radical produces a large number of NO_2 molecules by way of a chain reaction. However, this technique suffers from wall loss in the reaction chamber and "ghost" radical signals. Donald H. Stedman and Jia Hu of the University of Denver describe an improved amplification method that uses a Teflon filter–nitrogen wall to reduce wall loss and a smaller reactor to reduce the number of ghost signals. (p. 3384)

Photoreactive batik creates optical microsensor array

Photoinduced cross-linking and photolabeling have been used for a number of years in biochemistry to examine ligand binding sites in cell surface receptors and enzymes. Using a similar strategy, Karen S. Bronk and David R. Walt of Tufts University describe the fabrication and performance of sensor arrays that are photoprinted on the tip of a single imaging optical fiber. They first spin-coat the fiber with a fluorophor dye, then derivatize the coating with a photoreactive group. The sensors are formed by illuminating the derivatized coating in discrete spots to cross-link the dye to the fiber. (p. 3519)

Arsenic and cold LC/AAS

AAS detection for As and Se suffers from high absorption of incident radiation into the premixed flames at the principal resonance lines, which lie in the vacuum-UV range of the spectrum. Silica tubes that have been used as LC interfaces require an organic mobile phase, which limits the type of HPLC protocols that can be performed with AAS. Georges-Marie Momplaisir, Tian Lei, and William Marshall of McGill University (Canada) describe the performance of a fused-silica T-tube interface for LC/AAS that accommodates either aqueous or polar organic mobile phases and permits low-nanogram detection limits for As oxyanions, arsonium cations, Se anions, and Se amino acids. (p. 3533)

CHEMISTRY of MATERIALS...

All The Latest Directions And Innovations In Materials Chemistry!

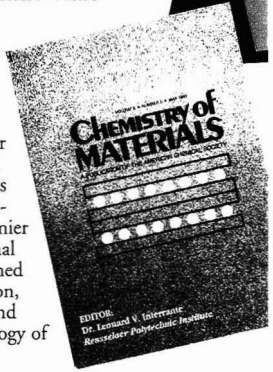

Chemistry of Materials is an indispensible reference source for chemists, chemical engineers, materials scientists, and technologists...the premier international journal for anyone concerned with the preparation, characterization, and processing technology of new materials.

If you do materials-related R&D and want to be kept informed on the latest developments, return this coupon card today!

ACS PUBLICATIONS
Essential Resources for the Chemical Sciences

CHEMISTRY of MATERIALS **Subscription Certificate**
Editor: Dr. Leonard V. Interrante
Rensselaer Polytechnic Institute

❑ **Yes! I want to subscribe to this critical research publication. I don't risk a thing with ACS's prompt, pro-rata refund policy for all unmailed issues. Please enter my subscription for:**

One Year (12 issues)

	US	Canada & Mexico	Europe Air Service	All Other Countries Air Service
Member:	❑ $50	❑ $63	❑ $81	❑ $90
Nonmember:	❑ $420	❑ $433	❑ $451	❑ $460

Name: _____

Title: _____ Member #: _____

Employer: _____

Address: ❑ Home ❑ Business _____

City: _____ State: _____ Zip: _____

Country: _____

Telephone (Home): _____ (Work): _____

Employer's Business: ❑ Manufacturing ❑ Academic ❑ Government ❑ Other

Method of Payment (Check one.):

❑ Bill me ❑ Payment enclosed (Payable to the American Chemical Society)

❑ Charge my ❑ VISA ❑ MasterCard

Account #: _____

Expiration Date: _____

Signature: _____

***Chemistry of Materials*, American Chemical Society**
1155 Sixteenth Street, NW, Washington, DC 20036

Member rates are for personal use only. Subscriptions outside the U.S. Canada, and Mexico are delivered via air service. Journal subscriptions based on calendar year. Foreign payment must be made in US currency by international money order, UNESCO coupons, or US bank draft. Orders accepted through your subscription agency. For nonmember rates in Japan, contact Maruzen Co., Ltd. Please allow 45 days for delivery of your first issue. Redeem until December 31, 1994

7882J

930/12/PH

Biochemistry. Critical research. On time. On target. On your must-read list!

Biochemistry is a must-read for researchers in chemistry, biochemistry, and molecular and cell biology. Every week (in over 12,000 pages a year), *Biochemistry* gives you fast-breaking, state-of-the-art research articles on a variety of important topics such as:

- Bioenergetics
- Carbohydrate chemistry
- Enzyme and protein biochemistry
- Gene structure and function
- Immunochemistry
- Lipid and cell membrane biochemistry
- Molecular and cell biology
- Virology

Before you begin your next research project or write your next proposal, subscribe to *Biochemistry* for the most relevant theories and methodologies in your field of endeavor.

Editor
Gordon G. Hammes
Duke University Medical Center

Associate Editors
Mary Barkley
Louisiana State University
Marc G. Caron
Duke University Medical Center
Earl W. Davie
University of Washington
Perry A. Frey
University of Wisconsin, Madison
Paul L. Modrich
Duke University Medical Center
William W. Parson
University of Washington
Joseph J. Villafranca
Bristol-Myers Squibb Co.
Leslie Wilson
University of California, Santa Barbara

ACS PUBLICATIONS
Essential Resources for the Chemical Sciences

1994 Subscription Rates

	U.S.	Canada, Mexico	Europe*	All Other Countries*
ACS Members				
One Year	$ 108	$ 200	$ 351	$ 422
Two Years	$ 194	$ 378	$ 680	$ 822
Nonmembers				
One Year	$1,328	$1,420	$1,571	$1,642

*Air service included.

Call toll free 1-800-333-9511 today. Outside the U.S., please call 614-447-3776. Or mail or fax your order to: American Chemical Society, Member & Subscriber Services, P.O. Box 3337, Columbus, OH 43210. FAX 614-447-3671.

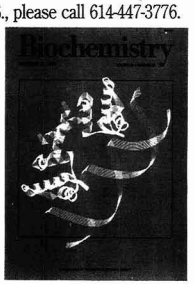

Synopses of significant analytical articles from other publications

CEing amplified DNA

The polymerase chain reaction (PCR) uses DNA-manipulating enzymes to amplify a desired DNA sequence and is especially helpful for analyses involving samples with a limited amount of DNA. Because the amplification is enzymatic, the efficiency of each PCR assay can vary. Bruce R. McCord and colleagues at the University of Virginia and the FBI Academy evaluated the use of CE with laser fluorescence detection to quantitate the PCR amplification products and compared their method with hybridization blots and spectrophotometric determinations.

Using a coated open-tubular capillary with a non-gel sieving buffer and a fluorescent intercalating dye, they obtained separations within 20 min. Unincorporated PCR primer oligonucleotides and PCR byproducts were separated from the desired PCR-amplified DNA, and peak migration time for an internal standard had an RSD < 0.1%. The researchers concluded that CE with fluorescence detection can be used to monitor the quality and quantity of the PCR product. (*J. Chromatogr. B* **1994**, *658*, 271–80)

Comparing gel electrophoresis techniques for protein separation

Traditional planar sodium dodecyl sulfate polyacrylamide gel electrophoresis (SDS PAGE) requires time-consuming gel preparation and visualization techniques but allows a large number of samples to be analyzed at the same time. Capillary SDS gel electrophoresis, a one-dimensional version of SDS PAGE, allows direct quantitation by on-column UV detection, fast single sample analysis, and the use of nanoliter sample volumes.

Andras Guttman and Judith Nolan of Hafslund Nycomed Pharma (Austria) and Beckman Instruments compared the results of planar SDS PAGE and capillary SDS gel electrophoresis for 65 different proteins with respect to performance, precision, and efficiency. They found that the advantage of capillary SDS gel electrophoresis is that the sieving material (non-cross-linked gel) in the capillary column can be replaced after each analysis, making the technique less labor intensive than planar SDS PAGE. They also found that the polyethylene oxide-based sieving matrix used in the experiments gives separation performance and estimated molecular weights that are slightly different from those obtained by planar SDS PAGE. (*Anal. Biochem.* **1994**, *221*, 285–89)

Detecting metals in pore water

In aquatic environments where there is a good supply of organic material, such as lakes, rivers, estuaries, and coastal waters, the sediment–water interface is characterized by marked chemical changes. Nutrients and metal ions can be released from the rapidly decaying organic materials, and the reduction of organic components can result in a sharp redox boundary. To understand the relationships between the various chemical changes, it is essential that the components be spatially defined. William Davison and colleagues at Lancaster University (U.K.) and the University of Oxford (U.K.) have used polyacrylamide gel probes to obtain depth-resolved iron and magnesium profiles in pore waters.

Both Fe(II) and Mn(II) diffuse freely within the gel matrix and, with the use of a 0.4-mm-thick gel, complete equilibration is achieved in 6 min. The gels are treated with NaOH or KOH to immobilize the Fe and Mn as their insoluble oxyhydroxides, and the concentration of Fe and Mn in the gel is measured using atomic absorption or proton-induced X-ray emission spectrometry. (*Environ. Sci. Technol.* **1994**, *28*, 1623–32)

Quantifying water in biomolecules by FT-IR

Because of their potential use as drugs, the pharmaceutical specification of peptides, enzymes, and other proteins are of interest. Determining water content, a minimum requirement for pharmaceutical preparations, may be difficult because these biomolecules are hygroscopic and difficult to dry completely.

Noting that the OH stretching bands of water in the IR region are extremely intense and can be used to measure the water absorbed in organic solvents, Teiki Iwaoka, Fumiko Tabata, and Shinya Tsutsumi of Sankyo Co., Ltd. (Japan) developed a method for determining water in biomolecules that involves extraction into an organic solvent under conditions that do not induce aggregation, followed by FT-IR measurement of the intensity of the OH stretching band at 3600 cm^{-1}. The extraction into acetonitrile was performed in a glove box that was purged with nitrogen to avoid errors caused by water in ambient air. The results for the analysis of peptides and enzymes were compared with those obtained by Karl Fisher titration, and measurements for loss of weight on drying in vacuo were also investigated. (*Appl. Spectrosc.* **1994**, *48*, 818–21)

CE and NMR coiled together

NMR spectroscopy can provide detailed information about molecular structure and has been successfully used as an on-line detector for LC. Coupling NMR spectroscopy to CE, however, has not been reported—primarily because of the inherently low sensitivity of NMR spectroscopy and because the NMR cell volumes typically used in LC (25–200 μL) are orders of magnitude too large to be used for CE. Jonathan V. Sweedler and colleagues at the University of Illinois have designed an rf microcoil wrapped directly around a fused-silica capillary that provides a detection cell of ~ 5 nL and detection limits in the nanogram range for short (< 1 min) NMR acquisitions.

The rf microcoil is formed with copper wire and typically has 17 turns for a total detection length of 1.1 mm. The coil and capillary are mounted so that they are perpendicular to the static magnetic field over the detection region. This arrangement provides a good filling factor for detection in the cell but causes significant susceptibility-induced line broadening. For a thin-walled capillary the linewidth is > 200 Hz; for a thick-walled capillary the linewidth is narrowed to 11 Hz. Uniform wrapping of the coil and positioning of the capillary/coil far from nonunity susceptibility materials reduces linewidth. (*J. Am. Chem. Soc.* **1994**, *116*, 7929–30)

Negative CI in the quadrupole ion trap

The quadrupole ion trap mass spectrometer is increasingly being used as a sensitive, small, and low-cost detector for GC. Most work with the quadrupole ion trap has involved the use of positive ions, although limited studies of negative ions have been reported. D. W. Berberich and R. A. Yost of the University of Florida have characterized the experimental parameters necessary for successful negative chemical ionization (CI) with reagent ion formation within the ion trap.

They investigated the effects of applied voltage and reaction times on the formation of negative ions via both electron capture and negative ion–molecule reactions and discovered that mass-selected ejection of undesired reagent ions and selective mass storage of only negative ions are required for practical negative CI. This can be achieved by the application of rf and dc voltages to the ring electrode to control the m/z of stored ions, as well as by the application of a supplemental rf voltage applied across the endcap electrodes to selectively eject ions of a particular m/z. (*J. Am. Soc. Mass Spectrom.* **1994**, *5*, 757–64)

Tracing the oil source

A ground survey completed 22 years after the tanker *Arrow* sank off Nova Scotia and released ~ 2.5 million gallons of oil showed that natural weathering processes have removed most of the oil along the contaminated shoreline. Scientists are interested in analyzing samples of any remaining oil to verify that it came from the *Arrow* spill and to obtain information about the oil's residual composition and changes in its characteristics as a result of exposure. Concentrations of key components or compound classes used to evaluate the behavior, fate, and toxicity of the spilled oil remaining in the environment could also be determined.

Because most saturated hydrocarbons and PAHs have been lost from the weathered oil, Zhendi Wang, Merv Fingas, and Gary Sergy of Environment Canada focused on characterizing biomarker compounds by GC/MS. They found that the relative abundance ratios of selected pairs of triterpanes and steranes, especially the ratio of C_{29}/C_{30} hopane that are displayed as major peaks in the m/z 191 ion chromatograms, are apparently independent of weathering effects and can be used to identify the source of the *Arrow* oil samples. (*Environ. Sci. Technol.* **1994**, *28*, 1733–46)

One parameter is not enough

The solvent strength of the mobile phase in RPLC is often measured by using ET(30), 2,6,-diphenyl-(2,4,6-triphenyl-*N*-pyridino) phenolate, as a solvent retention indicator. However, while investigating ET(33), a dichloro analogue with more stable pH dye interaction characteristics, Jung Hag Park, Andrew Dallas, Phoebe Chau, and Peter Carr at the University of Minnesota discovered that plots of the transition energy E_T for ET(33) versus E_T for ET(30) were not linear as the mobile phase composition varied, even though both dyes remained completely unprotonated under all phase compositions in the study.

The organic solvents used in the aqueous mobile phases were methanol, acetonitrile, isopropanol, and tetrahydrofuran, and each was mixed with water over the full range of composition. Nonlinearities in the plots of ln k' vs. E_T for ET(33) and ln k' vs. E_T for ET(30) strengthened the group's conclusion that a single-parameter solvent strength scale is insufficiently general for RPLC. (*J. Chromatogr. A* **1994**, *677*, 1–9)

Quantitating PCBs in marine benthic copepods

Because of their high hydrophobicity, PCBs in aqueous solutions strongly associate with organic carbon, clays, and silts and eventually deposit in estuarine sediments. The effect of these PCBs on benthic meiofauna, invertebrates that range in size from 0.063 to 1.00 mm and comprise an obligate food source for many fishes and shrimp, has not been well characterized, primarily because of a lack of techniques for accurate and precise quantification of the contaminant burdens in organisms this small. Edward F. Wirth and colleagues at the University of South Carolina have developed a microextraction method that uses 100 µL of total extraction volume and as few as 20 copepods (~ 25 µg of dry tissue mass) to quantify PCB body burdens in two species of meiobenthic copepods.

The copepods were homogenized and extracted in a 100-µL closed vial with alkaline media and isooctane spiked with an internal standard (hexachlorobenzene) to create a colloidal suspension. After centrifugation, Aroclor 1254 was directly determined from the organic solvent phase by GC-ECD. Spiked samples of Aroclor 1254 yielded recoveries of 95% ± 12 % (n = 11). Body burdens of sediment-exposed copepods were measured over a 12-day period, and predicted body burdens with 95% confidence intervals were calculated. (*Environ. Sci. Technol.* **1994**, *28*, 1609–14)

Balancing the synthesis of conducting polymers

Conducting polymers show potential as lightweight rechargeable batteries or in applications such as electrochemical gas detection. However, the composition of the organic medium used for synthesizing them affects their electroactive and physical characteristics. Patrice Topart and Mira Josowicz of the Universität der Bundeswehr (Germany) used an electrochemical quartz crystal microbalance to determine the effects of changing the water content of the background electrolyte during synthesis of poly(*N*-vinylcarbazole) films.

The frequency shifts showed that the polymerization efficiency decreased with increased water content in the background medium and became constant when water content was 10% or more by volume. The degree of cross-linking, the doping level, and the morphology of the films varied simultaneously with water content. (*Talanta* **1994**, *41*, 909–16)

Spend a Year Collecting Information, Testing New Theories and Conferring With International Experts.

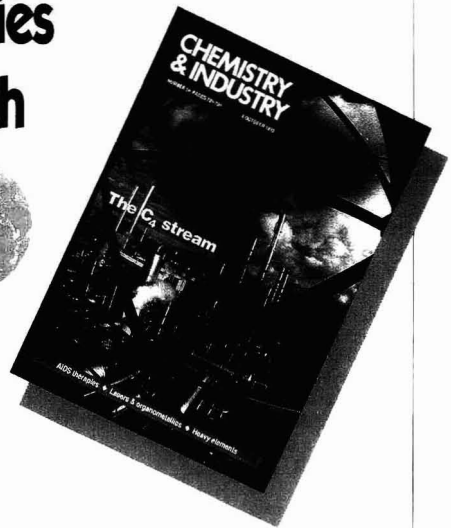

Stay on top of the industry's latest developments with an annual subscription to *Chemistry & Industry*. Discover the best source of global news, views and information — made, written and read by people like you. People involved in every aspect of the chemical industry, from academic and government scientists to R&D management, policy makers and opinion shapers from across Europe and around the world. Meet them all in the pages of *Chemistry & Industry*, the official publication of the Society of Chemical Industry, UK.

Twice a month, read the latest news, research and commentary about:

- applied chemistry
- food science
- biotechnology
- environmental issues
- science policy
- new materials
- pharmaceuticals
- energy

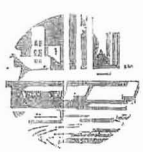

Subscribe today for the timely, innovative and international perspective that's exclusively *Chemistry & Industry*.

As lively as it is informative, *Chemistry & Industry* delivers a glimpse of future policy and research directions. Regular features include a quick-scan survey of European patent news, a section devoted to late-breaking research findings and reviews of the most current books and software.

IT'S THE NEWS YOU NEED FOR THE WORK YOU DO. SEND OR CALL FOR MORE INFORMATION.

Special subscription price for American Chemical Society members: $59 (non-members, $341). Air-shipped from Britain for expedited delivery in the U.S. Contact the American Chemical Society, P.O. Box 3337, Columbus, OH 43210. Phone: 800-333-9511 (U.S. only) or 614-447-3776 (outside the U.S.). Fax: 614-447-3671.

For orders outside the U.S., Canada and Mexico, please contact the Society of Chemical Industry, The Distribution Centre, Blackhorse Road, Letchworth, Herts SG6 1HN, England.

EXCLUSIVE OFFER: ONLY $59 ANNUALLY FOR ACS MEMBERS!

DAC programs promote analytical chemistry

"The Division of Analytical Chemistry [DAC] should prepare for growth in the areas of chemistry and biology, chemistry and physics, chemistry and materials, and chemistry and the environment by reaching out to these other communities, by educating its own members through symposia and workshops, and by defining and projecting a suitable public image of what we do." So says Edward S. Yeung, professor of chemistry at Iowa State University/Ames Laboratory and chair-elect of DAC.

DAC, one of the 33 divisions of the ACS, works to advance the field of analytical chemistry through a variety of programs. It provides a forum for discussions of the latest scientific advances, primarily through technical programming at ACS national meetings and by acting as a cosponsor for other technical meetings; makes other chemists, scientists, and the general public aware of the value of analytical chemistry; encourages chemistry students to select analytical chemistry as their field of study; advises the ACS on matters related to analytical chemistry; and, in general, provides analytical chemists with the opportunity to make professional contacts and lasting friendships.

DAC focuses on all areas of measurement science, including chromatography and separations, materials chemistry, electrochemistry, optical spectroscopy, MS, chemometrics, environmental analysis, surface analysis, and clinical chemistry. As of Dec. 31, 1993, DAC had 8264 members.

Since 1968 DAC and *Analytical Chemistry* have contributed to the education of future practitioners of the discipline through

1994–95 DAC officers

The Division is administered by an executive committee, which consists of the chair, chair-elect, secretary, treasurer, the four councilors, the four alternate councilors, the two immediate past chairs, and the Editor of *Analytical Chemistry*. The chair of DAC also serves as the ex-officio member of the *Analytical Chemistry* editorial Advisory Board. Members of the Division may serve on any of several committees: awards canvassing, education, financial planning, graduate fellowships, membership, nominating, professional status, program planning, publicity, regulatory affairs, and undergraduate awards. Elections are held each spring; winners are announced at the fall national meeting. Terms begin on Oct. 1.

This year's officers are Henry Blount III of the National Science Foundation, chair; Edward S. Yeung, chair-elect; Sarah Rutan of Virginia Commonwealth University, secretary; and Michelle Buchanan of Oak Ridge National Laboratory, treasurer. The Division councilors are William R. Heineman of the University of Cincinnati, Roland F. Hirsch of the U.S. Department of Energy, Karen B. Sentell of the University of Vermont, and Isiah M. Warner of Louisiana State University. Alternate councilors are Stanley R. Crouch of Michigan State University, Linda B. McGown of Duke University, Jon F. Parcher of the University of Mississippi, and James W. Serum of Hewlett Packard.

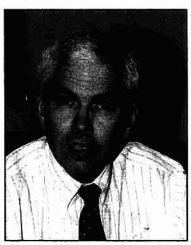

Henry Blount III

Edward S. Yeung

Sarah Rutan

Michelle Buchanan

the Undergraduate Awards Program. Every year, the journal and DAC provide eight-month, academic-year subscriptions to ~ 400 chemistry majors selected by the faculty at U.S. and Canadian colleges and universities with ACS-approved chemistry programs. The recipients also become honorary members of DAC for one year. This program is intended to recognize outstanding scholastic achievement and to stimulate interest in the field. For the 1994–95 school year, 384 subscriptions were awarded.

Since 1966 DAC has supported graduate students through the graduate fellowships program. The program began with two summer fellowships, awarding a stipend of $800 and tuition and fees. The following year, the program was increased to six summer fellowships, and in 1970 the first full-time fellowship was awarded. For the 1994–95 academic year, 11 fellowships were awarded: five full-year fellowships of $14,000 each and six summer fellowships of $4650 each. (See the Sept. 1 issue for details on the 1994 awardees.)

The graduate fellowships are intended to encourage basic research in analytical chemistry, to promote its growth in academic institutions, and to recognize future leaders of the profession. The awards are open to students working toward their Ph.D. on a full-time basis and who have completed at least one year of graduate work. In addition, their advisers must be members of DAC. A committee of professional analytical chemists selects the recipients on the basis of written applications and letters of recommendation.

The graduate fellowships program is fortunate to have the financial sponsorship of several of the country's leading chemical and instrument manufacturers as well as support from the Society for Analytical Chemists of Pittsburgh (SACP). Glaxo, DuPont, Eastman Chemical, Procter & Gamble, Perkin Elmer, Dow, and Eli Lilly each sponsored one full-time or summer fellowship this year. The fellowship winner often has the opportunity to visit the sponsor, allowing the student to observe the life of an analytical chemist in the industrial environment. This visit often helps the student decide what type of career to pursue after graduation. In addition to promoting good public relations, the companies benefit from improved industrial–academic relationships, and often the awardee comes to work for the sponsoring company after graduation.

Each year DAC also honors outstanding analytical chemists with four awards: the Award in Electrochemistry (sponsored by EG&G Princeton Applied Research), the Award for Excellence in Teaching (cosponsored by DAC and DuPont), the Award in Spectrochemical Analysis (sponsored by Perkin Elmer), and the Award in Chemical Instrumentation (sponsored by the Dow Chemical Foundation). The awards are presented at the fall national meeting, and each awardee receives a cash honorarium, a travel allowance to the meeting, and an inscribed plaque. (See the Oct. 1 issue for details on the 1994 awardees.)

The Subdivision of Chromatography and Separations Chemistry, a subgroup of DAC, tries to schedule two half-day sessions on the latest advances in chromatography and separations at each national meeting. At this year's fall national meeting in Washington, DC, they held a symposium entitled "Capillary Column Developments in Separations Chemistry" that covered column technology, capillary SFC, and various aspects of CE. The officers of the Subdivision are Peter C. Uden of the University of Massachusetts, chair; John G. Nikelly of Philadelphia College of Pharmacy and Science, chair-elect; and Mary Ellen P. McNally of DuPont, secretary.

DAC membership is open to scientists, engineers, college science students, and technically trained professionals with an interest in chemical separation and analysis. For more information about DAC and its programs, contact Sarah Rutan, Virginia Commonwealth University, Dept. of Chemistry, Box 2006, Richmond, VA 23284-2006 (804-367-7517; fax 804-367-8599; e-mail srutan@cabell.vcu.edu).

Janata receives Electrochemical Society award

Jiri "Art" Janata is the first recipient of the Electrochemical Society Sensor Division's Outstanding Achievement Award. Janata, associate director of materials and interfaces at the Environmental and Molecular Sciences Laboratory located at the Pacific Northwest Laboratory (PNL) and research professor of materials science at the University of Utah, is being honored for his work on chemically sensitive solid-state sensors. The award was presented at the annual meeting of the Electrochemical Society earlier this month.

Janata received his M.Sc. degree and his Ph.D. from Charles University (Czech Republic) in 1961 and 1965, respectively. He joined the faculty at the University of Utah in 1976 and PNL in 1991.

FOR YOUR INFORMATION

■ OSHA booklet

The Occupational Safety and Health Administration (OSHA) has published a new booklet entitled "Personal Protective Equipment" (OSHA 3077 1994). The booklet, which reflects revisions made in July to OSHA's personal protective equipment standards, discusses the concept of personal protective equipment; assessing the workplace for hazards; proper use of equipment; selection, fit, and maintenance of equipment; and water and night work hazards. To obtain a single copy, send a self-addressed label to OSHA Publications Office, Room N-3101, 200 Constitution Ave., N.W., Washington, DC 20210.

The Future of Polymer Research

...Is Yours Today With MACROMOLECULES

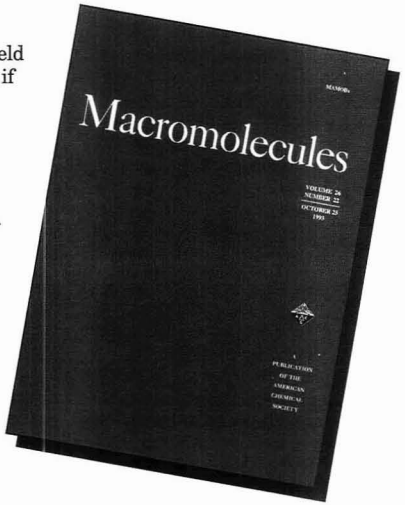

In the ever changing field of polymer chemistry, if you're not reading MACROMOLECULES, you're missing what your colleagues regard as the most authoritative, in-depth coverage anywhere.

Each biweekly issue of MACROMOLECULES will bring you up-to-date, peer-reviewed coverage of all aspects of polymer-chemistry including:

- ▲ synthesis
- ▲ polymerization mechanisms and kinetics
- ▲ chemical reactions
- ▲ solution characteristics
- ▲ bulk properties of organic polymers, inorganic polymers and biopolymers

For information you can trust to keep you on the cutting edge of the science of polymer chemistry, you simply cannot afford to do without a subscription to MACROMOLECULES.

To place your order simply call 1-800-333-9511 in the U.S.*, or send your order to:

American Chemical Society
Member and Subscriber Services
P.O. Box 3337
Columbus, OH 43210

*** Outside the U.S. dial (614) 447-3776,**

or you may fax your order to 614-447-3671.

1994 Subscription Prices				
	U.S.	Canada/Mexico	Europe	Elsewhere
ACS MEMBERS 1 YEAR	$ 84	$ 125	$ 186	$ 223
NONMEMBERS 1 YEAR	$1,030	$1,071	$1,132	$1,169

(Member rates are for personal use only. Journal subscriptions start January 1994.
For nonmember subscriptions in Japan, contact Maruzen Company, Ltd.)

ACS PUBLICATIONS
Essential Resources for the Chemical Sciences

MACROMOLECULES

Editor:
Field Winslow -- *AT&T Bell Laboratories*

Report

Injection Techniques in Capillary GC

Understanding the background of injection techniques will allow users to choose the most appropriate experimental conditions

Although capillary GC is more than 30 years old, injection methods have not achieved the degree of reliability needed for routine analysis. In fact, injection is the primary reason that capillary GC has acquired the reputation of producing relatively poor quantitative results. Not even the oldest technique, split injection, is understood to the extent required to give analysts reliable and comprehensive advice on how to apply split injection as a standard tool or to explain the mysterious phenomena regularly observed.

As GC instruments have evolved, they have become more elegant and easier to use. But one of the most essential parts, the injector, has generally been transplanted to each succeeding generation of instrument. Perhaps manufacturers do this because few potential customers are concerned about injectors when they buy a new instrument.

Injection problems cannot, on the other hand, be solved simply by buying the correct injector. Analysts must understand the background of the techniques they intend to use if they are to choose the most appropriate experimental conditions and solve any problems that occur. Several books describing injection techniques have been published (*1–4*). In this Report, I will briefly describe various injection techniques, review existing problems, and discuss promising ideas and concepts.

Basic concepts

Although many injection techniques have been developed for capillary GC, only the most commonly used of these are described below. Many other techniques, such as the capsule technique, the moving needle technique (solid injection), and gas sampling valves, have not been included.

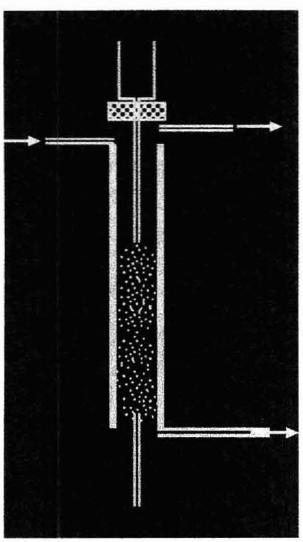

Konrad Grob
Kantonales Laborium Zürich

Split injection. During classical split injection, liquid samples are vaporized in a heated glass tube (injector liner or insert). The resulting vapors or gaseous samples are driven to the column entrance by the carrier gas and divided; a small portion enters the column and a larger portion leaves through the split outlet (Figure 1a). Split injection is most often used for relatively concentrated samples. Because no tool is available for introducing samples smaller than 0.1–1 μL into the injector, the amount of material entering the column is further reduced by splitting. Split injection is, however, also the only technique that can provide sharp initial bands and must be used when reconcentration of the initial bands is inconvenient or impossible (e.g., for headspace analysis).

In programmed temperature vaporizing (PTV) split injection, the sample is introduced into a cool chamber, which is rapidly heated after the syringe needle is withdrawn. Although on-column injection may involve splitting after the sample is vaporized in a precolumn (*5, 6*), it is rarely used in this way.

Splitless injection. The proper meaning of "splitless" is nonsplitting. The splitless injection technique, however, is more restrictive; it means nonsplitting injection into an injector that is also suitable for split injection. The split outlet remains closed during the so-called splitless period (Figure 1b) when sample vapors are transferred from the vaporizing chamber into the column. Flow through the split outlet is turned on again to purge the vaporization chamber after most of the sample has been transferred. Because al-

0003-2700/94/0366-1009A/$04.50/0
© 1994 American Chemical Society

most all of the sample material enters the column, splitless injection is used for trace analysis. Transfer into the column usually takes 30–90 s, resulting in broad initial bands that must be reconcentrated by cold trapping or solvent effects.

Conventional splitless injection involves a heated injector and a (normally) empty insert, whereas PTV splitless injection is performed with an initially cool injector and an empty or packed liner. Injection of large volumes by the overflow principle described below requires a packed insert. Quantitative results are less precise and reliable than those obtained by on-column injection. However, because on-column injection is hampered by nonvolatile sample byproducts, splitless injection is preferable for "dirty" samples.

Direct injection. Direct injection resembles splitless injection but is performed with an injector that does not have a split outlet (Figure 1c). As a result, the vaporizing chamber cannot be purged through the outlet at the end of the sample transfer. The technique is most widely used with instruments converted from packed columns to capillary columns, usually in combination with wide-bore (0.53-mm-i.d.) columns used at high flow rates. The septum-equipped temperature-programmable injector (Varian) allows PTV direct injection as well as a type of on-column injection.

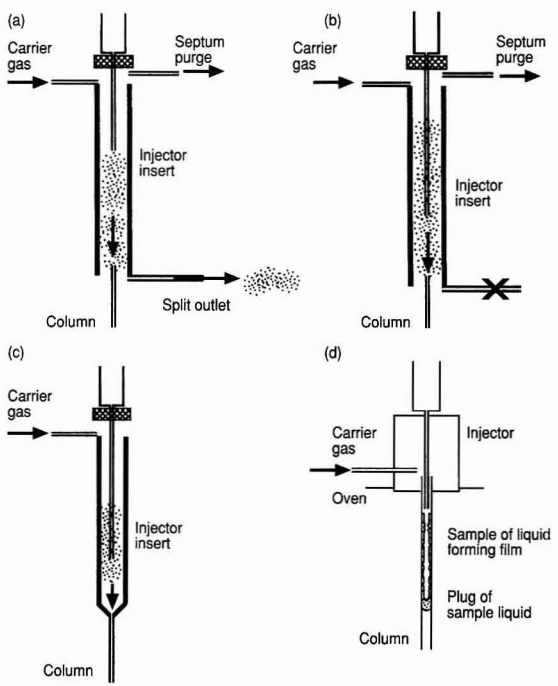

Figure 1. Injection techniques.

(a) In split injection, most sample vapors leave through the split outlet. (b) In splitless injection, the split outlet remains closed until nearly all sample material reaches the column and then serves as purge outlet. (c) In direct injection, the bottom of the vaporizing chamber is directly connected to the column inlet. (d) In on-column injection, the sample evaporates from the wall of the oven-thermostatted column inlet or precolumn.

Solvent split injection. Solvent split is a mode of PTV injection mainly used for injecting large volumes of sample. Solvent evaporation is performed at a low injector temperature with an open split outlet. Solvent evaporation (discharge) is fast, and only a small proportion of the solvent enters the column. The split outlet is then closed, the injector is heated, and the solute material is transferred into the column in the splitless mode. Volatile solutes are, of course, lost by evaporation together with the solvent.

Vapor overflow. This technique is used for splitless injection of large volumes into a hot or a PTV injector. Solvent vapors are not discharged from the vaporizing chamber by a carrier gas stream; rather, they are discharged by expansion and vapor pressure that exceeds the pressure of the environment (i.e., a temperature exceeding the pressure-corrected boiling point).

On-column injection. On-column injection deposits the sample liquid directly into the oven-thermostatted column inlet (Figure 1d) or into an uncoated precolumn (also known as a retention gap) connecting the column and injector. The injector is kept relatively cool to prevent solvent evaporation inside the syringe needle. The main functions of the injector are to hold the column and supply the carrier gas. The syringe needle passes completely through the injector and enters the column or precolumn. Upon injection, the flow of carrier gas redistributes the inserted plug of liquid into a film on the tubing wall. Sample evaporation occurs from this film. The outlet ends of some injectors must be heated to improve the release of higher boiling solutes when syringe needles are too short to adequately reach into the oven.

Critical steps

When one looks at the design of the various injectors in use today, injection techniques may appear to be more different than they actually are: The number of principles for achieving sample evaporation and transfer into the column is limited. It is important for users to understand them so that they can evaluate the various techniques and find the most suitable conditions in a systematic manner.

Analysts often select injection tech-

niques with a vague understanding of the principles involved or on the basis of some quick, poorly designed tests (e.g., with a simple mixture of some inert standards). Chromatographers tend to pragmatically accept test results as general evaluations and do not ask much about what caused specific problems or whether results were determined by accumulated positive or negative coincidences. I believe that a much more systematic approach is necessary. Each step of the injection process should be analyzed to understand weaknesses and sources of problems and to enable a definition of the range of samples and conditions for which the technique is optimally suited. This type of approach should help explain the puzzling phenomena observed almost daily and should improve techniques and equipment.

Separation of sample liquid from the needle. In cold on-column PTV injection of samples up to ~ 3 µL, separation of the sample liquid from the needle tip requires fast injection (*7*). (For samples larger than ~ 3 µL, other aspects become more important.) Slow injection leaves some liquid hanging at the needle tip. Volatile components evaporate from this liquid and reach the column, but high-boiling components are lost when the needle is removed, causing discrimination. Fast injection, however, often pulls a small amount of liquid out of the needle. This process increases the sample volume by ~ 0.1 µL but has no discriminative effect (*8*).

Sample evaporation in the needle. Accurate sample introduction into hot injectors is more difficult because the syringe needle is rapidly heated during the injection process. Solutions often start evaporating within the syringe needle (Figure 2), a process that can have two adverse results (*9, 10*). First, more sample is injected than is read on the barrel of the syringe, often a difference of nearly 1 µL or as much as 100%. It is impossible to inject volumes smaller than the internal needle volume. Second, losses on the needle wall increase with solute boiling point, resulting in discrimination of the high-boiling components. Losses of 80% are fairly common.

Evaporation inside the needle can be suppressed by using high-boiling solvents (*11*) which, however, often cause problems because of inadequate purity. Alternatively, fast autosamplers can inject the sample so quickly that the needle is withdrawn before evaporation begins. The temperature in the upper part of the injector, and particularly at the septum, is as important as the speed of injection. In many instruments the "injector temperature" is actually reached only in a short section near the center of the vaporizing chamber. The septum may be much cooler—below 150 °C when the injector temperature reads 350 °C. A cool injector head may cause high-boiling components to recondense but is particularly disadvantageous if the injector is also used for manual injection. If vaporization from the needle cannot be avoided, as during most manual injections, the cool rear portion of the needle (thermostatted by the cool injector head) will retain high-boiling solutes and result in strong discrimination of these solutes (*12*).

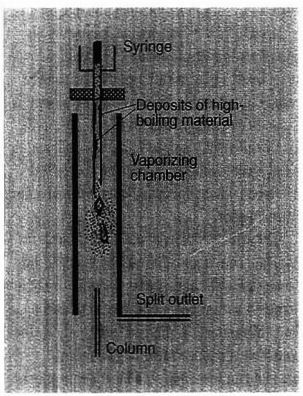

Figure 2. Injection into a conventional hot injector.

Partial evaporation empties the syringe needle (i.e., causes too much to be injected) but also results in the loss of high-boiling material.

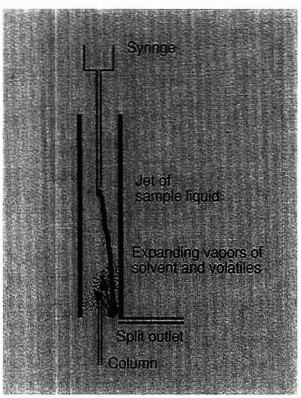

Figure 3. Incomplete sample evaporation.

Sample liquid shot to the bottom of the vaporizing chamber is neither correctly split nor efficiently transferred into the column.

Solvent evaporation. Because most samples introduced into capillary gas chromatographs are liquids, evaporation is a key step. We are, of course, interested in the solutes, but solvent evaporation is important because of solvent effects and because solvent evaporation may hinder solute volatilization more than commonly assumed.

On-column injection. Evaporation occurs from a sample layer on the surface of the oven-thermostatted column inlet or precolumn, a process that is highly reproducible and well described by solvent trapping and band broadening in space (*13*). The solvent evaporates from the rear to the front of the flooded zone, retaining most solutes up to the end of solvent evaporation. Solutes evaporate from the column wall, the same surface they contact during the chromatographic separation process.

PTV injection. Provided the injector temperature remains below the pressure-corrected solvent boiling point until solvent evaporation is completed, sample evaporation in PTV injectors proceeds in a manner similar to on-column injection, although in a less organized manner. The liquid coats the insert wall or a packing material (usually glass or quartz wool) and also evaporates from the rear to the front.

Conventional vaporizing injection. In a hot vaporizing chamber, the sample liquid must be evaporated before it reaches the column. Nonevaporated solute material shot past the column entrance (*10*) has hardly any chance of returning to the column (Figure 3). Sample evaporation is a complex process and is often poorly controlled. It may occur in the free volume of the vaporization chamber, which is a gentle process because it avoids contact with possibly adsorptive or chemically aggressive surfaces. Evaporation from a surface is, however, a more reliable process.

Because samples are usually dilute solutions, solvent evaporation is the first obstacle to overcome. The solute material does not evaporate to a significant extent before the solvent is completely vaporized because, even in a very hot injector, the temperature of the sample liquid remains at the solvent boiling point as long as the liquid contains a substantial concentration of solvent. The sample solvent, not the solutes, determines most of the evaporation process. Heat transfer to the liquid sample is one of the main problems; more than 99% of the heat is consumed for vaporization of the solvent (*10*, *14*). This situation causes some often neglected problems to become important.

As visual experiments have shown (*10*, *15*, *16*), the key to solvent evaporation is slowing the sample liquid leaving the syringe needle. At an initial velocity of 10–30 m/s the liquid would cover the distance to the column entrance in a few milliseconds. Heat transfer for solvent evaporation, however, takes between 100 ms and several seconds. Four ways to slow the liquid leaving the needle are shown schematically in Figure 4.

Nebulization. Sample liquid nebulized at the exit of the needle (Figure 4a) is slowed to the gas velocity by friction between the small droplets and the carrier gas. The carrier gas moves 100 times more slowly than the liquid even if the split flow rate is high. This provides a sufficient amount of time for heat transfer, provided the needle exit is relatively far above the column entrance and the evaporation energy of the solvent is modest.

Nebulization of the sample liquid is promoted by a solvent of low surface tension and a sample volume not exceeding ~ 1.5 µL. Most important, however, is partial evaporation inside the needle: Pressure built up in a hot needle probably causes the sample liquid to be overheated. Upon depressurization at the needle exit, this liquid may explode into small particles. No nebulization can be expected, however, when injecting by means of a fast autosampler.

Transfer to insert wall. It is difficult to imagine that a jet of non-nebulized liquid could be shot from the syringe needle through a channel ~ 40 mm long and a few millimeters in diameter directly to the column entrance without splashing against the insert wall. This view neglects the so-called Leidenfrost phenomenon, which is based on the fact that a liquid cannot touch a surface hotter than its boiling point. When a liquid approaches such a surface, heat transfer and the evaporation rate increase and the resulting vapors form a cushion repelling the liquid. The path of the liquid deviates (i.e., returns to the center of the liner) unless the surface is cooled to the boiling point of the liquid.

Deposition of the sample liquid onto a surface inside a hot vaporizing chamber (Figure 4b) therefore presupposes a high boiling point or the ability of the liquid to cool the surface to the boiling point. Undiluted samples with elevated boiling points or samples in high-boiling solvents are, in fact, easily transferred to the wall of an open tubular liner. Whether or not a sample liquid is capable of cooling a spot on a hot surface enough to wet it depends on the boiling point of the liquid and the temperature of the surface, the angle at which the liquid approaches the wall (or how easily its path is deviated), the thermal capacity of the spot, the heat of vaporization of the liquid (i.e., its cooling capacity), and the amount of liquid approaching the spot.

Evaporation from packing. Liquid samples can be reliably deposited onto light injector packing materials such as glass or quartz wool, even if they are solutions in volatile solvents. Packings with glass wool were recommended by Schomburg et al. (*17*) more than 15 years ago, but their effect could only recently be explained. Because of the low thermal mass of these materials, evaporation of a small fraction of the sample cools the top fibers to the solvent boiling point. The following liquid then falls into the network of the fibers and remains hanging there as a drop until it is evaporated (Figure 4c). One milligram of wool is sufficient, provided it is evenly spread across the insert with no holes through which the liquid can pass. An excess does not help sample evaporation, but increases adsorption. Deposition of the sample onto packings renders sample evaporation reliable and reproducible.

Injector liners with obstacles. Certain devices built into the injector liner have been reported to improve the analytical results (Figure 4d). The first one that found wide application was the "Jennings cup" or "in-

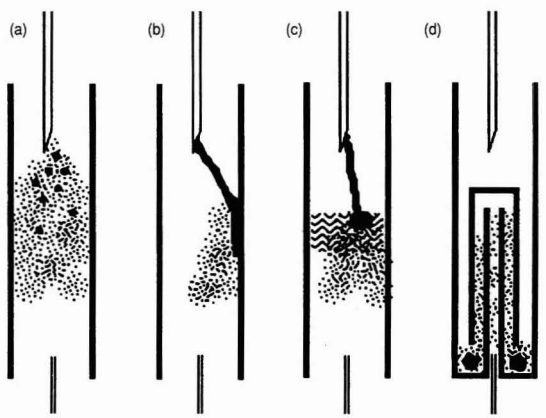

Figure 4. Methods for successful sample evaporation in a hot injector.
(a) Nebulization, (b) transfer to insert wall, (c) evaporation from packing, and (d) sample liquid trapped between obstacles.

verted cup" (*18*). Improvements have been demonstrated for test mixtures without direct evidence of how the device functions. Some of the claims are, in fact, difficult to substantiate.

Obstacles are assumed to help through mixing with carrier gas. If mixing is supposed to improve sample evaporation, the fact that the heat capacity of the carrier gas in the injector is far too small to provide a significant amount of heat has been overlooked. Furthermore, evaporation of a high-boiling solute can hardly be improved, because dilution with carrier gas is marginal (*10*). Mixing might, indeed, distribute the sample vapors more homogeneously across the insert, but this is most likely a minor advantage.

The consideration remains that obstacles might stop non-nebulized sample liquid from being shot to the column entrance. Do they really? Most obstacles were conceived to change the flow direction. The inverted cup, for instance, reverses it twice. The basis of this design was the assumption that droplets or jets of nonevaporated sample were unable to change direction and would, therefore, crash onto surfaces. Visual experiments showed, however, that baffles have no significant effect on sample evaporation. The stream of liquid performs a perfect slalom around the intrusions, guided by the Leidenfrost phenomenon. Nonevaporated sample liquid may, however, be stopped by narrow channels (*19*). Vapors generated at the hot walls hinder entry of the sample liquid. Narrow channels act like a sieve: Vapors pass whereas liquids are repelled. When obstacles stop a stream of sample liquid, evaporation usually occurs from a single droplet that is nervously turning around and "dancing" above the hot surfaces like a droplet of water on a hot griddle.

Solute evaporation. The impact of solute evaporation depends primarily on whether it occurs in the gas phase or from a surface. The inertness of the surface involved and the temperature are also important considerations.

Evaporation in the gas phase. The most gentle solute evaporation process occurs after nebulization from droplets suspended in the gas. Solvent evaporation causes droplets to shrink to aerosol particles, which finally turn into real vapor, provided the sample does not contain high-boiling or nonvolatile material. This kind of evaporation is achieved by hot needle injection into a hot, empty chamber (i.e., by conventional split or splitless injection without a fast autosampler).

When one looks at the design of the various injectors in use today, injection techniques may appear to be more different than they actually are

Because contact with surfaces in the injector is avoided, adsorptive or contaminated liners have little effect on the results obtained. It is, in fact, puzzling that free acids can be transferred using raw soft glass liners that exhibit strongly basic surfaces, or high-boiling analytes can be determined using liners coated with thick layers of strongly retaining carbonized material. Evaporation in the gas phase may also result in good transfer of extremely high-boiling components, provided the sample does not contain high concentrations of nonevaporating material. Solvent evaporation renders the droplets so small that they are swept into the column like vapors.

After being stopped by obstacles, sample liquid evaporates from a bigger drop that "dances" above hot surfaces. As the solvent evaporates, the boiling point increases, which may enable the remaining liquid, primarily consisting of solute material, to wet the surface. In such instances solute evaporation nevertheless occurs from a surface. High-boiling or nonvolatile byproducts may again have an important effect; they wet the surface without difficulty and tend to pull the solutes behind, "gluing" them to the surface.

Evaporation from surfaces. If the sample liquid is deposited onto the packing material (which implies that the sample is not nebulized and evaporated above the packing), volatilization of the solute material involves release from surfaces. However, sensitive compounds are degraded, adsorbed, or retained by layers of deactivating material. In splitless injection, relatively weak retention is sufficient to cause loss. During the splitless period, the flow rate is low and if the solute is released belatedly, most of it is lost through the split outlet.

On-column and PTV injection. With cold injection, solute evaporation inevitably proceeds from surfaces. Adsorption and degradation in packed PTV injectors is a well-known problem. Empty liners seem to be preferable, because insert surfaces are less adsorptive and more easily deactivated. In on-column injection, solute evaporation occurs from a well-deactivated column inlet, provided the latter has not been contaminated by adsorptive material. Temperature, however, corresponds to that of the oven. As higher temperatures overcome adsorptive forces, PTV or classical hot injection is superior in this respect. On-column injection, the method of choice for labile solutes, has not always proved to be the best injection technique for highly adsorptive components. In these cases, heating an uncoated precolumn to a higher temperature than the separation column (*20, 21*) has proved useful.

Expansion of sample vapors. Solvent evaporation creates a volume of vapor that tends to be underestimated: 2 µL of solvent form 300–1000 µL of vapor, depending on the solvent, pressure, and temperature inside the injector. In a hot injector, this volume is usually generated in < 1 s and creates a strong pressure pulse. If half of the injector volume is taken up by solvent vapor, the absolute pressure increases by 50% (e.g., as inlet pressure rises from 1 to 2 bar, absolute pressure increases from 2 to 3 bar). This increase is not generally observed because gas is displaced backward into the gas supply line and forward into the split outlet (Figure 5). The effects of the pulse depend on whether injection is performed in the split or splitless mode.

Split injection. The pressure pulse affects the split ratio in this injection tech-

nique because the flow rate into the column is unlikely to increase by the same proportion as that into the split outlet. The effect depends on the carrier gas supply system. Pressure regulators respond by closing the internal valve, and they begin delivering gas again only after pressure has returned to normal. Pressure rises relatively strongly, but because the column and split flow rate increase in a similar manner, changes in the split ratio are modest.

The system with a flow regulator delivering the carrier gas to the injector and backpressure regulation in the split outlet, proposed by German and Horning (*22*) and perfected by Hewlett Packard, reacts differently. Because the split flow rate is not directly flow-regulated, the extra volume created by sample evaporation is released immediately; the backpressure regulator fully opens. This keeps the pressure pulse weak, but the strong increase in the split flow rate causes the split ratio to increase substantially. The effect on quantitative results depends on the moment at which the solutes evaporate and pass the split point; there is no deviation if they are vaporized only when the pressure wave is over. If, however, some solutes evaporate together with the solvent, whereas others follow later, components are split by different ratios; that is, the sample composition is distorted and splitting is nonlinear (*23*).

The pressure wave is not the only mechanism that causes deviating split ratios and nonlinear splitting. Solvent recondensation into a cool column or a poorly warmed split outlet line may have even stronger effects (*10*).

In PTV split injection, pressure waves are weak and can be avoided almost completely by evaporating the solvent below its pressure-corrected boiling point. Other problems with the stability of the split ratio remain, however, explaining why PTV split injection still does not produce perfect quantitative results.

Splitless injection. The pressure pulse caused by sample evaporation has little effect on splitless injection. The flow rate into the column is increased, but not to a sufficient extent to accelerate sample transfer significantly. Expansion may, however, expel sample vapors from the injector liner because the vaporizing chamber is essentially open at both ends. Even a constriction such as a gooseneck does not stop escaping gas. Expulsion may have two causes: too large a volume of vapors generated by the sample injected and incorrect positioning of the vapor cloud within the vaporizing chamber.

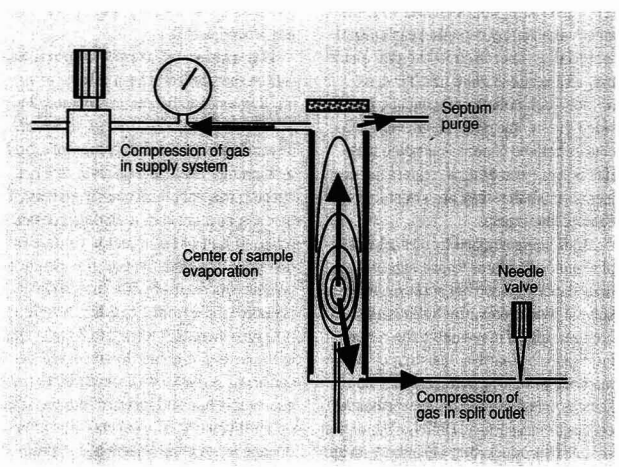

Figure 5. Expansion of sample vapors.

Sample evaporation produces a large volume of vapor and initiates a pressure pulse, shown here for a pressure regulator/needle valve system.

During the splitless period, injector systems with pressure-regulated carrier gas supply are closed except for the column (and possibly a small septum purge flow). Because pressure increases are small (hardly 0.1 bar), the sample vapors must displace a volume of gas phase from the vaporizing chamber that almost equals its own volume. Whether the sample vapors remain in the insert depends on the position of the center of evaporation and the accessible volumes at both sides of the vaporizing chamber. The classical concept aims at filling the vaporizing chamber from the bottom to the top. This requires a small volume in the split outlet and a larger one in the gas supply system (Figure 5), causing the carrier gas to be displaced backward.

The flow-regulated gas supply system is not really closed during the splitless period. The split flow is deviated into the septum purge line with a backpressure regulator but no flow restrictor. The top end of the vaporizing chamber is fully open, causing the pressure pulse to displace the carrier gas upward. As Hinshaw has shown (*24*), this configuration tends to result in higher losses of solute material in general and discrimination of the volatile sample constituents in particular. A liner with a gooseneck at the top end reduces losses by back diffusion. A gooseneck is unnecessary for the other gas system because the top end of the vaporizing chamber is essentially closed.

Splitless injection requires a long (7–8 cm) syringe needle to place the site of evaporation near the bottom of the liner. If the needle is only 5 cm long, as is unfortunately the case for many autosamplers, the needle tip does not even reach the center of the chamber. If the sample is nebulized near the needle tip, only the upper half of the chamber, which is often poorly heated, is used (Figure 6). A large part of the vapors are carried away by the gas stream discharged into the septum purge line. Furthermore, only carrier gas is transferred into the column during the first part of the splitless period, rendering sample transfer inefficient.

Maximum sample volume for splitless injection. If sample evaporation occurs in the gas phase, solvent and solute vapors (and perhaps aerosols) are mixed. To avoid losses, the entire mixture must be kept in-

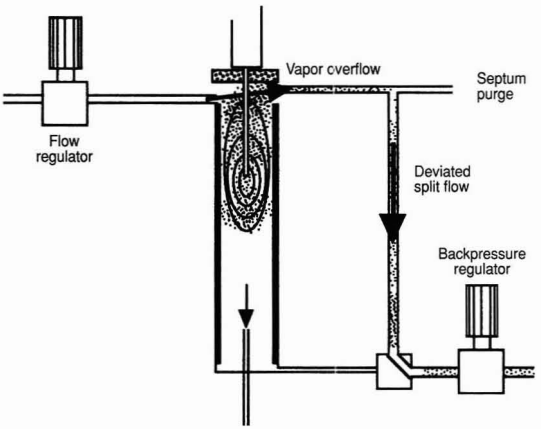

Figure 6. Splitless injection with a syringe needle that is too short.
The injection causes overflow of the vaporizing chamber and poor sample transfer shown here for a flow/backpressure-regulated system.

side the vaporizing chamber until it is transferred into the column. If the vaporizing chamber is filled from the bottom to the top, the vapor volume generated must remain somewhat smaller than that of the vaporizing chamber; some mixing with carrier gas is inevitable. Depending on the internal diameter of the liner, the inlet pressure, temperature, and the solvent used, maximum sample volumes range from 1 to 5 µL. If more is injected, the flow/backpressure-regulated system immediately removes the overflowing vapors, whereas in pressure-regulated systems the excess of vapor primarily penetrates the carrier gas supply line. This can cause memory effects that may persist for several weeks (*10*).

Wylie et al. have suggested using electronic pressure control to increase the maximum sample volume by increasing the inlet pressure during the splitless period (*25*). This compresses the vapors, increasing the capacity of the vaporizing chamber, and accelerates sample transfer. However, the gain in maximum sample volume is modest; the volume of the vapor cloud is proportional to the absolute pressure. If the inlet pressure is at 1 bar (2 bar absolute), doubling of the maximum sample volume requires increasing the inlet pressure to 3 bar (4 bar absolute).

Splitless injection with overflow. Because splitless injection is primarily used for trace analysis, the ability to introduce larger sample volumes would be an advantage. Injecting a volume of 1–3 µL does not make efficient use of the sample material available. A prepared sample may be reasonably reconcentrated to ~ 50 µL, and a 2-µL injection would correspond to merely 4% of the sample.

The overflow technique enables a spectacular increase of the sample volume, provided no highly volatile components are to be analyzed. Based on evaporation from surfaces, the method involves use of a packed insert (*10, 26*). Because the temperature of condensed solvent cannot exceed the (pressure-corrected) boiling point, deposition of sample liquid into a packing cools the site to the solvent boiling point (Figure 7). This causes evaporation to proceed stepwise: The solvent is volatilized first, whereas the solutes evaporate only when temperature is increased again after solvent evaporation is completed. Under such circumstances, solvent vapor can be released backward through the septum purge outlet without losing components of intermediate to high boiling points.

Discharge of the vapors by the overflow principle is self-regulating; there is no need to optimize conditions (*27*). The expanding vapors escape, driven by their vapor pressure. The maximum sample volume is determined by the amount of liquid that can be retained in the packing material against the strong current of escaping vapors. For a hexane solution, up to 2000 µL could be injected, whereas the limit for water using a 5-mm-i.d. liner, Tenax, and interrupted carrier gas supply was 400 µL (*28*). Losses of volatile compounds for 100-µL injections in pentane or hexane are significant for alkanes with up to 13–15 carbon atoms.

Discharge of solvent vapors in PTV injection. Introduction of the sample liquid into a PTV injector whose temperature is maintained below the pressure-corrected solvent boiling point causes solvent evaporation to be controlled by the gas flow. Passing carrier gas is saturated with solvent vapor, and the solvent cannot evaporate faster than the rate at which vapors are carried away. Because the vapor pressure is below the gas pressure, uncontrolled expulsion of vapors from the vaporizing chamber is ruled out.

PTV splitless injection. The maximum sample volume for PTV splitless injection is determined by the volume of liquid that can be retained in the vaporizing chamber without being pushed into the column

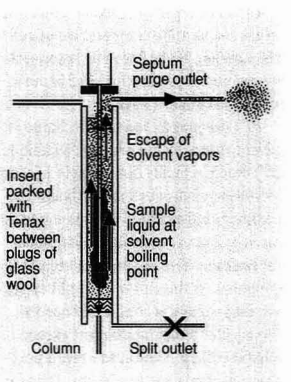

Figure 7. Splitless injection of large volumes by the overflow technique.

or the split outlet line by the carrier gas. This is 30–40 µL in a 1.2-mm-i.d. insert packed with glass wool. For a one-step injection, 25 µL seems to be a safe maximum volume (*29*). Solvent evaporation may take 3–5 min because all vapors are discharged through the column. In this way, no volatile solutes are lost. PTV splitless injection seems to be the technique of choice for trace analysis of dirty samples; for clean samples on-column injection is the first choice.

PTV solvent split injection. Solvent split injection, the more commonly used PTV method for large samples, was first described by Vogt et al. (*30*). A high carrier gas flow rate discharges the solvent vapors through the split outlet while the injector temperature is still low. The split outlet is then closed and the injector is heated to achieve splitless transfer of the solute material. If the entire sample liquid can be retained in the packing of the vaporizing chamber (up to 25 µL), introduction occurs at once.

Larger volumes, however, require adjustment of conditions so that the introduction rate is just slightly below the solvent evaporation rate. Generally some experimentation is required to optimize the first approximation of the conditions obtained by calculation (*31*). Too high an injection rate causes sample liquid to flow directly into the split outlet, whereas rates that are too low and delayed closure of the split outlet increase losses of volatile solute material. Strong cooling by solvent evaporation and inaccurate compensation by thermoregulation render the actual evaporation temperature uncertain. Losses of volatile solute material also depend on the packing material in the vaporizing chamber (*32–34*).

PTV overflow technique. Discharge of solvent vapors by the overflow technique (*27*) would simplify solvent split injection because any introduction rate below the maximum achievable evaporation rate produces optimum results in a self-regulating manner. The carrier gas supply is stopped, and the exit of the split or septum purge outlet is completely opened. The injector temperature must exceed the solvent boiling point at the given pressure (which may be a vacuum). There is, however, no practical experience with this technique yet.

If car engines worked as unreliably as capillary GC injectors, our world would still be crowded with horse carriages!

On-column injection. In this injection technique there is no problem with expanding solvent vapors because during injection the oven temperature must be kept below the pressure-corrected solvent boiling point (*13*). The vapor pressure remains below the inlet pressure, and the evaporation rate is controlled by the discharge of the vapors by the carrier gas flow.

Sample transfer in splitless injection. As the size of the vaporizing chamber of a conventional injector increases, so does (according to the classical concept) the volume of vapors that can be retained; thus, the amount of sample that can be injected becomes larger. The limit to the internal diameter of the insert is determined by the transfer of the solutes into the column. During splitless transfer, the flow rate through the injector corresponds to that through the column. The gas velocity in a 4-mm-i.d. vaporizing chamber is, however, some 250 times lower than in a 0.25-mm-i.d. capillary, which brings it to the limit beyond which diffusion in the injector enlarges the vapor cloud faster than the vapors are transferred. The minimum gas velocity in the vaporizing chamber that results in effective sample transfer is ~ 2.5 mm/s (*10*). This corresponds to a flow rate of ~ 2 mL/min in a 4-mm-i.d. insert and 3.2 mL/min in a 5-mm-i.d. insert. These flow rates are fairly high for capillary columns and particularly for GC/MS instruments with weak pumping systems. An 80 mm × 4 mm i.d. (1 mL) insert is just sufficiently large to safely house the vapors of ~ 2 µL of a solution in one of the commonly used solvents. Transfer requires 60–90 s (*10*).

Classical splitless injection may by affected by matrix effects. For example, the presence of nonvolatile byproducts hinders the transfer of the solute material into the column (*10*). It is still unknown whether this is a result of sample material that is shot to the bottom of the injector or to byproducts "gluing" the solutes to the insert wall. The presence of some glass wool above the column entrance almost eliminates the effect, which raises the question of whether the liner should be empty (as classically suggested). However, glass wool easily degrades or adsorbs the small amounts of solute injected by the splitless technique.

Sample transfer in PTV splitless injection is far more efficient because vaporizing chambers have internal diameters of ~ 1 mm. The minimum gas velocity needed to achieve satisfactory transfer is 16 times lower than that required for conventional splitless injection. Therefore, the minimum flow rate is just slightly greater than 0.1 mL/min. At 1 mL/min, a 5-cm chamber can be emptied into the column in < 3 s. Such efficient transfer should allow some retention by partitioning or adsorption in the vaporizing chamber. Matrix effects appear to be weak (*35*).

Solute reconcentration. The sharpness of peaks in capillary GC requires sharp initial bands, and because the system is small, it seems that only extremely small sample volumes would be suitable. However, only split injection introduces such small plugs of sample vapor. In splitless or direct injection, the transfer of the solutes into the column takes 30–90 s, resulting in strong band broadening over time (*10*). Cold trapping or solvent effects are required to reconcentrate the solute bands in the inlet of the column (*36, 37*). If the solute material is spread in the column inlet by flow in the liquid phase (on-column injection, splitless injection with solvent recondensation), bands are broadened in space (*38*). Initial bands (flooded zones) longer than 20–40 cm must be reconcentrated by the retention gap technique, which involves use of an uncoated precolumn (*13*).

For other introduction techniques,

some tricks can be used to resharpen initially broad bands. These reconcentration techniques are sufficiently powerful to enable injection of volumes far larger than those commonly used. The maximum volume that has been introduced by concurrent evaporation in on-line LC/GC stands at 20,000 µL (*39*).

Opportunities for development

Sample introduction is not only the most significant source of trouble in capillary GC, but it also provides unique possibilities. Many must still be perfected, making this field ripe for creative work. These opportunities fall broadly in three areas: larger sample volumes, selective sample introduction, and coupled techniques such as on-line LC/GC.

Larger sample volumes. The volume of sample introduced into the column can be varied by a factor of more than 1 million, namely from < 1 nL (splitting about 1000:1) up to > 1000 µL (concurrent evaporation with the loop-type interface, an injection technique that has been used routinely in coupled LC/GC for many years). The volume range from 1 nL to 1 µL was established in the early days of capillary GC and is suitable for the analysis of concentrated samples. In trace analysis, for which capillary GC is an excellent technique, injection of volumes between 10 and 100 µL would be important to increase sensitivity, to make better use of the sample, and to avoid tedious reconcentration to small volumes. Solvent evaporation performed during injection is easier, avoids the danger of sample contamination, and occurs under better controlled conditions. Several concepts for large-volume injections currently exist, and they are there, waiting to be perfected and implemented.

Selective sample introduction. Injection in capillary GC offers a number of elegant ways to accomplish selective sampling, fractionating a sample and/or enriching the components of interest before GC separation. Most of these techniques are probably far from being fully exploited, as, for instance, recently shown by the introduction of micro solid-phase extraction or injector–internal headspace analysis (*40*). Performed inside the injector, this technique broadens the range of solutes amenable to headspace analysis. Organophosphorus pesticides (*41*) can be determined in edible oils, which are injected into a vaporizing chamber at ~ 200 °C, where the components of interest are volatilized. The oil flows along the insert wall to the bottom of the injector and is collected there.

Coupled techniques. The term selective sampling was introduced by Schomburg, who demonstrated numerous techniques of two-dimensional GC as long as 20 years ago (*42, 43*). Capillary GC is, in fact, an excellent technique for final analysis in more complex systems and dedicated analyzers. This is primarily the result of the possibilities of efficient reconcentration by cold trapping, solvent effects, and the retention gap technique. On-line sample preparation or preseparation may occur in the gas phase by headspace, purge and trap, or GC (GC/GC); in the liquid phase by on-line extraction (*44*) or HPLC (LC)/GC (*45–47*); or in the supercritical fluid phase by on-line SFE/GC (*48*). Two factors promote the development of this type of coupled analyzer: An increasing proportion of all analyses is carried out routinely in large numbers, justifying a dedicated instrument, and computers enable the control of instruments performing extremely complex processes.

On-line LC/GC. The possibilities of on-line coupling of LC to GC can be illustrated by the analysis of sterol dehydration products, a procedure routinely performed to detect adulterated edible fats and oils (*49*). Because heat treatment of oils dehydrates a small amount of the sterols and their esters, the resulting olefins can be used to indicate raffination. This technique is of interest for the control of oils sold as unrefined, such as extra virgin olive oils. The method also can be used to detect the admixture of other oils.

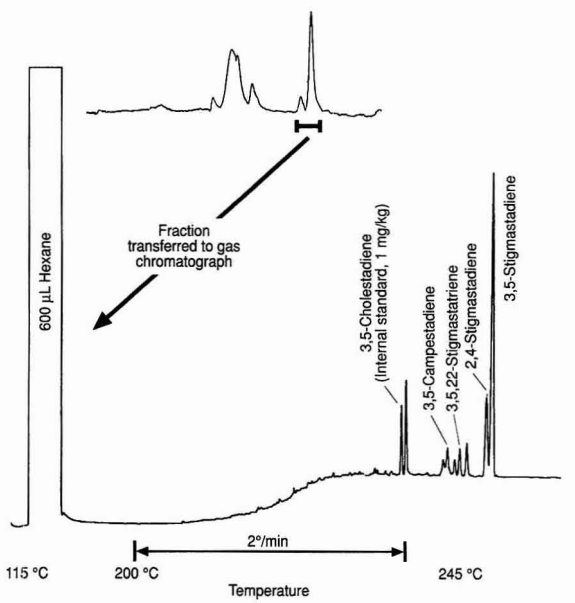

Figure 8. Chromatograms from on-line analysis of sterol dehydration products from a refined oil by LC/LC/GC-FID.

Top: UV chromatogram of the effluent from the second LC column monitored at 235 nm. Bottom: gas chromatogram obtained using a 25 m × 0.25 mm i.d. column coated with Superox 0.6, a polyethylene glycol.

Ideas flourish in this environment.

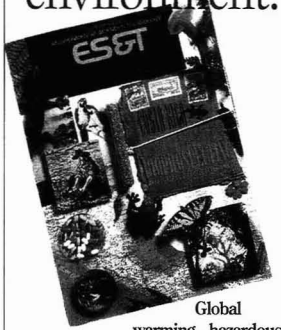

Global warming...hazardous waste...water scarcity...ecosystem ecology...risk communication... You'll explore today's most important environmental concerns in the critically-acclaimed *Environmental Science and Technology,* rated #1 of all environmental science journals in the latest *Science Citation Index. ES&T* provides breakthrough ideas, insightful analyses, and up-to-the-minute research every month.

Scientifically rigorous and international in scope, *ES&T* combines peer-reviewed research with a lively magazine section to present the latest thinking in environmental science and protection in a reader-friendly format.

Free Trial Issue

Call today and we will send you a copy of *ES&T* absolutely free with no obligation. Once you've reviewed it, you'll see why it pays to subscribe! Call toll free 1-800-333-9511 today. Outside the continental U.S., call 614-447-3776. FAX 614-447-3671.

1994 Subscription Rates

	U.S.	Canada, Mexico	Europe*	All Other Countries*
Members** One Year	$ 44	$ 66	$ 102	$118
Nonmembers** (personal) One Year	$ 90	$112	$148	$164
Nonmembers** (institutional) One Year	$497	$519	$555	$571

Member subscription rates for personal use only.
*Includes air service.
**2- and 3-year rates available; call for details.

Editor, William H. Glaze, University of North Carolina, Chapel Hill.

ACS PUBLICATIONS
Essential Resources for the Chemical Sciences

As applied currently, the technique involves on-line LC/LC/GC-FID. The first LC column isolates a broad range of olefins from a large amount (~ 20 mg) of oil. The olefins are further separated on a 25 cm × 2 mm i.d. silica gel LC column to pick out the dienes of interest. A fraction of 600–1000 µL in hexane is then transferred to the gas chromatograph and analyzed with a flame ionization detector (Figure 8). Detection by MS is possible but usually unnecessary.

In this application the first LC column performs a preseparation, removing the oil and some other components (such as squalene) that could also be carried out manually on a conventional LC column. The on-line mode, however, eliminates nearly all sample preparation work. A 20% solution of the oil is loaded into the autosampler and the analysis is fully automated. The second LC separation requires high resolution; no equivalent performance can be obtained by conventional LC. On-line transfer of the entire fraction to the gas chromatograph is necessary to achieve the required sensitivity. The method enables the analysis of more samples per day and achieves excellent efficiency in the cleanup. It also generates results that are more accurate and reliable than those obtained with other methods because the on-line mode rules out losses, and UV detection provides control over the preseparation, ensuring that the correct fraction is accurately segregated from the remainder of the sample.

Outlook

I believe that injection has never been optimized with sufficient professionalism, nor have the various techniques been evaluated with the care required before they are handed over to inexperienced users. If car engines worked as unreliably as capillary GC injectors, our world would still be crowded with horse carriages! For example, a few years ago—20 years after the technique was introduced—vaporizing chambers were often far too small to contain sample vapors. Many instrument manufacturers and users seemed to overlook this basic deficiency. Even today, syringe needles used for splitless injection are often too short.

Today's injection techniques often provide satisfactory results. However, more severe problems exist than those mentioned in the literature or during symposia. Many quantitative errors are not even recognized.

Why are so few people trying to solve the problems that exist and publishing their conclusions? It appears that only a few are actively working to enhance our understanding of the concepts underlying the technique—and they are doing it on Friday afternoon after their real jobs of analyzing samples are complete. Most users think injection techniques must be developed by instrument manufacturers. Many manufacturers, however, tend to invest their money in places other than basic research. Without more work in this field, I am concerned that capillary GC is in danger of stagnation and perhaps ultimately of degeneration.

References

(1) *Sample Introduction in Capillary GC*; Sandra, P., Ed.; Hüthig: Heidelberg, Germany, 1985.
(2) Lee, M. L.; Yang, F. J.; Bartle, K. D. *Open Tubular Column GC*; John Wiley and Sons: New York, 1984.
(3) Klein, M. S. *GC Inlets—An Introduction*; Hewlett Packard: Avondale, PA, 1990.
(4) Schomburg, G. *Gas Chromatography*; VCH: Weinheim, Germany, 1990
(5) Schomburg, G.; Husmann, H.; Schulz, F. *HRC & CC* **1982**, *5*, 565–67.
(6) Bicchi, C.; D'Amato, A.; Galli, A.; Galli, M. *HRC* **1990**, *13*, 649–51.
(7) Grob, K. *J. Chromatogr.* **1980**, *189*, 109–17.
(8) Grob, K.; Bronz, M. *HRC* **1993**, *16*, 121–22.
(9) Schomburg, G.; Dielmann, R.; Borwitzky, H.; Husmann, H. In *Proc. 12th Int. Symp. on Chromatography*; Schomburg, G.; Rohrschneider, L., Eds.; Elsevier: Amsterdam, The Netherlands, 1978; p. 157.
(10) Grob, K. *Split and Splitless Injection in Capillary GC*; Hüthig: Heidelberg, Germany, 1993.
(11) Schomburg, G.; Dielmann, R.; Borwitzky, H.; Husmann, H. *J. Chromatogr.* **1978**, *167*, 337–54.
(12) Grob, K.; Neukom, H. P. *J. Chromatogr.* **1980**, *198*, 64–69.
(13) Grob, K. *On-Column Injection in Capillary GC*; Hüthig: Heidelberg, Germany, 1987.
(14) Grob, K. *HRC* **1992**, *15*, 190–94.
(15) Grob, K.; De Martin, M. *HRC* **1992**, *15*, 335–40.
(16) Qian, J.; Polymeropulos, C. E.; Ulisse, R. *J. Chromatogr.* **1992**, *609*, 269–76.
(17) Schomburg, G.; Behlau, H.; Dielmann, R.; Weeke, F.; Husmann, H. *J. Chromatogr.* **1977**, *142*, 87–102.
(18) Jennings, W. G. *J. Chromatogr. Sci.* **1975**, *13*, 185–87.
(19) Grob, K.; Wagner, C. *HRC* **1993**, *16*, 429–32.
(20) Hagman, G.; Roeraade, J. In *Proc. 14th Int.*

Symp. on Capillary Chromatography; Sandra, P.; Lee, M. L., Eds.; Hüthig: Heidelberg, Germany, 1992.
(21) Hiller, J. F.; McCabe, T.; Morabito, P. L. *HRC* **1993**, *16*, 5–12.
(22) German, A. L.; Horning, E. C. *Anal. Lett.* **1972**, *5*, 619–28.
(23) Ettre, L. S.; Averill, W. *Anal. Chem.* **1961**, *33*, 680–84.
(24) Hinshaw, J. V. *HRC* **1993**, *16*, 247–53.
(25) Wylie, Ph. L.; Philips, R. J.; Klein, K. J.; Thompson, M. Q.; Hermann, B. W. *HRC* **1991**, *14*, 649–55.
(26) Grob, K.; Brem, S.; Fröhlich, D. *HRC* **1992**, *15*, 659–64.
(27) Grob, K. *HRC* **1990**, *13*, 540–46.
(28) Grob, K.; Fröhlich, D. *HRC* **1992**, *15*, 812–14; **1993**, *16*, 224–28; **1994**, in press.
(29) Grob, K.; Li, Z. *HRC & CC* **1988**, *11*, 626–32.
(30) Vogt, W.; Jacob, K.; Ohnesorge, A-B.; Obwexer, H. W. *J. Chromatogr.* **1979**, *174*, 437–39; **1979**, *186*, 197–205.
(31) Staniewski, J.; Rijks, J. A. *J. Chromatogr.* **1992**, *623*, 105–13.
(32) Staniewski, J.; Rijks, J. A. *HRC* **1993**, *16*, 182–87.
(33) Loyola, E.; Herraiz, M.; Reglero, G.; Martin-Alvarez, P. *J. Chromatogr.* **1987**, *398*, 53–61.
(34) Herraiz, M.; Reglero, G.; Loyola, E.; Herraiz, T. *HRC & CC* **1987**, *10*, 598–602.
(35) Grob, K.; Laubli, T.; Brechbühler, B. *HRC & CC* **1988**, *11*, 462–70.
(36) Grob, K.; Grob, K. *J. Chromatogr.* **1974**, *94*, 53–64.
(37) Grob, K. *J. Chromatogr.* **1983**, *279*, 225–32.
(38) Grob, K. *J. Chromatogr.* **1981**, *213*, 3–14.
(39) Grob, K.; Schmarr, H-G.; Mosandl, A. *HRC* **1989**, *12*, 375–82.
(40) Morchio, G. *Riv. Ital. Sostanze Grasse* **1982**, *59*, 335–39.
(41) Grob, K.; Biedermann, M.; Giuffre, A. M. *Z. Lebensm. Unters. Forsch.* **1994**, *198*, 325–28.
(42) Schomburg, G.; Husmann, H.; Weeke, F. *J. Chromatogr.* **1975**, *112*, 205–17.
(43) Schomburg, G. In *Sample Introduction in Capillary GC*; Sandra, P., Ed.; Hüthig: Heidelberg, Germany, 1985; pp. 235–60.
(44) Roeraade, J. *J. Chromatogr.* **1985**, *330*, 263–74.
(45) Grob, K.; Fröhlich, D.; Schilling, B.; Neukom, H. P.; Nägeli, P. *J. Chromatogr.* **1984**, *295*, 55–61.
(46) Grob, K. *On-Line LC–GC*; Hüthig: Heidelberg, Germany, 1991.
(47) Cortes, H. J.; Pfeiffer, C. D.; Richter, B. E. *HRC & CC* **1985**, *8*, 469–74.
(48) Hawthorne, S. B.; Miller, D. J. *J. Chromatogr.* **1987**, *403*, 63–71.
(49) Grob, K.; Artho, A.; Mariani, C. *Fat Sci. Technol.* **1992**, *94*, 394–400.

Konrad Grob studied chemistry at the University of Zürich (Switzerland) and received his Ph.D. in plant physiology from ETH Zürich in 1979. Since 1974 he has worked for the Kantonales Laborium (P.O. Box, CH-8030 Zürich, Switzerland), the laboratory of the government chemist of Zürich, in the field of food control.

THERMAL ANALYSIS IN POLYMER CHARACTERIZATION

THE RENOWNED FACULTY: EDITH A. TURI, COURSE DIRECTOR, RESEARCH PROFESSOR, POLYTECHNIC UNIVERSITY

HARVEY E. BAIR, TECHNICAL STAFF, AT&T BELL LABS

RICHARD P. CHARTOFF, PROFESSOR OF MATERIALS ENGINEERING, UNIVERSITY OF DAYTON

Monday-Tuesday, November 14-15, 1994, in Somerset, New Jersey
in conjunction with the 1994 Eastern Analytical Symposium

Ten Key Ways You Will Benefit from Attending This Course:

1. Learn the basic principles of thermal techniques
2. Understand the characteristics of commercial instruments: learn their applicability to your needs
3. Learn the systematic application of thermal analysis to a broad range of polymers
4. Learn ways to enhance polymer performance
5. Learn how to optimize experimental conditions and interpret thermal data obtained by different techniques
6. Optimize processes and quality control methods
7. Learn how to increase your direct input in achieving marketing objectives
8. Eliminate expensive trial-and-error experiments by cost-efficient, speedy, small-scale thermal analysis
9. Enhance your capability to conduct experiments targeted to improving quality and increasing productivity
10. Discuss with leading experts your specific questions such as problem solving, troubleshooting, and operation safety

For more information on this dynamic new course, call the Short Course Department at (800) 227-5558 (TDD: (800) 272-6306 or (202) 872-6306. FAX: (202) 872-6336. Or call the American Chemical Society's continuing education Short Course Department at (800) 227-5558 (TDD: (800) 272-6306 or (202) 872-6306.

YES! Please send me more information on the new ACS Short Course, *Thermal Analysis in Polymer Characterization*, to be held November 14-15,1994, in conjunction with the 1994 Eastern Analytical Symposium.

NAME _____

TITLE _____

ORGANIZATION _____

ADDRESS _____

CITY, STATE, ZIP _____

BUSINESS PHONE _____ FAX _____

Mail TO: American Chemical Society, Dept. of Continuing Education, 1155 16th Street, N.W., Washington, DC 20036

Modeling Made Easy

HyperChem

Molecular Visualization and Simulation

HyperChem

Hypercube Inc.
419 Phillip St.
Waterloo, Ontario, Canada N2L 3X2
519-725-4040; 800-960-1871;
519-725-5193 (fax); info@hyper.com (e-mail)
Release 4; $1995 commercial; $995 academic and government

HyperChem Release 4 is designed for molecular modeling, structural optimizations, and related manipulations. The program is easily installed and runs in the enhanced mode of Windows v. 3.1. The minimum hardware requirements are a 386-based computer equipped with a math coprocessor, 4 MB of RAM, and 20 MB of hard disk storage space. However, a faster computer with additional memory would be an advantage, particularly when manipulations are performed on larger molecules. Although the graphical and mathematical computations for smaller compounds are handled well using a standard 33-MHz 386-based computer, this type of hardware may be too slow for the larger systems. For proteins, it is especially time consuming to set up the initial structures from stored files and to carry out screen operations requiring enhanced graphics such as spherical versus stick-type representations. Because the program runs in Windows, information can be exported easily for postmanipulation and use in other programs.

HyperChem contains a number of useful features for both research-related activities and instructional purposes. These include the ability to create and manipulate the molecule structures, reconstruct proteins from existing databases, measure structural properties of displayed systems, and perform energy minimization and molecular orbital calculations as well as various other simulation experiments. In addition, Release 4 contains new features such as the ZINDO/1 and ZINDO/S semiempirical methods, spectroscopic simulations, and enhanced graphics. For scientists familiar with various computational methods, the software can be a convenient research tool. For those who are less familiar with the different molecular modeling/computational approaches, the software is equally valuable as an educational tool. In fact, the strength of HyperChem lies in its use as an educational tool, especially when the total product is judged (i.e., the software plus the accompanying manuals). The latest version, Release 4, contains bound updated manuals in place of the loose-leaf binder format of the earlier version. The computational chemistry manual, which covers various aspects of the calculations used in the program, is of textbook quality in its organization and description of techniques. It is divided into two major parts: a practical guide and a theory and methods section. This format is convenient for learning and for instruction; the manual could easily be used for formal teaching.

Hypercube has also released Chem Plus, a set of extension programs that provides enhanced features in terms of image presentation, conformational searches, and computations such as qualitative structure–activity relationships. This package is available separately ($695 commercial; $495 academic).

The tutorial and accompanying reference manuals were easy to follow and provided step-by-step details of the software features. In a relatively short time, a novice to the program can begin to comfortably use many of features and, with additional practice, should be able to master the more advanced features fairly quickly (assuming that the user has a general knowledge of computational methods). Another strong feature of the tutorial lessons and extensive reference manual is the numerous figures that show expected screen images or computed values. In addition, there are clear cross-references between the getting started manual, where concepts are introduced, and the reference manual, where more detailed information is found.

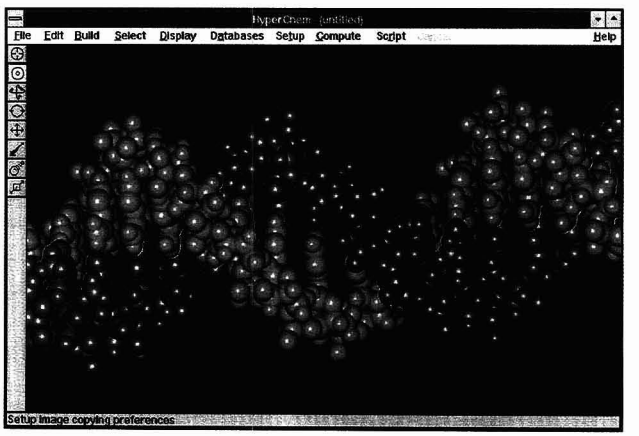

CPK (space filling) model of a β-form double-helix DNA generated by HyperChem.

In working through the various lessons, I found only two or three places where a few instructions seemed to be slightly out of sequence. However, these appeared later in the manual and perhaps were meant as a means of testing one's mastery of the program. Although a few practice exercises are suggested at the end of each lesson, a useful addition would be more exercises with accompanying answer keys at the end of the text. Such a feature would provide the user with immediate feedback.

Overall, HyperChem is a very user-friendly program. This is partly because of the layout of the working screen, which displays tool icons and descriptors as major menu headings and submenus.

I found only one feature to be somewhat inconvenient: the error messages. Although the error messages are probably adequate for those users who are already experienced with the various aspects of the program, they are perhaps less helpful to beginners. Thus I believe that a more interactive help menu that could explain error messages would be a valuable addition to the program and would help to avoid or minimize possible user frustration.

Another useful addition would be to include in the tutorial lesson a more detailed discussion of the icon/menu that allows changes in the degree of translational or rotational motion per distance of mouse movement. Currently this information appears only in the extended reference manual. As a consequence, this useful feature of the software can easily be missed.

In summary, HyperChem and the ChemPlus extensions are excellent packages and a pleasure to use. They will be helpful tools for the individual who does not have access to large computer-based molecular modeling systems or an educational tool by which to learn more about computational methods. I recommend that the software be used on a 486-based computer with a speed of 50–66 MHz.

Reviewed by R. K. Gilpin, Department of Chemistry, Kent State University

Faster FT-IR Analysis

Omnic

Nicolet Analytical Instruments
5225 Verona Rd.
P.O. Box 44451
Madison, WI 53711-4451
608-276-6100; 608-273-5046 (fax)
Version 1.2; $2500

The Basic Omnic software package for data stations, designed primarily for mid- and near-IR spectral analyses, includes Omnic 1.2, Omnic Macros/Basic, Omnic Spectral Interpretation Guide, Omnic Applications Bibliography, Omnic Search with sample libraries, Omnic file conversion utilities, and Smart Pad for Windows. Additional Omnic software packages offered by Nicolet include Omnic Data Collect, Omnic Quant IR, Omnic Macros/Pro with Visual Basic, Omnic Quick IR, and Omnic Series software for kinetics and chromatography applications. Here I will focus on the Basic package.

Because it follows all the conventions of standard Windows applications, the software is easy to learn. The fairly complete help section can minimize use of the manual, and the spectral display features are excellent. There are no roll and zoom buttons, unlike those found in spectral analysis software from other vendors and in earlier Nicolet software. I thought this omission would be a critical failure, but Nicolet's innovative use of the view finder and spectral panes makes manipulation of the spectral display regions quick and convenient. By using the mouse, one can easily manipulate right and left view finder bars on a small full-spectrum window representation of the selected spectrum to achieve both roll and zoom capabilities. Selecting spectral regions from the spectral pane is accomplished by using the mouse to draw a box around the region to be viewed. There are button capabilities for measuring peak areas and heights (both direct and baseline corrected), peak picking, and annotating spectra with either automatic frequency labels or input typed in by the user. Another button allows the screen cursor to follow the spectral data via mouse clicks or cursor keys.

Multiple spectra in different colors can be displayed within a single pane, or separate spectra can be displayed within multiple spectral panes. The spectral display can be set to autoscale or to matched, common, or offset scales. The only problem I found is that if multiple spectra are displayed in the same spectral pane, some display operations cause the spectra to change relative scales. The user is not always aware of this change; only the scale of the highlighted spectrum is shown, and the scale for nonselected spectra may be different, unbeknownst to the user.

Numerous spectral processing features are available, including conversions to % transmittance, absorbance, Kubelka–Monk, photoacoustic units, % reflectance, or $\log(1/R)$, as well as Fourier transform of interferograms, ratio of single-beam spectra, baseline correction (manual multipoint linear baseline correction or automatic baseline correction), dispersion corrections, correction for ATR, blank, straight-line generate, spectral subtraction, addition and multiplication, Fourier self-deconvolution, smooth, automatic smooth, change data spacing, first and second derivatives, peak picking, and noise analysis. Typical Windows editing features are also available. Special features include saving spectra as a group rather than singly, printing single and multiple spectral panes in various formats, and initiating and retaining a log of all the key strokes and selections of the spectra. One feature that is particularly useful for meeting U.S. Food and Drug Adminis-

tration requirements or for data related to legal cases is the automatic recording of all processing steps performed on the spectra. This sample history information is always stored with the spectral file and cannot be edited.

An additional feature that facilitates repetitive spectral processing is the ability to create and launch macros. The macros capability of Omnic Macros/Basic involves selecting options from a series of nearly 60 predefined functions or operations. However, the construction of macros with large numbers of steps caused a "toolbook memory error." To avoid this, one must make smaller macros and link them together to achieve the desired series of large numbers of macro steps.

Previous users of Nicolet's SX or DX spectral analysis software will notice the limitations of Omnic Macros/Basic. To achieve most of the capabilities of these packages, I recommend purchasing Nicolet's Omnic Macros/Pro with Microsoft's Visual Basic software ($950). It requires learning Visual Basic, but for the user with complex data processing on multiple files, Omnic Macros/Pro is a valuable addition to the Omnic package.

Omnic Search comes with six sample libraries that contain nearly 600 spectra. Full libraries can be purchased separately. This spectral search package has the flexibility to search multiple libraries, specified spectral regions, and individual spectral names and index numbers; examine the digitized library spectra with all of the Omnic software features; and create and search user libraries. The top search "hits," as determined by an unspecified match value, are listed and can be displayed automatically with the unknown spectrum for visual comparison. This latter feature, combined with access to the digitized library spectra, facilitates evaluation of the quality of spectral hits.

Three minor components of the standard Omnic software package include Smart Pad for Windows, Omnic Applications Bibliography, and Omnic Spectral Interpretation Guide. Smart Pad for Windows allows the user to add buttons to Omnic to simplify and streamline operations with single mouse clicks. A number of button options are supplied by Nicolet, and the user can create additional button options. The Omnic Spectral Interpretation Guide software is most useful for novices or for teaching the interpretation of mid-IR spectra. Some limited related information and text concerning 40 classes of compounds are available. A list of spectra in the software, as well as the ability to bring the spectra directly into Omnic for viewing and manipulating, would be useful. (It is available in the Omnic Interpret IR package.) The Omnic Applications Bibliography software is also useful primarily to people new to the field of IR spectroscopy. Its 1007 abstracted articles can form a good starting point for investigating topics in IR spectroscopy.

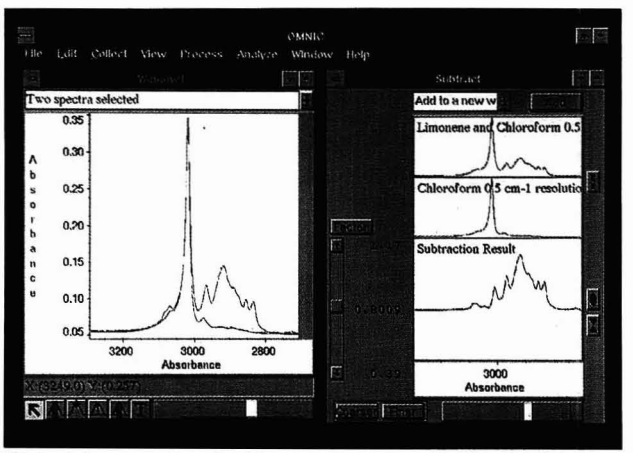

Window 1 shows a spectrum of cyclohexane and a spectrum of a mixture containing cyclohexane. In the subtract window, the cyclohexane spectrum is subtracted from that of the mixture, leaving the spectrum of the unknown (limonene).

Although I was generally pleased with the software, I identified several areas in which improvements would be helpful. Some of these are to be addressed in Omnic 2.0, scheduled for release in late September. For example, more types of file translators are needed to give the software general utility beyond Nicolet spectrometers. Especially useful would be conversions for spectra in LabCalc/Grams format (Galactic Industries) because that program has almost all spectral file converters available. In addition, some important information about calculations or operations (e.g., How does the automatic mode of the Savitsky–Golay smoothing work? What algorithm is used for the spectral search, and how is the match value determined?) is missing from the documentation. Although similar undocumented features are common, I do not like to process spectra with any operation that I do not fully understand.

I found the printer output of the plots to be very good for viewing the spectral data. However, the quality of the fonts, font sizes, and linewidths is substandard for publication. Although I could modify the output after Nicolet provided additional information about the .ini file associated with Omnic, I would prefer to control these features directly from the software. I also experienced applications errors without warning on occasion. In these cases, unsaved work was lost because the computer had to be rebooted.

In conclusion, the Omnic software is a very good first version of a spectral software package for users of the new family of Nicolet FT-IR spectrometers that are PC driven. Of all the spectral analysis software packages I have used, I found this one the easiest to learn. Nicolet should be commended for designing software that greatly reduces the time and effort required to become proficient at using the software. Some research spectroscopists might miss some of the capabilities of previous Nicolet software versions that are omitted from the Omnic software. For them, other third-party PC spectral analysis software packages can fill the gap until Nicolet upgrades Omnic with greater flexibility, more complete macros and programming capabilities, and a more complete set of spectral file converters. I use a variety of spectral software packages to achieve all the capabilities that facilitate spectral analyses. Omnic is an important addition to this suite of software.

Reviewed by David M. Haaland, Sandia National Laboratories

SOFTWARE RELEASED

Intro to CE

LC Resources
2930 Camino Diablo, Suite 110
Walnut Creek, CA 94596
510-930-9043; 800-379-5221;
510-930-9136 (fax)
$595

Designed to teach the principles and practice of capillary electrophoresis, Intro to CE consists of three modules covering basic to advanced concepts: Introduction to CE, Free Solution CE Method Development, and Micellar Electrokinetic Chromatography Method Development. Animated graphics illustrate the mechanisms involved in CE separations. The software runs on any IBM-compatible PC (386-CPU recommended) with Windows 3.0 or higher.

Molecules-3D

Molecular Arts
1532 East Katella Ave., Suite 1000
Anaheim, CA 92805-6627
714-634-8100; 714-634-1999 (fax);
info@molecules.com (e-mail)
Version 2.0; $29

Molecules-3D for Windows allows users to create presentation-quality graphics as well as high-quality models and images that can be transferred to and from other applications. More than 30 new features and upgraded capabilities have been incorporated, including an expandable structure library with more than 100 3D molecular structures; customizable molecular parameter settings; one-button wire-frame, ball-and-stick, and spacefill rendering; and a molecular syntax checker that identifies potential structure problems.

This release will operate on IBM-compatible PCs running Windows 3.1. Supported output devices include LaserJet printers, color printers, PostScript devices, and Hewlett Packard plotters.

ResearchStation

Megalon
400 Bel Marin Keys Blvd., Suite 102
Novato, CA 94949
415-884-3000; 415-884-2279 (fax);
info@megalon.com (e-mail)
$995

ResearchStation for Windows provides a dynamic electronic workspace in which scientists can consolidate, manipulate, and examine information about a research project or topic in any format: text, images, numerical data, graphics, video, and sound. Without leaving the program, users can work with multiple applications in a single window to capture, record, organize, visualize, and share data and information from many different sources. The ResearchStation Minder allows automation of routine and repetitive tasks. For collaborative work, security features protect record integrity and prevent unauthorized access to the system while enabling authorized users to share information across workspaces.

Based on Windows-standard OLE 2.0 architecture, the program runs on IBM-compatible 386/486-based PCs with Windows 3.1 or higher, 4 MB RAM, and 10 MB free hard disk space.

OMNIC™

LET OMNIC MAKE YOU MORE PRODUCTIVE

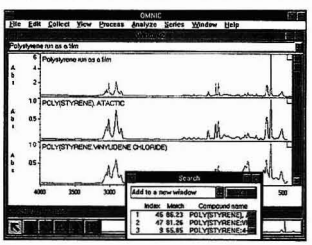

OMNIC Windows™compatible software simplifies FT-IR analysis, eliminates the need to know a complicated computer language and reduces training time. Its customizable user interface allows you to personalize screens and create icons using SmartPad™ for Windows for frequently used commands.

The OMNIC family also includes several optional software packages for quantitative analysis, spectral interpretation, macro writing and more; all with the same easy to learn and use point-and-click interface as basic OMNIC software. Adding a spectral library from Nicolet's extensive collection lets you quickly and easily identify an unknown sample.

OMNIC can operate Nicolet's Magna-IR,® Impact™ and Raman series spectrometers or act as a stand-alone data manipulation package for data collected from any FT-IR spectrometer.

With so many applications, it's no wonder that OMNIC is one of the best liked software packages for the laboratory. For your free OMNIC demo disk, call 1-800-356-8088, ext. 2442.

MICROSOFT® WINDOWS™ COMPATIBLE

Nicolet
ANALYTICAL

A subsidiary of Thermo Instrument Systems, Inc., a Thermo Electron company
5225 Verona Road • Madison, WI 53711-4495 • U.S.A. • Tel: 608-271-3333 • FAX: 608-273-5046

Microsoft is a registered trademark & Windows and the Windows logo are trademarks of the Microsoft Corp. SmartPad is a trademark of SoftMax.

CIRCLE 4 ON READER SERVICE CARD

Report

IN VIVO NMR OF

In vivo NMR spectroscopy can be used to determine drug concentrations directly in tissues of interest and may provide new information on drug efficacy and metabolism

Richard A. Komoroski
University of Arkansas for Medical Sciences

Magnetic resonance imaging (MRI) has achieved an amazing level of success in clinical medicine as a noninvasive diagnostic tool. Moreover, NMR spectroscopy is favored by chemists as a powerful technique for molecular structure determination. It therefore seems natural that these clearly related techniques should merge to yield noninvasive, spatially localized NMR spectroscopy for determining molecular structure and concentration in vivo.

Considerable effort has been directed toward developing in vivo NMR spectroscopy as a clinical diagnostic tool. This effort has centered largely on probing endogenous biochemical metabolites by ^{31}P and ^{1}H NMR. Discussions of in vivo NMR spectroscopy have appeared elsewhere (*1–3*). Less commonly, in vivo NMR spectroscopy has been used to monitor drugs as well as other xenobiotic agents directly in both human and animal studies. These studies, especially the human trials, are of great interest because of their potential clinical applications.

Why in vivo NMR of drugs?

The magnitude of the pharmacologic or toxic effect of a drug is expected to depend on the concentration at the receptor sites, which are generally located in the tissue cells of the target organ (*4*). Of necessity, most tissue cells are usually in close contact with extracellular fluid, which is in close contact with blood. Therefore, measuring drug levels in plasma is a reasonable method for monitoring drug therapy. It is also relatively noninvasive and inexpensive, and a wide range of analytical techniques, including high-resolution NMR spectroscopy (*5*), can be used for quantitation or identification of drug metabolites. It is also possible to monitor drugs and toxic agents in urine and other body fluids, although analyte concentrations in these fluids are often less reflective of drug concentration at the active site than blood levels are. Of course, biopsy is sometimes possible, but it is highly invasive and not suited for routine monitoring of therapy.

For a variety of reasons, however, the plasma concentration of a drug may not reflect the concentration at the active site. Individual variations in drug pharmacokinetics and metabolism, which are common, may arise from individual differences in physiological function, disease state, diet, and other factors. For example, a drug may accumulate to a high level in tissue with long-term administration, whereas plasma levels remain lower and relatively constant.

Therapeutic (and/or toxic) response, which is the ultimate clinical measure of correct dosage, may correlate better with the drug concentration in tissue than with that in plasma. An in vivo probe of drug concentration in tissue may be useful in a variety of clinical settings. For psychiatric illnesses, accurate diagnosis is often problematic. Therapeutic response can be difficult to measure, and drug levels in plasma are often inadequate predictors of response. Moreover, drug metabolism

0003-2700/94/0366-1024A/$04.50/0
© 1994 American Chemical Society

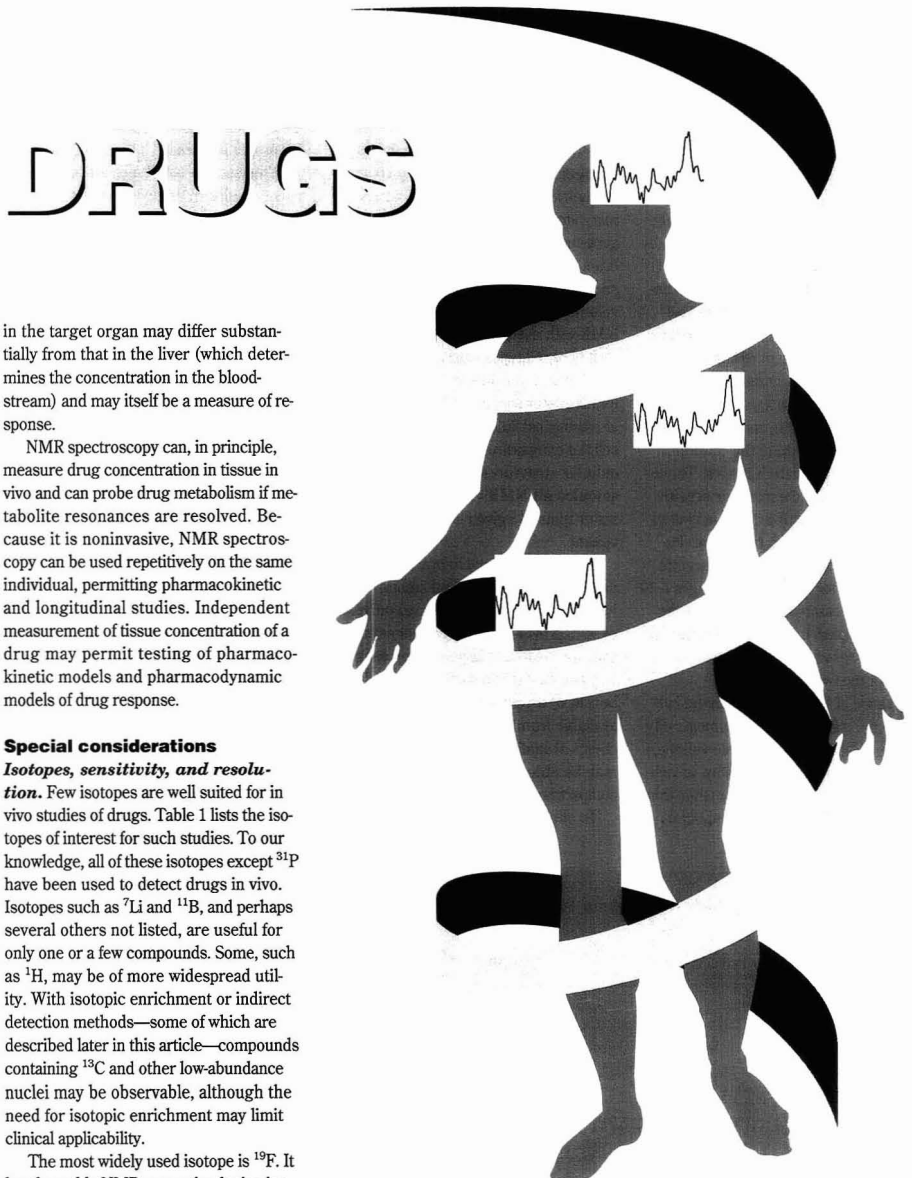

in the target organ may differ substantially from that in the liver (which determines the concentration in the bloodstream) and may itself be a measure of response.

NMR spectroscopy can, in principle, measure drug concentration in tissue in vivo and can probe drug metabolism if metabolite resonances are resolved. Because it is noninvasive, NMR spectroscopy can be used repetitively on the same individual, permitting pharmacokinetic and longitudinal studies. Independent measurement of tissue concentration of a drug may permit testing of pharmacokinetic models and pharmacodynamic models of drug response.

Special considerations

Isotopes, sensitivity, and resolution. Few isotopes are well suited for in vivo studies of drugs. Table 1 lists the isotopes of interest for such studies. To our knowledge, all of these isotopes except ^{31}P have been used to detect drugs in vivo. Isotopes such as ^{7}Li and ^{11}B, and perhaps several others not listed, are useful for only one or a few compounds. Some, such as ^{1}H, may be of more widespread utility. With isotopic enrichment or indirect detection methods—some of which are described later in this article—compounds containing ^{13}C and other low-abundance nuclei may be observable, although the need for isotopic enrichment may limit clinical applicability.

The most widely used isotope is ^{19}F. It has favorable NMR properties for in vivo

studies, including a nuclear spin of 1/2 and relatively narrow lines, high sensitivity (83% that of ^1H), and short spin–lattice relaxation times (T_1). In NMR a shorter T_1 permits more rapid signal averaging for sensitivity enhancement. Because ^{19}F is not present in biological systems to any significant extent, there is no background signal, and any ^{19}F signals observed must originate from the drug. Also, many drugs on the market contain fluorine as a part of their molecular structure.

The major limitation of in vivo NMR drug studies is low sensitivity. In normal use, most drugs do not reach sufficiently high tissue concentrations for detection by NMR in vivo. Table 1 gives estimated minimum detectable concentrations under favorable circumstances for the isotopes listed. These values are comparable to those given in a recent review (*6*).

Several factors, including intrinsic sensitivity, presence of background signal, magnetic field strength, and volume of tissue sampled, determine the minimum detectable concentration in vivo. Therefore it is difficult to compare the sensitivity of NMR for detecting drugs in biological fluids in vitro (*5*) with the in vivo situation. The typical in vivo tissue concentration necessary for detection of a drug is 1–10 times that necessary in vitro, because the volumes sampled, magnetic field strengths used, and resonance linewidths vary widely for the two situations (*6*).

Because of factors such as tissue heterogeneity, magnetic field inhomogeneity over the relatively large sample volume, and restricted molecular mobility, in vivo linewidths are substantially broader than those obtained for the pure compounds in solution. Of these factors, tissue heterogeneity probably makes the largest contribution to the in vivo linewidth. In addition, in vivo studies are usually conducted at lower magnetic field strengths than in vitro studies. Thus resolution in multicomponent spectra may be much lower in vivo, and compounds of similar molecular structure, such as drug metabolites, may not be resolved.

In vivo concentrations. A number of factors complicate the determination of endogenous metabolite or drug concentrations in vivo by NMR spectroscopy. Primary among these factors is the heterogeneous nature of biological tissue. The brain is a pertinent example—a relatively small volume of 0.5–1 mL (the smallest volume that can be sampled discretely by NMR with current technology) contains a variety of cell types (various types of neuronal and glial cells), vascular space, and extracellular space (perhaps including cerebrospinal fluid). Of course, within the cellular compartments is a variety of subcellular structures. NMR spectroscopy samples all NMR-visible (i.e., liquid-state) spins of a given isotope in the active volume.

Without additional information on the distribution of a compound among the various compartments, NMR can only be used to provide an average concentration over the relatively large volume sampled. In some cases, information on the distribution of a compound or an ion may be available from previous invasive or biochemical studies. In a limited way, NMR may be able to provide information on compartmental distribution (*7*).

In clinical applications, endogenous metabolite concentrations are often measured to assess the health of the tissue involved. However, metabolite NMR signals are sensitive both to decreases in metabolite concentration within the cell and to loss of cells from the tissue (with unchanged metabolite concentration in the remaining cells). Without additional histological information, the two possibilities cannot be distinguished by NMR, although such a distinction may be critical for proper diagnosis.

The issue of NMR measurement of concentration in tissue is somewhat different for drugs than for metabolites. For drugs, the compartmental distribution will be important in that the pertinent receptors probably reside in one compartment alone. However, even if the compartmental distribution is not available, the overall drug concentration in the tissue should be an acceptable alternative to concentration at the active site and should be highly superior to plasma concentration.

Measurement of absolute concentration, even with the above limitations, requires calibration to a signal of known concentration, such as tissue water or an external standard phantom. To avoid the problems of these methods, intensity ratios to an internal standard are often obtained. For a single-line spectrum, this solution is not possible, and an external standard may be necessary.

Signal visibility. The above considerations of in vivo concentration assume that all of a given species is in a liquid-like state and is contributing to the NMR signal of interest. The compound must reside in one of the fluid spaces in the tissue or be in rapid chemical exchange with the solution state if undergoing weak binding to macromolecules or membranes. These assumptions, however, are not always the case. Low molecular weight metabolites and drugs can bind strongly to a variety of macromolecules or to the cell membrane. This binding can greatly restrict the molecular mobility of the small molecules, broaden the NMR resonance, and render the metabolite or the drug invisible to high-resolution NMR.

Another factor is partitioning. Drugs are often lipophilic and may enter the cell membrane. The fraction of the total amount of drug that is represented by the in vivo NMR signal remains a question

Table 1. NMR isotopes for in vivo drug studies

Isotope	Natural isotopic abundance (%)	NMR receptivity[a]	Natural concentration (mmol/L)[b]	Minimum concentration (mmol/L)[c]
^1H	100.0	100.0	0.5–10	0.1
^7Li	92.6	27.2	—	0.1
^{11}B	80.4	13.3	—	5–10
^{13}C	1.1	0.018	10	50
^{19}F	100.0	83.4	—	0.05
^{31}P	100.0	6.65	1–20	1

[a] NMR receptivity relative to ^1H from Reference 26.
[b] Typical concentration of detectable endogenous metabolites.
[c] Estimated minimum detectable concentration under favorable circumstances.

that can be answered definitively only by in vivo measurement followed by in vitro analysis of the same tissue.

Instrumental requirements. In vivo studies of drugs are carried out with the same instrumentation used for studies of endogenous metabolites (*1–3*). Simple studies without spatial localization can be done on very small animals (mice and rats) by using standard high-resolution NMR systems. For some time, research-grade systems for small animal studies have been available with horizontal-bore magnets (of ~ 30–40 cm bore size) and offer the capability of generating the magnetic field gradients necessary for NMR imaging and spatially localized spectroscopy. Human studies are usually performed on clinical MRI scanners at a field strength of 1.5 T or greater. However, most MRI scanners, even at 1.5 T, do not have spectroscopic capability. Some have the capability for ^{1}H spectroscopy but lack the broadband electronics necessary for non-^{1}H studies.

In our laboratory at the University of Arkansas for Medical Sciences, animal studies are performed on a General Electric Omega CSI system with a 33-cm bore, 4.7-T magnet. Human studies are performed on a General Electric Signa 1.5-T clinical MRI system with multinuclear spectroscopic capability. For multinuclear studies on humans or animals, it is usually necessary to build the tuned radio-frequency (rf) coils in house. The frequency, size, and shape of such coils are designed for a particular experiment with the goal of maximizing sensitivity. Figure 1 shows the "birdcage" coil built for the ^{19}F studies of psychoactive drugs in human brain described below.

Spatial localization. The ability to restrict the spatial region that gives rise to an NMR spectroscopic signal in vivo is critical to clinical utility. The simplest method of spatial localization is restriction of the rf coil size and shape so as to excite and detect a signal from an approximate region of interest. Spatially localized spectroscopy using field gradients to define the region of interest has been undergoing rapid development, and many approaches are now available.

Successful performance of localized spectroscopy is dependent on several factors, but for drugs the most important is sensitivity. Most in vivo drug studies have been performed with only the crudest localization because of inadequate signal strength from regions of smaller size. Under these circumstances care must be exercised in interpreting such signals, which may arise from several different anatomical regions.

Multinuclear applications

For most in vivo drug studies, nonhydrogen NMR isotopes, primarily ^{19}F, have been used to measure concentration, distribution, or pharmacokinetics. A number of related biomedical applications of ^{19}F NMR, such as imaging of perfluorocarbon blood substitutes or of regional glucose metabolism by using fluorinated glucose analogues, have been reviewed by Thomas (*8*). The following multinuclear applications demonstrate the advantages and limitations of the technique.

Psychoactive drugs. In most cases, serum concentrations of psychoactive drugs used to treat mental illnesses provide little useful information concerning clinical response and side effects (*9*). A direct measure of drug concentration in brain tissue may be more relevant. Many psychoactive agents contain fluorine as a part of their molecular structure, although few reach sufficient concentration in the brain for detection by in vivo ^{19}F NMR. Initial work has centered on detection and quantitation of compounds containing trifluoromethyl groups, including the antidepressant fluoxetine (Prozac) and the antipsychotic agents trifluoperazine (Stelazine; TFP) and fluphenazine (*10*).

Figure 2 shows the ^{19}F NMR spectrum of the head of a 13-year-old patient who had been on a typical dose of 20 mg/day of fluoxetine for one month (*11*). The spectrum demonstrates a typical S/N, although patients on fluoxetine generally gave spectra with higher S/N than patients on the trifluorinated antipsychotics (*12*). The patient's brain had accumulated about the minimum concentration detectable for fluoxetine (~ 1.3 μg/mL). The second peak in the spectrum arises from a vial of a standard compound used to estimate the in vivo drug concentration. On the basis of data from 22 patients on fluoxetine treatment, we found that the brain concentration continued to increase

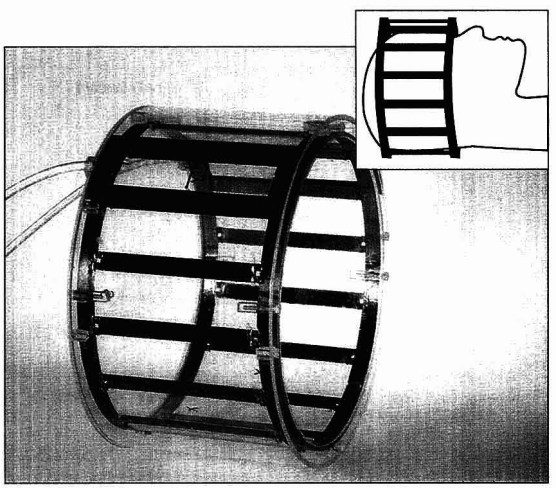

Figure 1. "Birdcage" volume rf coil designed for ^{19}F NMR studies of psychoactive drugs in human brain.
The coil is tuned to 60.1 MHz for operation on a 1.5-T clinical MRI system.

well after the clinical effects of the drug were evident and seemed to level off after a six- to eight-month period (*11*). The drug accumulated to levels of roughly 20 times those in plasma in the same patients. Because fluoxetine exerts a therapeutic effect within about two weeks, there appears to be no correlation of steady-state brain concentration with clinical response.

Fluoxetine metabolizes to the therapeutically active compound norfluoxetine in brain. As expected, the ^{19}F chemical shift of norfluoxetine is very close to that of fluoxetine, and the two compounds cannot be resolved in vivo. In vitro ^{19}F NMR studies of postmortem samples from a patient who had been on fluoxetine and confirmatory studies of brain extracts from rats given fluoxetine demonstrated that the in vivo signal arises in roughly equal proportion from fluoxetine and norfluoxetine. The in vivo spectra in Figure 2 were acquired using the coil shown in Figure 1. The coil detects drug in both brain and surrounding tissue; however, the contribution of drug and metabolites in nonbrain tissue to the in vivo signal was estimated at < 20% by low spatial resolution localized spectroscopy (*10*).

Antipsychotic drugs such as TFP, although given in oral milligram doses that are comparable to those for fluoxetine, do not visibly accumulate to the same extent in brain and give weaker ^{19}F NMR signals. Nevertheless, in unlocalized studies we observed signals for six responding patients taking different doses of TFP (*12*). A good correlation of brain concentration and daily dose was found. Interestingly, however, on four attempts we could not observe a signal from a nonresponding patient who was on a very high dose of the drug. This preliminary result suggests that the drug was not accumulating in that patient's brain at a detectable level. In vivo ^{19}F NMR may play a role in assessing the reasons for nonresponse to antipsychotic medication.

Lithium, typically given in the form of Li_2CO_3 tablets, is used to treat mania and manic-depressive illness. Serum Li concentrations are usually maintained in the therapeutic range of 0.5–1.2 mmol/L, although 20–40% of patients respond poorly or not at all. Serum Li concentrations above 2 mmol/L are often toxic, although neurotoxicity can also be seen in the nominal therapeutic range in some patients. These considerations suggest that the Li concentration in brain may be a better measure of efficacy and/or neurotoxicity than the concentration in serum. Moreover, the distribution of Li in brain may help elucidate its still unknown mechanism of action.

The ^{7}Li isotope is relatively favorable for in vivo NMR spectroscopy studies (Table 1). Moreover, the tissue concentration necessary for successful therapy is sufficiently high to make in vivo detection, and even low spatial resolution localized spectroscopy, feasible. Following the pioneering work of Renshaw and co-workers (*13*), several groups, including our own, have pursued in vivo ^{7}Li NMR in humans and animals. The topic has been recently reviewed (*14, 15*).

In animals, effort has been directed toward developing methods for measuring the pharmacokinetics of Li uptake in brain. Using a stimulated echo acquisition mode (STEAM) sequence for spatial localization, Ramaprasad et al. (*16*) found time constants of 48–98 min for the uptake of a single dose of Li in rat brain with signals that were uncontaminated by those from surrounding tissue. Because relatively high doses and long data acquisition times can be used for anesthetized animals, it was possible to obtain informative ^{7}Li NMR images in the rat.

Figure 3 shows sagittal ^{1}H and ^{7}Li images of the head of a rat dosed with Li. The quality of the ^{7}Li image is such that the overall shape of the head and neck is reasonably well defined. The strongest signals come from muscle at the back of the head and neck.

Intensities in the brain region are typically half of those for muscle. Within the brain region the intensity is relatively uniform, although the intensity in the cerebellum is lower than that in the frontal region. Before such images can be used reliably to measure local Li concentrations, issues concerning relaxation times, visibility, and compartmentalization must be resolved.

Most ^{7}Li work in vivo has centered on humans. Initial unlocalized studies mea-

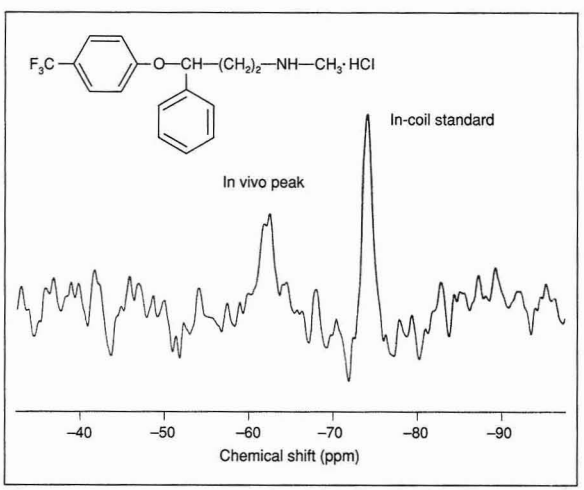

Figure 2. Chemical structure of fluoxetine and the in vivo ^{19}F NMR spectrum from the head of a 13-year-old.

The in vivo peak arises from fluoxetine and the metabolite norfluoxetine. The in-coil standard peak is from a vial of 12 mmol/L 2,2,2-(trifluoroethyl)-*p*-toluene sulfonate in $CDCl_3$ mounted on the side of the head with an elastic band. (Adapted with permission from Reference 10.)

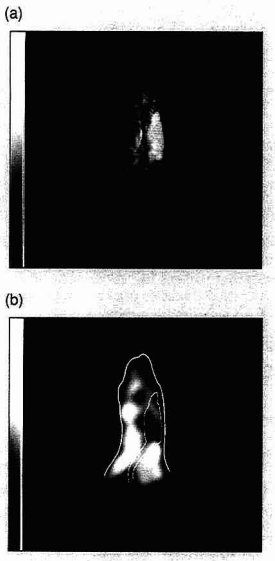

Figure 3. NMR images of the head of a rat dosed with lithium.

(a) Midline sagittal ^{1}H NMR image used for localization of ^{7}Li imaging. (b) ^{7}Li image after a multidose protocol of intraperitoneal LiCl. In this image, the outer line defines the shape and location of the rat head, and the inner line the brain and spinal cord. The pulse repetition time was 7 s, and the image took 4 h to acquire. The resolution was 4 mm in-plane, with a 7-mm slice thickness. (Adapted with permission from Reference 16.)

sured the pharmacokinetics of uptake and elimination and compared serum and brain concentrations (*14*, *15*, *17*, *18*). Several ^{7}Li studies in vivo confirmed that brain Li concentration is typically 0.1–0.6 mmol/L, which is 0.4–0.6 times the serum concentration.

Li is eliminated from the body relatively rapidly ($t_{1/2}$= 0.5–1 day). Figure 4a shows the results for a subject who had been on Li therapy for more than six months and was considered to be at steady state (*18*). After a single 300-mg dose of Li_2CO_3, the concentrations in brain and calf muscle (by ^{7}Li NMR) and in serum (by flame photometry) were monitored for 6 h. At the low time resolution of these experiments, the levels in serum and muscle peaked after ~ 2 h, whereas the level in brain peaked after ~ 4 h. Thus, although there is some delay for Li to cross the blood–brain barrier, the delay is short and cannot account for the well-known delay of ~ 1 week for Li to exert clinical efficacy.

Figure 4b shows serial results for the same subject after he was taken off of Li treatment because he developed a tremor (*19*). Initially the Li levels dropped rapidly. At six days after terminating Li therapy, ^{7}Li in vivo NMR no longer detected Li in muscle but did detect it in brain. At 10 days, no signal was detected from brain.

This result is of interest because the toxic symptoms took about a week to subside, a result that suggests that in vivo ^{7}Li NMR could be used to relate toxic effects to residual brain concentration. Preliminary spectroscopic imaging of the spatial distribution of Li in human brain has also been performed (*19*) and may shed light on the mechanisms of the therapeutic and toxic effects of Li.

Antineoplastic agents. A widely used cytotoxic drug for the treatment of colorectal and breast cancer is 5-fluorouracil (5-FU). The cytotoxic effect of 5-FU is attributed to the anabolic formation of fluoronucleosides and fluoronucleotides that interfere with DNA and RNA metabolism. The drug, which is used in combination with other compounds that modulate its metabolism, is effective in only ~ 20% of patients. Clinicians still cannot predict who will respond to the drug, despite its long history of use. Lack of response may be related to the effectiveness of the competitive catabolic pathway, in which 5-FU is metabolized in the liver in the manner of endogenous pyrimidines.

Both 5-FU and its major catabolite, α-fluoro-β-alanine (FBAL), are readily observable in human liver by ^{19}F NMR in vivo with a surface coil after a typical intravenous bolus injection of 1 g of the drug has been delivered over 10 min. Figure 5 shows a typical pharmacokinetic assay in the liver for a patient on prophylactic chemotherapy for breast cancer (*20*). Because they are quite different chemically, 5-FU and its catabolite FBAL are well resolved spectroscopically. Under these conditions of drug administration, sensitivity is sufficient to acquire a spectrum in several minutes, permitting pharmacokinetic analysis. Unfortunately, the therapeutically important metabolites are usually not seen, except with extensive signal averaging (*21*).

Of course, more important than the metabolism in healthy liver is the metabolism in tumors. Wolf (*22*), Presant (*23*, *24*), and co-workers have been using ^{19}F NMR in vivo to monitor the pharmacokinetics of 5-FU elimination from human tumors as a predictor of therapeutic response to the drug. They observe only the disappearance of 5-FU, not FBAL or therapeutic metabolites, in tumors. Their hypothesis, which is supported by human and animal data, is that responding tumors pool 5-FU and display a long $t_{1/2}$ for elimination; non-

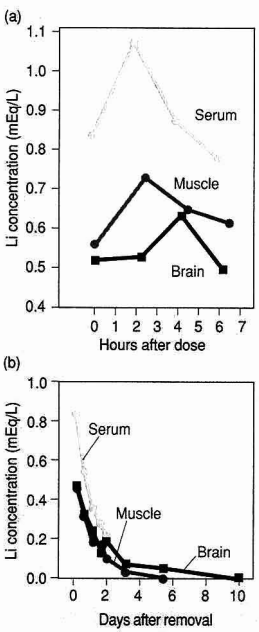

Figure 4. Li concentrations in serum, brain, and calf muscle.

(a) Concentration profiles for a subject at steady state after a 300-mg oral dose of Li_2CO_3. (Adapted with permission from Reference 18.) (b) Plots of Li concentrations for a subject removed from Li therapy. The serum values are plotted to the lowest level reported in the serum Li assay. (Adapted with permission from Reference 19.)

responding tumors tend to display a short $t_{1/2}$ like that in blood or liver.

Figure 6 shows the 5-FU elimination curves for tumors from responding and nonresponding patients that demonstrate this behavior and compares them with a control. The ability of some tumors to trap 5-FU is not well understood; it probably arises from factors such as vascularization of the tumor and transmembrane transport of the drug into tumor cells.

At last report (*24*), this trapping behavior was proving true for the 57 patients studied to that point, although many are still being evaluated for clinical response. Of 9 patients with tumors that demonstrated trapping, 8 had partial responses to 5-FU chemotherapy, whereas only 2 of 25 whose tumors did not trap the drug were considered responsive. The patients had primary tumors in a wide variety of sites, so the approach appears to be generally applicable, although with surface coils only tumors at least 2 cm in diameter and located within ~ 8 cm of the skin surface can be studied.

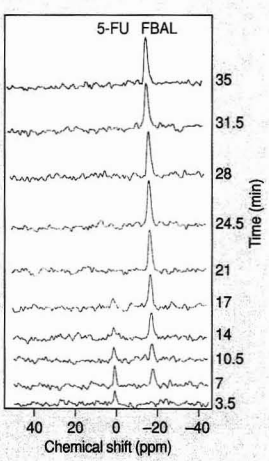

Figure 5. Stacked plot of sequential in vivo ^{19}F NMR spectra.

The patient received a bolus injection (600 mg/m^2 of body surface area 2 h after administering methotrexate) of 5-FU over 10 min (–5 to +5 min). Each spectrum is the baseline-corrected result of 200 acquisitions (~ 3.5 min/spectrum). The chemical shift scale is in ppm from 5-FU.

If the correlation between drug trapping and therapeutic response holds for a sufficiently large number of patients, this technique should be useful for developing and optimizing treatment protocols. It could also be considered for application to real-time clinical decision making in individual chemotherapy (*25*). For example, alternative chemotherapy could be considered more quickly for patients whose tumors do not trap 5-FU.

Neutron capture agents. In boron neutron capture therapy (BNCT), a pharmaceutical containing boron is administered to a cancer patient prior to irradiation of tumor-containing regions with thermal neutrons. Collision of the neutrons with ^{10}B nuclei releases alpha particles, which have relatively short trajectories and hence only damage cells in the immediate vicinity of the collision. A technique to probe the distribution of such pharmaceutical agents in tissue would be valuable for their development and perhaps even for guidance of BNCT in the clinic.

Of the two boron isotopes available for NMR, ^{11}B has the more favorable NMR properties (*26*). Kabalka and co-workers (*27*) have developed ^{11}B MRI and NMR spectroscopy, optimized for the short spin–spin relaxation time (T_2) of ^{11}B, to monitor the distribution and pharmacokinetics of BNCT agents in laboratory animals. A rat was administered the BNCT agent $B_{24}H_{22}S_2^{4-}$ (BSSB) by a surgically implanted osmotic pump that delivered 224 μg B/g body weight over seven days. A day after stopping infusion, the feasibility of the technique was demonstrated by performing ^{11}B NMR spectroscopy and MRI at 1 cm in-plane resolution.

Because the compounds administered to patients are highly enriched in ^{10}B, the ^{11}B approach may not be feasible in the clinic. Bendel et al. (*28*) have used indirect detection of ^{10}B via spin-coupled ^{1}H NMR, whereby the ^{1}H signal is detected with and without modulation (by heteronuclear decoupling or insertion of 180° pulses) of the ^{1}H–^{10}B coupling. Upon subtraction, only the protons coupled to ^{10}B remain and are detected at the higher ^{1}H sensitivity. The indirect detection of heteronuclei using spin-coupled protons is an approach that could see increasing use in a variety of drug studies in vivo.

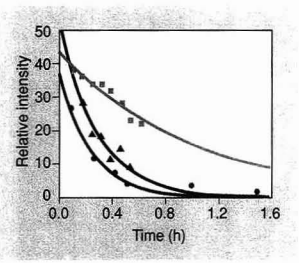

Figure 6. Clearance of 5-FU from tumors of responding (■) and nonresponding (▲) patients, and from the blood of a control patient (●).

The clearance times ($t_{1/2}$) were 41.3 ± 5.5, 15.5 ± 2.9, and 9.6 ± 1.4 min, respectively. (Adapted with permission from Reference 23.)

Anesthetics. Anesthesia during surgery is commonly maintained using fluorine-containing inhalation agents such as halothane and isoflurane. The mechanism of action of these anesthetics and their interactions with brain tissue are not well understood. Of particular interest are the distribution of anesthetic in the brain and the pharmacokinetics of elimination. Early studies demonstrated that such anesthetics could be observed in animal tissues using in vivo ^{19}F NMR spectroscopy, although there was considerable controversy concerning the pharmacokinetics of elimination, the spatial origin of the signals, and the number of signal components (*29–31*).

Particular care is required in unlocalized studies of such lipophilic molecules because of the possibility of contamination from components in fat; the multiple time constants for elimination; the short T_2s, which complicate observation of the total ^{19}F signal; and variable physiological factors. It appears that volatile fluorinated anesthetics may exist in more than one environment in brain, and measurable concentrations may persist for a relatively long time. Menon et al. (*32*) have demonstrated the possibility of observing cerebral halothane in patients up to 90 min after surgery by using ^{19}F NMR in vivo. More work is necessary to determine the spatial origin of the signals, the elimination pharmacokinetics, and the metabolism of these anesthetics before such studies can have clinical utility.

Measurement of oxygen tension. Because of their biochemical inertness and ability to dissolve large amounts of oxygen, liquid perfluorocarbon compounds have shown increasing utility as respiration and blood substitutes. ^{19}F MRI and NMR spectroscopy have been used to monitor these compounds in vivo (*8*). One particularly interesting spectroscopic property of these compounds is that their ^{19}F spin–lattice relaxation rates ($1/T_1$) depend linearly on the partial pressure of dissolved oxygen (P_{O_2}).

In a novel application, Wilson and coworkers (*33*) have used ^{19}F NMR to measure P_{O_2} at the surface of the retina in a human eye. Such a measurement is important in that retinal hypoxia may play a role in diseases such as diabetic retinopathy and retinal venous occlusion. In this study, a patient's retinal tear was repaired in a surgical operation that involved the use of a vitreous substitute of high specific gravity, perfluorotributylamine (FTBA), to flatten and position the retina. Although the FTBA was removed to the maximum extent possible after surgery, small (~ 3.1 μL) but visible droplets remained (Figure 7a), as is common but apparently inconsequential. These workers then measured the ^{19}F T_1s of the droplets in vivo (Figure 7b), and estimated the P_{O_2} to be 6–9 mm Hg from a calibration curve. This method should permit noninvasive, longitudinal measurement of P_{O_2} in the human eye to gain further insight into the evolution of ischemic ocular diseases.

Localized ^1H NMR of drugs in vivo

Given that most drugs do not contain an NMR label such as ^{19}F, it might be expected that the more generally applicable and sensitive nucleus ^1H would be preferable for detection of drugs in vivo. Applications of gradient-localized in vivo ^1H NMR spectroscopy are becoming widespread, and the technique is beginning to have clinical impact (*34*). However, the presence of signals from endogenous metabolites at ~ 1 mmol/L or greater substantially raises the minimum concentration of a drug that can be detected.

The relatively small range of chemical shifts and the necessity of suppressing the large H_2O peak make it more difficult to use the very large volumes commonly analyzed for ^{19}F NMR and thus also make ^1H NMR less desirable for in vivo detection of drugs. It may be possible to monitor drugs with a low therapeutic index (drugs that require administration of relatively large amounts to achieve therapeutic efficacy), drugs that accumulate in the organ of interest, or drugs that reach high local concentrations for short periods (e.g., 5-FU). Many drugs contain one or more aromatic rings in their molecular structure, and this region in the ^1H NMR spectrum in vivo is relatively free of potentially interfering background resonances.

Ethanol in brain. Ethanol has been detected by localized ^1H NMR spectroscopy in human and animal brain in vivo (*35–38*). Because ethanol freely penetrates the blood–brain barrier and is typically ingested in larger amounts than ther-

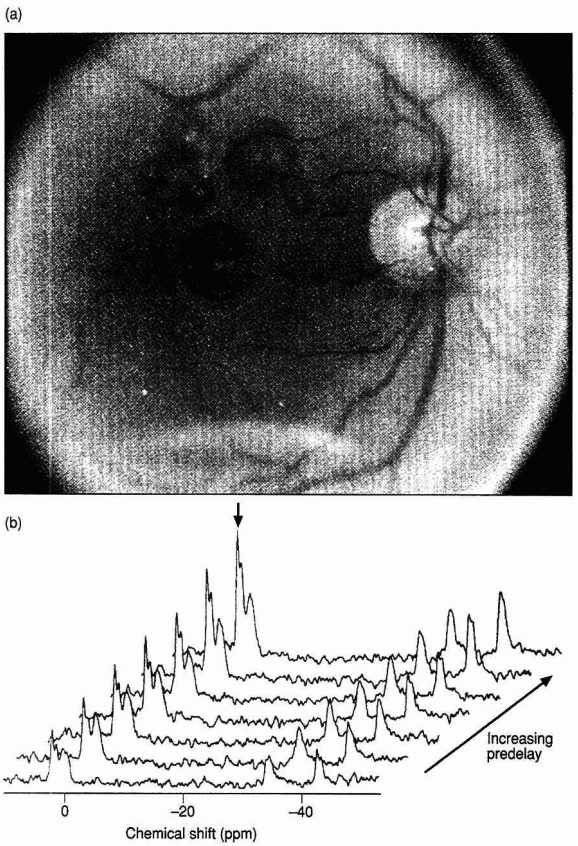

Figure 7. Fundus photograph of a human eye and ^{19}F T_1 measurement.

(a) After repair of a retinal tear and detachment with the use of intraoperative FTBA; residual FTBA droplets are shown. (b) In vivo ^{19}F T_1 of FTBA droplets in the eye. The intensity of the CF_3 peak (arrow) varied with predelay time (time between successive excitation pulses: 400, 500, 600, 800, 1000, 1200, and 4000 ms, front to back) and was used to measure T_1. (Adapted with permission from Reference 33.)

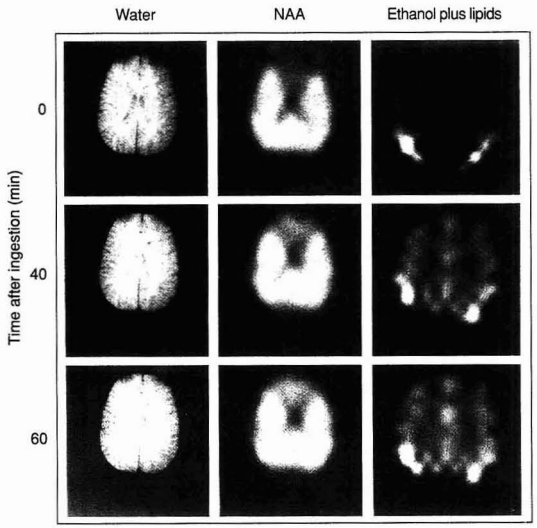

Figure 8. In vivo spectroscopic localization of water, NAA, and ethanol plus lipids in human brain.

Inversion time, 200 ms; echo time, 272 ms; repetition time, 2 s; 1.5 × 1.5 × 1.5 cm voxels; 17-min data acquisition; 16 × 16 spectroscopic images interpolated to 256 × 256 and shown with an edge-detected overlay of the water image to provide anatomical landmarks. (Adapted with permission from Reference 37.)

apeutic drugs, it is relatively straightforward to observe its CH_3 signal in vivo.

Initial studies (*35*) centered on measurement of brain alcohol concentration and correlation with blood alcohol concentration (BAC). However, issues surrounding signal visibility and interference from lipid signals have been raised, particularly with the work of Moxon et al. (*36*), in which signal visibility was found to be only 23% of BAC when *N*-acetylaspartate (NAA) was used as an internal reference. The reduced visibility was attributed to a combination of factors, including the suggestion of a pool of NMR-invisible ethanol, which might be bound in some manner to the phospholipid cell membranes in brain tissue.

More recent work (*37*), in which spectroscopic imaging (SI) was used at a spatial resolution of 1.5 cm, demonstrated that the distribution of ethanol in the brain is nonuniform. Figure 8 shows the SI results for a subject who had ingested 0.8–0.9 g of ethanol ~ 40–60 min before scanning. The image of ethanol distribution shows considerable nonuniformity; the apparent concentrations in cerebrospinal fluid, gray matter, and white matter were estimated as 23.0, 16.6, and 8.3 mmol/L, respectively. If the issues of signal visibility and multiple pools of ethanol can be clarified satisfactorily, such measurements may be useful for studying the relationship of ethanol's behavioral and physiological effects to brain concentration and distribution. The interaction of ethanol with membranes may be related to an individual's tolerance to the drug (*38*).

Silicone gel implants. Recently there has been considerable public controversy regarding the safety of silicone gel-filled breast implants. Concerns include the possible rupture of the silicone-rubber membrane encasing the gel and the bleeding of free silicone through the intact envelope into the surrounding tissue. Garrido and co-workers (*39, 40*) have used a modified SI technique and single-voxel localized spectroscopy to monitor the distribution of silicone in various organs in animals and humans. Observation of silicone is seemingly straightforward given the fact that the six equivalent $Si(CH_3)_2$ protons resonate upfield of common in vivo resonances. However, these workers found it necessary to modify existing pulse sequences to generate efficient suppression of both water and fat resonances.

Figure 9a shows a STEAM localized ^1H spectrum of a voxel from the liver of a patient who had silicone implants for 18 years. A strong resonance attributed to both hydrolyzed and chemically unchanged silicone was observed at ~ 0 ppm. No such resonance was seen for a subject without implants (Figure 9b). A silicone peak was present in localized ^1H spectra of liver for half of the six patients examined. Clearly, the above approach could be useful for detecting leakage and migration of silicone from implants in clinically important cases.

Future prospects

NMR spectroscopy and imaging are novel, noninvasive techniques for measuring the concentration, distribution, and pharmacokinetics of certain drugs in vivo in humans and animals. A potentially powerful feature of in vivo NMR is the ability to measure simultaneously the tissue con-

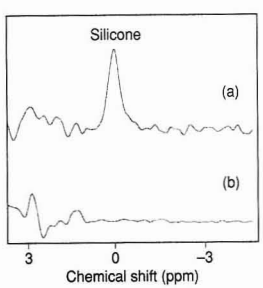

Figure 9. Localized ^1H spectrum of a voxel in the liver for (a) a patient with and (b) a subject without silicone implants.

The spectra were acquired using the STEAM pulse sequence combined with inversion recovery and chemical shift-selective saturation to suppress the large water and fat signals. Voxel volumes for (a) and (b) were 31 and 18 cm^3, respectively. (Adapted with permission from Reference 40.)

centration of a drug and related changes in brain metabolism, for example, by ^{1}H or ^{31}P NMR monitoring of endogenous metabolites (*41*). Although NMR techniques have significant limitations, in particular low sensitivity, their noninvasive character and unique information content ensure that new applications and methodological improvements will continue to appear. Higher magnetic fields, more sensitive detection coils, and postprocessing methods such as Bayesian statistical estimation of spectral parameters (*42*) should substantially reduce the minimum detectable drug concentration in vivo and/or improve spatial resolution.

Very recently, Albert et al. (*43*) obtained magnetic resonance images of mouse lungs using ^{129}Xe gas (a safe general anesthetic) that had been magnetically hyperpolarized by spin exchange with optically pumped Rb vapor. This procedure produced ~ 10^5-fold enhancement of the ^{129}Xe NMR signal, permitting rapid imaging of the distribution of Xe gas in the lungs and surrounding tissue. Beyond the obvious imaging applications in vivo, NMR spectroscopy of laser-polarized Xe in tissue may be a sensitive probe of the local environment or of O_2 concentration via the ^{129}Xe chemical shift or spin relaxation times.

I thank J.E.O. Newton for his careful reading of the manuscript.

References

(1) Gadian, D. G. *Nuclear Magnetic Resonance and Its Application to Living Systems*; Clarendon: Oxford, 1982.

(2) Cady, E. B. *Clinical Magnetic Resonance Spectroscopy*; Plenum: New York, 1990.

(3) *In Vivo Magnetic Resonance Spectroscopy I–III*; Rudin, M., Ed.; Springer-Verlag: Berlin, 1992.

(4) Shargel, L.; Yu, A.B.C. *Applied Biopharmaceutics and Pharmacokinetics*, 2nd ed.; Appleton-Century-Crofts: Norwalk, CT, 1985.

(5) Nicholson, J. K.; Wilson, I. D. *Prog. NMR Spectrosc.* **1989**, *21*, 449–501.

(6) Malet-Martino, M-C.; Martino, R. *Clin. Pharmacokinet.* **1991**, *20*, 337–49.

(7) Ernst, T.; Kreis, R.; Ross, B. D. *J. Magn. Reson. Ser. B* **1993**, *102*, 1–8.

(8) Thomas, S. R. In *Magnetic Resonance Imaging, Volume II: Physical Principles and Instrumentation*, 2nd ed.; Partain, C. L.; Price, R. R.; Patton, J. A.; Kulkarni, M. V.; James, A. E., Eds.; W. B. Saunders: Philadelphia, 1988; pp. 1536–52.

(9) Komoroski, R. A. *Am. J. Neuroradiol.* **1993**, *14*, 1038–42.

(10) Komoroski, R. A.; Newton, J.E.O.; Cardwell, D.; Sprigg, J.; Pearce, J.; Karson, C. N. *Magn. Reson. Med.* **1994**, *31*, 204–11.

(11) Karson, C. N.; Newton, J.E.O.; Livingston, R.; Jolly, J. B.; Cooper, T. B.; Sprigg, J.; Komoroski, R. A. *J. Neuropsychiatry Clin. Neurosci.* **1993**, *5*, 322–29.

(12) Karson, C. N.; Newton, J.E.O.; Mohanakrishnan, P.; Sprigg, J.; Komoroski, R. A. *Psychiatry Res.: Neuroimaging* **1992**, *45*, 95–104.

(13) Renshaw, P. F.; Haselgrove, J. C.; Leigh, J. S.; Chance, B. *Magn. Reson. Med.* **1985**, *2*, 512–16.

(14) Kato, T.; Takahashi, S.; Inubushi, T. *Lithium* **1994**, *5*, in press.

(15) Ramaprasad, S.; Komoroski, R. A. *Lithium* **1994**, *5*, 127–38.

(16) Ramaprasad, S.; Newton, J.E.O.; Cardwell, D.; Fowler, A. H.; Komoroski, R. A. *Magn. Reson. Med.* **1992**, *25*, 308–18.

(17) Renshaw, P. F.; Wicklund, S. *Biol. Psychiatry* **1988**, *23*, 465–75.

(18) Komoroski, R. A.; Newton, J.E.O.; Walker, E.; Cardwell, D.; Jagannathan, N. R.; Ramaprasad, S.; Sprigg, J. *Magn. Reson. Med.* **1990**, *15*, 347–56.

(19) Komoroski, R. A.; Newton, J.E.O.; Sprigg, J. R.; Cardwell, D.; Mohanakrishnan, P.; Karson, C. N. *Psychiatry Res.: Neuroimaging* **1993**, *50*, 67–76.

(20) Hutchins, L.; Nauke, S.; Sprigg, J.; Jagannathan, N.; Cardwell, D.; Tranum, B.; Mohanakrishnan, P.; Komoroski, R. A. *Abstracts of Papers*, 9th Annual Meeting, Society of Magnetic Resonance in Medicine, Aug. 18–24, 1990; New York, Abstract 949.

(21) Schlemmer, H-P.; Bachert, P.; Semmler, W.; Hohenberger, P.; Schlag, P.; Lorenz, W. J.; van Kaick, G. *Magn. Reson. Imaging* **1994**, *12*, 497–511.

(22) Wolf, W.; Presant, C. A.; Servis, K. L.; El-Tahtawy, A.; Albright, M. J.; Barker, P. B.; Ring, R. III; Atkinson, D.; Ong, R.; King, M.; Singh, M.; Ray, M.; Wiseman, C.; Blayney, D.; Shani, J. *Proc. Natl. Acad. Sci. USA* **1990**, *87*, 492–96.

(23) Presant, C. A.; Wolf, W.; Albright, M. J.; Servis, K. L.; Ring, R., III; Atkinson, D.; Ong, R. L.; Wiseman, C.; King, M.; Blayney, D.; Kennedy, P.; El-Tahtawy, A.; Singh, M.; Shani, J. *J. Clin. Oncol.* **1990**, *8*, 1868–73.

(24) Presant, C. A.; Wolf, W.; Waluch, V.; Wiseman, C.; Kennedy, P.; Blayney, D.; Brechner, R. R. *Lancet* **1994**, *343*, 1184–87.

(25) Price, P.; Griffiths, J. *Lancet* **1994**, *343*, 1174–75.

(26) *NMR and the Periodic Table*; Harris, R. K.; Mann, B. E., Eds.; Academic: London, 1978.

(27) Kabalka, G. W.; Cheng, G-Q.; Bendel, P.; Micca, P. L.; Slatkin, D. N. *Magn. Reson. Imaging* **1991**, *9*, 969–73.

(28) Bendel, P.; Zilberstein, J.; Salomon, Y. *Magn. Reson. Med.* **1994**, *32*, 170–74.

(29) Wyrwicz, A. M. *Ann. N. Y. Acad. Sci. (USA)* **1991**, *625*, 733–42.

(30) Litt, L.; Lockhart, S.; Cohen, Y.; Yasuda, N.; Kim, F.; Freire, B.; Laster, M.; Peterson, N.; Taheri, S.; Chang, L-H.; Sessler, D. I.; Moseley, M.; Eger, E. I., II; James, T. L. *Ann. N. Y. Acad. Sci. (USA)* **1991**, *625*, 707–24.

(31) Evers, A. S.; Berkowitz, B. A.; D'Avignon, D. A. *Nature* **1987**, *328*, 157–60; Correction: *Nature* **1989**, *341*, 766.

(32) Menon, D. K.; Lockwood, G. G.; Peden, C. J.; Cox, I. J.; Sargentoni, J.; Bell, J. D.; Coutts, G. A.; Whitwam, J. G. *Magn. Reson. Med.* **1993**, *30*, 680–84.

(33) Wilson, C. A.; Berkowitz, B. A.; McCuen, B. W., II; Charles, H. C. *Arch. Ophthalmol.* **1992**, *110*, 1098–1100.

(34) Kreis, R.; Ross, B. D.; Farrow, N. A.; Ackerman, Z. *Radiology* **1992**, *182*, 19–27.

(35) Mendelson, J. H.; Woods, B. T.; Chiu, T-M.; Mello, N. K.; Lukas, S. E.; Teoh, S. K.; Sintavanarong, P.; Cochin, J.; Hopkins, M. A.; Dobrosielski, M. *Alcohol* **1990**, *7*, 443–47.

(36) Moxon, L. N.; Rose, S. E.; Haseler, L. J.; Galloway, G. J.; Brereton, I.; Bore, P.; Doddrell, D. M. *Magn. Reson. Med.* **1991**, *19*, 340–48.

(37) Spielman, D. M.; Glover, G. H.; Macovski, A.; Pfefferbaum, A. *Alcoholism: Clin. Exp. Res.* **1993**, *17*, 1072–77.

(38) Chiu, T-M.; Woods, B. T.; Teoh, S. K.; Levisohn, L.; Mendelson, J. H. *Abstracts of Papers*, 11th Annual Meeting, Society of Magnetic Resonance in Medicine, Aug. 8–14, 1992; Berlin, Germany, p. 1958.

(39) Pfleiderer, B.; Ackerman, J. L.; Garrido, L. *Magn. Reson. Med.* **1993**, *29*, 656–59.

(40) Garrido, L.; Pfleiderer, B.; Jenkins, B. G.; Hulka, C. A.; Kopans, D. B. *Magn. Reson. Med.* **1994**, *31*, 328–30.

(41) Kato, T.; Takahashi, S.; Shioiri, T.; Inubushi, T. *J. Affective Disorders* **1993**, *27*, 53–60.

(42) Bretthorst, G. L.; Hung, C-C.; D'Avignon, D. A.; Ackerman, J.J.H. *J. Magn. Reson.* **1988**, *79*, 369–76.

(43) Albert, M. S.; Cates, G. D.; Driehuys, B.; Happer, W.; Saam, B.; Springer, C. S., Jr.; Wishnia, A. *Nature* **1994**, *370*, 199–201.

Richard A. Komoroski received his B.S. degree from St. Louis University in 1969 and his Ph.D. in physical chemistry from Indiana University in 1973. After completing a postdoctoral position at Florida State University, he spent 10 years in industry at Diamond Shamrock and B.F. Goodrich, applying advanced NMR techniques to polymers and other industrial materials. In 1986 he joined the faculty of the University of Arkansas for Medical Sciences (Departments of Radiology and Pathology, NMR Laboratory, Little Rock, AR 72205), where his research focuses on applications of in vivo NMR spectroscopy and imaging for biomedicine and materials science.

Conferences

Kemia '94 Finnish Chemical Congress and Exhibition
Nov. 8–10. Helsinki, Finland
Contact: Eeva Kotaaho, Program Secretary, Hietaniemenkatu 2, FIN-00100 Helsinki, Finland (358-0-408-022; fax 358-0-408-780)

1994 Eastern Analytical Symposium
Nov. 13–18. Somerset, NJ
Contact: EAS, P.O. Box 633, Montchanin, DE 19710-0633 (302-738-6218; fax 302-738-5275)

Materials Research Society Fall Meeting
Nov. 28–Dec. 2. Boston, MA
Contact: Materials Research Society, 9800 McKnight Rd., Pittsburgh, PA 15237 (412-367-3003; fax 412-367-4373)

9th International Forum Process Analytical Chemistry and 3rd International Conference: On-Site Analysis
Jan. 22–25, 1995. Houston (Montgomery), TX
Contact: InfoScience Services, Inc., Conference Division, 3000 Dundee Rd., Suite 313, Northbrook, IL 60062 (708-291-9161; fax 708-291-0097)

4th International Conference on Automation, Robotics, and Artificial Intelligence Applied to Analytical Chemistry and Laboratory Medicine
Feb. 7–10, 1995. Montreux, Switzerland
Contact: SCITEC, Av. de Provence 20, CH-1000 Lausanne 20, Switzerland (41-21-624-15-33; fax 41-21-624-15-49)

Pittcon '95
March 5–10, 1995. New Orleans, LA
Contact: Pittsburgh Conference, 300 Penn Center Blvd., Suite 332, Pittsburgh, PA 15235-5503 (412-825-3220; fax 412-825-3224)

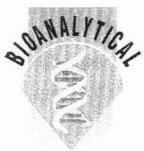

6th International Symposium on Pharmaceutical and Biomedical Analysis
April 23–26, 1995. St. Louis, MO
Contact: Shirley E. Schlessinger, Suite 1015, 400 East Randolph Dr., Chicago, IL 60601 (312-527-2011)

Symposium on Validation Practice for Biotechnology Products
April 24–25, 1995. Gaithersburg, MD
Contact: James K. Shillenn, Bioprocessing Resource Center, Penn State University, 519 Wartik Laboratory, University Park, PA 16802-9959 (814-863-3650; fax 814-863-1357)

5th International Symposium on Advances in Electrochemical Science and Technology
Nov. 24–26. Madras, India
Contact: The Secretary, Society for Advancement of Electrochemical Science and Technology, Karaikudi 623 006, India (91-4565-2368)

11th Montreux Symposium on LC/MS
Nov. 9–11. Montreux, Switzerland
Contact: M. Frei-Häusler, Postfach 46, CH-4123 Allschwil 2, Switzerland (41-61-481-27-89; fax 41-61-482-08-05)

7th Sanibel Conference on Physics and Chemistry of Multiply-Charged Ions
Jan. 21–24, 1995. Sanibel Island, FL
Contact: ASMS, 1201 Don Diego Ave., Santa Fe, NM 87501 (505-989-4517; fax 505-989-1073)

HPCE '95: 7th International Symposium on High-Performance Capillary Electrophoresis
Jan. 29–Feb. 2, 1995. Wurzburg, Germany
Contact: Shirley Schlessinger, Suite 1015, 400 East Randolph Dr., Chicago, IL 60601 (312-527-2011)

6th International Symposium on Chiral Discrimination
April 26–28, 1995. St. Louis, MO
Contact: Shirley Schlessinger, Suite 1015, 400 East Randolph Dr., Chicago, IL 60601 (312-527-2011)

1995 Winter Conference on Plasma Spectrochemistry
Jan. 8–13, 1995. Cambridge, England
Contact: Janice M. Gordon, Royal Society of Chemistry, Thomas Graham House, Science Park, Milton Rd., Cambridge, CB4 4WF; U.K. (44-223-420066; fax 44-223-420247)

Call for Papers

17th International Symposium on Capillary Chromatography and Electrophoresis
May 7–11, 1995. Wintergreen, VA
This symposium will focus on developments in capillary separation techniques, including capillary GC, microcolumn LC, CE, micellar electrokinetic capillary chromatography, analytical extraction and sample preparation, SFE, solid-phase extraction, automated techniques, chromatography-selective detection, and electrophoresis-selective detection. Authors should submit 300-word abstracts by Nov. 15. For more information, contact Milton L. Lee, Dept. of Chemistry, Brigham Young University, Provo, UT 84602-4672 (801-378-2135; fax 801-378-5474) or Joy Wise, P.O. Box 4153, Frederick, MD 21705-4153 (301-473-8311; fax 301-473-8312).

DTA HEATS UP Materials Analysis

As quality control and product development applications for DTA become increasingly important, instrument manufacturers respond by designing modular systems that offer enhanced flexibility.

As interest in materials chemistry increases, bench and research chemists are relying on a variety of tools to help characterize a wide spectrum of samples ranging from glasses to ceramics to polymers. One of these tools is thermal analysis (TA), a family of techniques involving the measurement of specific physical properties as a function of temperature.

Some materials, particularly ceramics and polymers, have properties that depend on the method of preparation rather than chemical composition. Determination of percent crystallinity, glass transition temperature, thermal stability, and mechanical properties are some of the unique capabilities of TA. When information obtained from these techniques is combined with that obtained by other means (e.g., X-ray diffraction, analysis of residues and evolved gases by MS or IR spectroscopy), one can obtain both quantitative and qualitative measures of solid-state properties and reactions.

TA has a variety of family members, most of whom are often referred to by their acronyms—TG (thermogravimetry), TMA (thermomechanical analysis), DMA (dynamic mechanical analysis), DSC (differential scanning calorimetry), and DTA (differential thermal analysis). Each technique uses different apparatus and provides analysts with different, although often complementary, information.

TG involves the measurement of the mass of a sample while its temperature is increased. From a plot of mass versus temperature, analysts can evaluate thermal stability, reaction rate, reaction processes, and sample composition. Many applications involve the study of polymers: their identification and decomposition mechanisms. TMA provides measurements of penetration, expansion, contraction, and extension of materials as a function of temperature. DMA is particularly useful for characterizing the modulus or stiffness of materials and for detecting transitions associated with polymer chain movements. It is based on the measurement of the resonant frequency and mechanical damping of a material forced to flex at a selected amplitude.

The two differential techniques, DTA and DSC, involve measurements made on a sample and a thermally inert reference material. Any transitions within the sample result in the liberation or absorption of energy by the sample and a corresponding deviation of its temperature from the reference sample. In power-compensated DSC, heat is added to the sample or to the reference material as needed so that the two substances remain at the iden-

tical temperature. The added heat is recorded and compensates for the heat loss or gain that results from endothermic or exothermic changes in the sample. In heat-flux DSC, the sample and reference material are simultaneously heated at a constant rate. The temperature difference between them is proportional to the difference in heat flow (from the furnace) between the two materials. In DTA, one plots the temperature difference between the sample and reference material (ΔT) as a function of the programmed temperature at which the system is changing. From this plot, analysts can identify the temperature of the transition and determine whether the transition is exothermic (i.e., adsorption, oxidation, or freezing) or endothermic (i.e., fusion, vaporization, sublimation, absorption, desorption, decomposition, or melting).

Analytical Chemistry consulted Neil D. Jespersen of St. John's University for help in understanding DTA and instrument options. Although Table 1 is not comprehensive, it includes representative products and common features of commercially available DTA systems. DSC instruments will be the subject of a future product review.

Historically, DSC provided more accurate information because of better heat transfer and thermal conductivity considerations, but advances in electronics and instrumentation have improved the accuracy and precision of DTA results. Today, DSC provides better information (higher sensitivity) over a temperature range from –180 °C to 725 °C, whereas DTA is most effectively used in evaluations between 600 °C and 1600 °C. Jespersen notes that the ability to use ceramic materials as sample holders in DTA allows for higher temperatures; operating temperatures are limited to 650 °C if sample holders are made from materials such as aluminum. Higher temperatures make it possible to characterize inorganic materials such as

Table 1. Summary of representative products

Product	Labsys[a]	Totalab	DTA 7
Company	Astra Scientific /Setaram 6900 Knoll Center Pkwy. Suite 417 Pleasanton, CA 94566 510-426-6900	Harrop Industries, Inc. 3470 East Fifth Ave. Columbus, OH 43219 614-231-3621	Perkin-Elmer Corporation 761 Main Ave. Norwalk, CT 06859 203-762-1000
List price (complete system)	INA	$25,000–$40,000	$34,000
Dimensions (l × w × h, in.)	20 × 22 × 18	11 × 17 × 16	20 × 9.75 × 15
Furnace	Metal resistor	Wire-wound, SiC, and molybdenum disilicide hairpin elements	Pt and Pt/30% Rh wound elements
Temperature range	Ambient to 1200 °C with platinel transducer; ambient to 1600 °C with Pt/Rh transducer	–150 °C to 1700 °C	Ambient to 1600 °C
Temperature detector	Platinel or Type S thermocouples	Type K or R cifferential thermocouples	INA
Δ T sensitivity	INA	1 μV	INA
Temperature accuracy	± 1 °C	± 1–2 °C	INA
Temperature precision	± 2 °C	± 2 °C	± 0.2 °C
Programmable heating rate	0.01–99.99 °C/min	INA	0.1–100 °C/min
Atmosphere	Static or controlled-flow gases	Static or controlled-flow gases	Static or dynamic with air, N_2, O_2, Ar, and other inert/reactive gases
Test atmosphere pressure	Ambient to 10^{-3} torr	10^{-3} torr to 1500 psi	Atmospheric or vacuum
Sample			
Available crucibles	Alumina, Pt	Alumina, Pt, quartz, Pyrex	Alumina, magnesia, Pt
Volume/size	100 μL	Up to 250 mm^3	Up to 100 mm^3
Data system			
Platform	486-based PC/Windows	486-based workstation/DOS	DEC PC/UNIX
Software features	Multitasking Windows-based software; data export in ASCII or Lotus; operation fully controlled by software	Input and data analysis software; Lotus 123; can be customized	7 Series/UNIX thermal analysis application software provides instrument control, automatic calibration, real-time data display, and automatic baseline correction
Instrument scope/applications	Designed for studies of chemicals, polymers, and materials; can be converted to simultaneous TGA/DTA or TGA/DSC	Can perform analyses simultaneously with other Harrop thermal analyzers	Can perform an analysis simultaneously with any other PE 7 Series thermal analyzer

INA = Information not available at press time
[a] Manufactured by Setaram (7 rue de l'Oratoire, 69300 Caluire, France; phone 33 78 29 38 38) and distributed in the U.S. by Astra

metals, glasses, ceramics, and minerals. Specific measurements include glass transitions, melting and boiling points, phase transitions, and assessments of oxidative and thermal stability.

Instrumentation

DTA system components include a circuit to measure temperature differences, a heating device (furnace) and temperature control unit, a means of amplifying and recording the observed signal, and a device to control the sample atmosphere.

Temperatures are measured with thermocouples. The selection of which thermocouple to use is based on the optimum temperature and lifetime desired. Different thermocouples have different temperature response characteristics; the computerized instrument control programs compensate for these as needed.

Because the thermocouples can be placed directly in the sample or attached to the sample container, DTA can provide high thermometric accuracy. This arrangement, however, increases the importance of thermal equilibrium. To minimize the effect of variations in temperature during heating, it is important to use the smallest sample size possible and to be certain that it is uniformly packed in the sample cup or tube.

The furnace in DTA instruments is generally designed to avoid electrical interference with the thermocouples. It may incorporate an inner metallic or ceramic chamber that holds both the sample and reference material such as aluminum oxide. Furnaces and sample block temperatures are increased in a linear fashion, most often at a rate of 5° C/min to 12 °C/min. Precise control of the furnace temperature is essential and is accomplished in today's thermal analysis systems by computer control. Most instruments are constructed to permit the circulation of inert or reactive gases; some can also operate at high pressure or in a vacuum.

DTA 92[a]	DTA 50	High-Temperature DTA	Labtronic II SDP
Setaram/Astra Scientific 6900 Knoll Center Pkwy. Suite 417 Pleasanton, CA 94566 510-426-6900	Shimadzu Scientific Instruments 7102 Riverwood Dr. Columbia, MD 21046 410-381-1227	TA Instruments 109 Lukens Dr. New Castle, DE 19720 302-427-4000	Theta Industries 26 Valley Rd. Port Washington, NY 11050 516-883-4088
$30,000–$50,000	$17,250–$30,000	$20,000–40,000	$29,000
INA	21.7 × 6.8 × 19.7	5.5 × 4.5 × 12.5 (cell only)	34 × 31 × 20
Metal resistor, graphite furnace	Alumina furnace tube	Alumina furnace tube	Wire-wound SiC tube furnace
Ambient to 1000 °C; ambient to 1600/1750 °C; ambient to 2400 °C	Ambient to 1600 °C	Ambient to 1600 °C	Ambient to 1600 °C
Platinel; Pt/Pt–10% Rh; Pt–6% Rh/Pt–30% Rh; W–Re	Pt/Pt–10% Rh alloy thermocouple (S-type)	Pt/Pt–18% Rh thermocouple pair	Platinel or Type S control thermocouples
INA	0.1 °C	0.004 °C	0.1 °C
± 1 °C	± 1 °C	± 1 °C or 1%	± 1 °C
± 2 °C	± 3 °C	± 0.5 °C	± 2 °C
0.01–100 °C/min	0.1–50.0 °C/min and 0.1–50.0 °C/h	0.01–200 °C/min	0.01–200 °C/min
Inert, oxidizing, reducing	Air, N_2, He, O_2, and other inert/reactive gases	Static or controlled flow. Air, N_2, O_2, Ar, or other inert/reactive gases	Air-controlled atmosphere
Atmosphere to vacuum	Vacuum to 10 torr	Ambient	10^{-4} torr
Al, alumina, Pt, W, graphite	Pt, Al, alumina, quartz, Ni, Cu, stainless steel	Pt, alumina	Pt, SiO_2, Al_2O_3, C
20–100 mm³	50 µL	Up to 75 µL	200 µL
PC/Windows	486-based PC/Windows	Thermal Analysts 2000, 2100, or 2200 486-, Pentium-based IBM PS/2	486-based PC
Instrument control; signal acquisition and processing	General and extended analysis functions; real-time data display; resident ASCII conversion; "snapshot" feature allows real-time sample analysis	General analysis; instrument control; automatic calibration, real-time data display	Thetasoft 3 software provides instrument control, data acquisition, temperature inputs, instrument calibration and verification tests; Lotus for Windows
Choice of DTA and DSC plate probes; permits thermal analysis of various types of materials from low to very high temperature	Stand-alone operation; simultaneous operation with other Shimadzu Series 50 thermal analyzers	Can be run simultaneously with up to three other TA techniques	Available as dilatometer attachment

The potential difference between the thermocouples is amplified and fed to a digital data acquisition and data handling system. This microprocessor-controlled system can also control the experiment, avoiding the need for operator intervention in operations such as baseline optimization and system calibration. These procedures are often tedious and contribute to experimental error.

The changing marketplace

Thermal analysis was commercialized in the early 1960s and was used primarily in industrial R&D labs for material characterization. Today, quality control and product development applications have become increasingly important, and instrument manufacturers have responded by designing modular thermal analysis systems that offer enhanced flexibility. Most DTA instruments can be expanded with the addition of modules that accommodate other thermal techniques such as DSC, TMA, and TG while allowing the analyst to use the same temperature controller and data system. Multitasking software permits users to process data from previous runs while acquiring new data and to control the operation of several modules from a single computer.

Tips for purchasers

What should laboratory managers who are considering adding DTA to their repertoire of instruments keep in mind? Says Jespersen, "Potential purchasers must remember that thermal analysis is not a high-throughput technique. You need to count on allotting 10 min to 1 h per sample." This is where instrument design can be important. Manufacturers recognize that by increasing the efficiency of the cooling system in the internal furnace, they decrease the time required for the system temperature to return to a useable level. This decreased cycle time leads to higher productivity for the laboratory.

Safety is a key issue, primarily because of the high temperatures at which these systems operate. Several manufacturers have incorporated locking devices that do not allow movement of the furnace assembly once the temperature has reached a preset, user-selectable point. Others have designed their instruments so that the furnace assembly remains on the instrument during sample loading, eliminating the possibility of placing a hot furnace on a combustible surface.

Finally, it's important not to forget the basics of any instrument purchase. Will the instrument company or supplier analyze a sample that you provide? How available and responsive is customer support? Many manufacturers have method development facilities as well as active applications laboratories that can help with the analysis of specific materials. Ask about the need for any special equipment or procedures. Sample preparation in DTA is normally nonexistent except for accurate weighing of milligram-sized samples. In terms of installation, it is important that the module be isolated from vibration sources and that an appropriate gas supply be available. Because a large number of TA instruments are run by technicians, the importance and availability of training cannot be overemphasized.

Louise Voress

Quality you can count on!
& still counting...

LPA
225 Reinekers Lane, Suite 625
Alexandria, Virginia 22314-2875
703-836-1360

We're the Laboratory Products Association.

When you buy from an LPA member company you can count on choosing from the best products & value, the broadest line of laboratory products, guaranteed delivery & service. By purchasing from an LPA member company you tap an invaluable source of leading manufacturers & distributors serving the scientific community. Our membership is constantly growing & expanding its network of information & services; all with the goal of providing you with what you need.

CIRCLE 10 ON READER SERVICE CARD

Laboratory Service Center

NOTICE

- ► You are manufacturers and/or producers of equipments and/or products meant for industrial and/or research laboratories.
- ► You want to export to Europe, and more especially to France.
- ► You require a specialized, technically competent and financially strong stockist-importer.

Please, send us a letter, we shall be loyal and efficient partners.

Address:

LABO-STANDA
14050 CAEN CEDEX FRANCE
Phone: 31 74 52 32 — Fax: 31 73 13 57

1-Acetyl-2-phenylhydrazine • p-Anisic Acid • Anthrone • DL-Aspartic Acid
Benzanilide • Benzoic Anhydride • D-Cellobiose • Chloramine T
Creatinine • 1,2-Diaminocyclohexanetetraacetic Acid • 1,3-Dibromopropane
4,6-Dichloropyrimidine • 3,5-Dimethylpyrazole • Dimethyl Succinate
Fructose • Imidazole • Malonic Acid • Methyl-p-toluenesulfonate
1-Naphtholphthalein • 4-(4-Nitrobenzyl)pyridine • Phenolphthalein
Rhamnose • Rubidium Chloride • Sodium Isethionate • Sodium Succinate
Succinic Acid • Sulfosalicylic Acid • Xylenol Orange • Xylitol

Write for our Products List of over 3,000 chemicals

Tel: 516-273-0900 • TOLL FREE: 800-645-5566 Telefax: 516-273-0858 • Telex: 497-4275

EASTERN CHEMICAL
ADMIRAL SPECIALTY PRODUCTS, INC.
P.O. Box 2500
DEPT. AC
SMITHTOWN, N.Y. 11787

FREE DATA, FAST

To quickly amass data on all of the products you need, consult the Lab Data Service Section on our *Analytical Chemistry* reader reply card insert.

LABORATORY SERVICE CENTER

(Equipment, Materials, Services, Instruments for Leasing). Maximum space — 4 inches per advertisement. Column width, 2-3/16"; two column width, 4-9/16". Artwork accepted. No combination of directory rates with ROP advertising. Rates based on number of inches used within 12 months from first date of first insertion.

Per inch: 1" — $200; 12" — $195; 24" — $190; 36" — $185; 48" — $180.

ANALYTICAL CHEMISTRY
1599 Post Road East
P.O. Box 231 Westport, CT 06881
203-256-8211 / FAX: 203-256-8175

Index to Advertisers

CIRCLE INQUIRY NO.	ADVERTISERS	PAGE NO.
9	*J. T. Baker, Inc. — Stiegler, Wells & Brunswick, Inc.	992A
10	LPA — LaMotte Company	1038A
4	*Nicolet Analytical Instruments	1023A
2, 3	*Perkin-Elmer Corporation — Lena Chow, Inc.	OBC
7	*Sigma-Aldrich Techware	IFC
1	Waters — Blitz Media	989A

Directory section, see page 1039A.
See ad in 1995 LabGuide Edition.

Advertising Management for the American Chemical Society Publications

CENTCOM, LTD.

President
James A. Byrne

Executive Vice President
Benjamin W. Jones

Joseph P. Stenza, *Production Director*

Laurence J. Doyle, *Director of Marketing*

1599 Post Road East
P.O. Box 231
Westport, Connecticut 06881-0231
(Area Code 203) 256-8211
Fax No. 203-256-8175

DIRECTOR, ADVERTISING SALES, LABORATORY PRODUCTS
Bruce E. Poorman

ADVERTISING PRODUCTION MANAGER
Jane F. Gatenby

SALES REPRESENTATIVES

Philadelphia, PA. . . . CENTCOM, LTD., The Meadows, 485 Devon Park Drive, Suite 106, Wayne, PA 19087. Telephone: 610-964-8061, FAX: 610-964-8071

New York/New Jersey . . . Dean A. Baldwin, John F. Raftery, CENTCOM, LTD., Schoolhouse Plaza, 720 King Georges Post Road, Fords, NJ 08863. Telephone: 908-738-8200, FAX: 908-738-6128

Westport, CT./Boston, MA. . . . Dean A. Baldwin, Michael J. Pak, CENTCOM, LTD., 1599 Post Road East, P.O. Box 231, Westport, CT 06881-0231. Telephone: 203-256-8211, FAX: 203-256-8175

Cleveland, OH. . . . Bruce E. Poorman, Dean A. Baldwin, CENTCOM, LTD., 19035 Old Detroit Road, Suite 203. Rocky River, OH 44116. Telephone: 216-331-5151, FAX: 216-331-3432

Chicago, IL. . . . Michael J. Pak, CENTCOM, LTD., 540 Frontage Rd., Northfield, IL. 60093. Telephone: 708-441-6383, FAX: 708-441-6382

Houston, TX./Atlanta, GA. . . . Edward M. Black, CENTCOM, LTD., P.O. Box 820966, Houston, TX 77082-0966. Telephone: 713-493-1560, FAX: 713-493-6673

San Francisco, CA. . . .Paul M. Butts, CENTCOM, LTD., Suite 808, 2672 Bayshore Parkway, Mountain View, CA 94043. Telephone: 415-969-4604, FAX: 415-969-2104

United Kingdom, Scandinavia and Europe (Except: Germany, Switzerland, Austria, France, Italy, Spain) . . . Malcolm Thiele, Technomedia Ltd., Wood Cottage, Shurlock Row, Reading RG10 OQE, Berkshire, England. Telephone: 0734-343302, FAX: 0734-343848

Germany, Switzerland, Austria . . . IMP InterMediaPartners, GmbH, Deutscher Ring 40, 42327 Wuppertall, Germany. Telephone: (0202) 711091, FAX: (0202) 712431

France . . . Gerard Lecoeur, Aidmedia, 31–33 Grand rue de Saint-Rambert, 69009 Lyon, France. Telephone: 78-64-20-37, FAX: 78-83-56-67

Italy, Spain . . . Tess Serranti, Serranti Communications, 43 Van Sant Road, New Hope, PA 18938. Telephone: 610-598-0668, FAX: 610-598-0670

Hong Kong. . .SEAVEX, LIMITED, 503 Wilson House, 19 Wyndham Street, Central, Hong Kong, Telephone: 868-2010, FAX: 810-1283

Japan. . . Shigeyuki Yasui, Intercommunications (Japan), Inc. 2F Ginza ElwaBldg. 8-18-7 Ginza, Chuo-ku, Tokyo 104, Japan. Telephone: (03) 5565-0861, FAX: (03) 5565-0860.

Korea. . .DooBee International Limited, Center Building (Byulgwan), 1-11 Jeong-dong, Choong-ku C.P.O. Box 4557, Seoul, Korea, Telephone: 822-776-2096, FAX: 822-755-9860

Singapore. . .SEAVEX, LIMITED, 400 Orchard Road, #10-01 Orchard Towers, Singapore 0923, Telephone: 734-9790, FAX: 732-5129

Taiwan. . .Epoch Limited, 2F No. 3, Lane 52, Nanking East Road, Section 4, P.O. Box 1642, Taipei, Taiwan, R.O.C. Telephone: 577-5441, FAX: 578-4308

South America . . .Bruce E. Poorman, CENTCOM, LTD., 19035 Old Detroit Road, Suite 203, Rocky River, OH 44116. Telephone: 216-331-5151, FAX: 216-331-3432

ANALYTICAL

Information Express

Get the product data you need fast...

By Phone: Use the reference list below, and contact the companies to fill an immediate need, or...

By Fax: Use the fax forms on the opposite page to send a direct written request.

Company	Page	Issue	RSN	Data+	Phone	Fax	Contact
ABC Instruments	712 A	7/1/94	402		800-533-0222	314-449-2988	Shelly Rittaers
Absolute Standards	707 A	7/1/94	3	●	203-466-7401	203-466-3404	Jack Grisco
Aldrich Chemical	OBC	7/1/94	1	●	414-273-3850	414-273-2094	Maryjean Essinger
Allison Associates	991 A	8/1/94	2	●	703-978-5100	703-978-5101	Sandra Kinney
Baird Analytical	710 A	7/1/94	406	●	617-276-6160	617-276-6510	Robin Tomulonis
Baltek	983 A	10/1/94	409		0625-434-127	0625-616916	Helen Williams
Bodman	713 A	7/1/94	409		800-241-8774	610-459-8036	Kirk Lind
Brinkmann Instruments	835 A	9/1/94	1		800-645-3050	516-334-7506	C. Shevchenko
Chem Service	896 A	9/15/94	2	●	800-452-9994	610-692-8729	Ron Gray
Chromapack	719 A	7/1/94	1	●	800-722-0000	800-722-0000	Judy Sparks
Dionex	712 A	7/1/94	403	●	800-346-6390	408-739-4398	Nancy Jensen
Discuss Energy	991 A	8/1/94	10, 11	●	800-530-4000	800-882-7650	Ruth Bozick
EM Science	713 A	7/1/94	410		800-222-0342	609-423-4389	Bruce Hyland
Fisons Instruments	879 A	9/1/94	410	●	508-524-1000	508-524-1100	Cathy Schaub
Galileo Electro-Optics	982 A	10/1/94	408		508-347-3191	508-347-3049	Laurie Fiacella
Hamamatsu	IFC	10/1/94	none		800-524-0504	908-231-1218	Robert Wisner
Hellma	992 A	10/1/94	408		516-671-6700	516-671-8810	Sheila Anderma
Hitachi Analytical	940 A	9/1/94	404		44-905-145995	44-905-410518	Ian D. Neale
InterAction Chromatography	983 A	10/1/94	410		408-894-9200	408-894-0405	David Hometchko
J&W Scientific	878 A	9/1/94	404	●	916-985-7888	916-985-1101	Brenda Meadows
JEOL USA	816 A	8/1/94	403	●	508-535-5900	508-536-2205	Brian Musselman
Labsphere	982 A	10/1/94	405	●	603-927-4266	603-927-4694	Joan A. Beaulieu
Leco	OBC	10/1/94	4		616-983-5531	616-983-4117	W. Stockwell
Maxtek	867 A	9/1/94	8		310-320-6604	310-320-6609	Valli K. Febbraro
Metrohm	940 A	10/1/94	0		41-071-500-505	41-071-500-001	R. Steiger
Midac	713 A	7/1/94	408		714-660-8558	714-660-9334	Heidi Auth
NIST	713 A	7/1/94	413	●	301-975-2208	301-926-0416	Lee Best
Novachem B.V.	983 A	10/1/94	411		31-85-2190	31-85-212332	
Parr Instrument	878 A	9/1/94	403	●	309-762-7716	309-762-9453	W. Sherman Hame
Perkin Elmer	OBC	10/15/94	2, 3	●	800-762-4000	203-762-6000	Mary Cooke Rager
Polaris Scientific	878 A	9/1/94	403		800-448-4750	201-933-2800	Russell Rabin
Radiometer Analytical SA	817 A	8/1/94	408	●	33-78-03-38-38	33-78-68-88-12	Patricia Dalmas
Rigaku/USA	982 A	10/1/94	402		508-777-2446	508-777-2604	Alan Rebsch
Rosemount Analytical	816 A	8/1/94	401	●	216-684-4423	216-684-4458	Blaine Shank
Sigma-Aldrich Techware	IFC	10/15/94	7	●	800-231-8327	800-962-9591	J. Russell Gant
SLM-Aminco	885 A	9/15/94	7		800-637-7669	716-248-4014	Jill Koepke
Supelco	IFC	7/1/94	9	●	814-359-3441	814-359-5459	Cathy Gates
Techne	991 A	10/1/94	0	●	800-432-3670	800-367-0177	Pam Summers
Talmar	879 A	9/1/94	402	●	800-543-4464	513-247-7050	Christine Wilson
Teledyne	IFC	9/1/94	18		415-962-6526	415-967-4353	Sharon Gomez
Varian	940 A	10/1/94	7-8	●	800-926-3000	713-240-6752	Chris Clark
VCH	779 A	8/1/94	3		49-6207-606/40	49-62016-06184	Christine Schweikart
Whatman	935 A	10/1/94	12		800-922-0361	201-472-6949	Sharman Pate
Wheaton	OBC	9/1/94	0-7	●	609-825-1100	609-825-9030	Frank Norman

Data+ Column: A bullet indicates that additional product and company information is available in the 1995 *Analytical Chemistry* LabGuide Edition.

Accelerated Articles

Anal. Chem. **1994,** *66,* 3289–3296

Electrospray Mass Spectrometric Study of Protein–Ketone Equilibria in Solution

J. C. Y. Le Blanc,† K. W. M. Siu,* and Roger Guevremont

Institute for Environmental Research and Technology, National Research Council of Canada, Montreal Road, Ottawa, Ontario, Canada K1A 0R6

The electrospray mass spectra of basic protein solutions containing ketones exhibit ions that are attributable to protein–ketone adducts whose relative abundances are in accordance with the relative concentrations of these adducts in solution. In a basic solution, the deprotonated (neutral) amino groups in a protein may be alkylated by ketone molecules to form Schiff bases. The extent of alkylation may be approximated by statistics if the reactivity of each amino group is identical. The relative ion abundances of these adducts have been found to follow their statistical distributions expected in solution. The reaction to form Schiff bases may be applied to the measurement of the number of primary amino sites (N-terminus plus lysine residues) in a protein. Excellent agreement with known numbers was observed for all 18 proteins measured.

Since Fenn and co-workers'[1] first demonstration of the analytical capabilities of electrospray mass spectrometry, the application of this technique has increased significantly, especially in the bioanalytical field. The ability to desorb multiply charged ions of high molecular mass compounds from aqueous solutions, and to mass analyze them using quadrupole filters whose upper m/z limits are comparatively low (<3000), enables an extension of the mass limit of the sample analyzed by mass spectrometry. The area where electrospray has generated most interest is, perhaps, in protein analysis. Protein molecular masses may be determined accurately and precisely by this technique.[2,3] Furthermore, adducts of proteins that are covalent[4] and noncovalent[5–7] in nature may also be characterized.

The electrospray mass spectra of protein cations exhibit multiply charged ions that have different numbers of protons attached to the protein, while those of protein anions have different numbers of protons abstracted from the neutral protein. In earlier work, we proposed an acid/base solution equilibrium model to account for the observed ion distributions in the electrospray mass spectra of proteins.[8,9] In this model, titration data were used to estimate the pK_as of adjacent groups to ionize; this information, together with the solution pH, enabled one to calculate relative protein ion distributions in solution. It should be pointed out, however, that the mass spectral record of the ionic species that exist in solution may be imperfect unless the variation of ion extraction (desorption) efficiencies with charge density is small[10–12] and the variation in collision-induced losses (in the so-called lens region) with ion charge is also relatively small and under control.[13] Compared with the charge densities of metal ions, the charge densities of multiply charged protein ions are relatively low because protein ions are far bulkier than metal or simple organic ions. Quantitative correlations between the ion distribution portrayed in the spectrum and that exists in solution were evident for smaller (and hence higher in charge density) ions only when ions of similar nature and identical in charge were compared.[10–12] Those of protein ions, however, were readily discernible provided the mass spectrometric

† Department of Chemistry, Queen's University, Kingston, Ontario, Canada K7L 3N6.

(1) Mann, M.; Meng, C. K.; Fenn, J. B. *Anal. Chem.* **1989,** *61,* 1702.
(2) Mann, M. *Org. Mass Spectrom.* **1990,** *25,* 575.
(3) Loo, J. A.; Edmonds, C. G.; Smith, R. D.; Lacey, M. P.; Keough, T. *Biomed. Environ. Mass Spectrom.* **1990,** *19,* 286.
(4) Bolton, J. L.; Le Blanc, J. C. Y.; Siu, K. W. M. *Biol. Mass Spectrom.* **1993,** *22,* 666.
(5) Katta, V.; Chait, B. T. *J. Am. Chem. Soc.* **1991,** *113,* 8534.
(6) Ganem, B.; Li, Y.-T.; Henion, J. D. *J. Am. Chem. Soc.* **1991,** *113,* 6294.
(7) Light-Wahl, K. J.; Springer, D. L.; Winger, B. E.; Edmonds, C. G.; Camp, D. G., II; Thrall, B. D.; Smith, R. D. *J. Am. Chem. Soc.* **1993,** *115,* 803.
(8) Guevremont, R.; Siu, K. W. M.; Le Blanc, J. C. Y.; Berman, S. S. *J. Am. Soc. Mass Spectrom.* **1992,** *3,* 216.
(9) Le Blanc, J..C.Y.; Guevremont, R.; Siu, K. W. M. *Int. J. Mass Spectrom. Ion Processes* **1993,** *125,* 145.
(10) Siu, K. W. M.; Gardner, G. J.; Berman, S. S. *Org. Mass Spectrom.* **1989,** *24,* 931.
(11) Cheng, Z. L.; Siu, K. W. M.; Guevremont, R.; Berman, S. S. *J. Am. Soc. Mass Spectrom.* **1992,** *3,* 281.
(12) Cheng, Z. L.; Siu, K. W. M.; Guevremont, R.; Berman, S. S. *Org. Mass Spectrom.* **1992,** *27,* 1370.
(13) Loo, J. A.; Udseth, H. R.; Smith, R. D.; *Rapid Commun. Mass Spectrom.* **1988,** *2,* 10.

0003-2700/94/0366-3289$04.50/0
© Published 1994 by the American Chemical Society

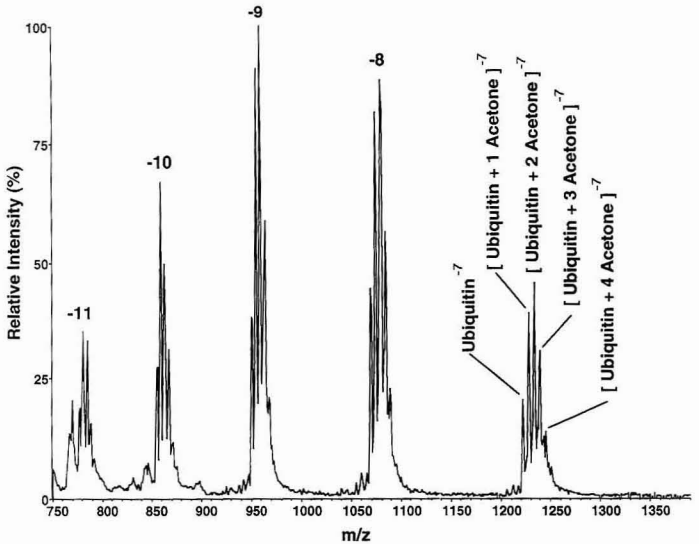

Figure 1. Electrospray mass spectrum of 20 μM bovine ubiquitin in water/methanol/acetone/piperidine (15/80/2/3 (v/v/v/v)). For clarity, only the –7 cluster is labeled (the *m/z* values of the five labeled ions are 1222, 1228, 1234, 1239, and 1245, respectively). The ions in the other clusters are identical except for their charges; e.g., for the –9 cluster, the ions are adducts with 0–4 units of acetone from low to high *m/z*, just as the –7 cluster. Note that the [ubiquitin + *x*acetone] label is an abbreviation for [ubiquitin + (acetone – H_2O)$_x$].

measurement system did not introduce significant charge[13] and/or mass-related[8,9] biases. Under these controlled conditions, we were able to demonstrate that the electrospray mass spectral ion distributions for several proteins under both positive[8] and negative ion[9] detection modes correlate well with the calculated protein ion distributions in acidic and basic solutions, respectively.

In an effort to further our appreciation of the extent of correlation between solution chemistry and electrospray mass spectrometry, and to demonstrate that electrospray mass spectrometry is a powerful technique for the study of solution equilibria under conditions where measurement biases are minimized, we have decided to investigate another type of solution equilibria: the condensation reaction between carbonyl compounds and amino groups on proteins. Aldehydes and ketones are known to react with free amine sites on proteins to form Schiff bases.

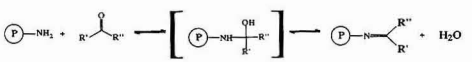

Reaction I

This reaction is simple and site specific and should result in minimal alteration of the protein charge state. The imino group formed has a pK_a similar to that of the parent amino group; the pK_a of the side-chain amino group on lysine is ~10.3.[14,15] Since the reaction involves a nucleophilic attack of the carbonyl compound by an amino group, but not an ammonium ion, the amount of Schiff base formed is pH dependent.[14,16,17] At low pH, the majority of the amino groups are protonated and little of the ketone adduct is formed. At high pH, most amino groups exist deprotonated and the concentration of adduct formed is proportionately higher.

Means and Feeney[17–20] have studied this reaction extensively using various aldehydes and ketones. The Schiff base formed was not very stable in dilute aqueous solution, but it could be reduced to a more stable secondary amine by means of sodium borohydride. With formaldehyde, this reductive alkylation yielded both the mono- and dimethyl derivatives (from the addition of one and two units of formaldehyde, respectively). When other aldehydes and ketones were used, the reductive alkylation yielded almost exclusively monoalkylated derivatives of the amino group on the N-terminus and the lysine residues. The extent of thereaction was also dependent on the nature of the carbonyl compound; aldehydes were much more reactive than ketones, and formaldehyde appeared to be the most reactive of all aldehydes.[19] This procedure has been used for ^{3}H- and ^{14}C-labeling of amino sites in proteins.[21] In this work, however, we focused our attention only on reaction I, the reversible formation of the Schiff base. It will be shown that this reaction may be used as a basis for a simple, rapid, and accurate determination of

(14) Jencks, W. P. *Catalysis in chemistry and enzymology*; McGraw-Hill, Inc.: New York, 1969; p 73.
(15) Stryer, L. *Biochemistry*, 3rd ed.; W. H. Freeman and Co.: New York, 1988, p 21.
(16) Sollendberger, P. Y.; Martin, R. B. In *The chemistry of the amino group*; Satay, P., Ed.; John Wiley & Sons, Ltd.: New York, 1968; pp 349–406.
(17) Feeney, R. E.; Blankenhorn, H.; Dixon, H. B. F. *Adv. Protein Chem.* **1975**, *29*, 135.
(18) Means, G. E.; Feeney, R. E. *Biochemistry* **1968**, *7*, 2192.
(19) Means, G. E. *Methods Enzymol.* **1977**, *47*, 469.
(20) Means, G. E.; Feeney, R. E. *Chemical modification of proteins*; Holden-Day, Inc.: San Francisco, 1971; pp 130–132.
(21) Rice, R. H.; Means, G. E. *J. Biol. Chem.* **1971**, *246*, 831.

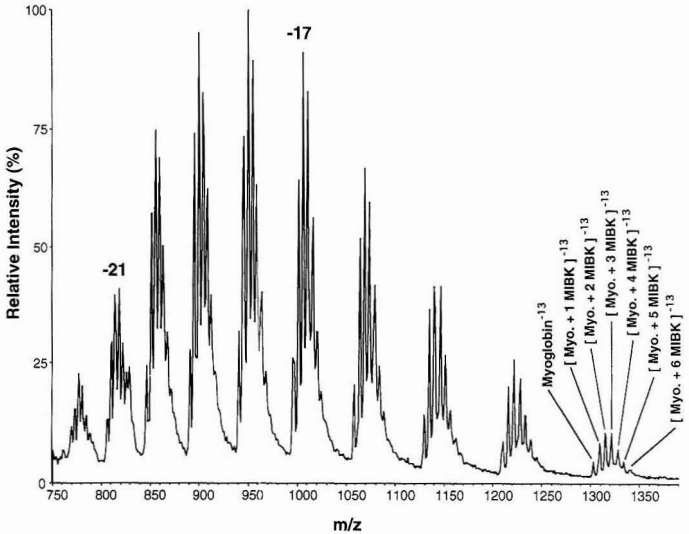

Figure 2. Electrospray mass spectrum of 40 μM equine myoglobin in a solution of water/methanol/MIBK/piperidine (44.8/47.8/4.6/2.8 (v/v/v/v)). See Figure 1 for explanation of the labels.

the number of amino groups (lysine residues plus N-terminal amino groups) in a protein. This application augments previous work[22,23] in applying electrospray mass spectrometry to real-time examinations of reactions in solution.

EXPERIMENTAL SECTION

Mass spectra were recorded on an atmospheric pressure ionization mass spectrometer (TAGA 6000E, SCIEX, Thornhill, ON, Canada) having an upper mass limit of 1400 m/z units. The electrospray probe was fabricated from an approximately 3-cm-long, 33-gauge stainless steel tube (Hamilton, ~100-μm i.d.) that had been attached to a length of $^1/_{16}$-in.-o.d. stainless steel tube with epoxy glue. The probe tip was electropolished prior to use. The optimum position was established on a daily basis for the protein of interest but was typically ~1–2 cm from the interface plate with the spray off-axis from the orifice. Biasing of the probe tip was achieved via a 50-MΩ current-limiting resistor in series with a high-voltage power supply (Tennelec, Model TC950) set typically between –2.7 and –3.0 kV. The electrospray current was monitored via a laboratory-built microammeter that could be floated above ground. The optimal potential difference between the orifice (OR) and the ac only quadrupole (R0) was typically 15 V. Mass spectra were acquired at a rate of 30–40 ms per m/z unit; seven to ten scans were averaged to generate a mass spectrum.

Micromolar protein solutions were continuously infused into the spray probe by means of a syringe pump (Harvard Apparatus, Model 22) at a typical flow rate of 20 μL/min. Electrical isolation of the probe was achieved by means of poly(tetrafluoroethylene) (Teflon) connection tubing.

(22) Lee, E. D.; Mück, W.; Henion, J. D.; Covey, T. R. *J. Am. Chem. Soc.*, **1989**, *111*, 4600.
(23) Wilson, S. R.; Perez, J.; Pasternak, A. *J. Am. Chem. Soc.*, **1993**, *115*, 1994.

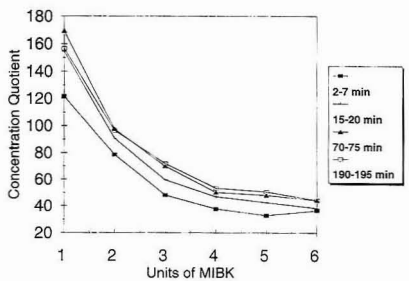

Figure 3. Variation of concentration quotients, $Q_{(x)}$s, of 40 μM equine myoglobin in water/methanol/MIBK/piperidine (44.8/47.8/4.6/2.8 (v/v/v/v)) with reaction time. The –18 ions were used for calculation. The concentration quotients as shown in eq 1 were calculated by multiplying $[H_2O]/[MIBK] = 58.7$ with the relative responses of the adduct ions.

All proteins were commercially available from Sigma Co. Methanol, acetonitrile, and acetone were Distilled-in-glass grade (Anachemia). Over 10 carbonyl compounds were examined; most work, however, was carried out with acetone, methyl isobutyl ketone (MIBK), and 2-pentanone (all Reagent grade, Aldrich).

RESULTS AND DISCUSSION

Schiff Base Formation. Ubiquitin has 76 amino acid residues with 1 α-amino group (N-terminus) and 7 ϵ-amino groups (lysine residues) where carbonyl compounds may react. The electrospray mass spectrum of ubiquitin anions exhibits an ion distribution that ranges from $z = -7$ to -11. Because of the low ion charges, even adducts with low molecular mass carbonyl compounds are well separated from the unmodified protein and from one another in a mass spectrum. Figure 1

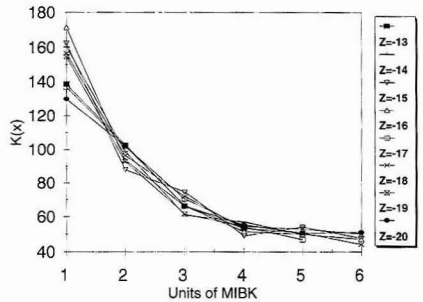

Figure 4. Equilibrium constants measured for equine myoglobin in water/methanol/MIBK/piperidine (44.8/47.8/4.6/2.8 (v/v/v/v)) using ion clusters with $z = -13$ to -20.

is a typical electrospray mass spectrum of ubiquitin electrosprayed from a solution of water/methanol/acetone/piperidine (15/80/2/3 (v/v/v/v)). The electrospray mass spectrum reveals two apparently distinct types of distributions: (1) the overall distribution of multiply charged ions present in solution of given molecular formulas charged to different degrees (i.e., the −7, −8, −9, etc., ion envelope) and (2) for each given charge state, a distribution of ions resulting from the equilibria of successive additions of an acetone molecule to a free amino site on ubiquitin. The molecular masses of the adducts are separated by multiples of 40, the difference between the molecular mass of acetone and that of water, which is lost as shown in reaction I. (On a m/z scale, the adducts are, of course, separated by multiples of $40/z$.) In Figure 1, as many as five protein species are evident: ubiquitin, and ubiquitin + (acetone − H_2O)$_x$, with x ranging from 1 to 4. What is apparent in this and subsequent spectra is that the proton abstraction spectra of the adducts (the distributions of the differently charged adduct ions) are very similar. These results confirm that the pK_as of the amino sites are not significantly altered by Schiff base formation. The potential difference in the lens region (OR − R0 = 15 V) was that used typically for electrospray. Increasing the potential difference to 30 V did not significantly affect the cluster distribution, but the absolute ion abundances decreased due to enhanced scattering.

Results similar to those shown in Figure 1 were obtained for other proteins and carbonyl compounds. Myoglobin has a total of 153 amino acid residues with 1 α-amino group and 19 ϵ-amino groups that can react with carbonyl compounds. Figure 2 shows an electrospray mass spectrum of 40 μM myoglobin in a solution of water/methanol/MIBK/piperidine (40/52/5/3 (v/v/v/v)). As in Figure 1, two types of equilibria are apparent: those that are due to different degrees of charging and those that are due to different degrees of alkylation. The following protein species are identifiable in the figure: myoglobin and myoglobin + (MIBK − H_2O)$_x$, where x ranges from 1 to 6.

Successive additions of ketones (or aldehydes) to the amino groups on a protein may be represented in the following scheme:

$$\text{protein}^{-z} + \text{ketone} \rightleftharpoons [\text{protein–ketone}]^{-z} + H_2O$$

$$[\text{protein–ketone}]^{-z} + \text{ketone} \rightleftharpoons [\text{protein–ketone}_2]^{-z} + H_2O$$

$$[\text{protein–ketone}_2]^{-z} + \text{ketone} \rightleftharpoons [\text{protein–ketone}_3]^{-z} + H_2O$$

$$\ldots + \ldots \rightleftharpoons \ldots + \ldots$$

$$[\text{protein–ketone}_{(n-1)}]^{-z} + \text{ketone} \rightleftharpoons [\text{protein–ketone}_n]^{-z} + H_2O$$

where n represents the maximum number of ketones (or aldehydes) that react with the protein and z denotes the charge state of the protein. The equilibrium constant for each of the steps is given by the following expression:

$$K_{(x)} = \frac{[H_2O][(\text{protein} + \text{ketone}_{(x)})^{-z}]}{[\text{ketone}][(\text{protein} + \text{ketone}_{(x-1)})^{-z}]} \quad (1)$$

The stepwise equilibrium constants, $K_{(x)}$s, can be measured from the electrospray mass spectrum provided [protein + ketone$_{(x)}$$^{-z}$]/[protein + ketone$_{(x-1)}$$^{-z}$] can be equated to the relative response of these adduct ions. This assumption is likely valid for adducts of the same charge (as in this case) because of the comparabilities of desorption efficiencies[10] and m/z-related transmission efficiencies.[8] Since in our experiments, the concentrations of water and of the ketone were in large excess relative to that of the protein, the equilibrium concentrations of water and the ketone were similar to their initial concentrations. The concentration quotient, $Q_{(x)}$ ($K_{(x)}$ is the $Q_{(x)}$ at equilibrium), as expressed in eq 1 for each addition step of MIBK to myoglobin was calculated over time and is shown in Figure 3. Equilibrium is apparently reached after 70 min at room temperature. The −18 ion cluster was used in the above calculations. Figure 4 shows that the equilibrium constants measured were independent of the protein charge states, a consequence of the similarity in the pK_as of alkylated and nonalkylated amino groups.

In a number of experiments, the concentration of the carbonyl compound was varied while the water and the protein concentration were kept constant to shift the equilibrium across the whole span of possible adducts. In a comparison of this type, it was important to maintain the protein in an identical conformational state throughout the experiment, and since organic solvents are known to denature proteins, the total organic solvent content (% methanol + % ketone) was kept constant in these experiments to minimize the risk of conformational changes. Figure 5 shows the electrospray mass spectra of ubiquitin in the presence of (A) 0.14 and (B) 2.71 M acetone with a total organic solvent content of 82%. As expected, increasing the acetone content resulted in an increased degree of alkylation. In 0.14 M acetone, ubiquitin + (acetone − H_2O)$_x$ adducts with x ranging from 0 to 3 are apparent, whereas in 2.71 M, x ranges from 3 to 8. In this example, it is difficult to determine the equilibrium constants of all the steps in a single spectrum. However, by varying the acetone concentration, it is possible to measure the equilibrium constant of every step as we shift the equilibrium to facilitate quantification. This is demonstrated in Figure 6A,B, where the equilibrium constants are plotted for an acetone concentration of 0.14–6.78 M in solutions of a total organic solvent content of (A) 57 and (B) 82%, respectively. The $K_{(x)}$s were similar in the two plots. Within each plot, discrepancies were

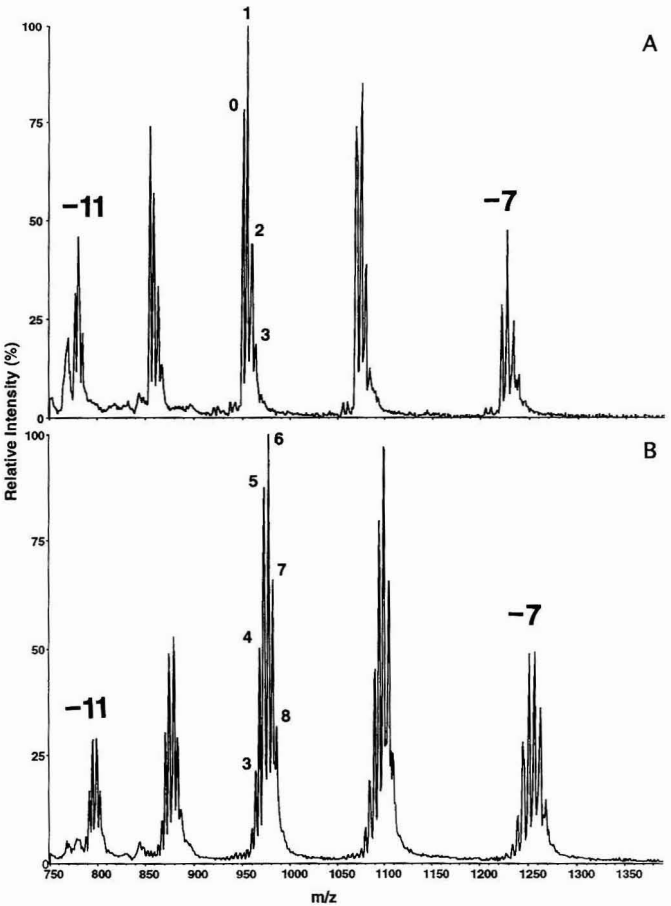

Figure 5. Electrospray mass spectra of 20 μM bovine ubiquitin in solutions of water/methanol/acetone/piperidine. Total organic content (% methanol + % acetone) = 82%; (A) 0.14 M acetone and (B) 2.71 M acetone. The number of acetone units is indicated for the two −9 clusters.

largest where x was relatively small (where low abundances and insufficient resolution compounded the errors in relative ion abundances). As in Figures 3 and 4, the composite of the K curves in Figure 6 shows a characteristic decrease with each alkylation step. The shape of the curve is a function of the number of amino groups in a protein and their reactivity.

Statistical Model. In a first approximation, we may assume that the amino groups in a protein have identical reactivity toward alkylation. That is to say, the probability of each group being modified is identical. Let P be the probability that a given amino group will be alkylated under a given set of conditions; the probability that the same group will not be alkylated is, therefore, $1 - P$. For a total of n amino groups, the probability $[A_{(x)}]$ that x of them will be alkylated is

$$A_{(x)} = \frac{n!}{(n-x)!x!}(P)^x(1-P)^{(n-x)} \qquad (2)$$

Since

$$\frac{[\text{protein} + \text{ketone}_{(x)}{}^{-z}]}{[\text{protein} + \text{ketone}_{(x-1)}{}^{-z}]} = \frac{A_{(x)}}{A_{(x-1)}}$$

$$K_{(x)} = \frac{[H_2O]A_{(x)}}{[\text{ketone}]A_{(x-1)}} = \frac{[H_2O]P(n-x+1)!(x-1)!}{[\text{ketone}](1-P)(n-x)!(x)!}$$

$$K_{(x)} = \frac{[H_2O]P(n-x+1)}{[\text{ketone}](1-P)x}$$

Or

$$K'_{(x)} = \frac{(n-x+1)}{x}\frac{P}{(1-P)} \qquad (3)$$

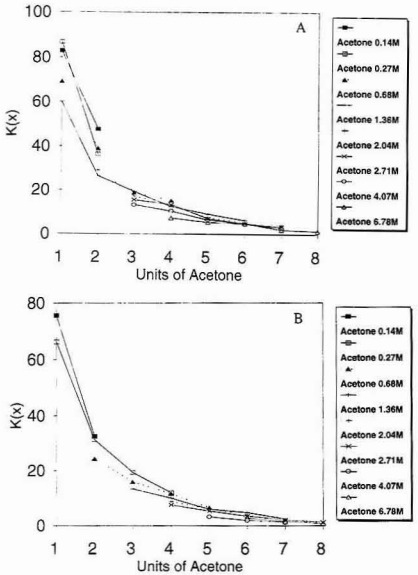

Figure 6. Equilibrium constants measured for bovine ubiquitin in water/methanol/acetone/piperidine solutions containing various concentrations of acetone. The water concentration was 22.2 M; total organic content, (A) 57 and (B) 82%.

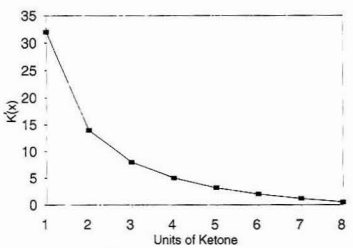

Figure 7. Calculated $K'_{(x)}$s (from eq 3) as a function of the number of the ketones attached for n (the total number of amino sites) = 8 and P = 0.8.

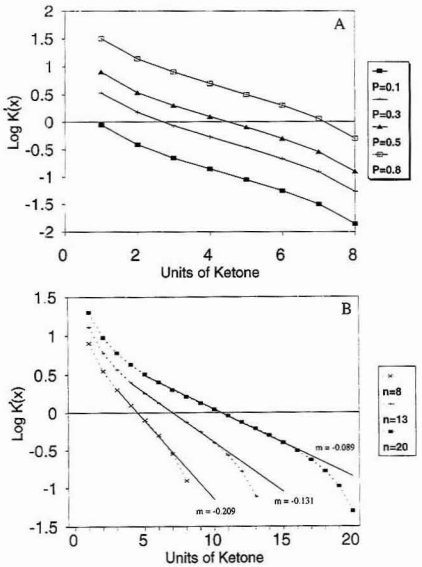

Figure 8. Effects of n and P on $K'_{(x)}$s as a function of the number of ketones attached: (A) n = 8 and P = 0.1, 0.3, 0.5, and 0.8; (B) P = 0.5 and n = 8, 13, and 20. m is the slope of the linear portion as shown.

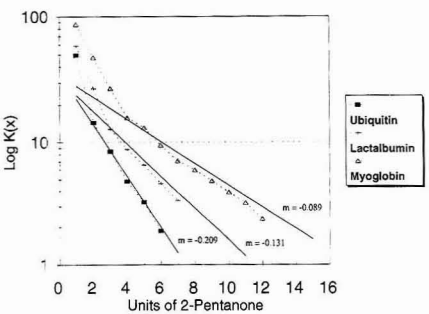

Figure 9. Measured equilibrium constants for bovine ubiquitin (n = 8), bovine α-lactalbumin (n = 13), and equine myoglobin (n = 20) as a function of the number of 2-pentanone attached. The proteins were in solutions of water/methanol/2-pentanone/piperidine, where the total organic content was 75% and the water concentration was 12.1 M. The theoretical slopes according to eq 3 (see Figure 8) are reproduced for ease of comparisons.

Figure 7 illustrates the relationship between $K'_{(x)}$ and x for n = 8 and P = 0.8; it is evident that the curve obtained is similar in characteristics to the plots of experimental data shown in the previous Figures. Panels A and B of Figure 8 are extensions of Figure 7 and show eq 3 in a semilogarithmic format for P = 0.1, 0.3, 0.5, and 0.8 at n = 8 in (A) and for n = 8, 13, and 20 at P = 0.5 in (B). We see that the characteristics of eq 3 are such that the plots are approximately linear except near the ends. Changing P at a constant n shifts the plots vertically but does not alter the slope (Figure 8A); the slope is changed only when n is varied (Figure 8B). Increasing n decreases the slope. Ubiquitin, α-lactalbumin, and myoglobin have 8, 13, and 20 amino groups available for alkylation, respectively; Figure 9 shows the equilibrium constants calculated for these three proteins reacting with 2-pentanone. Note that the characteristics and the slopes of these plots are very similar to those shown in Figure 8B (the slopes of the linear portions are reproduced in Figure 9 for ease of comparisons). The excellent agreement is in line with the hypothesis of a solution origin for electrospray-generated ions and corroborates previous observations[8-10,24] that the ion distributions in electrospray mass spectrometry reflect those in bulk solution provided measurement artifacts (biases) can be kept under control.

Schiff Base Equilibria versus Protonation Equilibria. The Schiff base formation reaction offers a window of observation

(24) Siu, K. W. M.; Guevremont, R.; Le Blanc, J. C. Y.; O'Brien, R. T.; Berman, S. S. *Org. Mass Spectrom.*, **1993**, *28*, 579.

that is different from that of protonation. Protonation reactions are believed to be very fast (submicroseconds) while the alkylation reactions require tens of minutes to reach equilibrium. Furthermore, protonation is pH dependent while Schiff base formation is pH independent. The three competing equilibria involving the $(m - 1)^-$ and m^- ions of a protein reacting with the ketone R_2CO are as follows; the net charges are left out for clarity:

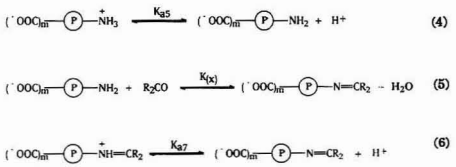

From (4)

$$K_{a5} = \frac{[(\text{`OOC})_m\text{—P—NH}_2]\,[H^+]}{[(\text{`OOC})_m\text{—P—}\overset{+}{\text{N}}\text{H}_3]}$$

From (5)

$$K_{(x)} = \frac{[(\text{`OOC})_m\text{—P—N=CR}_2]\,[H_2O]}{[(\text{`OOC})_m\text{—P—NH}_2]\,[R_2CO]}$$

From (6)

$$K_{a7} = \frac{[(\text{`OOC})_m\text{—P—N=CR}_2]\,[H^+]}{[(\text{`OOC})_m\text{—P—}\overset{+}{\text{N}}\text{H=CR}_2]}$$

Therefore,

$$K'_{(x)} = \frac{[(\text{`OOC})_m\text{—P—N=CR}_2]}{[(\text{`OOC})_m\text{—P—NH}_2]} = \frac{K_{a7}\,[(\text{`OOC})_m\text{—P—}\overset{+}{\text{N}}\text{H=CR}_2]}{K_{a5}\,[(\text{`OOC})_m\text{—P—}\overset{+}{\text{N}}\text{H}_3]}$$

Since $K_{a5} \approx K_{a7}$, the $K'_{(x)}$s of different charge states are identical. As well, the $K'_{(x)}$s are independent of pH as $[H^+]$ is absent while the K_as are pH dependent.

Measurement of *n* in a Protein. The alkylation reaction may be applied to the measurement of n, the total number of α- and ϵ-amino groups in a protein. In an experiment to demonstrate this possibility, the initial water concentration was at zero to ensure that the *n*th amino group had a significant probability of alkylation. For any given protein, *n* could be calculated from the data of two measurements using the following equation:

$$n = \frac{M_{(\text{protein+acetone}_n)} - M_{(\text{protein})}}{40.1} \qquad (7)$$

where $M_{(\text{protein+acetone}_n)}$ denotes the mass of the protein adduct with the largest number of acetone (presumed to be the saturated adduct) and $M_{(\text{protein})}$ the mass of the unmodified protein. The former was measured via electrospraying a solution of the protein with a large excess of acetone in a mixture of methanol and acetonitrile containing piperidine as the base while the latter was obtained via electrospraying a solution of the same protein in aqueous methanol containing piperidine. The denominator (40.1) is the difference between the mass of acetone and that of water. Figure 10 shows the two spectra obtained in such an experiment for myoglobin; *n* was calculated to be (17753.4 – 16945.6)/40.1 = 20.1, or 20, identical to the known sum of α- and ϵ-amino groups in that protein. The excellent agreement between the measured sums and the known sums for 18 proteins is shown in Table 1. It should be emphasized that to ensure formation of the *n*th

(25) Croft, L. R. *Handbook of protein sequence analysis: A compilation of amino acid sequences of proteins with an introduction to the methodology*, 2nd ed.; John Wiley & Sons: Chichester, U.K., 1980.

Table 1. Determination of the Numbers of α- and ϵ-Amino Groups in Proteins

protein	known no.[a]	determined no.
insulin (bovine)	3	3.0
ubiquitin (bovine)	8	8.1
β-casein (bovine)	12	11.9
β-lactoglobulin B (bovine)	16	16.2
β-lactoglobulin A (bovine)	16	16.2
cytochrome *c* (equine)	19	19.2
myoglobin (equine)	20	20.1
α-hemoglobin (canine)	12	12.0
β-hemoglobin (canine)	15	15.2
α-hemoglobin (porcine)	12	11.9
β-hemoglobin (porcine)	12	12.0
α-hemoglobin (goat)	12	12.0
β-hemoglobin (goat)	13	13.1
α-hemoglobin (bovine)	12	12.0
β-hemoglobin A (bovine)	14	14.0
α-hemoglobin (human)	12	12.0
β-hemoglobin (human)	12	12.1
α-lactalbumin (bovine)	13	13.2

[a] From published sequence information.[25]

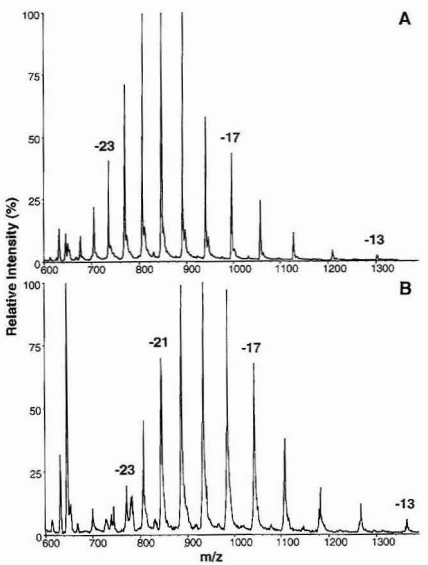

Figure 10. Electrospray mass spectra of 40 μM equine myoglobin in solutions of (A) water/methanol/piperidine (25/70/5 (v/v/v)) and (B) in methanol/acetonitrile/acetone/piperidine (47.5/37.5/10/5 (v/v/v/v)) showing the presence of the n = 20 adducts.

adduct, the protein sample must be dissolved directly in a mixture of acetonitrile, methanol, acetone, and piperidine; as well, it is advisable to analyze these solutions within 1 h to minimize the risks of side reactions and/or degradations.

CONCLUSION

The electrospray mass spectra of proteins in the presence of ketones and bases exhibit ions attributable to adducts of proteins with ketones in relative abundances that reflect their relative concentrations in solution as controlled by reaction statistics. The reactions have been applied to the measurement of the total numbers of free amino sites (i.e., N-terminus plus the number of lysine residues) in proteins.

ACKNOWLEDGMENT

Parts of this work were presented at the 41st ASMS Conference on Mass Spectrometry and Allied Topics, San Francisco, CA, May 30–June 4, 1993, and at the 34th Oak Ridge National Laboratory—Department of Energy Conference on Analytical Chemistry in Energy Technology, Gatlinburg, TN, October 5–7, 1993.

Received for review July 7, 1994. Accepted August 5, 1994.[⊗]

[⊗] Abstract published in *Advance ACS Abstracts,* September 1, 1994.

Articles

Anal. Chem. **1994,** *66,* 3297–3302

Gas-Phase Biosensor for Ethanol

Kohji Mitsubayashi,† Kenji Yokoyama, Toshifumi Takeuchi, and Isao Karube*

Research Center for Advanced Science and Technology, University of Tokyo, 4-6-1 Komaba, Meguro-ku, Tokyo 153, Japan

A gas-phase biosensor was constructed using an immobilized alcohol oxidase (AOD) enzyme electrode and a unique reaction cell with both gas- and liquid-phase compartments separated by a diaphragm membrane. The sensor was evaluated for the measurement of gaseous ethanol with two types of porous poly(tetrafluoroethylene) diaphragm membranes (pore size 30–60 μm, thickness 0.13 mm; pore size 1–2 μm, thickness 0.25 mm) and was used to measure ethanol in the gas phase from 0.358 to 1242 ppm, covering the sense of smell in humans and the concentration range encountered in breath after alcohol drinking. The sensor possessed high selectivity for ethanol in the presence of other gas-phase chemicals and gave a negligible response to these chemicals. The short lifetime of the device was caused by deactivation of the unstable AOD, which was consistent with previously reported results.

The detection and quantification of gaseous substances, such as odors and toxic and combustible gases, with high sensitivity and selectivity are required in many different areas. In addition, some substances in the gas phase can be related to human health and behavior. For example, chemical malodors can affect human mental and physical condition.[1] In several reports, analysis of the volatile components in the expiratory gas of patients can help in the diagnosis of diseases such as oral ailments,[2] hepatocirrhosis, and cancer of the lung,[3,4] head, and neck regions. Expiratory gas analysis would provide a noninvasive, convenient, and safe method of diagnosing and monitoring disease states.

One of the major applications of the breath analysis is in the quantification and detection of ethanol in expiratory gas after alcohol consumption. Blood ethanol concentration can be determined from its concentration in breath,[5] a blood/breath alcohol partition ratio of 2000 having been widely adopted.[6–8] The breath alcohol level can be related to the degree of intoxication [i.e., haziness 0.5–1.0 g·L^{-1} in blood (0.25–0.5 mg·L^{-1}, 130–260 ppm in breath); slight drunkenness 1.0–1.5 g·L^{-1} (0.5–0.75 mg·L^{-1}, 260–390 ppm); drunkenness 1.5–2.5 g·L^{-1} (0.75–1.25 mg·L^{-1}, 390–650 ppm)][5,10] and used as a measure of drunk driving.

In certain industrial fields, such as fermentation and distillation, the ethanol vapor concentration can reach toxic levels, causing inflammation of the nasal mucous membrane and conjunctiva, irritation of the skin and, at high levels, even alcohol poisoning. The maximum permitted concentration of ethanol vapor in the work place as defined by the American Conference of Governmental Industrial Hygienists (ACGIH) is 1000 ppm.

Since gaseous ethanol is a mal- or odorous substance for human (the ethanol selection and detection limits for the human sense of smell have been reported to be 6.1 and 0.36 ppm,[9] respectively), the continuous monitoring of ethanol concentration in the gas phase is significant for assessing the human health and behavior-related ethanol vapor from a physiological point of view.

A way is therefore required for measuring gaseous substances, including ethanol vapor, with high sensitivity and selectivity. Many types of gas sensors have been investigated and developed. Considerable effort has gone into improving the ethanol selectivity and sensitivity of semiconductor-type gas sensors.[11–13] For SnO_2-based devices this can be achieved by the addition of various basic oxides,[12] whereas in chromia semiconductors, heavy doping with MgO also enhances the selectivity.[13] Semiconductor sensors are still at present inadequate for sensing multianalyte samples such as expiratory gas, because the sensor response is based on only changes in electrical conductivity of the device following adsorption of gaseous substances.[1,11–14] Although an improvement in semiconductor sensors for gaseous ethanol has been reported, it is still far from the selectivity achievable using biological recognition systems such as enzymes.

In order to obtain highly selectivity for sensing gaseous substances, gas microchromatography has been attempted by applying micromachining technologies.[15] This method has

† Present address: Research Laboratories, Nippondenso Co., Ltd., 500-1 Minamiyama, Komenoki, Nisshin-cho, Aichi-gun, Aichi 470-01, Japan.

(1) Tonoike, M. *Circ. Jpn. Electrotech. Lab.* **1988,** *52*(5), 63–79.
(2) Kostelc, J. G.; Preti, G.; Zelson, P. R.; Brauner, L.; Baehmi, P. *J. Periodontal Res.* **1984,** *19,* 303–312.
(3) Watanabe, M. *J. Jpn. Assoc. Traffic Med. Eng.* **1992,** 39–46.
(4) Thomas, L., Ed. *Pam. Monell Chem. Senses Center* **1986.**
(5) Mizohata, M. *Jpn. J. Alcohol Drug Dependence* **1983,** *18*(2), 246–271.
(6) Jones, A. W. *J. Stud. Alcohol* **1978,** *10,* 5–10.
(7) Yamamoto, K. *Jpn. J. Stud. Alcohol* **1970,** *5,* 81–88.
(8) Ueda, M. *Jpn. J. Stud. Alcohol* **1967,** *2,* 32–33.
(9) Japanese Environmental & Sanitary Center. *A report of chemical malodor analysis* (a study for the Japan Enviromental Agency), 1980; pp 248–250.
(10) Sato, S.; Kitagawa, K. *The portable alcohol tester;* Traffic Safety Series; Japan Association of Traffic Medicine & Engineering: Mizuho Printing: Nagoya, Japan, 1993; pp 26–30.
(11) Hiranaka, Y.; Abe, T.; Murata, H. *Sens. Actuators B* **1992,** *9,* 177–182.
(12) Maekawa, T.; Miura, N.; Yamazoe, N. *Sens. Actuators B* **1992,** *9,* 63–69.
(13) Chen, Z.; Colbow, K. *Sens. Actuators B* **1992,** *9,* 49–53.
(14) Wang, X.; Yee, S.; Carey, P. *Sens. Actuators B* **1993,** *13–14,* 458–461.
(15) Terry, S. C. *IEEE Trans.* **1979,** *ED-26*(12), 1980.

0003-2700/94/0366-3297$04.50/0
© 1994 American Chemical Society

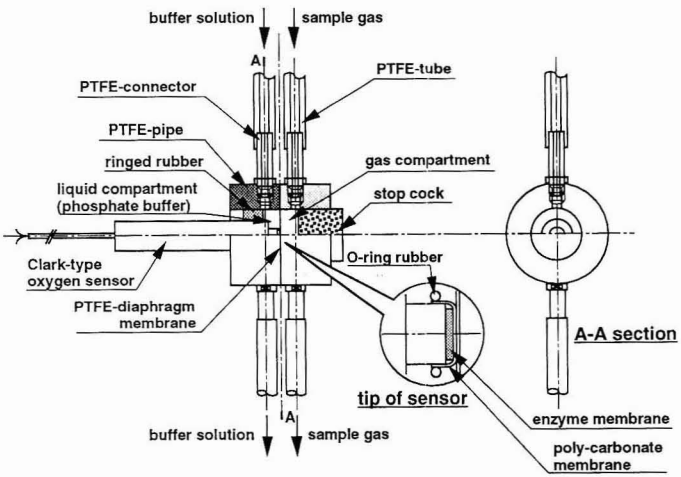

Figure 1. Structure of gas-phase biosensor.

some disadvantages, however, such as low response, structural complication, and the difficulty in applying it to continuous monitoring.

Biosensors have been extensively researched for the measurement of chemical substances in the liquid phase. Biosensors use biologically derived materials such as enzymes, microorganisms, antigens and antibodies, and organelles, which possess high specificity for their substrates.[16] An alcohol biosensor for the liquid phase has also been investigated and applied widely for the measurement of ethanol concentration in fermentation processes. Alcohol oxidase (AOD; EC 1.1.3.13) is commonly used in the construction of alcohol biosensors, catalyzing the oxidation of lower primary alcohols according to the reaction

$$RCH_2OH + O_2 \xrightarrow{AOD} RCHO + H_2O_2$$

It is difficult to use biosensors for detection of gaseous chemicals, however, because of deactivation of the biological component in the gas phase.

In this work, we have constructed a gas-phase biosensor using the enzyme catalytic reaction for measurement of gaseous substances. Ethanol vapor was chosen as a model analyte for the reasons described above. The performance, such as sensitivity, calibration behavior, selectivity, and lifetime, of the sensor is evaluated and compared with the performance of a commercially available semiconductor gas sensor.

EXPERIMENTAL SECTION

Construction of the Gas-Phase Biosensor. Figure 1 illustrates the structure of the gas-phase biosensor for measurement of ethanol vapor. The sensor consisted of an enzyme electrode, a homemade reaction cell with two compartments for liquid and gas phases, and a porous diaphragm membrane between these compartments. The enzyme electrode was constructed using a commercially available Clark-type dissolved oxygen electrode (Oriental Yeast Co., Ltd., Tokyo, Japan) with an enzyme membrane.

Alcohol oxidase (A-2404; EC 1.1.3.13, 1280 units·mL^{-1}, from *Pichia pastoris*; Sigma Chemical Co., St. Louis, MO) was used for constructing the enzyme electrode. The enzyme is specific for short-chain, linear aliphatic alcohols, primarily oxidizing methanol and ethanol, but will also oxidize the following substances at a slower rate: 1-propanol, 1-butanol, allyl alcohol, propargyl alcohol, methyl and ethyl mercaptan, and formaldehyde between pH 6.0 and 9.5 (information obtained from Sigma Research Technical Service, St. Louis, MO).

For enzyme immobilization, AOD was mixed with acrylamide gel monomer solution in a volume ratio of 1:4;[17] the resultant mixture was then sandwiched between two glass plates and irradiated with a UV lamp (254 nm, 15 W) for 5 min in order to photo-cross-link the monomer solution and immobilize the enzyme.[17] This method gave an enzyme membrane of approximately 130-μm thickness. The enzyme membrane was removed from the glass plate and immersed in phosphate buffer (0.067 M, pH 7.0). In order to prevent enzyme deactivation when not in use, the membrane was stored in buffer below 10 °C.

The enzyme electrode was constructed by cutting the enzyme membrane to the required dimensions using a scalpel and placing it onto the sensing area of the dissolved oxygen electrode. The enzyme membrane was covered with a supporting polycarbonate membrane (pore size 1.0 μm; thickness 10 μm; Nuclepore Corp., Pleasanton, CA) and secured with a rubber O-ring (see the enlargement of Figure 1).

Two hollow poly(tetrafluoroethylene) (PTFE) tubes (o.d. 40 mm, i.d. 20 mm) were cut to a length of 20 mm, and the

(16) Karube, I. *J. Agric. Food Chem.* **1984**, *32*, 315.

(17) Ikeda, S. *Denki Kagaku* **1978**, *46*(12), 667–672.

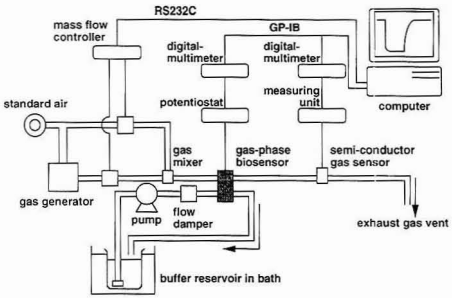

Figure 2. Schematic diagram of gas flow measurement system for gas-phase detection.

surfaces of the tubes were polished. Two 6-mm-diameter tapped holes were drilled across the entire diameter of each tube and four PTFE tube connectors (o.d. 6 mm, i.d. 2 mm) were screwed into the outside of all of the tapped holes. A porous PTFE membrane was sandwiched between the two tube blocks, which were then held firmly together using a mechanical clamp. In this way, the membrane acted as a separating diaphragm between the two hollow compartments of the tubes.

A cylindrical rubber stop cock (o.d. 20.5 mm) was inserted into the large hole of one of the tubes, thus forming the gas compartment of the reaction cell. The volume of the compartment was adjusted to 0.5 mL. A rubber O-ring was placed around the end of the enzyme electrode (o.d. 20.5 mm, i.d. 12 mm) and inserted into the hole of the other tube, thus producing the liquid compartment of the reaction cell. The tip of enzyme electrode was immersed in the liquid compartment filled with phosphate buffer (0.067 M, pH 7.0) and adjusted so as to directly touch the surface of the diaphragm membrane (see the enlargement of Figure 1). In order to investigate the effect of the diaphragm membrane, two kinds of porous PTFE membranes (pore size 1–2 μm, thickness 0.25 mm; pore size 30–60 μm, thickness 0.13 mm) were used in the reaction cell.

Gas and phosphate buffer solution could be flow individually through each inlet tube connector to the gas and liquid compartments of the reaction cell, respectively. Gaseous substances in the gas compartment could diffuse into the liquid compartment of the reaction cell through the PTFE diaphragm membrane.

When not in use, the gas-phase biosensor with phosphate buffer solution filling the liquid compartment was stored below 10 °C.

Gas Flow Measurement System. The gas-phase biosensor was used in a batch flow measurement system (Figure 2). A standard substance in the gas phase was supplied from a gas generator (Permeater, Type: PD-1B, Gastec Corp., Yokohama, Japan), which is a standardized machine approved by the Ministry for Labor and the Environmental Agency in Japan and by the Environmental Protection Agency (EPA) and the National Bureau of Standards (NBS) in the United States for gas calibration purposes.

A computer-controlled mass flow controller system (Type: SECU-1, Stec Inc., Kyoto, Japan) was used to adjust the flow rates of a standard air (Type: AIR-R, 21% oxygen, Takachiho Trading Co., Ltd., Tokyo, Japan) and the gases supplied from the gas generator, thus permitting the concentrations of gaseous substances into the gas compartment of the gas-phase biosensor to be varied with a final flow rate of 200 mL·min^{-1}.

Phosphate buffer solution (0.067 M, pH 7.0) in a carrier reservoir (2000 mL) with the temperature maintained at 2 °C flow and circulated into the liquid compartment of the gas-phase biosensor by means of a peristaltic pump (No. 7553-30, Cole-Parmer Instrument Co., Chicago, IL). In order to eliminate sensor noise caused by a pulsating stream from the pump, a homemade air damper system was added to the buffer flow tube between the pump and the gas-phase biosensor.

A computer-controlled potentiostat (HA-151, Hokuto Denko Ltd., Tokyo, Japan) was electrically connected to the gas-phase biosensor. A fixed voltage of −700 mV vs Ag/AgCl (counter electrode) was applied to the platinum working electrode of the dissolved oxygen electrode. The output current was monitored graphically on a continuous computer display and saved on floppy disk for later analysis.

Before measurement of ethanol, nitrogen gas (Type: N2-P, 99.99% nitrogen, Takachiho Trading Co., Ltd., Tokyo, Japan) was passed through the gas compartment, and the decrease in output current was used to confirm that the tip of the enzyme electrode was touching the diaphragm membrane.

A commercially available semiconductor gas sensor used for alcohol testing (Type: TGS822, Figaro Engineering Inc., Osaka, Japan) was also used simultaneously in the measurement system, and the characteristics of the two devices were compared. Other gaseous substances (*n*-pentane, benzene, methyl ethyl ketone, *n*-hexane, acetone, etc.), both individually and in a blended form, were also analyzed in order to investigate the selectivity of the sensors.

A liquid-phase AOD enzyme electrode was also constructed by use of an immobilized enzyme membrane fabricated by the same method as for the gas-phase biosensor. The characteristics of the enzyme electrode, such as lifetime, were compared with those of the gas-phase biosensor. When not in use, the AOD enzyme electrode was also stored below 10 °C.

RESULTS AND DISCUSSION

Evaluation of the Gas-Phase Biosensor. Figure 3 shows the current response of the gas-phase biosensor to ethanol in the gas phase at a concentration of 41.5 parts per million (ppm) for 5 min with and without buffer flow (1.9 L·h^{-1}) through the liquid compartment (before and after ethanol measurement, standard air was passed through the gas compartment). As the figure indicates, experiments both with and without buffer flow gave rectangular curves, in which the current decreased rapidly following application of ethanol, followed by a steady-state current which gradually increased to the initial output following standard air application. The decrease in output current relates to the concentration of ethanol in the gas phase, since ethanol that diffuses through the enzyme membrane is oxidized by AOD using oxygen as electron acceptor, causing a decrease in the concentration of dissolved oxygen (see the following equations).

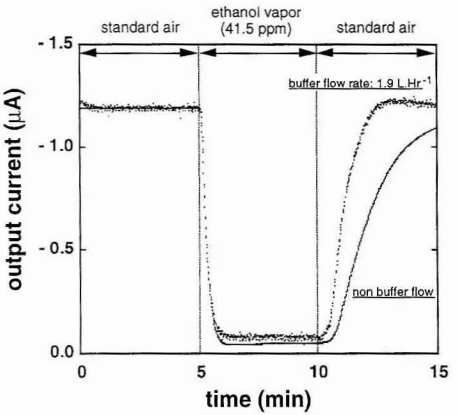

Figure 3. Typical responses for ethanol measurement in the gas phase using the gas-phase biosensor with buffer flow (1.9 L·h^{-1}) and without buffer flow.

enzyme reaction

$$RCH_2OH + O_2 \xrightarrow{AOD} RCHO + H_2O_2$$

working electrode

$$O_2 + 2H_2O + 4e^- \rightarrow 4OH^-$$

counter electrode

$$4Ag + 4Cl^- \rightarrow 4AgCl + 4e^-$$

Comparison of the curves showed that the sensor current without buffer flow had lower noise and slightly higher sensitivity than with buffer flow. With buffer flow, however, there was a more rapid recovery of the initial current following application of standard air.

Figure 4 shows the relationship between the buffer flow rate and the output recovery time of the gas-phase biosensor following application of 15.7 and 41.5 ppm ethanol in the gas phase. The output recovery time is represented by the time required to reach 90% of the steady current for standard air. As Figure 4 indicates, the output recovery time of the gas-phase biosensor decreases with increasing buffer flow rate. Namely, the buffer flow removes ethanol which diffuses through the diaphragm membrane into the liquid compartment and the enzyme membrane. Since there was little enhancement of the recovery time for buffer flow rates above 2.0 L·h^{-1} and the output current noise was greater, a buffer flow rate of 1.9 L·h^{-1} was generally used in all experiments with buffer flow.

The steady-state current value and the maximum slope calibration curves for ethanol in the gas phase are shown in Figure 5. The inset figure shows the typical response of the gas-phase biosensor to gaseous ethanol at various concentrations (1.57, 4.49, 7.86, 15.7, 41.5, 98.2, and 680 ppm). In these figures, the steady-state output signal is represented as a percentage of the current value for standard air. As Figure 5 indicates, the steady output and the slope of the response were related to the concentration of ethanol in the gas phase

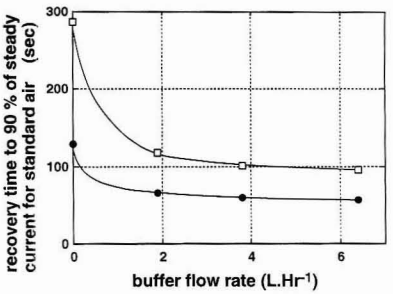

Figure 4. Effect of buffer flow rate on recovery time of the gas-phase biosensor (filled circle 15.7 ppm and open square 41.5 ppm ethanol in the gas phase).

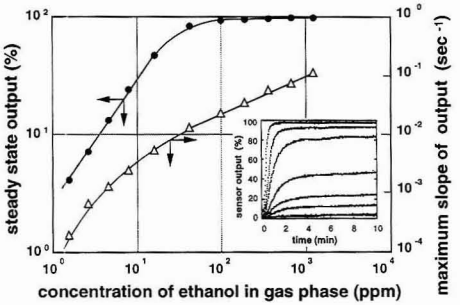

Figure 5. Calibration curves of gas-phase biosensor using steady-state output (filled circles) and maximum response slope (open triangles). Inset: typical response to varying concentrations of ethanol in the gas phase (1.57, 4.49, 7.86, 15.7, 41.5, 98.2, and 680 ppm).

over the range 1.57–41.5 ppm (correlation coefficient of 0.992) and 15.7–1242 ppm (correlation coefficient of 0.996), respectively, deduced from exponential regression analysis of the log–log plot by a method of least squares according to the following equations:

$$\text{output (\%)} = 3.00[\text{gaseous ethanol (ppm)}]^{0.943}$$

$$\text{slope (s}^{-1}\text{)} = 0.00091[\text{gaseous ethanol (ppm)}]^{0.685}$$

This calibration range using the maximum slope covers the maximum permissible concentration of ethanol vapor in the work place (1000 ppm), and the alcohol levels encountered in breath (over 130 ppm)[10] and can be utilized to determine the level of intoxication as described above. The gas-phase biosensor was calibrated by use of the steady-state output to give a detection limit for the sensor (diaphragm membrane pore size 1–2 μm, thickness 0.25 mm) of 1.57 ppm, which is lower than the ethanol-selective detection limit (6.1 ppm)[9] but higher than ethanol detection limit (0.36 ppm)[9] for the human sense of smell.

The detection limit of the device depends not only on the characteristics of the applied enzyme electrode but also on the pore size and thickness of the diaphragm membrane. If a more porous membrane is used as the diaphragm, ethanol can diffuse more easily into the liquid compartment and the

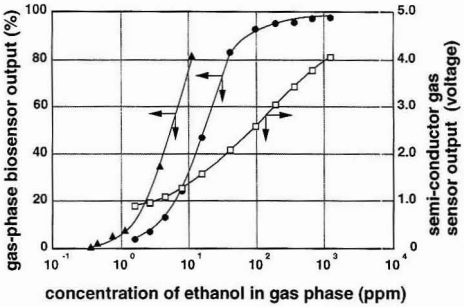

Figure 6. Comparison between the calibration curves of the gas-phase biosensors with two kinds of PTFE diaphragm membranes (filled circles, pore size of 1–2 μm, thickness of 0.25 mm; filled triangles pore size of 30–60 μm, thickness of 0.13 mm) and a commercially available semiconductor gas sensor (open squares).

enzyme membrane. The characteristics of the gas-phase biosensor can therefore be varied by changing the diaphragm membrane. This was examined by using a more porous and thinner type of diaphragm membrane (pore size 30–60 μm, thickness 0.13 mm).

Figure 6 shows the gaseous ethanol calibration curves for the gas-phase biosensor fabricated by using two different diaphragm membranes. In order to compare the sensor performance with a semiconductor-type gas sensor, the calibration curve of a commercially available semiconductor gas sensor is also shown in Figure 6. As this figure indicates, using the 30–60-μm pore membrane, the steady output was related to the concentration of gaseous ethanol over the range 0.358–11.46 ppm, with a correlation coefficient of 0.934 deduced by exponential regression analysis by a method of least squares according to the following equation:

$$\text{output (\%)} = 3.91[\text{gaseous ethanol (ppm)}]^{1.45}$$

By switching from a 1–2-μm pore size to a 30–60-μm pore size, it is possible to improve the detection limit from 1.57 to 0.358 ppm gaseous ethanol. As described above, the ethanol reported detection limit for sense of smell in humans is 0.36 ppm, which is equal to the sensitivity of the gas-phase biosensor. The calibration range of the semiconductor gas sensor was from 2.62 to 1242 ppm, which is wider than for the gas-phase biosensor. The gas-phase biosensor, however, is more versatile and can be modified to give a different calibration range by changing the pore size of the diaphragm membrane (i.e., for ethanol-sensitive detection like the human sense of smell) and by applying the maximum slope of the sensor output (i.e., for alcohol breath test).

One disadvantage of using a 30–60-μm pore size, was that the lifetime of the gas-phase biosensor was much reduced than when the 1–2-μm pore membrane was used. This decrease in the lifetime is not only caused by loss of enzyme from the enzyme membrane, but is also caused by deactivation of the enzyme. Namely, the enzyme membrane can dry out more easily when a more porous diaphragm is used, leading to enzyme denaturation. The diaphragm membrane must therefore be selected on the basis of the intended application of the sensor.

Because the AOD used in the enzyme electrode is unstable, the gas selectivity and lifetime of the gas-phase biosensor were investigated using the 1–2-μm pore membrane.

Gas Selectivity of Gas-Phase Biosensor. The selectivity of both the gas-phase biosensor and the commercially available semiconductor gas sensor for several gases and blends of gases is shown in Figure 7. The semiconductor gas sensor responded to all of the applied gases, confirming the extremely poor selectivity of such devices as generally known.[1,14] The gas-phase biosensor using an immobilized AOD electrode, however, gave negligible responses to all the chemicals other than ethanol.

The gas-phase sensor output using a mixture of ethanol (26.9, 89.5, and 268.6 ppm) and *n*-pentane (30.1, 100.0, and 301.0 ppm) was the same as the response to ethanol alone (26.9, 89.5, and 268.6 ppm, respectively) with a confidence level of 97.5% (determined from a paired *T*-test). The gas-

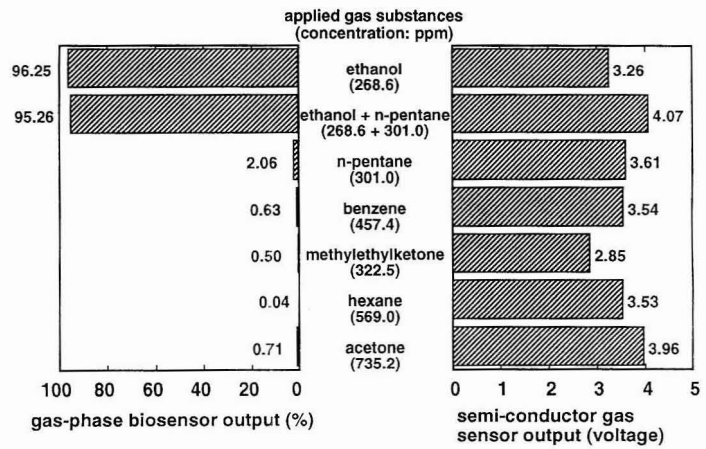

Figure 7. Gas selectivity of the gas-phase biosensor and semiconductor gas sensor for various substances in the gas phase.

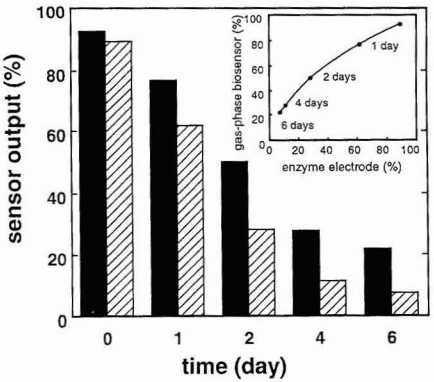

Figure 8. Lifetime of the gas-phase biosensor (filled bars, ethanol in gas phase 100.0 ppm) and immobilized AOD electrode (hatched bars, ethanol solution 94.7 mg·L^{-1}). Inset: relationship between lifetime of the gas-phase biosensor and immobilized AOD electrode.

phase biosensor thus possessed much greater selectivity and accuracy than the semiconductor gas sensor (same selectivity as for the enzyme electrode).

The AOD used in the sensor is from *Pichia pastoris* and has specificity for short-chain, linear aliphatic alcohols such as methanol and ethanol. It is possible to construct several kinds of AOD immobilized gas sensors with different characteristics, since the substrate specificity of the enzyme depends on the source microorganism [i.e., *Candida Sp.* (methanol 100%, ethanol 89%, 1-propanol 52%, 2-propanol 6%, and 1-butanol 29%);[18] *Candida methanosorbosa* (methanol 100%, ethanol 56.7%, 1-propanol 16%, 1-butanol 9.2%, 1-pentanol 4.2%),[19] etc.[20,21]]. Namely, using a sensor array system of these gas-phase biosensors and employing a pattern recognition method such as is found in neural networks,[22] it is possible to construct a gas-phase biosensor system with selectivity for a limited range of alcohols.

Lifetime of the Gas-Phase Biosensor. Figure 8 compares the lifetimes of the immobilized AOD gas-phase biosensor and enzyme electrode. The inset shows the relationship between the lifetimes of the two devices. The sensor outputs were obtained by applying 100 ppm ethanol vapor to the gas-phase biosensor and 94.7 mg·L^{-1} ethanol solution to the enzyme electrode and is represented as a percentage of the steady current value for standard air as described above.

As this figure indicates, both sensor outputs gradually decreased with time, the output of the gas-phase biosensor and the enzyme electrode after 4 days having decreased to a fourth and a tenth of the initial output, respectively. As the inset indicates, the decrease in output of the gas-phase biosensor is caused not only by applying the enzyme electrode to gas sensing but by deactivation and loss of AOD from the immobilization membrane. The short lifetime of the immobilized AOD electrode is in agreement with recently reported results.[19] The commercially available AOD used in these experiments has been reported to have low stability, low thermostability and short lifetime.[19] The slightly shorter lifetime of the enzyme electrode, as compared the gas-phase biosensor, may be caused by the easy loss of AOD from the enzyme membrane into the batch measurement solution. Since the lifetime of the gas-phase biosensor is also related to the pore size of the diaphragm membrane as described above, it is necessary that the membrane be selected to meet the application of the gas-phase biosensor.

CONCLUSIONS

The gas-phase biosensor for ethanol has a simple construction, high selectivity, and low detection limit, covering the concentration range encountered in breath after alcohol consumption and the sensing range of smell in humans. The calibration range of the sensor can be varied by selecting a diaphragm membrane of different porosity. Since a new AOD from *Candida methanosorbosa* which has high stability and long lifetime has been reported,[19] and several kinds of AOD with different substrate specificity depending on the source microorganism have become commercially available, the characteristics and lifetime of the gas-phase biosensor can be improved by applying these better enzymes. We are currently involved in applying these enzymes in the gas-phase biosensor, and the results will be reported in the near future.

The gas-phase biosensor can also be used for detection of other substances in the gas phase simply by changing the biomolecule (enzyme, microorganism, organelle, etc.) used in constructing the sensor. This would make the biosensor of value in many different areas, such as environmental monitoring, health and safety monitoring, and clinical analysis.

ACKNOWLEDGMENT

We thank Dr. Jonathan M. Dicks, who is a Japan Society for the Promotion of Science postdoctoral research fellow at RCAST, for his valued discussions and help in preparing the manuscript.

Received for review January 5, 1994. Accepted June 15, 1994.*

* Abstract published in *Advance ACS Abstracts,* August 1, 1994.

(18) Toyo Jozo enzyme catalogue, Toyo Jozo Co., Ltd., Tokyo, Japan, 1983; p 75.
(19) Suye, S. *Denki Kagaku* **1988**, *56*(12), 1122–1123.
(20) Kitagawa, Y. *Anal. Lett.* **1987**, *20*, 81.
(21) Janssen, F. W.; Ruelius, H. W. *Biochim. Biophys. Acta* **1968**, *151*, 330–342.
(22) Sommer, V.; Tobias, P.; Kohl, D. *Sens. Actuators B* **1993**, *12*, 147–152.

Anal. Chem. **1994,** *66,* 3303–3317

Interlaboratory Comparison of Autoradiographic DNA Profiling Measurements. 1. Data and Summary Statistics

James L. Mudd and F. Samuel Baechtel
Forensic Science Research and Training Center, Laboratory Division, Federal Bureau of Investigation Academy, Quantico, Virginia 22125

David L. Duewer, Lloyd A. Currie, and Dennis J. Reeder*
Chemical Sciences and Technology Laboratory, National Institute of Standards and Technology, Gaithersburg, Maryland 20899

Stefan D. Leigh and Hung Kung Liu
Computing and Applied Mathematics Laboratory, National Institute of Standards and Technology, Gaithersburg, Maryland 20899

The data obtained during an interlaboratory precision study sponsored by the Technical Working Group for DNA Analysis Methods are summarized. These data are representative of DNA restriction fragment length polymorphism (RFLP) autoradiographic measurements using laboratory protocols based upon procedures validated by the Federal Bureau of Investigation. Measurement reproducibility for a given RFLP fragment is a nonlinear function of the fragment's size, with the logarithm of the sample standard deviation (SD) approximately proportional to fragment size. The least-squares estimate of this relationship for fragments composed of 600 to 11 000 DNA base pairs (bp) is $SD = 10.4 \times 10^{(bp/8300)}$. Among-analyst and among-laboratory differences appear to contribute about equally to the variance in RFLP measurements. Autoradiographic imaging is a relatively small component of the overall variance for fragments ≤10 000 bp. Currently available data are sufficient to establish reliable tolerances for the expected interlaboratory variation for any given RFLP band size in this size range, assuming that relevant laboratories continue to use RFLP analysis protocols that are within the current "statistical population" (i.e., protocols similar to those used by the laboratories that participated in the interlaboratory study). This consistency may best be maintained through appropriate use of Standard Reference Materials, internal quality assurance programs, and external proficiency demonstrations.

The forensic use of DNA profiling methods (i.e., identifying an individual using DNA from blood or other tissue) has steadily increased in North America since its introduction in the 1987 trial *State of Florida v Tommie Lee Andrews*.[1,2] DNA restriction fragment length polymorphism (RFLP) analysis is a mature technology and is now recognized as valid and reliable.[2,3] While there are many newer analytical methods for demonstrating genetic differences among individuals, it is difficult to predict which technologies will predominate or when they will effectively supplant RFLP analysis.[4]

To realize the full potential of forensic DNA profiling, the Federal Bureau of Investigation (FBI) Laboratory is working in collaboration with state and local forensic laboratories to establish a DNA identification index system for the United States. This CODIS system (originally an acronym for *C*ombined *D*NA *I*ndex *S*ystem, now used as a name for the U.S. DNA index program) will enable law enforcement agencies to share DNA information when investigating violent crime and sex offenses.[5,6] It will do this by providing a central storage and exchange facility for selected DNA records submitted by local, state, and federal forensic DNA laboratories. For CODIS to meet the expectations of the forensic science community, all laboratories must produce comparable results when given samples from the same source.

The Technical Working Group on DNA Analysis Methods (TWGDAM) is an FBI-sponsored group of forensic scientists actively engaged in DNA testing or research.[7] The purpose of TWGDAM is to provide a forum for discussing issues, conducting studies, establishing quality assurance guidelines, and reaching consensus on DNA methodologies to be used in North American crime laboratories. The working group currently consists of 35 scientists representing university, Canadian, U.S. state and local forensic laboratories, the National Institute of Standards and Technology (NIST), and the FBI Laboratory.

In October 1989, TWGDAM initiated a three-phase interlaboratory study of the DNA RFLP profiling procedure based on the FBI Laboratory's choice of restriction enzyme

* Author to whom correspondence should be addressed: Tel: 301-975-3128; Fax: 301-330-3447; E-mail: DJReeder@micf.NIST.gov.

(1) *Andrews v State.* 533 SO. 2D 841; FL DIST CT APP, 1988.
(2) Office of Technology Assessment. Genetic Witness, Forensic Uses of DNA Tests (# 052-003-01203-1); Congress of the United States, U.S. Government Printing Office: Washington, DC, July 1990.
(3) National Research Council. *A Statement by the Committee on DNA Technology in Forensic Science*; National Academy Press: Washington DC, 1992.
(4) Weedn, W. V.; Roby, R. K. Overview of Future DNA Technologies; *Proc. Int. Symp. Hum. Identif.* **1992,** *3,* 117–133.
(5) Kirby, L. T. The Combined DNA Index System (CODIS): A Theoretical Model; *DNA Fingerprinting an Introduction*; Stockton Press: New York, NY, 1990; pp 279–317.
(6) *Legislative Guidelines for DNA Databases*; Assistant Director in Charge, Laboratory Division, Federal Bureau of Investigation: Washington, DC, November, 1991.
(7) Kearney, J. J. Summary of the First Meeting of the Technical Working Group for DNA Analysis Methods. *Crime Laboratory Digest* **1988,** *15* (4), 115–117.

This article not subject to U.S. Copyright.
Published 1994 by the American Chemical Society

Table 1. Participating Laboratories

Arizona Department of Public Safety
Broward County Sheriff's Office, Florida
California Department of Justice
Centre of Forensic Sciences, Ontario
Division of Forensic Science, Virginia
FBI Laboratory, Washington, DC
Florida Department of Law Enforcement
Georgia Bureau of Investigation
Institut für Rechtsmedizin, Bern, Switzerland
Kentucky State Police Forensic Laboratory
Metro-Dade Police Department, Florida
Minnesota Bureau of Criminal Apprehension
Nassau County Police Department, New York
National Institute of Standards and Technology
North Carolina State Bureau of Investigation Crime Laboratory
Orange County Sheriff's–Coroner Office, California
Royal Canadian Mounted Police Central Forensic Laboratory, Ontario
Texas College of Osteopathic Medicine, Department of Pathology
United States Army Criminal Investigation Laboratory, Europe
United States Army Criminal Investigation Laboratory, Georgia
Vermont Department of Public Safety
Washoe County Sheriff's Office, Nevada

and single locus probes.[8,9] A total of 22 laboratories (four U.S. Federal, 14 state and local, one university, two Canadian, and one European) participated in one or more phases of this study. Table 1 lists these laboratories. This study was *not* intended as a proficiency test for participating laboratories, but rather was designed to evaluate the interlaboratory reproducibility of DNA RFLP profiling analysis for pristine samples; determine what effect, if any, modifications to the TWGDAM-recommended general protocol have on the results obtained by these laboratories; and establish an expected RFLP measurement uncertainty estimate (a "window") to permit statistically valid interlaboratory comparison of data.

Due to the complexity and multiple foci of our analysis, we present the results of the TWGDAM sponsored interlaboratory DNA RFLP precision studies in three parts. Here, in Part 1, we present an overview of the TWGDAM-recommended RFLP general protocol and the design of the TWGDAM studies; summary data and relevant experimental details; various simple statistical and graphical summaries; graphical summaries of ancillary studies relevant to the TWGDAM data; an approximate allocation of various sources of measurement variance; and a determination of an interlaboratory measurement comparison "window". Part 2 will present an analysis of the sources and propagation of measurement uncertainty coming from the post-electrophoresis stages of RFLP profiling.[10] Part 3 details the known laboratory-specific protocol modifications and presents an analysis of the systematic effects these modifications introduce into band sizing.[11]

Interlaboratory evaluations, similar to this DNA RFLP study, will be required for informed use of any new DNA profiling technology. Several such studies are currently in progress. Discussion of these studies is beyond the scope of this present work.

METHODS AND MATERIALS

This section describes the design and evaluation of the TWGDAM interlaboratory precision study. Each participating laboratory received one set of replicate autoradiograms or specimens for each phase of the study and independently analyzed the autoradiograms or samples.

RFLP Procedure. The DNA RFLP analysis procedure used by TWGDAM study participants is described elsewhere.[8,9,12–15] In brief, this RFLP method involves *Hae*III restriction endonuclease digestion of DNA isolated from tissue or body fluid stains. Agarose gel electrophoresis separates the digested, double-stranded DNA fragments. The electrophoretic mobility is primarily proportional to fragment size; it also reflects fragment composition and conformation.[16] Fragment size is conventionally expressed as the number of constituent DNA base pairs (bp).

Alkali treatment denatures the double-stranded DNA fragments to single strands in the gel. Southern blotting transfers the denatured DNA fragments from the gel and immobilizes them onto a polymeric membrane support (or "blot").[17] Hybridization of the immobilized DNA with specific ^{32}P radiolabeled DNA probes enables autoradiographic imaging of fragments with complementary base sequences on X-ray-type film. Sequential hybridization with different probes is routine. A number of probes for use with *Hae*III-digested DNA have proven useful in forensic DNA profiling. Sufficient data exist to examine statistically the characteristics of five of these probes. The probe and the genetic locus each identifies are MS1 (for locus D1S7), YNH24 (D2S44), PH30 (D4S139), TBQ7 (D10S28), and V1 (D17S79). The locus designation will be used throughout the remainder of this work.

Each single locus DNA probe generally binds at a specific complementary sequence on a human chromosome. These probes typically bind with four single-stranded DNA fragments from a sample: two each from the maternal and paternal alleles. In some cases, where the maternal and paternal fragments are close in size, electrophoresis may fail to resolve both DNA fragments.[18,19]

The size of each fragment is estimated by interpolating its electrophoretic migration distance using DNA fragments of known sequence. A calibration set of DNA fragments is referred to as a "sizing ladder". The resulting calculated

(8) Budowle. B.; Baechtel, F. S. Modifications to improve the effectiveness of restriction fragment length polymorphism typing. *Appl. Theor. Electrophor.* **1990**, *1*, 181–187.

(9) Budowle, B. A protocol for RFLP analysis of forensic biospecimens. *Proc. Int. Symp. Forensic Aspects DNA Anal.* **1989**, 57–62 (June 19-23, Quantico, VA).

(10) Duewer, D. L.; Currie, L. A.; Reeder, D. J.; Leigh, S. D.; Liu, H. K.; Mudd, J. L. Interlaboratory Comparison of Autoradiographic DNA Profiling Measurements. 2. Measurement Uncertainty and Its Propagation. In preparation. (Preprints available from D. J. Reeder.)

(11) Leigh, S. D.; Liu, H. K.; Duewer, D. L.; Currie, L. A.; Reeder, D. J.; Mudd, J. L. Interlaboratory Comparison of Autoradiographic DNA Profiling Measurements. 3. Protocol Effects. In preparation. (Preprints available from D. J. Reeder.)

(12) Guidelines for a Quality Assurance (QA) Program for DNA Restriction Fragment Length Polymorphism (RFLP) Analysis. *Crime Lab. Dig.* **1990**, *16* (2), 40–59.

(13) The Guidelines for a Proficiency Testing Program for DNA RFLP Analysis. *Crime Lab. Dig.* **1990**, *17* (3), 59–64.

(14) Guidelines for a Quality Assurance (QA) Program for DNA Analysis. *Crime Lab. Dig.* **1991**, *18* (2), 44–75.

(15) Bashinski, J. Managing the Implementation and Use of DNA Typing in the Crime Laboratory. In *Forensic DNA Technology*; Farley, M. A., Harrington, J. J., Eds.; Lewis Publishers, Inc.: Chelsea, MI, 1991; pp 201–235.

(16) Holmes. D. L.; Stellwagen, N. C. The electric field dependence of DNA mobilities in agarose gels: A reinvestigation. *Electrophoresis* **1990**, *11*, 5–15.

(17) Southern, E. M. Detection of Specific Sequences Among DNA Fragments Separated by Gel Electrophoresis. *J. Mol. Biol.* **1975**, *98*, 503–517.

(18) Berry, D. A. Inferences Using DNA Profiling in Forensic Identification and Paternity Cases. *Statistical Science* **1991**, *6*(2), 175–205.

(19) Endean, D. J. RFLP Analysis for Paternity Testing: Observations and Caveats. *Proc. Int. Symp. Hum. Identi.* **1989**, 55–76.

fragment sizes are expressed as the number of DNA base pairs. This quantitative reduction of the information present on the autoradiogram is referred to as "band sizing". Most TWGDAM laboratories implement the sizing process with the FBI-developed computer-assisted image analysis system.[20] Other laboratories use one of several commercially developed imaging systems.

The TWGDAM-recommended RFLP general protocol has been optimized for sizing DNA fragments from about 1 000 to 11 000 bp. Very small fragments may be completely eluted from the gel during electrophoresis and therefore not detected. Very large fragments may not move sufficiently from the origin to be sized quantitatively. For the single locus probes in current use, however, most sample bands fall within the appropriate size range.

Standard Format of the Agarose Gel and Derived Autoradiograms. Although the specific arrangement of specimens, controls, and sizing ladders on the analytical gel and the resulting autoradiograms varies somewhat among laboratories, some standardization in this area has been achieved. The organization of the standard autoradiograms submitted to the laboratories, as well as the general organization of the analytical gels prepared for the submitted specimens, follows a format based on TWGDAM guidelines.[12–15] Figures 1 and 2 display examples of this format.

Each specimen, control, or sizing ladder sample is added to a separate well near the top (cathodic) edge of the rectangular agarose gel. DNA fragments from each such sample move in separate, parallel paths ("lanes") through the gel as they are drawn toward the anode during electrophoresis. An analytical gel may also include a visual or fluorescent marker, usually located in the left-most lane, which helps the analyst determine when to end electrophoresis. Early practice in some laboratories combined the visual marker with the first sizing ladder.

*Hae*III-digested DNA from an immortalized female human cell line (designated as K562) is to the immediate right of the first sizing ladder. (The original K562 cell line is maintained at the American Type Culture Collection, Rockville, MD.) The primary utility of this sample is to monitor the operational performance of the electrophoretic process. The analysis of bands from K562 DNA also provides an internal quality check on the quantitative conversion of band position to fragment size.

The extracted, *Hae*III-digested DNA specimens are applied in ordered lanes across the analytical gel, separated at appropriate intervals by sizing ladders. The specimens are divided into two subsets, "known" (K) from particular individuals and "questioned" (Q) from evidentiary samples. A sizing ladder typically brackets 2–5 DNA specimens.

Study Design. The TWGDAM precision study was divided into three phases, with phase 1 further divided into phases 1A and 1B: Phase 1A. Examine imaging steps only. Most participants had limited experience with equipment. Sample set consisted of duplicated autoradiograms. Phase 1B. Examine imaging steps only. Sent at the end of Phase 3, most participants had 18–24 months experience with equipment. Sample set consisted of duplicated autoradiograms. Phase 2. Examine all steps except sample preparation (i.e., electrophoresis, autoradiography, and imaging). Sample set consisted of *Hae*III-digested DNA. Phase 3. Examine the total RFLP process: sample preparation, electrophoresis, autoradiography, and imaging. Sample set consisted of bloodstains.

Phase 1A. Band Sizing from Duplicated Autoradiograms. This phase of the study, involving 22 laboratories, was initiated in October 1989 and completed in May 1991. It was designed to (1) ensure that all participating laboratories had the necessary equipment and skills needed to determine DNA fragment sizes from data present on autoradiograms and (2) provide an estimate of the reproducibility of interpreting the same autoradiograms across laboratories and analysts. No laboratory was excluded from this or any other phase of the study.

Three autoradiograms were selected from the FBI Forensic Science Research and Training Center's (FSRTC) collection. They were chosen to represent diversity in band size and good quality (by the criteria of the time) autoradiograms. The original autoradiograms were duplicated using Kodak X-OMAT C SO-408 duplicating film and a BXR Mark IV duplicator (Blu-Ray, Inc., Essex, CT). The duplicated autoradiograms were developed using a Kodak M 35A X-OMAT processor.

Each autoradiogram displays different DNA fragments of the same nine specimens. The autoradiogram for genetic loci D2S44 was obtained first, followed by D1S7 and D17S79. Of the nine specimens, four (K1, Q3, Q5, and Q7) were identified as coming from the same donor, four (K2, Q1, Q2, and Q6) were identified as coming from another donor, and one (Q4) was identified as an unmatched specimen. Each autoradiogram also contained a K562 DNA control. A sizing ladder which provided 30 bands ranging from 600 to 12 800 bp was used with these autoradiograms (Lifecodes Corp., Stamford, CT).

Parts a–c of Figure 1 present the phase 1A autoradiograms. Table 2 presents the following summary statistics for all data obtained for phase 1A: the extreme values, median, mean, standard deviation, and percent relative standard deviation. The raw data are available as supplementary material.

Phase 1B. Additional Band Sizing from Common Autoradiograms. This phase of the study was designed to complement phase 1A by examining the interlaboratory reproducibility of band sizing of very small and large fragments and to test for any changes in performance. It was initiated in June 1991 and completed in August 1991, with 21 laboratories participating. Each laboratory received a set of four duplicated autoradiograms, one autoradiogram each for genetic loci D1S7, D2S44, D4S139, and D17S79. The original autoradiograms were again selected from the FSRTC's collection using the criteria of diversity of band size and good autoradiogram quality. (Note that autoradiogram quality noticeably improved during the interval between studies.) The autoradiograms were duplicated and developed as described above for phase 1A.

Each autoradiogram in the set contained seven specimens from three anonymous donors. Unlike phase 1A, only the D1S7 and D2S44 autoradiograms in this phase were taken from the same blot. The D4S139 and D17S79 autoradiograms

(20) Monson, K. L.; Budowle, B. A system for semi-automated analysis of DNA autoradiograms. *Proc. Int. Symp. Forensic Aspects DNA Anal.* **1989**, 127–132 (June 19–23, Quantico, VA).

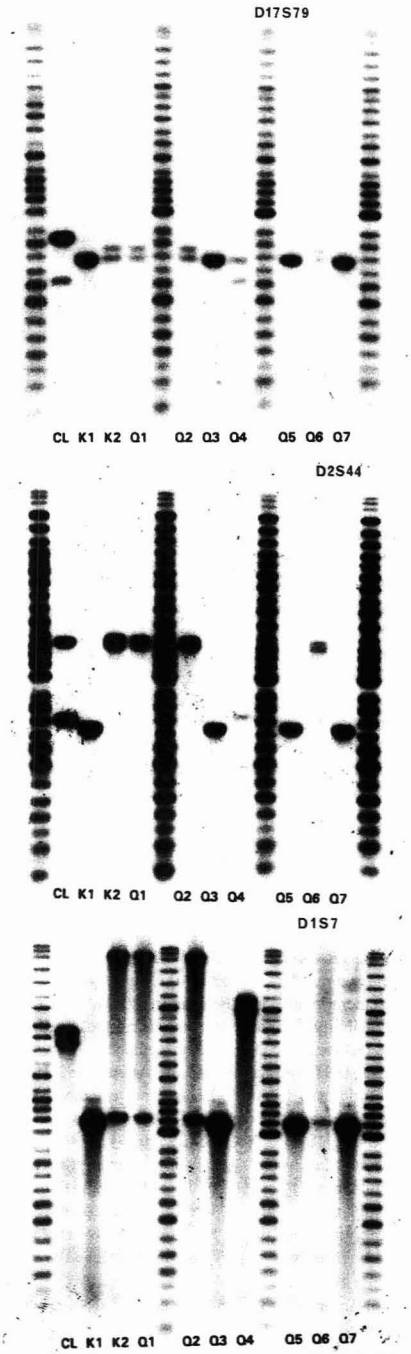

Figure 1. Autoradiograms used in TWGDAM phase 1A: (a, top) D1S7, (b, middle) D22S44, and (c, bottom) D17S79.

are from different blots. For the D1S7 and D2S44 autoradiograms, the specimen groupings are (K1, Q3, Q4), (K2, Q2, Q5), and Q1. For the D4S139 autoradiogram, the groupings are (K1, Q1, Q4), (K2, Q2, Q5), and Q3. For the D17S79 autoradiogram, the groups are (K1, Q1, Q4, Q5), (K2, Q3), and Q2. Each autoradiogram also contained a K562 DNA control.

The specimen in the first lane of the loci D1S7, D2S44, and D17S79 autoradiograms combined the phase 1A sizing ladder and a visual DNA marker. A sizing ladder that provided 30 bands ranging from 600 to 23 400 bp was used with the locus D4S139 autoradiogram (Lifecodes Corp., Stamford, CT).

Part a–d of Figure 2 present the phase 1B autoradiograms. Table 3 presents summary statistics for these data. The raw data are available as supplementary material.

Phase 2. Electrophoresis and Band Sizing of Predigested DNA Samples. The phase 2 study was designed to examine the variability of the total RFLP protocol excluding sample preparation. It was initiated in April 1990 and completed in April 1991, with 22 laboratories participating. Whole-blood aliquots collected from one of us (J.L.M., samples abbreviated JM) were extracted and treated with *Hae*III restriction endonuclease, as were K562 aliquots (Lifecodes Corp., Stamford, CT)[8,9] Digest from the same sources were mixed with loading buffer and pooled to ensure homogeneity. Individual 18-μL aliquots of the pools were prepared and kept frozen at –60 °C until shipped. Samples were shipped frozen. The JM samples were designated as JM1, JM4, and JM6. The K562 samples were designated C2, C3, C5, and C7. Each laboratory provided its own K562 control.

Participating laboratories were requested to provide DNA RFLP profiles for genetic loci D2S44 and D17S79. Table 4 presents the RFLP summary statistics for these phase 2 data. The raw data are available as supplementary material. Each participant's protocol modifications are presented in part 3.

Phase 3. Sample Preparation, Electrophoresis, and Band Sizing of Bloodstains. The phase 3 study was designed to examine the variability of the entire DNA profiling process. It was initiated in August 1990 and completed in August 1991, with 22 laboratories participating. Additionally, one laboratory submitted data obtained using two distinct variations of the general protocol. Bloodstains were prepared on washed white cotton sheeting from whole blood donated by FBI Laboratory employees JM, JA, KH, and SC. The DNA extracted from these donors provided a variety of band sizes. The bloodstains were sent through regular mail services to all participants. The KH samples were designated Q1, Q3, and Q5; the JM as Q2, Q6, and Q8; the JA as Q4; and the SC as Q7 and Q9. As in phase 2, each laboratory provided its own K562 control.

Participating laboratories were requested to provide DNA RFLP profiles for genetic loci D2S44 and D17S79. Table 5 presents summary statistics for these data. The raw data are available as supplementary material. Each participant's protocol modifications are presented in part 3.

RESULTS

All data obtained in this study were collated at FSRTC and evaluated at NIST. Band-sizing data were rounded to the nearest whole number of base pairs before analysis.

Table 2. TWGDAM Phase 1A Summary Statistics for Band Size (bp)[a]

			Band 1							Band 2						
Locus	Source	Sam	n	Low	Med	High	Mean	SD	%RSD	n	Low	Med	High	Mean	SD	%RSD
D1S7	K562	CL	42	4468	4544	4665	4546	32.2	0.71	42	4144	4196	4249	4195	19.0	0.45
	P1AK1	K1	43	2462	2493	2588	2499	26.7	1.07							
		Q3	43	2442	2483	2552	2484	22.8	0.92							
		Q5	43	2482	2508	2540	2507	14.0	0.56			*Single*	*band*	*pattern*		
		Q7	43	2454	2498	2535	2495	17.0	0.68							
			172	2442	2496	2588	2496	22.1	0.89							
	P1AK2	K2	43	10086	10393	10777	10405	165.1	1.59	43	2559	2570	2586	2570	5.4	0.21
		Q1	43	10086	10424	10804	10416	154.9	1.49	43	2553	2567	2578	2566	5.9	0.23
		Q2	43	10194	10430	10758	10422	126.6	1.21	43	2540	2557	2568	2556	6.8	0.26
		Q6	10	10533	10710	10793	10691	104.7	0.98	43	2523	2553	2567	2554	7.8	0.31
			139	10086	10433	10804	10434	162.5	1.56	172	2523	2562	2586	2562	9.3	0.36
	P1AQ4	Q4	43	6067	6135	6245	6142	45.6	0.74	43	5525	5630	5677	5628	26.7	0.47
D2S44	K562	CL	42	2910	2928	2944	2927	7.2	0.25	42	1783	1801	1818	1800	7.3	0.41
	P1AK1	K1	43	1672	1693	1710	1694	9.3	0.55							
		Q3	43	1682	1691	1707	1692	5.0	0.30							
		Q5	43	1692	1706	1716	1706	5.4	0.32			*Single*	*band*	*pattern*		
		Q7	43	1681	1696	1704	1695	5.4	0.32							
			172	1672	1696	1716	1697	8.5	0.50							
	P1AK2	K2	43	2953	2991	3029	2989	20.0	0.67	43	2834	2886	2933	2887	20.0	0.69
		Q1	43	2947	2984	3028	2983	17.7	0.59	43	2836	2893	2936	2891	21.0	0.72
		Q2	43	2941	2976	3009	2974	15.6	0.53	43	2843	2883	2920	2886	18.6	0.64
		Q6	43	2942	2964	2998	2967	13.3	0.45	43	2855	2877	2901	2879	11.8	0.41
			172	2941	2978	3029	2978	18.7	0.63	172	2834	2884	2936	2885	18.5	0.64
	P1AQ4	Q4	43	1827	1833	1846	1834	3.5	0.19	43	1319	1329	1345	1329	4.9	0.37
D17S79	K562	CL	42	1968	1992	2015	1992	9.3	0.47	42	1538	1544	1552	1545	3.0	0.19
	P1AK1	K1	43	1741	1751	1757	1750	3.9	0.23							
		Q3	43	1736	1746	1755	1746	4.7	0.27							
		Q5	43	1751	1760	1769	1760	3.9	0.22			*Single*	*band*	*pattern*		
		Q7	43	1737	1752	1769	1753	6.8	0.39							
			172	1736	1752	1769	1752	7.1	0.41							
	P1AK2	K2	43	1855	1867	1876	1867	4.8	0.26	43	1763	1774	1789	1774	5.4	0.31
		Q1	43	1854	1864	1874	1865	4.6	0.25	43	1762	1774	1789	1775	6.3	0.35
		Q2	43	1844	1860	1875	1861	5.3	0.29	43	1761	1769	1779	1769	4.2	0.24
		Q6	43	1845	1860	1873	1860	5.1	0.27	43	1755	1771	1790	1771	7.5	0.43
			172	1844	1863	1876	1863	5.7	0.30	172	1755	1772	1790	1772	6.3	0.36
	P1AQ4	Q4	43	1746	1754	1763	1754	4.4	0.25	43	1520	1532	1542	1531	4.3	0.28

[a] Locus, genetic locus; Source, label for DNA source; Sam, label for given sample; Band 1, statistics for larger band in lane; Band 2, statistics for smaller band in lane; *n*, number of analyses; Low, smallest size reported; Med, median of reported band sizes; High, largest size reported; Mean, arithmetic mean of reported band sizes; SD, standard deviation of reported band sizes; %RSD, percent relative standard deviation of reported band sizes.

Tables 2–5 report summary information for all phases of the TWGDAM precision study. All calculations are unweighted, treating every reported value as if it were from a separate laboratory. This approach minimizes assumptions about the potential sources of measurement variation. In practice, since most laboratories reported single sets of results for each phase of the study, this simple approach closely aligns with more complex models. A more detailed statistical analysis of these data is provided in part 3 of this series.

To enable independent review and analysis, we provide all data generated in the TWGDAM study as supplementary material. See the Supplementary Material Available section at the end of this article for further information.

Phases 1A and 1B. Although only a single set of autoradiograms was sent to each laboratory, the number of individuals who sized the set of autoradiograms varied among laboratories. In phase 1B, a number of individuals sized the autoradiograms several times.

Figure 3 displays the observed sample standard deviation (SD) and percent relative standard deviation (%RSD) for all bands in phases 1A and 1B as a function of mean band size (MBS). The logarithm of SD is seen to be an approximately linear function of MBS (i.e., SD is an exponential function of MBS). While %RSD is more constant than SD, it retains obvious dependence upon MBS. The least-squares linear fit of $\log_{10}$(SD) to MBS for Phase 1B data is:

$$\log_{10}(\mathrm{SD}) = (0.295 \pm 0.019) + \frac{\mathrm{MBS}}{(6025 \pm 130)} \quad (1)$$

with 56 data pairs and having a residual standard deviation of 0.076. The "±" terms in the intercept and slope parameters are estimated standard errors. The slope is expressed in reciprocal scale for the sake of interpretability. This relationship is shown in Figure 3 for both forms of the standard deviation values.

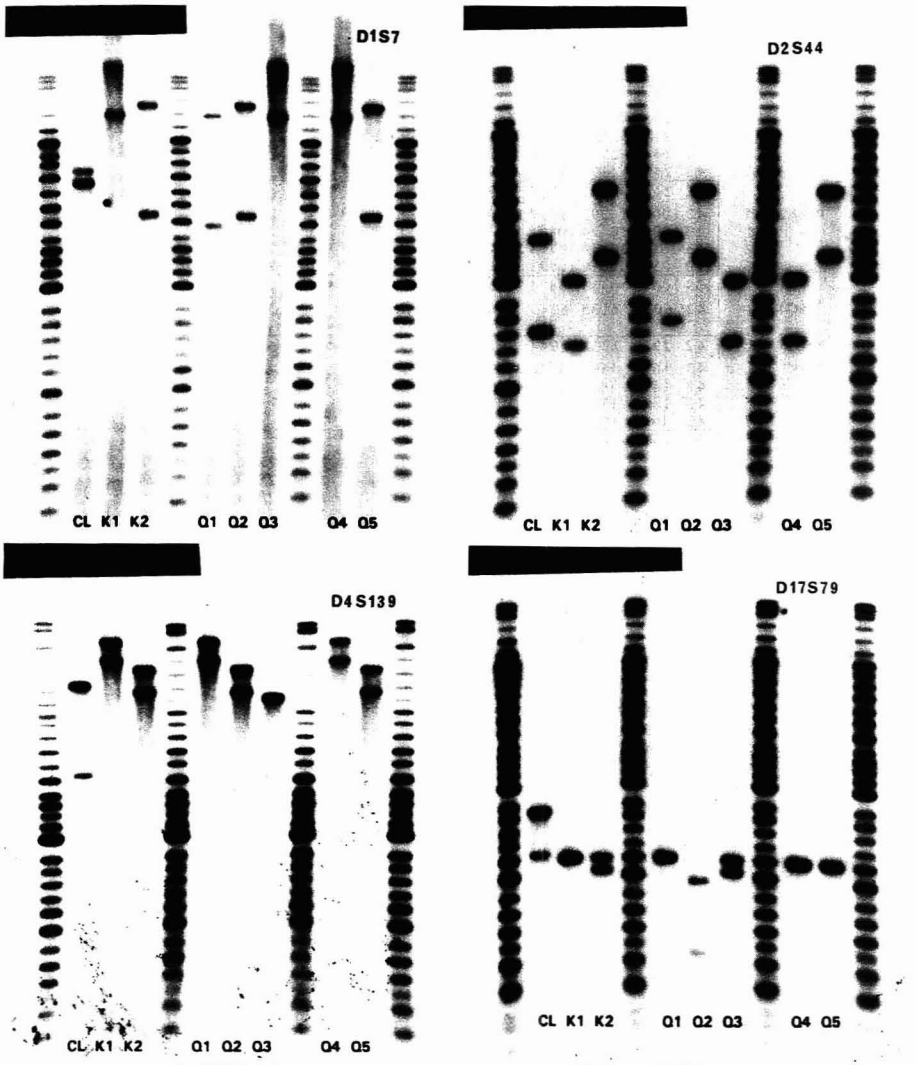

Figure 2. Autoradiogram used in TWGDAM phase 1B: (a, top left) D1S7, (b, top right) D2S44, (c, bottom left) D4S139, and (d, bottom right) D17S79. Casework identification code was originally in opaque area at upper left.

The sizings for several bands of the phase 1A study are much more variable than those of any band of comparable MBS in the phase 1B data. Even when the exceptional bands are excluded, the phase 1A data appear somewhat more variable than those of phase 1B. This suggests either general improvement in band-sizing reproducibility over the course of the TWGDAM study or systematic differences between the two sets of autoradiograms (see section below). An analysis of the sources and functional form of band sizing variation is presented in part 2 of this series.

Autoradiogram Homogeneity. The FSRTC conducted a study of both phase 1A and 1B autoradiograms that examined the uniformity of autoradiogram copies sent to the participating laboratories. Four randomly selected autoradiogram copies from each of the two sets were sized by one analyst ("rep" sizing) and the results compared to four sizings of one autoradiogram ("rad" sizing) by the same analyst. The average band sizes of the "rep" and "rad" sizings were all quite similar for the 104 bands in the two sets of autoradiograms, and were equally similar to the mean values obtained in the TWGDAM phase 1 interlaboratory comparisons. The median ratio of variances, SD^2_{rad}/SD^2_{rep}, was 0.93. The similarity of mean band sizes and the very modest increase in variance between the "rep" and "rad" sizings suggest that

Table 3. TWGDAM Phase 1B Summary Statistics for Band Size (bp)[a]

			Band 1							Band 2						
Locus	Source	Sam	n	Low	Med	High	Mean	SD	%RSD	n	Low	Med	High	Mean	SD	%RSD
D1S7	K562	CL	68	4540	4561	4587	4563	11.7	0.26	68	4180	4198	4213	4198	7.6	0.18
	P1B01K1	K1								60	7127	7183	7245	7187	27.0	0.38
		Q3				*Band too large to size*				60	7015	7094	7143	7092	31.2	0.44
		Q4								60	6919	7018	7105	7014	38.1	0.54
										180	6919	7100	7245	7098	77.9	1.10
	P1B01K2	K2	60	7903	7959	8051	7960	33.0	0.41	60	3470	3484	3498	3485	6.8	0.20
		Q2	60	7854	7931	8001	7940	35.8	0.45	60	3444	3457	3474	3458	6.1	0.18
		Q5	60	7696	7831	7908	7833	36.5	0.47	60	3449	3463	3476	3464	6.5	0.19
			180	7696	7926	8051	7911	65.9	0.83	180	3444	3465	3498	3469	13.1	0.38
	P1B01Q1	Q1	60	7081	7121	7164	7124	20.7	0.29	60	3249	3262	3273	3262	5.3	0.16
D2S44	K562	CL	68	2923	2936	2949	2936	6.1	0.21	68	1801	1810	1817	1810	3.3	0.18
	P1B01K1	K1	60	2332	2347	2359	2347	5.6	0.24	60	1676	1683	1688	1683	3.3	0.20
		Q3	60	2299	2313	2325	2313	4.6	0.20	60	1668	1677	1686	1678	3.5	0.21
		Q4	60	2317	2331	2345	2331	6.0	0.26	60	1668	1674	1682	1674	3.4	0.20
			180	2299	2331	2359	2331	14.9	0.64	180	1668	1678	1688	1678	4.9	0.29
	P1B01K2	K2	60	3849	3872	3888	3872	8.4	0.22	60	2631	2642	2658	2641	5.4	0.20
		Q2	60	3839	3858	3876	3858	8.8	0.23	60	2605	2621	2635	2621	6.5	0.25
		Q5	60	3821	3848	3868	3847	8.8	0.23	60	2620	2635	2649	2636	6.0	0.23
			180	3821	3859	3888	3859	13.4	0.35	180	2605	2634	2658	2633	10.3	0.39
	P1B01Q1	Q1	60	2941	2955	2968	2954	5.8	0.20	60	1882	1888	1897	1888	2.9	0.15
D4S139	K562	CL	68	6586	6644	6709	6644	26.1	0.39	68	3435	3449	3466	3450	7.3	0.21
	P1B04K1	K1	59	10892	11358	11600	11320	156.1	1.38	60	8316	8450	8541	8436	47.8	0.57
		Q1	59	10986	11479	11778	11427	186.7	1.63	60	8343	8453	8527	8442	48.5	0.57
		Q4	59	11012	11439	11628	11421	122.2	1.07	60	8305	8415	8487	8406	43.1	0.51
			177	10892	11403	11778	11389	163.9	1.44	180	8305	8425	8541	8428	48.9	0.58
	P1B04K2	K2	60	7518	7592	7664	7591	34.1	0.45	60	6132	6194	6255	6194	27.7	0.45
		Q2	60	7530	7608	7694	7611	42.6	0.56	60	6100	6154	6199	6150	24.1	0.39
		Q5	60	7464	7577	7669	7579	39.4	0.52	60	6056	6130	6196	6130	28.0	0.46
			180	7464	7592	7694	7594	40.9	0.54	180	6056	6156	6255	6158	37.8	0.61
	P1B04Q3	Q3	60	5731	5798	5849	5794	24.8	0.43			*Single*	*band*	*pattern*		
D17S79	K562	CL	68	2001	2015	2032	2015	6.9	0.34	68	1545	1554	1561	1553	3.5	0.22
	P1B17K1	K1	60	1513	1520	1531	1520	4.2	0.28							
		Q1	60	1501	1513	1522	1511	3.9	0.26							
		Q4	60	1497	1508	1521	1507	4.1	0.27			*Single*	*band*	*pattern*		
		Q5	60	1501	1510	1518	1509	4.1	0.27							
			240	1497	1511	1531	1512	6.5	0.43							
	P1B17K2	K2	60	1504	1512	1520	1512	3.0	0.20	60	1395	1402	1409	1402	3.2	0.23
		Q3	60	1500	1508	1515	1507	3.5	0.23	60	1389	1401	1410	1401	3.6	0.26
			120	1500	1509	1520	1509	4.0	0.26	120	1389	1401	1410	1402	3.4	0.24
	P1B17Q2	Q2	60	1315	1320	1326	1320	2.6	0.19	60	821	826	831	826	2.5	0.30

[a] Headings as in Table 2.

the copying process did not have much impact on autoradiogram sizing.

The *intralaboratory repeatability* observed in the "rep" and "rad" sizings paralleled that of the full *interlaboratory reproducibility* for all bands of all autoradiograms. The median ratio of intra- to interlaboratory variances, (SD^2_{rad} or SD^2_{rep})/SD^2_{phase1}, was 0.58. This suggests that more than half of the imaging variance can be attributed to intrinsic image processing effects rather than systematic differences among analysts or laboratory imaging systems. This will be examined in greater detail in part 2.

Even though the same experienced FSRTC analyst sized all autoradiograms of the "rep" and "rad" studies, the phase 1A autoradiograms produced more variable sizing than those of phase 1B. This strongly suggests that systematic differences in the quality of the autoradiograms themselves account for most of the improved repeatability and reproducibility of the phase 1B data. Casual examination of the autoradiograms displayed in Figures 1 and 2 indicates that some of the sample bands in the phase 1A autoradiograms are more intense and/or broader than any of the sample bands of phase 1B. This, too, will be examined in greater detail in part 2.

Phases 2 and 3. Figure 4 displays the observed SD and %RSD for all bands in phases 2 and 3 as a function of MBS. As in the phase 1 data, the logarithm of SD is an approximately linear function of MBS. The least-squares linear fit of $\log_{10}$(SD) to MBS is shown in Figure 4 for both measures of variation. The least-squares equation is

$$\log_{10}(SD) = (1.056 \pm 0.032) + \frac{MBS}{(9330 \pm 1390)} \quad (2)$$

for 70 data pairs with a residual standard deviation of 0.075.

Table 4. Phase 2 Summary Statistics for Band Size (bp)[a]

			Band 1							Band 2						
Locus	Source	Sam	n	Low	Med	High	Mean	SD	%RSD	n	Low	Med	High	Mean	SD	%RSD
D2S44	K562	CL	32	2838	2904	2961	2905	30.7	1.06	32	1747	1788	1821	1790	18.5	1.03
	K562	C2	30	2831	2888	2947	2886	27.0	0.93	30	1744	1785	1817	1785	16.2	0.91
		C3	30	2824	2889	2947	2887	28.1	0.97	30	1742	1784	1817	1783	16.4	0.92
		C5	30	2811	2889	2947	2886	30.0	1.04	30	1739	1787	1808	1783	17.2	0.97
		C7	30	2840	2892	2930	2886	21.7	0.75	30	1742	1787	1809	1783	15.5	0.87
			120	2811	2889	2947	2886	26.6	0.92	120	1739	1785	1817	1784	16.1	0.90
	JM	JM1	30	3050	3110	3143	3108	20.7	0.66	30	2046	2097	2121	2093	18.1	0.87
		JM4	30	3059	3109	3149	3108	19.0	0.61	30	2042	2087	2127	2089	18.6	0.89
		JM6	30	3056	3104	3165	3107	23.6	0.76	30	2046	2090	2123	2089	19.1	0.91
			90	3050	3108	3165	3107	21.0	0.67	90	2042	2092	2127	2090	18.5	0.89
D17S79	K562	CL	27	1946	1971	2017	1977	19.7	1.00	27	1499	1523	1555	1525	15.2	1.00
	K562	C2	26	1920	1972	2005	1968	22.1	1.12	26	1496	1527	1572	1527	14.9	0.98
		C3	26	1930	1965	2019	1969	23.8	1.21	26	1502	1529	1564	1529	15.5	1.02
		C5	26	1919	1965	2033	1966	24.2	1.23	26	1497	1525	1553	1526	13.7	0.90
		C7	26	1922	1966	2021	1969	20.2	1.03	25	1481	1526	1549	1524	17.4	1.14
			104	1919	1966	2033	1968	22.3	1.13	103	1481	1526	1572	1526	15.3	1.00
	JM	JM1	26	1722	1755	1797	1753	18.0	1.02	26	1272	1294	1317	1292	12.5	0.97
		JM4	26	1721	1755	1805	1755	17.9	1.02	26	1258	1296	1329	1294	16.6	1.28
		JM6	26	1720	1757	1789	1755	17.3	0.98	26	1247	1300	1336	1297	21.5	1.66
			78	1720	1756	1805	1755	17.5	1.00	78	1247	1296	1336	1295	17.2	1.33

[a] Headings as in Table 2.

Table 5. Phase 3 Summary Statistics for Band Size (bp)[a]

			Band 1							Band 2						
Locus	Source	Sam	n	Low	Med	High	Mean	SD	%RSD	n	Low	Med	High	Mean	SD	%RSD
D2S44	K562	CL	33	2867	2911	2939	2909	15.3	0.53	33	1766	1795	1830	1795	14.9	0.83
	KH	Q1	30	1765	1791	1823	1792	13.2	0.74	30	1647	1676	1729	1679	17.4	1.04
		Q3	29	1768	1788	1822	1790	13.6	0.76	29	1650	1676	1712	1679	18.2	1.08
		Q5	30	1759	1789	1815	1790	14.2	0.79	30	1637	1669	1705	1674	17.7	1.06
			89	1759	1790	1823	1791	13.5	0.76	89	1637	1673	1729	1677	17.7	1.06
	JM	Q2	30	3065	3140	3170	3131	25.7	0.82	30	2080	2104	2134	2106	14.5	0.69
		Q6	30	3066	3123	3173	3124	27.7	0.89	30	2070	2102	2143	2104	20.4	0.97
		Q8	30	3083	3134	3171	3131	24.6	0.79	30	2082	2109	2143	2109	18.3	0.87
			90	3065	3133	3173	3128	26.0	0.83	90	2070	2104	2143	2106	17.8	0.85
	JA	Q4	29	2889	2943	2980	2942	27.1	0.92	29	2222	2246	2294	2253	22.3	0.99
	SC	Q7	29	1541	1580	1603	1579	16.1	1.02							
		Q9	29	1555	1576	1599	1576	9.6	0.61			*Single*	*band*	*pattern*		
			58	1541	1579	1603	1578	13.2	0.84							
D17S79	K562	CL	28	1947	1985	2024	1986	18.4	0.93	28	1488	1529	1551	1529	14.4	0.94
	KH	Q1	26	1493	1533	1561	1534	16.0	1.04	26	1264	1295	1338	1302	20.3	1.56
		Q3	26	1500	1529	1564	1532	16.1	1.05	26	1275	1300	1338	1301	17.3	1.33
		Q5	26	1500	1524	1560	1529	15.4	1.00	26	1275	1294	1327	1299	16.8	1.29
			78	1493	1530	1564	1532	15.7	1.03	78	1264	1298	1338	1301	18.0	1.39
	JM	Q2	26	1729	1760	1795	1765	16.4	0.93	26	1268	1298	1334	1302	17.9	1.38
		Q6	26	1724	1763	1801	1764	20.6	1.17	26	1262	1298	1332	1299	19.8	1.53
		Q8	26	1729	1772	1794	1767	17.0	0.96	26	1255	1304	1340	1302	20.5	1.57
			78	1724	1764	1801	1765	17.9	1.01	78	1255	1299	1340	1301	19.3	1.48
	JA	Q4	26	1738	1757	1797	1762	18.4	1.05	26	1625	1644	1695	1653	21.4	1.30
	SC	Q7	29	1291	1331	1363	1332	17.9	1.34	25	1490	1535	1561	1532	18.8	1.23
		Q9	29	1307	1331	1363	1333	13.6	1.02	26	1512	1535	1571	1534	14.1	0.92
			58	1291	1331	1363	1333	15.8	1.18	51	1490	1535	1571	1533	16.4	1.07

[a] Headings as in Table 2.

The phase 1 data that fall within the phase 2 and 3 MBS range are plotted to facilitate comparison.

As anticipated, the variability in the complete RFLP analysis data is greater than observed for the simple autoradiogram image analysis data of phase 1. In both phase 2 and phase 3 studies, the median %RSD across all samples is about 1.0%. The least reproducible band in either study has a %RSD of 1.6%. Note that the phase 3 profiles, where

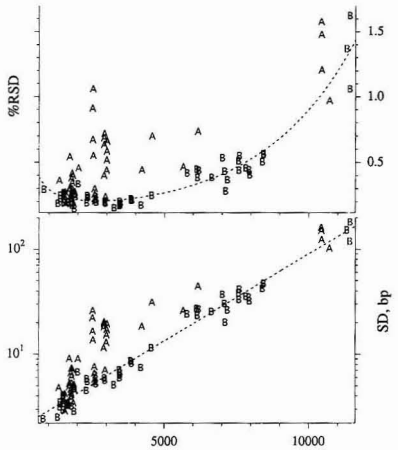

Figure 3. Observed standard deviation (SD) and percent relative standard deviation (%RSD) of the phase 1 autoradiogram sizings as a function of the mean band size (MBS). Values obtained for the 48 bands of the phase 1A study are denoted "A"; those for the 56 bands of phase 1B are denoted "B". The dotted line displays eq 1, the least-squares fit of MBS to $\log_{10}$(SD) through the Phase 1B data. The upper graph echoes all information presented in the lower, with the abscissa transformed from SD to %RSD.

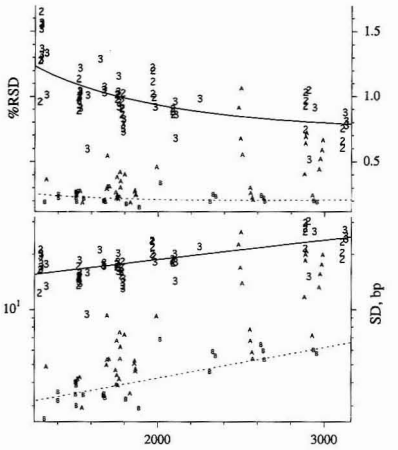

Figure 4. Observed SD and %RSD of the phase 2 and 3 sample sizings as a function of MBS. Values obtained for the 12 bands of the phase 2 study are denoted "2"; those for the 19 bands of phase 3 are denoted "3". The solid line displays eq 2, the least-squares fit of MBS to $\log_{10}$(SD) through the combined data. The phase 1 data that lies within the MBS spanned by the phase 2 and phase 3 values are marked with the small "a" and "b" symbols. The dotted line is as in Figure 3 (TWGDAM phase 1B). The upper graph echoes all information presented in the lower, with the abscissa transformed from SD to %RSD.

participants performed all steps of the RFLP protocol including DNA extraction, are no less reproducible than those of phase 2. This suggests that sample preparation steps do not contribute to measurement variability.

Ancillary Data. The MBS of all bands sized in phases 2 and 3 fell within the narrow range of 1250 to 3200 bp. Profiling data obtained in other studies that used methods related to the TWGDAM-recommended DNA RFLP protocol have been used to explore variation in bands with MBS below and above this range. Table 6 presents summary statistics for these studies and for all the TWGDAM Phases. Significant attributes of the various ancillary studies include the following:

NIST Prototype. A small interlaboratory comparison of only the D2S44 locus for K562 DNA and one set of blood-derived DNA, used to develop prototype materials, shipping methods, and analysis techniques for the larger interlaboratory study described below. The complete data are available as supplementary material.

NIST SRM. An interlaboratory comparison of all commonly probed loci for K562 DNA and several sets of blood-derived DNA, conducted to establish reference values for NIST Standard Reference Material 2390.[21] All data for bands having nine or more values are available as supplementary material. Only these bands were included in our summary analyses.

Cellmark Proficiency. A voluntary interlaboratory proficiency test available by subscription (sponsored by Cellmark Diagnostics Corporation, Germantown, MD). Data for all commonly probed loci were obtained for several different blood stains and each laboratory's K562 DNA. Only bands from *Hae*III restriction enzyme DNA digests having nine or more values were included in our summary analyses. Reference 22 details the data collected for this study, including some information regarding protocol modifications.

CTS Proficiency. A voluntary interlaboratory proficiency test available by subscription (sponsored by Collaborative Testing Services, Inc., Reston, VA). Data for all commonly probed loci were obtained for several different blood stains, a mixed blood and semen sample, and each laboratory's K562 DNA. Only bands from *Hae*III restriction enzyme DNA digests having nine or more values were included in our summary analyses. Reference 23 details the data collected for this study, including some information regarding protocol modifications.

FSRTC Postgraduate. A voluntary post-training service provided by the FBI's FSRTC to analysts who have graduated from the FBI's DNA Analysis School. On request, blood stains of known profile are provided to an analyst. Upon receipt of the profiling results for the samples and for the host laboratory's K562 DNA, the expected results are returned to the analyst. Only the sample identifier, the band sizes, and a laboratory identifier are retained by the FSRTC. Only data for loci D1S7, D2S44, D4S139, and D17S79 are available. All data obtained from this program as of early 1992 are available as supplementary material.

(21) National Institute of Standards and Technology. *Certificate of Analysis, Standard Reference Material 2390, DNA Profiling Standard*; Standard Reference Materials Program, NIST: Gaithersburg, MD, 1992.

(22) *International Quality Assessment Scheme, Forensic Analysis, Distribution 9201*, Cellmark Diagnostics: Germantown, MD, 1992.

(23) *DNA Profiling Report No. 91–15*; Forensic Laboratory Proficiency Testing Program, Collaborative Testing Services, Inc.: Herndon, VA, 1992.

Table 6. Summary of Recent TWGDAM-Recommended RFLP Protocol DNA Sizing Studies (bp)[a]

	number			data/band		band size		%RSD			
study	labs	data	band	min	max	min	max	min	med	max	Reference
TWGDAM phase 1A	22	2025	48	10	43	1329	10691	0.19	0.40	1.59	*b*
TWGDAM phase 1B	21	3421	56	59	68	826	11427	0.15	0.26	1.63	*b*
TWGDAM phase 2	23	901	12	27	120	1295	3107	0.67	1.00	1.33	*b*
TWGDAM phase 3	22	1069	19	26	90	1301	3128	0.53	0.99	1.48	*b*
NIST prototype	17	420	19	21	23	1287	3701	0.49	0.82	1.27	*b*
NIST SRM 2390	29	1126	60	10	34	1182	10979	0.47	0.94	2.00	*b*
FSRTC postgraduate	18	4525	39	27	104	805	9888	0.48	0.83	1.98	*b*
Cellmark proficiency	18	715	50	9	18	930	17383	0.45	1.00	4.76	22
CTS proficiency	26	1524	79	13	25	797	16379	0.40	1.24	6.12	23
TWGDAM population	14	7062	10	498	902	1184	6494	0.63	0.77	0.94	*b*
FBI casework	1	4626	8	302	911	1544	6584	0.41	0.58	0.62	*b*

[a] Study, name of study as used in text; number: labs, number of participating laboratories; number: data, total number of sizings reported; number: band, number of fragments identified (twice the number of unique samples); data/band: min, MBS of smallest fragment sized; data/band: max, MBS of largest fragment sized; %RSD: min, smallest %RSD for any fragment; %RSD: med, median %RSD for any fragment; %RSD: max, largest %RSD for any fragment; ref, source for original data. [b] Complete raw data available as supplementary material.

TWGDAM Population. This is a compilation of the valid K562 data obtained during an earlier TWGDAM-sponsored study that was designed to permit the estimation of the distribution of RFLP band sizes as a function of population differences.[24] Data were obtained for five loci commonly probed in North American forensic applications. All data for the resulting 10 bands obtained by the participating 14 forensic laboratories are available as supplementary material. The two bands for each probe are paired. Unlike the data in the TWGDAM phase 2 and 3 and the above ancillary studies, there is no determined relationship among the bands of the different probes.

FBI Casework. A compilation of the valid K562 data obtained during casework analysis at FBI Headquarters for loci D1S7, D2S44, D4S139, and D17S79. While only eight bands are available, this is by far the largest set of data for any single forensic laboratory. Data collected through early 1992 are available as supplementary material. As in the above TWGDAM population data, the two bands for each probe are paired but there is no determined relationship among the bands of the different probes.

Figure 5 presents the observed SD and %RSD for all bands of the ancillary data of MBS less than 11 000 bp, as well as the TWGDAM phase 2 and 3 values. Not only are the studies consistent, the linear relationship observed between the logarithm of SD and MBS holds well over the entire available data range. The least-squares line obtained using only the ancillary data is very similar to that obtained for the restricted MBS range TWGDAM phase 2 and 3 data:

$$\log_{10}(\mathrm{SD}) = (1.009 \pm 0.014) + \frac{\mathrm{MBS}}{(8215 \pm 238)} \qquad (3)$$

for 258 data pairs with a residual standard deviation of 0.125.

The data from the FBI casework and TWGDAM population studies are plotted as solid symbols in Figure 5. Both data sets show less variance than is predicted by the least-squares linear relationship (eq 3), with the FBI data generally being the least variable. The 4600+ *intra*laboratory FBI data are expected to display less variability than comparable

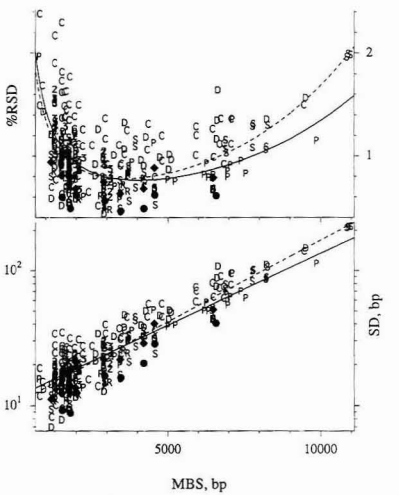

Figure 5. Observed SD and %RSD of ancillary data as a function of MBS for all bands of size ≤11 000 bp. Values obtained for the 19 bands of the NIST Prototype study are denoted "R"; values obtained for the 60 bands of the NIST SRM 2390 are denoted "S"; the 79 bands of the CTS proficiency are denoted "C"; the 50 bands of the Cellmark proficiency are denoted "D"; the 39 bands of the FSRTC postgraduate are denoted "P"; the 10 bands of the TWGDAM population are denoted as solid diamonds; and the 8 bands of the FBI casework are denoted as solid circles. The dashed line displays eq 3, the least-squares fit of MBS to $\log_{10}$(SD) through the ancillary data. To facilitate comparison, the values obtained for the phase 2 study are replotted and denoted "**2**" and those for the phase 3 are denoted "**3**". The solid line is as in Figure 4 (TWGDAM phase 2 and 3). The upper graph echoes all information presented in the lower, with the abscissa transformed from SD to %RSD.

*inter*laboratory reproducibility data. The 7000+ TWGDAM population data are from 14 experienced laboratories. While the observed SD values for these two studies are smaller than predicted from the full set of ancillary data, they are parallel to the fitted line between $\log_{10}$(SD) and MBS. The least-squares line for the FBI casework study data is

$$\log_{10}(\mathrm{SD}) = (0.779 \pm 0.047) + \frac{\mathrm{MBS}}{(7622 \pm 726)} \qquad (4)$$

for eight data pairs with a residual standard deviation of 0.056.

(24) Federal Bureau of Investigation. *VNTR Population Data: A Worldwide Study. Volume I-A Study Overview and HaeIII Histograms*; Forensic Science Research and Training Center, FBI Academy: Quantico, VA, Feb. 1993.

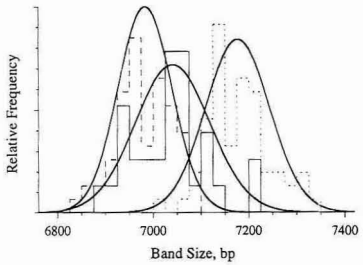

Figure 6. Univariate distributions for the sizings of one partially resolved band pair of the FBI postgraduate training data. The dashed lines represent the frequency histograms of the fully resolved bands; the light solid line represents the histogram of unresolved bands. The darker solid lines present normal curves having mean and SD of the corresponding three histograms.

DNA from one donor at one locus in the FSRTC postgraduate study is known to produce a closely spaced two-band pattern which at times is not electrophoretically resolved. This is consistent with the observed data in that these two bands were not resolved in 31 of the 93 analyses. In the 62 analyses that did resolve two bands, the mean ±SD sizes are 7177 ± 67 and 6983 ± 57 bp. These interlaboratory SD values agree well with the 64 and 73 bp SDs predicted from eqs 2 and 3, respectively, for MBS of 7000. The 31 analyses which did not resolve two bands give a mean ±SD size of 7036 ± 79 bp. Figure 6 presents approximate distributions for these data. It is clear that the sizing distribution of the unresolved single band sizings is not centered between the resolved band distributions but is biased toward that of the smaller band. While insufficient data are available to draw strong conclusions, this does suggest that closely spaced two-band patterns may need to be given special attention in any between-gel comparison.

K562 DNA Control Data. All the studies described include data for K562 DNA. There are 1527 values for the two bands of locus D1S7, 2231 for D2S44, 1121 for D4S139, 727 for D10S28, and 1231 for D17S79. Such large samples should permit reliable estimation of the measurement reproducibility distributions for these 10 fragments and of any correlation between measurements for the five band pairs.

Parts a and b of Figure 7 present TWGDAM phase 2 and 3 data for loci D2S44 and D17S79, along with corresponding data from the ancillary studies. The top segment of each figure summarizes the two frequency distributions. The bottom segment of each figure is a scattergram of the band size of the larger versus its smaller paired allele. The observed distributions of the TWGDAM and all other data are portrayed as frequency histograms at the top and right margins of the scattergram.

For both bands of both loci there are at least two distinct band-size groupings, with most of the TWGDAM sizings in a group that is 20–40 bp smaller than the other. These groupings appear to be related to protocol-specific differences such as the use of ethidium bromide during electrophoresis: this will be further discussed in part 3 of this series. Studies of other RFLP systems indicate that within-laboratory sizing distributions are approximately normal.[25,26]

Parts a–c of Figure 8 present the ancillary data for loci D1S7, D4S139, and D10S28. The format is the same as in Figure 7, parts a and b, except that there are no TWGDAM phase 2 or 3 data. There is less evidence for distinct groupings with these loci.

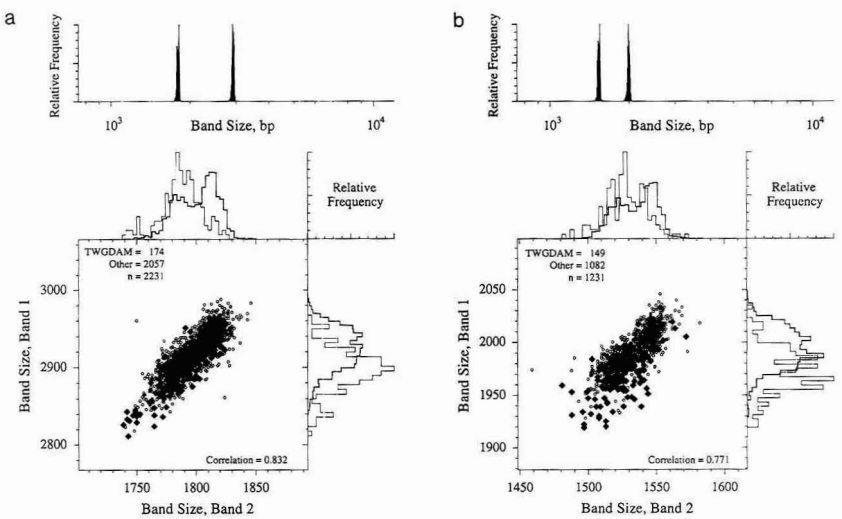

Figure 7. Distribution of sizings for both bands of K562 DNA at locus (a) D2S44 and (b) D17S79. The top histograms plot the relative frequency of occurrence of band size values against MBS for all available data. There are (a) 174 and (b) 149 measurements of the band from the TWGDAM phase 2 and 3 studies and (a) 2057 and (b) 1082 from the ancillary studies described in the text. The logarithmic band size scale roughly approximates the expected fragment distribution on the gel itself. The scattergrams show the bivariate distribution of the two bands for this locus. The TWGDAM data are indicated as (solid diamonds) and the other studies as (open circles).The histograms to the top and right of the scattergram show the univariate distributions of the TWGDAM (light line) and the other studies (dark line) band sizing values.

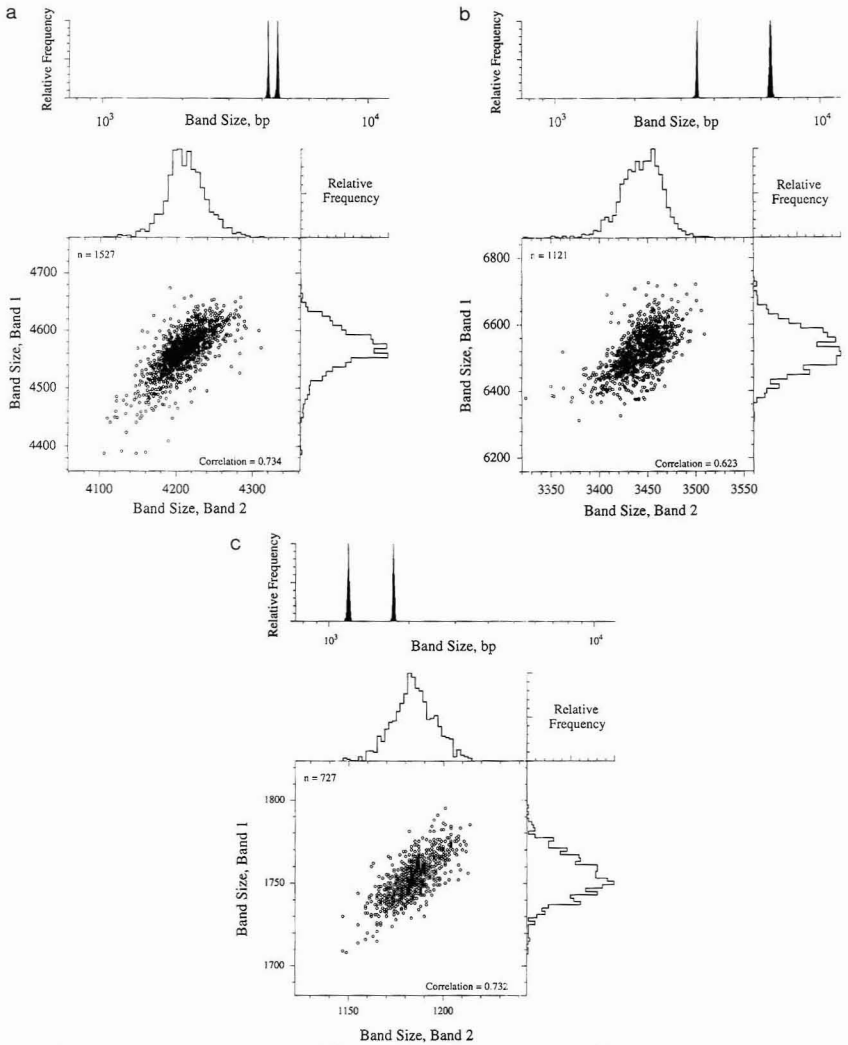

Figure 8. Distribution of sizings for both bands of K562 DNA at locus (a) D1S7, (b) D4S139, and (c) D10S28. Legend is as in Figure 7 (except that no TWGDAM precision data is available for these loci. There are (a) 1527, (b) 1121, and (c) 727 band sizings available from the other studies.

Two of the 2231 paired band sizings of locus D2S44 (Figure 7a) do not have the same correlation structure as the bulk of the data, although the size of each band taken alone is unexceptional. This deviation from the expected trend may be useful in flagging out-of-range data.

The correlation between bands at the same locus is comparable to that observed using the *Hin*fI restriction enzyme RFLP protocol advocated by the *E*uropean *DNA P*rofiling group (EDNAP),[25] although it is less strong than previously claimed for *Hae*III RFLP sizings.[27] The observed correlation cannot arise from any genetic source: K562 data are repeat sizings of DNA derived from one individual. In the absence of measurement differences and error, there can be no correlation between sizing values for K562 maternal and paternal bands. The observed correlation is a result of systematic variation due to analysts and laboratories as well as measurement artifacts within agarose gels.[25,28] This correlation in K562 band sizings has been incorrectly interpreted as limiting the forensic utility of RFLP profiling.[29] While the existence and magnitude of measurement correlation must be recognized when making use of RFLP measurements, techniques are currently available that explicitly address measurement variance and correlation issues.[19,30]

Table 7

loci	band	MBS ± SD phase 1B	MBS ± SD FBI casework	MBS ± SD TWGDAM phase 3	$SD^2_{phase1B}/SD^2_{phase3}$	SD^2_{FBI}/SD^2_{phase3}
D17S79	2	1553 ± 3.5	1544 ± 9.2	1529 ± 14.4	0.06	0.41
D2S44	2	1810 ± 3.3	1812 ± 8.8	1795 ± 14.9	0.05	0.35
D17S79	1	2015 ± 6.9	2006 ± 12.4	1986 ± 18.4	0.14	0.45
D2S44	1	2936 ± 6.1	2939 ± 16.5	2909 ± 15.3	0.16	1.16

Allocation of Sources of Variation in Complete Band-Sizing Process. It is possible to contrast interanalyst and interlaboratory variation using the available data. TWGDAM phase 3 involved many laboratories, with most laboratories represented by a single analyst. The FBI casework data is from a single laboratory, but represents results obtained by many analysts. Unfortunately, direct comparison of experimental variances is possible only with K562 D2S44 and D17S79 data. These data, along with data from the TWGDAM phase 1B image-analysis study, can be summarized as in Table 7.

At least for this very restricted fragment size range, the small $SD^2_{phase1B}/SD^2_{phase3}$ values imply that autoradiogram image analysis is a relatively minor contributor to the overall interlaboratory RFLP profiling variance. This result differs from previous work using manual autoradiogram interpretation where more than half of the observed variance was attributed to the digitizing process.[31]

The relatively large SD^2_{FBI}/SD^2_{phase3} values imply that variation within a single laboratory may account for a significant fraction of the total observed interlaboratory variance.

Comparison of the previously determined mathematical relationships between SD and MBS supports the above allocation of variation sources. Ratioing eqs 1 and 2,

$$SD^2_{T1B}/SD^2_{T2\&3} = \left(\frac{10^{(0.295 + MBS/6025)}}{10^{(1.056 + MBS/9330)}}\right)^2 \approx 0.173 \times 10^{MBS/17000} \quad (5)$$

suggests that autoradiogram imaging contributes perhaps 20% of the total profiling variance for small bands but becomes more important as band size increases. Ratioing eqs 4 and 2,

$$SD^2_{FBI}/SD^2_{T2\&3} = \left(\frac{10^{(0.779 + MBS/7622)}}{10^{(1.056 + MBS/9330)}}\right)^2 \approx 0.528 \times 10^{MBS/41600} \quad (6)$$

indicates that intralaboratory differences contribute somewhat more than half of the total interlaboratory variation over relevant band sizes.

%RSD as a Measure of Reproducibility. As is evident in Figures 3–5, %RSD is *not* proportional to MBS. Instead, the logarithm of SD is a linear function of MBS. While perhaps less convenient than the familiar "divide by the mean" form of %RSD, an exponential function for SD (e.g., eq 8) is clearly more appropriate. However, for the TWGDAM-recommended RFLP general protocol, %RSD can be approximated as a roughly constant 1% for fragments of about 1000 to 10 000 bp. It is less than 1% for the range 2000–8000 bp. The assumption of constant %RSD is inappropriate for fragments smaller than 1000 or larger than 10 000 bp.

Two recent EDNAP-sponsored interlaboratory comparisons reported *Hinf*I-protocol sample standard deviations as roughly proportional to MBS.[32,33] The average %RSD was 1.0–1.5% in the first of these studies and 0.8% in the second. The first study did not attempt to standardize across participating laboratories and examined an insufficiently wide range of band sizes to document any curvature in %RSD. The second study examined an insufficient number of fragments to document any relationship, although a broad minimum %RSD is present at midrange with distinct increases for both large and small fragments. The EDNAP-reported *Hinf*I %RSD values are quite compatible with TWGDAM %RSD observations.

Interlaboratory Statistical Interval "Window". The linear relationship between $\log_{10}$(SD) and MBS reported here has been previously noted.[34] This empirical relationship enables reliable estimation of the interlaboratory measurement variation as a function of observed band size. Figure 9 plots $\log_{10}$(SD) versus MBS for all data of 800–11 000 bp. The least-squares fit to these combined data is:

$$\log_{10}(SD) = (1.017 \pm 0.011) + \frac{MBS}{(8300 \pm 216)} \quad (7)$$

for 328 data pairs with a residual standard deviation of 0.12. The slope is expressed in reciprocal scale for the sake of interpretability. The "±" terms in the intercept and slope parameters are estimated standard errors.

A more convenient nonlinear expression for the identical relationship is obtained by exponentiation of both sides of eq 7:

$$SD = 10.4 \times 10^{(MBS/8300)} \quad (8)$$

Thus, from the intercept estimate of eq 7, the minimum expected SD for any fragment, regardless of size, is seen to be at least 10.4 bp.

Equation 7 is the linear least-squares estimate of the TWGDAM-recommended RFLP general protocol measure-

(25) Eriksen, B.; Bertelsen, A.; Svensmark, O. Statistical Analysis of the Measurement Errors in the Determination of Fragment Length in DNA-RFLP Analysis; *Forensic Sci. Int.* **1992**, *52*, 181–191.

(26) Pascali, V. L.; Moscetti, A.; Dobosz, M.; Pescarmona, M.; d'Aloja, E. Errors in sizing bands of hypervariable DNA profiles on autoradiograms: Are they Gaussian? *Electrophoresis* **1992**, *13*, 341–345.

(27) Devlin, B.; Rish, N.; Roeder, K. Forensic Inference from DNA Fingerprints. *J. Am. Stat. Assoc.* **1992**, *87* (418), 337–350.

(28) Youden, W. J. Graphical Diagnosis of Interlaboratory Test Results. *Ind. Qual. Control* **1959**, 15.

(29) Shapiro, M. M. Imprints on DNA fingerprints. *Nature* **1991**, *353* (12), 121–122.

(30) Evett, I. W.; Scrange, J.; Pinchin, R. Efficient Retrieval From DNA databases: Based on the Second European DNA profiling Group Collaborative Experiment; *Forensic Sci. Int.* **1991**, *53*, 45–50.

(31) Galbraith, D. A.; Boag, P. I.; Gibbs, H. L.; White, B. N. A study of precision for scoring DNA fingerprints. *Electrophoresis* **1991**, *12*, 210–220.

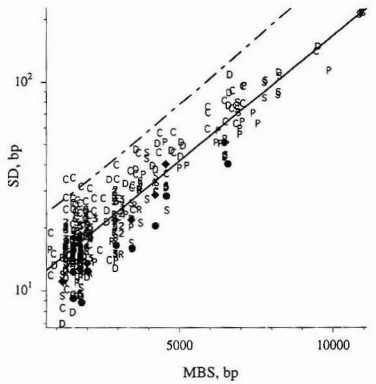

Figure 9. Observed SD of available sample sizings as a function of MBS for all bands with a MBS ≤ 11 000 bp. Data as in Figure 5. The dark solid line is the least-squares fit through all data. The dash–dot curve is the upper 95%–95% Lieberman–Miller simultaneous tolerance interval for the regression line: with 95% confidence, at least 95% of all measured interlaboratory SDs should lie beneath this curve.

ment interlaboratory SD for a fragment of a given size. This line understates the observed SD for roughly 50% of the data. For conservative prediction of the interlaboratory variance expected for a given band size, an equation capturing at least 95% of the data would be useful. Lieberman–Miller simultaneous tolerance intervals for regression can be used to bound a prechosen percent of observable data with prechosen confidence.[35] Strict application of Lieberman–Miller assumes a homogeneous, normally distributed, and homoscedastic population of residuals. While the $\log_{10}(SD)$ data may imperfectly satisfy these conditions, the following 95%–95% Lieberman–Miller upper interval should overstate SD about 95% of the time:

$$\log_{10}(SD) = 1.017 + \frac{MBS}{8300} + 0.116\left[2.12 + 2.73\left[\frac{1}{328} + \left(\frac{MBS - 3005}{37261}\right)^2\right]^{1/2}\right] \quad (9)$$

Part 2 of this series explores in more detail the empirically derived linear relationship between $\log_{10}(SD)$ and fragment size. It will be shown that this relationship is an approximation to an expected relationship that can be derived from considerations of the magnitudes and propagation of measurement uncertainties.

The "Statistical Population" of Laboratories. For the results presented above to be predictive of future RFLP measurement practice, the laboratories that participated in the various examined studies must be assumed to constitute a representative, statistically valid sample of the population of forensic laboratories. Analysis across all available RFLP DNA interlaboratory studies implies that this assumption is approximately valid as of late 1992. However, to avoid contamination of the proposed national CODIS database with incommensurate data, data quality control is necessary. Standard Reference Materials are available for self-evaluation of RFLP measurement performance.[21] In addition to internal proficiency testing programs, there are established sources of external proficiency tests.[22,23] Use of reference materials and participation in proficiency programs, in combination with various statistical tests of submitted data, should provide the necessary assurances of data quality. Periodic interlaboratory studies will be necessary to monitor measurement comparability as RFLP technology continues to evolve.

CONCLUSIONS

The 22 laboratories participating in the TWGDAM interlaboratory precision study represent a wide spectrum in laboratory resources and analyst experience in DNA analysis. The data obtained during this study are similar to data obtained in other RFLP studies. All available data suggest that this TWGDAM-recommended general protocol produces reliable, reproducible results that can be compared among laboratories.

Measurement reproducibility for a given RFLP fragment is a nonlinear function of fragment size. Thus, the assumption of constant %RSD is not appropriate. The logarithm of SD appears to be a linear function of fragment size, rendering SD proportional to $10^{(\text{fragment size/constant})}$. Overall, %RSD is 1% or less over the RFLP fragment size range of about 2000–8000 bp.

More than half of the variation observed in just the image processing steps of RFLP sizing is attributable to effects intrinsic to the process itself. The total image process variation is a small component of interlaboratory RFLP measurement variance for fragments ≤10 000 bp.

Intralaboratory processes appear to contribute about half of the overall interlaboratory RFLP measurement variance. There are small but systematic differences among sizing results obtained by different laboratories. Further RFLP protocol standardization could minimize some of these differences, leading to smaller interlaboratory RFLP measurement variances. Parts 2 and 3 in this series explore sources of RFLP measurement variance in some detail in an attempt to facilitate such variance reduction.

Current forensic practice appears adequate to support the development and use of a national DNA database system. Data obtained in the TWGDAM precision study and available from related studies are sufficient to establish reliable tolerances for the expected interlaboratory variation for any given RFLP band size. These expected tolerances are appropriate for data from laboratories which maintain measurement systems within the defining statistical population of RFLP protocols. System maintenance may best be achieved through appropriate use of Standard Reference Materials, internal quality assurance programs, and external proficiency demonstrations.

(32) Schneider, P. M.; Fimmers, R.; Woodroffe, S.; Werrett, D. J.; Bär, W.; Brinkmann, B. Eriksen, B.; Jones, S.; Kloosterman, A. D.; Mevåg, B.; Pascali, V. L.; Rittner, C.; Schmitter, H.; Thomson, J. A.; Gill, P. Report of a European Collaborative Exercise Comparing DNA Typing Results Using a Single Locus VNTR Probe. *Forensic Sci. Int.* **1991**, *49*, 1–15.

(33) Gill, P.; Woodroffe, S.; Bär, W.; Brinkmann, B.; Carracedo, A.; Eriksen, B.; Jones, S.; Kloosterman, A. D.; Ludes, B.; Mevåg, B.; Pascali, V. L.; Rudler, M.; Schmitter, H.; Schneider, P. M.; Thomson, J. A. A Report of an International Collaborative Experiment to Demonstrate the Uniformity Obtainable Using DNA Profiling Techniques. *Forensic Sci. Int.* **1992**, *53*, 29–43.

(34) Gill, P.; Sullivan, K.; Werrett, D. J. The analysis of hypervariable DNA profiles: problems associated with the objective determination of the probability of a match. *Hum. Genet.* **1990**, *85*, 75–79.

(35) Lieberman, G. J.; Miller, R. G., Jr. Simultaneous tolerance intervals in regression. *Biometrika* **1963**, *50*(1,2), 155–169.

The uni- and bivariate structure of the available K562 data suggest a number of data analytic techniques that may be appropriate for identifying potentially incommensurate data. Such screening could help maintain the necessary high data quality required for effective use of the proposed national DNA database system.

ABBREVIATIONS, ACRONYMS, SYMBOLS, AND TERMS

allele	one or more alternative forms of a given gene
band	the image of one particular DNA fragment separated by electrophoresis
band sizing	the process of estimating the number of DNA base pairs in a DNA fragment
blot	electrophoretically separated DNA transferred from a gel and immobilized on a polymeric membrane
bp	DNA base pairs, a unit of size for DNA fragments
CODIS	originally an acronym for *C*ombined *D*NA *I*ndex System; it is now applied to the U.S. national DNA identification index system
D1S7	genetic locus identified by single locus probe MS1
D2S44	genetic locus identified by single locus probe YNH24
D4S139	genetic locus identified by single locus probe PH30
D10S28	genetic locus identified by single locus probe TBQ7
D17S79	genetic locus identified by single locus probe V1
DNA profiling DNA typing	any method of identifying an individual through comparison of patterns arising from differences in DNA sequences
EDNAP	*E*uropean *DNA P*rofiling group, a group of scientists representing European forensic laboratories
FSRTC	FBI *F*orensic *S*cience *R*esearch and *T*raining *C*enter
*Hae*III, *Hin*fI	restriction endonucleases used to produce double-stranded DNA fragments
K	code for DNA from a known individual
lane	the path DNA fragments follow through an agarose gel during electrophoresis
MS1	single locus probe that identifies genetic locus D1S7
MBS	*M*ean *B*and *S*ize, the average of available sizing values for a given band
PH30	single locus probe that identifies genetic locus D4S139
Q	code for DNA from an evidentiary sample
restriction endonuclease restriction enzyme	a bacterial enzyme that recognizes unique DNA sequences and catalyzes the double-stranded cleavage of DNA at these sites
RFLP	*R*estriction *F*ragment *L*ength *P*olymorphism; differences in DNA sequence that result in DNA fragments of different size after digestion with a restriction enzyme
RFLP analysis	DNA profiling technique which detects variation in the DNA sequence by revealing size differences in DNA fragments produced by the action of a restriction enzyme
%RSD	percent relative standard deviation (or coefficient of variation), defined as 100(standard deviation)/mean
SD	sample standard deviation
SD^2_{FBI}	SD^2 for ancillary FBI casework data
SD^2_{Phase1}	SD^2 for TWGDAM phase 1A and 1B data
$SD^2_{Phase1B}$	SD^2 for TWGDAM phase 1B data
SD^2_{Phase3}	SD^2 for TWGDAM phase 3 data
SD^2_{rad}	SD^2 for single analyses of multiple autoradiogram copies
SD^2_{rep}	SD^2 for multiple analyses of one autoradiogram
single locus probe	radiolabeled single-strand DNA fragments that hybridize with denatured DNA fragments, generally at one position of a chromosome
sizing ladder	sets of DNA fragments of known sequence and size, used as internal standards
TBQ7	single locus probe that identifies genetic locus D10S28
TWGDAM	*T*echnical *W*orking *G*roup on *D*NA *A*nalysis *M*ethods, a group of scientists representing forensic laboratories in the United States and Canada
V1	single locus probe that identifies genetic locus D17S79
YNH24	single locus probe that identifies genetic locus D2S44

ACKNOWLEDGMENT

We thank all the analysts who participate in TWGDAM studies. Without their enthusiastic cooperation little progress could be made toward meaningful exchange of DNA information throughout North America. This study was enhanced by the efforts of Richard Berger and David Atkinson of the Washoe County Sheriff's Office, Reno, NV, who compiled all the K562 sizings taken during the TWGDAM population study. We also thank all FBI employees who have and continue to donate DNA samples to TWGDAM projects. Certain commercial equipment, instruments, or materials are identified in this report to specify adequately the experimental procedure. Such identification does not imply recommendation or endorsement by the Federal Bureau of Investigation nor the National Institute of Standards and Technology, nor does it imply that the materials or equipment identified are necessarily the best available for the purpose.

SUPPLEMENTARY MATERIAL AVAILABLE

Data for the TWGDAM phases 1A (4 pages), 1B (6 pages), 2 (2 pages), and 3 (3 pages); NIST SRM prototype (1 page); NIST SRM 2390 (3 pages); FSRTC postgraduate training (6 pages); TWGDAM population K562 (10 pages); and FBI casework K562 (6 pages) studies (42 pages total). Ordering information is given on any current masthead page.

Received for review November 11, 1993. Accepted June 15, 1994.®

® Abstract published in *Advance ACS Abstracts,* August 1, 1994.

Anal. Chem. **1994,** *66,* 3318–3322

Kinetic Method for the Quantitative Resolution of Structural Isomers Based on the Catalytic Properties of β-Cyclodextrin

Ellen Tuanying Chen and Harry L. Pardue*

Department of Chemistry, 1393 BRWN Building, Purdue University, West Lafayette, Indiana 47907-1393

This paper describes a new approach for the quantitative resolution of mixtues of structural isomers. The method is based on the observation that rate constants for the cyclodextrin-catalyzed hydrolysis of selected structural isomers are significantly different. By using cure-fitting methods, it is possible to use these differences in rate constants to resolve kinetic responses for mixtures into the responses for the individual components. The new approach is evaluated for the ortho-, meta-, and para-isomers of nitrophenyl acetate. At pH 10, with β-cyclodextrin as catalyst, ratios of rate constants for the three isomers differ by ratios of 1:6.7:1.6 in the order mentioned above. Results are reported for both two- and three-component mixtures. For two-component mixtures of the ortho- and para-isomers which have rate constants differing by only 1.6-fold, linear least-squares slope and intercept of determined vs prepared concentrations for the ortho-isomer were 1.00 ± 0.02 and 2 ± 2.2 μmol/L for three runs on each of five samples in the concentration range from 22 to 176 μmol/L. The pooled standard deviation for these 15 runs was 3.7 μmol/L, corresponding to a relative standard deviation of 3.7% for the average concentration. Similar results were obtained for other two- and three-component mixtures.

Cyclodextrins are macrocyclic compounds consisting of 6–12 glucose units joined at the α-1,4 positions. The most common forms consist of 6, 7, and 8 glucose units and are commonly identified as the α-, β-, and γ-cyclodextrins (α-, β-, and γ-CDs).[1] An interesting property of cyclodextrins is that they tend to mimic enzymes in the sense that they catalyze certain types of reactions such as hydrolysis of esters.[1-3] Although the catalytic properties of CDs have been studied extensively,[1-8] prior to our own studies,[9] there have been no attempts to exploit these properties for analytical purposes.

In a recent paper from this laboratory, it was shown that the catalytic properties of cyclodextrins can indeed be used to quantify selected species on the basis of selective catalysis of reactions that can be monitored continuously with appropriate detection systems.[9] The study focused on the use of error-compensating data processing methods for single-component (*p*-nitrophenyl acetate) determinations. In the course of that study, it was confirmed that the catalytic activity of any particular cyclodextrin was different for different structural isomers of any given compound. For example, it was confirmed that the catalytic activity of β-CD was significantly different for the ortho-, meta-, and para-isomers of nitrophenyl acetate (NPA)[1]. This observation opened the possibility of simulatneous quantitation of these isomers in mixtures based on differences in kinetic behavior.

Several papers from this and other laboratories describing simultaneous determinations based on kinetic differences among different compounds undergoing the same or similar reactions have been described in several monographs[10-12] and reviews.[13-15] Most of these studies have focused on entirely different compounds that undergo similar reactions to produce a common product. However, there have been a few studies, dating as far back as the 1930s, applied to the simultaneous quantitation of isomers of the same compound.[16-18] The present study was undertaken to determine if the catalytic properties of a cyclodextrin could be used to resolve mixtures of structural isomers quantitatively. The example chosen for study was quantitative resolution of the ortho-, meta-, and para-isomers of nitrophenyl acetate based on catalysis by β-CD of the hydrolysis of the isomers to produce the respective nitrophenolates (NP^-). The nitrophenolates were monitored by their absorption in the near-ultraviolet region.

EXPERIMENTAL SECTION

Instrumentation. Preliminary studies involving development of conditions for the measurement step were done by using a diode array-based rapid-scanning spectrophotometer (Model 8450A, Hewlett-Packard Co., Palo Alto, CA). Quantitative results for one-, two-, and three-component samples were obtained by using a multichannel centrifugal mixing/measurement system (Rotochem IIa, Travenol, Deerfield, IL). Data for absorbance vs time were recorded by

(1) Bender, M. L.; Komiyama, M. *Cyclodextrin Chemistry*; Springer-Verlag: Berlin, 1978
(2) Breslow, R.; Bovy, P.; Hersh, C. L. *J. Am. Chem. Soc.* **1980,** *102,* 2115–2117.
(3) Tabushi, I. *Acc. Chem. Res.* **1982,** *15,* 1566–1572.
(4) Szejtli, J. *Cyclodextrin Technology*; Kluwer Academic Publishers: Boston, MA, 1988.
(5) Stoddart, F. *Cyclodextrins*; Royal Society of Chemistry: London, 1989.
(6) Ikeda, H.; Kojin, R.; Yoon, C.-J; Ikeda, T.; Toda, F. *J. Incl. Phenom.* **1989,** *7,* 117–124.
(7) Breslow, R. *Acc. Chem. Res.* **1991,** *24,* 317–324.
(8) Schneider, H.-J.; Dürr, H. *Frontiers in Supramolecular Organic Chemistry and Photochemistry*; VCH: New York, 1991.
(9) Chen, E. T.; Pardue, H. L. *Anal. Chem.* **1993,** *65,* 2563–2567.
(10) Mark, H. B., Jr.; Rechnitz, G. A. *Kinetics in Analytical Chemistry*; Interscience Publishers: New York, 1968; pp 78–140.
(11) Mottola, H. A. *Kinetic Aspects of Analytical Chemistry*; John Wiley and Sons: New York, 1988; pp 122–146.
(12) Perez-Bendito, D.; Silva, M. *Kinetic Methods in Analytical Chemistry*; Ellis Horwood: Chichester, U.K., 1988; pp 149–189.
(13) Pardue, H. L. *Anal. Chim. Acta* **1989,** *216,* 69–107.
(14) Mottola, H. A.; Perez-Bendito, D. *Anal. Chem.* **1992,** *64,* 407R-428R.
(15) Quencer, B. M.; Crouch, S. R. *CRC Crit. Rev. Anal. Chem.* **1993,** *24,* 243–262.
(16) Hass, H. B.; Weber, P. *Ind. Eng. Chem., Anal. Ed.* **1935,** *7,* 231–233.
(17) Quintero, M. C.; Silva, M.; Perez-Bendito, D. *Talanta* **1989,** *36,* 717–722.
(18) Velasco, A.; Rui, X.; Silva, M.; Perez-Bendito, D. *Talanta* **1993,** *40,* 1505-1510.

0003-2700/94/0366-3318$04.50/0
© 1994 American Chemical Society

on-board computers with each system and then transferred to a high-speed microprocessor system (Model 4DX-33, Gateway 2000, North Sioux City, SD) for processing.

Gas chromatography (Model 3700, Varian Associates, Sugerland, TX) was used to test the purity of the nitrophenyl acetates.

Reagents. All aqueous solutions were prepared in doubly distilled (Corning megapure distillation apparatus, Corning Inc., Corning, NY) water and filtered through 0.2-μm pore size membrane filter (Nylon-66, Ranin Instrument Co., Inc., Woburn, MA).

Buffer Solutions. The two primary buffers used in this study were a phosphate buffer at pH 8.2 and a carbonate buffer at pH 10.0. The phosphate buffer (2 mmol/L) was prepared by dissolving 0.272 g of potassium phosphate (Aldrich Chemical Co., St. Louis, MO) in water, adjusting the pH to 8.2 with concentrated sodium hydroxide (18 mol/L), and diluting to 1.0 L. The carbonate buffer (0.13 mol/L) was prepared by dissolving 11.1 g of sodium carbonate (Aldrich) and 18 g of sodium chloride (Mallinckrodt Chemical Works, St. Louis, MO) in water, adjusting the pH to 10.0 with concentrated sodium hydroxide, and diluting to 1.0 L. Each buffer was filtered through a 0.2 μm pore size membrane filter (Nylon-66, Ranin) prior to use.

Substrates. The *o*- and *p*-nitrophenyl acetates (Aldrich) were recrystallized from hexane and tested for purity by using gas chromatography; the impurity level was judged to be less than 0.1%. The *m*-nitrophenyl acetate was synthesized according to a published method,[19] and the purity was tested as for the other isomers. Stock and diluted samples of all the isomers were prepared in freshly distilled acetonitrile (Fisher Scientific, Chicago, IL) and stored at 4 °C.

Cyclodextrin. The β-cyclodextrin (Aldrich) was used as received. Solutions were prepared in appropriate buffers each day. The β-CD for quantitative determinations was prepared in carbonate buffer (pH 10.0) containing 0.3 mol/L sodium hydroxide.

Procedure. A variety of common procedures were used for preliminary experiments designed to establish appropriate conditions for the quantitative determinations. For the quantitative determinations, 500 μL of 10 mmol/L β-CD in carbonate buffer was injected into the middle well of each position on the rotor of the centrifugal mixing system, 500 μL of phosphate buffer (2 mmol/L, pH 8.2) was injected into the inner well of each rotor channel, and then 10.0 μL of each sample in acetonitrile was injected into the phosphate buffer in each inner well of the rotor. This latter step was completed as rapidly was possible for all samples, usually within 4 min, and the rotor and measurement process was started as soon as the last sample was injected. Data acquisition was initiated 6.7 s after the rotor was started, and data points were collected at 6-s intervals; a total of 200 data points were collected for each sample.

Data Processing. Multicomponent mixtures were resolved by fitting models for two and three simultaneous first-order processes to data for absorbance vs time. The equations and general approach have been discussed elsewhere[20] and are not repeated here. The principal changes from earlier procedures involved the manner by which initial estimates were obtianed and the fact that rate constants were permitted to vary during the final fitting process.

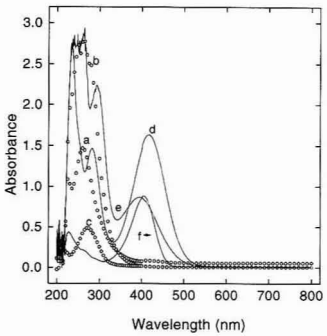

Figure 1. Spectra for the isomers of nitrophenyl acetates and the nitrophenolates: (a–c, O) *o*-, *m*-, and *p*-nitrophenyl acetates; (d–f, —) *o*-, *m*-, and *p*-nitrophenolates. Conditions: pH = 10, 25 °C, 0.15 mol/L NaCl. Concentrations: 200, 600, and 50 μmol/L for the ortho-, meta-, and para-isomers, respectively.

The curve-fitting method is an iterative process which requires initial estimates of the fitting parameters, namely the rate constant and the equilibrium absorbance corresponding to each component in each sample. Average values of rate constants determined for several concentrations of each isomer were used as initial estimates of rate constants. A method called successive integration was used to obtain initial estimates of absorbances used in the iterative process. This method has been described elsewhere.[21] The important point here is that it gives much more reliable initial estimates than procedures used previously. This permits more rapid convergence and, more importantly, more rugged resolution of data for mixtures.

RESULTS AND DISCUSSION

Unless stated otherwise, all random uncertainties are reported at the level of one standard deviation (±1 sd).

Absorption Spectra. Most applications of simultaneous kinetic determinations have involved similar reactions that produce a common product such that only one sensitivity factor for signal vs concentration is involved. The present study was complicated by the fact that the spectra for the different phenolate isomers were all different.

Absorption spectra for the esters and hydrolysis products are shown in Figure 1. The absorptivities for all the esters are very small near 400 nm, where the spectra for all the hydrolysis products have absorption maxima. Accordingly, the measurement region was selected in this range, namely 406 nm. At this wavelength, the molar absorptivities of the phenolate ions for the different isomers are quite different. At pH 10, the values (10^3 L/mol cm) for the ortho-, meta-, and para-isomers are 3.5, 1.1, and 14.4, respectively. Concentra-

(19) Spasov, A. *Ann. Univ. Sofia. II Faculte Phys.-Math., Livre* **1939**, *2*(35), 289–293.

(20) Willis, B. G.; Woodruff, W. H.; Frysinger, J. R.; Margerum, D. W.; Pardue, H. L. *Anal. Chem.* **1970**, *42*, 1350–1355.

(21) Matheson, I. B. C. *Anal. Instrum.* **1987**, *16*, 345–373.

Table 1. Apparent First-Order Rate Constants at 25 °C for the Hydrolysis of the Ortho-, Meta-, and Para-Isomers of Nitrophenyl Acetate

	apparent rate constants (10^{-3} s^{-1})					
	o-NPA[a]		*m*-NPA[a]		*p*-NPA[a]	
pH	without β-CD	with β-CD[b]	without β-CD	with β-CD[b]	without β-CD	with β-CD[b]
8.2[c,e]	0.01	0.01	0.02	0.04	0.02	0.02
9.5[c,e]	0.7	2.9	0.5	24	1.2	5.1
9.5[e,f]	0.6	2.3	0.45	16	0.9	3.5
10.0[d,f]	1.6 ± 0.01	8.2 ± 0.03	1.4 ± 0.002	53 ± 1.4	2.2 ± 0.01	12.6 ± 0.1

[a] Concentrations of ortho-, meta-, and para-isomers were 0.2, 0.6, and 0.05 mM, respectively. [b] pH 8.2, 9.5; 10 mM β-CD. pH 10; 5 mM β-CD. [c] One determination each. [d] Averages of three determinations on one concentration without β-CD and three determinations on each of five concentrations (*o*-NPA, 0.002–0.02 mM; *m*-NPA, 0.06–0.6 mM; *p*-NPA, 0.005–0.05 mM) with β-CD. [e] No control of ionic strength. [f] Ionic strength controlled at 0.15 M.

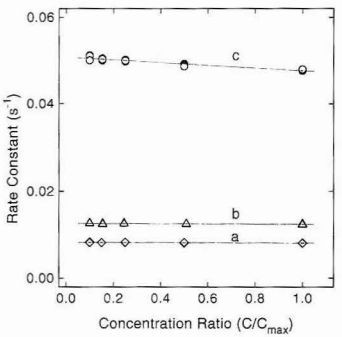

Figure 2. Dependencies of the apparent rate constants on concentrations of the esters. Conditions and maximum concentrations as in Figure 1.

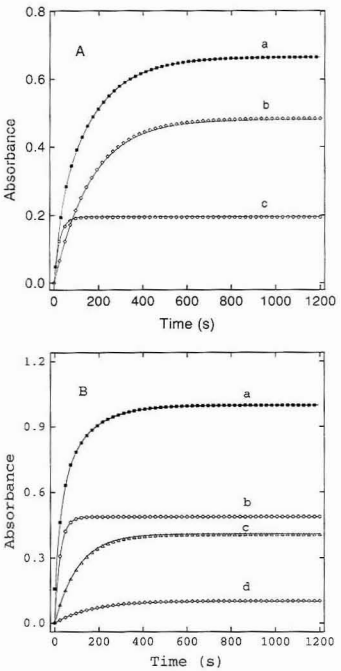

Figure 3. Experimental and fitted data for a two- and three-component mixture of the nitrophenyl acetates. Conditions as in Figure 1. (A) Curve a, experimental (■) and best-fit (solid curve) results for the mixture. Curves b and c, best-fit values for individual components (b, 154 μmol/L *o*-NPA; c, 198 μmol/L *m*-NPA) and expected values based on prepared concentrations, rate constants, and molar absorptivities (solid curves). (B) Same as A except for the components: b, 594 μmol/L *m*-NPA; c, 28 μmol/L *p*-NPA; d, 28 μmol/L *o*-NPA.

tions of the different isomers in mixtures were adjusted to give similar absorbance changes for each isomer.

Rate Constants. Preliminary studies were done to establish conditions for which the catalyzed hydrolyses of the *p*-nitrophenyl acetates followed pseudo-first-order kinetics and to compare rate constants for a range of pH values for the different isomers. Kinetic behavior was tested by using plots of $\ln(A_\infty - A_t)$ vs t and by fitting a first-order model to data for absorbance vs time. Both tests confirmed good pseudo-first-order behavior for all conditions reported in this paper. Moreover, there was good agreement among apparent first-order rate constants determined by the two data processing options. Rate constants obtained in these studies are summarized in Table 1. Results at pH 8.2 and 9.5 are reported only for the record because subsequent studies were done at pH 10 to take advantage of the faster rates and correspondingly shorter measurement times. In the course of these studies it was discovered that ionic strength had some small effects on rate constants (see data for pH 9.5). Accordingly, ionic strength was controlled for all subsequent studies.

Having chosen pH 10 for subsequent studies, rate constants were evaluated in more detail at this pH. Values and uncertainties at pH 10 in Table 1 are based on three runs each at each of five different concentrations for each isomer. Ideally, the rate constants should be independent of concentration. As shown in Figure 2, apparent rate constants obtained with β-CD as catalyst tended to decrease slightly with concentration for each isomer. Although the meta-isomer appears from the figure to exhibit the largest change, it should be noted that the concentration range for the meta-isomer is significantly larger than those for the other isomers. Linear least-squares slopes of rate constants (10^{-3} s^{-1}) vs concentration (μmol/L) for the ortho-, meta-, and para-isomers were −0.9, −5.3, and −3.4, respectively (last column in Table 2). Although this behavior is not ideal, the curve-fitting process used to resolve mixtures is expected to compensate for such nonidealities because the rate constants are used as fitting parameters.

Other features of the rate constants at pH 10 merit comment. Ideally, the differences between rate constants for catalyzed and uncatalyzed reactions should be large so that

Table 2. Calibration Results[a] and Concentration Dependencies of Rate Constants for Single-Component Samples

ester	range (mM)	slope (sd) (10^{-3} $\Delta A/\mu M$)	intercept (sd) (ΔA)	std error (ΔA)	correlation coefficient	slope k vs C (10^{-6} $s^{-1}/\mu M$)
o-NPA	0.002–0.2	3.54 (0.04)	0.006 (0.004)	0.011	0.999	–0.9 ± 0.2
m-NPA	0.06–0.6	1.11 (0.01)	0.004 (0.002)	0.007	0.999	–5.3 ± 0.5
p-NPA	0.005–0.05	14.4 (0.21)	0.003 (0.005)	0.016	0.998	–3.4 ± 1.3

[a] Three runs on each of five concentrations.

Table 3. Least-Squares Results[a] and Pooled Standard Deviations for Two- and Three-Component Mixtures

isomer	range (μM)	slope (sd)	intercept (sd) (μM)	std error (μM)	correlation coefficient	pooled sd[b] (μM)
			o-NPA + *m*-NPA			
o-NPA	22–176	1.00 (0.02)	2 (2.2)	4.4	0.997	3.7
m-NPA	132–593	1.00 (0.02)	–22 (7.6)	13.5	0.997	10.9
total	307–615	1.00 (0.03)	20 (14)	14.0	0.993	9.0
			o-NPA + *p*-NPA			
o-NPA	22–198	1.00 (0.02)	–9 (2.5)	4.8	0.997	4.2
p-NPA	5.7–52	1.00 (0.02)	0.5 (0.6)	1.4	0.996	1.0
total	74–204	1.00 (0.03)	–8 (4.7)	5.9	0.992	4.7
			o-NPA + *m*-NPA + *p*-NPA			
o-NPA	30–178	1.00 (0.02)	–3 (2.5)	6.3	0.995	3.6
m-NPA	198–594	1.00 (0.02)	–19 (7.5)	16	0.997	7.1
p-NPA	10–59	1.00 (0.02)	–2 (0.6)	1.5	0.997	0.84
total	336–653	1.00 (0.02)	16 (7.8)	15	0.997	7.8

[a] Determined vs prepared concentrations. [b] Pooled standard deviations based on three runs on each of five concentrations. Conditions: pH 10.0, 25 °C, 0.15 M NaCl, all fits over 10.5 half-lives of slower reaction.

the uncatalyzed reaction does not complicate the kinetic behavior. The ratios of rate constants for catalyzed vs uncatalyzed reactions for the ortho-, meta-, and para-isomers are 5, 38, and 5.7, respectively. Despite the small ratios for the ortho-, and para-isomers, kinetic responses for catalyzed reactions showed very close to first-order behavior. Accordingly, no attempt was made to compensate for the uncatalyzed reactions by using more complex curve-fitting models. However, the relatively large rates of the uncatalyzed reactions at pH 10 complicated the sample handling procedure. To avoid problems associated with the volatility of the organic solvent in which the esters were dissolved initially, it was desirable to prepare dilutions in aqueous media. To avoid excessive hydrolysis prior to the measurement step, samples in acetonitrile were injected into a buffer solution at pH 8.2 just before the mixing and measurement steps were begun. The buffer capacity of the solution was made low enough that it did not interfere with the adjustment to pH 10 in the final mixing and measurement step.

Because the resolution of the different isomers was to be based on kinetic differences, it is necessary that rate constants for the different isomers be different. For the catalyzed reactions at pH 10, the ratios of rate constants for the ortho-, meta-, and para-isomers respectively are 1:6.8:1.6. Thus, the ortho- and para-isomers are the most difficult to resolve in both two- and three-component mixtures.

Single-component Calibrations. Data used to evaluate apparent rate constants at pH 10 were also used to test linearity of absorbance changes vs concentration. All reactions were monitored for at least eight half-lives. Equilibrium absorbances were obtained by direct measurement and by a predictive method.[22] Direct measurement results were obtained by averaging several values near eight half-lives of each response. Predictive results were obtained by fitting a first-order model to data for absorbance vs time over selected data ranges (2–5 half-lives) and extrapolating the fits to infinite time.

All calibration plots were linear for both data processing options and there was excellent agreement between calibration results obtained by the direct measurement and predictive options. Some typical least-squares results for the predictive option are given in Table 2. Intercepts, standard deviations of slopes, and standard errors of the estimates are all small, and correlation coefficients are near unity, reflecting the good linearity observed visually. Very similar results were obtained with the direct measurement option. These results support the use of a first-order model for individual components and parallel first-order models for mixtures.

Mixtures. Results are reported here for two- and three-component mixtures. Two sets of two-component mixtures were examined. One set involved the ortho- and meta-isomers with relatively large differences between rate constants, and one set involved the ortho- and para-isomers with relatively small differences between rate constants. Concentrations of the different isomers used in the various studies are given in appropriate tables and figure legends below. All sets of mixtures used for quantitative determinations included low/low, low/high, high/low, and high/high concentration ratios of the different isomers. For example, for mixtures of the ortho- and meta-isomers containing 22–176 μM *o*-NPA and 132–593 μM *m*-NPA, the concentration ratios of the ortho-isomer to the meta-isomer varied from 22:593 to 176:132.

Response Curves. Figure 3A contains typical response data for a two-component sample. The top plot (curve a) represents the unresolved response for the mixture. The points represent experimental data, and the solid curve represents a

(22) Mieling, G. E.; Pardue, H. L. *Anal. Chem.* **1978**, *50*, 1611–1618.

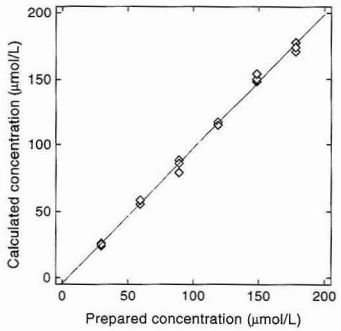

Figure 4. Comparison of prepared and determined concentrations for individual component in a three-component mixture. *o*-NPA with *m*- and *p*-NPA (see seventh row of Table 3).

fit of a model for two simultaneous first-order processes to the data. The model fits the data very well.

The two lower plots (curves b and c) represent the resolution of the overall response into the individual components of which it is composed. The absorbance change for the ortho-isomer (smaller rate constant) is about 2.5-fold that of the meta-isomer. The data points in these plots are the computed values based on the fit of the parallel first-order model to the overall response. The lines represent values computed by using the determined values of rate constants, prepared values of concentrations, and molar absorptivities of each component. Good agreement is obtained among determined (points) and expected (lines) results.

Figure 3B contains typical response data for a three-component sample. The different plots are as described above for two-component samples. The top plot represents the unresolved response, and the lower plots represent the contributions of the individual components. The model for three simultaneous first-order processes fits the overall data very well, and there is good agreement among the determined and expected results for the individual components.

Quantitative Results. A typical plot of determined vs prepared concentrations is given in Figure 4, and results for linear least-squares fits of determined vs prepared concentrations for several two- and three-component samples are summarized in Table 3. The plot respresents results for the component (*o*-NPA) with the smallest rate constant in several three-component mixtures. Both the plot and the least-squares results in the seventh row of Table 3 confirm good agreement among determined and prepared concentrations.

Plots of determined vs prepared concentrations for other mixtures were similar to the plot in Figure 4, and least-squares results in Table 3 permit quantitative comparisons. The components which are most difficult to resolve in both two- and three-component mixtures are the ortho- and para-isomers because the rate constants for these isomers differ by less than a factor of 2. Even so, least-squares statistics in rows 4, 5, 7, and 9 of Table 3 and results in Figure 4 confirm good performance for these components.

Pooled standard deviations are included in the last column of Table 3. Absolute values are in the range of 1–10 μmol/L. Values relative to average concentrations in each range at 3.7% or less.

Discussion. This study demonstrates the feasibility of resolving structural isomers quantitatively on the basis of differences in kinetic behavior. Reasonably good results were obtained despite some potential problems. The features expected to cause the most serious problems were the small differences among rate constants for the different components and between catalyzed and uncatalyzed reactions for each component. It is possible that other forms of cyclodextrins could enhance differences among rate constants for different isomers, but additional studies are necessary to determine if this is the case. Unmodified β-CD was used in this study because it is readily available. However, the effects of the uncatalyzed reactions could be reduced significantly by using a modified form of cyclodextrin with enhanced catalytic activity, such as that described in our earlier paper.[9]

It is possible that other curve-fitting methods such as the Kalman filter might give improved results. However, our focus was not on the curve-fitting method but on the potential use of the cyclodextrins as analytical reagents. In any event, the most serious limitation is that imposed by the large differences in molar absorptivities for the different isomers. These differences make it difficult to impossible to resolve similar concentrations of all the isomers by using a single wavelength. One possible solution to that problem would be to combine the kinetic-based resolution method with multi-wavelength data processing methods as used previously with phosphorescence[23] and other[15] data. For wavelengths longer than 450 nm, the absorptivities of the ortho- and meta-isomers approach and exceed those of the para-isomer, which should permit resolution of all the isomers in nearly equimolar concentrations. We did, in fact, intend to apply multiwavelength methods with these reactions. However, because the mixing times we were able to achieve in our multiwavelength instrumentation were too long for the faster-reacting components, we opted for the shorter mixing times achievable with the centrifugal mixing system which, unfortunately, does not have multiwavelength capability.

All results for mixtures reported above were based on fitting ranges corresponding to six or more half-lives of the component with the smallest rate constant. However, other data ranges were examined, and it was found that results degraded by factors of 2–4-fold relative to those reported above could be obtained by using fitting ranges as short as three half-lives of the component with the smallest half-life.

ACKNOWLEDGMENT

This study was supported in part by Grant No. GM 13326-26 from the National Institutes of Health.

Received for review March 1, 1994. Accepted July 1, 1994.[⊗]

(23) Goeringer, D. E.; Pardue, H. L. *Anal. Chem.* **1979**, *51*, 1054–1060.

[⊗] Abstract published in *Advance ACS Abstracts,* August 15, 1994.

Anal. Chem. **1994,** *66,* 3323–3327

Capillary Optical Sensors

Bernhard H. Weigl[†,‡] and Otto S. Wolfbeis[*,‡]

Joanneum Research, Institute for Sensor Interfaces, Steyrergasse 17, A-8010 Graz, Austria, and Institute for Organic Chemistry, Analytical Division, Karl Franzens University, Heinrich St. 28, A-8010 Graz, Austria

Glass or plastic tubings with a chemically sensitive coating on the inner surface are used for optical chemical sensing. Such devices possess several attractive features in that they (a) can act as a mechanical support for optically sensitive materials (coatings), (b) represent an optical waveguide structure and enable various methods of optical interrogation, (c) can serve as a sample cavity of well-defined volume, and (d) are suitable for direct sampling. The performance of such "capillary optrodes" is exemplified with a fast-responding and fully reversible carbon dioxide sensor chemistry. Its response time to gases (t_{90}) varies from 100 to 300 ms. We also give arrangements for optical readout devices and show that capillary sensors can overcome some of the problems of optrode membranes mounted in flow cells or on fiber tips.

Numerous solid supports for the immobilization of sensitive layers for optical (fiber) chemical sensors have been reported. For example, sensor materials have been deposited on fibers by dip-coating[1] and on planar supports by spin-coating,[2] photopolymerization[3] or covalent immobilization.[4,5] Others describe the spreading of chemically sensitive layers on polyester foils[6,7] which paves the way for mass manufacturing of sensor spots which, eventually, may be attached to fiber tips. Alternatively, they may be used in disposable (single-shot) sensors. Coated polyester membranes may also be obtained by spin-coating.[7-9]

Planar optical sensors usually are placed in flow cell type modules comprising light sources and detectors, sometimes along with optical fibers which guide light from the source to the cell with the membrane and back to an optoelectronic readout device. A sample (such as blood) is passed through the cell where it changes the optical properties of the sensor membrane. Such cells, frequently made from steel or durable plastic, are robust, bulky, expensive, and have relatively large internal volumes. Due to the nature of the measurement, the sensor membrane has to be fixed on one side of the cell with O-rings, springs, screws, or the like, or glued to the surface of a transparent cell wall. The cell–membrane interfaces, however, are a notorious source of error due to gas permeation, leakage, swelling, scratching, or delamination.

Alternatively, chemically sensitive optical materials also have been mounted at the tip of an optical fiber. Such devices, in principle, can be placed directly in the sample (such as blood in an artery). Hence, both sampling and transportation of the sample become unnecessary. However, this approach suffers from several shortcomings including (a) the fiber bending effect, (b) mechanical disrupture, (c) interferences by false light because of inadequate optical isolation and protection from both ambient light and sample fluorescence, and (d) the poor reproducibility of the thickness of the coatings on fiber tips. The most serious difficulty we encountered is the reproducible efficiency in coupling light into and out of the tip coating (or a tip membrane) which requires rather sophisticated optical alignments.

In addition to the use of optical fiber sensors, schemes have been reported in which capillaries have been used as waveguides. Giuliani et al.[10] and Reisfeld et al.[11] use a small glass capillary tube covered with a dye to sense ammonia in air. Another approach was reported[12] in which a glass tube was filled with porous sol–gel silica powder doped with a complexing agent which gave a color with the analyte. The length of the stained section of the tube was found to be a measure of the concentration of the analyte. The device resembles commercially available test tubes.

More recently, another configuration has been reported in which the chemically sensitive material was deposited at the tip of a micropipet using near-field photopolymerization.[3] The method lends itself to the fabrication of miniature fiber-optic pH sensors with an extremely small sample volume and very rapid response times. Due to the minute size of the fiber tip, these sensors are excellent research tools but fragile and unlikely ever to be used in an adverse environment or by unskilled personnel.

We describe an attractive alternative for making "integrated sensors" (in a sense that they can act as sampling device, sampling vessel, and optical element) by making use of small capillaries. We show how this has led to a new immobilization technique (referred to as "reversed pumping"), and that such "integrated capillary sensors" have attractive novel features iincluding (a) a new sampling format (by making the sensor the sample cuvette), (b) the use of capillaries as a new support for optical sensor materials, and (c) the use of capillaries as disposable sampling vessels of defined volume.

† Joanneum Research.
‡ Karl Franzens University.

(1) Munkholm, C.; Walt, D. R. *Talanta* **1988,** *35,* 109.
(2) Seiler, K.; Simon, W. *Anal. Chim. Acta* **1992,** *266,* 73.
(3) Tan, W.; Zhong-You, S.; Smith, S.; Birnbaum, D.; Kopelman, R. *Science* **1992,** *258,* 778.
(4) Harper, B. G. *Anal. Chem.* **1975,** *47,* 348.
(5) Wolfbeis, O. S.; Offenbacher, H.; Kroneis, H.; Marsoner, H. *Mikrochim. Acta (Vienna)* **1984,** *I,* 153.
(6) Wolfbeis, O. S.; Weis, L. J.; Leiner, M. J. P.; Ziegler, W. E. *Anal. Chem.* **1988,** *60,* 2028.
(7) Wolfbeis, O. S., Ed. *Fiber Optic Chemical Sensors and Biosensors;* CRC Press: Boca Raton, FL, 1991; Vol. I, Chapters 7 and 8.
(8) Jones, T. P.; Porter, M. D. *Anal. Chem.* **1988,** *60,* 404.
(9) Weigl, B. H.; Holobar, A.; Rodriguez, N. V.; Wolfbeis, O. S. *Anal. Chim. Acta* **1993,** *282,* 335–343.
(10) Giuliani J. F.; Wohltjen H.; Jarvis N. L. *Opt. Lett.* **1983,** *8,* 54.
(11) Chernyak V.; Reisfeld R.; Gvishi R.; Venezky D. *Sens. Mater.* **1990,** *2,* 117.
(12) Kuselman I.; Lev O. *Talanta* **1993,** *40,* 749.

0003-2700/94/0366-3323$04.50/0
© 1994 American Chemical Society

EXPERIMENTAL SECTION

Preparation of the Capillary Sensor. It was found that most sensor materials can be deposited inside glass or plastic tubes by pumping or sucking the sensor cocktail through the tubes. Disposable glass micropipets with an inner diameter of 0.7 mm (Brand, Wertheim, FRG) were used in this particular case. The capillaries were connected to a peristaltic pump and then dipped into the cocktail solutions (i.e., the mixtures prepared for immobilization). The pump speed was adjusted such that the solution was moving up at a rate of 5 mm/s. After the capillary was filled about half, the rotation of the pump was reversed. The pump speed depended largely on the viscosity and temperature of the immobilization solution. After the sensor material was pumped out, the capillary was dried by drawing air through the capillary using a water jet aspirator. After several minutes, the inner coating is completely dry. The capillary was then inserted into a suitable optical monitoring device (see below), or stored in clean ambient air until used.

For the experiments described in the following, carbon dioxide sensitive layers were used as an inner coating. The sensor cocktail comprises an ion pair consisting of an organic quaternary cation and a pH indicator anion.[13,14] The color change of the indicator dye was monitored. The following cocktail was employed: Solution *A* was prepared by dissolving 5.0 g of ethyl cellulose (Aldrich) in 45 g of toluene at room temperature. Solution *B* was prepared by stirring 1.368 g of tetraoctylammonium bromide (TOABr) (Aldrich) with 1.16 g of silver oxide (Aldrich) and 5 mL of methanol for 5 h at room temperature; the solid phase (silver bromide) was then removed. Solution *C1* was prepared by dissolving 13.77 mg of cresol red (Aldrich) in 22.5 mL of 0.1 M NaOH. Solution *C2* was prepared by dissolving 37.39 mg of TOABr in 3 mL of toluene. Solutions *C1* and *C2* were mixed and stirred for 5 min, and then the organic phase was removed and washed two times with 3 mL of 0.1 M NaOH. The resulting organic phase (solution *C*) contained the pure ion pair [cresol red$^-$/TOA$^+$] dissolved in toluene. One gram of solution *A*, 219 μL of solution *B*, 200 μL of solution *C*, 400 μL of tributyl phosphate (Aldrich), and 400 μL of toluene were mixed and homogenized by stirring for 5 min. This cocktail was used to coat the capillaries as described above. In one series of experiments, an additional coating was applied, in that a moisture-curing basic silicone (PS250, from Huels-Petrarch; obtained from ABCR, Karlsruhe, Germany) was deposited on the first layer, again by the "reversed pumping" technique.

When applied at room temperature, the cocktail deposited on the inner wall, after drying, has a thickness of around 2 μm, as estimated at a section of the capillary with a microscope and by comparison with steel spacers of defined thickness. The additional silicone coating applied in one series of experiments had an estimated thickness of about 3 μm. In order to obtain thinner coatings, the coating solution may be further diluted with toluene. Figure 1a shows a cross section of a capillary with one single sensor layer. However, several layers may be deposited consecutively by this technique, as it may become necessary in case of CO_2 sensors with an additional hydrophobic (proton-impermeable) layer of silicone rubber (such as the PS 250, from Huels-Petrarch). The additional coating prevents dye leaching and diffusion of protons into the sensing layer. Hence, the sensor becomes applicable to aqueous samples. Finally, an optical isolation may be placed on the chemistries so as to prevent ambient light from interfering. Figure 1b shows a cross section of a capillary having three sensor layers.

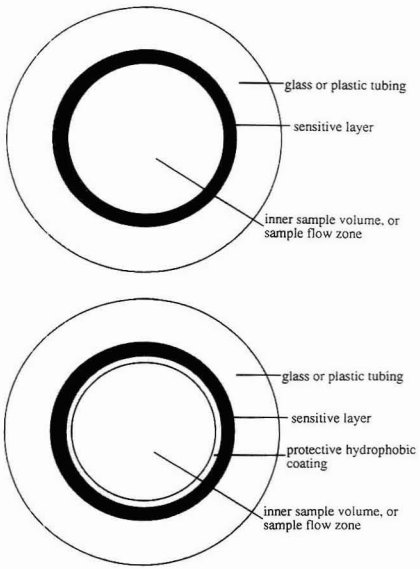

Figure 1. Cross section through typical capillary sensors. In a only one coating is deposited on the inner wall of the capillary, and the resulting sensor is preferably used for analyzing gaseous samples. In b two layers are deposited on the inner wall by the "reversed pumping" technique. The first layer is the carbon dioxide chemistry (polystyrene based), and the second a gas-permeable but proton-impermeable silicone layer. A third layer of black silicone may optionally be placed on layer 2 as an optical isolator.

Optical Arrangement. Figure 2 shows a conventional arrangement for monitoring the changes in the absorption or fluorescence of the tube sensors. A 1.5-mm diameter hole was drilled through an ST optical fiber coupler (Hirschmann, Vienna), into which the sensor capillary was inserted. Optical glass fibers (core diameter 125 μm) were attached to each side of the coupler so that the springs of the fiber connectors pressed the fibers against the capillary. One fiber was then attached to a yellow LED (λ_{max} 590 nm), and the other to a Hewlett-Packard 8153A lightwave multimeter. The capillary was connected to either the gas line with a short piece of polyethylene tubing or to a flow of buffered sample solutions which were equilibrated with gas mixtures of defined carbon dioxide partial pressure. The flow rate was 1 mL min^{-1}.

In the optical arrangement where the capillary acted as a waveguide for the 543.3-nm He–Ne laser line, an input and an output coupler, respectively, were created at each end of the capillaries. In essence, a 0.5- × 0.8-mm coupler spot was ground onto the outer surface using conventional optical grinding paper. The resulting, highly scattering surface acts

(13) Mills, A.; Chang, Q.; McMurray, N. *Anal. Chem.* **1992**, *64*, 1383.
(14) Raemer, D. B.; Walt, D. R.; Munkholm, C. U.S. Pat. 5,005.572, 1991.

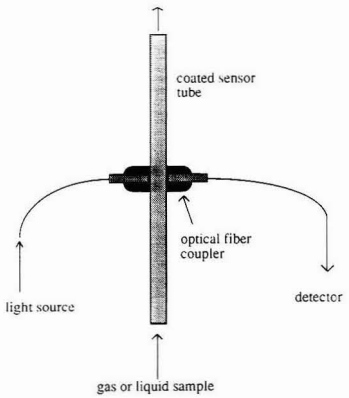

Figure 2. Optical capillary sensor with fiber coupler for absorption measurements. Note that the light beam passes through the sensing layer (the inner coating of the capillary) twice.

as a very efficient coupler, and the capillary with its index of refraction of 1.54 acts as the waveguide. The refractive index of the CO_2-sensitive coating (composed of mainly ethyl cellulose and acting as the "cladding" of the glass waveguide) is 1.35.

RESULTS AND DISCUSSION

The CO_2-sensitive capillaries, which show the blue color of cresol red in its base form, do not require further conditioning and can be tested immediately after being dried for several minutes at room temperature. They reversibly change color from blue via green to yellow when exposed to increasing levels of carbon dioxide.

The sensing mechanism is based on the reversible reaction between the blue [cresol red$^-$/TOA$^+$] ion pair and carbon dioxide, which results in the formation of a new ion pair consisting of the quaternary cation and a bicarbonate anion, thereby releasing a proton which converts the blue indicator anion into its yellow (protonated) form.[8] The process is fully reversible, and in the absence of CO_2 the blue color is obtained again.

Expired air contains 2–5% CO_2. The response time of this kind of sensor to gases is less than 0.3 s (t_{90}, the time of 90% of the total signal change to occur) because of the very thin coating. This makes it possible to instrumentally monitor the concentration of carbon dioxide in respiratory air (Figure 2), but also visually by observing the continuous color change (from blue to yellow and back) while breathing through the capillary.

In order to increase the resolution of the sensor, the capillary was inserted into the readout device shown in Figure 2. The measured response to varying concentrations of carbon dioxide in a gas mixture is shown in Figure 3. The gas mixtures also contained nitrogen and oxygen at atmospheric pressure. Also shown is a response curve of the same material, but immobilized on a polyester support and mounted in a planar flow-through cell arrangement. It clearly can be seen that response times are much shorter and the relative signal changes larger in case of the capillary sensor.

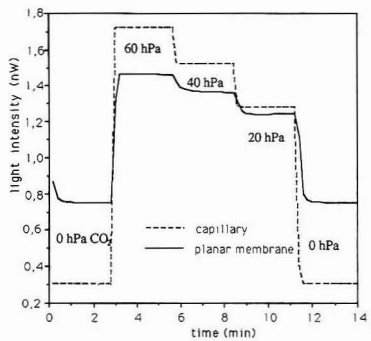

Figure 3. Response curves of a capillary sensor (this work) and a planar carbon dioxide sensor (with the chemistry placed on a planar polyester support), toward gaseous carbon dioxide. The same sensor layer chemistries and thicknesses were applied in both experiments. (1 hPa equals 1 mbar and 0.76 Torr).

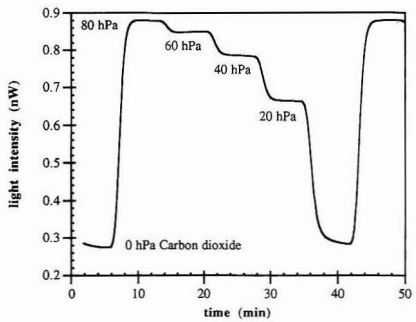

Figure 4. Response of the capillary sensor to carbon dioxide dissolved in water. (1 hPa equals 1 mbar and 0.76 Torr.)

In an experiment with aqueous samples, a capillary optrode with an additional hydrophobic coating (Figure 1b) was employed. The response to samples tonometered (gas-equilibrated) with gases of different pCO_2 is shown in Figure 4. Again, the sensor responds fully reversibly although response times are much slower, being in the order of 3 min for the forward response, and 4–7 min in the reverse direction. This is only partially due to the second coating which is required to prevent interferences by changes in pH but also acts as a diffusional barrier. The major reason for the slower response is the low concentration of CO_2 in the water sample which requires a substantial quantity of water to pass the membrane until it is equilibrated with carbon dioxide. To document insensitivity to pH, the capillary sensor was alternately exposed to 0.1 M buffer solutions of pH 4 and pH 9, both purged with nitrogen. No cross sensitivity to pH was found. However, when exposing it to 0.1 M HCl, the coating irreversibly turned yellow after less than 1 h. Not unexpectedly, ammonia interfered when present along with carbon dioxide.

The reproducibility of the insertion of the capillary into the optical arrangement (Figure 2) was tested by inserting and removing it 10 times, while the membrane was exposed to pure nitrogen. In a second experiment, 10 different

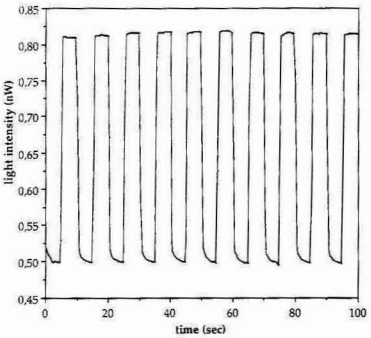

Figure 5. Response time, relative signal change, and reversibility of the capillary sensor for carbon dioxide, alternately exposed to 0 and 80 hPa carbon dioxide in dry nitrogen.

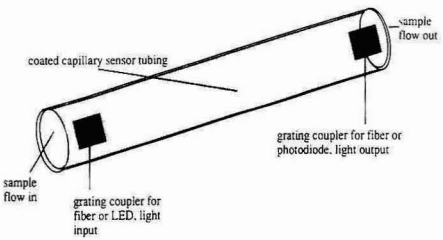

Figure 6. Capillary sensor used as a "tubular waveguide". The tubing is supplied with an input grating coupler for light from an optical fiber or directly from an LED and an output coupler from where light is directed to a photodiode. The optical changes are monitored via the evanescent field of the waveguide which hits the chemically sensitive inner coating.

capillaries having the same coating were inserted into the detector. The error due to misalignment (insertion) was less than 1%, whereas the error in absorption due to variations in manufacturing was less than 5% of the relative signal change.

In the arrangement shown in Figure 2, the optical damping due to absorption is twice as high as in a conventional sensor membrane placed in a cell, because the optical path passes through the membrane twice. Since the inner layers are mechanically protected by the capillary, a larger amount of plasticizer can be added to the coating solution. The addition of plasticizer is known[15] to reduce the response time by increasing the permeability for gases. However, large amounts of plasticizer cause the membrane to assume a sticky consistency which is a problem in case of planar sensor spots. In capillary sensors, in contrast, the inner coating is well protected from mechanical attack. Up to 80% tributyl phosphate (TBP) may be added to ethyl cellulose. This compares favorably to the maximally 50% TBP that can be added to ethyl cellulose when deposited on planar glass slides or polyester membranes. The response curve of this sensor, when exposed to 0 and 80 hPa carbon dioxide (i.e., 0 and around 8% CO_2 in gas mixtures at ambient pressure) is given in Figure 5. The response time (t_{90}) for the reaction from 0 to 80 hPa was 100 ms, the back-reaction occurred in less than 300 ms. These are among the shortest reported response times for chemical optical sensors based on a chemical reaction.[3,14,15]

Capillary sensors lend themselves to several other methods of optical interrogation. The capillary tube, when connected to a light source and a detector via grating couplers, can act as a "tubular waveguide". Changes in the absorption or fluorescence of the sensor layer within the evanescent field of the waveguide can be monitored. With this method, interferences by color and turbidity of the sample are widely eliminated, since the coating is thicker than the penetration depth of the evanescent wave which is in the order of 1 μm. Figure 6 shows the arrangement that has been used in experiments on evanescent wave absorptiometry (or fluorimetry). In a typical experiment, two gratings were ground into a CO_2-sensitive capillary close to each end (Figure 6). The green line of an He–Ne ion laser (λ 543.3 nm) was coupled into the capillary waveguide at one end, and attenuated light left the waveguide at the other end. Light was focused, via a standard lens, onto a silicone photdiode. When exposed to several levels of carbon dioxide in air (0–20%) by incorporating the tube into a gas line, a substantial and fully reproducible change in absorption was observed in all experiments.

In addition to absorption measurements, the capillary may as well be used to monitor changes in the refractive index of the sensor layer, because the depth of the evanescent field—and, consequently, the efficiency of the absorption—is a function of the ratio between the refractive indices of tube ("core") and sensor coating ("cladding"). The capillary then acts as sort of input/output coupler.[16] Without any coating, it is the refractive index of the sample passing the capillary which is measured.

Finally, the capillary can be considered as a useful sampling vessel and, at the same time, acts as a sensor, so that there is no need for sample transfer. Samples may be drawn by capillary action, and this is considered to be particularly promising in case of blood and other physiological liquids. Such a sampling technique is especially useful when only scarce amounts of sample are available.

CONCLUSIONS

We think that the capillary type sensor presented here has a number of interesting and novel features. These include a simple and reproducible immobilization procedure and a mechanical protection of the sensor surface. It can act as both a flow-through cell and a sampling vessel and applied to both liquids and gases. No leakage of sample, or air permeation into the tubing, both of which are common drawbacks in flow-cell type arrangements (because of poor membrane-to-cell alignment), can occur. Because of its geometry, air bubbles do not tend to reside in the tube area.

The sensors have extremely short response time for three reasons, namely because (a) the two sensing layers passed by the light beam when penetrating the capillary can be very thin, (b) equilibration of two thin layers is faster than that of a single layer of the same total thickness, and (c) the sample

(15) Brandrup, I., Immergut, E. H., Eds. *Polymer Handbook*, 3rd ed.; Wiley: New York, 1989; p VI/440.

(16) Clerc, D.; Lukosz, W. *Sens. Actuators* **1993**, *B11*, 461.

flow is laminar, resulting in a nonturbulent flow and a fast exchange of sample volume.

Conceivably, such sensors may also act as sampling devices, e.g. when drawing whole blood. Because of the use of low-cost materials and simple manufacturing techniques, such capillary sensors can be produced at low costs which, in turn, paves the way for disposable sensors. A final function of the capillary is that of a tubular waveguide. If appropriate means for coupling light into and out of the capillary are provided (such as shown in Figure 6), the evanescent field phenomena can be applied to optically interrogate the sensor. Initial experiments with this geometry are extremely promising.

The main disadvantage of capillary ("integrated") sensors over planar sensor geometries is a more sophisticated optical geometry which is required to couple light in and out of a curved capillary surface (Figure 2). However, we think that this kind of sensor allows the construction of a variety of simple and cost-effective measurement devices, and the capillaries may be disposable and easy to change and to handle.

Received for review December 1, 1993. Revised manuscript received June 15, 1994. Accepted June 16, 1994.®

® Abstract published in *Advance ACS Abstracts,* August 1, 1994.

Anal. Chem. **1994,** *66,* 3328–3336

Multicomponent Determination of Chlorinated Hydrocarbons Using a Reaction-Based Chemical Sensor. 1. Multivariate Calibration of Fujiwara Reaction Products

John M. Henshaw,† Lloyd W. Burgess,* Karl S. Booksh,‡ and Bruce R. Kowalski

Center for Process Analytical Chemistry, Department of Chemistry, BG-10, University of Washington, Seattle, Washington 98195

Multicomponent analysis for 1,1,1-trichloroethane, trichloroethylene, and chloroform is demonstrated by partial least squares modeling of absorbance data collected from the Fujiwara reaction of these analytes over time. Optimal calibration times are determined for each analyte dependent upon its reaction rate. This is the simplest example of trying to use the selectivity gained from a second data dimension or order. Problems associated with first-order calibration are demonstrated when interferences unaccounted for in the calibration model are present. Determination of 1,1,1-trichloroethane in the presence of the other two species is also demonstrated using the generalized rank annihilation method and trilinear decomposition for second-order calibration. A subsequent paper describes an approach using multivariate curve resolution to extract the analytical information from the spectral and temporal profiles of analytes in the Fujiwara reaction.

The Fujiwara reaction[1] has been used as the basis for a variety of analytical methods for both quantitative and qualitative determinations of several halogenated hydrocarbon species in blood,[2] water,[3] and air[4] samples. These methods rely on monitoring the absorbance at a single wavelength when the reaction between analyte and the Fujiwara reagent (pyridine, water, and base) is complete. An optical fiber-based chemical sensor for the determination of trichloroethylene (TCE) or chloroform (CHL) based on the Fujiwara reaction has been demonstrated by researchers at Lawrence Livermore National Laboratory (LLNL).[5] At least 22 different halogenated molecules have been shown to form visible light-absorbing species when exposed to the Fujiwara reagent.[6] This chemistry continues to enjoy popularity as it provides the ability to monitor the presence of chlorinated hydrocarbons by using visible light spectroscopy. However, the lack of selectivity, coupled with the instability of the Fujiwara product, has continued to plague researchers.

The selectivity of an absorbance-based measurement can be improved by monitoring more than one absorbing wavelength provided the analytes yield different absorbance spectra. This would be an improvement over traditional univariate Fujiwara reaction-based methods. Univariate methods must assume there are no interferences in the sample or bias will be added to the measurement. Any absorbance generated at the monitored wavelength will be attributed to analyte, thus causing analytical error when an unknown species contributes to the sensor response.

Examination of the full spectrum yields a vector of responses from an analyte and enables the application of multivariate statistical methods for response characterization and calibration. Multivariate calibration methods offer several advantages over univariate calibration methods.[8] Signal averaging is achieved since more than one measurement channel is employed in the analysis. Also, the concentrations of multiple species may be measured if they are present in the calibration samples. A calibration model is built by using responses from calibration standard solutions. The analysis of unknown samples will suffer if a species is present in the sample that is not accounted for in the calibration model. This is mitigated somewhat by the ability to detect whether a sample is an outlier from the calibration set.[9] This is especially important when the sample matrix is unknown, as is frequently the case in environmental samples. The work described here uses partial least squares (PLS) analysis for calibration of analyte spectral responses.

The analytes examined in this work include 1,1,1-trichloroethane (TCA), TCE, and chloroform in mixtures exposed to the Fujiwara reagent. Examination of the reaction product spectra reveal differences in both the visible light absorbance and reaction kinetics for the three analytes. This is not surprising, as different pathways for the species have been proposed.[10] The proposed reaction mechanisms involve first the reaction of the halogenated hydrocarbon with hydroxide ion to form a reactive intermediate. This intermediate species is proposed to be dichlorocarbene in the reaction of chloroform and dichloroacetlyene in the reaction of TCE.[10] The inter-

† Present address: ORS Environmental Systems, 7 Barnabas Rd., Marion, MA 02738.

‡ Present address: University of South Carolina, 700 S. Main St., Columbia, SC 29208.

(1) Fujiwara, K. *Sitzungsber. Abh. Naturforsch Ges. Rostock* **1916,** *6,* 33.
(2) Ross, J. H. *J. Biol. Chem.* **1923,** *58,* 641.
(3) Liebman, K. C.; and Hindman, J. D. *Anal. Chem.* **1964,** *36,* 348.
(4) Lugg, G. A. *Anal. Chem.* **1966,** *38,* 1532.
(5) Milanovich, F. P.; Garvis, D. G.; Angel, S. M.; Klainer, S. M.; Eccles, L. A. *Anal. Instrum.* **1986,** *15,* 137.
(6) Reith, J. F.; van Ditsmarsch, W. C.; de Ruiter, T. *Analyst* **1974,** *99,* 652.
(7) Angel, S. M.; Ridley, M. N. In *Chemical, Biochemical, and Environmental Fiber Sensors II*; Lieberman, R. A., Wlodarczyk, Eds.; SPIE: Bellingham, WA. 1990.
(8) Martens, H.; Naes, T. *Multivariate Calibration*; John Wiley & Sons: Chichester, England, 1989.
(9) Rousseeuw, P. J.; Leroy, A. M. *Robust Regression and Outlier Detection*; John Wiley & Sons: Chichester, England, 1987.
(10) Angel, S. M.; Daley, P. F.; Langry, K. C.; Albert, R.; Kulp, T. J.; Camins, I. In *Chemical, Biochemical, and Environmental Fiber Sensors II*; Lieberman, R. A., Wlodarczyk, Eds.; SPIE: Bellingham, WA, 1990.

0003-2700/94/0366-3328$04.50/0
© 1994 American Chemical Society

mediate species then reacts with pyridine in a series of steps to form the classic "Fujiwara product" (red-colored) and glutaconaldehyde.[11] The concentration of base affects both the spectral and kinetic profiles in the reaction. The LLNL sensor attains selectivity through modification of the base concentration to permit analysis of either TCE or chloroform.[7]

TCA reacts much slower than the other two analytes; this correlates well with the much lower reactivity of TCA with hydroxide as compared to TCE and chloroform.[12] The concentration of water also affects the analyte response.[13] The reaction is maintained under pseudo-first-order conditions by keeping the Fujiwara reagent in excess of the analyte.

When analytes react at different rates, the rate of reaction can be incorporated into the analysis. There are many kinetic-based methods that are based on differences in reaction rates.[14] These methods typically involve monitoring a reaction at a single measurement channel and examining the rate of appearance or disappearance of a chemical species. This approach maintains only one selective dimension and thus requires additional information about the system being monitored if multiple species are present. A more selective analysis can be made if analyte responses vary in both the temporal (kinetic) and spectral (chemical species) dimensions. This requires collection of absorbance spectra over time. A single sample measurement thus yields a matrix of data which is referred to as second-order data. Optimally, second-order data can provide the ability to predict the concentration of analytes in the presence of unknown interferences. This has been called the second-order advantage.[15]

Second-order data methods have been developed to handle these types of data.[15-17] The generalized rank annihilation method (GRAM) was developed by Sanchez and Kowalski[18,19] for the calibration of bilinear data. Bilinear data can be expressed as the outer product of two intrinsic factors representing the two-dimensional responses of a species. GRAM can extract the intrinsic factors in two orders along with an estimate of the concentration ratio of analyte in the sample to analyte in a calibration standard. GRAM uses a single calibration standard to predict the concentration of analyte in an unknown sample. This limits GRAM to the analysis of one sample at a time using only one standard. This can be time consuming when many samples require analysis. Also, responses that produce deviations from linearity will suffer increased error if the concentration of the analyte in the sample differs greatly from the concentration in the standard. Trilinear decomposition (TLD) has been developed in response to the desire to analyze stacks of response matrices, i.e., the data generated from a third-order tensor.[20] Data arrays that fit the trilinear model have a unique factor analysis decomposition that correspond to the true chemical factors that describe the data, i.e., the spectral, temporal, and concentration orders generated in this work.

A second-order sensor for the determination of metal ions has recently been introduced.[21,22] This sensor incorporates the elution profile of analyte ions from a cation exchange membrane and the absorbance spectrum of the analyte with a metal complexing agent as the two selective orders. GRAM and TLD are used to enable quantitation of cadmium and lead in the presence of several transition metal ions that would cause an interference in a uni- or bivariate analysis. The heavy metal sensor papers also present a good discussion on the theory of second-order sensing that will not be repeated here.

This paper discusses the use of chemometric methods for the spectroscopic determination of TCA, TCE, and chloroform in mixtures exposed to the Fujiwara reagent. The goal of this research is to determine whether selectivity can be gained by incorporating both the spectral and temporal domains of the Fujiwara reaction into the analysis. The research was initiated in an attempt to gain selectivity from the Fujiwara reaction which can then be incorporated into a more selective optical fiber-based chemical sensor. The temporal response of the sensor is dependent upon both the permeation rates of analytes through a membrane and the analyte-specific Fujiwara reaction kinetics. The kinetic aspect of the response has been studied first to determine the viability of the approach. Approaches to analysis of the two-dimensional kinetic/spectral data are presented here in a series of three reports. This paper describes the data and demonstrates the advantage of collecting multivariate data over univariate data. Second-order calibrations of TCA responses using the GRAM and TLD are also demonstrated. The second and third papers describe a multivariate curve resolution technique[23] and an iterative factor analysis technique[24] that enable estimation of the actual spectral and kinetic profiles of species formed in the reaction and subsequent calibration for the analytes.

EXPERIMENTAL SECTION

Reagent and Sample Preparation. The composition of the Fujiwara reagent used in the multivariate calibration experiments was 88.3% pyridine, 4.7% tetrabutyl ammonium hydroxide, and 7.0% water. These conditions were optimized for the fastest formation of visible light-absorbing products from TCA. The reagent was allowed to sit for 1 day following preparation to improve the clarity of the reagent solution. Standard analyte solutions of 1000 ppm TCA, TCE, and chloroform were prepared in pyridine. Aliquots of these solutions were taken using gas-tight syringes and then mixed with reagent to form the samples. Concentrations were selected at levels representative of those expected at a specific contaminated site.

Sample Analysis. The temporal and spectral profiles of the analytes reacting with the Fujiwara reagent were evaluated by monitoring the absorbance spectra at fixed time intervals of species in the reaction under temperature-controlled conditions. Absorbance spectra were collected of samples in

(11) Uno, T.; Okimura, K.; Kuroda, Y. *Chem. Pharm. Bull.* **1982**, *30*, 1876.
(12) Atkinson, R. *Chem. Rev.* **1985**, 85, 69.
(13) Henshaw, J. M. Ph.D. Dissertation, University of Washington, Seattle, WA, 1993.
(14) Mottola, H. A. *Kinetic Aspects of Analytical Chemistry*; John Wiley and Sons: Chichester, England, 1988.
(15) Sanchez, E. Ph.D. Dissertation, University of Washington, Seattle, WA, 1987.
(16) Sanchez, E.; Kowalski, B. R. *J. Chemom.* **1988**, *2*, 247.
(17) Wang, Y.; Borgen, O.; Kowalski, B. R.; Gu, M.; Turicek, F. *J. Chemom.* **1993**, *7*, 117.
(18) Sanchez, E.; Kowalski, B. R. *Anal. Chem.* **1986**, *58*, 496.
(19) Sanchez, E.; Kowalski, B. R. *J. Chemom.* **1988**, *2*, 265.
(20) Sanchez, E.; Kowalski, B. R. *J. Chemom.* **1990**, *4*, 29.
(21) Lin, Z.; Burgess, L. W. *Anal. Chem.* **1994**, *66*, 2544.
(22) Lin, Z.; Booksh, K. S.; Burgess, L. W.; Kowalski, B. R., *Anal. Chem.* **1994**, *66*, 2552.
(23) Tauler, R.; Smilde, A.; Henshaw, J. M.; Burgess, L. W.; Kowalski., B. R. *Anal. Chem.*, second paper of three in this issue.

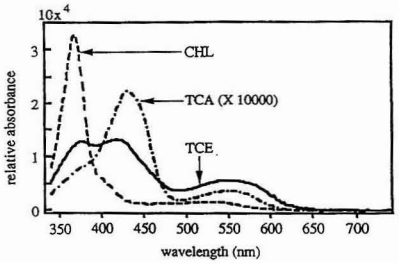

Figure 1. Absorbance spectra, divided by the initial molar concentration of analyte, of TCE (—), TCA (– · –) and CHL (- - -) Fujiwara reaction products at a fixed reaction time (TCE and CHL at 20 min, TCA at 60 min), 1% tetrabutylammonium hydroxide (TBAH), and fixed temperature (20 °C).

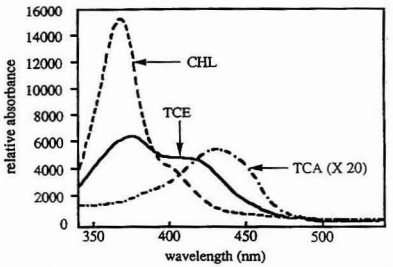

Figure 2. Absorbance spectra, divided by the initial molar concentration of analyte, of TCE (—), TCA (– · –), and CHL (- - -) Fujiwara reaction products at a fixed reaction time (TCE and CHL at 10 min, TCA at 60 min), 5% tetrabutylammonium hydroxide (TBAH), and fixed temperature (20 °C).

1 cm quartz cuvettes placed in a thermoelectrically stabilized cuvette holder by use of a Hewlett-Packard 8452A photodiode array spectrophotometer. Analytes were introduced into equilibrated cuvettes and mixed thoroughly at time zero. Data collection began 1 min after mixing the samples and reagent and proceeded at 1 min intervals for a period of 1 h. Duplicate samples were analyzed to determine the reproducibility of the experiments. No visible light absorbing products were seen in the standard solutions. The Fujiwara reagent did show an absorbance at 368 nm, similar to that of the product determined to be glutaconaldehyde.

Chemometric Data Analysis. The response matrices generated from each sample were transferred into Matlab software for data analysis and calibration purposes. Principal components analysis (PCA) was used to examine the variance in the response matrices generated from the collection of visible light absorbance spectra over time. PCA was done by performing the Matlab singular value decomposition on the response and examining the scores and loadings of the significant eigenvectors. All calibrations were done using software provided by the Laboratory for Chemometrics at the University of Washington's Center for Process Analytical Chemistry. PLS was used to calibrate the responses of the three analytes, TCE, TCA, and chloroform, at fixed points in time. GRAM and TLD were used to quantitate the second-order response of TCA in the presence of TCE and chloroform.

RESULTS AND DISCUSSION

Reagent Selection. The rates of appearance of visible light absorbance spectra of products formed upon reaction of analytes and the Fujiwara reagent are sensitive to both the base and water concentration and temperature and the analyte molecule. Figure 1 shows the absorbance spectra, formed at a fixed time following exposure of the three analytes to a reagent comprised of 92% pyridine, 7% water, and 1% tetrabutylammonium hydroxide at constant temperature. The differences in the spectra are apparent; each species has an absorbance maximum at ~368 nm, a second maximum in the region between 400 and 430 nm, and a third maximum at either 556 (TCE and TCA) or 534 nm (chloroform).

The spectra were normalized by dividing the absorbance by the molar concentration of precursor analyte for TCE and chloroform. This gives an indication of the sensitivity of this chemistry to these molecules. TCA was treated in a similar fashion; however, the normalized spectrum has been multiplied by 10 000 to put it on the same scale as the other spectra. This illustrates the relative insensitivity of this reagent composition to TCA, especially when the time difference (60 min for TCA vs 22 min for TCE and chloroform) is taken into consideration. This indicates that TCA would cause an insignificant interference to the determination of an equimolar concentration of TCE when a single wavelength (556 nm) is monitored, provided the reaction condition remains pseudo first order. However, an equimolar concentration of chloroform would yield a response equal to 15% of the absorbance produced by TCE at that wavelength at concentrations where Beer's law is obeyed.

The application under investigation is the determination of the three analytes at TCE and chloroform concentrations much greater than is accessible with the Fujiwara reagent described above. Also, although TCA is present at levels much higher than TCE or chloroform, the above chemistry is not sensitive enough for analysis. The concentration of base was evaluated to find conditions where TCA response was optimal and all three analtyes reacted. This was determined to be ~5% base; under these conditions, little Fujiwara product ($\lambda_{max} > 530$ nm) was formed and species absorbing at lower wavelengths dominated. A plot of the absorbance spectrum resulting from each of the three analytes at a single point in time is presented in Figure 2. Each analyte yields an absorbance centered at 368 nm; this is the dominant feature in the chloroform spectrum. The chloroform spectrum also contains a shoulder on this peak and a third absorbance maximum appears at 450 nm. The peak at 450 nm appears to grow and later diminish with time. This type of behavior is much more apparent in the peak centered at 414 nm for the reaction of TCE. The dominant feature in the TCA spectrum is centered at 430 nm and develops very slowly. This absorbance is continuing to increase one hour after the initiation of the reaction.

Panels a and b of Figures 3 depict the absorbance divided by the analyte concentration versus time at two wavelengths (368 and 430 nm) for each analyte. Again TCA yields a much lower absorbance per concentration of analyte than does either TCE or chloroform. However, the difference is much less than under the reduced base conditions described

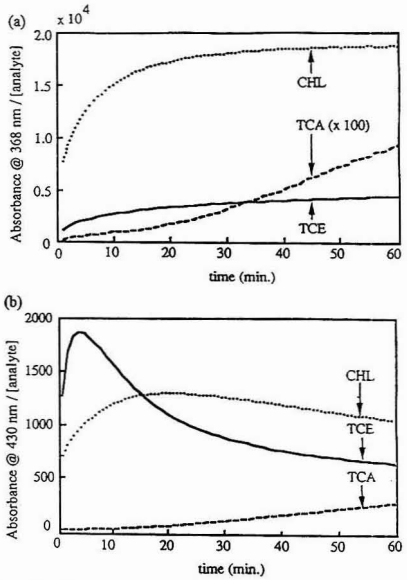

Figure 3. Absorbance divided by molar concentration of analyte at 368 and 430 nm (b) versus time for TCA (- - -), TCE(—), and CHL (•••) in the Fujiwara reaction at 5% TBAH.

above. This is due to the enhanced sensitivity to TCA and reduced sensitivity to TCE. The ratio of TCE absorbance per mole of analyte at 430 nm to that of TCA is reduced from ~5000 at 1% base concentration to ~3.5 at 5% base and long times. This is a significant improvement for the determination of samples containing TCA in samples containing TCE.

Chloroform sensitivity is also enhanced at higher base concentrations and suffers reduced linear dynamic range. Although chloroform analysis under these conditions can be demonstrated, actual analysis in unknown samples is problematic. Most of the response due to chloroform is at the 368 nm peak, which quickly yields nonlinear absorbances at much lower concentrations than any of the other spectral features of the analytes. The problem of limited dynamic range is compounded by several other features. This region of the spectrum suffers reduced detector response and source output and is attenuated over long distances of optical fibers. The absorbing product also forms via reaction between pyridine and the base. This background absorbance can be seen to increase slightly over time, contributing to a baseline drift. Finally, the commonality of this product to all analytes adds further to the analytical dilemma. Therefore it must be considered that minimizing the effect of chloroform upon the analysis of TCE and TCA is a more practical analytical goal.

Error Analysis. A set of mixtures of the three analytes were measured every minute for 1 h to examine the feasibility of doing multivariate calibration for the three analytes and also to provide the data for the self-modeling curve resolution research.[23] The samples ranged in concentration from 0 to 270 mg/L (ppm) TCA, 0 to 29.3 ppm TCE, and 0 to 7.4 ppm chloroform. Duplicates were analyzed for pure samples of each analyte. The differences between the duplicate sample matrices (61 × 100) were calculated and a root-mean-squared statistic was calculated at each wavelength. The root-mean-squared deviation for TCE was less than 2% over all absorbing wavelengths. The TCA error corresponded to 3.2% and 3.4% of the absorbance at the peak wavelength (430 nm) for the two duplicate samples. The chloroform error corresponded to 2.5% and 2.4% of the mean absorbance at the peak maximum (368 nm) of the duplicate samples. These figures suggest a level of the concentration error in the experiments.

Principal Components Analysis: Rank Determination. Determining the number of components or factors necessary to describe the response of a sample is critical to all multivariate statistical techniques.[25] The number of components is referred to as the rank of the response. The true rank of a response matrix would be equal to the number of chemical components which give rise to analytical signal if all responses were linear and no noise or analyte interactions were present. However, real data contain nonlinearities, noise, and analyte interactions. The true rank is oftentimes not determinable; therefore the term pseudorank is employed. The pseudorank of a matrix is the number of factors which can be used to describe the variance of the matrix to within the limit of the noise of the response. Determination of the pseudorank of a response matrix is frequently a difficult problem when dealing with experimental data. The noise added by incorporation of less significant factors must be weighed against losing potential chemical information if that factor is excluded. The ranks of the pure analyte and mixture responses were determined by examining the singular values resulting from singular value decompositions of the data.

Examination of Pure Analyte Responses. The response of the analytes to the Fujiwara reagent containing 5% tetrabutylammonium hydroxide occurred primarily in the wavelength region of from 340 to 540 nm. Data from higher wavelengths contained no chemical information and were thus truncated. The fractional variance of the first five principal components from the pure analyte response of TCA, TCE, and chloroform is presented for four concentrations of each analyte in Table 1. Selecting rank as the number of PCs with singular values greater than the mean singular value produces a rank 1 response for TCA and rank 2 response for both TCE and chloroform.

Response of Mixtures of Analytes. The analysis of mixtures of analytes poses a difficult problem when a kinetic reaction is the basis of the response. The primary concern is that the response of an analyte in a mixture be the same whether other species are present or not. A change in the rate of reaction induced by the presence of another species will create an interference in the measurement. The extent to which this interference hinders the analysis depends upon the type of calibration method employed as well as the magnitude of the interference. The determination of the analytes described here is further impeded by the formation of a common species, glutaconaldehyde, which absorbs light at a peak maximum of 368 nm. The rate and extent to which this species is formed varies from analyte to analyte. Chloroform generates much

(24) Smilde, A.; Tauler, R.; Henshaw, J. M.; Burgess, L. W.; Kowalski, B. R. *Anal. Chem.*, third paper of three in this issue.
(25) Wold, S. *Technometrics* **1978**, *20*, 397.

Table 1. Fractional Variance of First Five Principal Components from the Mean-Centered Pure Analyte Responses of TCA, TCE, and CHL in 5% TBAH Fujiwara Reagent

	Pure TCA Fractional Variance conc (ppm)			
PC no.	33.45	66.9	133.8	133.8
1	0.938	0.960	0.971	0.974
2	0.017	0.014	0.014	0.011
3	0.009	0.006	0.003	0.002
4	0.006	0.002	0.002	0.001
5	0.002	0.001	0.001	0.001
	Pure TCE Fractional Variance conc (ppm)			
PC no.	2.93	7.32	7.32	29.3
1	0.790	0.799	0.801	0.818
2	0.141	0.152	0.150	0.145
3	0.027	0.028	0.027	0.024
4	0.008	0.004	0.005	0.004
5	0.004	0.003	0.003	0.001
	Pure CHL Fractional Variance conc (ppm)			
PC no.	1.48	4.45	4.45	7.42
1	0.773	0.793	0.811	0.796
2	0.167	0.176	0.155	0.169
3	0.013	0.008	0.012	0.012
4	0.005	0.004	0.004	0.003
5	0.003	0.002	0.002	0.003

more of this species than does TCE, while TCA appears to yield negligible quantities. Under these reaction conditions (5% TBAH), the response of chloroform is primarily in this wavelength region (see Figure 2). If no interaction occurs between analytes, the response of a mixture of analytes to the Fujiwara reagent will be the sum of the responses of the individual analytes. A further discussion on the rank of these mixtures is presented in the second paper.[23]

The condition of bilinearity holds when each analyte yields a unit rank response. However, these data show nonbilinear behavior as multiple visible light-absorbing products are formed from TCE and chloroform yielding a nonunit rank. If the responses due to the analytes were additive, the rank of a mixture of analytes would be equal to the sum of the ranks of the pure analytes comprising the mixture. This is termed rank additivity. The presence of a common species breaks the condition of rank additivity. The response of a mixture would contain the spectrum of this species generated at a rate that would be the geometric mean of the two pure analyte responses for this species. Collinearity also affects rank additivity; if the response due to two different species changes at the same rate, a single factor can be used to describe both species.

The fractional variances of the first five principal components from the response of eight mixtures to 5% TBAH Fujiwara reagent are presented in Table 2. The first two mixtures, containing TCA and TCE with no chloroform, yield a rank of 3. The third component of the remaining mixture samples containing TCA explain ~2% of the total variance. If the condition of rank additivity were to hold, the rank of binary mixtures of TCA and TCE or chloroform should be 3. Additional information can be extracted by adding extra components; however, noise will also be incorporated. The ranks of the two samples containing TCE and chloroform and no TCA clearly do not show rank additivity as the rank of each pure analyte is 2. The formation of a common product from TCE and chloroform, which shows a peak absorbance at 368 nm, contributes to the nonadditive rank of the mixtures. A sample containing all three analytes showed a rank 3 response, which contains a larger percentage of the total variance in the third component than any of the other mixtures.

First-Order Calibration. The first approach was to examine multivariate calibration at each point in time. PLS models were built by using 20 samples at each point in time and evaluated by using leave-one-out cross validation. This technique builds a PLS model with all but one sample and then predicts the missing sample and obtains a prediction error. The missing sample is then returned to the calibration set, another sample withdrawn, and the process repeated until all samples have been excluded once and only once. A root-mean-squared error statistic is then calculated which yields an estimate of how well the data can be modeled. This process was conducted for each individual time slice for each of the three analytes. The root-mean-squared error of cross validation (RMSECV) obtained for two- and three-factor PLS models over time is presented in Figure 4a–c. The concentrations were scaled by dividing each analyte concentration by the maximum for each analyte in order to allow comparison between the errors for each analyte. Therefore the concentrations in the cross-validation modeling ranged from 0 to 1 for each analyte. The RMSECV statistic is thus comparable for each analyte and reflects how the model works for all samples combined.

The much slower reaction rate of TCA versus TCE and chloroform is evident from the time of best prediction for each of the analytes. TCA response exhibits best selectivity at later times, when the reaction of TCE and chloroform is nearly complete. Conversely, selectivity for TCE and chloroform is attained early in the reaction, when TCA does not present an interference. The results for TCA show similar minima for two- or three-factor models, however the three-factor model reached this minimum sooner. There appears to be some improvement in TCE prediction when a three-factor model is used at early times. Both TCE and chloroform two-factor models fail at later times when TCA contributes to the signal.

The number of factors required to model the data at any time was further investigated. Calibration models using two or three factors for TCE and chloroform, and one, two, or three factors for TCA, were built by use of all the analytes at four different times following mixing of analyte with the Fujiwara reagent. These models were then used to predict the concentrations of each analyte in a set of eight different samples. This work differs from the cross-validation modeling discussed above in that the samples have no weight in the calibration and are thus truly unknown. TCE and chloroform calibrations were examined at 5, 10, and 30 min while TCA data were used at 30 and 60 min. Two samples contained chloroform while TCA and TCE were each represented in five samples. The errors of prediction for the eight samples, along with the actual composition, are summarized in Table 3a–c for each model.

Table 2. Fractional Variance Described by the First Five Principal Components from Mixtures of TCA, TCE, and CHL in the Fujiwara Reaction

TCA conc (ppm)	33.5	66.9	133.8	33.5	66.9	0.0	0.0	33.5
TCE conc (ppm)	7.3	2.9	2.9	0.0	0.0	7.3	2.9	2.9
CHL conc (ppm)	0.0	0.0	0.0	4.5	1.5	1.5	4.5	1.5
principal component								
1	0.755	0.765	0.880	0.820	0.753	0.787	0.797	0.732
2	0.185	0.171	0.091	0.131	0.188	0.167	0.167	0.162
3	0.038	0.040	0.017	0.024	0.020	0.020	0.009	0.073
4	0.006	0.004	0.002	0.004	0.013	0.005	0.007	0.008
5	0.002	0.003	0.001	0.003	0.005	0.004	0.003	0.006

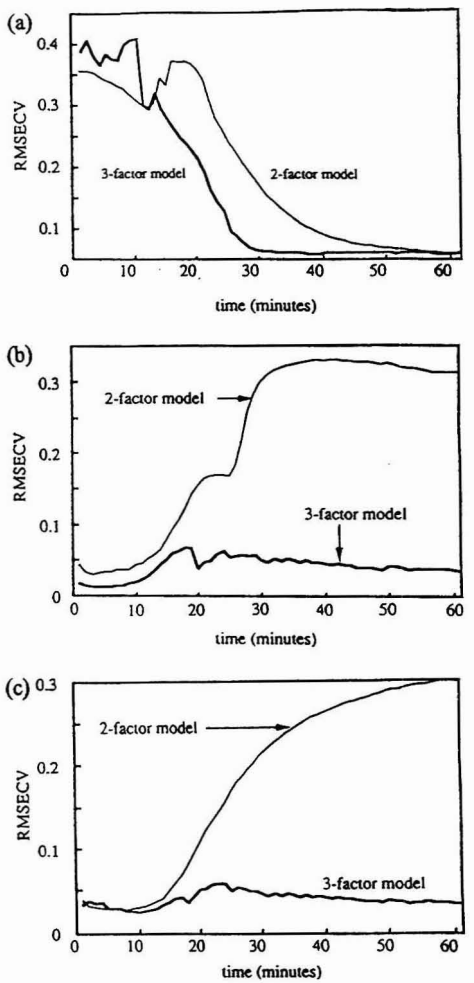

Figure 4. Root-mean-squared error of cross validation for the determination of TCA (a), TCE (b), and chloroform (c) in mixtures of the three analytes using two- and three-factor PLS models at different times.

The results for chloroform at 5 min are best when a two-factor model is used. This is also true at 10 min, with the exception of the sample with the higher chloroform concentration. The results obtained with a two-factor model at 5 and 10 min are comparable. There does appear to be an improvement in prediction at 10 versus 5 min when a three-factor model is used. The samples containing TCE caused an increased error in chloroform prediction when a three-factor model was used, this is especially true of the sample containing the highest concentration of TCE. Although the model predicts in the presence of an interferant, the performance is degraded when an extra factor is employed. The results from the cross-validation work above (Figure 4) showed no difference between two- and three-factor models at early analysis times. Prediction of chloroform at later times benefits from the fact that the reaction is approaching a steady state as the absorbance of the reaction products is changing very little (see Figure 3). However, at 30 min a third factor is required to reduce a false positive signal due to TCA.

The results from the analysis of TCE are generally better when a three-factor model is employed. This is true at all times, agreeing well with the results from cross validation. Prediction is also best at the shortest time, especially for samples containing high concentrations of TCE. This can be attributed to the fast reaction rate of TCE; samples with high concentrations of TCE will yield nonlinear absorbances at later times. As with chloroform, the presence of TCA causes increased error in time but has insignificant effect early in the reaction. The analysis for TCA after 30 min requires three-factors and is subject to much interference from both TCE and chloroform. After 60 min, the effect of these analytes declines and there appears to be no difference between the two- and three-factor models.

Second-Order Calibration: Generalized Rank Annihilation Method (GRAM). GRAM works very well when an analyte yields a bilinear response, i.e., the response matrix can be written as the product of two vectors, one from each domain, scaled by an appropriate singular value. This is the case for TCA. GRAM yields the ratio of the concentration in an unknown sample to the concentration in a single standard. GRAM was applied to data containing TCA alone or in the presence of interferences. GRAM works very well for the prediction of TCA in the presence of no interferences using one factor. Four samples containing only TCA were analyzed in pairs by using GRAM, with one sample acting as the standard and the other the unknown. Six combinations were determined; the samples ranged in concentration from 33.45 to 133.8 ppm. The standard error of prediction of these samples was 4.8 ppm. The mean recovery, as determined by taking the ratio of the predicted concentration to the actual concentration was 105.6% with a standard deviation of 5%.

Table 3. Prediction Errors for the Determination of CHL, TCE, and TCA in Eight Samples Using One to Three Factors after 5–60 min of Reaction Time

a. Determination of CHL

actual conc (ppm)			error in CHL					
			at 5 min		at 10 min		at 30 min	
TCA	TCE	CHL	2 factors	3 factors	2 factors	3 factors	2 factors	3 factors
0	0	4.45	1.1	1.4	1.1	0.81	0.64	0.57
0	29.3	0	0.01	2.0	0.00	1.3	0.145	0.02
0	1.46	0	0.04	0.42	0.06	0.26	0.784	0.2
33.5	2.93	1.48	0.001	0.98	0.00	0.17	0.000	0.005
33.5	7.32	0	0.03	0.07	0.04	0.27	0.309	0.18
66.9	0	0	0.05	0.11	0.06	0.09	0.048	0.060
133.8	0	0	0.05	0.05	0.04	0.01	0.175	0.000
133.8	2.93	0	0.04	0.05	0.03	0.24	0.195	0.001

b. Determination of TCE

actual conc (ppm)			error in TCE					
			at 5 min		at 10 min		at 30 min	
TCA	TCE	CHL	2 factors	3 factors	2 factors	3 factors	2 factors	3 factors
0	0	4.45	0.12	0.04	0.4	0.2	2.7	3.0
0	29.3	0	3.6	1.1	5.8	2.4	37.0	19.1
0	1.46	0	0.002	0.001	0.1	0.1	5.8	0.02
33.5	2.93	1.48	0.02	0.05	0.001	0.1	0.02	0.3
33.5	7.32	0	0.7	0.3	1.2	0.6	9.9	4.1
66.9	0	0	0.0003	0.000	0.001	0.002	0.05	0.007
133.8	0	0	0.009	0.003	0.09	0.07	18.3	0.5
133.8	2.93	0	0.002	0.0001	0.1	0.004	16.8	0.02

c. Determination of TCA

actual conc (ppm)			error in TCA					
			at 30 min			at 60 min		
TCA	TCE	CHL	1 factor	2 factors	3 factors	1 factor	2 factors	3 factors
0	0	4.45	173	292	38.3	87.5	59.0	1.7
0	29.3	0	2.9	3600	14.9	136.2	360	14.5
0	1.46	0	4300	21.7	13.0	4200	12.4	4.4
33.5	2.93	1.48	28.7	47.2	40.6	38.1	8.1	16.1
33.5	7.32	0	320	94.9	0.4	290	4.3	21.6
66.9	0	0	2.0	80.9	0.0	53.2	1.0	13.9
133.8	0	0	4500	730	70.8	3200	0.0	3.2
133.8	2.93	0	5500	420	43.4	4200	53.1	42.0

Theoretically the addition of interferences should not increase the prediction error using GRAM.[19] However, the many sources of variation due to the nature of the data along with the potential analyte interactions decrease the accuracy of the analysis when interferences are added. Samples containing TCA and TCE and/or chloroform were analyzed by use of GRAM. The best results were obtained using three-factor GRAM models. This corresponds to the theoretical rank of binary mixtures of TCA and TCE or chloroform. The actual rank of these mixtures was seen to be 2 or 3, depending upon the level of the noise.

Five mixture samples were analyzed four times each versus pure TCA standards at three different concentrations with one duplicate standard. The results of these analyses are presented in Table 4, which presents the fractional recovery of each sample versus each standard. The prediction of TCA in the mixture samples was biased low for all samples. The recovery of TCA, determined as the ratio of the observed concentration over the actual concentration, also decreased as the ratio of interference to analyte increased. The recovery also decreased as standards of lower concentration were used. This is due to a signal-to-noise problem; the higher concentrations yield better-determined profiles and thus suffer less fit error. Despite the reduction in recovery with concentration, the reproducibility among analyses was good. The standard errors of prediction (SEP) determined from these analyses is also presented in Table 4 along with the actual TCA concentration in each sample. The SEP was between 13 and 23 ppm for all samples.

Table 4. Fraction of Actual Concentration of TCA Determined by Use of GRAM on Mixture Samples Using the TCA Standard Listed in the Left-Hand Column

sample TCA conc (ppm)	133.8	66.9	33.5	66.9	33.5
sample TCE conc (ppm)	2.9	2.9	7.3	0.0	0.0
sample CHL conc (ppm)	0.0	0.0	0.0	1.5	4.5
std TCA conc (ppm)	fraction of TCA recovered				
133.8	0.893	0.680	0.592	0.764	0.634
66.9	0.831	0.637	0.552	0.722	0.596
33.5	0.824	0.644	0.548	0.716	0.592
SEP (ppm)	20.1	22.9	14.5	17.6	13.0

The success of a method for true application not only depends upon the ability to predict the concentration of

Table 5. Concentration of TCA Estimated by Use of GRAM on Samples Containing no TCA[a]

sample	composition: conc (ppm)	composition: analyte	predicted [TCA] (ppm)
c001	CHL	1.48	3.8
c002	CHL	4.45	8.6
c010	TCE	2.93	4.0
c020	TCE	7.32	9.2
c021	TCE	7.32	4.7
	CHL	1.45	
c012	TCE	2.93	2.6
	CHL	4.45	
mean			5.5

[a] Each predicted TCA concentration is the mean of four different determinations.

Table 6. Results from the Analysis of Samples Containing TCA Alone and in Mixtures Reacting with 5% TBAH Using Trilinear Decomposition for Prediction of TCA Concentrations

sample	TCA conc (ppm): actual	TCA conc (ppm): predicted	% recovery
C100	33.5	35	104.5
C200	66.9	68	101.6
C300a	133.8	135	100.9
C300b	133.8	130	97.2
C111	33.5	45	134.5
C102	33.5	40	119.4
C120	33.5	38	113.4
C201	66.9	64	95.7
C210	66.9	60	89.7

analytes present in a sample, but on the ability to predict whether an analyte is absent as well. False positive signals can be costly, especially when dealing with regulatory compliance and remediation of hazardous materials. The qualitative information obtained via PCA assists in determining the composition of a sample. However, direct application of GRAM to data containing no analyte will yield a predicted concentration. Table 5 contains the predicted concentration of TCA in six samples in which TCA is absent. The predicted concentration shown is the prediction error obtained from four samples compared to their actual value of 0 ppm TCA. The actual predicted concentrations were negative in all cases, further illustrating negative bias in the data. GRAM performed reasonably well for this data set, predicting concentrations below the SEP of samples containing TCA. This suggests that the predicted concentrations are not different from zero. Another interesting trend is seen whereby the predicted concentration increases as the interference concentration increases. This suggests that the chemistry does not exhibit the selectivity necessary to avoid the effects of interferences.

The application of GRAM to these data met with limited success. Analysis of TCA can be done in the presence of interferences; however, the recovery was less than desired. It is apparent that some interactions exist among the analytes. The ability to determine these species in mixtures at any level is an improvement over existing methods. Other approaches to GRAM analysis were investigated, including reducing the wavelength and time spaces to minimize interferences, and nonbilinear rank annihilation.[17] Reducing the size of the selective dimensions did not significantly improve the results. The nonbilinear rank annihilation approach helped to characterize which eigenvalues were correct for the multiple rank systems. This approach is to divide the concentration of analyte by some factor and determine which concentration ratios changed correspondingly. This helped only when there was some question as to which eigenvalue was correct; frequently this was obvious from either the recovered spectral and temporal profiles or the absurdity of the incorrect concentration ratios.

Second Order Calibration: Trilinear Decomposition (TLD). TLD was applied to the data collected at 5% TBAH concentration. TLD uses all the samples simultaneously and yields both spectral and temporal estimates for the analytes as well as the ratio of the concentrations in the sample and the mean standard. Best results were obtained when a greater number of factors than rank was used. A five-factor TLD worked best for the analysis of four samples containing TCA only and five mixture samples. If rank additivity was shown to hold, the rank of this data set would be 5 (rank TCA = 1; TCE = 2; chloroform = 2). However, since there is a common species formed from TCE and chloroform, and there is a high degree of overlap between the responses, the greatest rank of a single sample is 3. The results from the analysis of these samples are presented in Table 6. A five-factor TLD model yields five estimates for the concentration in each sample. The predicted concentrations for pure TCA were quite good. The results obtained from the mixtures are much better for TLD than GRAM. This is probably due to the use of multiple standards and samples together. The TLD results for samples containing high levels of interference yielded much higher estimates than did the samples containing less interferences. This suggests that the selectivity of this method is not sufficient to completely eliminate interferences and/or that sample interaction effects degrade the analysis.

Selection of the correct concentration estimates from TLD requires examining the estimated spectral and temporal profiles to determine which corresponds to the analyte of interest. This was done in a qualitative fashion, visually, and gave the estimates which also yielded the best predictions. Optimization of the TLD program will require addition of algorithms designed to automatically select the correct estimates as frequently the shapes of the profiles are similar. The qualitative information generated by TLD can help to mitigate the problem of a non-fully-selective method. This chemistry contains many pratfalls to this type of analysis, including nonbilinear and highly overlapped responses, several sources of experimental error, and an apparent interaction between analytes. Despite these negative aspects, the multivariate techniques described here show some level of success at determining analytes in the presence of unknown interferences.

CONCLUSIONS

The application of multivariate calibration methods to Fujiwara reaction-based data enables multicomponent determination of chlorinated hydrocarbons from a single analysis. PLS was demonstrated as a first-order calibration technique that can be applied at optimal reaction times for each of the analytes. However, when species are present that produce an absorbance that is unaccounted for in the PLS model, the

results are diminished considerably. Second-order calibration techniques were applied to the data matrices collected as analyte reacted in time. Both GRAM and TLD were applied, with TLD yielding better results than GRAM for the determination of TCA in the presence of unaccounted for interferences. Neither second-order method fully recovered the analyte concentrations due to changes in the reaction profile of TCA in the presence of interferences.

ACKNOWLEDGMENT

The Center for Process Analytical Chemistry (CPAC) is a National Science Foundation Industry/University Cooperative Research Center at the University of Washington.

Received for review March 15, 1994. Accepted June 30, 1994.[•]

[•] Abstract published in *Advance ACS Abstracts,* August 15, 1994.

Anal. Chem. **1994,** *66,* 3337–3344

Multicomponent Determination of Chlorinated Hydrocarbons Using a Reaction-Based Chemical Sensor. 2. Chemical Speciation Using Multivariate Curve Resolution

R. Tauler,[†] A. K. Smilde,[‡] J. M. Henshaw,[§] L. W. Burgess, and B. R. Kowalski*

Center for Process Analytical Chemistry, University of Washington, BG-10, Seattle, Washington 98195

A new multivariate curve resolution method that can extract analytical information from UV/visible spectroscopic data collected from a reaction-based chemical sensor is proposed. The method is demonstrated with the determination of mixtures of chlorinated hydrocarbons by estimating the kinetic and spectral profiles of the chemical species formed in the Fujiwara reaction. The three key aspects of the proposed method are (1) the initial estimation of the kinetic concentration profiles from evolving factor analysis; (2) the implementation of an alternating and constrained least squares method to optimize the determination of both the spectral and concentration profiles of the species present in the reaction, and (3) the development of a quantitative approach based on the simultaneous analysis of standards and unknowns for the determination of the initial concentration of the analytes in the mixtures.

Multivariate curve resolution has seen little application to the study of kinetic reactions despite its potential for the interpretation of the mechanisms of such reactions and their application in analytical chemistry.[1] The description and modeling of the evolution of a time-dependent chemical reaction is important for both theoretical and practical analytical reasons. Most of the kinetic-based analytical methods in the literature are of an univariate nature, i.e., only make use of one channel or wavelength in the analysis.[2,3] Even when multicomponent analysis is performed with these methods, the distinction between analytes (selectivity) is accomplished from univariate measurements based on the differences between rate constants and not on their global different spectroscopic responses. The methods described in the literature[4] that use a full-spectrum approach are chemical model-based methods (hard model approach), which means that the model has to be precisely determined and the parameters of that model estimated at the same time that the analytical information is obtained. The large number of parameters to estimate increases the possibility of uncertainties and artifacts in the numerical treatment.

In contrast to this situation, self-modeling curve resolution methods do not rely on the initial proposal of a specific kinetic model and do estimate directly the changes in concentration and unit responses of the species formed in the kinetic reaction without any previous assumptions. It is possible to determine what kind of kinetic model the reaction follows and the best approach to use that kinetic reaction for analytical purposes from the changes in concentration of the different species during the kinetic reaction.

Curve resolution decomposes a bilinear data matrix into the product of two simpler matrices which are related respectively to each one of the two orders (e.g., spectral and temporal) of the original data matrix. The goal of the curve resolution methods is the determination of those decompositions which have physical and chemical meaning.[5,6] The experiment involves periodically acquiring spectra during the progress of a chemical reaction. The spectra are placed in a matrix which is, hopefully, decomposed to yield one matrix containing the pure spectra of the individual reacting components and another containing concentration profiles as a function of time. Obtaining meaningful solutions from curve resolution decompositions requires some assumptions about the data such as nonnegative spectral intensities or closure.

However, in general, such treatments do not guarantee unique solutions because the rotational and intensity ambiguities inherent to factor analysis decompositions can still be present after applying the above-mentioned constraints.[7,8] As shown in the present work, these ambiguities can be partly overcome with the use of some special techniques. One of the most interesting which has not received much attention in kinetic analysis is evolving factor analysis (EFA).[9,10] EFA provides valuable information concerning the windows of existence and relative importance of the species formed in the unknown mixtures at any time during the kinetic reaction. When evolving factor analysis is applied to cases where selectivity for some component is present in any of the two orders, the determination of the concentration profile and spectroscopic response of such a component can be estimated at least qualitatively without any other additional requirement.

In addition, if different kinetic determinations are performed over different samples with different concentrations

[†] Present address: Department of Analytical Chemistry, University of Barcelona, Diagonal 647, Barcelona 08028, Spain.

[‡] Present address: Laboratory for Analytical Sciences, University of Amsterdam, Nieuwe Achtergracht 166, 1018 WV Amsterdam, The Netherlands.

[§] Present address: ORS Environmental Systems, 7 Barnabas Rd., Marion, MA 02738.

(1) Mottola, H. A.; Perez-Bendito, D. *Anal. Chem.* **1992,** *64,* 407R–428R
(2) Mottola, H. A.; *Kinteic Aspects of Analytical Chemistry,* John Wiley: New York, 1988.
(3) Perez-Bendito, D.; Silva, M. *Kinetic methods in Analytical Chemistry,* John Wiley: New York, 1988.
(4) Pardue, H. L. *Anal. Chim. Acta* **1989,** *216,* 69–107.
(5) Hamilton, J. C.; Gemperline. P. J. *J. Chemom.* **1990,** *4,* 1–14.
(6) Windig, W. *Chemom. Intell. Lab. Syst.* **1992,** *16,* 1–16.
(7) Lawton, W. H.; Sylvestre, E. A. *Technometrics* **1971,** *13,* 617–632.
(8) Borgen, O. S.; Kowalski, B. R. *Anal. Chim. Acta* **1985,** *174,* 1–26.
(9) Gampp, H.; Maeder, M.; Meyer, Ch.; Zuberbuhler, A. D. *Talanta* **1985,** *32,* 1133–1139.
(10) Gampp, H.; Maeder, M.; Meyer, Ch.; Zuberbuhler, A. D. *Talanta* **1986,** *33,* 943–951.

0003-2700/94/0366-3337$04.50/0
© 1994 American Chemical Society

of the analytes and at least one of the two orders is common between them (e.g., the same wavelength channels in the different spectra), the intensity ambiguities associated with the analysis of a single kinetic determination can be resolved.[11,12] Assuming that the same species in the different experiment has the same unit spectrum, the simultaneous analysis of the different experiments will give the relative amounts of the common species in the different mixtures analyzed. From these relative amounts, it is possible to estimate the initial concentration of the analytes in the samples if a set of standards is provided in the analysis. In the third paper of the present series,[13] a different approach is described that takes advantage of the full second order structure of the data[14,15] and makes possible the quantitation of the analytes in the presence of unknown and unmodeled interferents.

Multivariate reaction-based chemical sensors couple a selective chemical reaction with a multivariate analysis technique such as those based on spectroscopy. In the previous paper of this series[16] the Fujiwara reaction-based chemical sensor for the determination of mixtures of organohalides has been described.

In the Fujiwara reaction, halogenated hydrocarbons react with pyridine in basic medium giving different species, some of them characteristic of each analyte, and others common or very similar for different analytes.[17,18] The three analytes studied are 1,1,1-trichloroethane (TCA), trichloroethylene (TCE) and chloroform. Although the analytes themselves do not absorb in the spectral region under study, the product species of the Fujiwara reaction with these three analytes can be monitored using UV/visible spectroscopy.

However, the reaction is not selective for similar organohalides, and a considerable level of overlap and correlation is present in the two order responses of the different analytes, rendering traditional calibration unable to optimally analyze unknown mixtures of the analytes. In the present work, a recently developed multivariate curve resolution method[11,12] is used to determine the time-dependent concentration profiles and unit spectral responses of the species formed in the Fujiwara reaction. Resolving the pure species' spectral and temporal profiles enables the study of the reaction kinetics and the development of a method for the quantitation of the analytes in the mixtures.

EXPERIMENTAL SECTION

The experimental data used to illustrate the proposed multivariate curve resolution method was obtained using the experimental setup described in the Experimental Section of the first paper of the present series.[16] The selected experiments were those where the kinetic reaction was monitored in a thermostated spectrophotometric cuvette. The reagents and analytes were manually mixed, and the spectra were acquired at evenly spaced times using a diode array spectrophotometer and stored in the computer. The temperature was held constant at 20 °C.

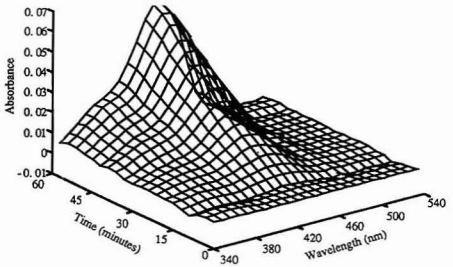

Figure 1. TCA (66.9 ppm) response in the Fujiwara reaction. Absorption increases during the reaction.

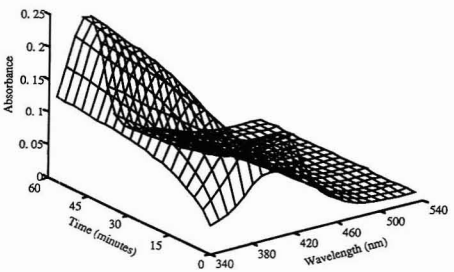

Figure 2. TCE (7.31 ppm.) absorption response in the Fujiwara reaction. Absortion increases and shifts to shorter wavelengths during the reaction.

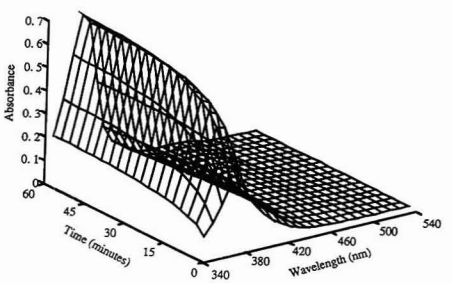

Figure 3. $CHCl_3$ (4.45 ppm) absorption response in the Fujiwara reaction. Absorption increases and shifts to shorter wavelengths during the reaction.

In Figures 1–3, examples of the spectra acquired during the analysis of the pure analytes 1,1,1-trichloroethane (TCA), trichloroethylene (TCE), and chloroform ($CHCl_3$) are respectively given. TCA shows a continuous growth of the same profile during the time of the experiment. TCE and $CHCl_3$ spectral profiles changed considerably in the first part of the experiment, suggesting that more than one chemical species is present in both systems. Observe also the presence of an isobestic point in the case of TCE. In Figure 4, an example of the spectra acquired in the analysis of a mixture of the three analytes is also given. In this figure, the contribution of TCA is at the higher wavelengths, whereas TCE and $CHCl_3$ are overlapped in the lower wavelength region.

(11) Tauler, R.; Izquierdo-Ridorsa, A.; Casassas, E. *Chemom. Intell. Lab. Syst.* **1993**, *18*, 293–300.
(12) Tauler, R.; Fleming, S.; Kowalski, B. R. *Anal. Chem.* **1993**, *65*, 2040–2047.
(13) Smilde, A. K.; Tauler, R.; Henshaw, J. M.; Burgess, L. W.; Kowalski, B. R. *Anal. Chem.*, third paper of the three in this issue.
(14) Sanchez, E.; Kowalski, B. R. *J. Chemometrics* **1988**, *2*, 265–280.
(15) Smilde, A. K. *Chemom. Intell. Lab. Syst.* **1992**, *15*, 143–157.
(16) Henshaw, J. M.; Burgess, L. W.; Booksh, K. S.; Kowalski, B. R. *Anal. Chem.* first paper of the three in this issue.
(17) Lugg, G. A. *Anal.Chem.* **1966**, *38*, 1532–1536.
(18) Reith, J. F.; van Ditmarsch, W. C.; de Ruiter, Th. *Analyst*, **1974**, *99*, 652–656.

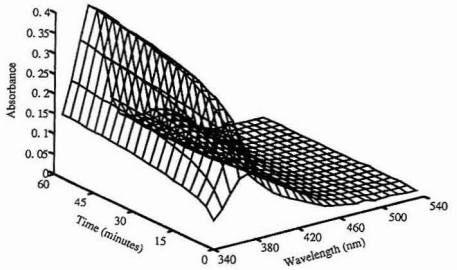

Figure 4. Absorption response of the mixture of TCA (66.9 ppm), TCE (2.93 ppm) and $CHCl_3$ (1.48 ppm).

In the following, it will be assumed that a plurality of spectra have been acquired during the analysis of each sample at evenly spaced time intervals until the kinetic reaction has reached a determined level. The spectral intensities are stored in a matrix **D** with one spectrum per row. The dimensions of **D** are the number of spectra acquired at different points in time during the reaction by the number of spectral channels (e.g., wavelengths). Each analyzed sample is characterized by a data matrix. The goals of the study are to determine the number of chemical species formed during the reaction, their pure spectra and concentration/time profiles, and the quantitation of the amount of analyte initially present in the sample. The term analyte will be used for the chemical compounds TCA, TCE, and chloroform to be determined in the analysis. The concentration of the analytes refers then to the initial concentration of these three compounds in the original samples before the reaction takes place. During the reaction, these analytes are consumed and new chemical species are formed. The term species refers to the actual different chemical species present at any time during the reaction. Not all species formed in the reaction can be detected spectroscopically; in particular, the species corresponding to the analytes themselves are not detected in the spectral range under study, and only some of the products of the reaction are detected. The total number of species in the system will be at least equal to or higher than the total number of analytes.

THEORY

Linear model. The linear model proposed is based on three fundamental assumptions which are validated during the analysis of the data. The eventual confirmation of such a model and of the underlying assumptions is derived from the final results obtained using the proposed multivariate curve resolution method.

Generalized Lambert–Beer's Law. The first important assumption relies on the matrix generalization of Beer's law. The spectroscopic data matrices obtained in the kinetic experiments are bilinear, such that

$$\mathbf{D} = \mathbf{CB} \tag{1}$$

$$d_{IJ} = \sum c_{IN} b_{NJ} \tag{2}$$

where **D** is the data matrix which contains the spectra acquired at fixed time intervals during the reaction. **C** and **B** are respectively the matrices of the concentration profiles and of the unit pure spectra for the spectroscopically active chemical species involved in the reaction. The dimensions of these matrices are $\mathbf{D}(I \times J)$, $\mathbf{C}(I \times N)$ and $\mathbf{B}(N \times J)$, where I is the number of spectra analyzed, J is the number of spectroscopic channels, and N is the number of chemical species in the mixtures. The goal of curve resolution methods is to obtain the actual **C** and **B** matrices from **D**.

Rank Analysis and Complexity of the Systems under Study. The second assumption is that the formation of the different chemical species in the pure analyte samples and in the mixture samples depends only on the initial concentration of the analyte. In addition, there must be no new species and no new interaction between the analytes, and consequently between the species, in the mixtures. To check these assumptions, the rank (pseudorank) of the data matrices obtained in the analysis of the pure analyte samples and of the data matrices obtained in the analysis of mixture analyte samples are calculated and compared in the following way:

(i) The rank of the pure analyte data matrices gives the number of spectroscopically active species given by that analyte in the kinetic reaction. As was mentioned before, the analytes do not absorb in the spectral range under study and will not contribute to the rank of the corresponding spectral data matrices. However, the rank associated with the global response of the analytes (TCA, TCE, $CHCl_3$) can be greater than 1, since they can produce more than one species in the chemical reaction.

(ii) The rank of the data matrices containing more than one analyte must be equal to or less (when some species are in common) than the sum of the ranks associated with the pure analyte responses present in the particular mixture, which is equal to the total number of spectroscopically active species identified in the analysis of the corresponding pure analyte samples.

(iii) The rank of the augmented data matrices formed by stacking the sample data matrices columnwise or rowwise (Figure 5) must be equal to or less than the total number of species identified in the analysis of the individual data matrices used to build the augmented data matrix.

When these three conditions are met, the pure spectral and kinetic concentration profile for every species in the different experiments is equal and allows the application of second-order methods.[13]

Kinetic Model. The kinetic experiments are assumed to be carried out under reproducible conditions. This assumption means that the concentration of the different species formed during the reaction of the analytes is always linearly related to the initial concentration of the analyte or parent molecule. For this assumption to be true, kinetic conditions of pseudofirst order hold.

The following kinetic model is proposed as the basis of the work. For TCA, the analyte gives irreversibly (because of the large excess of the other reagents) a single detectable product in the reaction (see below)

$$\mathrm{TCA} + \mathrm{py} + \mathrm{OH^-} \rightarrow \mathrm{P_1} \tag{3}$$

TCA is the analyte and P_1 is the product; py is the pyridine

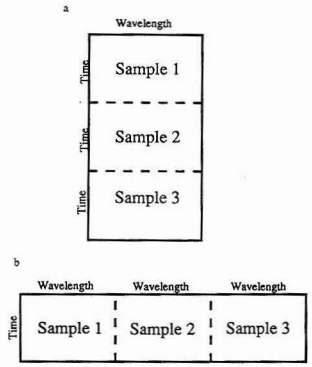

Figure 5. (a) Augmented data matrix formed by stacking columnwise (wavelength) three sample data matrices; (b) augmented data matrix formed by stacking rowwise (time) three sample data matrices.

reagent and OH^- is the base. Under excess concentration of pyridine and base, the reaction is of pseudofirst order. The concentration of TCA and of the product P_1 at any point in time during the reaction is directly proportional to the initial concentration of TCA. As the only species spectroscopically active in the wavelength region under study is the product P_1, measuring its concentration allows the determination of the initial concentration of TCA when compared to a calibration standard.

For TCE and $CHCl_3$, the situation is more complex because they give two products in a two-step reaction. In excess pyridine and base, the situation can be described as coupled first-order irreversible reactions

$$TCE + py + OH^- \rightarrow P_2 \rightarrow Q_1 \quad (4)$$

$$CHCl_3 + py + OH^- \rightarrow P_3 \rightarrow Q_2 \quad (5)$$

Solving the kinetic differential equations for the intermediate or transient products P_2 or P_3 gives the relation between the rate of change in concentration of them and the initial concentration of analyte, which is also linear[2,19,20] if the conditions of pseudofirst order prevail in the two stages of the reaction. The concentrations of the intermediate product and of the final product, species P, are linearly related to the initial concentration of the analyte. Since in the wavelength region under study, the only species which are spectroscopically active (see Experimental Section) are the intermediates and products of the reaction, monitoring the spectral changes will give the concentration changes of these species and provide the initial concentration of the analytes.

Multivariate Curve Resolution. Introduction. Data analysis can be carried out over one sample (one data matrix) or over different samples (several data matrices) simultaneously. Suppose there are K different samples at different initial conditions or starting concentrations of the analytes. In the analysis of each sample a data matrix $\mathbf{D_k}$ is obtained:

$$\mathbf{D_k} = \mathbf{C_k B}, \quad k = 1, 2, ..., K \quad (6)$$

$\mathbf{C_k}$ is the matrix of the time/concentration profiles of the chemical species spectroscopically active formed during the analysis of sample k, and $\mathbf{B}$ is the matrix of the unit or pure spectra of these species. As the number of columns (wavelengths) is the same for all the $\mathbf{D_k}$ matrices, the analysis can be performed simultaneously over more than one data matrix, as follows:

$$\mathbf{D} = \begin{bmatrix} \mathbf{D_1} \\ \mathbf{D_2} \\ \dots \\ \dots \\ \mathbf{D_K} \end{bmatrix} = \begin{bmatrix} \mathbf{C_1} \\ \mathbf{C_2} \\ \dots \\ \dots \\ \mathbf{C_K} \end{bmatrix} \mathbf{B} = \mathbf{CB} \quad (6)$$

The new augmented data matrix $\mathbf{D}$ is obtained by setting each of the sample data matrices $\mathbf{D_k}$ to be analyzed on top of the others, with the columns (wavelengths) in common and with a number of rows equal to the total number of acquired experimental spectra in the different sample analyses. In the case of the analysis of only one data matrix, this equation reduces to the usual case of the generalized Beer's law shown before. In the case of simultaneous analysis of different samples, the new augmented data matrix will be the product of an augmented concentration matrix times the unit spectra matrix. The augmented concentration matrix will contain the different submatrices $\mathbf{C_k}$ corresponding to the concentration of the species present in each of the data matrices $\mathbf{D_k}$ analyzed.

Selectivity and Evolving Factor Analysis. It is extremely important in multivariate curve resolution to detect and use the selective information present in the data to remove the rotational ambiguity. Evolving factor analysis[9,10] has been applied mostly to the study of spectroscopic experiments of multiequilibria systems[21,22,23] and to liquid chromatography with diode array detection.[24,25] The basic idea of this procedure is to provide an initial estimation of the concentration profiles by examining how the singular values evolve and change in magnitude the experiment (kinetic reaction in this case). From the results of evolving factor analysis, the selective regions in the data are usually detected, and the rotational ambiguities eventually solved.

Other similar methods have been proposed to detect and use the selectivity of the system such as local rank analysis,[26] window factor analysis,[27] fixed-size moving window evolving factor analysis,[28] the pure variable self-modeling mixture analysis method,[29] and the HELP method.[30] In the case of kinetic reaction-based data, it is better to take advantage of the intrinsic order in the time domain as in evolving factor analysis.

(19) Hughes, E. *J. Chem. Educ.* **1989**, *66*, 46.
(20) Schechter, I. *Anal. Chem.* **1991**, *63*, 1303–1307.
(21) Tauler, R.; Casassas, E. *J.Chemom.* **1988**, *3*, 151–161.
(22) Tauler, R.; Casassas, E. *Anal. Chim. Acta* **1989**, *223*, 257–268.
(23) Tauler, R.; Casassas, E.; Izquierdo-Ridorsa, A. *Anal. Chim. Acta* **1991**, *248*, 447–458.
(24) Maeder, M. *Anal. Chem.* **1987**, *59*, 527–530.
(25) Tauler, R.; Durand, G.; Barcelo, D. *Chromatographia* **1992**, *33*, 244–254.
(26) Geladi, P.; Wold, S. *Chemom. Intell. Lab. Syst.* **1987**, *2*, 273–281.
(27) Malinowski, E. R. *J. Chemometrics* **1992**, *6*, 29–40.
(28) Keller, H. R.; Massart, D. L. *Anal. Chim. Acta* **1991**, *246*, 379–390.
(29) Windig, W.; Stephenson, D. A. *Anal. Chem.* **1992**, *64*, 2735.
(30) Kvalheim, O. M.; Liang, Y.-z. *Anal. Chem.* **1992**, *64*, 936–946, 946–956.

Constrained Alternating Least-Squares Optimization of the Concentration Profiles and Unit Spectra. Analysis of a Single Kinetic Experiment. From the results of evolving factor analysis, the windows or range of existence of each species and its concentration profile can be obtained. These concentration profiles are used as initial values in a constrained alternating least-squares optimization procedure. At each iteration of the optimization a new estimation of the matrix of spectra **B** and of the concentration profiles **C** is obtained successively using the two following equations:

$$\mathbf{B} = \mathbf{C}^{+}\mathbf{D}^{*} \tag{7}$$

$$\mathbf{C} = \mathbf{D}^{*}\mathbf{B}^{+} \tag{8}$$

where the matrix $\mathbf{C}^{+}$ is the pseudoinverse of the matrix **C** and the matrix $\mathbf{B}^{+}$ is the pseudoinverse of the matrix **B**. Obviously, the selection of the right number of components in the calculation of $\mathbf{D}^{*}$ is essential. The use of this matrix instead of the experimental data matrix **D** will provide more stability in the calculations, since $\mathbf{D}^{*}$ is noise-filtered for the particular number of principal components.

In order to limit the number of possible solutions to these equations, the unit spectra are constrained to be nonnegative and the time/concentration profiles are constrained to be nonnegative[5-11,21-23,25] and of unimodal shape.[11,21-23,24,31] However, as was mentioned before, the solutions obtained from the analysis of a single sample data matrix are still ambiguous in their scale/intensity dimensions, and quantitation is not possible from them.

Simultaneous Analysis of Multiple Samples (Calibration and Unknowns). As a first step in the curve resolution method, the augmented matrix of the concentration profiles **C** is built up from the initial estimation of the $\mathbf{C}_1, \mathbf{C}_2, \ldots, \mathbf{C}_K$ submatrices obtained by evolving factor analysis of the $\mathbf{D}_1, \mathbf{D}_2, \ldots, \mathbf{D}_K$ submatrices, as described before. An initial estimation of the augmented **C** data matrix is then obtained simply by setting the estimation of the $\mathbf{C}_i$ matrices on top of each other in the same order as they are in **D**. The question about the presence or absence of a certain species in an experiment can be solved by looking at the pseudorank of the individual data matrices $\mathbf{C}_i$ and also by looking at the results of the individual alternating least-squares optimization. If the species spectra of two resolved species in different experiments are similar (fingerprint matching), then probably they correspond to the same species and so they will be postulated in the simultaneous analysis (common columns in matrix **C** and common rows in matrix **B**). Conversely, species with different spectra in different kinetic experiments correspond to different species in the simultaneous analysis. At each iteration of the alternating least-squares method a new estimation of the matrix of spectra **B** and of the concentration profiles **C** are obtained. The same procedure as before is used except now it is applied to the augmented matrix obtained by principal component analysis for the number of components $\mathbf{D}^{*}$. In addition to the constraints present in the single data matrix analysis, in the simultaneous analysis of multiple data matrices, there are two more constraints to apply:

(i) common species have the same spectrum in all the kinetic experiments[11,12]

(ii) common species have concentration profiles with equal shape in all the kinetic experiments:

Let $\mathbf{C}^{n}$ the n^{th} column of the augmented matrix **C** contain the current estimation of the concentration profiles of species n in the different K samples analyzed. This column can be folded in a matrix $\mathbf{C}'(I,K)$, where I is the number of spectra acquired in the analysis of every sample (synchronization is assumed between experiments). Under the assumption of equal shape, this matrix can be decomposed as the product of two vectors:

$$\mathbf{C}' = \mathbf{u}'^{*}\mathbf{t}^{\mathrm{T}} \tag{9}$$

where $\mathbf{u}'(I)$ is the unit concentration profile containing the common shape information of $\mathbf{C}'$, and $\mathbf{t}^{\mathrm{T}}(K)$ contains the relative amounts of this unit profile in $\mathbf{C}'$. The unit profile $\mathbf{u}'$ is equal to the first score vector of $\mathbf{C}'$ and the relative analyte concentrations **t** are obtained from the first loading of $\mathbf{C}'$ scaled by its first singular value.

This method assumes that the concentration profiles of the same species have the same shape in the different experiments and consequently that the matrix $\mathbf{C}'$ is rank one and **E** is at the level of the experimental error. An easy way to test this assumption during the analysis is to compare the magnitude of the next singular values with the first singular value.

(iii) Zero concentration components: when a species is known not to be present in the specific kinetic experiment, then the concentration of such species in **C** is forced to be equal to zero.

It is important to note that the use of the three described constraints leads to the second-order advantage[14,15] and the solutions obtained with the proposed method are very close to those obtained by using the second-order resolution methods.[13]

Testing the Number of Chemical Species. If the number of species is uncertain, the complete iterative alternating least-squares optimization is performed for the most plausible number of components. At the end, it is considered that the right number is the one which gives a best fit to the experimental data matrix **D** (not to $\mathbf{D}^{*}$) and physically meaningful solutions. This means that only those solutions with reasonable shapes for the unit spectra and concentration profiles are considered. The alternating least-squares procedure is repeated until convergence is achieved or until a predetermined number of cycles has occurred.

Quantitation of the Analytes. Once the concentration profiles have been determined using the proposed multivariate curve resolution method, the initial concentration of the analytes can be estimated. If the conditions previously described for linearity hold, the concentrations of the species formed at any point of the reaction are linearly related with the initial concentration of the analytes. Different methods of quantitation are tested and validated in the present work. The area under the concentration profile of a certain species (which can be determined from the sum of the concentration values of this species at the different measured times) will be then proportional to the initial concentration of the analyte which produced that species in the reaction.

(i) The simpler method of quantitation consists first of estimating the pure spectra of the different species from the

analysis of known pure analyte samples. Once they are determined, the concentration of the species present in any mixture of the analytes can be determined by least squares analysis from

$$\mathbf{C}_{unk} = \mathbf{D}_{unk}\mathbf{B}^{+} \qquad (10)$$

where $\mathbf{B}^{+}$ is the pseudoinverse of the unit spectra matrix $\mathbf{B}$ obtained in the analysis of the pure analyte samples, $\mathbf{D}_{unk}$ is the matrix of a new unknown sample, and $\mathbf{C}_{unk}$ is the matrix of the unknown kinetic concentration profiles.

The initial concentrations of the analytes in $\mathbf{D}_{unk}$ can then be determined from the ratio of the areas under the concentration profiles of the species in the unknowns compared with the areas under the concentration profiles of the corresponding species in the standards.

(ii) If several samples are analyzed simultaneously with the proposed procedure, the ratio between the areas of the concentration profiles for a particular species in the different samples will give the ratio between the initial concentrations of the analyte which produce this species in the reaction. If some of the samples are standards of known analyte concentration, the concentration of the analytes in unknown samples can be determined.

This method of quantitation is improved if the constraint of equal shape over the concentration profiles is applied. Under complete reproducible pseudo-first-order conditions, the intensity of the concentration profiles of the different species in the different experiments will only depend upon the initial concentration of the analyte. The relative amounts of the analytes in the different samples are directly recovered from the simultaneous constrained alternating least-squares optimization previously described.

RESULTS AND DISCUSSION

Rank Analysis. Results of rank analysis confirm that TCA only gives one spectroscopically active species, whereas TCE and $CHCl_3$ give two spectroscopically active species. From the analysis of the pure analyte data matrices, a maximum number of five different species is detected. The rank of the augmented data matrices formed by several samples of the same analyte at different concentrations is equal to the rank of any of the single pure analyte data matrices, regardless of the order used to form the augmented matrix, the wavelength variables, or the time variables.

The pseudorank of the mixture analyte data matrices is equal to or less than the sum of the pseudoranks of the pure analyte data matrices. The rank of the augmented data matrices is also equal to or less than the sum of the ranks of the data matrices present in the augmented matrix. These results are in agreement with the initial hypothesis that the same species are formed in the mixtures and in the pure analyte samples (no new species are formed in the mixtures) and that the kinetic behavior of the different analytes is independent of the presence of the other analytes. No new interactions appear in the analysis of the mixtures. The assumption of equal shape in the time profiles for the different species is then also confirmed in the rank analysis of the augmented data matrices.

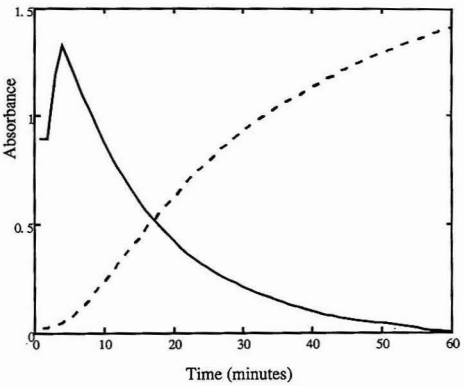

Figure 6. Concentration profiles of the two species obtained in the reaction of TCE initially estimated by evolving factor analysis (species 2, —; species 3, - - -).

Selectivity and Initial Estimates Using EFA. Evolving factor analysis of the different spectral data matrices provides the starting values for the concentration matrix in the alternating least-squares optimization. In Figure 6, the evolving factor analysis plot [9,10] of a pure TCE data matrix is shown for example. From this plot, an initial estimation of how the concentration of the two species change during the TCE reaction is obtained. Some selectivity for the two species given by TCE exists at the beginning and at the end of the reaction. Analogous observations can be made for $CHCl_3$, although here the selectivity is lower. For TCA, only one spectroscopically active species is present and there is no rotational ambiguity in the curve resolution analysis for this analyte.

Identification of the Species from the Pure Analyte Sample Analysis. Figure 7 shows the resolved pure unit spectra of the species formed in the analysis of the pure analyte samples using the multivariate curve resolution method previously described. Several samples at different concentrations of the same analyte were analyzed simultaneously with the outlined procedure. High overlap is observed for the species spectra of TCE and $CHCl_3$. Species 3 (TCE) and species 5 ($CHCl_3$) have unit spectra with similar shape and could correspond to the same chemical species. The spectra of these two species are also close to the spectrum obtained by the degradation of pyridine at high base concentrations, in agreement with the mechanisms proposed for the Fujiwara reaction in the literature.[17,18] Species 3 and 5 gave concentration profiles with a different slope, showing that TCE and $CHCl_3$ react with pyridine at different rates. The only significant differences between TCE and $CHCl_3$ are in the spectra of the intermediates, species 2 and 4, respectively, indicating a possible way to differentiate and quantitate them in the mixtures containing both. TCA gives species 1 with a unique spectrum (around 480 nm) and a different time/concentration profile (slower reaction). Therefore quantitation of TCA in the mixtures is simpler. In part 3 of the present series,[13] a better treatment is proposed to measure the similarities between the time profiles and unit spectra of the different

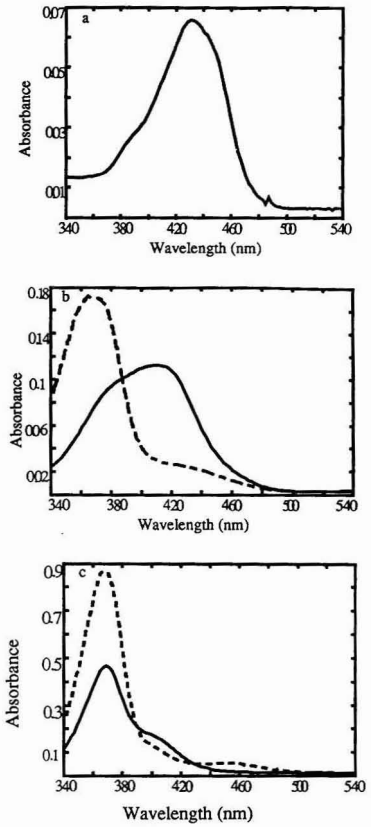

Figure 7. Unit spectra for the five detected species in the analysis of the pure analyte samples: (a) species 1 from TCA; (b) species 2 (—) and 3 (- - -) from TCE; (c) species 4 (—) and 5 (- - -) from $CHCl_3$.

species present in the system, as well as a global measurement of the similarities between the different analytes.

Quantitation of the Analytes Using the Pure Species Spectra. The results obtained in the analysis of the pure analyte samples confirm the initial assumptions made about the linear model for any of the species identified. Once the pure species spectra have been estimated from the pure analyte samples, quantitation in new samples is possible. Table 1 shows the results obtained by this procedure. For the quantitation of the pure analyte samples, the results are rather good, taking into account the experimental limitations[16] and that only one sample is taken as standard. The quantitation is not only possible in relative terms but also in absolute terms if the concentration of the analytes in some of the samples are known (standards). Quantitation using the pure species spectra is also done over four samples containing mixtures of the analytes. The results obtained are given in Table 1. The errors in prediction, although higher than in the analysis of pure analyte samples, are still reasonable when the high overlap between the TCE and $CHCl_3$ spectral and concentration profiles is considered.

Table 1. Results of Quantitation[a] Using the Pure Spectra

sample[b]	concn[3]	species[d]	area[e]	pred concn[f]	% error[g]
TCA	66.9	1	22.32	std	
TCA	133	1	45.98	138	3.6
TCA	267	1	100.5	301	13
TCA	267	1	87.29	262	2.0
TCE	7.31	2	22.43	7.43	1.6
		3	56.87	7.43	1.6
TCE	7.31	2	22.07	std	
		3	55.96		
TCE	29.3	2	75.89	24.7	15
		3	207.1	24.0	7.7
TCE	58.6	2	182.0	60.3	2.9
		3	451.5	59.0	0.6
TCE	1.46	2	3.340	1.11	24
		3	11.09	1.45	0.8
$CHCl_3$	1.48	4	7.150	1.48	0.1
		5	11.09	1.50	1.1
$CHCl_3$	4.45	4	21.53	std	
		5	32.98		
$CHCl_3$	7.42	4	41.80	8.65	16.6
		5	52.57	7.09	4.4
TCA	66.9	1	22.62	67.5	1.0
TCE	2.93	2	9.770	3.23	10
		3	20.63	2.69	8.0
$CHCl_3$	1.48	4	9.090	1.88	29
		5	14.35	1.94	31
TCE	2.93	2	11.57	3.83	31
		3	20.28	2.65	9.5
$CHCl_3$	1.48	4	22.42	4.63	4.0
		5	32.76	4.42	0.7
TCE	7.30	2	19.83	6.57	10
		3	47.44	6.19	15
$CHCl_3$	1.48	4	9.110	1.88	27
		5	13.13	1.77	19

[a] Results of the analysis of 15 samples using the pure species spectra. [b] Content of analyzed samples. [c] Concentration in ppm. [d] The species used for analyte quantitation (see Figure 7 for species identification). [e] Area under concentration profile (arbitary units). [f] Estimated concentration of the analyte. [g] Percent error in the prediction.

The use of the pure species spectra for the quantitation of the analyte in the samples is a full-model approach; this means that all the data variance is explained by the given species spectra. This approach fails in the presence of unknown overlapping interferences because then the estimated concentrations of the analytes will be in error.

Quantitation by Simultaneous Analysis of Standards and Unknowns. A different way to perform the quantitation using multivariate curve resolution is by the simultaneous analysis of a set of standard and unknown samples. In Table 2, a summary of the results obtained when this approach is used is shown. Unknown mixtures and pure analyte samples are analyzed simultaneously. A total number of 15 data matrices are simultaneously analyzed. In order to have the absolute concentrations, three pure analyte samples are used as standards. The values obtained along with the estimation of the errors in prediction are shown in Table 2. The results obtained with the proposed method are comparable to the results obtained in the quantitation when the unit species spectra of the different species were used, which is reasonable because both approaches are full-model descriptive approaches and there are no interferents. In the mixtures of TCE and $CHCl_3$, worse results are obtained for the analyte contributing less to the signal (at lower concentration). This method has some advantages as previously described since the quantitation is achieved in one step and the concentration profiles can be constrained to be positive, unimodal, and of equal shape.

Table 2. Results of Quantitation[a] Using the Profile Shapes

sample[b]	concn	species[d]	rel concn[e]	pred concn[f]	% error[g]
TCA	66.9	1	11.96	std	
TCA	133	1	24.64	137.6	3.4
TCA	267	1	49.93	279.3	4.6
TCA	267	1	45.73	255.8	4.2
TCE	7.31	2	32.80	7.54	3.1
		3	72.70	7.47	2.2
TCE	7.31	2	31.82	std	
		3	71.14		
TCE	29.3	2	116.0	26.7	8.6
		3	246.8	25.3	13
TCE	58.6	2	270.6	62.2	6.1
		3	614.9	63.2	7.8
TCE	1.46	2	5.765	1.32	9.8
		3	12.47	1.28	13
$CHCl_3$	1.48	4	20.13	std	
		5	19.14		
$CHCl_3$	4.45	4	44.49	3.27	26
		5	59.22	4.58	2.9
$CHCl_3$	7.42	4	70.14	5.16	30
		5	92.89	7.18	3.2
TCA	66.9	1	10.99	61.5	8.1
TCE	2.93	2	14.57	3.35	14
		3	24.72	2.55	13
$CHCl_3$	1.48	4	14.04	1.03	30
		5	24.72	1.91	29
TCE	2.93	2	17.10	3.93	34
		3	0.029	****	****
$CHCl_3$	1.48	4	41.28	3.03	32
		5	57.76	4.47	0.9
TCE	7.30	2	30.89	7.09	2.9
		3	59.10	6.07	17
$CHCl_3$	1.48	4	15.14	1.11	25
		5	23.69	1.83	26

[a] Results of the analysis of 15 samples using the pure species spectra. [b] Content of analyzed samples. [c] Concentration in ppm. [d] The species used for analyte quantitation (see Figure 7 for species identification). [e] Estimated relative concentration of the analyte compared to the other samples. [f] Estimated absolute concentration of the analyte. [g] Percent error in the prediction.

Quantitation in the Presence of Unknown Interferents. Finally, the curve resolution method presented here is tested by the quantitation of a certain analyte in the presence of an unknown interferent. The augmented data matrix is formed now by two data matrices, the unknown mixture data matrix containing the analyte and the interferent and the pure analyte data matrix. In Table 3, the results of three determinations are given for different mixtures. In the first case, the determination of TCE in a mixture of TCE and TCA is given; TCA is considered the interferent. As the first species of TCE is formed at earlier times in the reaction and its spectrum is quite different from that of TCA, quantitation is accurate (Table 3). In the second case, the determination of TCE in a mixture of TCE and $CHCl_3$ (now the interferent being $CHCl_3$) is given. The quantitation of TCE is also rather good using species 2 because of its unique spectral characteristics (see Figure 7b). Quantitation would be much worse if species 3 were used for the TCE quantitation, because this species

Table 3. Results of Quantitation in the Presence of Unknown Interferences

sample[a]	concn[b]	species[c]	rel concn[d]	pred concn[e]	% error[f]
TCE	7.31	2	22.99	std	
TCE	7.31	2	19.00	6.04	17
($CHCl_3$)	(1.48)				
TCE	7.31	2	17.98	std	
TCE	7.31	2	16.55	6.72	8.0
(TCA)	(66.9)				
$CHCl_3$	4.45	4	28.98	std	
$CHCl_3$	4.45	4	22.87	3.51	21
(TCE)	(2.93)				

[a] Content of analyzed samples. [b] Concentration in ppm. [c] The species used for analyte quantitation (see Figure 7 for species identification). [d] Estimated relative concentration of the analyte compared to the other sample. [e] Estimated absolute concentration of the analyte. [f] Percent error in the prediction.

overlaps highly with the species given by $CHCl_3$. The third case is the quantitation of $CHCl_3$ in the presence of TCE as interferent. The results are now worse because of the high overlap between the spectra of the two species given by $CHCl_3$ and also with the species 3 given by TCE.

CONCLUSIONS

Multivariate curve resolution has been shown to be a very useful technique for extracting qualitative and quantitative information from kinetic reactions. Multivariate curve resolution improves the selectivity of the analytical determinations obtained with reagent-based chemical sensors. In particular, the proposed multivariate curve resolution method allowed the identification and interpretation of the products (UV/visible spectroscopically active) given by TCA, TCE, and $CHCl_3$ in the Fujiwara reaction. The quantitation of the three analytes both in pure analyte samples and in their mixtures was possible in spite of the high overlap of their analytical signals. The method is proposed for the multicomponent determination of mixtures of chlorinated hydrocarbons using a reaction-based chemical sensor.

ACKNOWLEDGMENT

R.T. acknowledges the financial support from the DGICYT (Spain) for his stay at the Laboratory of Chemometrics at the University of Washington. A.K.S. acknowledges a grant from the Netherlands Organization for Scientific Research (NWO) for his stay at the Laboratory for Chemometrics at the University of Washington. The Center for Process Analytical Chemistry (CPAC) is a National Science Foundation Industry/University Cooperative Research Center at the University of Washington.

Received for review March 15, 1994. Accepted June 30, 1994.[⊗]

[⊗] Abstract published in *Advance ACS Abstracts*, August 15, 1994.

Anal. Chem. **1994,** *66,* 3345–3351

Multicomponent Determination of Chlorinated Hydrocarbons Using a Reaction-Based Chemical Sensor. 3. Medium-Rank Second-Order Calibration with Restricted Tucker Models

A. K. Smilde,[†] R. Tauler,[‡] J. M. Henshaw,[§] L. W. Burgess, and B. R. Kowalski*

Center for Process Analytical Chemistry, University of Washington, BG-10, Seattle, Washington 98195

The calibration of a chemical sensor for chlorinated hydrocarbon analytes based on the Fujiwara reaction is described. This sensor generates a particular type of data: medium-rank second-order data. With this type of data it is possible to calibrate the sensor in such a way that quantitation for the analytes in the presence of unknown interferents is possible. The calibration method developed is a new approach based on so-called restricted Tucker models that utilize all available chemical information.

In order to be able to monitor in situ multiple chlorinated hydrocarbons in contaminated soil, different approaches are available.[1] One of the approaches is based on the Fujiwara reaction of chlorinated hydrocarbons with pyridine and a base.[2] In this reaction, intermediates and final products are formed which can be detected with UV/visible spectroscopy.[3] One way to use this reaction is to measure the absorbance at a particular wavelength of the species being formed after the analyte permeates a membrane of a chemical sensor and encounters the Fujiwara reagent. Since the measurement is done at one wavelength, this is a zero-order measurement.[4] Therefore, calibration for the chlorinated hydrocarbons using this chemical sensor is called zero-order calibration. The disadvantage of using zero-order calibration is that the selectivity of such a calibration is low. There are usually more absorbing species at the particular wavelength and these species may be present in unknown concentrations in unknown samples. This puts a severe constraint on the applicability of zero-order calibration: an unknown interference cannot be detected and accounted for. This is called the background problem.

If the measurements are not performed at one particular wavelength but at multiple wavelengths simultaneously, the result is a vector of measurements acquired at a certain point in time. Calibration with a chemical sensor based on multiple wavelength absorbances at a certain point in time is called first-order calibration. For the chlorinated hydrocarbons chloroform, trichloroethylene, and 1,1,1-trichloroethane, calibration based on first-order measurements with a chemical sensor is described in the first part of this series.[5] Although less severe, the background problem is still present: an unknown interference can be detected but calibration for the analyte of interest is impossible.

The approach taken in this paper and in the second part of this series[6] uses not only the full spectrum at a certain time point but also temporal information of the successive UV/visible spectra. At regularly spaced time intervals, a UV/visible spectrum is collected. At each point in time such a spectrum has contributions from a mixture of the intermediate and final species. The data obtained from measuring one sample (containing a mixture of analytes of interest and unknown interferences) can be ordered in a matrix with dimensions equal to the number of time points by the number of wavelengths. This type of data is called second-order data.[7] Under certain conditions, calibration with second-order data yields the second-order advantage: the ability to quantify for analytes of interest in the presence of unknown interferents. Of course, it is possible to obtain first-order data using this matrix of measurements by stringing out the matrix in one long vector. The first-order calibration methods—like partial least squares—can then be used. This is also shown in the first part of this series. This stringing out and using the data in a first-order way however destroys the second-order advantage.

The analyte of interest enters the reaction chamber of the chemical sensor through a membrane. The Fujiwara reagent is added, the reaction starts, and intermediate and final species are formed. The development or vanishing in time of a particular intermediate or final species will be referred to as the time profile of that species. This particular species has a UV/visible spectrum which will be referred to as the species spectrum. The time profiles and the spectra of the species are not assumed to be known a priori. Estimates of these time profiles and spectra can be obtained from multivariate curve resolution methods.[8] This is shown in the second part of this series.[6]

In order to solve the background problem, a full second-order method should be used.[7] In case of response matrices

[†] Present address: Laboratory for Analytical Chemistry, University of Amsterdam, Nieuwe Achtergracht 166, 1018 WV Amsterdam, The Netherlands.

[‡] Present address: Department of Analytical Chemistry, University of Barcelona, Diagonal 647, Barcelona 08028, Spain.

[§] Present address: ORS Environmental Systems, 7 Barnabas Rd., Marion, MA 02738.

(1) Liebman, K. C.; Hindman, J. D. *Anal. Chem.* **1964**, *36*, 348.
(2) Fujiwara, K. *Sitzungsber. Abh. Naturforsch Ges. Rostock* **1916**, *6*, 33.
(3) Reith, J. F.; van Ditsmarsch, W. C.; de Reuter, T. *Analyst* **1974**, *99*, 652.
(4) Sanchez, E.; Kowalski, B. R. *J. Chemom.* **1988**, *2*, 247–264.
(5) Henshaw, J. M.; Burgess, L. W.; Booksh, K. S.; Kowalski, B. R., *Anal. Chem.*, first paper of three in this issue.
(6) Tauler, R.; Smilde, A. K.; Henshaw, J. M.; Burgess, L. W.; Kowalski, B. R. *Anal. Chem.* second paper of three in this issue.
(7) Sanchez, E.; Kowalski, B. R. *J. Chemom.* **1988**, *2*, 265–283.
(8) Tauler, R.; Kowalski, B. R.; Fleming, S. *Anal. Chem.* **1993**, *65*, 2040.

0003-2700/94/0366-3345$04.50/0
© 1994 American Chemical Society

generated by a pure analyte with rank one, the generalized rank annihilation method can be used.[7] This method is able to quantitate for specific analytes in the presence of unknown interferences.

For pure analyte responses of rank higher than one (caused by multiple absorbing species) the calibration becomes more complicated. The challenge is, of course, to retain the second-order advantage. Recently, a second-order calibration method suited for medium-rank cases was developed.[9] The calibration of the reagent-based chemical sensor fits exactly in the framework of medium-rank second-order calibration. This medium-rank second-order calibration method is based on restricted Tucker models.

The first paper in this series deals with the description of the sensor and zero- and first-order calibration.[5] The second paper describes the curve resolution of the response matrices, i.e., the estimation of the underlying spectra and time profiles.[6] The second paper also describes details concerning the kinetics of the applied reactions and a calibration procedure based on the full-response matrices. This third paper describes the results of applying medium-rank second-order calibration to the Fujiwara reaction-based data. A short description of the theory will be given.

THEORY

Medium-Rank Second-Order Calibration with Restricted Tucker Models. In the following, italic lower and upper case characters refer to scalars, bold lower case characters refer to vectors, bold uppercase characters refer to matrices and bold underlined uppercase characters refer to three-way matrices (also called third-order tensor). (Note: scalars, vectors, and matrices designated in this third paper of the series do not directly correspond to those of the same name in the first and second parts of the series.)

A short description of the theory will be given as more detailed information is given elsewhere.[9] One calibration example is used as an illustration in order to explain the theory. Suppose that the analyte 1,1,1-trichloroethane (TCA) generates one unique absorbing species, the analyte trichloroethylene (TCE) generates two absorbing species, and the analyte chloroform ($CHCl_3$) also generates two absorbing species. The number of species generated by the analytes can be established with rank analysis of the response matrices. Principal component analysis or curve resolution can be used for this purpose. Assume that the second species being formed by TCE and $CHCl_3$ has the same spectrum; i.e., it is the same species but with a different time profile for analytes TCE and $CHCl_3$. The calibration problem can be stated as follows:

$$\mathbf{N}_1 = z_{11}\mathbf{x}_1\mathbf{y}_1^t + \mathbf{E}_1 \tag{1a}$$

$$\mathbf{N}_2 = z_{22}\mathbf{x}_2\mathbf{y}_2^t + z_{22}\mathbf{x}_3\mathbf{y}_3^t + \mathbf{E}_2 \tag{1b}$$

$$\mathbf{N}_3 = z_{33}\mathbf{x}_4\mathbf{y}_4^t + z_{33}\mathbf{x}_5\mathbf{y}_5^t + \mathbf{E}_3 \tag{1c}$$

$$\mathbf{M} = z_{41}\mathbf{N}_1^* + z_{42}\mathbf{N}_2^* + z_{43}\mathbf{N}_3^* + \mathbf{U}_m + \mathbf{E}_m \tag{1d}$$

where z_{lk} represents the true concentration of analyte k in mixture l. The $\mathbf{x}$ vectors are the true time profiles of the species, the $\mathbf{y}$ vectors the true spectra of the species, $\mathbf{U}_m$ is the interferent in the mixture sample $\mathbf{M}$, and the $\mathbf{E}$ matrices are error matrices. The rank of $\mathbf{U}_m$ can vary between 0 (no interferent) and any positive number. From now on $\mathbf{N}_1$ refers to TCA, $\mathbf{N}_2$ refers to TCE, and $\mathbf{N}_3$ refers to $CHCl_3$. $\mathbf{N}_k^*$ is the unit concentration response of analyte k = 1, 2, 3 (TCA, TCE, and $CHCl_3$, respectively); i.e., $\mathbf{N}_k^* = \mathbf{N}_k/z_{kk}$. With NBRA[10] the presence of $\mathbf{N}_1$, $\mathbf{N}_2$, and $\mathbf{N}_3$ in $\mathbf{M}$ can be established. The rank of $\mathbf{U}_m$ can be established by analyzing the rank of $\mathbf{M}$, using the information of the presence of the analyte, and with knowledge about the level of the measurement error. It is assumed that the unit time profiles and spectra of the species are equal in the pure samples and in the mixtures. It is important to stress the fact that the time scale of the measurements represented in $\mathbf{N}_1$, $\mathbf{N}_2$, $\mathbf{N}_3$, and $\mathbf{M}$ is the same; i.e. the recording of the spectra starts at time zero and evolves at the same points in time for each analyte and mixture.

The quantitation of TCA ($=\mathbf{N}_1$) can be found with the generalized annihilation method (GRAM[7]) since the rank of $\mathbf{N}_1$ (eliminating the noise) is one. Hence, the contribution of $\mathbf{N}_1$ can be substracted from $\mathbf{M}$.

For illustrative purposes it is assumed that there is no interferent present. Examples of other calibration models which take care of interferents will be discussed later in this paper.

Assuming absence of TCA and no interferent in M the calibration problem is

$$\mathbf{N}_2 = z_{12}\mathbf{x}_2\mathbf{y}_2^t + z_{12}\mathbf{x}_3\mathbf{y}_3^t + \mathbf{E}_2 \tag{2a}$$

$$\mathbf{N}_3 = z_{23}\mathbf{x}_4\mathbf{y}_4^t + z_{23}\mathbf{x}_5\mathbf{y}_5^t + \mathbf{E}_3 \quad \text{with} \quad \mathbf{y}_5 = \mathbf{y}_3 \tag{2b}$$

$$\mathbf{M} = z_{32}\mathbf{N}_2^* + z_{33}\mathbf{N}_3^* + \mathbf{E}_m \tag{2c}$$

where the values of z_{32} and z_{33} are desired (quantitation) together with estimations of the x and y vectors (qualitative information). Calibration proceeds by stacking $\mathbf{N}_2$, $\mathbf{N}_3$, and $\mathbf{M}$ to form the three-way matrix $\underline{\mathbf{D}}$ ($I \times J \times 3$), where I and J are the dimensions of $\mathbf{N}_2$, $\mathbf{N}_3$, and $\mathbf{M}$. Let $\mathbf{X}$, $\mathbf{Y}$, and $\mathbf{Z}$ be the matrices consisting of the $\mathbf{x}$, $\mathbf{y}$, and $\mathbf{z}$ vectors. The estimated counterparts of these matrices will be called $\mathbf{A}$, $\mathbf{B}$, and $\mathbf{C}$, respectively.

Two different models for analyzing three-way data are useful in this calibration. The first model is the PARAFAC or trilinear model.[11,12] An element d_{ijk} of $\underline{\mathbf{D}}$ is modeled as

$$d_{ijk} = \sum_{q=1}^{Q} a_{iq}b_{jq}c_{kq} + e_{ijk} \tag{3}$$

where Q is chosen in such a way that $\underline{\mathbf{E}}$ with elements e_{ijk} has a small norm (i.e., $\sum e_{ijk}^2$ is small). Define the vectors $\mathbf{a}_q$, $\mathbf{b}_q$, and $\mathbf{c}_q$ as vectors with elements a_{iq}, b_{iq}, and c_{iq}, respectively. The outer tensor product of $\mathbf{a}_q$, $\mathbf{b}_q$, and $\mathbf{c}_q$ is called the qth triad in the PARAFAC decomposition and is obtained by multiplying a_{iq}, b_{jq}, and c_{kq} for each i, j, and k. The PARAFAC model as represented in eq 3 is visualized in Figure 1.

(9) Smilde, A. K.; Wang, Y.; Kowalski, B. R. *J. Chemom.* **1994**, *8*, 21.

(10) Wang, Y; Borgen, O.; Kowalski, B. R.; Gu, M.; Turecek, F. *J. Chemom.* **1993**, *7*, 117.

(11) Harshman, R. A; Lundy, M. In *Research Methods for Multimode Analysis*; Law, H. G., Snyder, C. W., Hattie, J. A., McDonald, R. P., Eds.; Prager: New York, 1984.

(12) Smilde, A. K. *Chemom. Intell. Lab. Syst.* **1992**, *15*, 143–163.

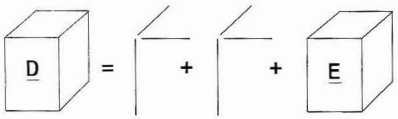

Figure 1. PARAFAC model. The three-way matrices **D** and **E** are explained in the text. The sticks to the right of the equal sign represent the vectors **a**, **b**, and **c** of the PARAFAC model.

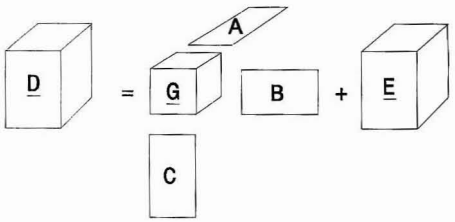

Figure 2. Tucker model. The matrices **A**, **B**, **C**, **D**, **E**, and **G** are explained in the text.

Another way to decompose $\underline{\mathbf{D}}$ is the Tucker model.[12,13] Again, let d_{ijk} be an element of $\underline{\mathbf{D}}$, then

$$d_{ijk} = \sum_{p=1}^{P} \sum_{q=1}^{Q} \sum_{r=1}^{R} a_{ip} b_{jq} c_{kr} g_{pqr} + e_{ijk} \qquad (4)$$

is the Tucker decomposition of $\underline{\mathbf{D}}$. The elements g_{pqr} are the typical elements of the three-way array $\underline{\mathbf{G}}$ ($P \times Q \times R$) which has a much smaller size than $\underline{\mathbf{D}}$. The three-way array $\underline{\mathbf{G}}$ is called the core array. P, Q, and R are parameters to be chosen in such a way that $\underline{\mathbf{E}}$, with elements e_{ijk}, has a small norm. The Tucker model, as represented in eq 4, is visualized in Figure 2. From this figure it is obvious that the vectors $\mathbf{a}_p$, $\mathbf{b}_q$, and $\mathbf{c}_r$ (defined in the same way as above) are connected (multiplied) with each other by the core element g_{pqr}. In eq 4 this is accomplished by the triple summation.

From eqs 3 and 4 it is clear that PARAFAC is a special case of the Tucker model. Taking $P = Q = R$ and $g_{pqr} = 1$, if and only if $p = q = r$, transforms the Tucker model into the PARAFAC model. For the PARAFAC model the core array is a $P \times P \times P$ cube with ones on the superdiagonal. The Tucker model is more general due to the possibility of an unequal number of loading vectors in each dimension and because of a more general core array.

One of the latest developments in three-way analysis is the restricted Tucker model.[14] The Tucker model can be restricted by setting specific core array elements to zero. The result is a much more parsimonious model in terms of the number of parameters to be estimated. Only particular multiplications of $\mathbf{a}_p$, $\mathbf{b}_q$, and $\mathbf{c}_r$ are allowed. The zero elements in the core array can be selected by theory or chemical knowledge about the system.

Other restrictions also apply to the Tucker model. Since the pure underlying time profiles, spectra, and concentrations

(13) Kroonenberg, P. M. *Three-mode Principal Component Analysis*; DSWO Press: Leiden, The Netherlands, 1983.
(14) Kiers, H. A. L. *Stat. App.* **1992**, *4*, 659–667.

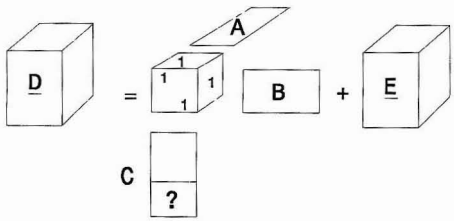

Figure 3. Restricted Tucker model. This model is a special case of the Tucker model of Figure 2. The core array has ones (or nonzero's) at particular places. The **C** matrix contains the concentrations, and part of **C** (the upper part) is known. The other part of **C** is unknown (?) and has to be estimated together with **A** and **B**.

Table 1. Unfolded Core Array of the PARAFAC Four-Component Model of the Theory Example

	1	2	3	Q	1	2	3	Q	1	2	3	Q	1	2	3	Q
1	1	0	0	0	0	0	0	0	0	0	0	0	0	0	0	0
2	0	0	0	0	0	1	0	0	0	0	0	0	0	0	0	0
3	0	0	0	0	0	0	0	0	0	0	1	0	0	0	0	0
P	0	0	0	0	0	0	0	0	0	0	0	0	0	0	0	1
			1				2				3				R	

Table 2. Unfolded Core Array of the Theory Example after Applying $\mathbf{y}_3 = \mathbf{y}_5$

	1	2	Q	1	2	Q	1	2	Q	1	2	Q
1	1	0	0	0	0	0	0	0	0	0	0	0
2	0	0	0	0	1	0	0	0	0	0	0	0
3	0	0	0	0	0	0	0	0	1	0	0	0
P	0	0	0	0	0	0	0	0	0	0	1	0
		1			2			3			R	

are nonnegative, this can also be assumed for the estimated counterparts **A**, **B**, and **C**. Moreover, part of **C** is known: the part describing the concentrations in the standard solutions. All of these constraints can be incorporated in the restricted Tucker model. The estimation procedure becomes a combination of an alternating least squares and a nonnegative least squares algorithm.[15]

Counting the number of vectors in the calibration problem represented by eqs 2a–c present in the X, Y, and Z domain, the maximum is four (in the X domain). In order to provide "space" for the X-domain vectors a four-component PARAFAC model must be used to model eqs 2a–c simultaneously. The core array of this four-component PARAFAC model is a $4 \times 4 \times 4$ three-way array with ones on the superdiagonal. If each horizontal slice of this core array is placed next to each other (unfolded or strung out[12]), the result is presented in Table 1.

In Table 1, $P = 4$, $Q = 4$, and $R = 4$ stand for the number of components in the X, Y, and Z domain, respectively. More specifically, $\mathbf{x}_2$–$\mathbf{x}_5$ correspond to $P = 1$ to $P = 4$, respectively, and likewise $\mathbf{y}_2$–$\mathbf{y}_5$ correspond to $Q = 1$ to $Q = 4$. The z vectors are represented by $R = 1$–4. Applying the knowledge that $\mathbf{y}_3 = \mathbf{y}_5$ gives the unfolded core array of Table 2.

In Table 2 the column associated with $q = 4$ ($\mathbf{y}_5$) is added to the column associated with $q = 2$ ($\mathbf{y}_3$) of Table 1. Therefore, the value of Q changes from 4 to 3 in Table 2. The first two

(15) Lawson, Ch. L.; Hanson, R. J. *Solving Least Squares Problems*; Prentice-Hall: Englewood Cliffs, NJ, 1974.

Table 3. Final Unfolded Core Array of the Theory Example

	1	2	$Q = 3$	1	2	$Q = 3$
1	1	0	0	0	0	0
2	0	1	0	0	0	0
3	0	0	0	0	0	1
P	0	0	0	0	1	0
		1			$R = 2$	

columns of **Z** in the four-component PARAFAC model are equal because both dyads $\mathbf{x}_2\mathbf{y}_2^t$ and $\mathbf{x}_3\mathbf{y}_3^t$ represent the contribution of $\mathbf{N}_2$. Both $\mathbf{z}_1$ and $\mathbf{z}_2$ will describe the concentration of $\mathbf{N}_2$ in $\mathbf{N}_2$, $\mathbf{N}_3$, and **M**. Obviously, $\mathbf{z}_1 = \mathbf{z}_2$, and likewise, $\mathbf{z}_3 = \mathbf{z}_4$, where $\mathbf{Z} = [\mathbf{z}_1\ \mathbf{z}_2\ \mathbf{z}_3\ \mathbf{z}_4]$. In order to accommodate these relationships the $r = 2$ ($\mathbf{z}_2$) block is added to the $r = 1$ ($\mathbf{z}_1$) block and the $r = 4$ ($\mathbf{z}_4$) block is added to the $r = 3$ ($\mathbf{z}_3$) block of Table 2. The resulting unfolded core array is shown in Table 3.

The core array shown in Table 3 has exactly the right size ($4 \times 3 \times 2$) since the model has to support four x vectors, three y vectors, and two concentration vectors (**z**). The restricted Tucker model is estimated using the core array of Table 3, applying nonnegativity constraints to the estimation of **A**, **B**, and **C**, and using the known concentrations in **C**.

Estimation of the restricted Tucker models starts with starting values for **A**, **B**, and **C**. Multivariate curve resolution (MCR) of the pure analyte responses gives estimates of the true time profiles (**A**) and spectra (**B**).[6,8] This is explained in detail in the second paper of this series. These estimated time profiles and spectra will be used as starting values. The first two rows of **C** are (z_{22} 0) and (0 z_{33}), respectively. In the third row of **C**, arbitrary positive constants are used as starting values. After convergence of the iterative estimation procedure, the final row in **C** gives the estimates of the concentrations of $\mathbf{N}_2$ and $\mathbf{N}_3$ in **M**.

Complexity of the Calibration Problems. The calibration method developed will be illustrated with two data sets. The experimental setup of both data sets is described in part 1 of this series. The difference between both data sets is that the first one is measured at room temperature and the second one at 10 °C. It is expected that the same absorbing species are being formed, but of course at different reaction rates. The complexity of the first data set will be described in detail, and the complexity of the second data set differs mainly with respect to the temporal profiles and will be discussed shortly.

In part 2 of this series, the estimated unit spectra (spectra at unit concentration) and time profiles of the different species formed by the analytes in the Fujiwara reaction were presented. These spectra and time profiles can be helpful for assessing the complexity of the calibration problems.

If each spectrum is understood as a vector in the 100-dimensional space (the number of wavelengths at which absorbances are measured equal 100), then the cosine of the angle between the vectors serves as a measure of similarity of the spectra. These cosines are presented in Table 4.

The cosine varies between 0 and 1, where a 0 means that the spectra are very dissimilar and a 1 means that the spectra are very similar. From this table it is clear that there is a high overlap between the second species formed by TCE (TCE2) and both species formed by $CHCl_3$ ($CHCl_3$1 and $CHCl_3$2). Also, the spectra of both species formed by $CHCl_3$ are very similar (0.97) to each other. Since the second species formed by TCE and $CHCl_3$ are both final products in the Fujiwara reaction and have a very high spectral overlap, it is assumed that these species are identical.

Table 4. Spectral Similarities

	TCA	TCE1	TCE2	$CHCl_3$1	$CHCl_3$2
TCA	1	0.86	0.47	0.49	0.40
TCE1	0.86	1	0.70	0.76	0.62
TCE2	0.47	0.70	1	0.98	0.98
$CHCl_3$1	0.49	0.76	0.98	1	0.97
$CHCl_3$2	0.40	0.62	0.98	0.97	1

Table 5. Time Profile Similarities

	TCA	TCE1	TCE2	$CHCl_3$1	$CHCl_3$2
TCA	1	0.15	0.93	0.30	0.94
TCE1	0.15	1	0.36	0.95	0.37
TCE2	0.93	0.36	1	0.56	0.999
$CHCl_3$1	0.30	0.95	0.56	1	0.56
$CHCl_3$2	0.94	0.37	0.999	0.56	1

The analyte TCA forms one species that has spectral differences with respect to the ones formed by TCE and $CHCl_3$. This makes the calibration for TCA easier, and also the calibration of TCE and/or $CHCL_3$ in the presence of TCA should be possible.

A similar approach can be taken with respect to the time profiles. Again a cosine is calculated between the different time profiles understood as vectors in the 61 dimensional space (measurements were taken at 61 regularly spaced time points). Note that the cosine gives information about the angle between time profiles and is therefore a measure of similarity of the unit time profiles: the time profiles scaled to unit concentration. In other words, the cosine is a measure of similarity in shape. This holds, of course, also for the spectral similarities.

In Table 5, the time profile similarities are shown. The first species formed by TCE and $CHCl_3$ overlap; the second species overlaps even more. There is also some overlap in time profile shapes of the species formed by TCA and the second species formed by TCE and $CHCl_3$. This overlap counteracts the spectral differences between the species formed by TCA and the ones formed by TCE and $CHCl_3$ (see Table 4).

In the calibrations, the full response matrices of the analytes are used. It is therefore useful to look at the full response matrices of each species and of the analytes. The response matrices of the five different species can be approximated by taking the outer product of the spectrum and the time profile for each species. Thus, five different response matrices are obtained, assuming five different species. Each response matrix is therefore of rank one. A congruence coefficient between these matrices can be calculated according to

$$\frac{\|\mathbf{A}^t\mathbf{B}\|}{\|\mathbf{A}^t\mathbf{A}\|^{1/2}\|\mathbf{B}^t\mathbf{B}\|^{1/2}} \tag{5}$$

where $\|\mathbf{A}\|$ is the Frobenius norm of a matrix.[16] This congruence coefficient varies between 0 and 1, where 0 means no similarity and 1 means perfect similarity between the matrices **A** and

(16) Golub, G. H.; van Loan, Ch. F. *Matrix Computations*; John Hopkins University Press: Baltimore, MD, 1989.

Table 6. Pure Species Similarities

	TCA	TCE1	TCE2	$CHCl_3$1	$CHCl_3$2
TCA	1	0.02	0.86	0.09	0.88
TCE1	0.02	1	0.13	0.90	0.14
TCE2	0.86	0.13	1	0.32	0.997
$CHCl_3$1	0.09	0.90	0.32	1	0.32
$CHCl_3$2	0.88	0.14	0.997	0.32	1

Table 7. Analyte Similarities

	TCA	TCE	$CHCl_3$
TCA	1	0.71	0.68
TCE	0.71	1	0.998
$CHCl_3$	0.68	0.998	1

B. In Table 6, the similarities between the different species are presented. It is clear that the first species formed by TCE (TCE 1) and formed by $CHCl_3$ ($CHCl_3$1) are similar (0.90) and the two second species (TCE_2 and $CHCl_3$2) are assumed to be equal, which is supported by the similarity of 0.997.

There is no direct relationship between the values in either Table 4 or 5 and Table 6. However, some conclusions can be drawn. The high similarity between the time profile shapes of TCA and those of TCE2 and $CHCl_3$2 is counteracted to some extent by a low spectral agreement. Still, the similarity of the total TCA species and the second TCE and $CHCl_3$ species is moderate (0.86 and 0.88, respectively). The first species of TCE and $CHCl_3$ are overlapped (0.90). This is a consequence of a high spectral similarity.

As a final step, the total similarity between analytes is calculated. In order to do this, the two total species responses TCE1 and TCE2 are added. The same is done for $CHCl_3$. For TCA, the total species response is the same as the total analyte response since TCA generates only one species. The congruence between the total response matrices generated by the pure analytes can be calculated using eq 5. The results are reported in Table 7.

Table 7 clearly shows the difficulty of the calibration problem. There is a high similarity between TCE and $CHCl_3$. This means that the quantitation of, for example, TCE in the presence of the unknown interferent $CHCl_3$, or vice versa, is a very difficult task. The analyte TCA as an interferent should not present too much difficulty.

If the experiment is performed at a lower temperature (10 °C; second data set) a difference in time profiles is expected. This is exactly what happens, and the time profile similarities show less overlap than in the first data set and result in lower species similarities. The analyte similarity of TCE and $CHCl_3$ is 0.46, which is low compared to the analogous similarity in the first data set (0.998).

While it is true that thus far only three analytes are dealt with which would yield good results if they are the only ones present, the real aim is to do the analysis in the presence of unexpected interferents. Therefore, one should consider the analysis of, for example, TCE in a case where TCA, $CHCl_3$, and other interferents are present. In order to illustrate the calibration methods, TCE will be used as an interferent in the calibration of $CHCl_3$ in a mixture and vice versa. These cases represent the hardest calibration cases, since the responses of TCE and $CHCl_3$ overlap severely. The results extend easily to cases of more unknown interferents.

Table 8. Unfolded Core Array of Example 2

	1	2	$Q = 3$	1	2	$Q = 3$
1	1	0	0	0	0	0
2	0	1	0	0	0	0
3	0	0	0	0	0	1
P	0	0	0	0	1	0
		1			$R = 2$	

EXPERIMENTAL SECTION

In this section different calibration examples are described which are used to test the restricted Tucker calibration methodology. The calibrations differ with respect to the presence of an interferent. Results for both data sets will be presented, but the structures of the calibration problems are the same for both data sets. Throughout it will be assumed that TCE and $CHCl_3$ have the second (final) species in common: the spectra of the second species being formed by TCE and $CHCl_3$ are equal, but their time profiles are not equal since the reaction kinetics differ. The structure of the calibration problems will be discussed in this section, whereas the results for the two different data sets will be presented in the Results section.

Example 1. The first calibration is already formalized in eqs 2a–c and will be called example 1. The model is estimated by using the constraints that **A**, **B**, and **C** are nonnegative and the first two rows in **C** are (z_{12} 0) and (0 z_{23}), respectively. Starting values for **A** and **B** are obtained from multivariate curve resolution.

Example 2. In the second example, the analyte $CHCl_3$ is used as an unknown interferent. The standard $\mathbf{N}_2$ is the response of pure TCE, and the mixture consists of TCE and $CHCl_3$. This is the real second-order challenge: is it possible to quantify for TCE in the presence of an unknown? Of course, it must first be determined whether TCE is in the mixture. There are several ways of doing this.[10] The equations that describe example 2 are

$$\mathbf{N}_2 = z_{12}\mathbf{x}_2\mathbf{y}_2^t + z_{12}\mathbf{x}_3\mathbf{y}_3^t \quad (6a)$$

$$\mathbf{M} = z_{12}\mathbf{N}_2^* + \mathbf{U}_m \quad (6b)$$

$$\mathbf{U}_m = z_{mu}\mathbf{x}_4\mathbf{y}_4^t + z_{mu}\mathbf{x}_5\mathbf{y}_5^t \quad \text{with} \quad \mathbf{y}_5 = \mathbf{y}_3 \quad (6c)$$

where z_{mu} stands for the concentration of the unknown $\mathbf{U}_m$ in **M**. The error matrices are left out for convenience. The unfolded core array associated with example 2 is presented in Table 8.

In Table 8, $P = 4$ (X domain), $Q = 3$ (Y domain), and $Q = 2$ (concentration domain). The first row of **C** is (z_{12} 0). Since $CHCl_3$ acts as an interferent in example 2, the associated starting columns in **A** and **B** are chosen randomly. The columns in **A** and **B** associated with TCE have starting values obtained from multivariate curve resolution.

Example 3. In this example, a mixture of TCE and $CHCl_3$ is used and only $CHCl_3$ is used as a standard. Hence, it is the reverse of the previous example. The calibration model is nearly the same; the core arrays associated with examples 2 and 3 are equal. Of course, the proper arrangements have to be made in matrices **A**, **B**, and **C**.

RESULTS AND DISCUSSION

Quality of the First Data Set (Room Temperature). In part 1 of this series, a general description of the experimental

Table 9. Results of Example 1 Data Set 1

	TCE conc	max abs	$CGCl_3$ conc	max abs	SD
N	7.31	0.24	1.48	0.24	
M	7.31	0.24	1.48	0.24	
	7.14 (2.3%)		1.58 (7.0%)		0.0027

Table 10. Results of Example 2 Data Set 1

	TCE conc	max abs	$CHCl_3$ conc	max abs	SD
N	7.31	0.24			
M	7.31	0.24	1.48	0.24	
	8.26 (13.2%)				0.0018

Table 11. Results of Example 3 Data Set 1

	TCE conc	max abs	$CHCl_3$ conc	max abs	SD
N			4.45	0.71	
M	2.93	0.09	4.45	0.71	
			3.84 (13.7%)		0.0025

Table 12. Results of Example 1 Data Set 2

	TCE conc	max abs	$CHCl_3$ conc	max abs	SD
N	0.488	0.055	0.995	0.28	
M	1.464	0.165	0.995	0.28	
	1.520 (3.8%)		0.975 (2.0%)		0.00065

setup is given. The pure experimental error of the data in this data set is between 3.2 and 3.4% (relative error) for TCA and between 2.4 and 2.5% for $CHCl_3$. For TCE, a similar number is expected. These values are calculated as averages over time for absorbances at particular wavelengths. Another way to approach reproducibility is by calculating

$$100\frac{\|\mathbf{A}-\mathbf{B}\|}{\|0.5\mathbf{A}+0.5\mathbf{B}\|} \tag{7}$$

where $\|\mathbf{A}\|$ denotes the Frobenius norm of **A** and the matrices **A** and **B** are responses of reproduced measurements. For TCE at a concentration of 7.31 ppm this number is 3.04%. A similar number is expected for $CHCl_3$. These numbers give an indication of the range of relative errors in concentrations due to measurement error.

In a similar way, a standard deviation value can be calculated by dividing $\|\mathbf{A}-\mathbf{B}\|$ by 61×100 (number of time-points times number of wavelengths) and taking the square root. These numbers are 0.0059 and 0.0113 for the above-mentioned TCE and TCA standards, respectively. The SD values given in Tables 9–11 can be compared with the range 0.0059–0.0113.

Quality of the Second Data Set (10 °C). The only difference between the second and first data set is the temperature. Experimental details are given in part 1 of this series.

For $CHCl_3$ the results of using eq 7 was 3–5%, and for TCE this number was 5–8%. These values give an indication of the experimental error in the second data set. A standard deviation value, analogous to the first data set, was calculated. These values were 0.0063 and 0.0048 for $CHCl_3$ and TCE, respectively. The SD values reported in Tables 12–14 can be compared with these values.

Results for Data Set 1. *Example 1.* It is clear from Table 7 that the analytes TCE and $CHCl_3$ have a very similar

Table 13. Results of Example 2 Data Set 2

	TCE concn	max abs	$CHCl_3$ conc	max abs	SD
N	0.488	0.055			
M	1.464	0.165	0.995	0.28	
	1.418 (3.1%)				0.00068

Table 14. Results of Example 3 Data Set 2

	TCE conc	max abs	$CHCl_3$ conc	max abs	SD
N			0.995	0.28	
M	1.464	0.165	0.995	0.28	
			0.742 (25.4%)		0.00055

response. In the mixture of example 1, the analytes TCE and $CHCl_3$ are present in the same amount as in the standards. Table 9 shows the results of the calibration. The relative prediction errors are low, and the SD value indicates a very good fit of the model. Hence, despite the similar response of the analytes TCE and $CHCL_3$, calibration is possible provided that a mixture behaves well: linear additivity should hold, and each analyte has to contribute to a certain extent to the signal in the mixture. The latter can be checked by comparing the maximum absorbance contribution of the analytes to the mixture. For both analytes this maximum was 0.24, indicating that both analytes contribute in the same order of magnitude to the overall absorbance of the mixture. The results of this example are better than the corresponding ones in part 2 (Table 2, part 2).[6]

Example 2. In this example, the real second-order challenge is obtained: the mixture contains an unknown interferent. This is important since it tests the ability of the method to calibrate in the presence of an unknown interferent. The results are reported in Table 10. The interferent has approximately the same contribution to the mixture response signal as the analyte. The quantitation for TCE is performed with a relative prediction error of 13.2%. Given the high overlap between the analyte and the interferent this error is very reasonable, also compared to an experimental error in the order of 3–4%. The prediction errors are of the same order of magnitude as in part 2 (Table 2, part 2).[6] The fit of the model to the data is good again.

An analogous case of predicting the concentration of TCE in the presence of the interferent $CHCl_3$ was performed in part 1.[5] This resulted in a prediction error of 105%. The difference between 13.2% on the one hand and 105% on the other hand clearly shows the second-order advantage of the restricted Tucker model approach.

Example 3. This example is the reverse of the previous one. Now TCE acts as an interferent and the results are reported in Table 11. The interferent in this example has a lower contribution to the mixture response signal than the analyte. The relative prediction error in the concentration of $CHCl_3$ is 13.7%. This error is reasonable, also compared with the error of the same calibration in part 2 (Table 2, part 2)[6] and an experimental error of 3–4%. The SD value is low, indicating a good fit of the model.

The error of predicting the concentration of $CHCl_3$ in the presence of TCE in part 1[5] is 42.7%. Example 3 clearly gives a better result.

Results for Data Set 2. *Example 1.* The setup of the calibration is the same as for the first example of data set 1.

The results of the calibration are shown in Table 12. The prediction errors are very low, and the predictions can be considered as being very good. The model fits the data very well.

Example 2. This example shows the second-order advantage: calibration of TCE in the presence of an unknown interferent ($CHCl_3$). Table 13 presents the result of this calibration. The prediction error of TCE in the mixture is very low (3.1%). The prediction is very good: on the order of magnitude of the experimental error. The model fits the data very well.

Example 3. In this example, TCE serves as the unknown interferent in a mixture also containing the analyte $CHCl_3$. Table 14 presents the result. The prediction error of $CHCl_3$ is higher than in example 2. This is because the two species being formed by $CHCl_3$ have very similar spectra (a cosine value of 0.99); this causes instability in the estimated model, especially in the **B** matrix. Since the model fits the data very well, the conclusion is that the error surface is rather flat in the neighborhood of the minimum error: relatively small changes in parameter values (e.g., the estimated concentration) do not change the error very much.

General Comments. The starting values of the algorithm for the unknown parts in **C** are important. Calculations have shown that different starting values give slightly different calibration results. Good starting values can perhaps be found using nonbilinear rank annihilation.[10] More research is needed in this area.

The problem encountered in example 3 of data set 2 can be circumvented by designing better algorithms. Such algorithms should be more robust to similarities in spectra (estimation of **B**) and time profiles (estimation of **A**).

In all the above examples, only one standard was used to quantitate for an analyte in a mixture. The restricted Tucker model approach can be augmented easily to support more than one standard. The results should be better when multiple standards that span a range of concentrations are used.

GENERAL CONCLUSIONS

A complete new class of calibration models is described for second-order calibration. It is shown with experimental data that quantitation of analytes in mixtures containing unknown interferences is possible. The restricted Tucker model approach makes it possible to develop fully selective reaction-based chemical sensors.

ACKNOWLEDGMENT

A.K.S. acknowledges a grant from the Netherlands Organization for Scientific Research (NWO) for his stay at the Laboratory for Chemometrics at the University of Washington. R.T. acknowledges the financial support from the DGICYT (Spain) for his stay at the Laboratory for Chemometrics at the University of Washington.

Received for review March 15, 1994. Accepted June 30, 1994.*

* Abstract published in *Advance ACS Abstracts,* August 15, 1994.

Anal. Chem. **1994,** *66,* 3352–3361

Submersible, Osmotically Pumped Analyzers for Continuous Determination of Nitrate in Situ

Hans W. Jannasch,* Kenneth S. Johnson, and Carole M. Sakamoto

Monterey Bay Aquarium Research Institute, 160 Central Avenue, Pacific Grove, California 93950, and Moss Landing Marine Laboratories, P.O. Box 450, Moss Landing, California 95039

A continuous flow analyzer powered by osmotic pumps has been developed to monitor nitrate concentrations while submerged in freshwater or seawater. Osmotic pumps driven by a NaCl gradient propel both sample and reagents through a miniature continuous flow manifold. The analyzer operates with sample and reagent flow rates of about 12 and 1 μL h^{-1}, respectively ($\approx$8 and 0.7 mL month^{-1}), shows a linear response from 0 to 20 μM nitrate with a detection limit of 0.1 μM, and has a 90% response time of approximately 30 min. The analyzer can automatically standardize itself by correcting for baseline and sensitivity drift by periodically injecting and analyzing known standard solutions. The system has operated continuously for month-long periods in freshwater and seawater and can be easily adapted to a variety of colorimetric analyses. Potential applications for this analyzer include environmental and oceanographic monitoring and process control.

Electrochemical sensors such as pH and oxygen electrodes[1] as well as newer technologies including solid-state ChemFET's,[2] fiber optical probes,[3,4] and biosensors[5] have been developed for monitoring dissolved compounds in aquatic environments. With few exceptions,[6] however, these sensors are still not stable nor sensitive enough for most long-term environmental monitoring requirements. Common difficulties associated with sensors are detector drift, the inability to self-calibrate, a lack of sensitivity and selectivity (especially in a seawater matrix), and the formation of organic films and biofouling on the sensor surface.

Environmental chemists are, therefore, still limited to the collection of samples followed by transport to the laboratory for analysis. This lack of chemical detectors for long-term environmental monitoring of dissolved chemicals poses a series of problems, including (a) the limited number of data points that can be obtained by conventional methods due to the effort, time, and expense associated with collecting and transporting samples in an appropriate manner; (b) the potential for sample contamination and alteration during sample transfer, transport, or storage; and (c) the lag time in obtaining the desired data.[7,8]

An approach which circumvents these issues is to adapt continuous flow analyzers to operate autonomously for extended periods. Chemical *analyzers*, where sample and reagents are pumped through a reaction manifold and detector, can determine analyte concentrations with well-proven irreversible chemistries. They differ from *sensors*, which are dependent on diffusion to transport the analyte onto or through an easily fouled surface and which generally require reversible chemistries. Continuous flow analyzers that can operate underwater have been used to measure concentrations of nutrient compounds, including nitrate and silicic acids[9–13] and trace elements[14,15] to depths of several thousand meters in the ocean. These submersible analyzers, however, use either peristaltic or piston pumps to propel both sample and reagents, which require significant quantities of power ($\sim$10 W) and reagents (>150 mL d^{-1}) when run in a continuous mode. The tubing in peristaltic pumps also requires periodic replacement. Such analyzers are, therefore, best suited for short-term, high-resolution spatial mapping of dissolved chemicals.

This lack of chemical sensors or analyzers that are capable of unattended long-term deployments has led us to begin developing an unsegmented continuous flow analyzer specifically for monitoring dissolved species in aquatic environments for longer times. Our initial results, shown in this paper, describe a chemical analyzer designed to operate while completely submerged for periods of 1 month or longer for the determination of dissolved nitrate. This system uses osmotic pumps[16] to propel both the sample and reagents through a microconduit, flow-injection-style manifold.[17] Nitrate is determined by reduction to NO_2 in the presence of a Cd surface, followed by reaction of the NO_2 to form an azo dye that is detected colorimetrically.[18] The system has a number of advantages, including (a) a system for automatic in situ calibrations using standards with known nitrate concentrations; (b) mechanical simplicity and ruggedness to ensure reliability; (c) minimal use of electrical power (<35 mW) to allow battery operation at remote sites; and (d) its relatively small size and

(1) Langdon, C. *Deep-Sea Res.* **1984,** *31,* 1357–1367.
(2) Wohltjen, H. *Anal. Chem.* **1984,** *56,* 87A–103A.
(3) Saari, L. A. *Trends Anal. Chem.* **1987,** *6,* 85–90.
(4) Barnard, S. M.; Walt, D. R. *Nature* **1991,** *353,* 338–340.
(5) Schultz, J. S. *Sci. Am.* **1991,** 64–69.
(6) Wallace, D. W. R.; Wirick, C. D. *Nature* **1992,** *356,* 694–696.
(7) Johnson, K. S.; Coale, K. H.; Jannasch, H. W. *Anal. Chem.* **1992,** *22,* 1065A–1075A.
(8) Dickey, T.; Marra, J.; Granata, T.; Langdon, C.; Hamilton, M.; Wiggert, J.; Siegel, D.; Bratkovich, A. *J. Geophys. Res.* **1991,** *96,* 8643–8663.
(9) Johnson, K. S.; Beehler, C. L.; Sakamoto-Arnold, C. M.; Childress, J. J. *Science.* **1986,** *231,* 1139–114.
(10) Johnson, K. S.; Beehler, C. L.; Sakamoto-Arnold, C. M. *Anal. Chim. Acta* **1986,** *179,* 245–257.
(11) Johnson, K. S.; Childress, J. J.; Hessler, R. R.; Sakamoto-Arnold, C. M.; Beehler, C. L. *Deep-Sea Res.* **1988,** *35.* 1723–1744.
(12) Johnson, K. S.; Sakamoto-Arnold, C. M.; Beehler, C. L. *Deep-Sea Res.* **1989,** *36,* 1407–1413.
(13) Taylor, C. P.; Howes, B. L.; Doherty, K. W. *Mar. Technol. Soc. J.* **1993,** *27,* 32–44.
(14) Coale, K. H.; Chin, C. S.; Massoth, G. J.; Johnson, K. S.; Baker, E. T. *Nature* **1991,** *352,* 325–328.
(15) Chin, C. S.; Johnson, K. S.; Coale, K. H. *Mar. Chem.* **1992,** *37,* 65–82.
(16) Theeuwes, F.; Yum, S. I. *Annu. Biomed. Eng.* **1976,** *4,* 343–353.
(17) Ruzicka, J.; Hansen, E. H. *Anal. Chem.* **1984,** *173,* 3–25.
(18) Stickland, J. D. H.; Parsons, T. R. *A Practical Handbook for Analysis of Seawater;* Fisheries Board of Canada: Ottawa, 1972.

0003-2700/94/0366-3352$04.50/0
© 1994 American Chemical Society

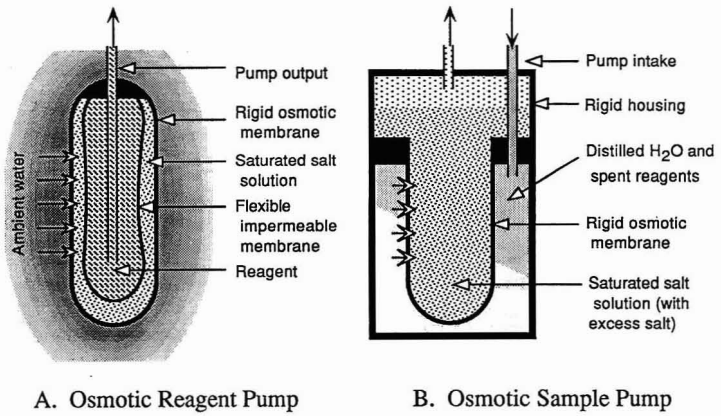

Figure 1. Fluid flow in an osmotic pump is driven by the osmotic pressure differential developed across the semipermeable membrane separating a saturated brine from a solution with a lower salinity. The net flow of water diffusing across the semipermeable membrane results in reagents being propelled out of a reagent pump (A) and liquids being drawn into a sample pump (B).

cost. Although this work focuses on the determination of nitrate, the analyzer can be easily adapted to other chemistries.

EXPERIMENTAL SECTION

Apparatus. (A) Osmotic Pumps. Flow within an osmotic pump is caused by the osmotic pressure created across a rigid semipermeable membrane separating a saturated salt solution from a solution of lower salinity[16] (Figure 1A). The diffusion of water through the membrane results in a net flow from the dilute to the more saline solution. This flow of water through the rigid membrane then squeezes a flexible impermeable bag containing the reagents to be pumped, driving a reagent flow. Flow rates are dependent only on the membrane (area, thickness, and porosity), the osmotic pressure gradient, and the diffusion coefficient of water, which depends primarily on temperature. The osmotic pressure is maintained throughout a pump's life by keeping the brine solution saturated with an excess quantity of salt. In practice, variations in flow rates of osmotic pumps are predominantly dependent on temperature and are further discussed below. The inherent simplicity of osmotic pumps make them an excellent replacement for electromechanical pumps in autonomous chemical analyzers that will be used for extended time periods in harsh aquatic environments and where high response rates are not essential.

We used commercially available osmotic pumps (Model 2ML4 from Alza, Inc.) with flow rates of about 1 μL h^{-1} at 20 °C to add reagents to the flow stream. In order to pull the sample into and through the analyzer, we modified Model 2ML1 Alza pumps with flow rates of ~4 μL h^{-1} at 20 °C (nominal flow rates are 10 μL h^{-1} at 37 °C) by removing the inner bag and mounting the rigid permeable membrane in an enclosed volume (sample pump, Figure 1B). The upper and lower compartments are filled with a saturated brine solution and distilled water, respectively. When water begins flowing across the membrane, the under-pressure created in the lower compartment draws the sample and reagents into and through the analyzer. Sample pump flow rates must equal the combined flow rate of the reagent pumps plus the desired flow rate of sample. Our sample pumps, therefore, usually contain at least four 2ML1 membranes for a total flow rate of at least 12 μL h^{-1} at 20 °C. A further optional modification includes using a flexible impermeable membrane to contain the saturated brine and to avoid losing salt to the environment.

The endurance of osmotic pumps is limited by the volumes of the osmotic agent and the reagent bags. Alza 2ML4 pumps used to propel reagents have a 2-mL internal volume and lifetimes of about 10 weeks at 20 °C. Our sample pump modifications increased their internal volume to ~100 mL, which increases their lifetime from about 2 weeks for unmodified 2ML1 pumps to about 1 year at flow rates of ~12 μL h^{-1}. Similar modifications can also increase the lifetime of the reagent pumps.

(B) Flow Manifold and Detector. A schematic of a nitrate analyzer manifold and the associated osmotic pumps is shown in Figure 2. Reagent pumps deliver chemicals to the sample stream pulled along the analyzer's flow path by the sample pump. The determination of nitrate requires three reagent pumps as well as an in-line cadmium-reducing surface. An analyzer with a four-membrane sample pump pulling in 12 μL h^{-1} draws 9 μL h^{-1} of sample through its intake, with three 1 μL h^{-1} reagent pumps connected to the manifold.

In order to obtain reasonable response times at the low flow rates of osmotic pumps, the volume of the flow path must be kept to a minimum. Miniature flow manifolds were made by using microconduits similar to those described by Ruzicka and Hansen.[17] This technique involves cold-forging PVC by pressing a wire (0.5 mm) that has been bent in the shape of the desired flow path into the surface of a flat-milled sheet (4 × 8 × 1 cm) of rigid PVC (Figure 3). For nitrate analyses, we insert a disk of solid cadmium (2 mm thick by 10 mm diameter) into the PVC plate before milling. The wire is bent into a sinusoidal shape where it contacts the Cd to allow the sample a reaction time long enough to achieve a >95% nitrate reduction efficiency. After removal of the wire, 0.5-mm holes are drilled through to the back of the plate for connections to the sample intake tube, the reagent and sample pumps, and

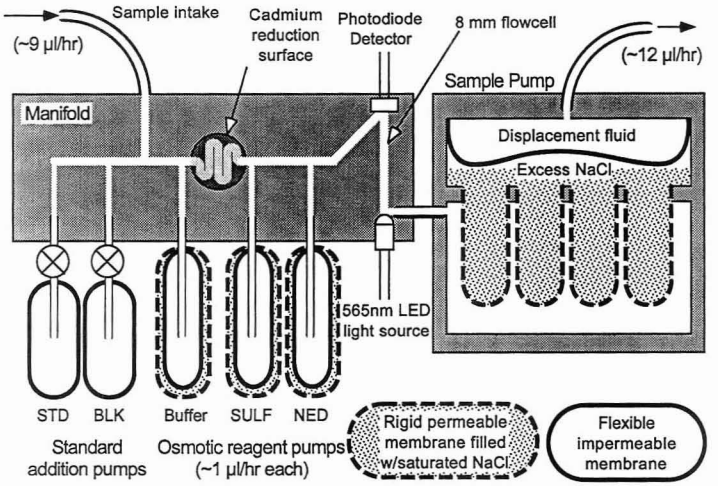

Figure 2. Schematic of an osmotically pumped nitrate analyzer (see text for further description).

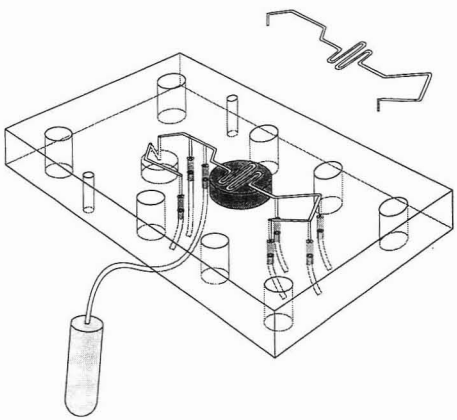

Figure 3. Microconduit reaction manifold. The manifold is forged by pressing a wire (shown at top right) into the surface of a flat-milled sheet of PVC previously fitted with a Cd disk. Connections are made through the back of the plate. One Alza osmotic pump is shown for clarification.

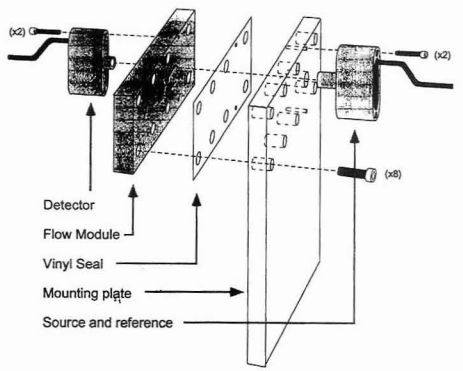

Figure 4. Assembly of the osmotic analyzer. The manifold is sealed by screwing it to an acrylic mounting plate with a 0.4-mm vinyl gasket. The LED light source and the photodiode detector are attached directly to the ends of the flow cell, which is perpendicular to the forged flowpath.

the detector flow cell. Tubing is connected to the manifold by tapping the holes on the backside with a no. 10–32 thread and using an O-ring compressed under a nut to seal the tube. The front of the flow manifold is sealed with a 0.4-mm vinyl sheet held firmly in place by a rigid sheet of clear acrylic (Figure 4). This design allows visual inspection of the flow path, easy dismantling for cleaning, and rapid reproducible fabrication.

The nitrate analyzer uses a simple LED/photodiode detector[19] to determine the concentrations of the azo dye. To further minimize the internal volume of the analyzer, the 0.5 by 8 mm detector flow cell is bored directly into the manifold perpendicular to the plane of the forged flow path.[17] An ultrabright green LED (Hewlett-Packard HLMP-3950) with a 565-nm peak emission wavelength and a broadband photodiode (Hamamatsu, G1118) are used as the light source and detector, respectively, and are mounted directly on the ends of the flow cell (see Figure 4). A reference photodiode is also located next to the LED to monitor any intensity changes. The output signals of the two photodiodes are converted to voltages and amplified using a simple op-amp circuit.[19] These current to voltage circuits are located directly adjacent to the photodiodes to reduce noise. The optical components, as well as the current to voltage circuits, are potted with polyurethane (Fluid Polymer Systems; HMP 85-1-ic). The amplified signal is digitized and stored by a datalogger contained in a separate water-tight housing.

The output signal of the sample photodiode is proportional to the percent of transmittance (%T) and gives a near-zero

(19) Betteridge, D.; Daglass, E. L.; Fields, B.; Graves, N. F. *Analyst* **1978**, *103*, 897–908.

signal with the LED turned off. The maximum detector signal is adjusted by regulating the LED current with distilled water in the flow cell. The signal is digitized with a 12-bit A/D converter (4096 counts of resolution).

(C) Standard Addition Micropumps. Automatic calibration is required to correct for detector drift and changes in reagent stability over extended periods of time. Hydrodynamic injections[20] are used to periodically add standard solutions with known concentrations of nitrate into the flow stream (see Figure 2). Solenoid-operated micropumps (The Lee Co.; LPLA0520050L) inject standard solutions into the sample stream by back-flushing the intake tube from a "T" on the manifold upstream of where the reagents are added. The standard solutions flow out of the sample intake because the system downstream of the "T" is a closed volume. These pumps deliver 50 μL/stroke of the solenoid, which is more than enough to completely flush the intake tube with the standard. The resulting standard slug remaining in the intake tube is then drawn into the manifold and analyzed in the same manner as the sample. The length of the intake tube determines the volume of standard to be analyzed and the duration of the standard signal. We use an 8 cm by 0.5 mm i.d. intake tube, which requires about 2 h for the standard to pass completely through the detector cell at 20 °C.

The present analyzer is equipped with two standard addition pumps (blank and standard) for a two-point calibration. The pumps are contained in an oil-filled pressure compensated container to isolate them from ambient water. The intake is attached to a collapsible bag filled with standard or blank, and the output is connected to the reaction manifold. The frequency of standard additions is regulated by the software programmed into the datalogger.

(D) Control and Datalogging Electronics. The osmotic analyzer is controlled by a low-power electronics package. We use a TattleTale programmable datalogger (Onset Computer Corp. Model 4a) that powers the LEDs, digitizes the photodiode signals, logs the data, and activates the standard addition pumps. This datalogger has a Hitachi 6303 microprocessor, 16 I/O channels, and a 12-bit A/D converter connected to an eight-channel multiplexer. A custom-made signal conditioning board was designed to control the LEDs and standard pumps.

The software can control the analyzer in both a real-time interactive mode and in a low-power data logging mode. During logging, the controller powers the LED for 5 s, digitizes the outputs of the sample and reference photodiodes, and stores the data in 512 KB of static RAM before going into a low-power sleep mode. This cycle is repeated every 2 min.

Reagents. The chemistry is based on the well-proven colorimetric nitrate method,[18,21] where dissolved nitrate is reduced to nitrite on a copperized cadmium catalyst, followed by the production of an azo dye by reaction of nitrate with *p*-aminobenzenesulfonamide (sulfanilamide) and *N*-(1-naphthyl)ethylenediamine dihydrochloride (NED). The three reagents used for nitrate determinations are an imidazole buffer (0.681 g of imidazole and 0.19 mL of concentrated HCl in 100 mL of deionized water), an acidified sulfanilamide reagent (1.0 g of sulfanilamide and 10 mL of concentrated HCl in 100 mL of deionized water), and an NED solution (0.1 g of NED in 100 mL of deionized water). Working nitrate and nitrite standards are prepared by the dilution of 10 mM $NaNO_3$ and $NaNO_2$ solutions in deionized water.

The Cd surface was initialized by successively gravity feeding the following solutions through the manifold at approximately 0.5 mL min^{-1} for 5 min each: (a) 10% HCl; (b) the imidazole buffer; (c) a 1 + 1 (v/v) mixture of a 2% $CuSO_4 \cdot 5H_2O$ (80 μM) solution and imidazole buffer; and (d) the imidazole buffer again. Care was taken to prevent any air from entering the column during or after initialization to avoid premature oxidation of the copperized cadmium surface. All solutions and reagents were also degassed under vacuum to eliminate potential bubble formation within the analyzer.

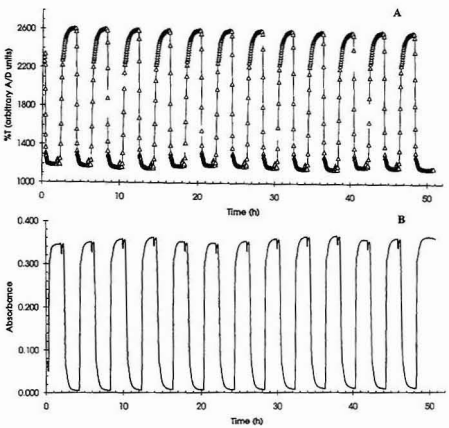

Figure 5. Alternating 0 and 20 μM nitrate standards as measured by the osmotically pumped nitrate analyzer over 48 h. The top panel (A) shows the raw data (A/D counts proportional to %*T*) with a 2-min interval. The absorbance (B) is calculated from the same raw data.

RESULTS

The analyzer was initially operated while submerged in a 40-L aquarium filled with deionized water kept at room temperature (20 ± 2 °C). At this temperature, freshly filled Alza reagent pumps and our sample pumps require about 2 days before pumping smoothly. After all the pumps are operating properly, they are connected to the manifold. The analyzers must then equilibrate overnight to allow the reagent to fill the manifold. Figure 5 shows the analyses of alternating solutions of 0 and 20 μM NO_3, which are plotted as both raw data (A/D counts proportional to %*T*) and the calculated absorbance. The absorbance (A) was calculated from the A/D counts of the sample (C_{SAM}) and distilled water (C_{BLK}), where the absorbance $(A) = -\log(C_{SAM}/C_{BLK})$. A constant value for C_{BLK} was used to calculate the entire record. The analyzer gave reproducible results, where the absorbances of 12 replicate 0 and 20 μM NO_3 injections over a 48-h period of operation were 0.000 ± 0.001 (±1 standard error) and 0.353 ± 0.005 or <1.5%.

Response Times. Response times of the analyzers were determined from the rate of change in signal when step changes

(20) Ruzicka, J.; Hansen, E. H. *Flow Injection Analysis*, 2nd ed.; Wiley: New York, 1988.
(21) Brewer, P. G.; Riley, J. P. *Deep-Sea Res.* **1965**, *12*, 765–772.

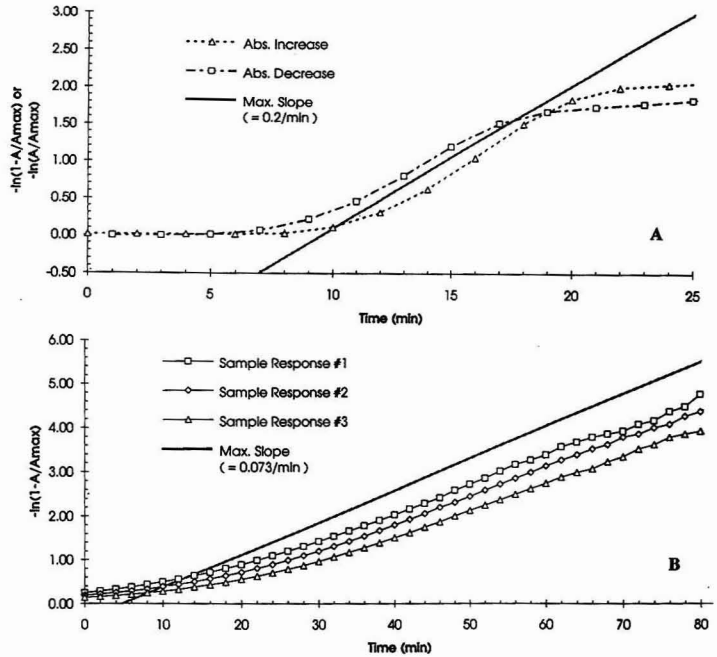

Figure 6. ln $(1 - A/A_{max})$ and ln (A/A_{max}) vs time is plotted for concentration transitions from 0 to 20 and from 20 to 0 μM NO_3, respectively. Maximum slopes of these plots correspond to a 63% (1 – 1/e) response time of about 5 min for standard injections (A) and 13 min for samples (B).

of nitrate concentrations (0–20 and 20–0 μM) were introduced by standard injections. We assumed an exponential response for the absorbance signal, where $A = A_{max}(1 - e^{-kt})$ for an increasing absorbance, and $A = A_{max}(e^{-kt})$ for a decreasing absorbance. A_{max} is the absorbance of the 20 μM NO_3 standard, k is the response rate (min^{-1}), and t is the time (min). At 20 °C, the slopes of ln (A/A_{max}) and ln $(1-A/A_{max})$ vs time plots (k) are about 0.2 min^{-1} when 0 and 20 μM NO_3 standards were injected (Figure 6A). This corresponds to a 63% (1 – 1/e) standard response time of about 5 min and a 90% response time in 12 min.

Samples, however, enter the analyzer through the intake tube and travel further than do interfaces between standards (which are formed at the "T" on the manifold). A concentration gradient in the sample will therefore have a longer time to smear by diffusion than injected standards. This results in longer sample response times. With a 8 cm by 0.5 mm i.d. intake tube (~16 μL), the sample response time calculated in the same way as described above is about 13 min to attain a 63% signal, corresponding to a 90% response time of less than 30 min (Figure 6B). These response times can be decreased by shortening the intake tube and minimizing dead volumes but will increase at lower temperatures.

Standard Curve. The standard curve for the nitrate analysis determined from 0 to 20 μM nitrate standards is

$$NO_3\ (\mu M) = (-0.11 \pm 0.07) + (56.7 \pm 0.5)A$$

where the coefficient of determination (r^2) is 0.998 and the errors are calculated as ±1 standard error (Figure 7A). Figure 7B shows an enlargement of the 0–5 μM data with the same linear regression line passing through the data.

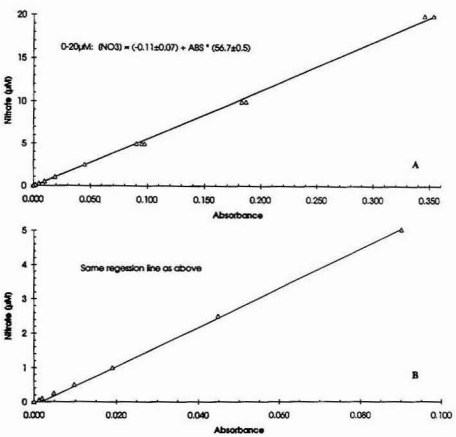

Figure 7. Standard curve for the osmotically pumped analyzer from 0 to 20 μM nitrate. Also shown is the enlargement of the 0–5 μM portion of the data. The least-squares fit of the data is NO_3 (μM) = $(-0.11 \pm 0.07) + (56.7 \pm 0.5)A$, $r^2 = 0.998$.

The slope of the standard curve, 56.7 μM, is similar to the predicted value from Beer's law. The absorption of the nitrite azo dye at 565 nm (the dominant emission of the green LED)

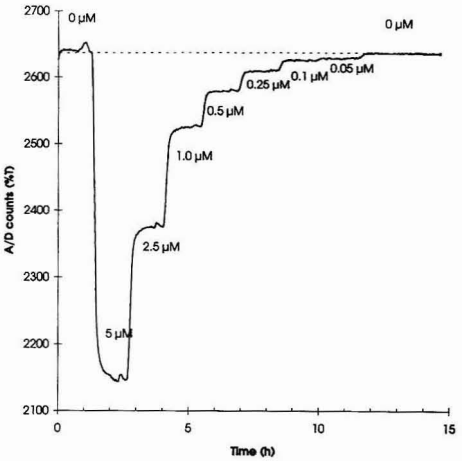

Figure 8. Raw data (A/D counts proportional to % T) obtained during the analysis of NO_3 standards from 0 to 5 μM.

is approximately 69% of the value at 540 nm (the peak absorbance of the azo dye). Assuming that the molar absorptivity (ϵ) has a similar ratio for the two wavelengths, ϵ_{565nm} is calculated as 32 026 L mol^{-1} cm^{-1} or 69% of ϵ_{540nm} (46 000 L mol^{-1} cm^{-1}).[22] Given an 0.8-cm optical path length and a sample dilution of 0.75 (9 μL h^{-1} sample in 12 μL h^{-1} total sample and reagents flowing through the flow cell), the slope of the calibration line should be

$$\text{slope } (\mu M) = \frac{10^6\ \mu\text{mol mol}^{-1}}{32\,026\ \text{L mol}^{-1}\ \text{cm}^{-1} \times 0.8\ \text{cm} \times 0.75} = 52.0\ \mu M$$

The difference between this calculated value and the 56.7 μM slope shown in Figure 7 is <8% and is probably due to errors in path length (±0.2 mm) and deviations of ϵ_{565nm} due to the bandwidth of the LED.

Detection Limit. Figure 8 shows the detector response for a series of NO_3 standards at concentrations <5 μM. This figure demonstrates that the analyzer is capable of resolving an 0.05 μM NO_3 concentration with a signal-to-noise ratio of about 5:1. The fluctuations in the data just before each standard change are due to pressure pulses caused by the injections of the standard. The real detection limit, however, depends on the long-term stability of the baseline. We estimate it as three times the standard deviation of the 12 blank determinations analyzed over 48 h after the baseline was corrected by a linear interpolation between the first and last blank analyses (Figure 5). This gives a detection limit of about 0.11 μM NO_3 if the analyzer is standardized every 2 days.

Month-Long Record. An analyzer was fully submerged in a 40-L aquarium and run continuously for 1 month without physical intervention. Figure 9A shows the raw data (>24 000 data points) consisting of the analyses of a series of 20 and 0 μM NO_3 standards with tank water analyses in-between. During the first 4 days, standards were added every 4 h, with blanks following 2 h later, and no tank water was analyzed. As the experiment progressed, the interval between the standard and blank injections was lengthened, and the analysis of the tank water is shown in-between. The erratic data at the end of the 4-month record occurred when the reagent pumps expired.

The uncorrected absorbance of blank injections rose steadily over the full month from 0.000 to 0.070, which corresponds to a baseline drift of ~15% relative to a 20 μM signal (0.354). This baseline drift could be caused by either the slow color formation in the NED reagent or the dye precipitating in the flow cell. The analyzer's sensitivity (the absorbance difference between the 0 and 20 μM signals) is reduced by about 15% (from 0.354 to 0.291) over the same time. This decrease in sensitivity was potentially a result of either the slow decay of the nitrate standard or the efficiency of the Cd reduction surface. The baseline drift and change in sensitivity are accounted for in Figure 9B, where nitrate concentrations are calculated using only one calibration point at each end of the record (arrows represent the calibration times). The standard error of the concentrations obtained for the 20 μM NO_3 standard, which was treated as an unknown at times between the two calibrations, was about 1.6 μM (8%). This error was reduced to 0.4 μM (2%) when the signal was calibrated weekly (Figure 9C, arrows represent the calibration times). Concentrations at all points between the calibrations were obtained by linear interpolation of the baseline and slope of the calibration curves.

The NO_3 concentrations in the tank were raised and lowered during the experiment. The aquarium NO_3 concentrations started at 10 μM and were lowered by adding a bag of activated charcoal to the filtering system attached to the aquarium. Concentrations were raised by slowly pumping a 50 mM standard solution into the tank. The results of these concentration changes can be seen in Figure 9 between the standard analyses. The accuracy of the analyzer measurements of NO_3 in the tank water were validated by analyses of discrete samples collected from the aquarium. The results of these discrete measurements are also shown on Figure 9B,C (as diamonds). The standard deviation of the concentration differences between the discrete samples and the values determined by the osmotic analyzer is 0.3 μM using either the monthly or weekly calibrations.

Seawater Analysis. The analyzers have also been successfully tested in seawater. An analyzer was submerged to a depth of 8.5 m in the 500 000-L kelp tank of the Monterey Bay Aquarium. This tank is completely flushed with fresh seawater from Monterey Bay every 90 min, and trends in nitrate concentrations within the tank follow those of the Bay. The record (Figure 10A) shows calculated nitrate concentrations in the kelp tank interspersed with periodic 25 μM NO_3 standards and blanks similar to those in the 1-month freshwater record. Nitrate concentrations determined on discrete samples agree well with the analyzer data (Figure 10A, diamonds).

The nitrate concentrations are, as expected, inversely proportional to the seawater temperature (Figure 10B). This NO_3 vs T inverse relationship is well known and is caused

(22) Grasshoff, K.; Ehrhardt, M.; Kremling, K. *Methods of Seawater Analysis*, 2nd ed.; Verlag Chemie: Weinheim, Germany, 1976; Chapter 9.

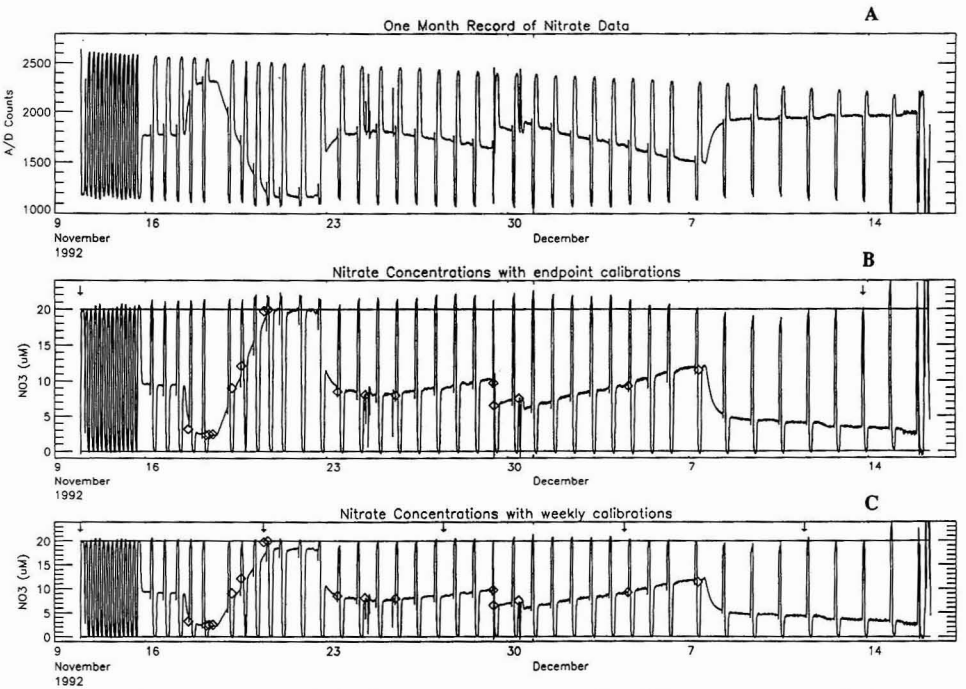

Figure 9. One-month record of the detector signal and calculated NO_3 concentrations obtained with the osmotic analyzer fully submerged in a 40-L test tank. The panels show (A) the raw data (A/D counts proportional to % *T*), nitrate concentrations calculated (B) with only monthly (2) calibrations (arrows) and (C) with weekly (5) calibrations. Nitrate concentrations determined from discrete samples analyzed by standard methods are also shown (diamonds).

by the mixing of cold deep waters enriched in nitrate with warmer surface waters which have been depleted of nitrate by phytoplankton. On a finer scale, however, nitrate concentrations show fluctuations which cannot be explained merely by temperature. These variations are seen as scatter or a nonlinearity in the NO_3 vs temperature relationships. They are of great interest in oceanography and are likely caused by biological activity consuming or excreting excess nitrate.

Temperature Dependence. Flow rates produced by osmotic pumps are temperature dependent and are a function of the diffusion coefficient of water. The flow rate equation for the Alza 2-mL pumps is given by

$$Q_T = Q_o(0.141 \times e^{0.051T} - 0.007\pi + 0.12)$$

where Q_T is the pumping rate at temperature T, Q_o is the specified pumping rate at 37 °C, π is the osmolality of the outside solution from 0 to 25 atm, and T is the temperature (in °C) from 4 to 42 °C.[23] Flow rates measured in our lab agreed well with calculated values, which are about 43% at 20 °C and 21% at 5 °C of the nominal flow rate at 37 °C. Ambient temperatures, therefore, have a significant effect on the reagent and sample flow rates.

Our design minimizes this temperature effect by using only membranes with the same flow rate coefficient. If both the reagent and sample pumps within an analyzer warm and cool simultaneously, then the sample and reagents will still be mixed in the same proportions regardless of temperature. The sample and reagent concentrations in the reaction manifold should therefore remain essentially constant.

Secondary temperature effects may occur if the pump housings and the solutions they contain have a different thermal expansion coefficient, or with rapid temperature changes, where the pump housing and their solutions expand or contract at different rates. The pump housings are made of cast acrylic, which was chosen because it has a volumetric expansion coefficient similar to that of water. A warming of the sample pump, for example, will first cause the 92-mL intake chamber of the housing to swell, resulting in volume increases of 17 μL °C^{-1} for the acrylic housing the 19 μL °C^{-1} for the contained water. If the solutions and pump housings change temperature at the same rate, they should experience only a net 2 μL °C^{-1} change. If thermal cycling is slow enough, this volume change results in a net flow rate change significantly smaller than the nominal flow rate of the pump, and the analyzer should be relatively immune to the originating temperature variations.

(23) *Alza Technical Information Manual*; Alza Corporation: Palo Alto, CA, 1989; p 11.

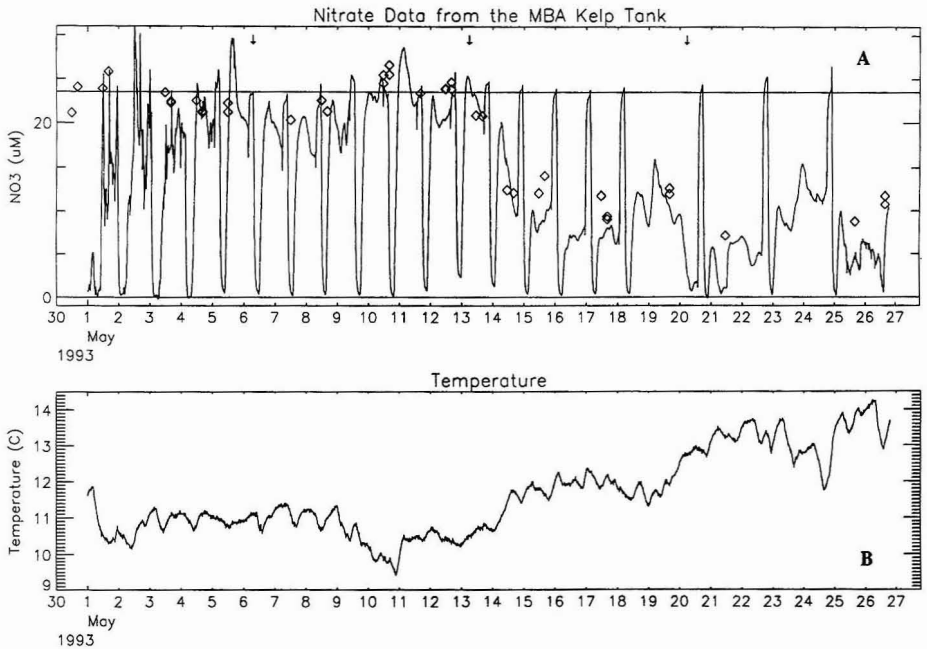

Figure 10. One-month record of calculated NO_3 concentrations and water temperature obtained with the analyzer submerged in the kelp tank of the Monterey Bay Aquarium. Nitrate concentrations determined from discrete samples analyzed by standard methods are also shown (diamonds).

More rapid ambient temperature changes, on the other hand, may cause a thermal disequilibrium between the pump housing and solution. Such temperature fluctuations may cause oscillations of the pump's flow rate due to the external pump housing expanding or contracting more rapidly than the solution inside. For example, the warming of the same pump described above will first cause the 92-mL housing to swell 17 μL °C^{-1}, resulting in an increase of the intake flow rate depending on the temperature rise time and the rate of thermal transfer. If the enclosed fluid warms more slowly, the intake flow rate decreases by a net volume of 19 μL °C^{-1}. These phase-shifted temperature changes, therefore, result in temporal variations in flow rate. Since these flow rate responses differ between the reagent and sample pumps (the much larger pumps being more sensitive due to their larger volume and longer thermal equilibration time), the sample and reagent may not be mixed in the proper proportions, resulting in spurious signals.

The effect of temperature can be reduced by several methods including (a) insulating the whole analyzer to reduce the temporal thermal gradients to an acceptable level; (b) designing sample and reagent pumps with more similar thermal responses; and (c) increasing the sample flow rate so that the flow rate changes have less on an effect. The effects of increasing the sample flowrate on the signal artifacts caused by temperature changes are shown in Figure 11. Lines A–C show the fluctuations in absorbance of a 20 μM nitrate solution as detected by analyzers with sample pump rates of 12, 24, and 36 μL h^{-1}, respectively. The temperature was changed in 1.0, 0.5, and 0.25 °C steps over 2-h periods (Figure 11). These data show that the signal artifacts due to temperature fluctuations are reduced with larger sample pump flow rates.

Temperature fluctuations were not a serious problem in our relatively well-controlled aquarium in the lab ($dT/dt \leq 2$ °C d^{-1}), although some of the variability in Figure 5A may be temperature related. Temperature may likely cause more of the signal fluctuations found in the kelp tank record.

Chemical Stability. An important aspect of operating long-term analyzers is the stability of the reagents, catalysts, and standards. In the case of NED, a working strength solution may oxidize to a visibly brown color within 1 week at room temperature. We noticed, however, no significant deterioration in either color or ability to produce the azo dye when the reagent was stored in a pump over periods of 1 month, even at 20 °C, as long as the pump was kept out of direct light and the reagent was vacuum-degassed before filling the pump.

Similarly, we were able to avoid significant decay in the nitrate standards by vacuum-degassing the solution before filling the standard bags and keeping the insides of the bags and pumps as clean as possible. For seawater standards, low-nutrient seawater was filtered to 0.45 μm and microwaved to just below boiling conditions for 10 min before the addition of NO_3. Significant care was taken when refilling the pump bags to avoid contamination by nitrate-consuming organisms.

The cadmium reduction surface showed <15% deterioration in its capacity to reduce nitrate to nitrite for the month-long time periods of running freshwater samples. The only problems

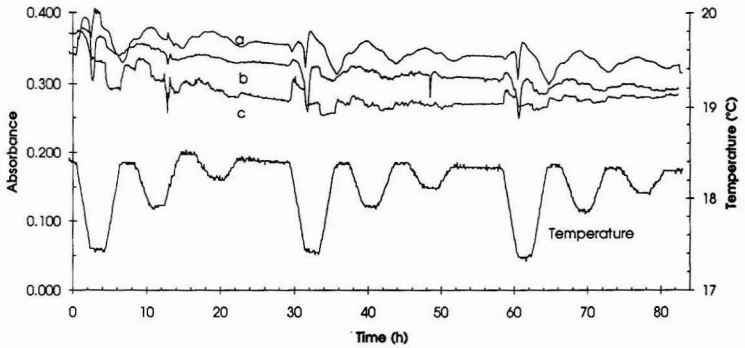

Figure 11. Effect of temperature variations on analyzer performance for three analyzers with sample pump rates of 12(a), 24(b), 36(c) μL h^{-1} sampling a 20 μM nitrate solution. The temperature was cycled in 1.0, 0.5, and 0.25 °C steps over 2-h periods.

were created when extreme temperature jumps produced flow reversals that caused the acidic sulfanilamide reagent to backwash over the Cd and thereby desorb the Cu from the surface.

DISCUSSION

Miniaturization of CFA. The low flow rates of osmotic pumps allow a continuous flow analyzer to operate for extended periods of time without using large quantities of reagents. A pump operating at 12 μL h^{-1} consumes only 8 mL month^{-1}. These slow flowrates, however, also require a significant miniaturization of the flow path to permit reasonable response times. Theoretical limits to miniaturization have been discussed previously.[24] The limits are bounded by a flow path diameter of 0.2 mm due to flow restriction, diffusive mixing, and the volume of liquid required by a detector. We used a flow path diameter of 0.5 mm, which is both small enough to allow reasonable response times and large enough to avoid clogging of the flow stream by natural particles. This diameter also allows sufficient light for an ultrabright green LED to reach the photodiode so that the detector electronics are not limiting precision.

The 0.5-mm flow path diameter and the 12 μL h^{-1} total flowrate used in most of the work presented here yield a theoretical response time of ~10 min, which is based on the time required to flush the 8-mm flow cell assuming plug flow. In practice, however, the detector responds to 90% of a step change in concentration in about 13 min. The longer response time that we observed is probably due to dispersion of the gradient between the standards and the sample that is driven by molecular diffusion as the solution flows through the manifold.

A delay time proportional to the total volume of the intake tube and manifold must also be accounted for. We find that the analyzers have a delay time of about 2 h at 20 °C and 3 h at 10 °C. The sample has about 10 min to react with the last reagent (NED) before entering the flow cell, which is the maximum time required for full color development.[18]

Other Chemistries. Although we were initially concentrating on the determination of nitrate, the analyzer can be adapted to other chemistries. Many reliable and proven methods exist for the detection of environmentally important compounds, which are based on simple, colorimetric reactions. Other types of detectors (including spectrophotometric, fluorimetric, or electrochemical detectors) could also be incorporated into the osmotic analyzer.

The major consideration for adapting other analyses to the osmotic analyzer is the long-term stability of the reagents and standards. Many dissolved reagents are highly sensitive to light and oxygen over longer time frames at the dilute concentrations required in chemical analyses. Thorough reagent and standard stability tests will, therefore, be needed for all long-term chemistries. These tests must also account for the environments the analyzers are to be used in (e.g., temperature).

Similarly, any catalyst or solid reactant must also be stable over the lifetime of the analyzer. In the case of the cadmium surface used for the reduction of nitrate, potential enhancements can include enlarging the Cd surface for operation in colder waters (where there reduction capacity is significantly reduced),[25] using a Cd/Cu alloy in place of the copperized Cd surface,[26] or putting a Cu surface ahead of the Cd catalyst in the manifold[27] to increase its longevity.

The long-term stability of standards must also be accounted for and is especially important for labile compounds in the dilute solution. Nutrients such as nitrate are easily degraded by bacteria and should be sterilized for long-term use. Work by Aminot and Kerouel[28] have shown that NO_3 and PO_4 standards in seawater degrade by <1.2% after 14 months of storage at room temperature following autoclaving at 125 °C for 20 min. Similar stabilities over the required time frames must be shown for other standards.

Biofouling. Biological growth within the analyzers during long-term deployments in natural waters has the potential of interfering with the analysis. During tests conducted so far in both fresh and seawater, however, biofouling does not seem to be a problem. Although algae and barnacles have been observed growing on the outside of the analyzer, the comparison

(24) van der Linden, W. E. *Trends Anal. Chem.* **1987**, *6*, 37–40.

(25) Nydahl, F. *Talanta* **1976**, *23*, 349–357.

(26) Hydes, D. J.; Hill, N. C. *Estuarine Coastal Shelf Sci.* **1985**, *21*, 127–130.

(27) van Staden, J. F.; Joubert, A. E.; van Vliet, H. R. *Fresenius Z. Anal. Chem.* **1986**, *325*, 150–152.

(28) Aminot, A.; Kerouel, R. *Anal. Chim. Acta* **1991**, *248*, 277–283.

of discrete samples shows that this growth does not result in a noticeable effect on the osmotic analyzer. This suggests that the analyzers are immune to internal biofouling for at least the time frames the analyzers have been deployed so far. This does not rule out potential effects of biofouling during longer deployments, on the analyzers in areas with higher levels of algal and bacterial growth, or with other chemistries. One potential solution to internal fouling of the analyzer is the addition of poisons to the blank or standard solutions, which periodically flush the intake tube during calibrations.

CONCLUSIONS

An osmotically pumped continuous flow analyzer has been developed to continually monitor dissolved chemical species in aquatic environments. The analyzer is designed to be completely submersible and should function at any ambient pressure. The inherent simplicity and small size of osmotic pumps allow the analyzers to be used to continually monitor dissolved chemicals at remote sites for limnological, estuarine, and oceanographic studies.

With flow rates of 12 μL h^{-1} and a flow path diameter of 0.5 mm, the analyzer has a 90% response time of less than 30 min, which is rapid enough for many environmental monitoring situations and for studying aquatic processes with diel time scales or slower. Data collected in the Monterey Bay Aquarium kelp tank shows that the analyzer can be used in the field and can monitor rapidly changing natural nitrate concentrations with time scales less than 1 h.

Although the analyzers were designed for environmental monitoring, they should also be useful for many other applications including industrial process control. Their main advantages over collecting samples from the field and running laboratory analyses include higher data densities at a greatly reduced cost, minimal contamination potential, near real-time data feedback, and long-term fully automated data collection.

ACKNOWLEDGMENT

We are grateful to Ed Mellinger for designing the electronics, to Luke Coletti for building the dataloggers and writing the software, and to Clarisa Peer of Alza Corp. for her generous advice on osmotic pumps. Funding was supplied by MBARI Project S-213 and ONR Grant N00014–89–J–1070. This article is MBARI contribution JA94-98.

Received for review November 15, 1993. Accepted June 30, 1994.[⊗]

[⊗] Abstract published in *Advance ACS Abstracts,* August 1, 1994.

Anal. Chem. **1994,** *66,* 3362–3370

This Research Contribution is in Commemoration of the Life and Science of I. M. Kolthoff (1894–1993).

Raman Spectroscopy of Covalently Bonded Alkylsilane Layers on Thin Silica Films Immobilized on Silver Substrates

Wade R. Thompson and Jeanne E. Pemberton*

Department of Chemistry, University of Arizona, Tucson, Arizona 85721

Results are presented which demonstrate the use of Raman spectroscopy for the characterization of alkylsilane layers covalently bound to silica surfaces. Raman spectra of molecular assemblies of octadecylsilane have been studied by use of a thin silica gel/Ag sandwich structure as the substrate. The Ag surface, used to provide electromagnetic enhancement to the octadecylsilane overlayer, is modified with a monolayer of (3-mercaptopropyl)trimethoxysilane, which is used as a molecular adhesive for anchoring the thin silica gel film. Spin coating a silica sol on the modified Ag surface results in the formation of a thin silica gel layer which contributes minimal fluorescence background to the Raman spectra. The spectral data have been interpreted in terms of the alkyl chain conformation within a layer of octadecylsilane, used as a model of a reversed-phase chromatographic stationary phase, on dry silica surfaces as well as in the presence of solvents commonly used in chromatography. The Raman data from the ν(C–C) and ν(C–H) spectral regions suggest that the alkyl chains comprising the layer are predominantly in an ordered configuration. These data represent the first Raman spectra reported for alkylsilane layers on oxide surfaces and demonstrate the feasibility of acquiring conformational information from alkylsilane layers covalently bound to silica surfaces.

A number of oxide surfaces such as silica, alumina, zirconia, tin oxide, and titanium dioxide are used to support covalently anchored alkylsilane films.[1] Less stable films are also formed on oxidized boron, iron, and carbon surfaces.[1] The structures of these oxide-bound alkylsilane layers are of particular importance due to the diversity of applications in which these surface-immobilized species are used, including catalysis,[2,3] chromatographic separations,[2] electrochemistry,[4–6] microsensors,[5] and adhesion.[3,7–12] Although the study of organically modified oxide surfaces has received intense interest in recent years, research in this area has suffered from the lack of spectroscopic techniques capable of adequately characterizing the organic/oxide interface.

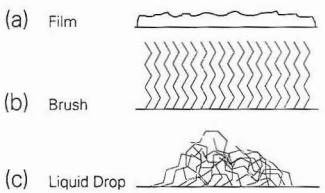

Figure 1. Models of molecular organization of stationary-phase chains in RPLC.

These issues are specifically relevant to the characterization of the organically modified silica surfaces used in reversed-phase liquid chromatography (RPLC). RPLC is one of the more popular separation techniques used for the isolation of nonpolar molecules. Retention and separation are accomplished through the interactions of nonpolar analytes with a polar mobile phase and a nonpolar stationary phase.

Stationary phases used in RPLC are typically formed by covalent attachment of either C_2, C_8, or C_{18} alkylchlorosilanes to a silica gel support using mono-, di-, or trichloroalkylsilanes. The Cl atoms are highly reactive toward surface silanols and anchor the alkylsilanes to the silica gel surface through siloxane (Si–O–Si) bond formation. Di- and trichlorosilanes have multiple reaction sites which allow cross-linking and possible multilayer formation. Therefore, chromatographic materials made from these precursors are referred to as "polymeric" stationary phases. Monochlorosilanes have a single reactive Cl group and form a single siloxane bond with the silica gel surface. Chromatographic materials made from these precursors are referred to as "monomeric" stationary phases. Although chemists have a general understanding of the role of monomeric and polymeric stationary phases in retention, the specific molecular interactions that occur at, on, or in the stationary phase and which lead to separation and retention are still not understood.

Several models have been proposed to describe the interfacial interactions of the stationary phase involved in retention, including possible contributions from alkyl chain conformation. Originally, the stationary phase was pictured as a silica surface covered with a thin, nonpolar film as shown in Figure 1a.[13] Later models described a more dynamic stationary phase. In the stick/brush model shown in Figure

(1) Arkles, B. In *Silicon Compounds: Register and Review*, 5th ed.; Anderson, R., Larson, G. L., Smith C., Eds.; Hüls America, Inc.: Piscataway NJ, 1991; pp 59–60.
(2) Evans, J. In *Silane Surfaces and Interfaces*; Leyden, D. E., Ed.; Gordon and Breach Science Publishers: New York, 1985; p 203.
(3) Pinnavaia, T. J.; Lee, J. G.; Abedini, M. In *Silylated Surfaces*; Lyden, D. E., Collins, W. T., Eds.; Gordon and Breach Science Publishers: New York, 1980; pp 333–345.
(4) White, H. S.; Murray, R. W. *Anal. Chem.* **1979**, *51*, 236–239.
(5) Yongan, Y.; Bein, T. *J. Phys. Chem.* **1992**, *96*, 9387–9393.
(6) Untereker, D. F.; Lennox, J. C.; Wier, L. M.; Moses, P. R.; Murray, R. W. *J. Electroanal. Chem.* **1977**, *81*, 309–318.
(7) Porro, T. J.; Pattacini, S. C. *Appl. Spectrosc.* **1990**, *44*, 1170–1175.
(8) Lee, L. H. *J. Colloid Interface Sci.* **1968**, *27*, 751–760.
(9) Ishida, H.; Koenig, J. L. *J. Colloid Interface Sci.* **1978**, *64*, 565–576.

0003-2700/94/0366-3362$04.50/0
© 1994 American Chemical Society

1b, the stationary phase is envisioned with the alkyl chains extending away from the silica surface, moving freely in the mobile phase and accessible to both solute and solvent molecules.[14,15] The "liquid drop" model (Figure 1c) has also been proposed in which the stationary phase exists as self-associated aggregated islands of hydrocarbon chains lying on the silica surface.[16–18]

Evidence for these models has been obtained using an assortment of techniques including fluorescence spectroscopy[18–24] nuclear magnetic resonance (NMR) spectroscopy,[25–28] infrared (IR) spectroscopy,[29–34] and chromatography.[35–37] The results of these studies suggest that the stationary phase is a dynamic molecular assembly that responds to changes in temperature, mobile-phase solvent, and surface coverage.[38] However, many questions concerning the effect of experimental conditions on the molecular orientation of the stationary phase and the retention process still remain unanswered. These issues can only be addressed with more information that is molecularly specific using techniques that are sensitive to alkyl chain conformation. The aforementioned techniques have difficulty of providing this information due to sensitivity limitations, strong interference from bulk silica, or the fact that they require probe molecules. Raman spectroscopy is one of the few vibrational techniques that might provide the desired information with relative immunity to these limitations.

The major drawback of Raman scattering, particularly for the study of alkane-containing molecules, is that it is inherently a weak phenomenon. Development of a procedure to enhance the Raman scattering efficiency would make Raman spectroscopy a more viable tool for the study of weak Raman scatters on oxide surfaces. Walls and Bohn recently developed a rather novel approach based on the electromagnetic enhancement properties of Ag. These workers used flat Ag island structures, sputtered with a thin SiO_2 overlayer, to study the adsorption interactions of *p*-nitrobenzoic acid and phthalazine with the SiO_2 surface.[39,40] The premise on which their layered approach is based is that the Ag island structures should provide long-range electromagnetic enhancement to the species adsorbed at the silica surface via the surface-enhanced Raman scattering (SERS) phenomenon.[41,42] Their results suggest that the thin Ag island structures do, in fact, provide nominal enhancement to these adsorbed species, but not significant enough for studying weak Raman scatters such as alkane systems. Experimental evidence from SERS studies and predictions from electromagnetic calculations suggest that the strength of the enhanced electric field at the surface of Ag particles scales with the degree of curvature of the Ag surface.[41,42] The flat Ag islands used by Bohn and co-workers exhibit the greatest degree of curvature at their edges. Therefore, the majority of the enhanced electromagnetic field for this layered structure is parallel to the interface, not directed toward the SiO_2/adsorbate interface, and cannot provide the desired enhancement. In order to maximize the enhancement realized at the surface of a thin dielectric overlayer such as SiO_2, the electromagnetic field needs to be enhanced in a direction perpendicular to the SiO_2/Ag interface. A solution to the limitation inherent Bohn's approach is described in this report.

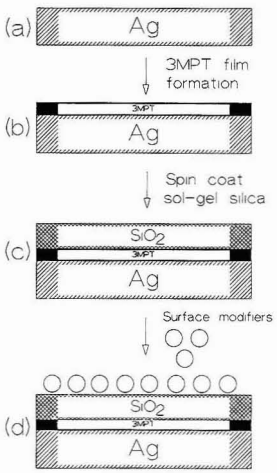

Figure 2. Schematic showing "sandwich" approach for Raman spectroscopy on silica surfaces: (a) Ag surface, (b) Ag surface modified with a monolayer of 3MPT, (c) 3MPT-modified Ag surface with a thin layer of silica gel, and (d) attachment of alkylchlorosilanes to silica surface.

The use of a similar layered structure based on a thin silica film on a Ag substrate for the Raman spectroscopic study of adsorbates or chemically anchored modifiers at silica surfaces is presented here. Particular attention is directed to the determination of molecular conformation of the alkyl chains of covalently attached alkylsilanes and conformational changes induced by typical mobile phases.

THE METHOD

Raman spectra of molecular assemblies of octadecylsilane were studied on the thin silica gel/Ag sandwich structures through use of the electromagnetic enhancement properties of Ag. The basic outline of the method is described in Figure 2. The first step involves formation of a self-assembled layer

(10) Boerio, F. J.; Williams, J. W.; Burkstrand, J. M. *J. Colloid Interface Sci.* **1983**, *91*, 485–495.
(11) Pantano, C. G.; Wittberg, T. N. *Surf. Interface Anal.* **1990**, *15*, 498–501.
(12) Bascom, W. C. *Macromolecules* **1972**, *5*, 792–798.
(13) Gilpin, R. K. *J. Chromatogr. Sci.* **1984**, *22*, 371–377.
(14) Karch, K.; Sebestian, I.; Halasz, I. *J. Chromatogr.* **1976**, *122*, 3–16.
(15) Scott, R. P. W.; Simpson, C. F. *J. Chromatogr.* **1980**, *197*, 11–20.
(16) Lochmuller, C. H.; Wilder, D. R. *J. Chromatogr. Sci.* **1979**, *17*, 574–579.
(17) Lochmuller, C. H.; Colborn, A. S.; Hunnicutt, M. L.; Harris, J. M. *Anal. Chem.* **1983**, *55*, 1344–1348.
(18) Lochmuller, C. H.; Colborn, A. S.; Hunnicutt, M. L.; Harris, J. M. *J. Am. Chem. Soc.* **1984**, *106*, 4077–4082.
(19) Lochmuller, C. H.; Marshall, D. B.; Wilder, D. R. *Anal. Chim. Acta* **1981**, *130*, 31–43.
(20) Carr, J. W.; Harris, J. M. *Anal. Chem.* **1986**, *58*, 626–631.
(21) Carr, J. W.; Harris, J. M. *Anal. Chem.* **1987**, *59*, 2546–2550.
(22) Bjarneson, D. W.; Petersen, N. O. *Langmuir* **1991**, *7*, 2821–2826.
(23) Wirth, M. J.; Burbage, J. D. *Anal. Chem.* **1991**, *83*, 1311–1317.
(24) Burbage, J. D.; Wirth, M. J. *J. Phys. Chem.* **1992**, *96*, 5943–5948.
(25) Sindorf, D. W.; Maciel, G. E. *J. Am. Chem. Soc.* **1983**, *105*, 1848–1851.
(26) Kelusky, E. C.; Fyfe, C. A. *J. Am. Chem. Soc.* **1986**, *108*, 1746–1749.
(27) Shah, P.; Rogers, L. B.; Fetzer, J. C. *J. Chromatogr.* **1987**, *388*, 411–419.
(28) Bayer, E.; Paulus, A.; Peters, B.; Laupp, G.; Reiners, J.; Albert, K. *J. Chromatogr.* **1986**, *364*, 25–37.
(29) Sander, L. C.; Callis, J. B.; Field, L. R. *Anal. Chem.* **1983**, *55*, 1068–1075.
(30) Ohtake, T.; Mino, N.; Ogawa, K. *Langmuir* **1992**, *8*, 2081–2083.
(31) Tripp, C. P.; Hair, M. L. *Langmuir* **1992**, *8*, 1120–1126.
(32) Tillman, N.; Ulman, A.; Penner, T. L. *Langmuir* **1989**, *5*, 101–111.
(33) Netzer, L.; Sagiv, J. *J. Am. Chem. Soc.* **1983**, *105*, 647–676.
(34) Netzer, L.; Iscovici, R.; Sagiv, J. *Thin Solid Films* **1983**, *99*, 235–241.

of (3-mercaptopropyl)trimethoxysilane (3MPT) on a smooth Ag surface. This monolayer, which acts as a molecular adhesive for a thin silica gel film, is hydrolyzed to remove the organic methoxy groups. The hydrolysis reaction results in essentially complete cross-linking of the terminal silane groups and produces a stable thin film, as shown in Figure 2b. A thin silica layer is then formed by spin coating a small portion of a tetramethoxysilane- (TMOS-) based sol–gel solution onto the 3MPT-modified Ag surface, as shown in Figure 2c.

Although silica systems such as sol–gel silica, chromatographic silica, vapor-deposited SiO_2, and quartz are stoichiometrically equivalent, the physical and chemical properties of the silica systems can be radically different. For example, chromatographic and sol–gel silica are hydrated and amorphous materials. Vapor-deposited SiO_2 is amorphous but anhydrous, and quartz is crystalline and anhydrous.[43] Unlike vapor-deposited SiO_2 or quartz, sol–gel and chromatographic silica also exhibit a range of microstructures depending on the experimental conditions used for the formation of the silica.[43–48] The microstructural attributes of particular importance in RPLC are particle diameter and pore size. Sol–gel and chromatographic silica are similar, because both forms are products of hydrolysis reactions of tetrafunctional silanes. Chromatographic silica is generally formed from the hydrolysis of $SiCl_4$,[43] whereas sol–gel silica is generally formed from the hydrolysis of tetraalkoxides, $Si(OR)_4$ (R = OCH_3 or OCH_2CH_3).[49] Therefore, the thin silica films created by sol–gel techniques should model the chemical and physial environment of chromatographic grade silica better than vapor deposited SiO_2 films or quartz.

After formation of the thin silica film on the modified Ag substrate, the silica layer is dried and reacted with the alkylchlorosilane or interest, as shown in Figure 2d. The Ag/3MPT/silica "sandwich" structure used to study organic modifier/silica interactions provides long-range electromagnetic enhancement to the surface of the silica and an attachment mechanism for the silica gel overlayer that facilitates the acquisition of Raman spectra of covalently bound alkylsilanes at the silica gel surface.

EXPERIMENTAL SECTION

Instrumentation. Raman spectral data were obtained using 100 mW of 514.5-nm radiation from a Coherent Innova 90–5 Ar^+ laser on a Spex 1877 Triplemate spectrometer as described previously.[50–52] The detector in these experiments was a Princeton Instruments charge-coupled device (CCD) system based on a Tektronix TK-512T, 512 × 512, thinned, back-illuminated, antireflection-coated CCD chip cooled with liquid N_2 to −120 °C.

XPS measurements were made using a Vacuum Generators ESCALAB MKII electron spectrometer equipped with a concentric hemispherical analyzer and Channeltron electron multiplier. X-rays from an AlKα line at 1486.6 eV were used as the excitation source. Electrons were collected in the constant analyzer energy (CAE) mode with a pass energy of 20 keV. Spectra were corrected for sample charging using the C 1s peak at 284.6 eV. Peak areas were calculated using a Gaussian fit program. Relative peak ratios were then calculated using previously published photoionization cross sections.[53]

Ellipsometric measurements were made with a Rudolph Research Model 43603-200E ellipsometer using a He–Ne laser at an incident angle of 70°. Readings were taken on vapor deposited Ag surfaces to establish the bare substrate optical constants prior to any surface modification. The Ag surfaces were either used directly after deposition or sputtered with Ar^+ to remove surface oxides prior to analysis. The surfaces were transferred from the ultrahigh-vacuum chamber and stored for short periods of time in a container purged with UHP argon. A refractive index of 1.45 was used for the 3MPT layer,[54] and a refractive index of 1.46 was used for the thin silica layer.[55] The ellipsometry results were used to calculate the corresponding thickness values by use of DafIBM version 2.0, a computer program supplied by Rudolph Research and implemented on a DOS-based PC system.

Procedures. The thin silica films were made by spin coating a dilute, prehydrolyzed tetramethoxysilane (TMOS) solution onto a modified Ag surface. The Ag surfaces were first mechanically polished to a mirror finish using successively finer grades of alumina down to 0.05 μm. Trapped alumina was removed by sonicating the surfaces for 2–5 min in water.

To promote adhesion, the Ag surfaces were modified with a monolayer of 3MPT by immersion in a solution of 20 mM 3MPT in ethanol for 3 h. After formation, the surfaces were removed and rinsed with ethanol. The 3MPT layer was then hydrolyzed in an aqueous acidic solution (0.1 M HCl for 12 h) prior to spin coating, as described previously.[56] Raman spectroscopy indicated the presence of a small number of surface silanols on the 3MPT monolayer after hydrolysis.[56] These SiOH groups provide reaction sites and points of attachment for the spin-cast thin silica film.

The TMOS sol was prepared using the procedure developed by Bertoluzza and co-workers.[57] This preparation uses 4.0 mL of TMOS, 5.5 mL of methanol, 16.3 mL of water, and 0.03 mol of HCl/mol of TMOS. The solution was mildly heated for 0.5 h to facilitate the hydrolysis process. A small portion of the TMOS solution (0.25–0.5 mL/0.32 cm^2 Ag)

(35) Gilpin, R. K.; Gangoda, M. E.; Krishen, A. E. *J. Chromatogr. Sci.* **1982**, *20*, 345–348.
(36) Schunk, T. C.; Burke, M. F. *Int. J. Environ. Anal. Chem.* **1986**, *25*, 81–103.
(37) Cole, L. A.; Dorsey, J. G. *Anal. Chem.* **1992**, *64*, 1317–1323.
(38) Martire, D. E.; Boehm, R. E. *J. Phys. Chem.* **1983**, *87*, 1045–1062.
(39) Walls, D. J.; Bohn, P. W. *J. Phys. Chem.* **1989**, *93*, 2976–2982.
(40) Bohn, P. W. *Prog. Anal. Spectrosc.* **1989**, *12*, 41–72.
(41) Wang, D. S.; Kerker, M.; Chew, H. *Appl. Opt.* **1980**, *19*, 4159–4173.
(42) Gersten, J. I. *Chem. Phys.* **1980**, *72*, 5779–5780.
(43) *The Chemistry of Silica*; Iler, R. K., Ed.; John Wiley and Sons; New York, 1979.
(44) Stöber, W.; Fink, A.; Bohn, E. *J. Colloid Interface Sci.* **1968**, *26*, 62–69.
(45) Tan, C. G.; Bowen, B. D.; Epstein, N. *J. Colloid Interface Sci.* **1987**, *118*, 290–293.
(46) Van Helden, A. K.; Jansen, J. W.; Vrij, A. *J. Colloid Interface Sci.* **1981**, *81*, 354–368.
(47) Brinker, C. J.; Scherer, G. W. *J. Non-Cryst. Solids* **1985**, *70*, 301–322.
(48) LeCloux, A. J.; Bronckart, J.; Noville, F.; Dodet, C.; Marchot, P.; Pirard, J. P. *Colloids Surf.* **1986**, *19*, 359–374.
(49) Brinker, C. F.; Scherer, G. W. *Sol–Gel Science: The Physics and Chemistry of Sol–Gel Processing*; Academic Press, Inc.: San Diego, 1990.
(50) Bryant, M. A.; Pemberton, J. E. *J. Am. Chem. Soc.* **1991**, *113*, 8284–8293.
(51) Pemberton, J. E.; Bryant, M. A.; Sobocinski, R. L.; Joa, S. L. *J. Phys. Chem.* **1992**, *96*, 3776–3782.
(52) Bryant, M. A.; Pemberton, J. E. *J. Am. Chem. Soc.* **1991**, *113*, 3629–3637.
(53) Scofield, J. H. *J. Electron Spectrosc. Relat. Phenom.* **1976**, *8*, 129–137.
(54) Walczak, M. M.; Chung, C.; Stole, S. M.; Widrig, C. A.; Porter, M. D. *J. Am. Chem. Soc.* **1991**, *113*, 2370–2378.
(55) *Handbook of Chemistry and Physics*, 60th ed., Weast, R. C., Ed.; Chemical Rubber Co.: Boca Raton, FL, 1981.
(56) Thompson, W. R.; Pemberton, J. E. *Chem. Mater.* **1993**, *5*, 241–244.
(57) Bertoluzza, A.; Fagnano, C.; Morelli, M. A.; Gottardi, V.; Guglielmi, M. *J. Non-Cryst. Solids* **1982**, *48*, 117–128.

was used to spin-coat (at ca. 3.5 kHz) the Ag surface. These surfaces were then dried in a desiccator overnight.

The silica surfaces were modified by use of two different reaction strategies. Initial experimental conditions followed standard chromatographic procedures reported in the literature, with minor alterations.[58] The silica surfaces were immersed in a solution of 0.1 M alkylchlorosilane in distilled toluene for 24 h at room temperature. These surfaces were removed and cleaned by Soxhlet extraction, first in distilled toluene (3 h) and then in methanol (3 h), to remove excess alkylsilane. Raman spectroscopy of the surfaces prior to and after Soxhlet extraction suggests that the majority of alkyl chains are strongly adherent to the silica surface, since only minor changes are observed in the spectra. The only change observed is a slight decrease in the $\nu_s(CH_2)_{FR}$ band intensity at 2917 cm^{-1} after the Soxhlet extractions. This change is attributed to removal of minor amounts of excess octadecylsilane from the surface. In addition, Raman spectral intensities of the modified silica surfaces in the ν(C–H) region reveal that this silanization procedure results in inconsistent alkylsilane surface coverages. Different spectral intensities can be observed for similar surfaces immersed in the same solution for equivalent immersion times.

To improve the reproducibility of the silanization reaction on these thin silica gel films, an alternative procedure was investigated. The second silanization procedure resembles the experimental conditions used by Sagiv[33,59,60] and Ohtake[30] for the formation of alkylsilane organized molecular assemblies. The silica surfaces were prepared by immersion in a solution of 0.1 M alkylchlorosilane in distilled toluene at room temperature for 0.5 h, rinsed with distilled toluene, reimmersed for another 0.5 h, and rinsed with distilled toluene. This procedure for creating alkylsilane films on our silica surfaces was more reproducible than the first. The second method resulted in alkylsilane films that could be readily sensed by Raman spectroscopy ~70% of the time versus ~25% for the first method. Although the second method does improve the reproducibility of the silanization reaction, it is still inadequate. Carbon loadings continue to vary from sample to sample. The lack of reproducibility of the silanization reaction may be due to variations in water content from gel to gel. The amount of residual water would have a profound effect on hydrolysis and cross-linking of the alkylchlorosilane at the silica surface. On chromatographic silica, water adsorbs to the surface in three distinct layers.[61,62] The water molecules closest to the silica surface interact with the surface silanols through hydrogen bonding, forming a highly adherent monolayer which can only be completely removed by heating the silica to temperature in excess of 650 °C. The second layer of water is weakly adsorbed and is removed at 120 °C, under low vacuum, or with drying agents. The third layer of water is removed at 70 °C or with drying solvents such as methanol. Silica gels formed by sol–gel chemistry are expected to contain at least two to three monolayers of water, similar to chromatographic silica. Further studies on the influence of surface water on the silanization reaction are underway in this laboratorry and will be reported at a later time.

Materials. Polishing supplies including alumina and polishing pads were purchased from Buehler. (3-Mercaptopropyl)trimethoxysilane (3MPT, >97%) was purchased from either Hüls America or Aldrich and vacuum distilled prior to use. Octadecyltrichlorisilane (>97%) was obtained from Hüls America. Hexane (99+%) and tetramethoxysilane (98%) were obtained from Aldrich. Anhydrous grade methanol was purchased from Mallinkrodt. Ethanol (absolute) was purchased from Midwest Grain Products. Toluene (reagent grade), obtained from EM Science, was distilled and stored over molecular sieves prior to use. Reagents were used as received unless indicated otherwise.

RESULTS AND DISCUSSION

I. Predicted and Observed Alkylsilane Coverages. The theoretical coverage of silanols on a silica surface is estimated to be ca. ~4.5 OH^-/100 $Å^2$.[63] This places each surface hydroxyl ~5 Å apart at a surface concentration of ~8 × 10^{-10} mol/cm^2.[63] Interestingly, a comparable surface density of potential bonding sites is encountered for Ag or Au single crystal surfaces used as substrates for self-assembled monolayer films of alkanethiols. These systems have been shown to form close-packed, ordered layers on such substrates with a measured surface coverage of ~(7–9) × 10^{-10} mol/cm^2.[54] Similarly, self-assembled monolayers formed from alkylsilanes on silicon surfaces have been found to form close-packed, ordered layers of alkyl chains.[64] Thus, the maximum predicted coverage of alkylsilane layers is ~8 × 10^{-10} mol/cm^2.

For the average polymeric stationary phase used in RPLC, the alkyl chains are estimated to be ~5.7 Å apart, at a coverage of ~5 × 10^{-10} mol/cm^2.[63] This places the alkyl chains in the polymeric stationary phase, on average, only slightly farther apart than the alkyl chains of the self-assembled monolayers formed on metal and silicon surfaces. Therefore, it is reasonable to assume that the hydrocarbon chains that comprise the polymeric stationary phase also form relatively ordered, densely packed molecular arrays on the silica surface.

Monomeric stationary phases used in RPLC applications typically have considerably smaller surface coverages of ~(2–3) × 10^{-10} mol/cm^2. At these concentrations, the alkyl chains are ~8.2 Å apart and unable to completely cover the silica surface. Accordingly, the alkyl chains are not expected to form densely packed, molecular arrays and are more likely to contain alkyl chain defects.

II. Surface Characterization of Polymeric Stationary Phases. Ellipsometry Characterization of the Thin Silica Film. The thicknesses of the silica films formed by our spin-coating procedure were estimated using ellipsometry. The optical constants for each uncoated Ag sample were determined prior to surface modification. The optical constants varied slightly for each sample due to sample preparation and oxide formation at the surface. The thicknesses of the thin silica films formed in this manner were found to be 80 ± 5 nm.

Scanning Electron Microscopy Characterization. After the silica surface is modified with octadecyltrichlorosilane, the low-resolution scanning electron microscopy (SEM) image

(58) Snyder, L. C.; Wise, S. A. *CRC Crit. Rev. Anal. Chem.* **1987**, *18*, 299–415.
(59) Gun, J.; Iscovici, R.; Sagiv, J. *J. Colloid Interface Sci.* **1984**, *101*, 201–213.
(60) Cohen, S. R.; Naaman, R.; Sagiv, J. *J. Phys. Chem.* **1986**, *90*, 3054–3056.
(61) Scott, R. P. W.; Traiman, S. *J. Chromatogr.* **1980**, *196*, 193–205.
(62) Fungkee Fung, C. Ph.D. Dissertation, University of Arizona, 1993.
(63) Dorsey, J. G.; Dill, K. A. *Chem. Rev.* **1989**, *89*, 331–346.
(64) Wasserman, S. R.; Whitesides, G. M.; Tidswell, I. M.; Ocko, B. M.; Pershan, P. S.; Axe, J. D. *J. Am. Chem. Soc.* **1989**, *111*, 5852–5861.

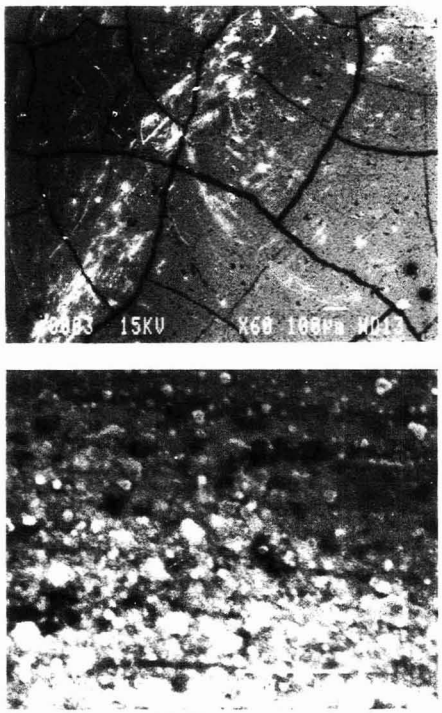

Figure 3. SEM images of the thin silica surface after modification with octadecyltrichlorosilane: (a, top) low resolution; (b, bottom) high resolution.

of the surface (Figure 3a) shows a number of large fissures. Even though the film is fractured, it still remains strongly adherent to the Ag surface. Cursory visual observation of the gels, using a Central Scientific binocular microscope at 3× magnification, indicates that these fractures are caused by shrinking of the gel during Soxhlet extraction and are not associated with the chemical modification of the silica surface. Cracks in the gel predominantly occur on the edges of the Ag surface, sometimes occurring during the toluene extraction, sometimes during the methanol extraction, and other times not at all. The inconsistent cracking of the silica surfaces may be attributed to sample-to-sample variation or across one sample variation in silica film thicknesses, with a greater degree of fragmentation expected for thicker films. However, the ellipsometry measurements described above suggest that the thicknesses of these silica films are fairly reproducible. Nonuniformity of the Ag surface may be an alternative explanation. As the Ag surfaces are mechanically polished, they develop rounded edges and uneven ridges. Therefore, as the gel solidifies these surface morphologies may introduce uneven stresses, which eventually crack the gel.

At lower resolution (Figure 3a), the SEM images of the modified silica surfaces appear reasonably flat and smooth. At higher resolution (Figure 3b), the films appear to contain a variety of surface features. The high-resolution SEM image

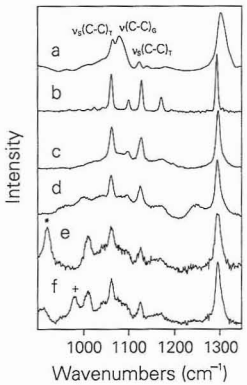

Figure 4. Raman spectra in ν(C–C) region of (a) neat liquid octadecyltrichlorisilane, (b) solid octadecyltrichlorosilane, (c) hydrolyzed octadecylsilane, (d) octadecylsilane attached to the thin silica film, (e) octadecylsilane attached to the thin silica layer in the presence of acetonitrile (*), and (f) octadecylsilane attached to the thin silica layer in the presence of deuterated methanol (+).

indicates that there is a considerable amount of roughness associated with the silica surface. The increased roughness is believed to be the result of the covalent immobilization chemistry of the alkylchlorosilanes. The formation of the Si–O bond in the reaction between the surface silanol and the alkylchlorosilane is a highly exothermic reaction, and HCl is a byproduct of the reaction. It is believed that the HCl released during the silanization reaction etches the silica surface, generating these microscopic surface features.

Raman Spectroscopic Characterization in the ν(C–C) Region. Figure 4 shows the Raman spectra between ~800–1300 cm^{-1} for neat octadecyltrichlorosilane (a), frozen (solid) octadecyltrichlorosilane (b), hydrolyzed bulk octadecyltrichlorosilane (c), the polymeric phase covalently attached to a silica surface (d), the silica surface polymeric phase in the presence of acetonitrile (e), and the silica surface polymeric phase in the presence of deuterated methanol (f). The bands of interest in this region are the ν(C–C)$_T$ and ν(C–C)$_G$ from octadecylsilane, ν_s(C–C) from acetonitrile, and ν(O–C) from deuterated methanol. The band assignments and peak frequencies are tabulated in Table 1.

For neat liquid octadecyltrichlorosilane (Figure 4a), the large ν(C–C)$_G$ intensity at ~1080 cm^{-1} relative to the two ν(C–C)$_T$ bands at ~1065 and 1124 cm^{-1}, and the broad CH$_2$ twist$_{T,G}$ at 1303 cm^{-1}, suggest that the alkyl chains are considerably disordered. Cooling octadecyltrichlorosilane to liquid nitrogen temperatures (Figure 4b) causes the alkyl chains to become more ordered.[65] The ν(C–C)$_G$ band disappears from the spectrum while the two ν(C–C)$_T$ bands increase in relative intensity and shift ~3 cm^{-1} to lower frequencies. The CH$_2$ twist band at ~1300 cm^{-1} also increases in intensity, shifts ~10 cm^{-1} to lower frequencies, and becomes much narrower and highly symmetric.

When bulk octadecyltrichlorosilane is hydrolyzed (Figure 4c), the chlorosilanes cross-link to form a siloxane network,

(65) Mizushima, S. I.; Shimanouchi, T. *J. Am. Chem. Soc.* **1949**, *71*, 1320–1324.

Table 1. Raman Band Assignments and Peak Frequencies (cm^{-1}) for Octadecyltrichlorosilane (OTS) in the ν(C–C) and ν(C–H) Regions

neat liquid OTS	frozen OTS	gelled OTS	surface OTS	surface OTS + CH_3CN	surface OTS + D_3COD	surface OTS + H_2O	assignment[a]
890		890	888	887	890		CH_3 rk_T
				921			$\nu_s(C–C)_T - CH_3CN$
					981		$\nu(O–C) - D_3COD$
			1000	1009	1008		$\nu(C–C)_T$ 3MPT
1065	1062	1061	1062	1062	1061		$\nu_a(C–C)_T$
1080	1081 sh[b]		sh	sh	sh		$\nu(C–C)_G$
	1100	1099	1097	sh	sh		CH_2 $twist_T$
1124	1128	1129	1126	1127	1126		$\nu_s(C–C)_T$
1303	1293	1296	1297	1297	1297		CH_2 $twist_{T,G}$
2724	2725	2725	2724	2723			
2851	2847	2848	2849	2848	2847	2846	$\nu_s(CH_2)$
2890	2881	2882	2882	2882	2881	2879	$\nu_a(CH_2)$
2927	2930	2929	sh	sh	2917	2917	$\nu_s(CH_2)_{FR}$
2957	2958	2957	sh	sh	sh	sh	$\nu_s(CH_3)$
	2970	sh					$\nu_s(CH_3)$

[a] Assignments are for OTS unless otherwise noted. [b] sh, shoulder.

similar to what is observed for 3MPT, as discussed previously.[56] In contrast to the behavior of bulk 3MPT, however, which remains relatively disordered upon condensation, the intensities of the two $\nu(C–C)_T$ bands of the octadecylsilane relative to the $\nu(C–C)_G$ band suggest that the hydrocarbon chains in this long alkane chain molecule adopt a relatively ordered configuration upon condensation. Further evidence for the proposed order in the hydrolyzed bulk octadecylsilane comes from the shape of the CH_2 twist band at $\sim$1296 cm^{-1}. This band remains relatively narrow after the hydrolysis and condensation processes, which also suggests that the alkyl chains are in a predominantly ordered configuration. Perfect order is not likely, however, since the CH_2 twist band is broadened slightly to higher frequencies and is only shifted 6 cm^{-1} to lower frequencies compared to 10 cm^{-1} in the spectrum of solid octadecylsilane. Octadecylsilane has a much longer alkane chain than 3MPT, which may provide stronger van der Waals forces for self-association and the ordered orientation. Thus, in total, the spectral results suggest that the alkyl chains in the hydrolyzed bulk octadecylsilane are not completely ordered and contain defects.

When a polymeric octadecylsilane phase is covalently anchored to the thin silica surface (Figure 4d) the alkyl chains appear to adopt a predominantly ordered configuration. The $\nu_a(C–C)_T$, $\nu_s(C–C)_T$, and CH_2 twist bands are observed at $\sim$1062, 1126, and 1297 cm^{-1}, respectively; these frequencies correspond to those observed for solid octadecyltrichlorosilane, suggesting that the chemical environment of the alkyl chains is similar in each case. The peak frequency of the CH_2 twist and the shoulder on the $\nu_a(C–C)_T$ band, assigned to a weak $\nu(C–C)_G$ mode at $\sim$1080 cm^{-1}, indicate that these films contain some minimal gauche defect structure, resulting in films which are not perfectly ordered. Nonetheless, these films clearly do not resemble liquid-phase alkanes as has been proposed previously[16,17,18] on the basis of the Raman spectral evidence in this region.

A series of spectra were acquired from these films while they were exposed to two solvents commonly employed in RPLC. The spectra from these experiments are shown in Figure 4e and f. Exposing this silica surface polymeric phase to acetonitrile (Figure 4e) does not appear to disrupt the alkyl chain order significantly. However, the two $\nu(C–C)_T$ peaks

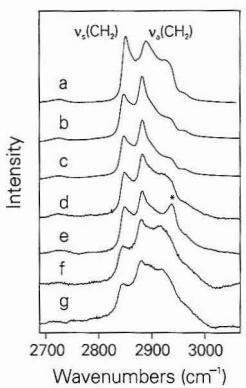

Figure 5. Raman spectra in ν(C–H) region of (a) neat liquid octadecyltrichlorosilane, (b) solid octadecyltrichlorosilane, (c) hydrolyzed octadecylsilane, (d) octadecylsilane attached to the thin silica film, (e) octadecylsilane attached to the thin silica layer in the presence of acetonitrile (*), (f) octadecylsilane attached to the thin silica layer in the presence of deuterated methanol, and (g) octadecylsilane attached to the thin silica layer in the presence of water.

and the CH_2 twist peak appear to decrease in intensity and broaden slightly, signifying greater mobility of the alkyl chains. With deuterated methanol (Figure 4f), the two $\nu(C–C)_T$ bands and the CH_2 twist band appear to be slightly narrower, suggesting less influence of this solvent than acetonitrile in this region. Intermolecular interactions between the solvent and the chain can be either specific or nonspecific. Yonker et al. observed that acetonitrile is prefentially retained within C_{18} stationary phases over methanol due to nonspecific dispersion interactions.[66] The $\nu(C–C)_G$ band does not appear to be significantly affected by either mobile phase.

Raman Spectroscopic Characterization in the ν(C–H) Region. Figure 5 shows the Raman spectra between $\sim$2700 and 3100 cm^{-1} for neat octadecyltrichlorosilane (a), frozen (solid) octadecyltrichlorosilane (b), hydrolyzed octadecyltrichlorosilane (c), the polymeric phase on silica (d), the silica surface polymeric phase in the presence of acetonitrile (e),

(66) Yonker, C. R.; Zwier, T. A.; Burke, M. F. *J. Chromatogr.* **1982**, *241*, 269–280.

the silica surface polymeric phase in the presence of deuterated methanol (f), and the silica surface polymeric phase in the presence of water (g). The bands of interest in this region are the $\nu_s(CH_2)$, $\nu_a(CH_2)$, $\nu_s(CH_2)_{FR}$, $\nu_a(CH_3)$ from octadecylsilane, and $\nu_s(CH_3)$ from acetonitrile. Deuterated methanol and water do not have vibrational bands in this frequency region. The band assignments and peak frequencies are tabulated in Table 1.

Neat liquid octadecyltrichlorosilane (Figure 5a) exhibits four primary bands in this region at about 2851, 2890, 2927, and 2957 cm^{-1} assigned to the $\nu_s(CH_2)$, $\nu_a(CH_2)$, $\nu_s(CH_2)_{FR}$, and $\nu_a(CH_3)$ modes, respectively. When octadecyltrichlorosilane is frozen (Figure 5b), the hydrocarbon chains adopt a more ordered or "crystalline" orientation. The increase in degree of order is exhibited in the methylene [$\nu_a(CH_2)$ and $\nu_s(CH_2)$] modes through a small change in peak frequency and a more noticeable change in relative peak intensity.[67] The transformation from liquid (disordered) to solid (crystalline) is reflected in the intensity ratio of the two of the CH_2 group vibrations, $[I\nu_a(CH_2)/I\nu_s(CH_2)]$, which can be used as an indicator of conformational change with alkyl chains.[68] For liquid octadecyltrichlorosilane, this ratio is 0.938 ± 0.005; upon solidification, this ratio increases significantly to 1.92 ± 0.02. Gaber and Peticolas observed similar intensity ratios for liquid and solid hexadecane.[68] Since the C–H vibrational envelope contains a number of vibrational modes, the CH_2 group intensity ratio exhibits a range of values, depending upon the molecule of interest and complexity of the C–H frequency region. Therefore, the value of this ratio lies not in comparing absolute numbers but in being able to monitor the relative effects of specific environmental influences on given a system.

When bulk octadecyltrichlorosilane is hydrolyzed and condensed (Figure 5c), the CH_2 group intensity ratio (1.38 ± 0.02) is indicative of hydrocarbon chains in a more ordered state, consistent with the observations in the ν(C–C) region. Although the spectrum of hydrolyzed and condensed octadecylsilane appears more ordered than that from the liquid, the CH_2 group intensity ratio is actually substantially lower than that for solid octadecylsilane. This difference implies that the octadecyl chains are not completely ordered after condensation and contain a number of gauche defects.

For the modified silica surfaces (Figure 5d–g), two prominent bands associated with the $\nu_s(CH_2)$ and $\nu_a(CH_2)$ vibrations of octadecylsilane at ~2849 and 2882 cm^{-1}, respectively, are observed. The shoulder at ~2929 cm^{-1} is assigned to the $\nu_s(CH_2)_{FR}$ from both octadecylsilane and 3MPT. The CH_2 group intensity ratio for these modified silica surfaces ranges from ~1.45 to 1.70, suggesting that, although the hydrocarbon chains are still not completely crystalline, they are fairly ordered. This picture of these systems is consistent with that provided by the Raman spectral data in the ν(C–C) region. The variances observed in the CH_2 group ratio for octadecylsilane covalently attached to thin silica films are attributed to variation in the spectral contribution from the 3MPT/silica substrate and to different carbon loadings for each sample.

Comparison of the CH_2 group intensity ratio for the octadecylsilane gel (Figure 5c) with that for the silica surface octadecylsilane (Figure 5d) suggests that the alkyl chains are slightly more ordered on the silica surface than in the gel. This result suggests that the polymeric stationary phases formed on the thin silica surfaces do not resemble bulk hydrolyzed octadecylsilane, but rather, an ordered hydrocarbon film influenced by its attachment to the silica surface.

In order to quantitatively assess changes in the stationary-phase spectral response due to interaction with solvent molecules, the CH_2 group intensity ratio was determined as a percent change relative to this ratio prior to solvent exposure. Therefore, changes that occur in this ratio should reflect an adjustment of the alkyl chains to the different chemical environment.

Exposure of the octadecylsilane film to acetonitrile decreases the CH_2 group ratio by ~8%, suggesting slightly more disorder in the presence of acetonitrile relative to air. Using a slightly less polar mobile phase, deuterated methanol (D_3-COD), the CH_2 group intensity ratio decreases by ~11% relative to air. For water, this ratio decreases by ~4%. Collectively, these data suggest that the spectral response of the octadecyl chains is capable of responding to different solvent interactions. Acetonitrile and deuterated methanol appear to disrupt the alkyl chains more significantly than water. These observations are consistent with those recently reported by Burbage and Wirth.[24] Wirth observed that wetting solvents, such as alcohols, cause slight perturbations in the stationary phase, resulting in a greater orientational distribution of partitioning molecules and a more disordered stationary phase than nonwetting solvents, such as water. Although the Raman data suggest that the stationary phase is slightly perturbed by the presence of acetonitrile and deuterated methanol, the octadecyl chains still maintain a predominantly ordered configuration and do not resemble a "liquid-like" environment.

Surface Coverage Measurements by X-ray Photoelectron Spectroscopy. XPS was used in an attempt to estimate thickness of the octadecylsilane layer using the relationship in eq 1 relating the signal intensity of the underlying substrate

$$I_s = I_{s^\circ} \exp[-d/\lambda \sin \alpha] \quad (1)$$

(I_s) to the thickness of the overlayer (d), the escape depth of electrons through the overlayer (λ), the angle at which the electrons are ejected from the surface (α), and the signal intensity of the pure bulk substrate at zero coverage (I_{s°). Recasting eq 1 in a logarithmic form results in the following linear relationship:

$$\ln I_s = \ln I_{s^\circ} - d(1/\lambda \sin \alpha) \quad (2)$$

Therefore, a plot of $1/\lambda \sin \alpha$ versus $\ln I_s$ (intensity of underlying substrate) at various angles should result in a line with a slope equal to the thickness of the overlayer (d). When α is 90°, $\sin \alpha$ is equal to 1 and the vertical sampling depth is maximized. As α decreases, the path length of the X-rays through the overlayer increases, which decreases the vertical sampling depth.

(67) Wallach, D. F. H.; Verma, S. P.; Fookson, J. *Biochim. Biophys. Acta* **1979**, *559*, 153–208.
(68) Gaber, B.; Peticolas, W. L. *Biochim. Biophys. Acta* **1977**, *465*, 260–274.

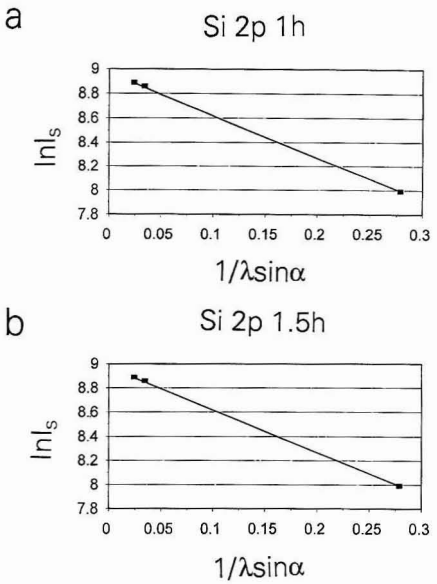

Figure 6. Plot of the natural log of the XPS signal from the Si 2p electrons versus (1/λ sin α) for immersion times of (a) 1 and (b) 1.5 h.

Five variables are associated with eq 2. I_s^∞ is left as an unknown and included in the y-intercept term, α is an instrumental variable, and I_s is the detected XPS signal. Therefore, the only unknown variables are d and λ. In order to determine d, λ must be known. Bain and Whitesides have estimated λ for organic thin films (self-assembled alkanethiol monolayers) at Au surfaces by measuring the attenuation of the Au XPS signal as a function of the thiol chain length.[69] They estimated escape depths of 42 Å at 1402 eV, 34 Å at 1151 eV, and 28 Å at 940 eV. Other reported values range from 15 to over 100 Å.[70-72]

The relationship between measured signal intensity and α are plotted for the Si 2p electrons using immersion times of 1 and 1.5 h in parts a and b of Figure 6, respectively. The self-assembled monolayer films used by Bain and Whitesides are used as a reasonable model of the alkylsilane films formed on our silica surfaces. The escape depths used in the thickness calculations are based on the data provided by Bain and Whitesides.[69] An escape depth of 39.77 Å was used for Si 2s electrons (154 eV) and 41.12 Å for Si 2p electrons (104 eV). The corresponding thickness measurements are tabulated in Table 2. The measurements made with the Si 2p electrons and the Si 2s electrons are in excellent agreement, as expected. Interestingly, the estimated film thicknesses do not increase for extended immersion times, suggesting that octadecylsilane film formation is complete after 1 h.

Table 2. Octadecylsilane Thickness Estimates

	immersion time (h)	λ	d (Å)
Si 2s	1.0	39.77	3.5
	1.5	39.77	3.2
Si 2p	1.0	41.12	3.2
	1.5	41.12	3.5
Si 2s	1.0	100	6.4
	1.5	100	8.1
Si 2p	1.0	100	7.7
	1.5	100	8.6

Assuming that the octadecylsilane films form a single monolayer on a smooth silica surface and that the alkyl chains are extended out away from the silica surface, the thickness of a monolayer octadecylsilane film is predicted to be ~25–30 Å thick, comparable to octadecanethiol films formed by self-assembly on metal surfaces.[73,74] However, using the escape depths provided by Bain and Whitesides, the XPS measurements suggest that the octadecylsilane films formed on the thin silica surfaces are only ~3 Å, significantly less than predicted for a perfectly ordered monolayer film.

The XPS thickness measurements depend significantly on the values of λ used. Substituting increasingly larger values for λ into eq 2 results in larger thicknesses, as shown in Table 2. Using an escape depth of 100 Å (the upper range of λ based on the XPS literature), the thickness of the polymeric stationary phase is estimated to be ~8 Å, still substantially smaller than that predicted for an ordered monolayer.

The uncertainty associated with the approximation of λ suggests that XPS may not provide a good quantitative estimate of film thickness for these octadecylsilane overlayers. However, the XPS results do qualitatively suggest that the silica surface polymeric films are fairly thin, on the order of monolayer or less in coverage, and not oligomeric phases similar to what have been prepared by Sanders and Wise.[75] One conclusion from these results might be that the alkylsilane layers adhere to the silica surface as collapsed, densely packed, thin films. This explanation is not consistent with the Raman spectral data or the plethora of chromatographic evidence that suggests that these films are more ordered.

Attenuation of film thickness would also be observed if the octadecylsilane bonded to the silica surface in patchy islands and not in a uniform layer. More likely, however, is the influence of surface roughness on the accuracy of film thickness measurements for these systems. Surface roughness in the underlying silica layer would prohibit a certain fraction of the octadecylsilane film from producing measurable signals, since the silica roughness features would shield this fraction from X-ray excitation. The predicted thickness values assume a smooth, flat silica surface. For these surfaces, X-rays at a grazing angle sample more of the octadecylsilane overlayer, as shown in Figure 7a. For a porous or rough silica surface, the surface roughness features shield the octadecylsilane layer and sample more of the silica layer at grazing angles, as shown in Figure 7b. Consequently, surface roughness results in attenuation of the octadecylsilane film thickness. In any case,

(69) Bain, C. D.; Whitesides, G. M. *J. Phys. Chem.* **1989**, *93*, 1670–1673.
(70) Hupfer, B.; Schupp, H.; Andrade, J. D.; Ringsdorf, H. *J. Electron Spectrosc. Relat. Phenom.* **1981**, *23*, 103–107.
(71) Cadman, P.; Gossedge, G.; Scott, J. D. *J. Electron Spectrosc. Relat. Phenom.* **1978**, *13*, 1–6.
(72) Brundle, C. R.; Hopster, H.; Swalen, J. D. *J. Chem. Phys.* **1979**, *70*, 5190–5196.
(73) Porter, M. D.; Thomas, B. B.; Allara, D. L.; Chidsey, C. E. D. *J. Am. Chem. Soc.* **1987**, *109*, 3559–3568.
(74) Bain, C. D.; Troughton, E. B.; Tao, Y. T.; Evall, J.; Whitesides, G. M.; Nuzzo, R. G. *J. Am. Chem. Soc.* **1989**, *111*, 321–335.
(75) Sanders, L. C.; Wise, S. A. *Anal. Chem.* **1984**, *56*, 504–510.

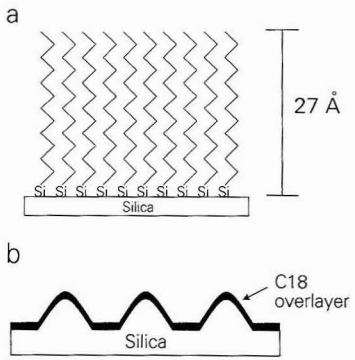

Figure 7. Diagram of overlayer on (a) smooth silica surface and (b) rough silica surface.

the thickness measurements made by XPS are consistent with the estimates of surface coverages made by chromatographers for this type of system in that they are not thick polymer layers, in spite of what the name implies but, instead, are relatively thin films no more than several monolayers at most, and more typically monolayer or submonolayer in coverage.[63]

CONCLUSIONS

The results presented here demonstrate the utility of Raman spectroscopy for studying alkyl conformational changes for common chromatographic RPLC stationary phases. The spectra indicate the the hydrocarbon chains are predominantly in an ordered configuration similar to what might be expected on the basis of the brush model of an alkylsilane stationary phase. In the presence of common mobile phases such as acetonitrile, deuterated methanol, and water, the alkyl chains undergo subtle conformational changes and appear to be in dynamic equilibrium with their surrounding environment.

Detection limits could be improved by decreasing the thickness of the thin silica layer or increasing the surface area of the silica gel which would permit a greater range of studies, such as those on monomeric stationary phases, to be pursued. Further applications of this "sandwich" approach are currently being investigated. A variety of insulating oxides and semiconducting surfaces can be created with sol–gel chemistry techniques which should result in a range of surface adsorbate characterizations using Raman spectroscopy.

ACKNOWLEDGMENT

The support of this work by the National Science Foundation (Grant CHE-9023678) is gratefully acknowledged.

Scientific Parentage of the Authors. W. R. Thompson, Ph.D. under J. E. Pemberton, Ph.D. under R. P. Buck, Ph.D. under D. N. Hume, Ph.D. under I. M. Kolthoff.

Received for review April 21, 1994. Accepted June 17, 1994.[⊗]

[⊗] Abstract published in *Advance ACS Abstracts,* August 1, 1994.

Anal. Chem. **1994,** *66,* 3371–3378

Monodisperse Dried Microparticulate Injector: A New Tool for Studying Fundamental Processes in Inductively Coupled Plasmas

John W. Olesik* and Steven E. Hobbs

Laboratory for Plasma Spectrochemistry, Mass Spectrometry and Laser Spectroscopy, Department of Geological Sciences, The Ohio State University, 1090 Carmack Road, Columbus, Ohio 43210

Spatially and temporally resolved inductively coupled plasma (ICP) emission intensities produced when samples are introduced by the monodisperse dried microparticulate injector (MDMI) are reported for the first time. The MDMI produces monodisperse droplets of controllable size on demand and reproducibly introduces the droplets into an ICP with 100% efficiency. Emission intensity peak heights and peak areas (in time) had a relative standard deviation of 1–6% except near the point of analyte particle vaporization. Sr atom emission intensity appears to be high only when the analyte particle is being vaporized. Analyte particle vaporization times were less than 80 μs. By variance of the furnace temperature and the gas flow rate through the furnace, the drop size can be controlled. The height in the plasma where analyte particle vaporization occurs can be controlled from below the load coil to more than 30 mm above the load coil.

The processes leading to inductively coupled plasma emission and mass spectrometry signals include aerosol droplet desolvation, particle vaporization, atomization, ionization, and excitation. If any of these processes are sample-dependent, matrix effects could lead to errors in analysis. It is difficult to assess which of the processes are most influenced by large concentrations of concomitant species without being able to separately investigate each process. If a single droplet of sample could be followed in the plasma, the drop desolvation and particle vaporization processes would be clearly separated in time and space. It may also be possible to observe the kinetics of ionization. This requires that either a single droplet of sample or a train of monodisperse droplets must be reproducibly introduced into the inductively coupled plasma (ICP). However, conventional pneumatic nebulizers produce polydisperse aerosols with more than 10^8 droplets/s entering the plasma.

The optimum drop size to be introduced into the ICP is not known. The size of the largest droplets that can be completely vaporized in the plasma is not precisely known, although some estimates (10–20 μm) have been made from a combination of aerosol drop size distribution and aerosol transport rate measurements made when the plasma is not operating and laser light scattering measurements made in the operating ICP.[1] There is evidence that the signal per gram of analyte entering the plasma is drop size dependent.[2,3] If individual droplets of known, controllable size could be introduced into the ICP, more direct, reliable measurements to address these points could be made.

The potential to gain new insight into the fundamental processes that control signals in atomic sources using a monodisperse droplet generator has been demonstrated with laminar flames. Hieftje and Malmstadt[4] first described such experiments in 1968 as well as analytical applications in 1969.[5] Subsequently, many fundamental studies using a monodisperse droplet generator with flames that have been reported include investigations of desolvation,[6] vaporization,[7,8] the spatial distribution of atoms surrounding a vaporizing analyte particle,[9,10] and matrix effects.[11]

Recently, investigations focusing on the effect of individual droplets and particles on emission,[12–16] laser-induced fluorescence,[16] and mass spectrometry[17] signals have led to a new understanding of the factors controlling ICP emission and mass spectrometry signals. When conventional nebulizers are used, a significant number of droplets (although a small percentage of the total number of droplets in the aerosol) remain incompletely desolvated within the ICP.[1,12,13] Each incompletely desolvated droplet affects the plasma ionization and excitation processes within 1–2 mm of the drop, acting as a local heat sink.[1] As a result, even if only one out of one million aerosol droplets are incompletely desolvated in the ICP, time-integrated signals can be significantly influenced. The region near desolvated analyte particles is also affected.[16]

The results of these studies have many implications. Incompletely desolvated droplets are a key factor controlling vertical emission profiles as a function of power and center gas flow rate.[14] Models of the ICP based on steady state

(1) Olesik, J. W.; Fister, J. C. III *Spectrochim. Acta* **1991,** *46B,* 851.
(2) Koropchak, J. A.; Aryamanya-Mugisha, H. *J. Anal. At. Spectrom.* **1989,** *4,* 291.
(3) Olsen, S. D.; Strasheim, A. *Spectrochim. Acta* **1983,** *38B,* 973.
(4) Hieftje, G. M.; Malmstadt, H. V. *Anal. Chem.* **1968,** *40,* 1860–1867.
(5) Hieftje, G. M.; Malmstadt, H. V. *Anal. Chem.* **1969,** *41,* 1735–1744.
(6) Clampitt, N. C.; Hieftje, G. M. *Anal. Chem.* **1972,** *44,* 1211–1219.
(7) Bleasdell, B. D.; Wittig, E. P.; Hieftje, G. M. *Spectrochim. Acta* **1981,** *36B,* 205–213.
(8) Hieftje, G. M.; Miller, R. M.; Pak, Y.; Wittig, E. P. *Anal. Chem.* **1987,** *59,* 2861–2872.
(9) Boss, C. B.; Hieftje, G. M. *Anal. Chem.* **1979,** *51,* 895–901.
(10) Boss, C. B.; Hieftje, G. M. *Anal. Chem.* **1979,** *51,* 1897–1905.
(11) Bastiaans, G. J.; Hieftje, G. M. *Anal. Chem.* **1974,** *46,* 901–910.
(12) Cicerone, M. T.; Farnsworth, P. B. *Spectrochim. Acta* **1989,** *44B,* 897.
(13) Olesik, J. W.; Smith, L. J.; Williamsen, E. J. *Anal. Chem.* **1989** *61,* 2002.
(14) Fister, J. C. III; Olesik, J. W. *Spectrochim. Acta* **1991** *45B,* 869.
(15) Ogilvie, C. M.; Farnsworth, P. B. *Spectrochim. Acta* **1992,** *47B,* 1389.
(16) Hobbs, S. E.; Olesik, J. W. *Spectrochim. Acta* **1993,** *48B,* 817.
(17) Hobbs, S. E.; Olesik, J. W. *Anal. Chem.* **1991,** *64* , 274.

0003-2700/94/0366-3371$04.50/0
© 1994 American Chemical Society

assumptions[18–22] must be applied with caution. Apparent deviations from local thermodynamic equilibrium (LTE) could be due to time-varying plasma conditions resulting from local cooling by individual droplets[16] and bias introduced into time-integrated measurements.[23] Evaporation of sample in the plasma has been proposed to affect excitation flow in the ICP.[24] Noise resulting from signal fluctuations due to individual droplets and particles contributes to imprecision in ICP measurements. The effect of incompletely desolvated droplets and vaporizing particles helps to explain the success or failure of internal standards[25] under different operating conditions. Measurements using Fourier transform interferometers are deleteriously affected by signal fluctuations due to incompletely desolvated droplets and vaporizing particles.[26] Molecular oxides that act as spectral interferences in ICP-MS may be formed mainly near incompletely desolvated droplets.[17,27]

Fundamental processes in the ICP could be much more clearly investigated by introducing a reproducible train of droplets of controlled size and number into the ICP rather the by using conventional nebulizers. However, this is much more difficult to accomplish experimentally in ICPs than in large, laminar flow flames. Because of the high temperature, spatial heterogeneity, and small size of the ICP, droplets could not be introduced from the side of the plasma, as was done with large, laminar flames.

This paper reports initial ICP-OES studies using a new sample introduction device developed by French and coworkers.[28] The monodisperse dried microparticulate injector (MDMI) produces monodisperse droplets of solution from an on-demand micropump, injects the droplets into a flowing stream of gas nearly isokinetically, desolvates the droplets to any desired extent in a furnace and reproducibly carries the droplets or desolvated particles into the center of a conventional ICP.

The MDMI also has a number of potential practical applications including analysis of small volumes of sample, reduction of oxides in ICP-MS[28] and potential signal-to-noise advantages using frequency-selective detection.

In this paper, spatially and temporally resolved emission intensity measurements using the MDMI are reported for the first time. The reproducibility of the MDMI system is assessed via time-resolved laser light scattering and emission measurements. Vertical emission profiles using the MDMI are compared to those using a conventional nebulizer/spray chamber. The relationship between vertical emission profiles and particle vaporization is discussed. Control of the drop size and its affect on vertical emission profiles is explored.

Table 1. Instrumentation and Experimental Parameters

power supply	Plasma Therm 2500W, 27.12 MHz (HFP-2500D)
impedance matcher	Plasma Therm (AMNPS-1)
incident power	1.0 kW
outer gas-flow rate	12.0 L/min
intermediate gas-flow rate	0.6 L/min
central gas-flow rate	varied (see text)
torch	Perkin-Elmer
samples	50 ppm Sr as $SrCO_3$
spectrometer	McPherson Model 2016B with 3600 g/mm holographic grating
imaging detector	Princeton Instruments Model 576G/R intensified charge coupled device detector (with Thompson 384 × 578 CCD chip)
photomultiplier tube	Hamamatsu R636 (−1000 to −1200 V applied)
spectral lines	Sr I, 460.73 nm; Sr II, 421.55 nm

EXPERIMENTAL SECTION

Experimental parameters and instrumentation used to measure time and space-resolved emission intensities are listed in Table 1.

Laser-Light-Scattering Measurements. Light from a 15 mW HeNe laser (Aerotech model OEM10R) was scattered by droplets approximately 3 mm above the MDMI furnace. Scattered light was collected in a forward direction about 4.4° from the laser beam. A single 15 cm focal length, fused silica, planoconvex lens was used to collect scattered light. A 0.35 m Heath Czerny-Turner monochromator with 1200 g/mm grating was used with a Hamamatsu R636 photomultiplier tube with an applied voltage of −1200 V. A Keithley Model 427 current amplifier was used with a gain of 10^6 V/A and a rise time of 10 μs. A Nicolet Model 3091 digital oscilloscope was used to measure the time-resolved voltage waveforms. Data were transferred to a Gateway 2000 DX-33 microcomputer via an RS-232 interface and ASYST software.

Time-Resolved Emission Measurements. Time-resolved data were acquired with one of two spectrometers. Each spectrometer viewed a horizontal slice of the ICP. In one case a 0.35 m Heath monochromator was mounted on its side so that the slit was horizontal. Alternatively, the ICP image was rotated 90° using a pair of beam steerers[29] and focused on the entrance slit of a 1 m McPherson Model 2061 monochromator with a 3600 g/mm holographic grating. An image of the ICP was formed on the entrance slit with a magnification of 1.1. The slit width was 50 μm, leading to an effective viewing height in the plasma of approximately 46 μm (or larger, depending on optical aberrations). A Keithley Model 427 current amplifier was used with a rise time of 10 μs to convert the PMT output current into a voltage monitored by a Nicolet Model 3091 digital oscilloscope. Data were transferred via an RS-232 interface to a PC.

Emission Spatial Profiles. Initially, vertical emission profiles were acquired sequentially using the instrumental system described in the preceding paragraph and a translation stage on which the ICP torch box was mounted. Subsequently, two dimensional spatial profiles were acquired simultaneously

(18) Blades, M. W.; Horlick, G. *Spectrochim. Acta* **1981**, *36B*, 861.
(19) Raaymakers, I. J. M. M.; Boumans, P. W. J. M.; Van Der Sijde, B.; Schram, D. C. *Spectrochim. Acta* **1983**, *38B*, 697.
(20) Boumans, P. W. J. M.; deBoer, F. J. *Spectrochim. Acta* **1977**, *32B*, 365.
(21) Hasegawa, T.; Umemoto, M.; Haraguchi, H., Hsiech, C.; Montaser, A. In *Inductively Coupled Plasma in Analytical Atomic Spectrometry*, 2nd ed.; Montaser, A., Golightly, D. W., Eds.; VCH Publishers: New York, 1992.
(22) Olesik, J. W. *Spectrochim. Acta* **1989**, *44B*, 625.
(23) Olesik, J. W.; Den, S.-J. *Spectrochim. Acta* **1990**, *45B*, 731.
(24) Fey, F. H. A. G.; de Regt, J. M.; van der Mullen, J. A. M.; Schram, D. C. *Spectrochim. Acta* **1992**, *47B*, 1447.
(25) Myers, S. A.; Tracy, D. H. *Spectrochim. Acta* **1983**, *38B*, 1227.
(26) Travis, J. C.; Winchester, M. R.; Salit, M. L.; Wythoff, B. J.; Scheeline, A. *Spectrochim. Acta*, in press.
(27) Tanner, S. D. *J. Anal. At. Spectrom.* **1993**, *8*, 891–897.
(28) French, J. B.; Etkin, B.; Jong, R. *Anal. Chem.* **1994**, *66*, 685–691.
(29) Olesik, J. W.; Williamsen, E. J. *Appl. Spectrosc.* **1989**, *43*, 933.

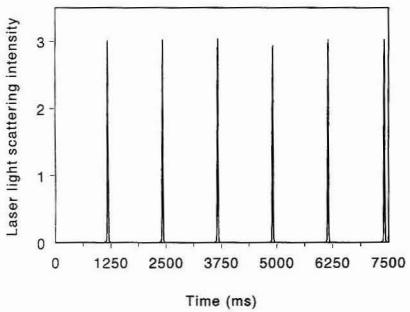

Figure 1. Time-resolved laser-light-scattering measured 3 mm above the top of the MDMI furnace.

using a slitless spectrograph[30] with astigmatism compensating focussing optics[31] and an intensified CCD detector. Signals produced from analyte contained in between 60 and 600 droplets were integrated.

Monodisperse Dried Microparticulate Injector. Two different versions of the MDMI,[28] constructed of stainless steel and quartz, respectively, were used during these studies. The MDMI was oriented vertically below the plasma. The center, demountable quartz tube of the ICP torch was inserted into the end of stainless steel MDMI furnace. The quartz MDMI furnace terminated in a socket. A quartz center tube of the ICP torch, terminating in a ball joint, was connected to the MDMI furnace socket. The tip of the center tube of the ICP torch had an inner diameter of 1.5 mm.

RESULTS AND DISCUSSION

Reproducible Production, Desolvation, and Transport of Sample Droplets. The reproducibility of the production and transport of individual droplets through the furnace in a train can be seen by observing time-resolved laser light scattering signals (Figure 1) at the exit of the furnace. When the initial droplet velocity entering the furnace and the gas velocity through the furnace were optimized to minimize jitter in the arrival times of successive droplets (produced at a rate of 800/s) at the exit of the furnace, the jitter was about 7 μs. Precision of the laser light scattering peak height, which is related to drop size, was typically better than 1% and as low as 0.1% under optimum conditions.

The reproducibility of transport of droplets into the ICP is shown by the time-resolved Sr atom and ion emission intensities measured at 30 mm above the load coil (Figure 2). Each peak in atom and ion emission intensity was produced from about 3 pg of Sr that was originally contained in a single, 65 pL (60 μm diameter) droplet. The variation in the time between Sr atom emission intensity peaks (nominally 1.67 ms) had a standard deviation of between 11 and 65 μs, depending on the day and specific MDMI experimental settings. At a gas velocity of about 24 m/s,[12] this corresponds to a distance of approximately 0.26–1.6 mm. At the same gas velocity and a drop production frequency of 600 Hz, the distance between droplets in the plasma is 40 mm. The jitter

(30) Olesik, J. W.; Hieftje, G. M. *Anal.Chem.* **1985**, *57*, 2049–2055.
(31) Olesik, J. W.; Bradley, K. R. *Spectrochim. Acta* **1986**, *42B*, 377.

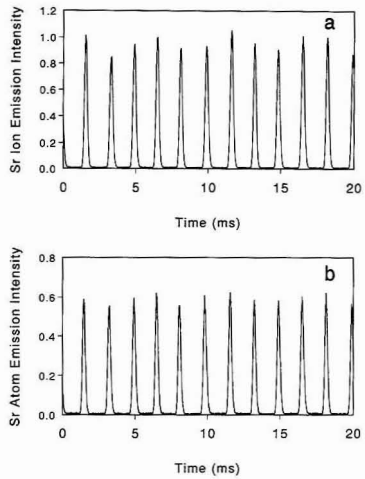

Figure 2. Time-resolved Sr atom and ion emission intensity observed at 30 mm above the load coil. Center gas-flow rate was 1.4 L/min.

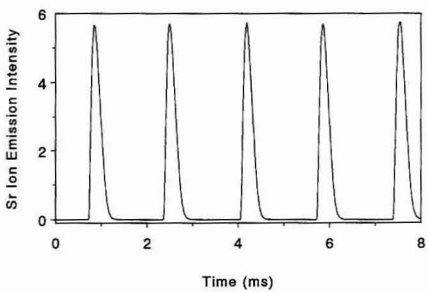

Figure 3. Time-resolved Sr ion emission intensity observed at 14 mm above the load coil. Center gas flow rate was 0.9 L/min.

time measured in the ICP may be higher than the jitter time measured at the exit of the furnace because of turbulence created near the joint between the furnace and center tube of the ICP torch, between the top of the center tube of the torch and the plasma, or in the plasma itself.

The short-term relative standard deviation of the Sr ion emission intensity peak heights (and areas) produced following vaporization of individual analyte droplets varied from day to day between 1% (Figure 3, center gas flow rate was 0.9 L/min) and 6% (Figure 2, center gas flow rate was 1.4 L/min). A short-term precision of 2–3% was routinely achieved. Hieftje and Malmstadt[4] reported a relative standard deviation of 3% in flame emission intensity when monodisperse droplets were introduced.

Near the point of analyte particle vaporization, fluctuations in the drop-to-drop atom and ion emission intensities were much larger, with a relative standard deviation for peak heights and areas between 30% and 35% (Figure 4). It is likely that the large variations in emission intensity at this height are due to differences in the extent of vaporization (due to differences in the height in the ICP where particle vaporization begins).

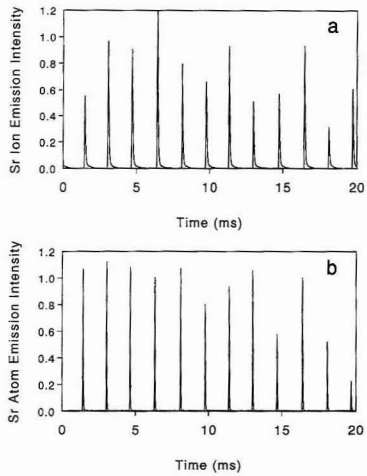

Figure 4. Time-resolved Sr atom and ion emission intensity observed at 14 mm above the load coil. Center gas-flow rate was 1.4 L/min.

This could be the result of gas-velocity fluctuations in the furnace or plasma or small fluctuations in the initial drop size leading to different heights (times) when desolvation is complete. The time to vaporize the analyte particle produced from a 60 μm droplet of 50 ppm Sr is less than 80 μs, corresponding to less than a 2 mm distance in the plasma. Therefore, it is not surprising that large variations in the peak emission intensity (from sample originally in individual sample droplets) are observed near the height where particle vaporization begins.

Comparison of MDMI and Conventional Nebulizers. Unlike conventional nebulizers, the MDMI introduces samples into the ICP as monodisperse droplets (or dried particles) with 100% efficiency. There is no drain or waste.

Water loading, as both liquid and vapor, are different for the MDMI than conventional nebulizer/spray chamber sample introduction systems. When pneumatic nebulizers and double-pass spray chambers are used, aerosol transport rates are typically 7–20 mg/min of sample solution.[32–34] Furthermore, the argon passing through the spray chamber becomes saturated with water vapor. At room temperature, this corresponds to about 20 mg of water vapor/L of Ar. So, at a nebulizer (center) gas flow rate of 1 L/min, as much as 40 mg of water (aerosol and vapor) enter the ICP each minute. The total amount of water entering the plasma when the MDMI is used depends on the initial drop size and the drop production rate. If the droplets produced by the on-demand drop generator are 60 μm in diameter and the drop production frequency is 600 drops/s, a total of about 4 mg of water (aerosol and vapor) enters the plasma per minute. For a drop production rate of 2000 drops/s, a total of 13.6 mg of water enters the plasma per minute. The relative amount of water vapor versus liquid aerosol introduced by the MDMI depends on the extent of desolvation in the furnace, which is in turn a function of the gas flow rate (velocity through the furnace) and the furnace temperature, as discussed below.

Table 2. Comparison of Gas Velocities at Tip of Center Tube of ICP Torch and Transit Times for Drops from Tip of Center Tube to Top of Load Coil[a]

gas-flow rate	gas temp (°C)	gas velocity (m/s)	time to travel (ms)
0.6	25	11.0	1.8
0.6	200	17.5	1.1
1.0	25	6.6	3.0
1.0	200	10.5	1.9

[a] Center tube inner diameter assumed to be 1.4 mm in diameter. Tip of inner tube assumed to be 20 mm from top of load coil.

The velocity of the gas exiting the center tube of the torch depends on the inner diameter of the end of the tube, the gas flow rate, and the gas temperature. If the gas temperature is 200 °C (473 K) at the end of the center tube, the gas velocity using the MDMI will be approximately 1.6 times higher than if the same torch and gas-flow rate were used with a conventional nebulizer at room temperature (298 K).

Calculations[35,36] and experimental measurements[12,37] show that the plasma gas velocity is virtually independent of center gas flow rate at or above the load coil. Therefore the "residence time" of sample in the plasma above the load coil is unaffected by changes in center gas-flow rate. However, the velocity between the tip of the center tube and the plasma will be a function of the center gas flow rate. So, the time a drop spends between the tip of the center tube and its entry into the ICP will be different for the MDMI versus a conventional nebulizer/spray chamber operated at room temperature. Table 2 shows some simple estimates of the time required for a drop to travel from the tip of the center tube to the top of the load coil. As can be seen from these data, the increased temperature of the gas exiting the MDMI will result in a shorter time for a drop of sample to travel from the torch to the top of the load coil. Although this time is not the residence time in the plasma, some desolvation likely occurs during this time.

Vertical Emission Profiles. The vaporization, ionization, excitation, and diffusion processes control vertical atom and ion emission intensity profiles in the ICP. However, conventional nebulizers produce a wide range of droplet sizes. As a result, the height in the plasma where vaporization and production of free atoms and ions begins is dependent on the original size of the sample droplet. Because the MDMI produces a train of monodisperse droplets that are reproducibly transported into the plasma, the locations in the plasma where droplet desolvation, particle vaporization, and ionization occur should be more easily separated.

Time-integrated Sr atom and ion vertical emission profiles produced using a pneumatic nebulizer and spray chamber are compared to those using the MDMI in Figure 5. In particular, the width of the vertical Sr atom emission intensity profile is much narrower (in terms of height in the plasma) when the MDMI is used in place of the pneumatic nebulizer. Also, the

(32) Browner, R. F.; Boorn, A. W.; Smith, D. D. *Anal. Chem.* **1982**, *54*, 1411–1419.
(33) Farino, J.; Miller, J. R.; Smith, D. D.; Browner, R. F. *Anal. Chem.* **1987**, *59*, 2303–2309.
(34) Bates, L. C.; Olesik, J. W. *J. Anal. At. Spectrom.* **1990**, *5*, 239–247.
(35) Barnes, R. M.; Scheicher, R. G. *Spectrochim. Acta* **1981**, *36B*, 81.
(36) Mostaghimi, J.; Proulx, P.; Boulos, M. I. *Plasma Chem. Plasma Proc.* **1984**, *4*, 199.
(37) Barnes, R. M.; Jenna, J. L. *Spectrochim. Acta* **1981**, *36B*, 299.

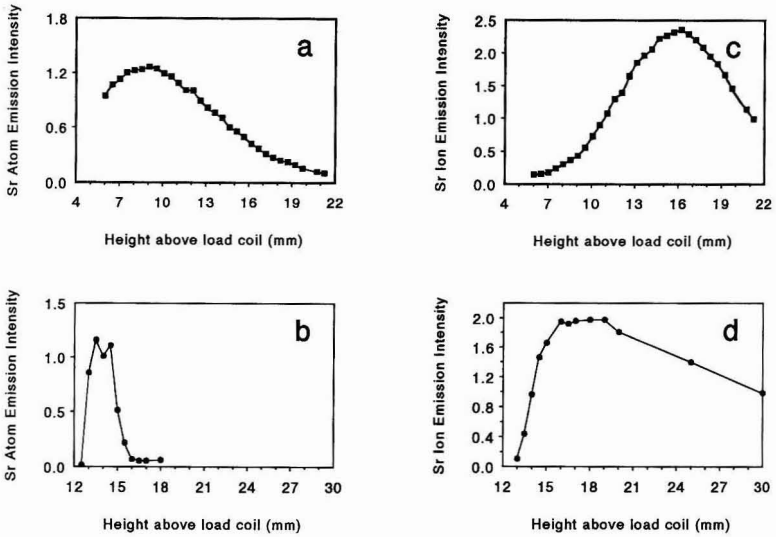

Figure 5. Comparision of time-integrated Sr atom and ion vertical emission profiles produced using a conventional nebulizer/spray chamber and using the MDMI. (a) Sr I–nebulizer; (b) Sr I–MDMI; (c) Sr II–nebulizer; (d) Sr II–MDMI.

leading edge of the peak in the Sr ion emission intensity is much steeper when the MDMI is used.

When a conventional nebulizer is used, small sample droplets are vaporized low in the plasma while some large droplets survive into the analytical zone. The atom emission intensity is large only in cool regions of the plasma near incompletely desolvated droplets. Conversely, ion emission from most lines is depressed near incompletely desolvated droplets. The leading edge of both the atom and ion vertical emission profiles is then related to the number of incompletely desolvated droplets at each height.[14] As a result, the leading edge of the vertical emission profiles rises slowly. Fister and Olesik[14] showed that there was a relatively constant number of incompletely desolvated droplets at the height of peak atom emission (or ion emission) intensity even when the location of the peak was varied by adjusting the nebulizer gas flow rate or plasma power.

In contrast, when the MDMI is used, the height in the plasma where vaporization begins (for a particular set of experimental conditions) is very similar for all drops because they are monodisperse and reproducibly transported with a fixed separation in time (distance) into the plasma. The leading edge of the Sr atom emission intensity will be related to the vaporization of the desolvated analyte particle.

When a conventional nebulizer is used, the Sr atom vertical emission intensity profile falls off at a height in the plasma where the number of incompletely desolvated droplets is decreasing rapidly. Then the time-averaged atom concentration in the observation volume is falling faster than the fraction of atoms that are excited is increasing. The ion vertical emission intensity falls off at heights where either diffusion dilutes the number of ions in the observation zone or the plasma temperature decreases (resulting in a smaller fraction of ions that are excited).

When the MDMI is used, the ionization process is probably the main cause of the rapid fall in the atom vertical emission profile. While the particle is vaporizing, it cools a local region of the plasma. It is also likely that the region near a vaporizing particle may have been cooled during droplet desolvation and not yet heated to the temperature of the surrounding plasma gas. In either case, the fraction of analyte as atoms (rather than ions) should be higher in the cooler regions of the plasma.[16] The distance over which the atom vertical emission profile falls and the ion vertical emission profile rises is probably controlled by a combination of the ionization kinetics and the rate of temperature increase of the center channel of the plasma after the particle vaporization is complete. The ion vertical emission profile falls off mainly due to diffusion of ions out of the observation zone. At some point, the plasma temperature will fall off as it mixes with the surrounding atmosphere which decreases the fraction of ions that are excited.

Further investigation is needed to determine if the above explanations of the vertical emission profiles using the MDMI, which are consistent with the data, are correct. In particular, one must use great care in interpreting the emission data because the emission intensity depends on the fraction of atoms (or ions) excited as well as the number of atoms (or ions) in the observation volume.

Connecting Vertical Emission Profiles to Particle Vaporization. Figure 6 shows an expanded view of the Sr atom and ion vertical emission profiles at the heights (8.5–11.5 mm above the load coil) where emission is first observed. Following the above line of reasoning, the initial rise in Sr atom (460 nm) emission intensity is consistent with initial vaporization of the desolvated analyte particle, followed by atomization and excitation. The atomization and excitation processes are likely rapid compared to vaporization. The fall in Sr atom

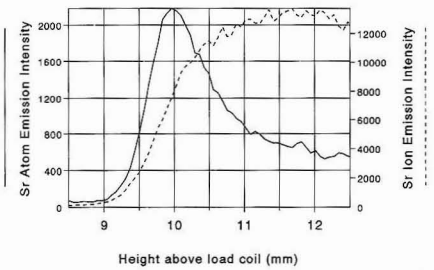

Figure 6. Comparison of time-integrated Sr atom and ion vertical emission profiles near the point of analyte particle vaporization.

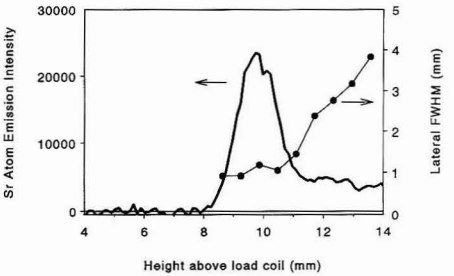

Figure 7. Sr atom emission intensity and lateral full width at half-maximum as a function of height above the load coil.

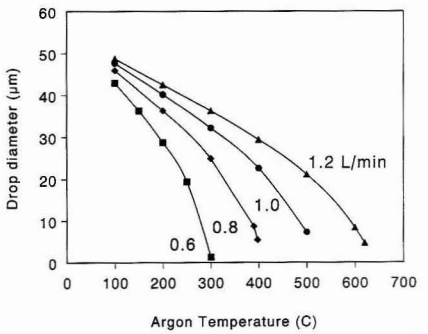

Figure 8. Estimated (model calculated) drop size at the exit of the MDMI furnace as a function of gas-flow rate and furnace temperature.

emission intensity is likely due to more complete ionization of Sr when the particle vaporization is finished. If this explanation for the rise and fall of the Sr atom emission intensity as a function of height in the plasma is true, then the Sr atom emission intensity may be used as a sensitive probe of analyte particle vaporization.

If the gas velocity in the plasma is known, then it is possible to determine the vaporization time of analyte particles in analytical ICPs using the MDMI. This would make it possible to determine how vaporization time is related to initial desolvated particle size by varying the analyte concentration in the original liquid sample. The sample was 50 ppm Sr as $SrCO_3$. If the desolvated particle is assumed to be spherical with a density equal to that of pure $SrCO_3$, the initial diameter of the particle would be 0.39 μm. If the plasma gas velocity is approximately 24 m/s,[12] then the 1–2 mm width of the Sr atom vertical emission profile corresponds to a vaporization time of 40–80 μs.

To test the idea that the Sr atom vertical emission profile width is related to the particle vaporization, lateral emission profiles were also observed with the imaging spectrometer. While the particle is vaporizing, it acts as a local source of atoms, as well as a heat sink. As a result, the Sr atom emission intensity should be strongly peaked near the particle (in the center channel of the plasma). After the particle is vaporized, both lateral diffusion and ionization will reduce the concentration of atoms in the center of the plasma. Furthermore, the lateral emission profile should rapidly become wider due to lateral diffusion.

Figure 7 shows a plot of Sr atom emission intensity and the full width at half-maximum (fwhm) of the lateral emission profile as a function of height in the plasma. The fwhm of the lateral profiles does not appear to change during the peak in the Sr atom vertical emission profile. This is consistent with the idea that the peak in Sr atom emission intensity occurs while the particle is vaporizing. However, it is also possible that jitter in the lateral position of the particle is large compared to the width of the atom cloud near a single particle. The jitter could then be the main controlling factor for the fwhm of the lateral profile until diffusion produces a wider atom cloud. Detection of the vertical and lateral emission profile from a single particle could address this question. Alternatively, the lateral emission profiles could be controlled by expansion of hot plasma gas inward, i.e., the center channel.

There are two potential sources of error that could make the apparent vaporization time, based on Sr atom emission intensity behavior, erroneously long. If the position of the initial vaporization point is not constant from one drop to the next, the vaporization time obtained from data acquired by averaging the signals due to multiple drops will be biased high. This possibly occurs because of the observed jitter time between emission peaks from consecutive droplets and the large variation in emission intensities observed near the vaporization point. Furthermore, the vaporization time is based on emission intensities. This assumes that the time between vaporization and atomization/excitation are short relative to the vaporization time. There is some evidence that this may not be true in flame sources.[38,39]

Varying the Drop Size. For fundamental experiments and perhaps some practical applications, it is desirable to be able to control (vary) the size of the sample droplets entering the plasma. In the MDMI system, drop size can be controlled by adjusting the furnace temperature or gas-flow rate (which in turn controls the time that the drop spends in the furnace).

Using the model described by French et al.,[28] the drop diameter can be related to the furnace temperature and gas-flow rate (Figure 8). It should be possible to produce a drop diameter anywhere between the original drop size (before desolvation) and a completely desolvated particle.

As the gas-flow rate is increased, the size of the droplets

(38) Childers, A. C.; Hieftje, G. M. *Anal. Chem.* **1993**, *65*, 2753–2760.
(39) Childers, A. G.; Hieftje, G. M. *Anal. Chem.* **1993**, *65*, 2761–2765.

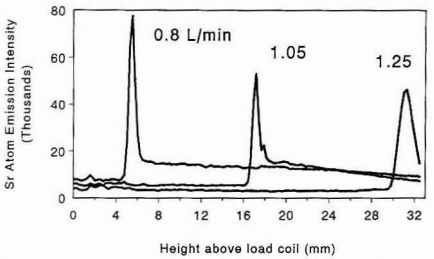

Figure 9. Sr atom vertical emission profiles at center gas flow rates of 0.8, 1.05, and 1.25 L/min.

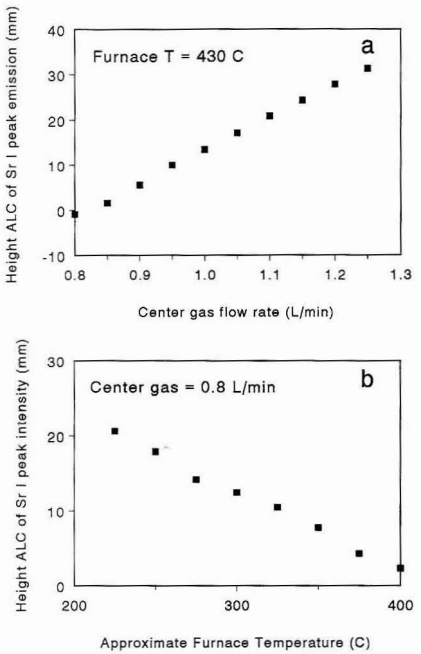

Figure 10. Height in the ICP where analyte particle vaporization occurs (as indicated by the peak in Sr atom emission intensity) as a function of center gas flow rate and furnace temperature.

exiting the furnace should increase. The height in the plasma where Sr atom emission was first observed moved upward in the plasma as the gas-flow rate was increased (Figure 9), consistent with larger drops entering the plasma. Figure 10 shows how the height of peak Sr atom emission intensity varied as a function of furnace temperature and gas-flow rate. As can be seen from these data, the point where vaporization of the desolvated analyte particle begins can be controlled from below the load coil to more than 30 mm above the load coil. This suggests that the drop size exiting the furnace can be controlled and varied over a fairly wide range, as the model predicts.

Calculations by Etkin[28,40] estimate the drop size (at the exit of the furnace) corresponding to the furnace temperatures

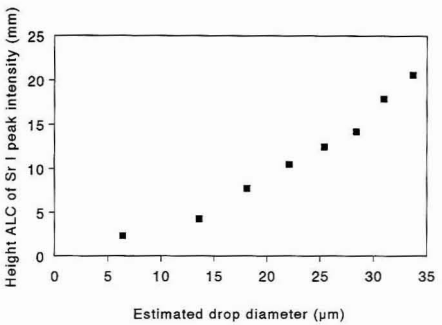

Figure 11. Estimated size of droplets that survive to various heights in the plasma.

and gas-flow rates used in these experiments to be variable from 3 to more than 30 μm in diameter. Figure 11 shows the relationship between the location (height) in the ICP where the Sr atom emission intensity peaks and the estimated original size of the drop when it exited the furnace based on the model.[28]

The combination of the model predicted drop sizes and measured vertical emission profiles leads to upper limits on the original size of drops that are completely desolvated in the plasma. These results are in the same range as values measured previously using a conventional nebulizer.[1] At a central gas-flow rate of 0.8 L/min, previous results indicated that droplets with a diameter larger than 12 μm when entering the plasma survived to 8 mm above the load coil and that droplets 23 μm in diameter survived to 18 mm above the load coil. The new results based on our emission measurements with the MDMI and the model predicted drop diameter suggest that droplets 16 μm or larger survive to 8 mm above the load coil and droplets 31 μm or larger in diameter survive to 18 mm above the load coil. Considering the potential sources of error and differences in experimental conditions, these results agree quite well.

CONCLUSIONS

The MDMI system reproducibly introduced a train of droplets of monodisperse droplets into the ICP. Emission from picogram quantities of analyte originally contained in a 60 μm diameter droplet was easily detectable. Short-term precision in the emission intensity peak heights (or areas) originating from individual sample droplets was between 1% and 6%.

Vertical atom emission intensity profiles were much narrower when the MDMI is used in place of a conventional nebulizer. This is likely because vaporization of the desolvated monodisperse droplets occurs over a small, well-defined range of heights in the ICP. Sr atom vertical emission profiles appear to be directly related to the vaporization of the desolvated analyte particles. The Sr atom emission intensity was large only while the particle is vaporizing. Sr ion vertical emission intensity profiles had a much sharper leading edge when the MDMI was used rather than a conventional nebulizer. This

(40) Etkin, B., personnel communication, March 1993.

is likely due to the narrow range of heights over which particle vaporization occurs and rapid ionization of the analyte.

The size of droplets introduced into the plasma can be varied by adjusting the gas-flow rate through the MDMI furnace and the furnace temperature. The height in the ICP where vaporization occurs can be varied from below the load coil to more than 30 mm above the load coil by selection of the drop size.

A number of practical questions remain to be addressed regarding the operation of the MDMI for fundamental experiments. Vertical emission profiles from single droplets must be measured to assess the contribution of jitter in the point of initial vaporization to the measured vaporization times. Independent drop size measurements must be made. Drop size and transport precision must be evaluated. The effect of sample matrix on the drop generation process or the desolvation of the droplet in the furnace, if any, must be assessed.

The results presented in this paper demonstrate only a small part of the huge potential of the MDMI for fundamental studies of inductively coupled plasmas.

ACKNOWLEDGMENT

Barry French, Ben Etkin, and Ray Jong (University of Toronto Institute for Aerospace Science) are thanked for developing the MDMI and for many exciting discussions concerning both their results and those reported here. Dennis Yates is also acknowledged for helpful comments on this paper. Perkin-Elmer Corp. is acknowledged for donation of the ICP power supply and impedance matcher used in these studies. This research was supported by the National Science Foundation (Grant CHE 9217170), Perkin Elmer Corp., and The Ohio State University.

Received for review February 21, 1994. Accepted June 22, 1994.®

® Abstract published in *Advance ACS Abstracts,* August 1, 1994.

Anal. Chem. **1994,** *66,* 3379–3383

Surface-Enhanced Raman Gene Probes

T. Vo-Dinh,* K. Houck, and D. L. Stokes

Advanced Monitoring Development Group, Health Sciences Research Division, Oak Ridge National Laboratory, Oak Ridge, Tennessee 37831-6101

We report for the first time a new type of DNA gene probe based on surface-enhanced Raman scattering (SERS) label detection. The surface-enhanced Raman gene (SERG) probes do not require the use of radioactive labels and have great potential to provide both sensitivity and selectivity. The SERG probe can be used to detect DNA biotargets (e.g., gene sequences, bacteria, viral DNA fragments) via hybridization to DNA sequences complementary to that probe. The analytical figures of merit and its applications in environmental and biomedical areas are discussed.

There is currently strong interest in the development of nonradioactive DNA probes for use in a wide variety of applications, such as gene identification, gene mapping, DNA sequencing, medical diagnostics, and biotechnology. We report here for the first time the development of a new type of DNA probe based on surface-enhanced Raman scattering (SERS) label detection. These surface-enhanced Raman gene (SERG) probes do not require the use of radioactive labels and have a great potential to provide both sensitivity and selectivity.

Raman spectroscopy is a useful tool for chemical analysis due to its excellent capability of chemical group identification. One limitation of conventional Raman spectroscopy is its low sensitivity, often requiring the use of powerful and costly laser sources for excitation. However, a renewed interest has recently developed among Raman spectroscopists as a result of observation that Raman scattering efficiency can be enhanced by factors of up to 10^8 when a compound is adsorbed on or near special metal surfaces.[1,2] Spectacular enhancement factors due to the microstructured metal surface scattering process is responsible for increasing the intrinsically weak normal Raman scattering (NRS) signal. The technique associated with this phenomenon is known as surface-enhanced Raman scattering (SERS) spectroscopy. The Raman enhancement process is believed to result from a combination of several electromagnetic and chemical effects between the molecule and the metal surface.[1]

For the past few years we have concentrated our efforts to develop efficient SERS-active substrates for trace organic analysis in environmental and biological applications.[3–10] The possibility of using Raman and/or SERS for in situ monitoring has also been reported.[9,11–14] The SERS technique has been recently applied to trace detection of pesticides, dyes, food products, and metabolites of chemical exposure.[15–20] In this article we report the use of the SERS technique as a tool for detecting specific nucleic acid sequences. An example of hybridization experiment using the SER-gene probe illustrates the usefulness of this technology. Hybridization of a nucleic acid probe to DNA biotargets (e.g., gene sequences, bacteria, viral DNA) permits a very high degree of accuracy for identifying DNA sequences complementary to that probe. The potential applications of the SER-gene probe in environmental monitoring and in biomedical diagnostics are discussed.

EXPERIMENTAL SECTION

Instrumentation. Raman measurements were conducted with a SPEX Model 1403 double-grating spectrometer (SPEX Ind.) equipped with a thermoelectrically cooled gallium arsenide photomultipler tube (RCA, Model C31034), operated in the single-photon-counting mode. Data storage and processing were handled using a personal computer (PC) with SPEX Datamate software. The monochromator bandpass was 2 cm^{-1}. Laser excitation was the 620-nm line extracted from the emission band of a rhodamine 6G loaded dye laser (Coherent, CR-599–21) pumped by an argon ion laser (Coherent, Innova-70). Tuning of a birefringent filter plus the use of a bandpass filter permitted a narrow excitation bandpass centered at 620 nm. Laser power was 25 mW for all measurements. A right-angle geometry of the laser excitation source and the scattered radiation was employed. SERS measurements were performed using two experimental systems. The SPEX-based system was used to generate the basic SERS spectra. An ICCD-based system was used to generate spectra in hybridization experiments. In this system

(1) Chang, R. K., Furtak, T. E., Eds., *Surface-Enhanced Raman Scattering*; Plenum: New York, 1982.
(2) Jeanmarie, D. J.; Van Duyne, R. P. *J. Electroanal. Chem.* **1977,** *84,* 1.
(3) Vo-Dinh, T.; Hiromoto, M. Y. K.; Begun, G. M.; Moody, R. L. *Anal. Chem.* **1984,** *56,* 1667.
(4) Vo-Dinh, T.; Meier, M.; Wokaun, W. *Anal. Chim. Acta.* **1986,** *181,* 139.
(5) Moody, R. L.; Vo-Dinh, T.; Fletcher, W. H. *Appl. Spectrosc.* **1987,** *41,* 966.
(6) Alak, A.; Vo-Dinh, T. *Anal. Chem.* **1989,** *61,* 656.
(7) Vo-Dinh, T.; Miller, G. H.; Bello, J.; Johnson, R. D.; Moody, R. L.; Alak, A.; Fletcher, W. H. *Talanta,* **1989,** *36,* 227.
(8) Bello, J. M.; Stokes, D. L.; Vo-Dinh, T. *Anal. Chem.* **1989,** *61* 1779.
(9) Bello, J. M.; Vo-Dinh, T. *Anal. Chem.* **1990,** *44,* 63.
(10) Bello, J. M.; Narayana, V. A.; Stokes, D. L.; Vo-Dinh, T. *Anal. Chem.* **1990,** *62,* 2437.
(11) Carraba, M. M.; Edmonds, R. B.; Rauh, R. D. *Anal. Chem.* **1987,** *59,* 2559.
(12) Angel, S. M.; Katz, L.; Archibald, D.; Honigs, D. *Appl. Spectrosc.* **1989,** *43,* 367.
(13) Garrison, A. A.; Trimble, D. S.; Muly, E. C.; Roberts, M. J.; Kercel, S. W. *Amer. Lab.* **1990,** *Feb,* 19.
(14) Alarie, J. P.; Stokes, D. L.; Sutherland, W. S.; Edwards, A. C.; Vo-Dinh, T. *Appl. Spectrosc.* **1992,** *46,* 1608.
(15) Enlow, P. D.; Buncick, M.; Warmack, R. J.; Vo-Dinh, T. *Anal. Chem.* **1986,** *58,* 1119.
(16) Vo-Dinh, T.; Uziel, M.; Vo-Dinh, T. *Appl. Spectrosc.* **1987,** *41,* 605.
(17) Vo-Dinh, T.; Alak, A.; Moody, R. L. *Spectrochim. Acta B* **1988,** *4/5,* 605.
(18) Vo-Dinh, T. Surface-Enhanced Raman Spectroscopy. In *Chemical Analysis of Polyaromatic Compounds*; Vo-Dinh, T., Ed.; Wiley: New York, 1989.
(19) Narayanan, V. A.; Bello, J. M.; Stokes, D. L.; Vo-Dinh, T. *J. Raman Spectrosc.* **1991,** *22,* 327.
(20) Narayanan, V. A.; Bello, J. M.; Stokes, D. L.; Vo-Dinh, T. *Analusis* **1992,** *19,* 307.

0003-2700/94/0366-3379$04.50/0
© 1994 American Chemical Society

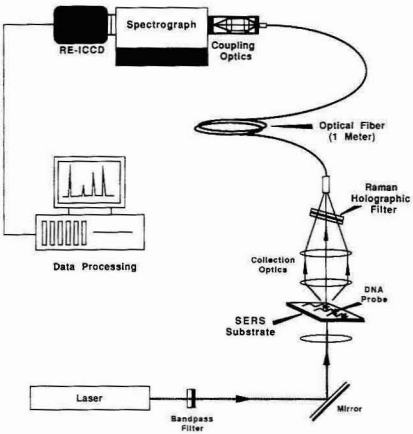

Figure 1. RE-ICCD research system: Instrument set-up to detect the SERG probe.

the 632.8-nm line from a helium–neon laser was used with an excitation power of approximately 5 mW. A bandpass filter was used to spectrally isolate the 632.8-nm line before focusing onto the sample. Scattered radiation was collected with a two-lens system which efficiently coupled the collected radiation to a 600 μm diameter silica fiber (NA-0.26, General Fiber Optics). Signal collection was performed at 180° with respect to the incident laser beam. A Raman holographic filter was used to reject the Rayleigh scattered radiation prior to entering the collection fiber. The collection fiber was finally coupled to a spectrograph (ISA, HR-320) which was equipped with a red-enhanced intensified charge-coupled device (RE-ICCD) detection system (Princeton Instruments, RE-ICCD-576S). ICCD control and data processing was enabled by a Princeton Instruments ST-130 control unit and CSMA software installed on a PC. Figure 1 shows a schematic diagram of the detection system of the SERG probe. Fluorescence measurements were performed with the Perkin-Elmer fluorimeter (Model LS-50).

Chemicals. The agglomerate-free alumina (0.1 μm nominal particle diameter) used to prepare the SERS substrates was provided by Baikowski Int. Corp. The alumina was suspended in distilled Milli-Q Plus water by sonication.

Procedure. The properties of the SERS substrates based on microparticles were described in detail.[17,18] SERS substrates were prepared in the following manner. Three drops of a 5% aqueous suspension of the alumina were dropped and spread evenly on the surface of a precleaned rectangular glass strip (2.5 cm × 1.25 cm; 1 mm thick) cut from a microscope slide. The glass strip was then placed on a spinning device and spun at 2000 rpm to spread the alumina uniformly. Next, a 100-nm layer of silver was thermally evaporated onto the alumina-coated glass strip at a pressure of 2×10^{-6} Torr.

MATERIALS AND METHODS

Preparation of Buffers and Solutions. The highest grade of reagents available were used. All solutions were prepared with distilled, deionized Milli-Q Plus water. All nucleic acid solutions were sterilized by autoclaving or by filtration through a 0.22-μm filter. Exposure of labeled DNA to light was minimized by using opaque siliconized glassware, aluminum foil covering, or reduced room-lighting conditions.

Preparation of Nitrocellulose Blot. Oligonucleotides for binding to nitrocellulose were prepared from homopolymers of adenosine or thymidine. Samples were heated for 10 min at 100 °C, rapidly chilled on ice, and diluted to 50% with 1 M NaOH. Alkaline-treated DNA was then incubated for 30 min at room temperature before neutralization with the following solution: 0.5-M Tris, 1 M NaCl, 0.3 M sodium citrate, 1 M HCl. Samples were then immediately chilled on crushed ice. A nitrocellulose filter (Sigma) was cut into 3 mm × 3 mm squares and turned onto virgin parafilm. DNA (25 μL) was loaded onto the nitrocellulose in 5 μL aliquots, added sequentially to the same spot, leaving sufficient time to absorb the material between additions. The amount of DNA affixed to the membrane was 2.5 μg. Filters were air dried for 2 h and then washed with 50 mL of SSC-20X solution (175.3 g of NaCl, 88.2 g of Na citrate in 1 L H_2O; pH 7.0). After washing the DNA loaded nitrocellulose, the filters were redried and baked for 2 h at 75–85 °C in a vacuum oven.

Synthesis of SERG Probes. Solutions of cresyl fast violet (Fluka), erythrosin, and aminoacridine (Sigma) were prepared at 0.15–0.25 M concentrations. Labeled oligonucleotides were synthesized as 5′-phosphoramidates using a modification of the procedure described by Chu and coworkers.[21] Briefly, solutions of deoxyribonucleotide oligomers (either 9 or 18 residues in length; Sigma) were converted to 5′-phosphorimidazolide intermediates with 0.2 M imidazole and 0.5 M 1-ethyl-3-(dimethylamino)propyl carbodiimide by incubation at 50 °C for 3 h. The 5′-phosphorimidazolides were then reacted with equal volumes of the SERS active labels (e.g., cresyl fast violet dye) for 18 h at 50 °C. Unreacted label was removed from the reaction mixture by gel filtration on Bio-spin 6 columns (Bio-Rad). The resultant labeled oligonucleotide samples were concentrated by lyophilization.

Hybridization Procedures. Nitrocellulose filters containing the DNA to be hybridized were placed in siliconized 1.5 mL microfuge tubes. Distilled water was added to the tube and was boiled in a water bath. The water was then removed by gentle aspiration. Negative controls consisted of labeled DNA that was not complimentary to the immobilized DNA.

The filters were incubated overnight at 40 °C in hybridization solutions containing 2 ng/mL of the labeled probe. DNA which did not hybridize was removed by washing three times with SSPE-20X solution (174 g of NaCl, 27.6 g of NaH_2PO_4 in 1 L of H_2O; pH 7.4) containing 0.1% SDS at room temperature.

Material which hybridized to the nitrocellulose was recovered as follows. Filters were washed twice with 1 mL of SSC solution (0.1 N NaOH) for 30 min at room temperature and three times with 1 mL of SSC followed by vortexing. The wash buffer was aspirated, neutralized, pooled, and lyophilized before SERS analysis. The reconstitution volume was 30 μL, and only 1 μL was spotted onto the SERS substrate.

(21) Chu, B. C. F.; Orgel, L. E. *Nucleic Acids Res.* **1983**, *11*, 6513.

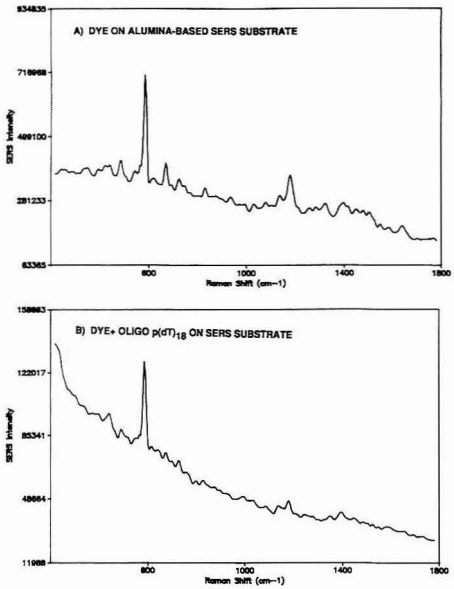

Figure 2. (A) SERS spectrum of cresyl fast violet (CFV) label alone. (B) SERS Spectrum of CFV label attached to 18 deoxyribonucleotide oligomers, $p(dT)_{18}$.

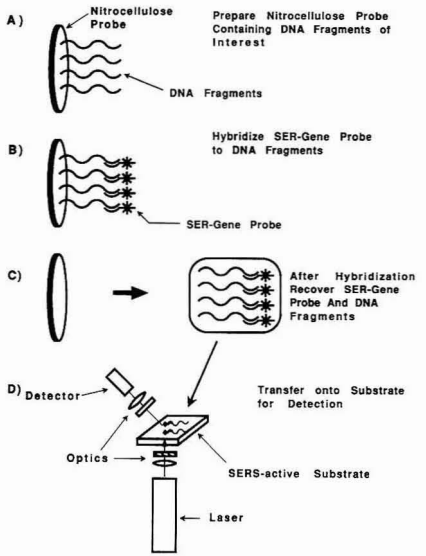

Figure 3. Schematic diagram of SERG probe hybridization and detection.

RESULTS AND DISCUSSION

SERS Spectrum of Cresyl Fast Violet SERS Label. Figure 2A shows a SERS spectrum of a dye, cresyl fast violet (CFV), that was used in this study for DNA labeling. The measurement was performed using a silver-coated alumina substrate. The laser wavelength was 620 nm, and the excitation power only 25 mW. The SERS spectrum of cresyl violet exhibits a series of narrow lines with the strongest at 590 cm^{-1}. This intense and sharp line can be attributed to the benzene ring deformation mode. Another less intense but sharp line at 1195 cm^{-1} could be related to benzene ring breathing vibrations. Another group of small peaks between 1000 and 1400 cm^{-1} could be associated with aromatic ring substitution-sensitive modes. Finally several peaks, which could correspond to benzene stretch vibrations, occur between 1500 and 1650 cm^{-1}.

SERS Detection of the CFV-Labeled Oligonucleotides. Cresyl fast violet, which was used as the model DNA label in this study, was covalently attached to a nucleic acid fragment consisting of 18 deoxyribonucleotide oligomers of thymine, $p(dT)_{18}$. The SERS spectrum of this labeled DNA fragment is shown in Figure 2B. The SERS-active substrate used for this figure is identical to that used to obtain the SERS spectrum of the CFV label alone (Figure 2A). Figure 2B demonstrates that it is possible to detect the spectral characteristic features of the CVF label even when it is bound to a large $p(dT)_{18}$ oligonucleotide fragment. Comparison of parts A and B of Figure 2 indicates that the presence of the oligonucleotides induces a decrease in the SERS intensity of the CFV label, as one can expect, but the spectral features of the label are still visible. Although there is an increase of the background emission when the CFV label is attached to the DNA fragment, the sharp peak associated with the label at 585 cm^{-1} remains the most prominent SERS line of the labeled DNA fragment. It is noteworthy that a slight shift of this band is observed between the labeled dye (586 cm^{-1}, Figure 2B) and the dye alone (590 cm^{-1}, Figure 2B). Careful inspection of Figure 2B indicates that several other small peaks in the label oligonucleotide system (445, 490, 675, 725, 1140, 1180 cm^{-1}, Figure 2B) are similar to those detected in the label (450, 490, 675, 730, 1145, 1195 cm^{-1}, Figure 2A).

SERG Probe in DNA Hybridization. To demonstrate the applicability of the SERS method in DNA gene probe technology, we performed a series of hybridization and SERS detection experiments. Hybridization, which involves the joining of a strand of nucleic acid with its corresponding mirror image, is a powerful technique to identify DNA sequences of interest. Figure 3 shows a schematic diagram of the hybridization and SERS detection of the probes. Figure 4 shows the results obtained with the different samples investigated. In these experiments we employed DNA fragments to be hybridized, viz., $p(dA)_{18}$ oligonucleotides which are complementary to the SERS-labeled $p(dT)_{18}$ probes discussed previously. The SERS-labeled probes that hybridized to the DNA oligomers attached on nitrocellulose were recovered by washing the nitrocellulose and spotted on a SERS-active substrate (silver-covered alumina) for analysis. Negative controls, which consisted of labeled DNA that was not complementary to $poly(dT)_{18}$ fragments, for example, CFV-labeled $p(dC)_9$ oligonucleotides, were also analyzed. Figure 4A shows clearly the SERS peak of the labeled $p(dT)_{18}$ probes that have hybridized to $p(dA)_{18}$. On the other hand, negative

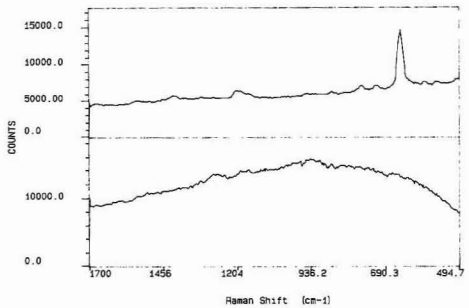

Figure 4. (A) Detection of the SERG probe that has hybridized to a DNA fragment complementary to the probe. (B) No SERS detection indicates that the DNA fragments are not complementary to the SER-Gene probe.

controls exhibit no SERS signals since the SERG probes do not hybridize to the $p(dC)_9$ oligonucleotides (Figure 4B).

Analytical Applicability of SERG Probe. Among the various methods for gene identification, technologies using radioactive labels are currently the most widely used. Radioactive label techniques suffer from several disadvantages however. The principal isotope used, phosphorus-32, has a limited shelf life because it has a 14-day half-life. Second, because there is one principal label for gene probes, DNA can only be probed for one sequence at a time. Due to material limitations, probing immobilized DNA with different ^{32}P-labeled sequences can only be performed a few (3–4) times. Therefore, the researcher must have some idea about the sequence prior to probing. In addition to these inconveniences, the potential safety hazard associated with use of radioactive materials makes the technology undesirable. Shipping, handling, and waste disposal of radioactive materials are strictly regulated by federal and state guidelines.

Because SERG probes rely on chemical identification, rather than emission of radioactivity, they have a significant advantage over radioactive probes. SERG probes are formed with stable chemicals which do not emit potentially dangerous ionizing radiation. Furthermore, the probes offer the excellent specificity inherent in Raman spectroscopy. While isotope labels are few, many chemicals can be used to label DNA for SERS detection. Potentially up to hundreds of different SERG probes could be constructed. A large number of probes with different labels could be used to simultaneously probe one immobilized DNA or RNA of interest.

Recently luminescence labels (e.g., fluorescent or chemiluminescent labels) have been developed for gene detection.[22] Although sensitivities achieved by luminescence techniques are adequate, alternative techniques with improved spectral selectivities must be developed to overcome the need for radioactive labels and the poor spectral specificity of luminescent labels.

The spectral specificity of the SERG probe is excellent in comparison to the other spectroscopic alternatives. For comparison purposes, we compare the detection of the dye cresyl violet in UV absorption, fluorescence, and SERS. As

(22) Richterich, P.; Church, G. M. *Methods Enzymol.* **1993**, *218*, 187.

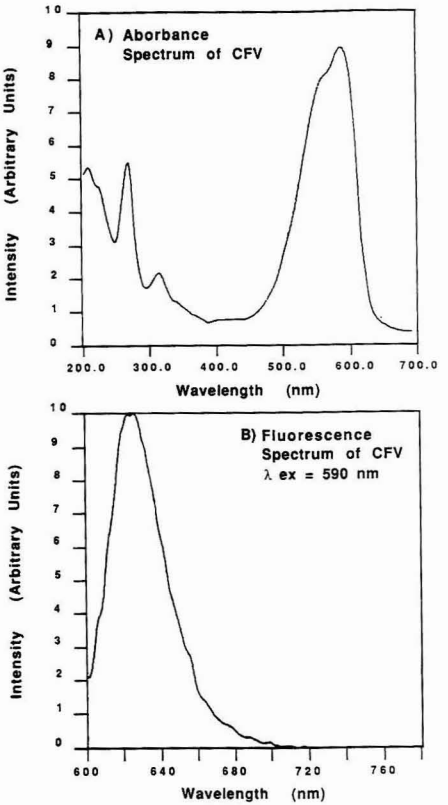

Figure 5. (A) Absorption spectrum of cresyl fast violet. (B) Fluorescence spectrum of cresyl fast violet.

shown in Figure 5, the spectral bandwidth of cresyl fast-violet in UV absorption and fluorescence are broad (typically 50–100 nm half-widths), whereas the bandwidth of the SERS spectrum of the same CFV dye is much narrower (<1 nm half-width, limited here by Raman spectrometer resolution; see Figure 2). For this reason, the Raman approach has a major advantage over the absorption or luminescence techniques. In a typical Raman spectrum, a spectral interval of at least 2000 cm^{-1} can provide 2000/2 or 10^3 available individual spectral "intervals" at any given time. Even allowing a factor of 10 due to possible spectral overlap, it should be possible to find 10^2 labels that can be used for simultaneous detection of different gene biotargets.

CONCLUSION

This work demonstrates the feasibility of DNA probes based on a SERS label. The SERG probe could have a wide variety of applications in areas where nucleic acid identification is involved. The results of this work indicate that single strands of DNA fragments can be prepared and labeled with SERS probes. The SERG probes may then be used to identify genes or to detect bacterial and viral components. The SERG probes

may also be used in polymerase chain reaction (PCR) applications for biotechnology and medical diagnostic applications.

ACKNOWLEDGMENT

This work was sponsored by the Office of Health and Environmental Research under Contract DE-AC05-84-OR21400 with Martin Marietta Energy Systems, Inc. T.V.-D. also acknowledges the support of ORNL-LDRD and of BMDO, managed by the Office of Naval Research (IAG DOE No. 1866-E030-A1, Navy No. N00014-91-F-0042). The assistance of S. A. Poston in performing preliminary measurements is acknowledged. The authors also acknowledge the helpful comments of Dr. V. Ananthanarayanan in the spectral assignment of the SERS spectra.

Received for review January 3, 1994. Accepted June 23, 1994.[⊗]

[⊗] Abstract published in *Advance ACS Abstracts,* August 1, 1994.

Anal. Chem. **1994,** *66,* 3384–3393

Free Radical Detector for Tropospheric Measurement Using Chemical Amplification

Jia Hu and Donald H. Stedman*

Department of Chemistry, University of Denver, Denver, Colorado 80208

An improved chemical amplifier for atmospheric RO_x ($HO + HO_2 + RO + RO_2$) radical measurement is reported. The reaction chamber in this version was equipped with a Teflon filter–nitrogen wall to maintain the nature of the wall constant and reduce the free radical wall loss. The results of laboratory studies were consistent with theoretical calculations assuming a radical wall loss coefficient of 1 s^{-1}. Radical calibration gave relatively stable chain lengths, i.e., 26% variability over a period of 3 months. In addition, the zero modulation and the interferences from the ambient PAN and PNA were reduced by using a smaller reactor which yielded a short residence time. The details of the instrumentation and chain length measurement procedure are described. Results of a local field study in the summer of 1993 using this chemical amplifier are presented.

Free radicals in the earth's atmosphere play significant roles in tropospheric chemistry. The hydroxyl radical, HO, the most important tropospheric gas-phase oxidant, comes from the ultraviolet photolysis of ozone (O_3), nitrous acid (HONO), and various precursors. HO can initiate the reactions of hundreds of trace gases, both natural and anthropogenic, in many instances as the first and rate-determining step.[1] For example, nitrogen and sulfur oxides are converted respectively to nitric and sulfuric acids, and nonmethane hydrocarbons (NMHC) are oxidized to organic acids after reacting with HO.[2] Reactions of HO with hydrocarbons and CO lead to the production of hydroperoxy, HO_2, organic oxy, RO, and organic peroxy, RO_2, radicals. HO_2 is also formed following formaldehyde photolysis, nitrate radical (NO_3) reactions, and the reactions of alkenes with ozone.[3–9] These RO_x radicals ($HO + HO_2 + RO + RO_2$) are known to be involved in the production and removal of ozone in photochemical cycles through the competition between the oxidation of NO by RO_2 and O_3, which govern the so-called $NO–NO_2–O_3$ photostationary-state system in the atmosphere.[10] In addition, HO_2 and RO_2 are the only gas-phase precursors for peroxide compounds H_2O_2 and ROOH, which also contribute to acid precipitation.[2] Finally, HO_2 can participate in a number of oxidation reactions in the aerosol phase because it is soluble in aqueous aerosols.[11]

Many methods have been attempted to measure RO_x radicals. As a consequence of their high reactivity, the tropospheric RO_x concentrations are very low. The calculated total midday maximum varies from about 7×10^8 molecule/cm^3 (28 parts per trillion by volume (pptv) mixing ratio) for clean conditions to around 5×10^9 molecule/cm^3 (200 pptv) for the more polluted case.[12] The daytime value for HO_2 was predicted to be 10–100 pptv, and a 1991 measurement suggested that atmospheric RO_2 was at the same level as HO_2.[13] HO concentrations are perhaps 100–1000 times less, with midday photostationary-state concentrations ranging from $\sim 1 \times 10^7$ molecule/cm^3 (0.5 pptv) to $\sim 1 \times 10^6$ molecule/cm^3 or less.[14,15] RO concentrations are estimated to be much smaller, about 1×10^4 molecule/cm^3 (0.0005 pptv).[16] Consequently, the measurement of RO_x radicals represents a challenge. Determining the concentration of HO generally makes use one of the following four techniques: laser-induced fluorescence (LIF),[17–20] long-path absorption,[21–26] a radiochemical tracer method in which HO reacts with ^{14}CO to produce $^{14}CO_2$,[27–29] and titration/selected-ion chemical

(1) Ehhalt, D. H.; Dorn, H.-P.; Poppe, D. *Proc. R. Soc. Edinburgh* **1991**, *97*, 17.
(2) Thompson, A. M. *Science* **1992**, *256*, 1157.
(3) Calvert, J. G. *Proceedings of the NATO Advanced Study Institute on Atmospheric Ozone: Its Variation and Human Influences*; Report No. FAA-EE-80-20; U.S. Department of Transportation, Federal Aviation Administration, U.S. Government Printing Office: Washington, DC, 1979; p 153.
(4) Moortgat, G. K.; Cox, R. A.; Schuster, G.; Burrows, J. P.; Tyndall, G. S. *J. Chem. Soc., Faraday Trans. 2* **1989**, *85*, 809.
(5) Atkinson, R.; Plum, C. N.; Carter, W. P. L.; Winter, A. M.; Pitts, J. N., Jr. *J. Phys. Chem.* **1984**, *88*, 1210.
(6) Cantrell, C. A.; Stockwell, W. R.; Anderson, L. G.; Busarow, K. L.; Perner, D.; Schmeltekopf, A.; Calvert, J. G.; Johnston, H. S. *J. Phys. Chem.* **1985**, *89*, 139.
(7) Cantrell, C. A.; Davidson, J. A.; Busarow, K. G.; Calvert, J. G. *J. Geophys. Res.* **1986**, *91*, 5347.
(8) Su, F.; Calvert, J. G.; Shaw, J. H. *J. Phys. Chem.* **1980**, *84*, 239.
(9) Kan, C. S.; Su, F.; Calvert, J. G.; Shaw, J. H. *J. Phys. Chem.* **1981**, *85*, 2359.
(10) Crutzen, P. J. *Tellus* **1974**, *26*, 47.
(11) Mozurkewich, M.; McMurry, P. A.; Gupta, A.; Calvert, J. G. *J. Geophys. Res.* **1987**, *92*, 4163.
(12) Mozurkewich, M.; Calvert, J. G. *J. Geophys. Res.* **1990**, *95*, 5697.
(13) Cantrell, C. A.; Lind, J. A.; Shetter, R. E.; Calvert, J. G.; Goldan, P. D.; Kuster, W.; Fehsenfeld, F. C.; Montzka, S. A.; Parrish, D. D.; Williams, E. J.; Buhr, M. P.; Westberg, H. H.; Allwine, G.; Martin, R. *J. Geophys. Res.* **1992**, *97*, 20671.
(14) Eisele, F. L.; Bradshaw, J. D. *Anal. Chem.* **1993**, *65*, 927A.
(15) Kanakidou, M.; Singh, H. B.; Valentin, K. M.; Crutzen, P. J. *J. Geophys. Res.* **1991**, *96*, 15395.
(16) Finlayson-Pitts, B. J.; Pitts, J. N., Jr. *Atmospheric Chemistry: Fundamentals and Experimental Techniques*; John Wiley and Sons, Inc.: New York, 1986.
(17) Hard, M. T.; O'Brien, R. J.; Chan, C. Y.; Mehrabzadeh, A. A. *Environ. Sci. Technol.* **1984**, *18*, 768.
(18) Rodgers, M. O.; Bradshaw, J. D.; Sandholm, S. D.; KeSheng, S.; Davis, D. D. *J. Geophys. Res.* **1985**, *90*, 12819.
(19) Davis, L. I., Jr.; Gao, C.; James, J. V.; Morris, P. T.; Postiff, R.; Wang, C. C. *J. Geophys. Res.* **1985**, *90*, 12836.
(20) Chan, C. Y.; Hard, T. M.; Mehrabzadeh, A. A.; George, L. A.; O'Brien, R. J. *J. Geophys. Res.* **1990**, *95*, 18569.
(21) Perner, D.; Ehhalt, D. H.; Patz, H. W.; Pllat, U.; Roth, E. P.; Volz, A. *Geophys. Res. Lett.* **1976**, *3*, 466.
(22) Dorn, H.-P.; Callies, J.; Pllat, U.; Ehhalt, D. H. *Tellus* **1988**, *40B*, 437.
(23) Hofzumahaus, A.; Dorn, H.-P.; Callies, J.; Ehhalt, D. H. *Atmos. Environ.* **1991**, *25A*, 2017.
(24) Mount, G. H. *J. Geophys. Res.* **1992**, *97*, 2427.
(25) Hübler, G.; Perner, D.; Platt, U.; Tonnissen, A.; Ehhalt, D. H. *J. Geophys. Res.* **1984**, *89*, 1309.
(26) Armerding, W.; Herbert, A.; Spiekermann, M.; Walter, J.; Comes, F. J. *Fresenius' Z. Anal. Chem.* **1991**, *340*, 654.
(27) Campbell, M. J.; Sheppard, J. C.; Au, B. F. *Geophys. Res. Lett.* **1979**, *6*, 175.
(28) Campbell, M. J.; Farmer, J. C.; Fitzer, C. A.; Henry, M. N. *J. Atmos. Chem.* **1986**, *4*, 413.

0003-2700/94/0366-3384$04.50/0
© 1994 American Chemical Society

ionization MS.[30] Measuring RO_2 and HO_2 concentration has been accomplished in the atmosphere and in the laboratory with techniques including matrix isolation with electron paramagnetic resonance (MIEPR),[31–33] which may measure HO_2 and speciated RO_2, and some spectroscopic methods. LIF may also measure HO_2 by converting HO_2 to HO.[17] More details of the measurement methods for RO_x radicals in the atmosphere can be found in review articles.[14,34,35]

Cantrell and Stedman[36] and Cantrell et al.[37] developed a technique for the measurement of total RO_x radicals in the early 1980s. They utilized a chemical amplification method in which each initial radical produced a large number of NO_2 molecules through a chain reaction involving HO, HO_2, RO, and RO_2 with NO and CO. The chain reaction may be initiated, for example, by letting HO_2 or RO_2 react with NO to form NO_2 and an HO or RO:

$$HO_2 + NO \rightarrow NO_2 + HO \quad (1)$$

$$RO_2 + NO \rightarrow NO_2 + RO \quad (2)$$

Through the addition of a large amount of CO, the HO radical produced in reaction 1 reforms HO_2 by the following reactions:

$$HO + CO \rightarrow CO_2 + H \quad (3)$$

$$H + O_2 + M \rightarrow HO_2 + M \quad (4)$$

RO radical from eq 2 reacts efficiently with O_2 to form an HO_2 or RO_2 radical and a carbonyl molecule:

$$RO + O_2 \rightarrow R'CHO \text{ (or } R'R''CO) + HO_2 \text{ (or } R'''O_2) \quad (5)$$

There are several reactions which remove free radicals from the system. The most significant chain termination processes were considered to be the following reactions:

$$HO + NO + M \rightarrow HONO + M \quad (6)$$

$$HO_2 + NO_2 + M \rightarrow HO_2NO_2 + M \quad (7)$$

$$HO_2 + \text{wall} \rightarrow \text{nonradical products} \quad (8)$$

Actually, the chain can be initiated at any of reactions 1–5 by any of the radicals, and thus the sum of HO, HO_2, RO, and RO_2 is determined by this technique. In practice, N_2 gas is added periodically to replace CO so that the chain reaction is turned off, and a blank signal resulting from O_3, NO_2, and other possible interfering molecules is recorded. The difference between the signals with and without CO, or the modulated NO_2 signal, is proportional to the radical concentration. The NO_2 produced is monitored, in most cases, using a sensitive detector based on the chemiluminescent reaction of NO_2 with luminol.[38,39]

The number of NO_2 molecules produced per radical, or the chain length (CL), is a crucial factor in determining measured radical concentrations. This number is dependent on the rates of reactions 1–5, the processes that remove the radicals from the system, and the experimental conditions such as the flow rates of the reagent gases and the reaction time.

In the past decade, several groups around the world have adopted this chemical amplification method in their research. In addition to measuring free radicals, this technique was employed to detect PAN and radon decay in the ambient air.[40–43] One of the major problems often encountered is the uncertainty of the free radical wall loss in the reaction chamber, resulting in the instability of measured chain lengths. Another is so-called zero modulations, which are fake radical signals occurring when no free radicals are considered to be present.

Described in this paper is an improved free radical detector which, to a certain extent, solved the two problems mentioned above. The results of laboratory studies and ambient air measurements are presented and discussed.

EXPERIMENTAL SECTION

Chemical Amplifier. The instrumentation is composed of three parts: a reactor where the chemical amplification takes place and NO_2 is produced from the chain reactions, a detector in which the NO_2 concentration is determined, and a gas system to supply the reagent gases and appropriately ventilate the exhaust.

(i) Reactor or Chemical Amplifier. Several reactor designs were used in our study. The original configuration was developed by both Buhr and Ghim.[44,45] Later, a cone-shaped chamber with a Teflon filter wall was constructed.[46] After an informal comparison between these two reactors and a reactor designed by Hastie et al.,[40,46] a new version of the University of Denver chemical amplifier was configured as shown in Figure 1.

In the original reactor used in this laboratory during 1980s, the reaction chamber (250 mL volume) was fabricated from stainless steel coated with halocarbon wax. This configuration yielded chain length estimates ranging from 10s to over 1000.[44,45] After a series of tests on the factors affecting the chain length determination, it was found that the major problem was the radical wall loss. In our final configuration,

(29) Felton, C. C.; Sheppard, J. C.; Campbell, M. J. *Environ. Sci. Technol.* **1990**, *24*, 1841.
(30) Eisele, F. L.; Tanner, D. J. *J. Geophys. Res.* **1991**, *96(D5)*, 9295.
(31) Mihelcic, D.; Ehhalt, D. H.; Kulessa, G. F.; Komfass, J.; Trainer, M.; Schmidt, A.; Rohrs, H. *Pure Appl. Geophys.* **1978**, *116*, 530.
(32) Mihelcic, D.; Musgen, P.; Ehhalt, D. H. *J. Atmos. Chem.* **1985**, *3*, 341.
(33) Mihelcic, D.; Volz-Thomas, A.; Patz, H. W.; Kley, D.; Mihelcic, M. *J. Atmos. Chem.* **1990**, *11*, 271.
(34) Cantrell, C. A.; Shetter, R. E.; McDaniel, A. H.; Calvert, J. G. In *Measurement Challenges in Atmospheric Chemistry*; Newman, L., Ed.; Advances in Chemistry Series 232; American Chemical Society: Washington, DC, 1993; p 291.
(35) O'Brien, R. J.; Hard, T. M. In *Measurement Challenges in Atmospheric Chemistry*; Newman, L., Ed.; Advances in Chemistry Series 232; American Chemical Society: Washington, DC, 1993; p 323.
(36) Cantrell, C. A.; Stedman, D. H. *Geophys. Res. Lett.* **1982**, *9(8)*, 846.
(37) Cantrell, C. A.; Stedman, D. H.; Wendel, G. J. *Anal. Chem.* **1984**, *56*, 1496.
(38) Maeda, Y.; Aoki, K.; Munemori, M. *Anal. Chem.* **1980**, *52*, 307.
(39) Wendel, G. J.; Stedman, D. H.; Cantrell, C. A. *Anal. Chem.* **1983**, *55*, 937.
(40) Hastie, D. R.; Weissenmayer, M.; Burrows, J. P.; Harris, G. W. *Anal. Chem.* **1991**, *63*, 2048.
(41) Anastasi, C.; Gladstone, R. V.; Sanderson, M. G. *Environ. Sci. Technol.* **1993**, *27*, 474.
(42) Blanchard, P.; Shepson, P. B.; Schiff, H. I.; Drummond, J. W. *Anal. Chem.* **1993**, *65*, 2472.
(43) Ding, H.; Hopke, P. K. *J. Atmos. Chem.* **1994**, *17(4)*, 375.
(44) Buhr, M. P. M.S. Thesis, University of Denver, Denver, CO, 1986.
(45) Ghim, B. T. M.S. Thesis, University of Denver, Denver, CO, 1988.
(46) Stedman, D. H.; Hu, J. *Proc. Annu. Meet.—Air Waste Manage. Assoc., 86th* **1993**, Paper No. 93-WA-68A.03, 16 pp.

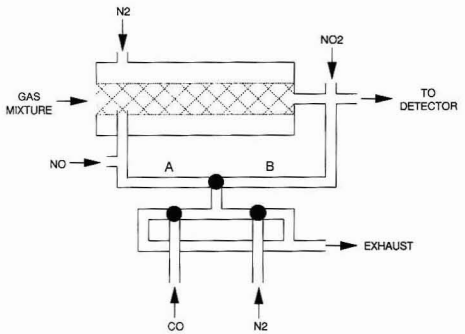

Figure 1. Schematic diagram of the chemical amplifier. The Teflon filter or nitrogen wall reaction chamber is drawn with the dashed lines. Letters A and B refer to the two carbon monoxide addition points.

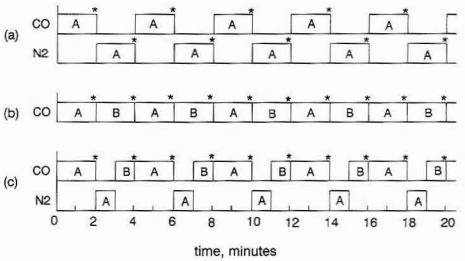

Figure 2. Schematic diagrams of three modulation patterns used in (a) original system, CO flow is replaced with equal N_2 flow; (b) Hastie et al.'s system, CO is added at two points; (c) this study, a combination of a and b. The asterisks mark the points at which data were collected. Letters A and B stand for the two CO addition points as in Figure 1.

the reaction chamber is a tubular Teflon filter (Fiberfilm T60A20, Pallflex Inc.). A piece of 20.4 cm × 7 cm Teflon filter was vertically rolled up and sprung inside a coarse galvanized wire mesh (mesh size, 1 in.) cylinder which was mounted inside a 20.8 cm long, 5.1 cm i.d. leak-free PVC pipe. The final dimension of the Teflon filter reactor is 20.4 cm long with 1.85 cm i.d., corresponding to a volume of 55 cm^3. An N_2 gas flow of about 400 mL/min enters the PVC pipe and passes through the Teflon filter wall, or nitrogen wall as it is called, into the chamber so that a nitrogen layer is formed around the wall, in an attempt to prevent the free radical molecules from contacting with the wall, thereby reducing the wall loss of the radicals. It is quite possible that some radicals might still diffuse into the nitrogen layer and be lost on the wall. However, the fraction of the radical molecules colliding directly with the wall is expected to be decreased with this design.

At a typical total flow of 3 L/min, the residence time of radicals in the reactor is 1.1 s, which is the same as that of Hastie et al.'s reactor.[40] This smaller chamber was adopted partly to reduce the zero modulation and the interferences caused by PAN and PNA in the atmosphere, as discussed later.

Another change we made was to take off the air or gas mixture "inlet". In the original RO_x detector, air was drawn into the reactor through an inlet tube of 1/4 in. stainless steel where the reagent gases NO, CO, and/or N_2 were added. In the new version, the reaction chamber itself is a Teflon filter "tubing" of less than 3/4 in. i.d., which also functions as an air inlet. The reagent gases are sent to the chamber through the Teflon filter wall at the front of the reactor as demonstrated in Figure 1. This improvement eliminates possible free radical loss in the narrow stainless steel inlet.

(ii) NO_2 Detector. The luminol detector used in our work is similar to those described elsewhere.[38,39] The luminol solution is pumped by a peristaltic pump at a rate of 0.3 mL/min and flows over a 4.7 cm diameter fiberglass cloth which is held on the back wall of the detection cell. The gas mixture from the reactor is passed between the fiberglass cloth and a glass window that seals the cell from the photomultiplier tube (RCA 4507). The blue chemiluminescence occurring at the gas–liquid surface from the reaction of NO_2 with luminol is measured, and the photocurrent generated is amplified by an electrometer. The output is displayed on a chart recorder (Cole-Parmer Instrument 8387-32) and is also collected by a personal computer using the Lab Master program.

(iii) Gas System. All gas flows are controlled by mass flow controllers (Tylan Corp.) and calibrated using a bubble flow meter for slow flow rates or a gas sampling test meter (Singer, American Meter Division) for larger ones. The total flow is measured between the reactor and the detector. The solenoid valve timing sequence is controlled by a Chrontrol CT-4 table top timer. Since a high concentration of carbon monoxide is used, care is taken to ensure that the system is leak-free and that the laboratory area is equipped with an alarm (Enmet ISA-3) to warn of dangerous levels. The exhaust from the detector and CO/N_2 switch system is properly vented.

(iv) Modulation Experiments. As described in the introduction section, in the conventional system, a radical zero was obtained by replacing the flow of CO with an equal flow of N_2[36,37,44,45] (Figure 2a). In Hastie et al.'s system, the chain mechanism was suppressed by moving the point at which the CO was added closer to the NO_2 detector[40] (Figure 2b). Besides these two modulation patterns, a new one combining the features of conventional and Hastie's systems (Figure 2c) was also tested. As shown in Figure 1, three 3-way solenoid valves were used in the RO_x detector. The modulation frequency was 0.25 min^{-1} since experiments showed that about 90 s was needed for a signal to reach its maximum. The first 2 min in each modulation cycle supported the chain reaction, CO being added into the reactor at the front of the chamber and N_2 going to the vent. At the third minute, CO and N_2 were switched, N_2 being sent to the chamber and a signal zero being achieved. For the last minute, N_2 was sent to the vent again, and CO was added between the reactor and the detector. No chain reaction was expected in this situation. Notice that the chain reaction was shut off during the last 2 min by both replacing CO with N_2 (third minute) and moving the CO addition point (fourth minute). Without N_2, CO flow is temporarily doubled at point B when CO is switched from point A to B. This causes a spike in the output reading which we essentially eliminated using the N_2 addition. Data were collected as 1 s average values every 2 min (1 s before the switch of with/without chain reactions) for all three modula-

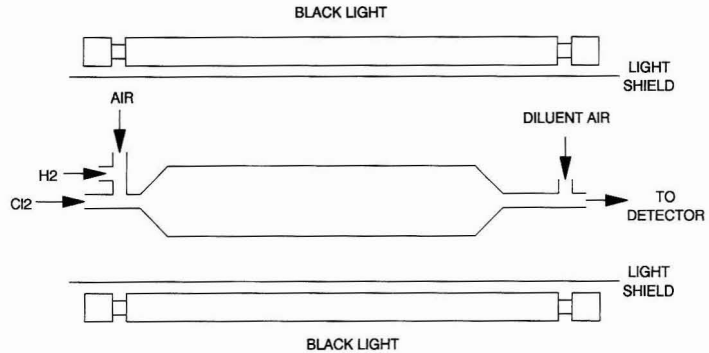

Figure 3. Schematic diagram of Cl_2/H_2/air photolysis system used as a free radical (HO_2) source.

tion patterns as indicated by the asterisk marks in Figure 2. With this data acquisition system, a point-to-point precision of ±3% was observed using a stable free radical source in the laboratory.

Free Radical Source. A free radical or HO_2 source was established using the Cl_2/H_2/air photolysis system which was studied by Cox et al. in 1977.[47] For $[H_2]/[Cl_2] > 20$, HO_2 radicals are produced in a flow tube by the following mechanism:

$$Cl_2 + h\nu\ (320\ nm) \rightarrow 2Cl \qquad j \qquad (9)$$

$$Cl + H_2 \rightarrow HCl + H \qquad k_{10} \qquad (10)$$

$$H + O_2 + M \rightarrow HO_2 + M \qquad k_{11} \qquad (11)$$

$$2HO_2 \rightarrow H_2O_2 \rightarrow O_2 \qquad k_{12} \qquad (12)$$

$$2HO_2 + M \rightarrow H_2O_2 + O_2 + M \qquad k_{13} \qquad (13)$$

The radical destruction processes also include wall loss, eq 8, when the $[HO_2]$ is low. The photolysis flow tube setup is shown in Figure 3. The large portion of the tube is 7.5 cm i.d. × 23.5 cm, and the narrower region is 1.65 cm i.d. × 37 cm, giving a total volume of 1.09 L and reaction time of 150 s when a flow of 410 mL/min is used. The inner surface of the flow tube is coated with halocarbon wax (Halocarbon Products Corp.) to reduce wall reactions. Four GE black lights rich in 320 nm radiation are arranged around the tube. The air flow providing O_2 for the reactions and hydrogen flow are maintained in excess to minimize undesirable reactions. The final flow is diluted with a large air flow near the reactor inlet. The free radical concentrations can be varied by changing either Cl_2 or dilution air flow. In the latter case, the radical source itself remains unchanged.

NO_2 Calibration Technique. NO_2 was added in concentrations from 0 to 250 ppbv at the front of the reaction chamber with the reagent gases NO, CO, and/or N_2. The photocurrents from the electrometer were recorded. As a comparison, the experiments were performed under three conditions: with NO_2 only, with 6 ppm NO added, and in the radical detection mode.

Radical Calibration Technique. Free radical calibration or chain length measurement was made in this study using the Cl_2/H_2/air photolysis system. When the HO_2 concentration is large enough that homogeneous radical destruction dominates over wall loss, the following equations hold from reactions 9–13:

$$d[Cl]/dt = 2j[Cl_2] - k_{10}[Cl][H_2] = 0 \qquad (14)$$

$$d[H]/dt = k_{10}[Cl][H_2] - k_{11}[H][O_2] = 0 \qquad (15)$$

$$d[HO_2]/dt = k_{11}[H][O_2] - 2(k_{12} + k_{13})[HO_2]^2 \qquad (16)$$

For the initial period after all flows are established and the light shields are rapidly removed, the term $2(k_{12} + k_{13})[HO_2]^2$ is assumed negligible. Then:

$$d[HO_2]/dt = k_{11}[H][O_2] = k_{10}[Cl][H_2] = 2j[Cl_2] \qquad (17)$$

For the steady state:

$$d[HO_2]/dt = 2j[Cl_2] - 2(k_{12} + k_{13})[HO_2]^2 = 0 \qquad (18)$$

Combining eqs 17 and 18 and letting the chain length, CL, equal $[NO_2]/[HO_2]$, the final chain length calculation formula is given:

$$CL = 2(k_{12} + k_{13})[NO_2]_{ss}^2/IS \qquad (19)$$

where $[NO_2]_{ss}$ refers to NO_2 concentration at steady state and IS stands for initial slope, $d[NO_2]/dt$, which equals $2j[Cl_2]$-CL.

Thus, in this method, we measured two NO_2 signals from which the chain lengths or instrumental sensitivity to free radicals might be derived from eq 19: (1) the initial change of NO_2 signal with time and (2) the steady-state signal. Experimentally, the initial slope was obtained by uncovering

(47) Cox, R. A.; Derwent, R. G. *J. Chem. Soc., Faraday Trans. 1* **1977**, *73*, 272.

Table 1. Modeling Conditions

	Environment	
temperature	298 K	
pressure	630 mmHg (Denver area)	
relative humidity	15%	
	ambient	reagent
	Initial Conditions	
HO_2	30 pptv	
HO	0.2 pptv	
H_2O_2	2 ppbv	
NO_2	40 ppbv	
NO	20 ppbv	6 ppmv
CO	2 ppmv	8%
PAN	2 ppbv	
CH_3COO_2 (PA)	10 pptv	
CH_2O	50 ppbv	
O_3	60 ppbv	
HNO_3	20 ppbv	
HONO	5 ppbv	
HO_2NO_2 (PNA)	0.5 ppbv	
CH_4	1.5 ppmv	
CH_3NO_4	50 pptv	
RO_2	30 pptv	
RO	0.0005 pptv	
CH_3O_2	3 pptv	
CH_3O	0.003 pptv	
H_2O	4690 ppmv	
O_2	20%	

the black lights to start the photolysis reactions and measured during the first 10 s. During this period, the signal rose steeply and nearly linearly with time. Steady-state NO_2 signals were measured about 20 min later after the steady state was achieved.

In practice, the chain lengths were measured for a range of HO_2 concentrations in which eq 19 held. This range was determined experimentally.

Local Field Measurements. The field measurement site was located in a parking lot near our laboratory building. The free radical detector was set in a trailer. Atmospheric ozone concentrations and solar UV fluxes were measured simultaneously with an O_3 monitor and an Eppley radiometer, respectively.

Computer Simulation. The behavior of the chemical amplifier under the conditions of laboratory research and ambient air study was modeled using the PHASEPLANE computer program.[48] The program input was in the form of differential equations or rate expressions. The reaction mechanism and rate coefficients were largely based on recommendations of references.[40,42,49,50] Table 1 lists the model conditions for the ambient air study with the initial gas mixing ratios for the case of the field measurement in the parking lot. Simulations were performed for daytime only, so the reactions concerning species like N_2O_5 and NO_3 were not included. The modeling results are presented in the form of chain lengths.

Reagents. The gases used in this work were CO (General Air, CP grade); N_2 (General Air, CP grade); 1300 ppm NO in N_2 (Scott Specialty Gases, Certified Master Gas); 50 ppm NO_2 in air (Scott Specialty Gases, Certified Master Gas); H_2 (General Air, CP grade); and 0.1% Cl_2 in N_2 (General Air). The CO was passed through an activated charcoal/iodine trap to remove metal carbonyl compounds, principally Ni$(CO)_4$ and Fe$(CO)_6$.[44] The NO was passed through dry $FeSO_4$ to reduce to NO any NO_2 formed in the cylinder. Stainless steel instead of Teflon tubing was used to carry NO to prevent the inward diffusion of O_2 which led to formation of NO_2. Building compressed air was used and passed through activated charcoal to remove hydrocarbons and NO_x, through ascarite to remove CO_2 and water, and through Purafil to remove CO before entering the photolysis tube.

The composition of the luminol operating solution was 0.05 M NaOH, 0.2 M Na_2SO_3, 1×10^{-4} M luminol (3-aminophthalhydrazide, Aldrich, 97%), 1.5×10^{-4} M EDTA, and 0.1% (v/v) Triton, as recommended by both Cantrell et al.[50] and Blanchard et al.[42] Triton, a surfactant, was added to cause the solution to flow homogeneously over the fiberglass cloth and thus reduce the base line noise, as reported by Blanchard et al. The base line noise of the system with this solution was 0.05 mA, compared to 0.1 mA with the solution we previously[46] used. In addition, we observed higher sensitivity and better linearity for the NO_2 detector. All reagents were used without further purification with the exception of the luminol, which was recrystallized from alkaline aqueous solution as described by Burkhardt.[51]

RESULTS AND DISCUSSION

Theoretical Behavior of the Chemical Amplifier. A general description of chemical amplifier behavior as a function of reagent concentrations, initial radical concentrations, residence time, and rate constants for pertinent reactions, especially the wall loss of radicals, can be found in the literature.[36,37,40,50] Presented in this paper are model results concerning our chemical amplifier under the specific operating conditions used, in order to get a better understanding of the instrument. For example, 1.1 s was used as the reaction time in the chamber for all the simulations with the exception of chain lengths as a function of reaction time.

(i) Influence of Instrumental and/or Operational Parameters. The calculated chain lengths versus [NO] added to the system as a reagent are shown in Figure 4 by the solid line. The wall loss coefficient for radicals, k_{wall}, is chosen to be 1 s^{-1}, as discussed later. The optimum NO concentration appears at 4 ppmv. Normally, we work at an NO concentration of 6 ppmv.

The modeled chain lengths versus [CO] added in the chemical amplifier is displayed by the dotted line in Figure 4. Here, again, the calculation is performed with radical wall loss equal to 1 s^{-1}. This result indicates that the sensitivity of the instrument is continuously increased by raising the carbon monoxide concentration within the range of our calculations. Considering the lower explosion limit of CO in air, 12.5%,[52] a CO concentration of 8% is used in practice for safety reasons.

Shown as the downward sloping line in Figure 4 is the chain length as a function of k_{wall}. The RO_x concentrations

(48) Ermentrout, B. *Phaseplane: The Dynamical Systems Tool*; Brooks/Cole Publishing Co.: Pacific Grove, CA, 1989.
(49) DeMore, W. B.; Sander, S. P.; Golden, D. M.; Hampson, R. F.; Kurylo, M. J.; Howard, C. J.; Ravishankara, A. R.; Kolb, C. E.; Molina, M. J. *Chemical Kinetics and Photochemical Data for Use in Stratospheric Modeling*, NASA Panel for Data Evaluation, Evaluation Number 10, JPL (Jet Propulsion Laboratory) Publication 92-20; Pasadena, California, 1992.
(50) Cantrell, C. A.; Shetter, R. E.; Lind, J. A.; McDaniel, A. H.; Calvert, J. G.; Parrish, D. D.; Fehsenfeld, F. C.; Buhr, M. P.; Trainer, M. *J. Geophys. Res.* **1993**, *98*, 2897.
(51) Burkhardt, M. R. Ph.D. University of Denver, Denver, CO, 1989.
(52) *CRC, Handbook of Chemistry and Physics*; Weast, R. C., Ed., CRC Press: Cleveland, OH, 1974.

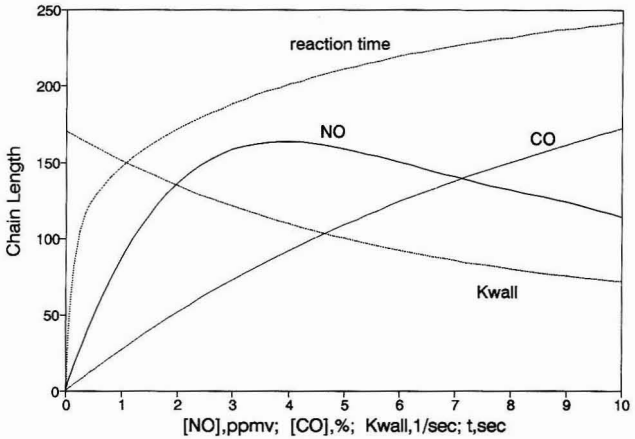

Figure 4. Calculated chain lengths as a function of the instrumental/operational parameters: reagent gases [NO] (solid line) and [CO] (dotted line), radical wall-loss coefficient, k_{wall} (downward sloping line), and reaction time (dashed line).

are 30 pptv for both HO_2 and RO_2, and the normal operating conditions are applied, that is, the reagents are 6 ppmv and 8% for NO and CO, respectively. The k_{wall} of our system is estimated by comparing the chain lengths measured in the laboratory and calculated at various k_{wall} using the laboratory model. At the point of $k_{wall} = 1\ s^{-1}$, the calculated chain length, 160, from the simulation of laboratory study is consistent with those obtained before and after the field study (average value of 158). For ambient air modeling, the calculated chain length for a k_{wall} of $1\ s^{-1}$ is 151, very close to both the observed data and calculated value based on the laboratory model. Therefore, a radical wall loss of $1\ s^{-1}$ is chosen for all the model calculations. The calculated effect of varying the residence time on the chain lengths is demonstrated by the dashed line in Figure 4. Notice that the chain reaction continues to increase in length even at $t = 10$ s in this simulation.

The calculated value of chain length from this model is lower than those in the literature because a polluted ambient air condition was adopted. For example, high concentrations of O_3 and NO_2 are involved as found over a typical urban parking lot, and both may cut chain length down as discussed below. If $[O_3]$ and $[NO_2]$ were set at zero, a calculated chain length of 310 would be achieved for $k_{wall} = 0$ at reaction time of 1.1 s, which would be consistent with the results of Hastie et al., 270,[40] and Cantrell et al., 450.[50]

(ii) Interferences from Atmospheric Species. The ambient air is a complex mixture that contains a number of species to which the luminol NO_2 detector responds. For example, NO_2 is often present, and ozone will convert the added NO to NO_2 in the instrument. Both may contribute directly to the signal and act as interferents. This background signal is determined by shutting off the chain reactions for a part of the measurement time. NO_2 and ozone may also alter chain lengths as indicated by the modeled results.

Summarized in Figure 5 by solid line and dotted line are the calculated impacts on chain length by ozone and NO_2, respectively, in the ambient air. The chain lengths are reduced as $[O_3]$ increases, because of the formation of NO_2 by the reaction between ozone and reagent NO. However, this background-dependent sensitivity is small compared to the effect of other factors. Atmospheric NO_2 has a more significant effect on calculated chain lengths. This is because of the extra termination of the chain reactions by the reaction between NO_2 and HO radicals when the NO_2 concentration is high.

Two atmospheric molecules have been identified as the principal interferents in both the radical measurement and the NO_2 detection system. PAN (peroxyacetyl nitrate, $CH_3COO_2NO_2$) and PNA (pernitric acid, HO_2NO_2) could decompose in the reactor, releasing NO_2 as well as peroxyacetyl radicals and HO_2. Because these contributions to the signal are comparable to the signal from RO_x radicals, it is necessary that they be determined regularly to correct the measured radical signals. However, the decomposition ratios are dramatically decreased by shortening the reaction time.[40] The simulated results show that both PAN and PNA concentrations increase at the very beginning of the chain reactions, and the decompositions occur after about 0.2 and 0.25 s, respectively. At 1.1 s residence time, [PAN] is still higher than its initial concentration, and the fractional decomposition of PNA is 0.8%, corresponding to an HO_2 concentration of 4 pptv at the ambient [PNA] of 500 pptv as illustrated by the modeling conditions in Table 1. Interference from PAN and PNA is not expected to be a problem in this system under the normal operating conditions. By contrast, for a radical reactor of 10 s residence time, the fractional decomposition would be 0.13% and 30% for PAN and PNA, respectively, which would produce free radicals of 2.6 pptv from PAN and 150 pptv from PNA (if 2 ppbv PAN and 500 pptv PNA were presented in the ambient air as shown in Table 1). Under these conditions, one would overestimate the radical concentration by more than 200% when the chemical amplifier was measuring 60 pptv RO_x radicals.

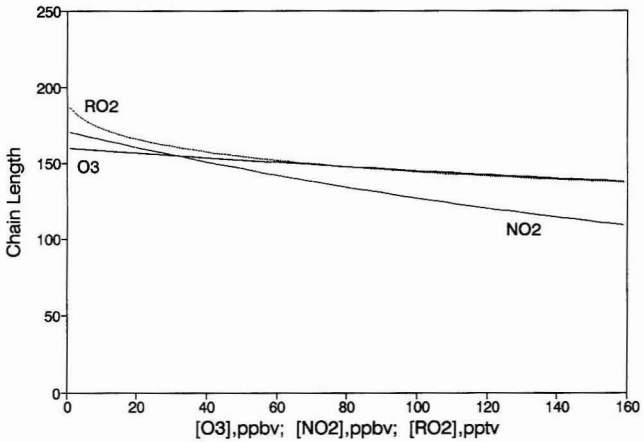

Figure 5. Calculated chain lengths as a function of concentrations of ambient species: O_3 (solid line), NO_2 (dotted line), and free radicals (dashed line).

Finally, the calculated chain lengths versus total initial free radical concentrations, which are the sum of $[HO_2]$ and $[RO_2]$ with the ratio of $[HO_2]$ to $[RO_2]$ set at 1:1, are plotted on the dashed line in Figure 5. The nonlinear response in the model is due to the PNA chemistry. PNA decomposes when both HO_2 and NO_2 concentrations are low and is formed at high HO_2 and NO_2 levels.

Laboratory Studies. (i) Modulation Experiments. The output from the radical detector when HO_2 is measured from a stable radical source with three modulation patterns is shown in Figure 6. Spikes were observed for both Hastie's and the combined pattern when CO was switched between the two addition points. Replacing CO with N_2 (the conventional style) resulted in a slowly changing, time-dependent free radical signal. Fundamentally, the radical sensitivities were the same for all three. The combined modulation pattern generated by three valves was employed throughout our studies, both laboratory and field, since more stable readings were obtained with small spikes.

(ii) NO_2 Calibration. Figure 7 shows the results of calibrations under three experimental conditions: with NO_2 only, with addition of 6 ppm NO, and in the radical detection mode. It has been reported that for large concentrations of NO (>~5 ppmv) a decrease in sensitivity and a nonlinear behavior for the NO_2 detector occurred.[37,50] These results were also observed in our system. Moreover, the sensitivity decreased further when the radical detection mode was applied. The reason for this phenomenon is not clear yet. It is inferred that the following reaction might occur at the gas–liquid surface:

$$CO + NO_2 + H_2O \rightarrow H_2CO_3 + NO \qquad (20)$$

The calibration curve used is that for the radical detection mode. The linear response region for NO_2 is from 40 to 250 ppb in this case. In practice, a small, constant flow of NO_2 corresponding to 40 ppb is added into the system downstream of the reactor in order to ensure the linearity of the detector. The sensitivity is about 0.1 mA/ppb NO_2, and the system is able to detect ppt levels of NO_2.

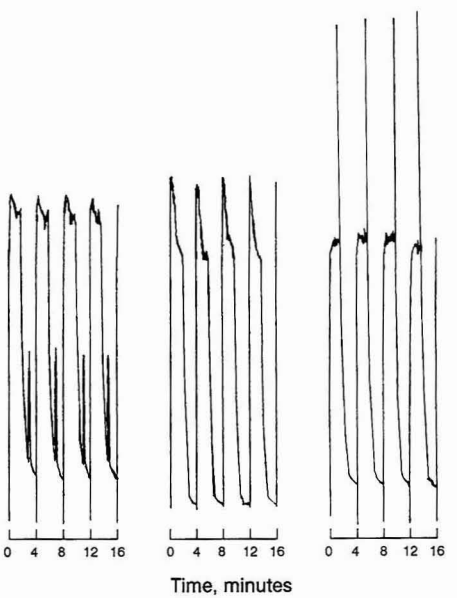

Figure 6. Output from the radical detector for the measurement of HO_2 radicals from a stable source using the three modulation patterns described in the text. Left, this study; middle, conventional system; right, Hastie et al.

An apparent free radical modulation was still observed in the absence of free radicals but at a much lower level than with other configurations (typically about 2.5% of NO_2 signals). This zero signal was subtracted from all data except

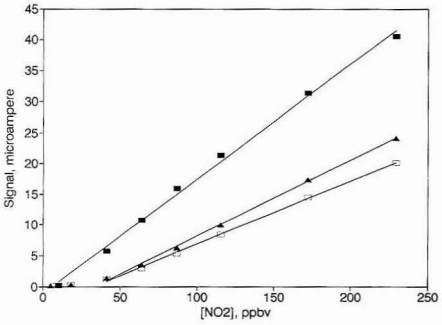

Figure 7. NO_2 calibration of reactor and detector system for three conditions: with NO_2 only (■), 6 ppmv [NO] added (▲), and in the radical detection mode (□).

Table 2. Chain Lengths Determined Using Cl_2/H_2/Air Photolysis System as Radical Source

date	no.	$[HO_2]$, pptv	chain length
July, 1993	1	35.9	133.7
	2	39.4	131.5
	3	53.1	118.8
	4	156.5	112.7
	5	137.2	157.7
	6	101.6	146.5
	7	58.4	131.9]
	8	25.2	138.9
	9	3.4	150.4
	10	7.2	162.1
	11	49.0	151.5
		average	139.6 ± 10.5
October, 1993	1	69.0	176.5
	2	62.9	181.4
	3	57.5	169.7
		average	175.8 ± 10.8

those from some laboratory studies in which a constant NO_2 background signal existed. Hastie et al.[40] found that the magnitude of these zero signals was dependent on the amplifier reaction time and attributed it to the production of radicals from the thermal decomposition of PAN in the chemical amplifier. They designed a radical reaction chamber with consideration to the lifetime of PAN, and their final configuration had a much shorter residence time than conventional reactors. As described previously, one of the improvements we made on our chemical amplifier was to build a small reaction chamber which gave a reaction time of 1.1 s. With this design, the zero modulation observed in NO_2 calibration decreased from 7.5% (yielded by a Teflon filter reactor with a reaction time of 3.5 s[46]) to 2.5% of NO_2 signals. In typical field measurements, a background reading of 140 ppb NO_2 (40 added at the reactor and 100 from ambient NO_2 plus O_3) gave a background modulation of about 3.5 ppb. The ambient free radicals provided an added modulation of about 20 ppb. NO_2 calibration in this study was performed in the laboratory with the building compressed air in which no PAN was supposed to exist. The zero modulation observed during the experiments indicated some other causes besides the decomposition of peroxy nitrates. The NO_2 calibration curves (Figure 7) were plotted using the average of the signals in the radical modulation mode.

(iii) Response to a Stable Radical Source. A stable radical source was set up using the Cl_2/H_2/air photolysis system. The chlorine, hydrogen, and reagent air flows were constant, and the flow rates were 2.7, 29.8, and 378.8 mL/min, respectively. The large dilution air flow acted as an independent variable, varying from 2.4 to 9.8 L/min. The results show that the chemical amplifier system is linear to changes in $[HO_2]$. The linearity of response is fairly good, with R^2 values of 99.8%.

(iv) Relationship between HO_2 Produced and Cl_2 in the Photolysis Tube. In this study, the flow rates of hydrogen, reagent air, and dilution air were 29.8, 378.8, and 3400 mL/min, respectively, and fixed, but that of chlorine varied from 0.4 to 8.0 mL/min. At low Cl_2 concentrations, a linear relationship between $[Cl_2]$ and final NO_2 signals was obtained since the dominant radical removal process was wall loss. When the chlorine flow rate was greater than 2.5 mL/min, corresponding to over 6.1 ppmv $[Cl_2]$ in the flow tube, the plot of radical signals versus Cl_2 concentrations was not linear, but the relationship between the signals and $[Cl_2]^{1/2}$ (square root of $[Cl_2]$) was. This is consistent with the radical production mechanism of HO_2–HO_2 combination dominating over free radical wall loss. From eq 18, the following expression may be derived:

$$[HO_2] = [j[Cl_2]/(k_{12} + k_{13})]^{1/2} = K([Cl_2])^{1/2} \quad (21)$$

where $K = [j/(k_{12} + k_{13})]^{1/2}$.

(v) Determination of Chain Lengths. Chain length calibrations were performed in the laboratory before and after the ambient air measurement with HO_2 produced in the Cl_2/H_2/air photolysis tube. The flow rates of hydrogen and reagent air were held constant at 29.8 and 378.8 mL/min, respectively, and that of chlorine changed from 2.7 to 8.0 mL/min, which was within the linear region of radical signal versus $[Cl_2]^{1/2}$. At the outlet of the tube, the gas mixture was diluted by the large air flow (flow rates varied from 3 to 13 L/min) so that the magnitude of the recorded modulated signals were within the range observed in the field measurement. Only a small portion of the flow from the photolysis tube entered the amplifier, where it was further diluted by the reagent gases, principally N_2 and CO. Both the initial slope and the steady-state NO_2 signal were corrected for zero modulation.

The results of the chain length calibration are presented in Table 2. HO_2 concentrations listed are obtained by dividing the steady-state $[NO_2]$ by the calculated chain lengths and represent the final radical mixing ratios in the chemical amplifier. The chain length determined prior to the field study was 140, with a variability of ±10.5 at the 95% confidence interval. The radical calibration repeated after the field study gave a chain length of 176, with a variability of ±10.8 at the same confidence interval. These are consistent with a free radical wall loss rate coefficient of about 1 s^{-1}, based on the calculations discussed earlier. In comparison, Hastie et al. reported a chain length of 240, which was consistent with a wall loss coefficient of 2.5 s^{-1} for their system,[40] and the radical calibration made by Cantrell et al. during a 1-month field measurement yielded chain lengths from 51 ± 22 to 131 ±

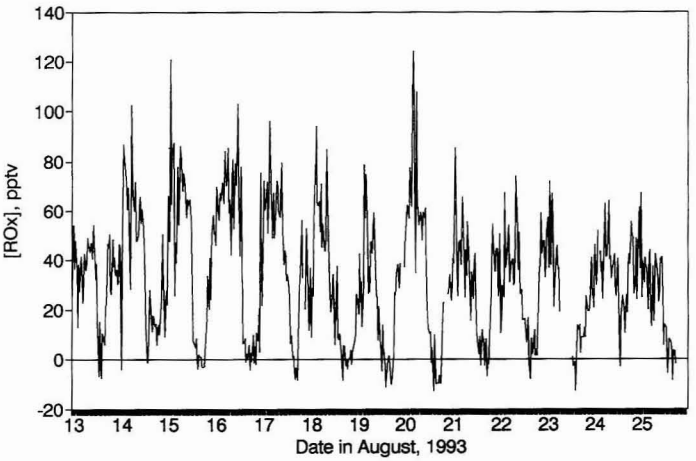

Figure 8. 30-min averages of RO_x concentrations measured in the parking lot outside the S. G. Mudd Building at the University of Denver, August 13–25, 1993.

30, which corresponded to a calculated k_{wall} of 5 s^{-1}.[13,50,53]

Combining the results of both NO_2 and free radical calibrations, the sensitivity of this free radical detector is estimated to be 0.016 mA/pptv RO_x, with a detection limit of about 5 pptv with a stable background signal.

As we expected, the wall loss of the radicals at the Teflon–nitrogen gas wall was fairly low. Furthermore, stable chain lengths resulting from a relatively invariant wall loss rate coefficient are achieved. These results imply that the character of the "nitrogen wall" formed on the Teflon filter in the reactor seems constant, with the fresh nitrogen continuously carried in. This improvement appears to solve a major problem of the marked and variable effect of the reactor wall on the sensitivity of the instrument.

Ambient Air Measurements. A local field measurement was carried out in the summer of 1993 from August 8 to September 12 outside our laboratory building at the University of Denver, about 7 miles southeast of downtown Denver. The free radical detector, along with an ozone monitor and an Eppley radiometer, were set up in a trailer with the inlet pointed northward to avoid sunshine. The temperature inside the trailer was kept at about room temperature using an air conditioner or, occasionally, a heater. The operating conditions were the same as for the laboratory studies. All instruments were calibrated before and after the measurement.

Since free radicals are easily destroyed by any surface, no trap or filter was employed for the ambient air before it entered the chemical amplifier. This caused a problem in that the cleanliness of the system deteriorated rapidly during the field study, particularly in the reactor exit tubing. As a precaution, the Teflon filter and its galvanized wire cylinder support were changed and the tubing around the reactor and the cell in the NO_2–luminol detector were cleaned about every 2 weeks. The tubing, especially the ferrules, became dirty with some kind of dark green material apparently from the atmosphere. In the detection cell, some solid material was formed from the alkaline luminol solution. However, the Teflon filter of the chemical amplifier was relatively clean. Only a pale brown spot was found on the position opposite the reagent gas inlet. The air flow drawn into the radical detection system and NO_2 sensitivity of the luminol detector decreased with the measurement time. Both changes were determined by measuring the total flow rate of the system and making the NO_2 calibration right before and after each successive run.

Our site was located in a parking lot, leading to high and often rapidly fluctuating NO_x mixing ratios that appeared in the free radical base line. This fluctuation made discerning the modulated signal due to ambient RO_x difficult, and the data were therefore collected, averaged, and analyzed using a personal computer.

The system was operated from August 13 to September 12. Figure 8 shows the RO_x concentrations measured from August 13 to August 25. The free radical detector ran continuously from the morning of August 13 (Friday) to early morning on August 26 (Thursday) with occasional suspension for maintenance. In the data processing, the background-related zero modulation was subtracted from the radical signals, and the RO_x mixing ratios were reduced to 30 min average values.

The weather for this period was quite changeable, with frequent thunder storms, but generally clear and sunny and sometimes very hot. The conditions were conducive to radical formation. The daytime free radical mixing ratios ranged from 15 to 140 pptv, with around 60 pptv typical, peaking in the early afternoon at about 2:00 p.m. each day. The nighttime mixing ratios of RO_x were more variable than we expected, from −17 to 15 pptv, with average >5 pptv, which was within the nighttime radical range theoretically predicted by Cantrell et al.[7] This might reflect the generation of free radicals through

(53) Cantrell, C. A.; Shetter, R. E.; Calvert, J. G.; Parrish, D. D.; Fehsenfeld, F. C.; Goldan, P. D.; Kuster, W.; Williams, E. J.; Westberg, H. H.; Allwine, G; Martin, R. *J. Geophys. Res.* **1993**, *98*, 18355.

nighttime chemistry by the reactions of NO_3 radicals with CH_2O, CH_3CHO, and other biogenic hydrocarbons.[6,7,54,55] Negative values also were reported occasionally during daytime because of the rapid fluctuation of the background which resulted from O_3 and NO_2 in the atmosphere, whose fluctuations were sometimes faster than the 4 min instrument cycle time.

Only part of the data from the RO_x radical measurement are displayed here to demonstrate the ability of this improved chemical amplifier to detect normal atmospheric free radical levels under difficult conditions. Data analysis, comparison to ozone concentrations, solar UV fluxes, $j(NO_2)$ values, etc. will be presented in a later paper.

Received for review April 15, 1994. Accepted July 6, 1994.*

* Abstract published in *Advance ACS Abstracts,* August 15, 1994.

(54) Stockwell, W. R.; Calvert, J. G. *J. Geophys. Res.* **1983**, *88*, 6673.
(55) Sabljić, A.; Güsten, H. *Atmos. Environ.* **1990**, *24A*, 73.

Anal. Chem. **1994,** *66,* 3394–3399

Electrospray Mass Spectrometric Analysis and Photocatalytic Degradation of Polyethoxylate Surfactants Used in Wool Scouring

Kim B. Sherrard, Philip J. Marriott,* and Malcolm J. McCormick
Department of Applied Chemistry, Royal Melbourne Institute of Technology, GPO Box 2476V, Melbourne, 3001 Australia

Ray Colton
School of Chemistry, La Trobe University, Bundoora, 3083, Australia

Geoff Smith
CSIRO Division of Wool Technology, Belmont, 3216, Australia

Electrospray mass spectrometry (ESMS) has been used to identify the mixture of components in three nonionic surfactants, nonylphenol ethoxylate (NPE), secondary alcohol ethoxylate (SAE), and primary alcohol ethoxylate (PAE). In each case singly protonated species are observed with the number of ethylene oxide units ranging from 4 to 16. Collisionally activated decomposition of protonated SAE leads to cleavage of the secondary carbon–oxygen bond to give protonated ethylene oxide fragment ions. ESMS is used to show that the products of the photocatalytic decomposition of SAE are the same as those produced by the collisionally activated decompositions. The surfactants can also be singly ionised in solution by addition of sodium or potassium ions, and the products observed by ESMS.

Nonionic surfactants are being used increasingly as an effective and less environmentally harmful alternative to their ionic equivalents for a range of industrial applications. They comprise the second most important class of surfactants after the anionic class.[1] The three nonionic surfactants discussed here, nonylphenol ethoxylate (NPE), secondary alcohol ethoxylate (SAE), and primary alcohol ethoxylate (PAE), are commonly used for wool scouring. Despite their relatively low toxicity, degradation due to the metabolic activities of aquatic microbial communities may produce more toxic products that are potential environmental hazards.

Effluent containing these surfactants therefore requires further treatment prior to disposal in order to reduce detrimental environmental effects. An important example of this problem is the effluent resulting from wool scouring. Scouring of greasy wool produces large volumes (360 000 L per day for a typical modern scour line) of a highly stable, complex mixture of components ranging from inorganic ions to grease.[2] It also contains significant amounts of surfactants. Currently, treatments of scour effluent range from basic primary treatment (centrifuging to recover grease and dirt) through to secondary and tertiary treatments. Secondary treatments include such processes as acid cracking, biological treatment, e.g. activated sludge, ultrafiltration, and chemical flocculation. Tertiary treatments are usually highly expensive and include solvent extraction and evaporation. Lagooning is also widely used in Australia.[2] In general, these processes have the disadvantage of using nondestructive technologies which transfer contaminants from one phase to another rather than destroying them. The resultant sludge provides a substantial disposal problem that must be considered as part of the overall treatment process.

A possible alternative treatment of the scour effluent prior to being discharged or recycled is photocatalytic degradation. This involves irradiating an aqueous slurry of fine particles of the catalyst, TiO_2, with long wavelength ultraviolet light. The light must possess energy greater than the band gap of the TiO_2 (2.9–3.2 eV) which is equivalent to light of wavelengths between 390 and 420 nm or less[3] to produce electron–hole pairs. These can migrate to the surface of the catalyst and undergo redox reactions. It is believed that the positive holes oxidize hydroxide ions, present in the aqueous environment, to hydroxyl radicals[4] and dissolved oxygen to superoxide ions.[5,6] These active species then oxidize compounds present in solution, eventually mineralizing them to CO_2, H_2O, and simple inorganic ions, e.g. Cl^-. The TiO_2 catalyst is a harmless and common component of industrial and consumer products and is found in white paint pigment and as a "whitening" agent in the food and pharmaceutical industry. Photocatalytic degradation has been shown to be successful in degrading many organic pollutants commonly present in waste waters.[7-9] A further application is in the analysis of total organic carbon (TOC).[10,11]

(1) Llenado, R. A.; Jamieson, R. A. *Anal. Chem.* **1981,** *53,* 174R–182R.
(2) Bateup, B. O. *Scouring Effluent Treatments*; Proceedings of the Seminar; Adding Value to Australian Wool, CSIRO Division of Wool Technology, Geelong, Australia, March 1992.
(3) Schrauzer, G. N.; Guth, T. D.; Salehi, J.; Strampach, N.; Hui, L. N.; Palmer, M. R. In *Homogeneous and Heterogeneous Photocatalysis*; Pelizzetti, E., Serpone, N., Eds.; D. Reidel Publishing Company: Holland, 1986; pp 509–520.
(4) Ollis, D. F.; Turchi, C. *Environ. Prog.* **1990,** *9,* 229–234.
(5) Bickley, R. I.; Jayanty, R. K. M.; Vishwanathan, V. In *Homogeneous and Heterogeneous Photocatalysis*; Pelizzetti, E., Serpone, N., Eds.; D. Reidel Publishing Co.: Holland, 1986; pp 555–565.
(6) Tseng, J.; Huang, C. P. In *ACS Symp. Ser.* **1990,** *422,* 12–39 (Tedder, D. W., Pohland, F. G., Eds.).
(7) Ahmed, S.; Ollis, D. F. *Sol. Energy* **1984,** *32,* 597–601.

0003-2700/94/0366-3394$04.50/0
© 1994 American Chemical Society

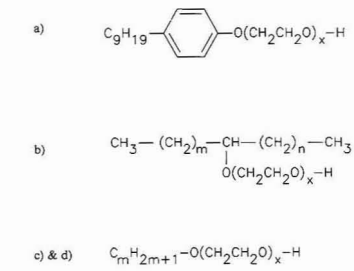

Figure 1. Structural formulas of (a) NPE, $x = 8$ (nominal value); (b) SAE, $x = 9$, $m + n = 9–11$; (c) PAE(12–8), $x = 8$, $m = 12–14$; and (d) PAE(9–6), $x = 6$, $m = 9–11$.

The surfactants NPE, SAE, and PAE (Figure 1) exist as a mixture of isomers and homologues of the hydrocarbon chain, combined with a series of homologues of the polyethoxylate chain differing from each other simply by one ethylene oxide unit. The ratio of the average number of ethylene oxide units to the hydrocarbon chain length gives the surfactant its characteristic properties.

Currently, NPE, SAE, and PAE are in use at commercial scour plants around the world. However, the use of NPE is being restricted in some countries. It is banned from use in scouring plants in several European countries because of its slow biodegradation rate and toxicity of its biodegradation products relative to SAE and PAE.[12]

A method of analysis was required to give information on the mixture of compounds present in each surfactant. The method needed to be comprehensive for a broad range of molecular weights so that, after photodegradation of the SAE, identification of the lower molecular weight products together with any remaining starting material would be possible. We have found electrospray mass spectrometry to be ideally suited to this particular analytical problem.

Electrospray (ES) mass spectrometry is a relatively new technique that has been of widespread interest over the last five years.[13] It enables the transfer of large, complex, and fragile ions from solution to the gas phase, with minimal fragmentation, and so it represents a true soft ionization method. Its applications include inorganic and organometallic compounds[14–16] and organic compounds,[13,17–19] with large biomolecules such as proteins and peptides being of special interest.[20,21] The report by Fenn and co-workers[18] on the observation of multiple sodium ion adducts of high molecular weight poly(ethylene glycol)s is particularly relevant to the present studies.

EXPERIMENTAL SECTION

NPE, PAE(12–8), and PAE(9–6) were obtained from commercial sources.

Electrospray Mass Spectrometry. Electrospray mass spectra were obtained using a VG Bio-Q triple quadrupole mass spectrometer (VG Bio-Q, VG Bio-Tech, Altrincham, Ches., U.K.). A water/methanol/acetic acid (50:50:1%) mobile phase was used with a flow rate of 5 μL min^{-1}. Solutions for analysis were prepared by dissolving one drop of the surfactant in water (1 mL) and this solution was then diluted 1/10 with a methanol/acetic acid mixture resulting in an approximate concentration of surfactant of 0.2 mM. The diluted solution was injected directly into the spectrometer via a Rheodyne injector fitted with a 10-μL loop. The potential applied to the first skimmer (B_1) was varied between 90 V and the minimum possible voltage consistent with retaining a stable ion jet. This was found to be 40 V. Unless otherwise stated $B_1 = 40$ V.

Nitrogen was used as both the drying gas (3 mL min^{-1}) and as the nebulizer (100 mL min^{-1}). Pressure in the mass analyzer region was usually about 3×10^{-5} Torr. Typically 8–12 signal-averaged spectra were required to give a good signal to noise ratio.

Photocatalytic Degradation. A 2000-mL solution of 2000 ppm (w/v) SAE was prepared in Milli-Q ultrapure water (Millipore Australia). TiO_2 powder (Degussa P25, Frankfurt, Germany) was added resulting in a final loading of 0.1%. The 2-L slurry, in a large glass jar, was stirred vigorously with an overhead stirrer. A 25-W, U-shaped black light lamp (UVS Ultra Violet Pty Ltd, Scoresby, Victoria, Australia) was immersed directly into the slurry. The wavelength range emitted by this lamp was between 300 and 400 nm with a maximum at 365 nm. The photoreactor was opened to the atmosphere to allow dissolution of atmospheric oxygen, and the entire system was surrounded by aluminum foil. Samples were taken by syringe via Teflon tubing (1.0 mm i.d.) at regular time intervals. These were then centrifuged at 6000 rpm for 30 min and a liquid–liquid extraction was performed using 100 mL aqueous to 1×40 mL dichloromethane (HPLC grade, AJAX Chemicals, NSW, Australia). Both a saturated NaCl solution and hydrochloric acid (2 M) (laboratory reagent), 5 mL each, were added to aid separation. The organic layer was removed, dried, filtered, and reduced to dryness under vacuum. ESMS analysis as described above was conducted on the sample.

RESULTS

The electrospray mass spectra of NPE and SAE are shown in Figure 2.

These samples are expected to be protonated in the acidic solvent used for dissolution. The homologous series for each

(8) Hsiao, C.-Y.; Lee, C.-L.; Ollis, D. F. *J. Catal.* **1983**, *82*, 418–423.
(9) Legrini, D.; Oliveros, E.; Braun, A. M. *Chem. Rev.* **1993**, *93*, 671–698.
(10) Matthews, R. W.; Abdullah, M.; Low, G. K. C. *Chem. Aust.* **1990**, 85–89 (April).
(11) Matthews, R. W.; Abdullah, M.; Low, G. K.-C. *Anal. Chim. Acta* **1990**, *233*, 171–179.
(12) Kurata, N.; Koshida, K.; Yokoyama, H.; Goto, T. *Monohydric Alcohols. ACS Symp. Ser.* **1981**, *159*, 113–157.
(13) Mann, M.; Shen, S.; Fenn, J. B. In *Mass Spectrometry in the Biological Sciences; A Tutorial*; Gross, M. L., Ed.; Kluwer Academic Publishers: The Netherlands, 1992; pp 145–163.
(14) Colton, R.; Dakternieks, D. *Inorg. Chim. Acta* **1993**, *208*, 173–177.
(15) Canty, A. J.; Traill, P. R.; Colton, R.; Thomas, I. M. *Inorg. Chim. Acta* **1993**, *210*, 91–97.
(16) Colton, R.; Klăui, W. *Inorg. Chim. Acta* **1993**, *211*, 235–242.
(17) Wong, S. F.; Meng, C. K.; Fenn, J. B. *J. Phys. Chem.* **1988**, *92*, 546–550.
(18) Nohmi, T.; Fenn, J. B. *J. Am. Chem. Soc.* **1992**, *114*, 3241–3246.
(19) Fenn, J. B.; Mann, M.; Meng, C. K.; Wong, S. F.; Whitehouse, C. M. *Mass Spectrom. Rev.* **1990**, *9*, 37–70.
(20) Meng, C.-K.; McEwen, C. N.; Larsen, B. S. *Rapid Commun. Mass Spectrom.* **1990**, *4*, 147–150.
(21) Fenn, J. B.; Mann, M.; Meng, C. K.; Wong, S. F.; Whitehouse, C. M. *Science* **1989**, *246*, 64–71.

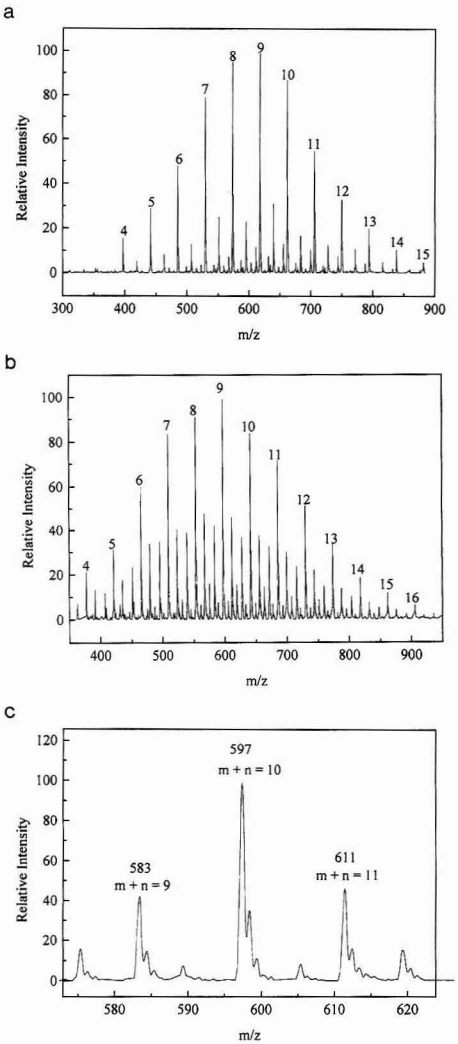

Figure 2. ES mass spectra of the nonionic surfactants. The values of x are given for each peak (a) NPE, (b) SAE, and (c) expansion of SAE x = 9 peaks.

surfactant approximates a statistically normal distribution. Both spectra show clearly the $[M + 1]^+$ ion for each compound present. Each main peak is separated from its neighbor by 44 m/z units corresponding to one ethylene oxide unit.

The spectrum of NPE in Figure 2a indicates that the ethylene oxide chain length for NPE varies from $x = 4$ (m/z 397) to $x = 15$ (m/z 881). Assuming that mass discrimination effects are minimal due to the similar nature of all compounds present in a single sample of surfactant, the nominal value (most abundant oligomer) of NPE is 9. The manufacturer claims the EO mole number (number of moles of EO per mole

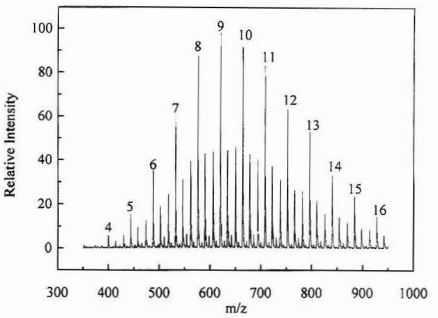

Figure 3. ES mass spectrum of SAE with addition of NaCl.

of alkylphenol) to be between 8 and 9 which correlates well with our result. The smaller peaks between the main series are due to the impurity ions Na^+ and K^+ replacing the proton with a resultant difference of 22 and 38 m/z units. The strongest peak at $x = 9$ (m/z 617) represents $[M + H]^+$ where M is $C_9H_{19}C_6H_4O(CH_2CH_2O)_9H$.

The ES mass spectrum of SAE shown in Figure 2b is more complex. The family of strongest peaks has a separation between peaks of 44 m/z units, corresponding to a difference of one ethylene oxide unit, with the strongest peak at $x = 9$ (m/z 597) representing $(m + n) = 10$ (see Figure 1). Each main peak is flanked on either side by smaller peaks at ±14 m/z values which correspond to species with $m + n = 9$ and 11 respectively (Figure 2c). The series of homologues ranges from $x = 4$ to $x = 16$, so there are 39 distinguishable components in this surfactant. Additional peaks of low intensity are assigned to the Na^+ adducts.

The ES mass spectrum of the PAE(9–6) surfactant (the PAE spectra are not shown here) is similar to that of SAE in the sense that the major family of peaks is due to species with $x = 2$–14 and $m = 10$ (Figure 1), with each peak flanked by others due to species with $m = 9$ and $m = 11$. The most intense peak is at m/z 467 which corresponds to $x = 7$ and $m = 10$.

The ES mass spectrum of PAE(12–8) is again similar except the values of m are 12, 13, and 14 with peaks due to $m = 12$ the most intense of the three. Values of x range from 3 to 17, with the strongest peak being at m/z 583 corresponding to $x = 9$, $m = 12$. In the mass spectra of both PAE surfactants, the peaks due to replacement of H^+ by Na^+ and K^+ are more significant than in the NPE and SAE spectra.

The above data indicate that all the surfactants show an ability to form adducts with Na^+ and K^+ impurities in the mobile phase which in turn form cations which are observed in the ES mass spectra. To confirm the identity of these adducts, deliberate addition of a solution of either NaCl or KCl to give about a 2-fold molar excess was made to the surfactant before injection into the mass spectrometer.

Figure 3 shows the ES mass spectrum of SAE to which has been added some NaCl solution. The spectrum has the familiar envelope shape but all the main peaks are shifted 22 m/z units higher compared to the spectrum of protonated SAE (Figure 2b). Similar spectra were obtained for all the surfactants

with both Na^+ and K^+ addition, with K^+ addition shifting the spectrum to 38 *m/z* units higher.

High molecular weight poly(ethylene glycol)s are able to sustain multiple charges by attachment of more than one Na^+ to each molecule[17–19,21] and it was concluded that one sodium ion is attached per 17 ethylene oxide units.[18,21] In this present case only single charging was possible because the number of ethylene oxide units is much lower.

Collisionally Activated Mass Spectra. Collisionally activated mass spectra of SAE were observed at several skimmer (B_1) voltages. Figure 4 illustrates the ES mass spectra of SAE at several skimmer voltages.

The ES mass spectra of SAE at B_1 = 40 V is given in Figure 4a. The pattern shown for B_1 = 55 V (Figure 4b) is altered from that of B_1 = 40 V by the appearance of a new set of equidistant peaks separated by 44 *m/z* units at lower *m/z* values formed by collisionally activated fragmentation within the source. The new peaks are attributable to the protonated ethylene oxide chains previously attached to the hydrocarbon chain series and have the general formula $[HO(CH_2CH_2O)_xH + H]^+$ with lengths x = 3 (*m/z* 151) to at least x = 11.

For B_1 = 85 V (Figure 4c) only the new, symmetrical pattern is observed at lower molecular weights with the most intense peak at x = 10 (*m/z* 459). The hydrocarbon chain has been completely separated from the surfactant mixture by collisional activation leaving the protonated ethylene oxide series as the only series detected. A comparison of part a and c of Figure 4 clearly shows that the nonfragmented sample (Figure 4a) contains a mixture of three hydrocarbon chain lengths (C12, C13, C14) for each ethylene oxide homologue, whereas the fragmented sample (Figure 4c) displays only single peaks separated by 44 *m/z* units.

In contrast to SAE, NPE shows little fragmentation in its collisionally activated decomposition (CAD) mass spectrum, although at B_1 = 90 V the base peak (*m/z* 177) is attributable to $[(CH_2CH_2O)_4H]^+$; another peak at *m/z* 291 is unidentified. The other surfactants PAE(9–6) and PAE(12–8) also show considerable resistance to collisionally activated fragmentation. The relative ease of fragmentation of SAE may be connected to its relative ease of biodegradation.

One interesting feature of the CAD mass spectra is that at high B_1 voltages the relative intensity of peaks due to Na^+ and K^+ adducts increase, suggesting that they are less susceptible to fragmentation than the protonated species.

Photocatalytic Degradation. Photocatalytic degradation of SAE was performed using the conditions described. The ES mass spectra of the photodegradation products were observed with B_1 = 40 V so that no collisionally activated decomposition would be induced. Therefore only the starting material and protonated species resulting from photocatalytic degradation are detected. Spectra are shown for irradiation times of 0, 48, and 77 h in Figure 5.

Comparison of the spectra of samples taken at 0 and 48 h (Figure 5, parts a and b) shows a shift in the envelope of peaks to lower *m/z* values. The number-average x-value is 9.01 at t = 0 h, correlating very well with 9.07, the value obtained for untreated SAE. This indicates that the complete envelope of homologues is extracted from the mixture without bias. After 48 h of irradiation time, the number-average

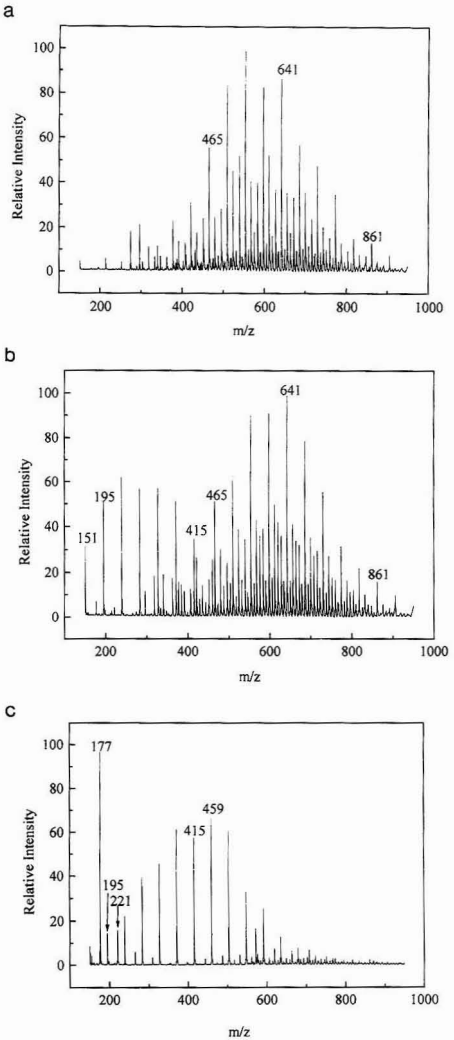

Figure 4. ES mass spectra of SAE with varying B_1 voltages of (a) 40, (b) 55, and (c) 85 V.

x-value is 7.09, indicating photocatalytic degradation has occurred. This is illustrated by the relative increase in intensity of the *m/z* 465 peak (x = 6) and decrease of the *m/z* 641 peak (x = 10).

There is further evidence of photocatalysis after 77 h of irradiation (Figure 5c). The peaks observed at *m/z* 61, 75, and 89 suggest protonated ethanoic, propanoic, and butanoic acids. A second and third series of peaks occurs between 107 and 591 *m/z* units and 261 and 613 *m/z* units respectively, with peaks in each series separated by 44 *m/z* units. The second series is consistent with $[HO(CH_2CH_2O)_xH + H]^+$ where x = 2–13 (marked *), and the third series is consistent

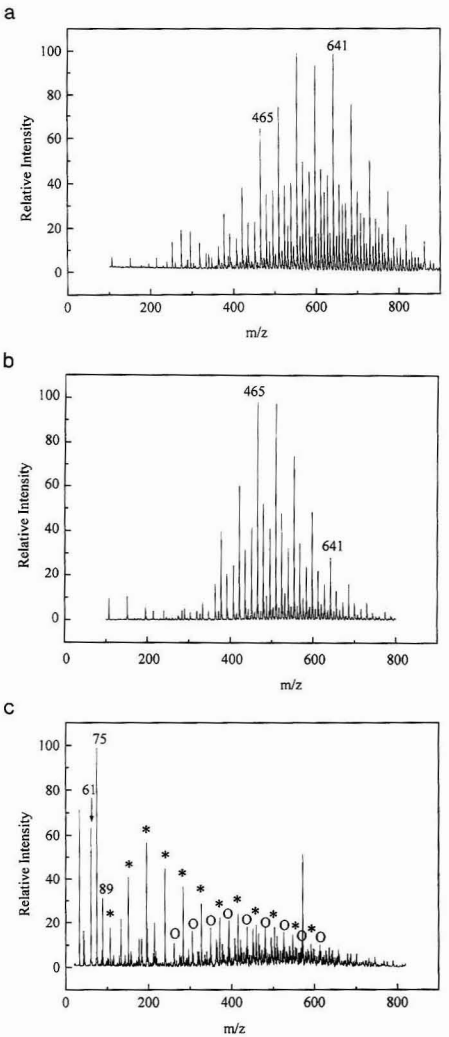

Figure 5. ES mass spectra of SAE after photocatalytic degradation of (a) 0, (b) 48, and (c) 77 h.

with $[C_{11}H_{23}O(CH_2CH_2O)_xH + H]^+$ where $x = 1$ to $x = 11$ (marked O).

Between 48 and 77 h of irradiation time the TiO_2 particles began to agglomerate rather than remaining as a suspension of fine particles. The clumps and some of the remaining aqueous layer were solid–liquid extracted with CH_2Cl_2 under similar conditions to the liquid–liquid extraction described earlier. The spectrum of the extracted TiO_2 is shown in Figure 6.

Several groups of peaks were identified as compounds more hydrophobic than the starting material. These compounds are likely to preferentially adhere to surfaces, for example

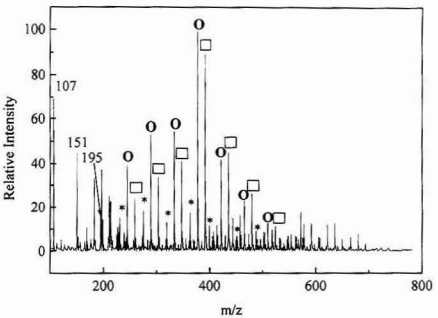

Figure 6. ES mass spectrum of the extract from the agglomerated TiO_2 particles containing SAE derivatives where $m + n = 10$ (*), 11 (O), and 12 (□).

glass container walls and TiO_2 particles, rather than remain in solution and this is a probable reason for agglomeration of the particles. The peaks at m/z 107, 151, and 195 are consistent with $[HO(CH_2CH_2O)_xH + H]^+$ where $x = 2$–4. The other main peaks between m/z 231 and 523 are consistent with another series of homologues with the general structure

$$[CH_3(CH_2)_m\underset{\displaystyle O(CH_2CH_2O)_xH}{\underset{|}{CH}}(CH_2)_nCH_3 + H]^+$$

where $x = 1$–7, and $m + n = 9$–11 (marked *, O, and □ respectively). Overall, the compounds adhered to the TiO_2 generally have relatively short ethylene oxide chains and long hydrocarbon chains and are thus more hydrophobic than the starting material.

DISCUSSION

SAE is found to decompose by collisional activation more readily than the other three surfactants. This is demonstrated by the degree of fragmentation observed for SAE at intermediate skimmer voltages (e.g. $B_1 = 55$ V) which is not observed for PAE and NPE unless they are exposed to high B_1 voltages (e.g. $B_1 = 90$ V). CAD of SAE appears to be, at least in part, a nonrandom process. An ordered series of homologues is the observed result (Figure 4), whereas in contrast, CAD spectra of NPE and PAE result in peaks that are much less regular and possess no obvious series. This suggests that SAE is more readily decomposed by collisional activation than the other surfactants. The ordered distribution of fragment ions in SAE may also be interpreted as originating from cleavage of the secondary carbon–oxygen bond, and that the higher abundance of these fragment ions versus other bond cleavages in SAE, NPE, and PAE suggests that this is a labile bond toward collisional activation. The majority of derivatives produced by photocatalytic degradation of SAE also suggest cleavage at the secondary carbon–oxygen bond. The more labile secondary carbon–oxygen bond, relative to the other carbon–oxygen bonds in the molecules studied is most likely to be related to the more stable secondary carbon-centered cation or radical that would result versus the higher energy primary cations and radicals that result from cleavage

of other carbon–oxygen bonds. Enthalpies of formation of SAE protonated at different oxygen positions along the ethylene oxide chain were calculated using the MNDO semiempirical quantum mechanical method. The difference in these values suggests protonation at the first oxygen (i.e. adjacent to the secondary carbon) occurs more rapidly than protonation of other oxygen atoms within the molecule. This, together with the fact that secondary carbocations are more stable than primary carbocations, accounts for the apparent lability of the secondary carbon–oxygen bond toward collisional activation. Although predominantly occurring at the secondary carbon–oxygen bond, the radical attack believed to initiate the photodegradation process also cleaves terminal ethylene oxide units, but to a smaller extent.

Experimental data indicates that the cationized forms of SAE are more resistant to CAD than the equivalent protonated forms and are thus still present at high B_1 voltages. In other words, the protonated analogues may be decomposed in the CAD process in preference to those with alkali metal ions attached. This results in an apparent increase in the relative abundance of the $[M + Na]^+$ peaks with respect to their protonated analogues and can be seen in Figure 4, part b vs a.

All of the four surfactants produce a peak at m/z 177 when analyzed at high B_1 voltages (90–100 V). This suggests that the peak corresponds to a relatively stable protonated derivative of the ethylene oxide chain.

ES mass spectral data on poly(ethylene glycol)s, a series of compounds with structures very similar to these surfactants, shows little or no mass discrimination.[13] Other mass spectrometric techniques show a similar minimal mass discrimination. With the use of field desorption, electrohydrodynamic ionization, and fast-atom bombardment mass spectrometry, the mean molecular weight of the protonated form of the poly(ethylene glycol) is found to agree well with that derived from classical methods and values declared by the suppliers.[22] Conversely, discrimination on the basis of mass has been shown for poly(ethylene glycol)s using other mass spectrometric techniques such as laser desorption-Fourier transform ion cyclotron resonance mass spectrometry (LDI-FTICR).[23] The production of gaseous charged species in ES mass spectrometry does not involve the steps used in LDI-FTICR and is therefore not likely to be subject to this bias. The assumption that a linear concentration–response relationship exists is therefore reasonable, as is the qualitative comparison of relative peak height intensities.

Ultimately mineralization to CO_2 and H_2O is the result of photocatalytic degradation but it is desirable that the intermediates of the photooxidation process are neither persistent nor toxic derivatives of the starting material. The intermediates observed here are the result of oxidative radical attack. For example, the carboxylic acids result from oxidation close to the secondary carbon and they will be present at very low concentrations during photocatalysis of scour effluent. Since they are not known for their environmental persistence or toxicity, they pose little problem in the overall disposal following the scouring process.

ACKNOWLEDGMENT

The authors are indebted to Dr. Graham Wills-Johnson for the MNDO calculations and also thank La Trobe University for providing a SCAEF grant to assist in the purchase of the electrospray mass spectrometer and the Wool Research and Development Corporation for provision of a student scholarship (K.S.) that made this research possible.

Received for review March 9, 1994. Accepted June 16, 1994.[⊗]

[⊗] Abstract published in *Advance ACS Abstracts,* August 1, 1994.

(22) Seraglia, R.; Traldi, P.; Mendichi, R.; Sartore, L.; Schiavon, O.; Veronese, F. M. *Anal. Chim. Acta* **1992**, *262*, 277–283.
(23) Hogan, J. D.; Laude, D. A., Jr. *Anal. Chem.* **1992**, *64*, 763–769.

Anal. Chem. **1994,** *66,* 3400–3407

Low-Pressure Inductively Coupled Plasma Ion Source for Molecular and Atomic Mass Spectrometry

E. Hywel Evans,* Warren Pretorius,† Les Ebdon, and Steve Rowland

Department of Environmental Sciences, University of Plymouth, Drake Circus, Plymouth PL4 8AA, U.K.

A low-pressure inductively coupled plasma system is described which can be used for both molecular and atomic mass spectrometry. Element-selective detection of organotin, organolead, organoiron, and organohalide compounds was possible using this source coupled with gas chromatography. Detection limits were as follows: tetraethyllead, 13 pg; tetrabutyltin, 35 pg; ferrocene, 33 pg; iodobenzene, 25 pg; bromobenzene, 50 pg; and chlorobenzene, 500 pg. By decreasing the power and plasma gas flow it was possible to sustain a helium plasma using only the carrier gas from the gas chromatograph, and mass spectra were obtained for chlorobenzene, bromobenzene, and iodobenzene that were similar to those obtainable using an electron impact ionization source. The molecular ion for chlorobenzene was observed to 10 ng injected on-column. The effect of power on the mass spectrum was investigated. By adjusting the plasma gas flow and forward power, it was possible to influence the degree of fragmentation of the organic species. The potential exists for the development of a variable ion source with the ability to adjust the degree of fragmentation simply and rapidly.

Inductively coupled plasmas (ICPs) have been used extensively as ion sources for elemental mass spectrometry (MS). Other plasmas such as microwave-induced plasmas (MIPs) and glow discharges (GDs) have been used less commonly. Conventionally, procedures such as electron impact (EI), chemical ionization (CI) fast atom bombardment (FAB), thermospray, and electrospray have been utilized as ion sources for molecular MS. However, the appropriate ion source will depend on the analyte to be studied and the degree of fragmentation which is desired. For instance, for molecular weight determinations of proteins, FAB would be the method of choice; and for total elemental determinations, the ICP would be the best source.

The conclusion that can be drawn from this is that, to gain the appropriate degree of fragmentation, it is necessary to use the correct ion source. Evidently, it would be advantageous if a single ion source could fulfill all of the roles cited above. Microwave-induced plasmas have been investigated as a possible "soft" ionization source for molecular MS[1–4] for the production of molecular fragment ions, although the most common use of a MIP is as a source of monoatomic ions. Heppner[1] investigated a MIP formed with helium or hydrogen at between 30 and 150 W of forward power and at a pressure of between 10 and 200 Torr, in conjunction with GC sample introduction and mass spectrometry. Compounds such as hexane and toluene were injected into a MIP using GC, though no actual chromatography was performed. The compounds were almost totally destroyed in the MIP and broken down to constituent elements which recombined to form simple polyatomic forms such as CH, CH_4, and CO in the MIP tail flame. These compounds were then extracted into a mass spectrometer where they were ionized by using EI and mass spectrometrically analyzed. Poussel et al.[2] utilized a MIP formed with argon, xenon or krypton and maintained at a power of between 25 and 50 W, at pressures of between 2×10^{-2} to 6×10^{-2} mbar. Compounds such as cyclohexane and dodecane were introduced into the tail flame of the MIP discharge, where they were fragmented and ionised. These species were extracted into a mass spectrometer through a skimmer cone of 1.2-mm diameter and yielded spectra similar to those obtained using EI ionization. Similar work was performed by Olson et al.,[3] who obtained spectra for chlorobenzene and toluene similar to the EI spectra. They also introduced compounds through the whole length of a MIP discharge and found that the molecular ions disappeared, with a consequent increase in the intensity of the monoatomic ions. These experiments were performed by introducing the pure compound itself, or headspace vapor, so were not representative of analysis at trace levels.

Atmospheric pressure ionization (API) sources have also been developed utilizing a MIP[4] or glow discharge.[5] The latter workers noted that the predominant ions produced using the API source were the M^+ and $(M + 1)^+$ ions, while the same glow discharge source used under reduced pressure produced molecular ions accompanied by fragmentation. However, these workers used continuous sample introduction, and no work was performed with transient signals.

The need for element-selective techniques for the detection and speciation of metals in the environment has lead to the development of numerous chromatographic techniques being coupled to element-selective detectors.[6–9] The most promising element-selective detectors for coupling to chromatography are ICPMS, MIPMS, and MIP or ICP atomic emission detection (AED). Most of the chromatographic work with coupled plasma MS systems has focused on the use of high-performance liquid chromatography (HPLC) coupled to plasma mass

† Present addresss: Port Elizabeth Technikon, Private Bag X6011, Port Elizabeth 6000, South Africa.

(1) Heppner, R. A., *Anal. Chem.* **1983**, *55*, 2170.
(2) Poussel, E.; Mermet, J. M.;, Deruaz, D.; Beaugrand, C. *Anal. Chem.* **1988**, *60*, 923.
(3) Olson, L. K.; Story, C. W.; Creed, J. T.; Shen, W.; Caruso, J. A. *J. Anal. At. Spectrom.* **1990**, *5*, 471.
(4) Shen, W.; Satzger, R. D. *Anal. Chem.* **1991**, *63*, 1960.
(5) Chien, B. M.; Michael, S. M.; Lubman, D. M. *Anal. Chem.* **1993**, *65*, 1916.
(6) Ebdon, L. C.; Hill, S. J.; Ward, R. W. *Analyst* **1987**, *112*, 1.
(7) Ebdon, L. C.; Hill, S. J.; Ward, R. W. *Analyst* **1986**, *111*, 1113.
(8) Vela, N. P.; Olson, L. K.; Caruso, J. A. *Anal. Chem.* **1993**, *65*, 585A.
(9) Hill, S. J.; Bloxham, M. J.; Worsfold, P. J. *J. Anal. At. Spectrom.* **1993**, *8*, 499.

0003-2700/94/0366-3400$04.50/0
© 1994 American Chemical Society

spectrometry sources, but relatively little work has been done on gas chromatography (GC) systems.[10] Gas chromatography coupled to a plasma detector is generally limited to volatile organometallic compounds (e.g., alkylleads, alkyltins, etc.) and halogenated or other heteroatomic volatile organic compounds. The work carried out with GC/plasma-MS to date can be divided into studies using helium MIPMS and those using argon ICPMS. The use of atmospheric capillary GC/ICPMS has been applied to organotin and organolead compounds;[11,12] more recently a high temperature GC/ICPMS system has been developed for the analysis of metalloporphyrins in geological samples.[13] These systems require only slight modifications to the ICPMS instrument and do not require any form of solvent venting.

Low-pressure MIPs have also been used for element-specific analysis of organic compounds.[14–17] In that work, GC was coupled to low-pressure MIPMS for the element-selective determination of P, S, and Cl in a variety of organic compounds including pesticides; however, no molecular fragmentation studies were performed. Other workers have used a furnace to introduce a dry aerosol.[18]

Initial investigations of low-pressure (LP) ICPMS systems, using argon[19,20] and helium[21] as the plasma gases, have demonstrated the applicability of the technique for element-selective detection of organic compounds using GC sample introduction. In the work described in the present study a helium/argon LP-ICP has been used to obtain both atomic and molecular ions by introducing subnanogram amounts of compounds, via GC, directly into the plasma discharge. By adjusting the plasma gas flow and forward power, it was possible to influence the degree of fragmentation of the organic species. The preliminary results presented here suggest that LP-ICPMS is capable of being tuned for either elemental or molecular MS.

EXPERIMENTAL SECTION

Low-Pressure Plasma. All experiments were performed with a modified inductively coupled plasma mass spectrometer (VG PlasmaQuad 2, Fisons Instruments Elemental, Winsford, UK). The instrument was modified in several respects. First, the standard sampling cone was replaced with a low-pressure sampler machined from aluminium (Machine shop, University of Plymouth), with a 2-mm orifice and an ultratorr fitting for a $^1/_2$-in. pipe. Using this design, it was possible to form a vacuum seal between the low-pressure torch and sampler. The torch was constructed from quartz and was simply a 140-mm-long quartz tube of $^1/_2$-in. o.d., with a $^1/_4$-in.-o.d. side arm through which the plasma gas could be introduced. Second, the pumping rate at the interface was increased from 44 to ~75 L min^{-1} by the addition of a second pumping port at ~135° to the original port, linked to the same rotary vacuum pump (Edwards E1M-18, Edwards High Vacuum, Crawley, Sussex, UK). Typical operating conditions are shown in Table 1.

Table 1. Typical Operating Conditions Used for LP-ICPMS

	element-selective detection	molecular fragmentation
forward power (W)	200	15–50
reflected power (W)	35	7–30
argon plasma gas flow (L min^{-1})	1.0	0
helium GC gas flow (mL min^{-1})	~3.5	~3.5
skimmer/sampler spacing (mm)	4.5	4.5
pressure in interface (mbar)	2.1	not measd
pressure in torch (mbar)	13	not measd

Gas Chromatography. A gas chromatograph (HRGC 5300, Carlo Erba) was interfaced to the rear of the low-pressure torch by means of a heated transfer line maintained at a temperature of 200 °C. The GC column passed through the transfer line and into the torch so that it was positioned 10 mm behind the rearmost turn of the ICP load coil. The vacuum seal between the column and the torch was made using Swagelock and ultratorr fittings. Two types of capillary column were used: a DB-1 HT, 0.32 mm × 15 m with a 0.1-μm film thickness (J&W, Fisons, Loughborough, UK); and a DB-5, 0.32 mm × 20 m with a 0.1-μm film thickness (J&W). The GC program was typically 50–200 °C at 20 °C/min with a column head pressure of 54 kPa using helium as the carrier gas, which resulted in a gas flow of 3.5 mL min^{-1}. The instrumental setup is shown in Figure 1.

Data Acquisition Parameters. Data were acquired by single ion monitoring and multiisotopic peak jumping. For element-selective detection it was only necessary to acquire data for one selected mass at a time; however, for the molecular fragmentation study the mass range between m/z 60 and 209 was monitored. Data acquisition parameters for both element-selective detection and molecular fragmentation are given in Table 2. It should be noted that the software supplied with the instrument was designed for multielement analysis of monoatomic ions, so was not ideally suited for a full mass range, data-capture experiment.

Reagents and Standards. Standards were diluted in hexane (HPLC grade, Rathburn Chemicals, Scotland, UK) to the required concentration. Tetrabutyltin, tetraethyllead, iodobenzene, chlorobenzene, bromobenzene, and ferrocene were obtained from Aldrich Chemicals (Gillingham, UK).

RESULTS AND DISCUSSION

Element-Selective Detection. *Optimization of Plasma Gas.* The plasma was sustained with argon gas introduced through the side arm of the low-pressure torch. The plasma gas flow was a critical parameter with respect to the analytical utility of the low-pressure ICP. The effect of plasma gas flow on the signals for bromobenzene and tetraethyllead, when determined

(10) Pretorius, W.; Foulkes, M.; Ebdon, L.; Rowland, S. *HRC & C, J. High Resolut. Chromatogr. Chromatogr. Commun.* **1993**, 16, 157–160.
(11) Kim, A.; Hill, S.; Ebdon, L.; Rowland, S. *HRC & C, J. High Resolut. Chromatogr. Chromatogr. Commun.* **1992**, *15*, 665–668.
(12) Kim, A.; Foulkes M. E.; Ebdon, L.; Hill, S.; Patience, R. L.; Barwise, A. G.; Rowland, S. J. *J. Anal. At. Spectrom.* **1992**, *7*, 1147.
(13) Pretorius, W. G.; Ebdon, L.; Rowland, S. J. *J. Chromatogr.*, in the press.
(14) Creed, J. T.; Davidson, T. M.; Shen, W.; Caruso, J. A. *J. Anal. At. Spectrom.* **1990**, *5*, 109.
(15) Creed, J. T.; Mohamad, A. H.; Davidson, T. M.; Ataman, G.; Caruso, J. A. *J. Anal. At. Spectrom.* **1988**, *3*, 923.
(16) Story, W. C.; Olson, L. K.; Shen, W.; Creed, J. T.; Caruso, J. A. *J. Anal. At. Spectrom.* **1990**. *5*, 467.
(17) Story, W. C.; Caruso, J. A. *J. Anal. At. Spectrom.* **1993**, *8*, 571.
(18) Eberhardt, K.; Buchert, G.; Herrmann, G.; Trautmann, N. *Spectrochim. Acta* **1992**, *47B*, 89.
(19) Evans, E. H.; Caruso, J. A. *J. Anal. At. Spectrom.* **1993**, *8*, 427.
(20) Evans, E. H.; Pretorius, W.; Ebdon L.; Worsfold, P. J.; Rowland, S. Presented at the XXVIII Colloquium Spectroscopicum Internationale, York, UK, June 29–July 4, 1993; paper FL6.1.
(21) Castillano, T. M.; Giglio, J. J.; Evans, E. H.; Caruso, J. A. *J. Chromatogr.*, submitted for publication.

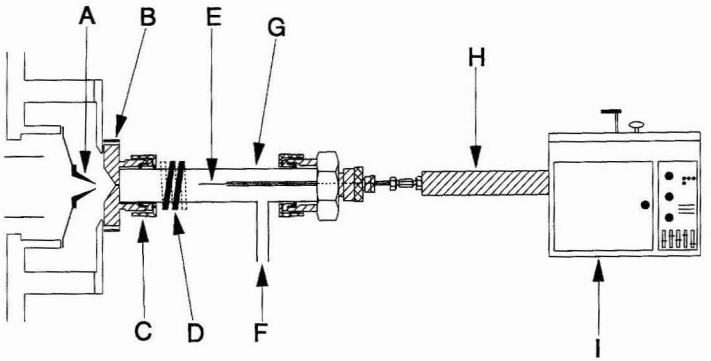

Figure 1. GC/LP-ICPMS instrumentation used in this work: A, skimmer; B, low-pressure sampler; C, vacuum fitting; D, ICP load coil; E, tip of GC column; F, plasma gas; G, quartz torch; H, heated transfer line; I, gas chromatograph.

Table 2. Mass Spectrometer Data Acquisition Parameters

	element-selective detection	molecular fragmentation
mode	single ion	peak jumping
no. of masses	1	150
points per mass	n/a[a]	1
mass range (m/z)	n/a	60–209
dwell time (ms)	164	1.28
no. of sweeps per time slice	n/a	2
no. of channels	4096 max	n/a

[a] Not applicable.

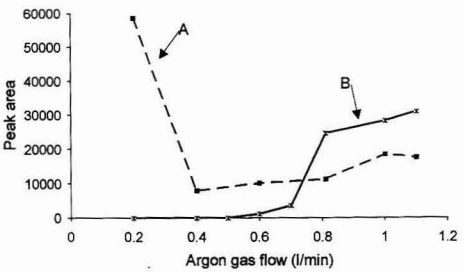

Figure 2. Effect of plasma gas flow on peak area signal: (A) Br^+ (m/z 79) from bromobenzene; (B) Pb^+ (m/z 208) from tetraethyllead.

in element-selective mode at m/z 79 and 208, respectively, are shown in Figure 2. Evidently the effect on signal was dependent on the type of compound studied. The signal for tetraethyllead was not detectable below a flow rate of 0.6 L min^{-1}, whereas the bromobenzene signal was unaffected and was considerably enhanced when the flow was reduced to 0.2 L min^{-1}. Several explanations may be considered to explain the contradictory behavior of the two compounds. First, the increase in signal at m/z 79 when the gas flow was reduced to 0.2 L min^{-1} could have been caused by the formation of polyatomic ions. However, a similar effect was observed for the iodobenzene signal at m/z 127 so this seems unlikely to be the explanation.

Evidently, it would be useful to ascertain the effect of the gas flow on ionization, ion sampling, and throughput in order to try and explain the contradictory behavior of bromobenzene and tetraethyllead. At a gas flow of 0.2 L min^{-1} the plasma was quite diffuse and extended from the tip of the GC column. As the gas flow rate was increased, the base of the plasma was pushed further forward and the plasma itself became progressively denser and brighter, until it was confined completely within the load coil at a gas flow greater than 0.8 L min^{-1}. Hence, the effect of the gas flow was to condense the plasma at higher flows. Unfortunately, another consequence of reducing the gas flow was an apparent reduction in the gas temperature (i.e., the quartz torch no longer glowed red and did not soften below a gas flow of 0.8 L min^{-1}), with a probable decrease in the ionization temperature. A lower ionization temperature would explain the apparent decrease in the number of Pb^+ ions formed, though not the increase in Br^+. The lower gas temperature may have resulted in incomplete dissociation of the tetraethyllead molecules, though a similar effect on the bromobenzene molecules would also be expected, and in any case, this seems unlikely due to the extremely unstable nature of tetraethyllead.

Another important consideration is the effect of gas flow on the sampling and skimming processes of ions from the plasma into the mass spectrometer. Sampling/skimming interfaces for plasma-MS have been designed,[22,23] using criteria derived for molecular beam experiments.[24] The plasma gas is sampled from a relatively high pressure environment through an orifice into a low-pressure expansion chamber. In the expansion chamber the gases undergo adiabatic expansion to form a barrel shock region. Within the barrel shock is the so-called "zone of silence", which is thought to be representative of the sampled plasma gases. The barrel shock takes the form of a cone with its apex at the orifice. The base of the cone is a diffuse collisional region where the expanding gas meets the background gas known as the "Mach disk". In order to obtain the greatest ion throughput into the mass spectrometer, the gases must be sampled within the zone of silence and upstream of the Mach disk. The position of the Mach disk is dependent on the pressure differential between the sampled gas and the gas in the expansion chamber; and the orifice

(22) Douglas, D. J.; French, J. B. *J. Anal. At. Spectrom.* **1988**, *3*, 743.
(23) Olivares, J. A.; Houk, R. S. *Anal. Chem.* **1985**, *57*, 2674.
(24) Campargue, R. *J. Phys. Chem.* **1984**, *88*, 4466.

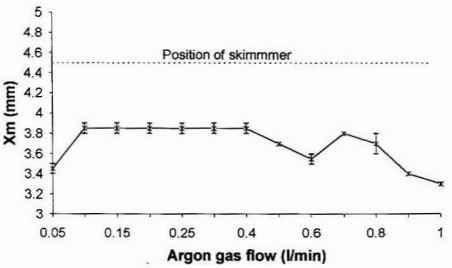

Figure 3. Effect of plasma gas flow on the distance of the Mach disk downstream of the sampling orifice (X_m).

diameter,[24] as shown in eq 1, where X_m is the distance of the

$$X_m = 0.67D_0(P_0/P_1)^{1/2} \quad (1)$$

Mach disk downstream of the sampling orifice, D_0 is the diameter of the sampling orifice, i.e., 2.0 mm, P_0 is the pressure in the torch, and P_1 is the pressure in the expansion stage of the interface.

In this work, the pressure was measured in the absence of the GC column at the rear of the torch, where the GC transfer line would normally be interfaced, and at the side arm to the expansion chamber. The influence of helium from the GC column (3.5 mL min^{-1}) was ignored because it was considered to be negligible in comparison with the argon gas flow (between 0.05 and 1 L min^{-1}). The position of the Mach disk was calculated by use of eq 1, and the effect of argon gas flow on its position is shown in Figure 3. It is evident that the gas flow had very little effect on the position of the Mach disk (i.e., the P_0/P_1 ratio remained relatively constant). The actual skimming distance used was 4.5 mm, so the expanding gases were skimmed downstream of the Mach disk, though the extent of the Mach disk itself is ill defined. This means that the skimmed ions were not necessarily representative of those sampled from the plasma source because of the liklihood of collisional processes occurring outside the zone of silence, and the onset of background gas penetration through the skimmer.

The nature of the gas flow through an orifice can be charaterized by the Knudsen number (Kn):[25]

$$Kn = \lambda/D \quad (2)$$

where λ is the mean free path and D is the orifice diameter.

The mean free path can be calculated by use of simple kinetic theory:[26]

$$\lambda = 3\eta/mN(8kT/\pi m)^{1/2} \quad (3)$$

where η is the viscosity of argon at the specified temperature, m is the mass of argon (6.642×10^{-26} kg), and N is the number density. For the low-pressure plasma at a gas flow of 1 L min^{-1}, the gas temperature was estimated to be ~1900 K, because of the tendency for the quartz torch to glow red and soften. Douglas and French[22] have calculated that the local plasma temperature does not depart from the source temperature until very close to the sampling orifice. Assuming that the source conditions prevail at the sampling orifice, then for the low pressure torch, T = 1900 K; P_0 = 13 mbar (1300 Pa), $N_0 = 4.96 \times 10^{22}$ m^{-3}, and $D_0 = 2 \times 10^{-3}$ m. Using these values, then $\lambda = 8 \times 10^{-5}$ m and Kn_0 = 0.04 (the Knudsen number for the sampling orifice). This indicates that the flow through the sampling orifice is transitional between viscous and molecular flow ($1 < Kn < 0.01$) for the low pressure plasma.

Campargue[24] has shown that the skimming distance which gives maximum beam intensity is given by

$$X_s/D_0 = 0.125[(1/Kn_0)(P_0/P_1)]^{1/3} \quad (4)$$

where X_s is the optimum skimmer distance, Kn_0 is the Knudsen number at the sampling orifice, P_0 is the pressure in the source, and P_1 is the pressure in the expansion stage. For the low-pressure plasma at a gas flow of 1 L min^{-1}, X_s is calculated to be 1.4 mm, which is much less than the distance of 4.5 mm used in this work.

To describe the flow through the skimmer it is necessary to calculate the mean free path at the skimming distance used (4.5 mm in this case). The theory that describes flow through the skimmer has been derived for skimming processes within the zone of silence. As already stated, in this work skimming was performed outside the zone of silence, but it is neverthless instructive to calculate the skimming Knudsen number to gain some idea of the skimming processes. The local Mach number is given by[22,27]

$$M(x/D_0) = 3.26(x/D_0)^{2/3} - 0.61(x/D_0)^{-2/3} \quad (5)$$

where M is the local Mach number, x is the skimming distance downstream of the sampler, and D_0 is the sampling orifice diameter).

The local temperature is given by[22]

$$\frac{T_0}{T_x} = 1 + M^2\frac{(\gamma - 1)}{2} \quad (6)$$

where T_0 is the source temperature, T_x is the local temperature, M is the Mach number, and γ is the specific heat ratio of argon (5/3).

For the low-pressure plasma at a gas flow of 1 L min^{-1} and a skimming distance of 4.5 mm, then M = 2.33, T_x = 680 K, the number density at the skimmer $N_x = 1.6 \times 10^{21}$ m^{-3}, and $\lambda = 2 \times 10^{-3}$ m. Hence, the skimmer Knudsen number Kn_s = 2, assuming a skimmer orifice diameter of 1.0 mm. This indicates that molecular flow is occurring through the skimmer, though the assumption has been made that the theory is applicable when skimming downstream of the Mach disk.

(25) Dushman, S. In *Scientific Foundations of Vacuum Technique*, 2nd ed.; Lafferty, J.M., Ed.; Wiley: New York, 1962; p 80.
(26) Atkins, P. W. *Physical Chemistry*, 4th ed; Oxford University Press: Oxford, U.K., 1992; pp 722–745.
(27) Ashkenas, H.; Sherman, F. S. Rarified Gas Dynamics. *In Proceedings, 4th International Symposium of Rarified Gas Dynamics*; de Leeuw, J. H., Ed.; Academic Press: New York, 1966; Vol. II, p 84.

Table 3. Summary of Performance Parameters for the Low-Pressure Plasma at Different Gas Flows and Source Temperatures[a]

			in source			at skimming position		
gas flow (L min^{-1})	source temp (K)	X_s (mm)	λ ($\times 10^{-4}$ m)	N ($\times 10^{22}$ m^{-3})	Kn	λ ($\times 10^{-3}$ m)	N ($\times 10^{20}$ m^{-3})	Kn
1.0	1900	1.4	0.8	5.0	0.04	2.0	16	2
0.2	1900	1.0	2.2	1.7	0.1	5.9	5.5	6
0.2	1500	1.1	1.7	2.2	0.08	4.4	6.9	4
0.2	1100	1.3	1.2	3.0	0.06	2.7	9.4	3

[a] X_s, optimum skimming distance; λ, mean free path; N, number density; Kn, Knudsen number.

Table 4. Detection Limits Obtained for a Selection of Standards, Using Element-Specific Detection[a]

compound	m/z monitored	detection limit (pg)
chlorobenzene	35	500[b]
ferrocene	56	33[c]
bromobenzene	79	50[b]
tetrabutyltin	120	35[c]
iodobenzene	127	25[b]
tetraethyllead	208	13[c]

[a] Argon plasma gas 1.0 L min^{-1}; Helium carrier gas ~3.5 mL min^{-1}. [b] Three times the signal-to-noise ratio. [c] Three times the standard deviation of blank.

Table 3 contains a summary of the critical parameters for ion sampling and skimming, calculated for different gas flows and source temperatures. As can be seen, there is not a great deal of difference in the mean free path, the number density, or the Knudsen number for the different gas flows and source temperatures, so it is difficult to explain the contradictory behavior of the two analytes in terms of ion sampling and skimming. However, since skimming was performed downstream of the Mach disk, the calculated values may not be representative of the actual conditions at the skimmer, and it is quite possible that further recombination and ionization reactions could be occurring. Another possibility is that, because of the relatively large sampling orifice diameter used and hence the small pressure differential between the source and the expansion chamber (<10:1), a barrel shock region does not actually form in the expansion stage of the low-pressure plasma. This would result in considerable further interactions between the species in the plasma both in the expansion stage and possibly downstream of the skimmer.

Optimization of Carrier Gas. Initial experiments were performed with a column head pressure of 42.5 kPa, which resulted in a flow rate of ~3.0 mL min^{-1}. It was impossible to measure the column flow rate exactly since it was set at atmospheric pressure using a constant head pressure control, and subsequent coupling to the low-pressure plasma probably caused the flow to change somewhat because of the lower pressure at the end of the column. Nevertheless, similar resolution and retention was obtained using a flame ionization detector at atmospheric pressure. A chromatogram for tetraethyllead, monitored at m/z 208, is shown in Figure 4a and exhibits considerable band broadening. When the head pressure was increased to 54 kPa (Figure 4b), which resulted in a carrier gas flow of ~3.5 mL min^{-1}, the retention time of the peak was shortened and the efficiency of the column was greatly increased. It was initially thought that the broadening

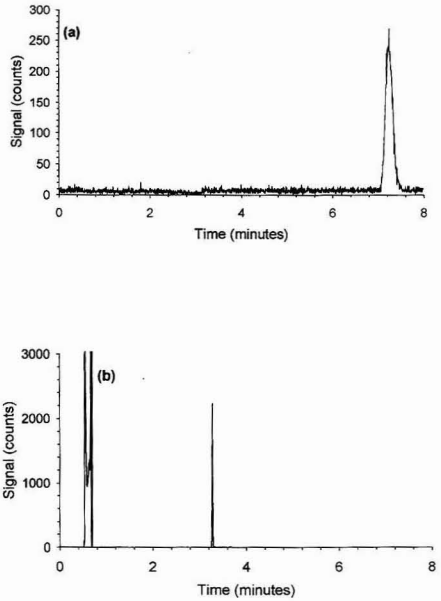

Figure 4. Effect of column head pressure on band broadening. Chromatograms for tetraethyllead at head pressures of (a) 42.5 and (b) 54 kPa.

was a result of torch dead volume, since at 42.5-kPa pressure the eluent from the column, which was 10 mm behind the back of the load coil, caused an indentation in the base of the plasma which was clearly visible when the solvent eluted. When the pressure was raised to 54 kPa the carrier gas punctured the plasma, resulting in an annular plasma similar to that obtained with an atmospheric plasma. Thus, the plasma was subject to less mixing, and less band broadening was observed. However, subsequent experiments have indicated that the band broadening may have been caused by uneven heating of the transfer line between the GC and the plasma rather than the effect of head pressure.

Analysis of Standards. Table 4 shows the results for the analysis of a number of standards. The detection limits were all below 1 ng on-column. Typical chromatograms for ferrocene, tetrabutyltin and bromobenzene are shown in Figure 5a–c. The peaks within the first minute of each chromatogram are solvent peaks, presumably caused by a combination of the quenching effect of the solvent on the plasma, dissociation, and subsequent recombination in the expansion stage. The solvent perturbed the plasma, but did not extinguish it, and the plasma returned to its normal state after the solvent had been eluted. This is an advantage over the MIP system for which solvent venting has conventionally to be employed.

The relative standard deviation for repeat injections of tetraethyllead over a 5-h period was 6.1%. This stability in the signal was also reflected in day-to-day runs with the area per nanogram remaining relatively constant (i.e., within 15%). This is considerably more constant than an atmospheric GC/ICPMS system in our experience.

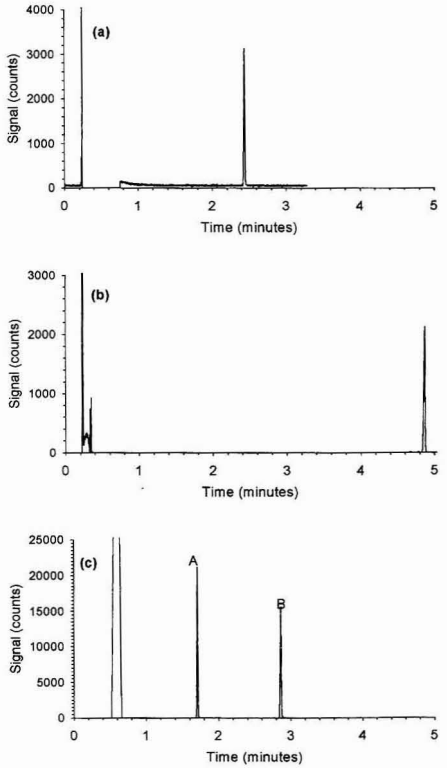

Figure 5. Element-selective chromatograms for (a) 10 ng of ferrocene, at *m/z* 56; (b) 55 ng of tetrabutyltin, at *m/z* 120; and (c) (A) 10 ng of bromobenzene and (B) 10 ng of benzyl bromide, at *m/z* 79.

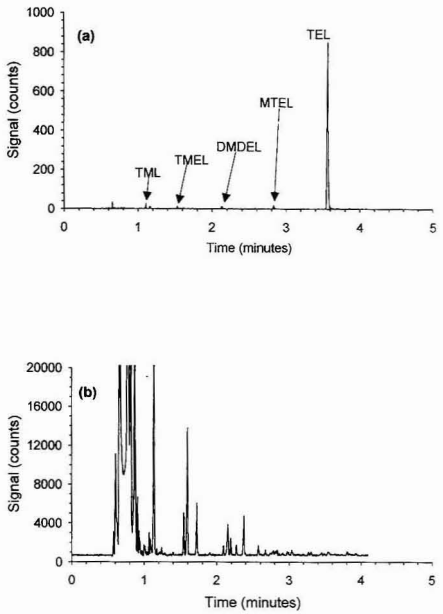

Figure 6. Element-selective chromatograms obtained for a sample of petrol in hexane containing tetraethyllead (TEL), methyltriethyllead (MTEL), dimethyldiethyllead (DMDEL), trimethylethyllead (TMEL), and tetramethyllead (TML). Monitored at (a) *m/z* 208 and (b) 12.

Analysis of Lead in Petrol and Naphtha. Chromatograms of lead (*m/z* 208) and carbon (*m/z* 12) for the petrol and naphtha samples are shown in Figure 6 and Figure 7, respectively. The petrol was found to contain 226 ± 22 μg/mL tetraethyllead. The high background on the carbon trace could have been due in part to residual carbon from the solvent, on the torch walls. The carbon trace (*m/z* 12) compared well with the GC-FID trace for the naptha sample as shown in Figure 7c, which also illustrates that minimal band broadening was observed with the low-pressure system. A comparison between the chromatograms illustrates the greater sensitivity and specificity that was achieved using element-selective detection at *m/z* 208.

Molecular Fragmentation Study. For molecular fragmentation, the LP-ICP was initially operated at a forward power of 50 W (30 W reflected), using only the carrier gas from the GC column (~3 mL min^{-1} He) to sustain the plasma. A 1-μl sample of a mixture of chlorobenzene, iodobenzene, and bromobenzene (500 μg mL^{-1} of each in hexane) was injected on-column, and the mass range between *m/z* 60 and 209 was monitored in a time-resolved manner, so that the total ion beam chromatogram shown in Figure 8 was obtained. The mass spectra for the chromatographic peaks are shown in Figure 9a–c. The mass range below *m/z* 60 was not monitored because of the presence of many polyatomic ions arising from the plasma gas and ablation from the quartz torch, so the unequivocal identification of the base peak was not possible. However, in the case of chlorobenzene, the most intense peak was at *m/z* 77, with the molecular ion peaks at *m/z* 112 and 114 being the next most intense (Figure 9a). In comparison, the molecular ion peaks for bromobenzene at *m/z* 156 and 158 (Figure 9b) and iodobenzene at *m/z* 204 (Figure 9c) were more intense than that at *m/z* 77. The mass spectra shown in Figure 9a–c are comparable to mass spectra obtainable using an electron impact (EI) ionization source, even though the relative intensities are slightly different and a comparison was not made below *m/z* 60. Also, the (M + 1) peaks were more intense with the LP-ICP source, indicating that some recombination also occurred. It is clear, however, that the potential exists for molecular fragmentation of organic compounds using the LP-ICP source.

One potential problem that was encountered was a concentration-dependent effect on the relative intensities of the total ion beam peaks. The relationships between concentration and signal for powers of 50 and 15 W is shown in Figure 10a–c for the molecular ions, phenyl ions, and halogen ions of chlorobenzene, bromobenzene, and iodobenzene, respectively. As can be seen, the relationship between concentration and signal was not exactly linear for the molecular ions or the phenyl ions. This was thought to be due

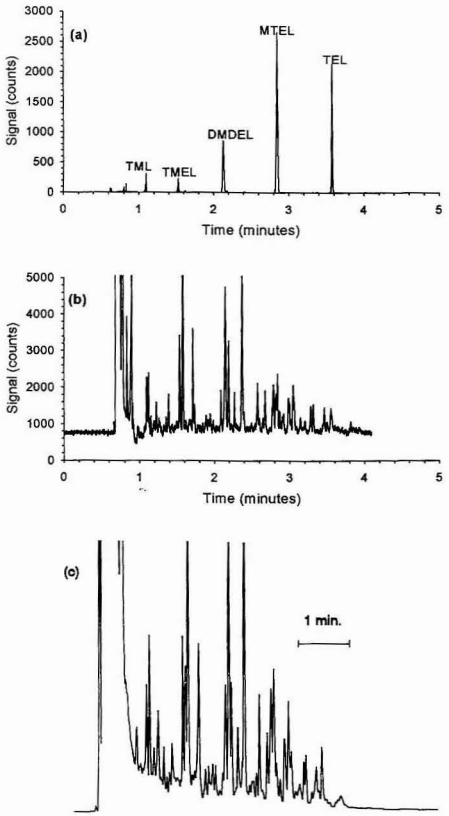

Figure 7. Chromatograms obtained for a sample of naptha in hexane containing TEL, MTEL, DMDEL, TMEL, and TML. See Figure 6 legend for definitions. Monitored at (a) *m/z* 208, (b) *m/z* 12, and (c) using flame ionization detection.

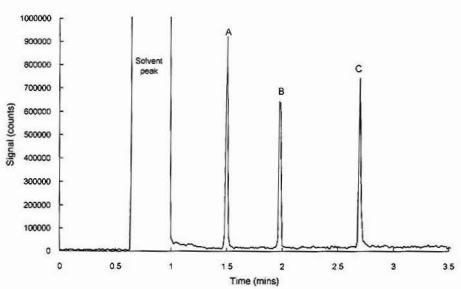

Figure 8. Total ion beam chromatogram for a mixture of (A) chlorobenzene, (B) bromobenzene, and (C) iodobenzene in hexane (500 ng of each).

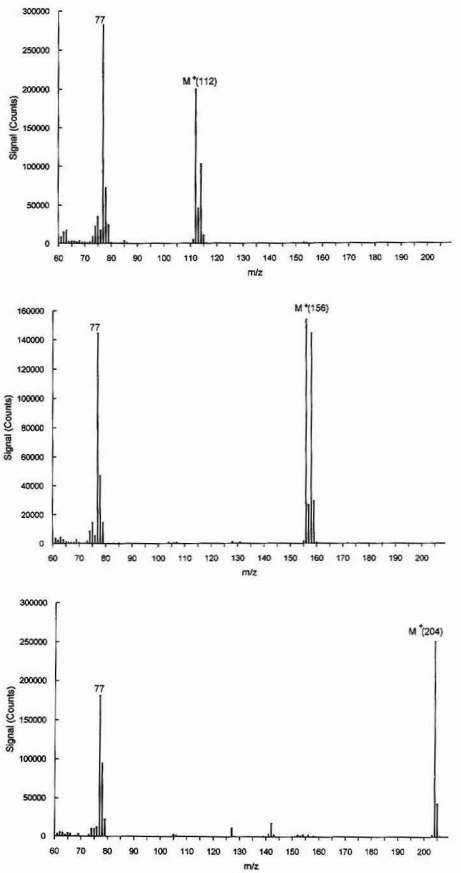

Figure 9. Mass spectra for (a) chlorobenzene, (b) bromobenzene, (c) iodobenzene (500 ng of each).

to a quenching or "self-matrix" effect of the analyte, which affected the fragmentation and ionization conditions. Another critical parameter was the power, also shown in Figure 10a–c. For example, at a concentration of 125 ppm (125 ng on-column), the signals observed for the molecular and phenyl ions of chlorobenzene and bromobenzene increased dramatically when the power was decreased from 50 to 15 W, with a similar though less pronounced effect for iodobenzene. The power dependency is shown more clearly in Figure 11a–c. As the power was increased from 15 to 100 W there was an exponential decrease in the molecular and phenyl ions of chlorobenzene (Figure 11a), presumably because the molecule was completely atomized in the plasma. The effect of power on the molecular and phenyl ion signals of bromobenzene and iodobenzene was even more pronounced (Figure 11b and c), with these ions disappearing almost entirely as the power was increased from 15 to only 25 W. This is in agreement with electron impact ionization where the molecular ion of chlorobenzene is more stable than that of bromobenzene or iodobenzene. At 15-W power the molecular ions for chlorobenzene and bromobenzene (though not iodobenzene) were evident at 50 ng, and the molecular ion for chlorobenzene was evident at 10 ng. It was not possible to reduce the power

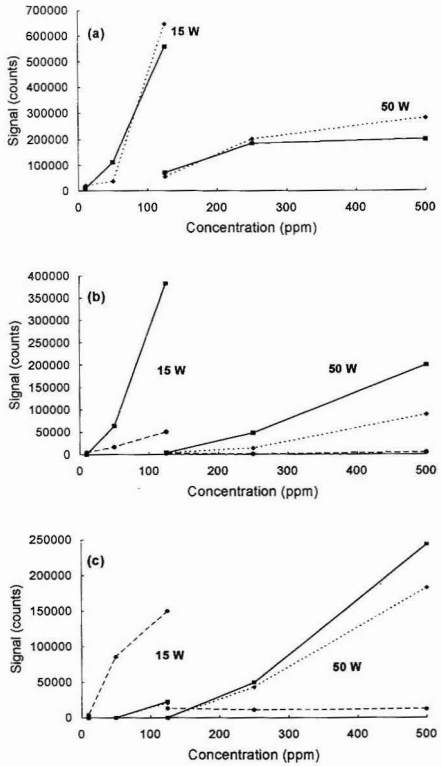

Figure 10. Relationship between concentration and signal of the molecular ion (■), phenyl ion (◆) and the halogen ion (●) for (a) chlorobenzene, (b) bromobenzene, and (c) iodobenzene at 15 (left side) and 50 W (right side) of power.

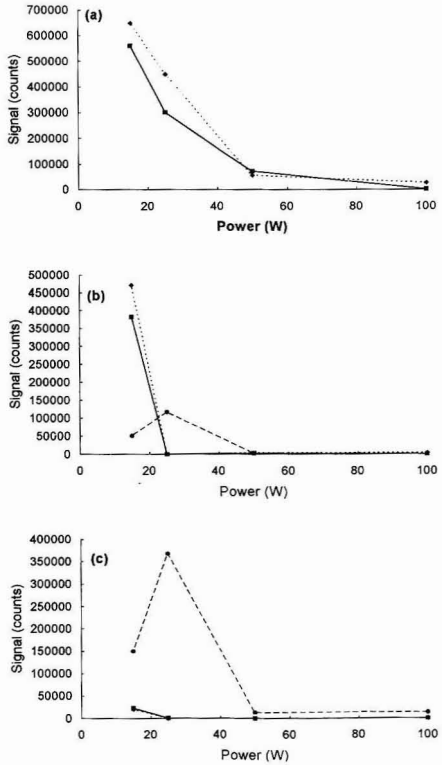

Figure 11. Influence of power on the signal for the molecular ion (■), phenyl ion (◆), and the halogen ion (●) for 125 ng of (a) chlorobenzene, (b) bromobenzene, and (c) iodobenzene.

below ~15 W because the radio-frequency generator was designed to operate at powers in excess of 1000 W, so it was impossible to set the power with an acceptable degree of accuracy or reproducibility below 50 W. The reproducibility of the forward power setting was further degraded by the high degree of reflected power, which was typically 60% of the forward power.

It is also evident from Figure 11b and c that the signals for $^{79}Br^+$ and $^{127}I^+$ first increased then decreased as the power was increased. A continuous increase in these signals with increasing power would be expected if the molecules were atomized to a greater extent at higher power. The results indicate that ion sampling and throughput may also be affected by power.

It is envisaged that, with finer control over the forward power, the fragmentation process could be controlled to a much greater extent.

CONCLUSIONS

Low-pressure inductively coupled plasma was shown to offer considerable potential as an ion source for both atomic and molecular mass spectrometry, with the ability to select a specific degree of fragmentation using a single source. Better control of power and further optimization of the sampling interface is expected to yield improved performance and extend the areas of application. It is already evident, however, that the LP-ICPMS is capable of producing both elemental and molecular information by adjusting the gas mixture, power, and pressure in the plasma. The plasma can be simply controlled by adjusting the power setting so as to adopt the charactersitics of a conventional ICP or a glow discharge without the need to change instrumentation. Further, LP-ICPMS shows promise of offering similarly facile variability of the nature of fragmentation and ionization. Work is progressing in this regard to evaluate more fully the potential.

ACKNOWLEDGMENT

W.P. thanks the FRD (South Africa) and the University of Plymouth for funding.

Received for review March 30, 1994. Accepted June 28, 1994.[⊗]

[⊗] Abstract published in *Advance ACS Abstracts,* August 1, 1994.

Anal. Chem. **1994,** *66,* 3408–3415

Chemical Electron-Transfer Reactions in Electrospray Mass Spectrometry: Effective Oxidation Potentials of Electron-Transfer Reagents in Methylene Chloride

Gary J. Van Berkel* and Feimeng Zhou

Chemical and Analytical Sciences Division, Oak Ridge National Laboratory, Oak Ridge, Tennessee 37831-6365

Cyclic voltammetry (CV), UV/visible absorption spectroscopy, and electrospray mass spectrometry (ES-MS) are used in conjunction to study the mono- and/or dications produced in solution from the reaction of three model compounds (β-carotene, cobalt(II) octaethylporphyrin ($Co^{II}OEP$), nickel(II) octaethylporphyrin ($Ni^{II}OEP$)), in three different solvent/electron-transfer reagent systems (methylene chloride/0.1% trifluoroacetic acid (TFA) (v/v), methylene chloride/0.1% TFA/2,3-dichloro-5,6-dicyano-1,4-benzoquinone (DDQ) (v/v/200 μM), methylene chloride/0.1% TFA/0.1% antimony pentafluoride (SbF_5) (v/v/v)). The reactions were carried out on-line with ES-MS by means of flow injection. Correlation of the CV data for these analytes with the ionic species determined to be in the solution on the basis of UV/visible absorption spectra and/or on the basis of the ionic species observed in the gas phase by ES-MS, along with our previously published data on these solvent/reagent systems, allowed an effective oxidation potential range, E, to be assigned to these solvent/reagent systems: methylene chloride/0.1% TFA (v/v), 0.6 V ≤ E_{TFA} < 0.7 V; methylene chloride/0.1% TFA/DDQ (v/v/200 μM), 0.8 V ≤ $E_{TFA/DDQ}$ < 1.0 V; methylene chloride/0.1% TFA/0.1% SbF_5 (v/v/v), 1.3 ≤ E_{TFA/SbF_5} < 1.5. Knowledge of the solvent/reagent oxidation potentials and the electrochemical redox potentials of a particular analyte of interest allows a solvent/reagent system to be chosen to selectively ionize an analyte, or a range of analytes, to a desired ionic state for subsequent analysis by ES-MS. The ability to detect, in the gas phase, an ionic species produced in solution by chemical electron transfer will depend, however, on the stability of the ion in the given solvent/reagent system and on whether the ion can survive intact the transfer to the gas phase via the ES process.

Electrospray (ES) is a relatively new ionization method that affords the transfer of ions in a liquid solution into the gas phase, where they can be analyzed by mass spectrometry (MS).[1-5] The nature of the ES process, though not fully understood,[6-13] is such that observation of gas-phase analyte ions is dependent upon the presence of those analyte ions in solution. That is, the ES process does not *normally* ionize the analyte directly,[13,14] but merely assists the transfer of "preformed" ionic analyte species in solution into the gas phase. Therefore, the types of ions normally observed in ES mass spectra, both singly and multiply charged, are those ionic species that are stable in solution. For the most part, these types of ionic species include the cations or anions of salts and pseudomolecular ions, e.g., $(M + nH)^{n+}$, $(M - nH)^{n-}$, and $(M + nNa)^{n+}$, that are formed from species containing acidic or basic sites that can be ionized in solution via Brønsted or Lewis acid/base chemistry. Furthermore, the work of Siu and co-workers[7,8] and Kebarle and co-workers,[6,11,12] among others, indicates that the ionic abundance distribution observed in an ES mass spectrum, in the absence of severe matrix-induced ion signal suppression or gas-phase charge-changing reactions, is at least qualitatively related to the abundances of these same ionic species in solution.

Radical cations, radical anions, or other ionic species formed by gain or loss of electrons from neutral organic molecules in solution are not *typically* observed in ES mass spectra since these types of ions are not formed by simple acid/base chemistry nor are they generally stable in solution for long periods. However, Van Berkel et al.,[13] and more recently Xu et al.,[14] have demonstrated that some easily oxidized compounds (e.g., metallocenes, metalloporphyrins, and polycyclic aromatic hydrocarbons (PAHs)) can be ionized in solution at the ES needle/solution interface via an electrochemical oxidation process inherent to ES[6] and can be detected in the gas phase as their respective radical cations. Analytes with oxidation potentials less than 0.3 V appear to be almost completely oxidized by this process, but the "efficiency" of this oxidation process for ionization of analytes with oxidation potentials greater that 0.3 V dramatically decreases.[14] For analytes with oxidation potentials greater than 0.5–0.6 V, the analytical utility of this ionization phenomenon in terms of analyte detection is limited to samples of very high concentration (i.e., 0.1 mM or greater). If analyte oxidation potentials

(1) Fenn, J. B.; Mann, M.; Meng, C. K.; Wong, S. K.; Whitehouse, C. M. *Science* **1989**, *246*, 64–71.
(2) Fenn, J. B.; Mann, M.; Meng, C. K.; Wong, S. K.; Whitehouse, C. M. *Mass Spectrom. Rev.* **1990**, *9*, 37–71.
(3) Smith, R. D.; Loo, J. A.; Edmonds, C. G.; Barinaga, C. J.; Udseth, H. R. *Anal. Chem.* **1990**, *62*, 882–899.
(4) Huang, E. C.; Wachs, T.; Conboy, J. J.; Henion, J. D. *Anal. Chem.* **1990**, *62*, 713A–725A.
(5) Mann, M. *Org. Mass Spectrom.* **1990**, *25*, 575–587.
(6) Ikonomou, M. G.; Blades, A. T.; Kebarle, P. *Anal. Chem.* **1991**, *63*, 1989–1998.
(7) Guevremont, R.; Siu, K. W. M.; Le Blanc, J. C. Y.; Berman, S. S. *J. Am. Soc. Mass Spectrom.* **1992**, *3*, 216–224.
(8) Cheng, Z. L.; Siu, K. W. M.; Guevremont, R.; Berman, S. S. *J. Am. Soc. Mass Spectrom.* **1992**, *3*, 281–288.
(9) Fenn, J. B. *J. Am. Soc. Mass Spectrom.* **1993**, *4*, 524–535.
(10) Ashton, D. S.; Beddell, C. R.; Cooper, D. J.; Green, B. N.; Oliver, R. W. A. *Org. Mass Spectrom.* **1993**, *28*, 721–728.
(11) Kebarle, P.; Tang, L. *Anal. Chem.* **1993**, *65*, 972A–986A.
(12) Tang, L.; Kebarle, P. *Anal. Chem.* **1993**, *65*, 3654–3668.
(13) Van Berkel, G. J.; McLuckey, S. A.; Glish, G. L. *Anal. Chem.* **1992**, *64*, 1586–1593.
(14) Xu, X.; Nolan, S. P.; Cole, R. B. *Anal. Chem.* **1994**, *66*, 119–125.

0003-2700/94/0366-3408$04.50/0
© 1994 American Chemical Society

exceed 1.0 V, detection even at much higher concentration is tenuous.

In several reports,[15–19] we have demonstrated chemical electron-transfer reactions to be a more efficient and analytically useful means to generate molecular radical cations, and anions, of aromatic, heteroaromatic, and other highly conjugated systems in solution for subsequent transport to and detection in the gas phase using ES-MS. Recently, we have reported the ability to form molecular dications[18] and dianions[19] in solution and the ability to transfer them to the gas phase using similar techniques. In a clever application of this methodology, Anacleto et al.[20] used chemical electron-transfer reactions as a postcolumn "derivatization", affording the analysis of fullerenes (as their radical cations or anions) by HPLC/ES-MS.

A number of chemical reagents including Brønsted acids, Lewis acids, halogens, metal salts, and charge-transfer reagents might be used to ionize highly conjugated molecules in solution via electron-transfer reactions for subsequent analysis by ES-MS.[21] A limiting factor in the analytical utility of these, or other, solvent/electron-transfer systems is the fact that the precise mechanism by which analyte oxidation occurs is not always known. Furthermore, although the oxidation of highly conjugated systems in solution by reaction with strong Brønsted acids such as trifluoroacetic acid (TFA),[21] charge-transfer reagents such as 2,3-dichloro-5,6-dicyano-1,4-benzoquinone (DDQ),[22] and Lewis acids such as antimony pentafluoride (SbF_5)[23] is well documented, and has been used successfully with ES-MS for analyte ionization/detection,[15–20] the oxidizing strength, or "oxidation potential", of such solvent/reagent systems can generally only be loosely categorized as either "strong" or "weak".[17] Therefore, the choice of a solvent/reagent system for the oxidation of a particular analyte in conjunction with ES-MS detection has been carried out largely in a "hit" or "miss" fashion. Knowledge of the solvent/reagent oxidation potentials, in combination with the electrochemical redox potentials of a particular analyte of interest, would enable one to judiciously choose a solvent/reagent system to ionize the analyte to the desired ionic state (e.g., $M^{\bullet+}$ or M^{2+}). The ability to detect in the gas phase an ionic species produced in solution by chemical electron transfer will depend, however, on the stability of the ion in the given solvent/reagent system and on whether the ion can survive intact the transfer to the gas phase via the ES process.

In the work presented here, cyclic voltammetry (CV), UV/visible absorption spectroscopy, and ES-MS are used in conjunction to study the mono- and/or dications produced in solution from the reaction of three model compounds (β-carotene, cobalt(II) octaethylporphyrin ($Co^{II}OEP$)), nickel(II) octaethylporphyrin ($Ni^{II}OEP$)), in three different solvent/electron-transfer reagent systems we have found particularly effective and relatively simple to employ with ES-MS (methylene chloride/0.1% TFA (v/v), methylene chloride/0.1% TFA/DDQ (v/v/200 μM), methylene chloride/0.1% TFA/0.1% SbF_5 (v/v/v)).[15–18] Correlation of the CV data for these analytes with the ionic species determined to be in the solution, on the basis of UV/visible absorption spectra and/or on the basis of the ionic species observed in the gas phase by ES-MS, allowed an effective oxidation potential range to be assigned to these solvent/reagent systems. By carrying out these reactions on-line with ES-MS, by means of a flow injection technique, the time between formation of the ions in solution and their subsequent transfer to the gas phase could be minimized.[15–19] In this way, transient ionic species, e.g., the dication of β-carotene, which has a solution half-life of only a few seconds,[18] as well as more solution-stable species, could be studied to determine these effective oxidation potentials.

EXPERIMENTAL SECTION

Samples. All analytes and reagents were obtained from commercial suppliers and used without further purification. HPLC-grade methylene chloride (J. T. Baker, Phillipsburg, NJ) was dried by elution through a bed of activated basic alumina (Bio-Rad, Richmond, CA) and stored in an air-tight flask over alumina. Analyte stock solutions were prepared daily at about the 1000 μM level in freshly dried methylene chloride. From these stock solutions, sample solutions were prepared by serial dilution with this solvent.

Mass Spectrometry. All ES-MS experiments were carried out using a modified version of a Finnigan-MAT ion trap mass spectrometer (ITMS) adapted to sample from ambient air.[24–26] For continuous-infusion experiments, a syringe pump (Harvard Apparatus, Inc., Cambridge, MA) and a glass syringe were used to pump analyte/oxidant solutions at a rate of 10–15 μL/min through a short length of 500-μm-i.d. Teflon tubing that connected to a 120-μm-i.d. (500-μm-o.d.) dome-tip needle within a pneumatically assisted ES source. Nitrogen gas, at a backing pressure of 280 kPa, was used for pneumatically assisting the ES process.

Flow injection experiments were carried out at 10–15 μL/min by use of the syringe pump to deliver the solvent/oxidant mixture at a constant rate, through Teflon tubing, to a Rheodyne (Cotati, CA) Model 7520 injector with a 0.5-μL internal sample chamber and then through a short length ($\sim$15 cm) of 100-μm-i.d. silica capillary to which the pneumatically assisted ES source was connected. The analyte, dissolved in methylene chloride, was injected into the flowing stream so that reaction with the oxidant occurred in the silica capillary just prior to the ES needle.

UV/Visible Absorption Spectroscopy. UV/visible absorption spectra acquired during flow injection experiments made

(15) Van Berkel, G. J.; McLuckey, S. A.; Glish, G. L. *Anal. Chem.* **1991**, *63*, 2064–2068.
(16) Asano, K. G.; Van Berkel, G. J. In *Proceedings of the 41st ASMS Conference on Mass Spectrometry and Allied Topics*, San Francisco, CA, May 30–June 4, 1993; ASMS: Santa Fe, NM, 1993; pp 1068a–1068b.
(17) Van Berkel, G. J.; Asano, K. G. *Anal. Chem.* **1994**, *66*, 2096–2102.
(18) Van Berkel, G. J.; Asano, K. G.; McLuckey, S. A. *J. Am. Soc. Mass Spectrom.* **1994**, *5*, 689–692.
(19) Zhou, F.; Van Berkel, G. J.; Donovan, B. T. *J. Am. Chem. Soc.* **1994**, *116*, 5485–5486.
(20) Anacleto, J. F.; Quilliam, M. A.; Boyd, R. K.; Howard, J. B.; Lafleur, A. L.; Yadav, T. *Rapid Commun. Mass Spectrom.* **1993**, *7*, 229–234.
(21) Bard, A. J.; Ledwith, A.; Shine, H. J. In *Advances in Physical Organic Chemistry;* Gold, V., Bethell, D., Eds.; Academic Press: New York; 1976; Vol. 13, pp 155–278.
(22) Foster, R. *Organic Charge Transfer Complexes*; Academic Press: New York, 1969.
(23) Brouwer, D. M.; Van Doorn, J. A. *Recl. Trav. Chim. Pays-Bas* **1972**, *91*, 1110–1116.
(24) Van Berkel, G. J.; Glish, G. L.; McLuckey, S. A. *Anal. Chem.* **1990**, *62*, 1284–1289.
(25) McLuckey, S. A.; Van Berkel, G. J.; Glish, G. L.; Henion, J. D.; Huang, E. C. *Anal. Chem.* **1991**, *63*, 375–383.
(26) Van Berkel, G. J.; McLuckey, S. A.; Glish, G. L. *Anal. Chem.* **1991**, *63*, 1098–1109.

use of a SoloNet140 diode array detector system (Groton Technology, Inc., Concord, MA). In this case, the syringe pump was used to deliver the solvent/oxidant mixture at a constant rate, through Teflon tubing, to the Rheodyne injector and then through a short length (~12 cm) of 254-μm-i.d. Teflon tubing connected to the detector flow cell (4.5-mm path length, 5-μL volume) constructed of methylene chloride resistent Kel-F. The solution exited the cell through an additional length of 254-μm-i.d. Telfon tubing directed to waste. Operating this system at a flow rate of 40 μL/min resulted in a time from sample injection to initial detection in the flow cell of ~9 s with a peak width of ~15 s. This "reaction time" is comparable to that experienced by the analytes in the flow injection experiments carried out on-line with ES-MS at a flow rate of 10–15 μL/min.

Cyclic Voltammetry. Electrochemical experiments were performed with a PAR 173 potentiostat (Princeton Applied Research Corp., Princeton, NJ), a PAR 175 universal programmer, and a Hewlett-Packard *x–y* recorder. A 1-mm-radius platinum disk electrode was used as the working electrode, a platinum mesh as the auxiliary electrode, and a silver wire as a quasi-reference electrode. Samples were dissolved in dry methylene chloride at ~1.5 mM with 0.1 M tetrabutylammonium tetrafluoroborate ((TBA)BF_4; Johnson Matthey Corp., Ward Hill, MA) added as the supporting electrolyte. Cyclic voltammograms were obtained at a scan rate of 100 mV/s. After the cyclic voltammogram of each compound was obtained, bis(pentamethylcyclopentadienyl)-iron (Cp*Fc; Strem Chemicals, Inc., Newburyport, MA) was added to each solution and used as the reference redox system.

RESULTS AND DISCUSSION

Analyte Redox Behavior Determined via Cyclic Voltammetry. Each of the three model compounds investigated in this study, viz., β-carotene,[27–30] cobalt(II) octaethylporphyrin (Co^{II}OEP),[31] and nickel(II) octaethylporphyrin (NiOEP)[32] are relatively easy to oxidize in solution to their respective mono- and dications. The individual electrochemical behavior of these species is quite different, however, as evidenced by the cyclic voltammograms (CVs) recorded in methylene chloride shown in Figure 1. The peak potential for oxidation of β-carotene (E_{pa}) is observed at ~0.75 V versus the SCE (Figure 1a). Previous electrochemical studies have shown the oxidation of β-carotene to be a simple two-electron transfer reaction forming the dication, M^{2+} (E_rE_r mechanism).[27–30] Only one CV wave, corresponding to a two-electron transfer, is observed as the radical cation formed by the oxidation of the neutral molecule is oxidized to the dication at a potential only 42 mV more positive than the potential at which the radical cation is formed.[28] The peak current ratio for the cathodic and anodic waves, i_{pc}/i_{pa}, is only 0.57 ($i_{pc}/i_{pa} \approx 1.0$ for a reversible redox couple[33]), indicating that the dication undergoes a following chemical reaction (C_i). A reduction wave is observed at ~0.23 V, also indicating that the dication undergoes a chemical reaction and that the product of this reaction is electroactive. The chemical followup reaction must be relatively slow, however, because an appreciable reduction wave can be observed during the reverse scan even at the relatively slow CV scan rate of 100 mV/s. Therefore, an $E_rE_rC_i$ mechanism can be assigned to the two-electron oxidation CV wave of β-carotene.

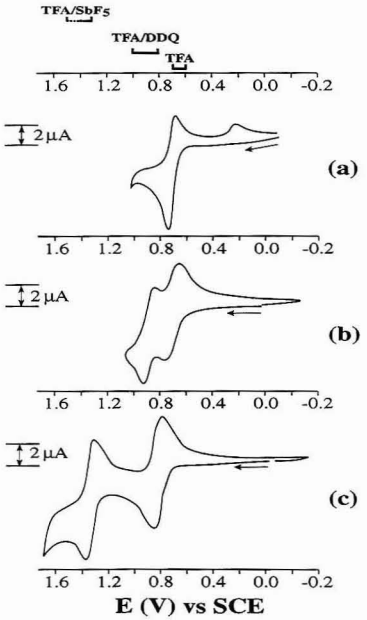

Figure 1. Cyclic voltammograms (scan rate, 100 mV/s) of (a) 1.6 mM β-carotene, (b) 1.5 mM Co^{II}OEP, and (c) 1.6 mM Ni^{II}OEP obtained in methylene chloride using (TBA)BF_4 (0.1 M) as the supporting electrolyte. Arrows indicate the initial scan direction. The effective oxidation potential range of each solvent/reagent system as determined in this study is delineated by a bar on top of the potential scale.

In contrast to β-carotene, the CV of Co^{II}OEP in Figure 1b indicates that this compound undergoes two reversible one-electron transfer reactions (E_rE_r, E_{pa1} = 0.76 V and E_{pa2} = 0.92 V) and the mono- and dication products are both stable (i_{pc1}/i_{pa1} = 1.0 and i_{pc2}/i_{pa2} = 0.97). Moreover, the peak potential separation ($\Delta E = E_{pa} - E_{pc}$) of the first wave is 65 mV and that of the second 75 mV. These values are quite close to the theoretical value of 59 mV for a reversible redox couple,[33] given the highly resistant solvent system used and the fact that no correction for uncompensated solution resistance was made during the measurement. Therefore, the electrochemical oxidation behavior of Co^{II}OEP can be described by an E_rE_r mechanism.

The CV of Ni^{II}OEP in Figure 1c indicates that this compound also undergoes two reversible one-electron transfer

(27) Mairanovsky, V. G.; Engovatov, A. A.; Ioffe, N. T.; Samokhvalov, G. I. *J. Electroanal. Chem.* **1975**, *66*, 123–137.
(28) Grant, J. L.; Kramer, V. J.; Ding, R.; Kispert, L. D. *J. Am. Chem. Soc.* **1988**, *110*, 2151–2157.
(29) Khaled, M.; Hadjipetrou, A.; Kispert, L. D. *J. Phys. Chem.* **1990**, *94*, 5164–5169.
(30) Khaled, M.; Hadjipetrov, A.; Kispert, L. D.; Allendoerfer, R. D. *J. Phys. Chem.* **1991**, *95*, 2438–2442.
(31) Dolphin, D.; Muljiani, Z.; Rousseau, K.; Borg, D. C.; Fajer, J.; Felton, R. H. *Ann. N.Y. Acad. Sci.* **1973**, *206*, 177–209.
(32) Fuhrhup, J.-H.; Mauzerall, D. *J. Am. Chem. Soc.* **1969**, *91*, 4174–4181.
(33) Bard, A. J.; Faulkner, L. R. *Electrochemical Methods*; John Wiley & Sons, Inc.: New York, 1980.

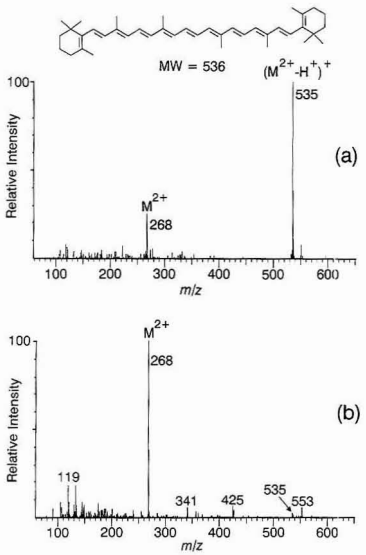

Figure 2. Background-subtracted, averaged ES mass spectrum obtained from the injection of 5 pmol (0.5 μL) of β-carotene (MW = 536, dissolved in methylene chloride) into a flowing stream (10 μL/min) composed of (a) methylene chloride/0.1% TFA (v/v) and (b) methylene chloride/0.1% TFA/0.1% SbF_5 (v/v/v).

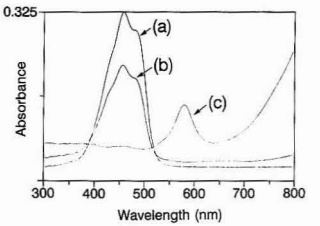

Figure 3. Photodiode array UV/visible absorption spectra obtained from the flow injection of 50 pmol (0.5 μL) of β-carotene (dissolved in methylene chloride) into a flowing stream (40 μL/min) composed of (a) methylene chloride, (b) methylene chloride/0.1% TFA (v/v), and (c) methylene chloride/0.1% TFA/0.1% SbF_5 (v/v/v).

reactions ($E_r E_r$; $i_{pc1}/i_{pa1} = 0.96$, $\Delta E = 75$ mV and $i_{pc2}/i_{pa2} = 0.94$, $\Delta E = 78$). The monocation is formed at a potential ($E_{pa1} = 0.84$ V) midway between the potentials needed to form the monocation and dication of $Co^{II}OEP$ while the dication is formed at a much more positive potential ($E_{pa2} = 1.37$ V).

Analyte Oxidation via Chemical Electron Transfer. Similar electron-transfer chemistry occurs with these compounds upon their reaction in solution with chemical electron-transfer reagents. Since these compounds are normally neutral in solution, chemical electron-transfer reactions provide a means for the solution-phase ionization/gas-phase detection of these compounds, and compounds of similar electron-transfer characteristics, by ES-MS.[15–20] To ionize an analyte to its mono- or dication, however, requires that the solvent/reagent system have a sufficient "oxidation potential".

A. β-Carotene. The ES response of β-carotene in methylene chloride at the low levels used in this study (i.e., 5 pmol) was found to be negligible unless some chemical measure was taken to make the compound ionic in solution. Figure 2a is the background-subtracted, averaged mass spectrum of β-carotene obtained from a flow injection experiment in which 5 pmol of β-carotene was injected into a flowing stream (10 μL/min) of methylene chloride/0.1% TFA (v/v). At this flow rate the analyte remained in contact with the oxidizing solvent system, from the time of injection until peak elution, for 10–16 s (peak width, 6 s). The two major peaks in the spectrum appear at the *m/z* value expected for the molecular dication of β-carotene, M^{2+} (*m/z* 268), and at the *m/z* value corresponding in mass to $(M - 1)^+$ (*m/z* 535), respectively.

The ion at *m/z* 268 was confirmed to be that of the dication, rather than a singly charged ion at half the molecular mass, by observing in real time that the isotope peaks occurred at half-mass intervals as expected for a doubly charged ion.[18] Furthermore, the MS/MS spectrum obtained by collision-induced dissociation (CID) of the ion at *m/z* 268 contained product ions at both *m/z* values lesser and *m/z* values greater than that of the parent ion.[18] Such an MS/MS spectrum, in the absence of ion/molecule reactions, is only possible if the parent ion is multiply charged.[34]

Although the mechanism of this oxidation reaction is not known, these results demonstrate that TFA can oxidize β-carotene to the dication. However, previous work on the reactions of β-carotene and TFA would indicate that neither the dication nor the ion observed at *m/z* 535 is that expected. On the basis of UV/visible absorption spectra, Ioffe et al.[35] reported that the reaction of β-carotene with TFA resulted in formation of protonated β-carotene, $(M + H^+)^+$. The UV/visible absorption spectrum of β-carotene obtained under flow injection conditions mimicking the experimental conditions of the flow injection experiments carried out on-line with ES-MS are shown in Figure 3. Curve a, which is the absorption spectrum obtained for 50 pmol of β-carotene injected into a stream of methylene chloride, compares well with the literature spectrum of neutral β-carotene.[35] Curve b is the UV/visible spectrum obtained for 50 pmol of β-carotene injected into a stream of methylene chloride/0.1% TFA (v/v). In this spectrum, the absorption peak due to the neutral compound has decreased and a broad peak that maximizes somewhere beyond 800 nm has appeared. These are the same spectral changes noted by Ioffe et al.[35] upon mixing β-carotene and TFA.

On the basis of the ions observed in the ES mass spectrum, it appears that these spectra are indicative not of the protonated molecule, but a combination of the dication and a reaction product corresponding in mass to $(M - 1)^+$. The work of Mairanovsky et al.[27] and Kispert and co-workers,[28–30] as well as our other studies of this analyte/solvent/reagent system,[18,36] indicate that the ion at *m/z* 535 corresponds to $(M^{2+} - H^+)^+$ formed in solution by rapid loss of a proton from the dication

(34) Busch, K. L.; Glish, G. L.; McLuckey, S. A. *Mass Spectrometry/Mass Spectrometry: Techniques and Applications of Tandem Mass Spectrometry*; VCH Publishers: New York, 1988.
(35) Ioffe, N. T.; Engovatov, A. A.; Mairanovskii, V. G. *Zh. Obshch. Khim.* **1976**, *46*, 1638–1644.
(36) Van Berkel, G. J.; Zhou, F. *Anal. Chem.*, in preparation.

(eq 1). Furthermore, it is this ion which is the product of the

$$M^{2+} \rightarrow (M^{2+} - H^+)^+ + H^+ \quad (1)$$

chemical followup reaction indicated by the CV data. In fact, the observation of the dication is only possible because the flow injection experiment allows for rapid transport of this species, which is short-lived in solution, to the gas phase where it is stable. On the basis of the relative abundances of dication and the $(M^{2+} - H^+)^+$ species in the ES-MS obtained from the flow injection experiments carried out at various flow rates (10, 20, 30, and 40 μL/min), we were able to determine the half-life of the dication in this solvent system to be 6.3 s. A similar solution half-life was determined from a simulation of the β-carotene CV based on this $E_rE_rC_i$ mechanism.

Solvent/reagent systems comprised of methylene chloride/TFA/DDQ were found in our previous studies to be better oxidants than methylene chloride/0.1% TFA (v/v).[17] However, no ions that could be correlated with β-carotene were observed under flow injection conditions using methylene chloride/0.1% TFA/DDQ (v/v/200 μM) as the solvent/reagent system. Moreover, the ES mass spectra obtained by continuous infusion of a solution of β-carotene dissolved in this solvent system showed little evidence of ions that could be directly related to β-carotene.[18] Dissolution of β-carotene in this solvent/reagent system was accompanied by a solution color change indicative of a chemical reaction that might be expected to form an ionic product. However, the β-carotene dication and $(M^{2+} - H^+)^+$, if formed, apparently have much shorter solution lifetimes in this solvent/reagent system than in methylene chloride/0.1% TFA (v/v). This result again points out that a particular solvent/reagent system must not only be capable of oxidizing the analyte to the desired ionic state, but also that the ionic product formed must have a sufficiently long solution lifetime (i.e., a lifetime of several seconds under present experimental conditions) to survive until it can be transferred to the gas phase and detected.

Previous work with methylene chloride/TFA/SbF_5 as the solvent/reagent system demonstrated it to be the strongest oxidizing system among the three under study.[17,18] The present results are consistent with these earlier observations. Figure 2b is the background-subtracted average mass spectrum obtained from a flow injection experiment in which 5 pmol of β-carotene was injected into a flowing stream (10 μL/min) of methylene chloride/0.1% TFA/0.1% SbF_5 (v/v/v). The major peak observed in the ES mass spectrum is that due to the dication at *m/z* 268. Other ions of lesser intensity are seen to appear at low mass (e.g., *m/z* 119), which may be fragment ions formed upon ion injection into the trap.[26,37] In this solvent system, β-carotene is ionized forming the dication which, given the absence of other ions in the spectrum, is apparently much longer lived in this solvent system than in the previous two discussed.

Curve c in Figure 3 is the UV/visible spectrum obtained for 50 pmol of β-carotene injected into a stream of methylene chloride/0.1% TFA/0.1% SbF_5. This spectrum is quite different from the spectrum in curve b obtained for the reaction

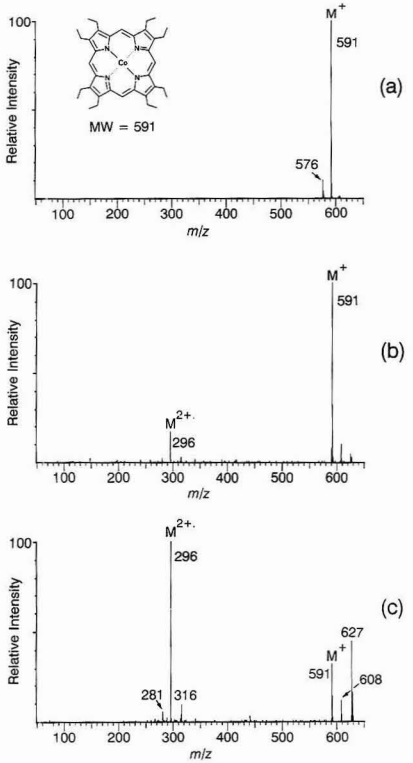

Figure 4. Background-subtracted, averaged ES mass spectrum obtained from the injection of 40 pmol (0.5 μL) of $Co^{II}OEP$ (MW = 591, dissolved in methylene chloride) into a flowing stream (15 μL/min) composed of (a) methylene/0.1% TFA, (b) methylene/0.1% TFA/DDQ (v/v/200 μM), and (c) rnethylene/0.1% TFA/0.1% SbF_5 (v/v/v).

of β-carotene with TFA. Note also the complete disappearance of the absorption peaks due to the neutral molecule indicating complete conversion of the neutral to another species. On the basis of the ES mass spectrum obtained under similar conditions (Figure 2b), this UV/visible spectrum would appear to be that of the dication, M^{2+}. To our knowledge the UV/visible spectrum of the β-carotene dication has not previously been reported, apparently due to its short solution lifetime in most solvent systems.

B. $Co^{II}OEP$. Like β-carotene discussed above, $Co^{II}OEP$ is neutral when dissolved in methylene chloride and, at the analyte levels used here, has minimal ES response unless it is somehow ionized in the solution prior to the ES process. The ES mass spectrum of $Co^{II}OEP$ in Figure 4a was obtained in a flow injection experiment in which 40 pmol of $Co^{II}OEP$ was injected into a flowing stream (15 μL/min) of methylene chloride/0.1% TFA (v/v). The major peak observed in the spectrum at *m/z* 591 corresponds in mass to the monocation, M^+, formed by one-electron loss from the neutral porphyrin. (Note that neutral $Co^{II}OEP$ is paramagnetic with Co coordinated in a square-planar $3d^7$ configuration; hence, the first oxidation product is an even-electron species.)

(37) Loo, J. A.; Udseth, H. R.; Smith, R. *Rapid Commun. Mass Spectrom.* **1989**, *2*, 207–210.

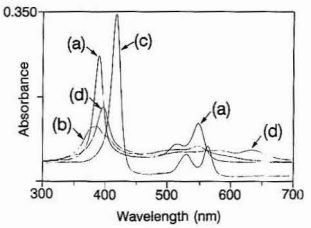

Figure 5. Photodiode array UV/visible absorption spectra obtained from the flow injection of 50 pmol (0.5 μL) of $Co^{II}OEP$ (dissolved in methylene chloride) into a flowing stream (40 μL/min) composed of (a) methylene chloride, (b) methylene chloride/0.1% TFA (v/v), (c) methylene chloride/0.1% TFA/DDQ (v/v/200 μM) and (d) methylene chloride/0.1% TFA/0.1% SbF_5 (v/v/v).

UV/visible absorption spectra of $Co^{II}OEP$ obtained under similar flow injection conditions are shown in Figure 5. Curve a, which is the absorption spectrum obtained for 50 pmol of $Co^{II}OEP$ injected into a stream of methylene chloride, compares well with the literature spectra of neutral Co^{II}-OEP.[31,32] Curve b is the UV/visible spectrum obtained for 50 pmol of $Co^{II}OEP$ injected into a stream of methylene chloride/0.1% TFA. This spectrum is very similar to that reported by Dolphin et al.[31] for the monocation of $Co^{II}OEP$ formed via one-electron electrochemical oxidation in methylene chloride. Thus, the ES mass spectrum and UV/visible spectra show that $Co^{II}OEP$ is oxidized to the monocation in methylene chloride/0.1% TFA. It should be noted that an ES mass spectrum identical to that obtained under flow injection conditions was obtained by continuously infusing a methylene chloride/0.1% TFA (v/v) solution of $Co^{II}OEP$ (40 μM). This observation supports the CV data, which indicates that the monocation is very stable in methylene chloride.

Figure 4b is the ES mass spectrum obtained by injecting 40 pmol of $Co^{II}OEP$ into a flowing stream (15 μL/min) of methylene chloride/0.1% TFA/DDQ (v/v/200 μM). The base peak in this spectrum is the monocation, but the dication, $M^{\bullet 2+}$, is also observed. (Note that the ion trap data acquisition program used to acquire these spectra forces an integer m/z value upon ions that occur at half-mass values. As such, the m/z value assigned to the dication of $Co^{II}OEP$ is m/z 296. Calibration of the spectrum in real time found the m/z value of the dication to be 295.5 as expected.) Further confirmation of this ion as the dication was demonstrated through the use of interface fragmentation.[26,37] Fragmentation of this ion in the atmospheric sampling region of the instrument resulted in the formation of doubly charged fragment ions as expected based on previously published tandem mass spectrometry investigations of porphyrin dications.[38,39]

Curve c in Figure 5 is the UV/visible spectrum obtained for 50 pmol of $Co^{II}OEP$ injected into a stream of methylene chloride/0.1% TFA/DDQ (v/v/200 μM). In this spectrum, the absorbance peaks characteristic of neutral $Co^{II}OEP$ are all shifted to longer wavelength. This spectrum is not that expected for either the mono- or dication of this compound[31] and may in fact be that of a charge-transfer complex formed between $Co^{II}OEP$ and DDQ. On the basis of this spectrum, the actual ionic species created in this solvent/reagent system cannot be determined. Nonetheless, the ES mass spectrum in Figure 4b demonstrates that the net oxidizing strength of this solvent/reagent system is sufficient to form the dication of $Co^{II}OEP$.

Figure 4c is the ES mass spectrum obtained by injecting 40 pmol of $Co^{II}OEP$ into a flowing stream (15 μL/min) of methylene chloride/0.1% TFA/0.1% SbF_5 (v/v/v). The base peak in this spectrum is the dication. Three other ions of significant abundance appear in this spectrum, viz., the monocation at m/z 591 and two ions which correspond in mass to $(M + 17)^+$ (m/z 608) and $(M + 36)^+$ (m/z 627), respectively. The appearance of the monocation under these conditions might result from incomplete oxidation to the dication. The origin of the other two ions is not certain, but they may result from reaction of the dication with trace impurities (possibly water) in the solvent. When $Co^{II}OEP$ was dissolved in methylene chloride/0.1% TFA/0.1% SbF_5 (v/v/v) and continuously infused, the dication and monocation were observed in the ES mass spectrum, but a number of other unidentified ions, including peaks at m/z 608 and m/z 627, were observed as well. The number and intensity of these unidentified peaks increased with time following initial preparation of the sample, indicating that, on the time scale of the continuous infusion experiment (i.e., several minutes), the initially formed analyte ions are not stable with respect to further chemical reaction in this solvent system. In the flow injection experiment, formation of products of chemical followup reactions of the initially formed dications is minimized by rapidly transferring the ions from solution to the gas phase.

Curve d in Figure 5 is the UV/visible spectrum obtained for 50 pmol of $Co^{II}OEP$ injected into a stream of methylene chloride/0.1% TFA/0.1% SbF_5. This spectrum is very similar to that reported by Dolphin et al.[31] for M^{2+} of $Co^{II}OEP$ formed by electrolysis in methylene chloride. Thus, the ES-MS and UV/visible spectra show that $Co^{II}OEP$ is essentially completely oxidized to the dication in this solvent/reagent system.

C. $Ni^{II}OEP$. Compared to $Co^{II}OEP$, $Ni^{II}OEP$ is slightly more difficult to oxidize to the monocation, but much more difficult to oxidize to the dication (see Figure 1). As with β-carotene and $Co^{II}OEP$, the signal for $Ni^{II}OEP$ when sprayed out of methylene chloride is minimal. Figure 6a is the ES mass spectra obtained in a flow injection experiment in which 8.5 pmol of $Ni^{II}OEP$ was injected into a flowing stream (15 μL/min) of methylene chloride/0.1% TFA (v/v). The base peak in the spectrum at m/z 590 corresponds in mass to the radical cation, $M^{\bullet +}$. Of significant note here is a comparison of the UV/visible spectra of $Ni^{II}OEP$ in Figure 7 that were acquired under flow injection conditions using methylene chloride (curve a) and methylene chloride/0.1% TFA (v/v) (curve b) as the solvent/reagent systems. Curve a, which is the absorption spectrum obtained for 50 pmol of $Ni^{II}OEP$ injected into a stream of methylene chloride, is the UV/visible spectrum expected for the neutral molecule.[32] Curve b is the UV/visible spectrum obtained for 50 pmol of $Ni^{II}OEP$ injected into a stream of methylene chloride/0.1% TFA. This spectrum is only slightly different from that in curve a (i.e., a slight reduction in the absorption peak maximum is noted), indicating

(38) Beato, B. D.; Yost, R. A; Quirke, J. M. E. *Org. Mass Spectrom.* **1989**, *24*, 875–884.
(39) Van Berkel, G. J.; McLuckey, S. A.; Glish, G. L. *J. Am. Soc. Mass Spectrom.* **1992**, *3*, 235–242.

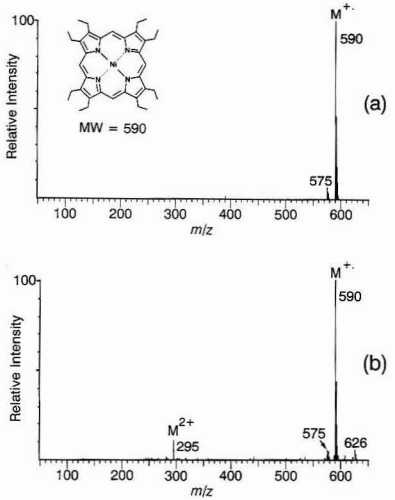

Figure 6. Background-subtracted, averaged ES mass spectrum obtained from the injection of 8.5 pmol (0.5 μL) of $Ni^{II}OEP$ (MW = 590, dissolved in methylene chloride) into a flowing stream (15 μL/min) composed of (a) methylene/0.1% TFA (v/v) and (b) methylene/0.1% TFA/0.1% SbF_5 (v/v/v).

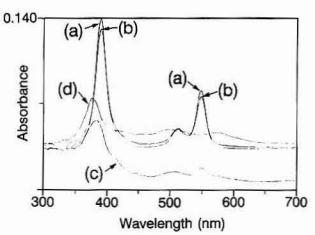

Figure 7. Photodiode array UV/visible absorption spectra obtained from the flow injection of 50 pmol (0.5 μL) of $Ni^{II}OEP$ (dissolved in methylene chloride) into a flowing stream (40 μL/min) composed of (a) methylene chloride, (b) methylene chloride/0.1% TFA (v/v), (c) methylene chloride/0.1% TFA/DDQ (v/v/200 μM) and (d) methylene chloride/0.1% TFA/0.1% SbF_5 (v/v/v).

that the bulk of $Ni^{II}OEP$ remains neutral in this solvent/reagent system.

Although the absolute signal in the ES mass spectrum owing to the radical cation of $Ni^{II}OEP$ increases by a factor of 2–3 (a relatively minor increase) when methylene chloride/0.1% TFA (v/v) is used as the solvent/reagent system, compared to methylene chloride alone, the UV/visible spectra discussed above indicate that this increase in signal may not be due to chemical electron-transfer ionization of the compound in solution. Formation of the radical cation of $Ni^{II}OEP$, rather than occurring by a direct chemical reaction in solution, might be attributed in this case to the electrochemical oxidation phenomenon inherent in the electrospray process.[6,13] The role of TFA in this process may be to "stabilize" or otherwise protect the electrochemically generated radical cations from reaction in solution. However, given the inherent stability of the radical cation of $Ni^{II}OEP$ in methylene chloride (see Figure 1), it may be that the TFA somehow acts to enhance the electrochemical oxidation process, as we have previously noted.[13] The ability of TFA to enhance the electrochemical oxidation phenomenon is not observable in the case of β-carotene or $Co^{II}OEP$ as these analytes are very efficiently oxidized chemically by this acid. In any case, these data indicate that the oxidizing potential of methylene chloride/0.1% TFA (v/v) is lower than that necessary to ionize $Ni^{II}OEP$.

The ES mass spectrum obtained by injecting 8.5 pmol of $Ni^{II}OEP$ into a stream comprised of methylene chloride/0.1% TFA/DDQ (v/v/200 μM) was identical to that shown in Figure 6a. However, the absolute signal intensity of the radical cation was increased by ~1 order of magnitude over the signal intensity observed in the spectrum in Figure 6a. Curve c in Figure 7 is the UV/visible spectrum obtained by injecting 50 pmol of $Ni^{II}OEP$ into a stream of methylene chloride/0.1% TFA/DDQ (v/v/200 μM). This UV/visible spectrum is very similar to the spectrum reported by Fuhrhop and Mauzerall[32] for $M^{\bullet+}$ of $Ni^{II}OEP$ formed by chemical oxidation with ferric perchlorate in chloroform/methanol (4:1 v/v). Therefore, the order of magnitude increase in the ES-MS signal owing to the radical cation when using this solvent/reagent system is used, over methylene chloride/0.1% TFA (v/v), is due to the fact that in this solvent/reagent system $Ni^{II}OEP$ is oxidized to the radical cation.

Figure 6b is the ES mass spectrum obtained by injecting 8.5 pmol of $Ni^{II}OEP$ into a flowing stream (15 μL/min) of methylene chloride/0.1% TFA/0.1% SbF_5 (v/v/v). The base peak in this spectrum is also the radical cation, but the dication at m/z 295 is observed at an intensity of ~10 percent of the base peak. As with $Co^{II}OEP$, confirmation of this ion as the dication was demonstrated through the use of interface fragmentation, which resulted in the formation of the expected doubly charged fragment ions.[37–39] Reference to the UV/visible spectrum obtained under similar flow injection conditions (Figure 7, curve d) indicates that the porphyrin is largely converted to the radical cation. The slight differences between the UV/visible spectra in curves c and d, both of which are thought to reflect the presence of the radical cation in solution, may be a result of the different solvent/reagent systems employed. However, the differences may be due in part to the presence of a small amount of the dication in the solution from which the spectrum in curve d was recorded.

Oxidation Potentials of the Various Solvent/Reagent Systems. The ability to oxidize the three model compounds to the mono- or dication in solution, as determined by the UV/visible and ES-MS data above, allows an effective oxidation potential range to be assigned to these different solvent/reagent systems. The oxidation potential necessary to form the mono- or dications of the model analytes in methylene chloride is equal to the potential at the foot of the respective CV oxidation wave in Figure 1 (i.e., β-carotene, M^{2+} = 0.6 V; $Co^{II}OEP$, M^{+} = 0.6 V, $M^{\bullet 2+}$ = 0.8 V; $Ni^{II}OEP$, $M^{\bullet+}$ = 0.7 V, M^{2+} = 1.3 V). Therefore, if a particular ionic species is formed by a chemical electron-transfer reaction in solution, the oxidation potential of the particular solvent/reagent system being used is effectively at least as much as the potential at the foot of the CV wave that corresponds to electrochemical formation of this ionic species. If a particular

ionic species cannot be formed using a particular solvent/reagent system, then the effective oxidation potential of the solvent system is less than the potential at the foot of the CV wave that corresponds to electrochemical formation of that ionic species. On the basis of these data and data from our previously published work[17] discussed below, the effective oxidation potential, E, of the solvent/reagent systems under study are determined to be

methylene chloride/0.1% TFA (v/v)

$$0.6\ \text{V} \leq E_{\text{TFA}} < 0.7\ \text{V}$$

methylene chloride/0.1% TFA/DDQ (v/v/200 μM)

$$0.8\ \text{V} \leq E_{\text{TFA/DDQ}} < 1.0\ \text{V}$$

methylene chloride/0.1% TFA/0.1% SbF_5 (v/v/v)

$$1.3 \leq E_{\text{TFA/SbF}_5} < 1.5$$

These effective oxidation potentials are designated by the bars on top of the potential scale in Figure 1.

As determined from the data in this work alone, the oxidation potential range for methylene chloride/0.1% TFA (v/v) is quite narrow ($\Delta E_{\text{TFA}} = 0.1$ V), but the oxidation potential range is fairly wide in the case of methylene chloride/0.1% TFA/DDQ (v/v/200 μM) ($0.8\ \text{V} < E_{\text{TFA/DDQ}} < 1.3$ V, $\Delta E_{\text{TFA/DDQ}} = 0.5$ V). However, our previous work on the oxidation of perylene in each of the three solvent systems[17] indicates that the upper potential limit for the methylene chloride/0.1% TFA/DDQ (v/v/200 μM) system may be ~1.0 V. The potential at the foot of the CV wave that corresponds to formation of the radical cation of perylene in methylene chloride is ~0.95 V. Our previous work showed that perylene could be oxidized to its radical cation in methylene chloride/0.1% TFA/DDQ (v/v/60 μM), but the oxidation was not complete. However, perylene was completely oxidized in methylene chloride/0.1% TFA/0.5% SbF_5.[17] Therefore, the upper limit for the oxidation potential of methylene chloride/0.1% TFA/DDQ (v/v/200 μM) is probably closer to 1.0 V rather than 1.3 V, as would be determined from the data presented in this paper alone.

The upper limit for the oxidation potential of the methylene chloride/0.1% TFA/0.1% SbF_5 (v/v/v) system cannot actually be determined from the data gathered in the present work. The low abundance of the Ni^{II}OEP dication formed in methylene chloride/0.1% TFA/0.1% SbF_5 (v/v/v) suggests that the upper limit is probably not much greater than the 1.3 V needed to form the dication of Ni^{II}OEP. However, when using methylene chloride/0.1% TFA/0.5% "magic acid" (v/v/v) (25% magic acid = 4:1, (v/v) fluorosulfonic acid:antimony pentafluoride) we were able to form the radical cation of C_{60}.[17] Since the potential at the foot of the oxidation wave for formation of the radical cation of C_{60} is 1.5 V,[40] methylene chloride/0.1% TFA/0.5% magic acid (v/v/v) must have a minimum oxidation potential of at least 1.5 V. The oxidation potential of the methylene chloride/0.1% TFA/0.1% SbF_5 (v/v/v) system is probably similar. Therefore, we have assigned the oxidation potential of this solvent system to range from a minimum of 1.3 V to a loosely set upper limit of 1.5 V.

(40) Dubois, D.; Kadish, K. M.; Flanagan, S.; Wilson, L. J. *J. Am. Chem. Soc.* **1991**, *113*, 7773–7774.

SUMMARY

In this work, CV, UV/visible, and ES-MS data were used in combination to determine the ionic species produced in solution by the reaction of three model compounds in three different solvent/electron-transfer reagent systems. On the basis of these data, an effective oxidation potential range could be assigned to each of the three solvent/reagent systems. Other solvent/electron-transfer reagent systems that one might use to ionize analytes in solution for detection by ES-MS could be "calibrated" in a similar fashion. Knowledge of the oxidation potential of the solvent/reagent system can significantly enhance the analytical utility of this methodology for analyte ionization/detection in ES-MS. With the solvent/reagent oxidation potentials, and the electrochemical redox potentials of a particular analyte of interest, a solvent/reagent system can be chosen to selectively oxidize in solution an analyte, or range of analytes, to a desired ionic state for subsequent detection in the gas phase using ES-MS. This is in contrast to the "hit" or "miss" methodology of solution-phase ionization that must be employed when the oxidation potential of the solvent/reagent system is unknown or poorly defined.[15–17] The ability to detect in the gas phase the ionic species produced in solution will, of course, depend on the stability (i.e., lifetime) of the ion in the given solvent/reagent system and on whether the ion can survive intact the transfer to the gas phase via the ES process. Using the flow injection technique described here, the ionic species that can be ionized in solution and detected in the gas phase spans the range from very solution-stable ionic species, like the porphyrin ions, to species, like the dication of β-carotene, which have a solution lifetime of only a few seconds.[18,36]

ACKNOWLEDGMENT

This research was sponsored by the United States Department of Energy, Office of Basic Energy Sciences under Contract DE-AC05-84OR21400 with Martin Marietta Energy Systems, Inc. The authors thank Dr. Michael E. Sigman (ORNL) for a loan of the electrochemical equipment, Prof. J. Martin E. Quirke (Florida International University) for providing the cobalt(II) octaethylporphyrin, and Dr. Scott A. McLuckey (ORNL) for critical review of the manuscript. F.Z. acknowledges an appointment to the United States Department of Energy, Laboratory Cooperative Postgraduate Research Training Program, administered jointly by the Oak Ridge Institute for Science and Education (ORISE) and ORNL.

Received for review March 11, 1994. Accepted June 16, 1994.*

* Abstract published in *Advance ACS Abstracts*, August 1, 1994.

Anal. Chem. **1994,** *66,* 3416–3422

Accumulation and Storage of Ionized Duplex DNA Molecules in a Quadrupole Ion Trap

Mitchel J. Doktycz,† Sohrab Habibi-Goudarzi,‡ and Scott A. McLuckey*,‡

Biology Division and Chemical and Analytical Sciences Division, Oak Ridge National Laboratory, Oak Ridge, Tennessee 37831–6365

Evidence for the accumulation and storage of ionized duplex DNA molecules in a quadrupole ion trap is presented. Aqueous solutions of complementary single-strand molecules of DNA were annealed to form duplexes in solution and subjected to electrospray ionization. The ions liberated in this process were transported through an atmosphere/vacuum interface and injected into a quadrupole ion trap operated with a bath gas present at a pressure of 1 mTorr. Despite the roughly 2 order of magnitude poorer signal levels noted for electrospray of aqueous solutions relative to those observed for single-strand oligonucleotides in methanol solutions, aqueous solutions were used to avoid denaturing the duplexes. Ion trap mass spectra are reported here for duplexes consisting of two complementary 20-mer single strands and two complementary 10-mers. Tandem mass spectrometry results are also reported for the 10-mer duplex. These results are significant in that they indicate that the ions are kinetically stable under the ion injection, storage, and mass analysis conditions of the quadrupole ion trap operated with a relatively high pressure of bath gas. The tools of ion trap mass spectrometry can therefore be applied to this important class of compounds.

Electrospray ionization has enjoyed remarkable success in forming gaseous ions from biopolymers in solution.[1–5] Indeed, much of its popularity derives from its utility in biomedical research as an interface for high-performance separations and mass spectrometry.[6] A particularly interesting, and so far unique, feature of electrospray is its ability to form gaseous ions of noncovalently bound species of biological relevance that are known to exist as specific complexes under physiological conditions.[7–23] Although it is difficult to prove conclusively that a gaseous ionized complex observed in a mass spectrometer originated as a specific complex in the condensed phase, strong and rapidly growing evidence suggests that this is so. Examples of such complexes include peptide–protein complexes,[7,8,11] protein tetramers,[23] DNA duplexes[14,15] and quadruplexes,[13] and protein–prosthetic group complexes.[9,18,19,21] The ability to form such species as gaseous ions provides important new opportunities for mass spectrometry to make contributions to biochemical and biological research.

We are specifically interested in the role quadrupole ion trap mass spectrometry might play in the analysis of ions derived from specific complexes formed in the condensed phase. The ion trap has already been demonstrated as a mass analyzer for covalently bound biomolecule ions derived from cesium ion bombardment,[24] matrix-assisted laser desorption,[25–29] and electrospray.[30–33] A number of useful experiments have been demonstrated with these ions including high-mass resolution,[31,34,35] multiple stages of mass spectrometry,[36] and ion/molecule reactions.[37–39] In addition to its merits as an analytical mass spectrometer, the relatively small size and

† Biology Division.
‡ Chemical and Analytical Sciences Division.

(1) Fenn, J. B.; Mann, M.; Meng, C. K.; Wong, S. F.; Whitehouse, C. M. *Science* **1989**, *246*, 64.
(2) Fenn, J. B.; Mann, M.; Meng, M. K.; Wong, S. F.; Whitehouse, C. M. *Mass Spectrom. Rev.* **1990**, *9*, 37.
(3) Smith, R. D.; Loo, J. A.; Edmonds, C. G.; Barinaga, C. J.; Udseth, H. R. *Anal. Chem.* **1990**, *62*, 882.
(4) Smith, R. D.; Loo, J. A.; Ogorzalek Loo, R. R.; Busman, M.; Udseth, H. R. *Mass Spectrom. Rev.* **1991**, *10*, 359.
(5) Smith, R. D.; Loo, J. A.; Ogorzalek Loo, R. R.; Busman, M.; Udseth, H. R. *Mass Spectrom. Rev.* **1992**, *11*, 434.
(6) Huang, E. C.; Wachs, T.; Conboy, J. J.; Henion, J. D. *Anal. Chem.* **1990**, *62*, 713A.
(7) Ganem, B.; Li, Y. T.; Henion, J. D. *J. Am. Chem. Soc.* **1991**, *113*, 6294.
(8) Ganem, B.; Li, Y. T.; Henion, J. D. *J. Am. Chem. Soc.* **1991**, *113*, 7818.
(9) Katta, V.; Chait, B. T. *J. Am. Chem. Soc.* **1991**, *113*, 8534.
(10) Ganguly, A. T.; Pramanik, B. N.; Tsarbopoulos, Covey, T. R.; Huang, E.; Fuhrman, S. A. *J. Am. Chem. Soc.* **1992**, *114*, 6559.
(11) Baca, M.; Kent, S. B. H. *J. Am. Chem. Soc.* **1992**, *114*, 3992.
(12) Smith, R. D.; Light-Wahl, K. J.; Winger, B. E.; Loo, J. A. *Org. Mass Spectrom.* **1992**, *27*, 811.
(13) Goodlett, D. R.; Camp, D. G., II; Hardin, C. C.; Corregan, M.; Smith, R. D. *Biol. Mass Spectrom.* **1993**, *22*, 181.
(14) Light-Wahl, K. J.; Springer, D. L.; Winger, B. E.; Edmonds, C. G.; Camp, D. G., II; Thrall, B. D.; Smith, R. D. *J. Am. Chem. Soc.* **1993**, *115*, 803.
(15) Ganem, B.; Li, Y. T.; Henion, J. D. *Tetrahedron Lett.* **1993**, *34*, 1445.
(16) Jaquinod, M.; Leize, E.; Potier, N.; Albrecht, A.; Shanzer, A.; Van Dorsselaer, A. *Tetrahedron Lett.* **1993**, *34*, 2771.
(17) Huang, E. C.; Pramanik, B. N.; Tsarbopoulos, A.; Reichert, P.; Ganguly, A. K.; Trotta, P. P.; Nagabushan, T. L.; Covey, T. R. *J. Am. Soc. Mass Spectrom.* **1993**, *4*, 624.
(18) Li, Y. T.; Hsieh, Y. L.; Henion, J. D.; Ganem, B. *J. Am. Soc. Mass Spectrom.* **1993**, *4*, 631.
(19) Feng, R.; Konishi, Y. *J. Am. Soc. Mass Spectrom.* **1993**, *4*, 638.
(20) Smith, R. D.; Light-Wahl, K. J. *Biol. Mass Spectrom.* **1993**, *22*, 493.
(21) Loo, J. A.; Giordani, A. B.; Muenster, H. *Rapid Commun. Mass Spectrom.* **1993**, *7*, 186.
(22) Li, T.-Y.; Hsieh, T. L.; Henion, J. D.; Senko, M. W.; McLafferty, F. W.; Ganem, B. *J. Am. Chem. Soc.* **1993**, *115*, 8409.
(23) Light-Wahl, K. J.; Winger, B. E.; Smith, R. D. *J. Am. Chem. Soc.* **1993**, *115*, 5869.
(24) Kaiser, R. E., Jr.; Louris, J. N.; Amy, J. W.; Cooks, R. G. *Rapid Commun. Mass Spectrom.* **1989**, *3*, 225.
(25) Cox. K. A.; Williams, J. D.; Cooks, R. G.; Kaiser, R. E., Jr. *Biol. Mass Spectrom.* **1992**, *21*, 226.
(26) Chambers, D. M.; Goeringer, D. E.; McLuckey, S. A.; Glish, G. L. *Anal. Chem.* **1993**, *65*, 14.
(27) Doroshenko, V. M.; Cornish, T. J.; Cotter, R. J. *Rapid Commun. Mass Spectrom.* **1992**, *6*, 753.
(28) Jonscher, K.; Currie, G.; McCormack, A. L.; Yates, J. R., III *Rapid Commun. Mass Spectrom.* **1993**, *7*, 20.
(29) Schwartz, J. C.; Bier, M. E. *Rapid Commun. Mass Spectrom.* **1993**, *7*, 27.
(30) Van Berkel, G. J.; Glish, G. L.; McLuckey, S. A. *Anal. Chem.* **1990**, *62*, 1284.
(31) Schwartz, J. C.; Syka, J. E. P.; Jardine, I.; *J. Am. Soc. Mass Spectrom.* **1991**, *2*, 198.
(32) Lin. H.-Y.; Voyksner, R. D. *Anal. Chem.* **1993**, *65*, 451.
(33) Mordehai, A.; Henion, J. D. *Rapid Commun. Mass Spectrom.* **1993**, *7*, 205.
(34) Williams, J. D.; Cox, K. A.; Cooks, R. G.; Kaiser, R. E., Jr.; Schwartz, J. C. *Rapid Commun. Mass Spectrom.* **1992**, *5*, 327.
(35) Schwartz, J. C.; Jardine, I. *Rapid Commun. Mass Spectrom.* **1992**, *6*, 313.
(36) Cooks, R. G.; Kaiser, R. E., Jr. *Acc. Chem. Res.* **1990**, *23*, 213.
(37) McLuckey, S. A.; Van Berkel, G. J.; Glish, G. L. *J. Am. Chem. Soc.* **1990**, *112*, 5668.

0003-2700/94/0366-3416$04.50/0
© 1994 American Chemical Society

low cost of the ion trap are attractive features which can make it more widely accessible to researchers than more expensive forms of mass spectrometry. For these reasons, it is of interest to explore the possibility for injecting and storing noncovalently associated biomolecule ions in a quadrupole ion trap for the purpose of mass analysis and for determining what other types of information might be obtainable.

The quadrupole ion trap operated with a light bath gas, such as helium, is unique among mass analyzers in that the ions can undergo many collisions in the processes of ion injection, storage, and mass analysis. Collisions between the DNA ions and helium at greater than thermal energies, which occur upon ion injection into the ion trap and ion ejection out of the ion trap, can heat the ions. During storage, the ions tend to assume an internal energy distribution determined by the temperature of the bath gas. A major issue in the quadrupole ion trap mass spectrometry of noncovalently bound ions is the likelihood of survival of these species over the course of a typical ion trap experiment. We have recently reported the injection, storage, and mass analysis of myoglobin ions, which contain a noncovalently bound heme group, in a quadrupole ion trap.[40] We have also focused our attention on duplex DNA molecules as an extension of our ion trap studies of nucleic acid constituents.[41-44] Studies to date have emphasized the electrospray, interface, and ion-trapping conditions required to observe these species. We demonstrate here that relatively small duplex DNA molecules can survive the ion trap experiment and describe the required conditions.

EXPERIMENTAL SECTION

Samples and Electrospray Conditions. The DNA samples used in this study were synthesized on a PCR Mate DNA synthesizer (Applied Biosystems, Fountain City, CA) on either a 0.2- or 1-μmol scale by use of standard phosphoramidite chemistries. After deprotection the samples were taken up in 200–500 μL of water, filtered through a 0.45-μm filter, and ethanol precipitated two times with 3.5 M ammonium acetate. The samples were then taken up in 200–500 μL of water, and an aliquot was quantitated by absorbance. Denaturing polyacrylamide gel electrophoresis was performed on all samples to check purity.

The 20-base-long samples were further purified from failure products from the synthesis by preparative denaturing gel electrophoresis. This was accomplished by electrophoresis on a 15% gel with 8 M urea after which the product was identified by UV shadowing and subsequently electroeluted from the gel slice.[45] This material was bound to a column of DEAE Sephadex A-25 (Pharmacia Biotech, Piscataway, NJ), washed with at least 10 column volumes of 50 mM ammonium formate, and eluted with 2 M ammonium formate. These DNA samples were then precipitated twice with ethanol in the presence of ammonium acetate and quantitated as before. Samples were prepared for electrospray by diluting the concentrated stock with either water or methanol to the appropriate concentration.

Methanol solutions were infused at a rate of 1 μL/min through a 120-μm-i.d. stainless steel needle held at a potential of –3.5 to –4.0 kV. Aqueous solutions were infused at a rate of 3–5 μL/min through a concentric two-needle arrangement. Nitrogen was passed through the larger diameter needle to assist in nebulizing the sample solution as it exited the central needle.

Ion Trap Mass Spectrometry. Two essentially identical ion trap mass spectrometers (Finnigan, San Jose, CA) modified for electrospray[30,39] were used to acquire the data described here. Slightly different pressures, however, were present in the interface region (0.45 vs 0.5 Torr). Electrospray mass spectra were acquired by use of an ion accumulation time of 0.5–0.7 s and a radio frequency trapping voltage amplitude of 1038–1500 V 0–p (low m/z cutoff of m/z 90–130). After ion accumulation, a rapid scan (10–20 ms) of the radio frequency trapping voltage from 577 to 3462 V 0–p in conjunction with a 800–1200 mV p–p resonance excitation signal applied across the end caps was performed to accelerate desolvation of wet ions in the ion trap.[46] Mass analysis was effected using resonance ejection[24] (3000 mV p–p applied across the end caps) extending the nominal upper mass/charge limit of the ion trap from m/z 650 to as high as m/z 3900. A correction for the mass/charge scale of the data system was derived using the ions, derived from electrospray, of the synthetic 15-mer 5′-d(TCG ATC GAT GCA TGC)-3′. The mass accuracy using this correction is ~0.1%. No attempt was made in these studies to improve either the mass resolution via reduced scan speed[31,34] or the mass accuracy via the use of internal standards.[47]

The mass spectrometry/mass spectrometry (MS/MS) data reported for the 10-mer duplex were acquired using a special version of the Finnigan scan editor program referred to as MASSEXT. This program allows for resonance excitation of ions of higher mass/charge values than can be accessed with the normal scan editor software. In addition to the ion accumulation and ion desolvation periods, the MS/MS experiment involved isolation of a mass/charge range containing the parent ions of interest by means of two resonance ejection periods[48] and a resonance excitation period of 100 ms employing a resonance excitation amplitude of 600 mV p–p between end caps.

Figure 1 shows a side-view schematic diagram of the electrospray/ion trap combination used in this work. The electrical elements that most influence the electrospray mass spectra are those labeled A1, AL1, and AL2. The electrospray mass spectra of DNA duplexes are particularly sensitive to the voltage levels of these electrical elements in the interface. Another important parameter is the pressure in the interface region defined by the aperture plates labeled A1 and A2. We

(38) McLuckey, S. A.; Glish, G. L.; Van Berkel, G. J. *Anal. Chem.* **1991**, *63*, 1971.
(39) McLuckey, S. A.; Van Berkel, G. J.; Glish, G. L.; Schwartz, J. C. In *Modern Mass Spectrometry: Practical Aspects of Ion Trap Mass Spectrometry*; March, R. E., Ed.; CRC Press: Boca Raton, FL, 1994; Vol. 1, Chapter 11.
(40) Ramsey, R. S.; McLuckey, S. A. *J. Am. Soc. Mass Spectrom.* **1994**, *5*, 324.
(41) McLuckey, S. A.; Van Berkel, G. J.; Glish, G. L. *J. Am. Soc. Mass Spectrom.* **1992**, *3*, 60.
(42) Ramsey, R. S.; Van Berkel. G. J.; McLuckey, S. A.; Glish, G. L. *Biol. Mass Spectrom.* **1992**, *21*, 347.
(43) McLuckey, S. A.; Habibi-Goudarzi, S. *J. Am. Chem. Soc.* **1993**, *115*, 12085.
(44) McLuckey, S. A.; Habibi-Goudarzi, S. *J. Am. Soc. Mass Spectrom.*, in press.
(45) Sambrook, J.; Fritsch, E. F.; Maniatis, T. *Molecular Cloning: A Laboratory Manual*, 2nd ed.; Cold Spring Harbor Press: Cold Spring Harbor, NY, 1989.
(46) McLuckey, S. A.; Van Berkel, G. J.; Glish, G. L.; Huang, E. C.; Henion, J. D. *Anal. Chem.* **1991**, *63*, 375.
(47) Cooks, R. G.; Julian, R. K., Jr.; Cleven, C. D.; Lammert, S. A.; Soni, M. *Proceedings of the 41st ASMS Conference on Mass Spectrometry and Allied Topics*; San Francisco, CA, 1993; p 789.
(48) McLuckey, S. A.; Goeringer, D. E.; Glish, G. L. *Anal. Chem.* **1992**, *64*, 1455.

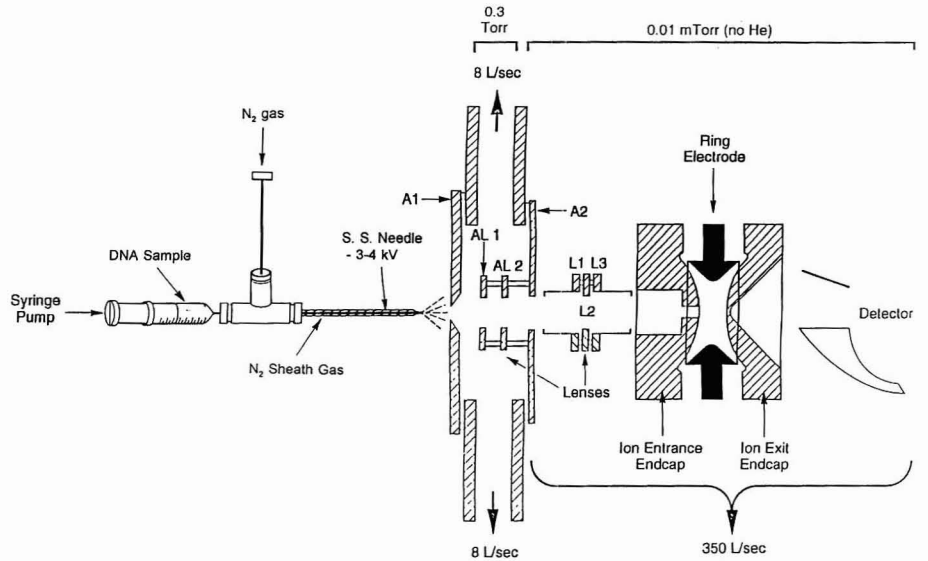

Figure 1. Side-view schematic diagram of the electrospray/ion trap combination emphasizing the electrical elements of the system that influence ion transport through the atmosphere/vacuum interface. A1 is a plate containing an aperture that separates atmosphere from the interface region held at ~0.5 Torr. A2 is a plate containing an aperture that separates the 0.5-Torr region from the vacuum system of the ion trap. AL1 and AL2 are lens elements in the interface.

found that the A1, AL1, and AL2 lens settings on a given system were quite reproducible over periods of months. However, we did not find that the voltage settings applied to one of the systems could be used to provide comparable data on the other system. We speculate that this may be due to the slightly different pressures in the interface regions (0.45 vs 0.5 Torr). The interface regions differ in pressure due to different pumping speeds applied to the respective interfaces. However, different A1 aperture plates, although nominally identical, were also used. Slight differences in aperture size could, for example, affect the gas dynamics in the interface. In any case, it is apparent that some subtle difference in the interface can significantly affect optimal interface lens potentials. Comparisons of results illustrating the effects of interface conditions on electrospray mass spectra are therefore restricted to data acquired with the same instrument, thereby avoiding ambiguities arising from different pressures and, perhaps, different aperture geometries.

RESULTS AND DISCUSSION

The goal of this work was to find electrospray, interface, and ion trap conditions necessary for the observation of duplex DNA ions. For this reason, essentially all data were acquired using water solutions to avoid precipitating or denaturing the duplex molecules in organic solvent that could cause dissociation of the two DNA strands. Signal levels acquired with aqueous solutions tend to be roughly 2 orders of magnitude lower than those acquired with methanol as the solvent. An example is given in Figure 2 which compares electrospray mass spectra of a 20 μM solution of 30-mer 5′-d(TCA AGG ACA GGA AAG ACA TTC TGG CCT GGC)-3′ in 9:1 methanol/water (Figure 2a) and 100% water (Figure 2b). All interface and ion trap conditions were held constant, and an equal number of scans were averaged. Optimal electrospray

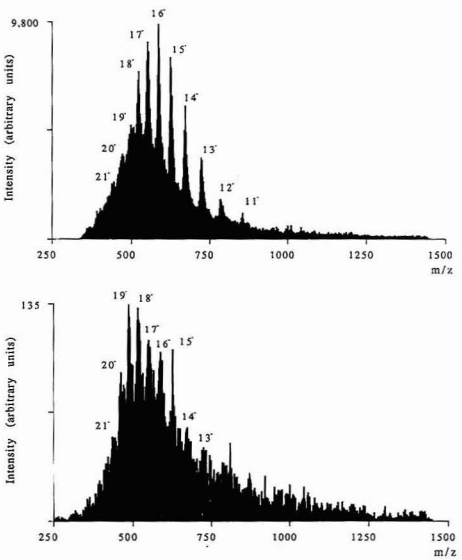

Figure 2. Electrospray mass spectra of 20 μM solutions of the 30-mer 5′-d(TCA AGG ACA GGA AAG ACA TTC TGG CCT GGC)-3′ in 9:1 methanol/water (a, top) and in water (b, bottom).

conditions were used for each solvent composition. In the case of the 90% methanol solution, a flow rate of 1 μL/min was used and no pneumatic nebulization was employed. In the case of the aqueous solution, a flow rate of 3 μL/min and pneumatic nebulization with N_2 were used. The spectra represent an average of 300 individual experiments each of which consumed roughly 0.7 s, thereby yielding a total data accumulation period of 3.5 min. Seventy picomoles of 30-mer was therefore consumed for Figure 2a whereas 210 pmol was consumed for Figure 2b due to the differences in flow rates used for the different solvent compositions. Despite the greater analyte consumption associated with the aqueous solution, the signal level measured with this solution must be multiplied by a factor of 73 to make it compare directly with the signal level obtained with the methanol solution. This comparison suggests that spectral quality similar to that of Figure 2b can be expected with largely methanol solutions with analyte consumption in the low picomole to high femtomole range. However, no duplex DNA ions have yet been observed from any solvent composition not comprised of a large water component. The mass spectra shown here, derived from electrospray of water solutions, typically required the consumption of hundreds of picomoles of analyte. While this does not reflect the quantities of oligonucleotides necessary in general to obtain electrospray data, the solvent system constraints associated with preserving duplex DNA, as they are currently understood, place greater limitations on the achievable sensitivity with duplex DNA than on single-strand DNA.

The peaks in the spectra of Figure 2, as well as those in the other spectra shown in this paper, are tens of m/z units wide. Due to the fact that the ions are multiply charged, the peaks can be hundreds of mass units wide. Ions of a range of masses contribute to the peak at each charge state. In the case of oligonucleotides, it is well-known that common cations, such as sodium ions and potassium ions, can replace protons as the counterions associated with the phosphodiester groups.[3] Therefore, at each charge state, except that which results from the removal of all cations from the phosphodiester linkages, a mixture of anions can contribute to the signal when a mixture of cations is present in solution. We took no special measures, other than precipitation, to desalt these solutions, and therefore, there are substantial numbers of cations other than protons attached to the oligonucleotides in these studies. Furthermore, the number of these cations tends to increase with decreasing charge state due to the greater number of total cations present. The mass/charge resolution of the ion trap is sufficient to resolve the peaks with different numbers of sodium adducts, the major source of peak multiplicity within a given charge state, under these experimental conditions. However, due to limitations in the software used to average and display the data,[30,44] discrete peaks for each adduct are not apparent. The peaks here simply show the envelope of ions contributing to a charge state. A count of the number of sodium ions associated with the oligonucleotide can be useful in distinguishing a single-strand ion from a double-strand ion. For example, a doubly charged 10-mer can hold a maximum of 7 sodium ions whereas a quadruply charged 10-mer double strand can contain a maximum of 14 sodium ions. Nevertheless, as shown below, the mass/charge resolution displayed in these spectra is sufficient to make a strong case for the observation of duplex DNA ions without recourse to a discrete count of number and type of counterions.

Just as solvent composition is expected to be critical for the observation of noncovalently bound biomolecular ions, interface conditions have also been shown to affect the likelihood of survival of the complex.[7-23] Our experience has proved to be no exception, although the home-built electrospray arrangements used in our laboratory are somewhat different from most of the more commonly used electrospray ion sources.[1-6] For example, no attempt is made at drying the ions before the interface. That is, no dry gas is used outside of the vacuum system to assist in desolvation and no heated capillary is used to transport ions into the interface region. Furthermore, the commonly employed nozzle/skimmer arrangement is not used in our interface. Rather, two aperture plates are used with two lenses mounted between them (see Figure 1). However, fragmentation in the interface can occur under some interface conditions[49] as seen earlier with the nozzle/skimmer fragmentation induced by creating a voltage gradient between the nozzle and skimmer. The efficiency of ion transmission through the interface is expected to depend upon a variety of factors including, for example, the lens voltages, pressure, ion mass, ion charge, and collision cross section. Optimal conditions for efficient transmission of some ions are inappropriate for transmission of others. In the case of high-mass, multiply charged biopolymers, we have observed that the charge-state distribution observed in the electrospray mass spectrum can be affected somewhat by the interface conditions. That is, conditions can be established to favor either high-charge states (low mass/charge) or low-charge states (high mass/charge). This observation was also noted for the oligonucleotides used in this study, as illustrated in Figure 3, which compares electrospray mass spectra, acquired at two interface lens voltage settings, of a 20 μM solution of the 30-mer in water. Figure 3a shows conditions that optimize the transmission of higher charge states (i.e., A1 = –129 V, AL1 = –78 V, AL2 = –117 V) whereas Figure 3b shows conditions that tend to favor transmission of lower charge states (i.e., A1 = –208 V, AL1 = –213 V, AL2 = –55 V). Given the general tendency for noncovalently bound ionic complexes to appear at high mass/charge values relative to ions formed from uncomplexed biopolymers and the specific examples illustrating this generalization already described for duplex DNA anions,[14,15] the conditions used to acquire the data of Figure 3b are expected to be more appropriate for transmission of duplex DNA anions than those used for the spectrum of Figure 3a.

A 20-mer duplex was formed in solution by mixing two 10 μM solutions of the complementary 20-mers 5′-d(GAC AGG AAA GAC ATT CTG GC)-3′ and 5′-d(GCC AGA ATG TCT TTC CTG TC)-3′ in 10 mM ammonium acetate. The solution was heated to ~90 °C and allowed to cool slowly to room temperature prior to electrospray. Duplex formation under these conditions was confirmed by electrophoresis experiments. The electrospray mass spectrum of this solution, acquired using lens conditions similar to those used to acquire the spectrum of Figure 3b, is shown in Figure 4a. For comparison, the electrospray mass spectrum of the single-

(49) Van Berkel, G. J.; McLuckey, S. A.; Glish, G. L. *Anal. Chem.* **1991**, *63*, 1098.

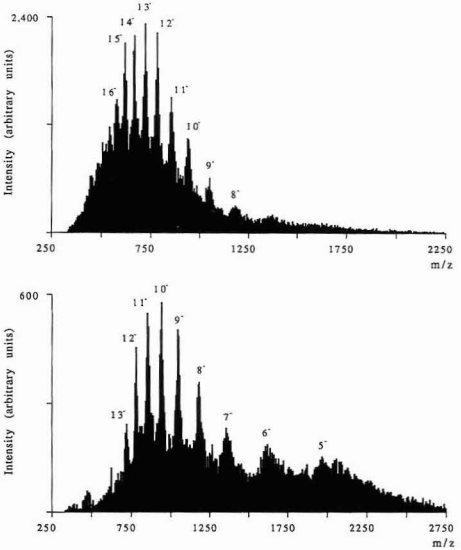

Figure 3. Electrospray mass spectra of 20 μM aqueous solutions of the 30-mers of Figure 2 acquired with the interface lens elements held at A1 = −129 V, AL1 = −78 V; AL2 = −117 V; A2 = 0 V (a, top) and with the interface lens elements held at A1 = −208 V; AL1 = −213 V; AL2 = −55 V; A2 = 0 V (b, bottom).

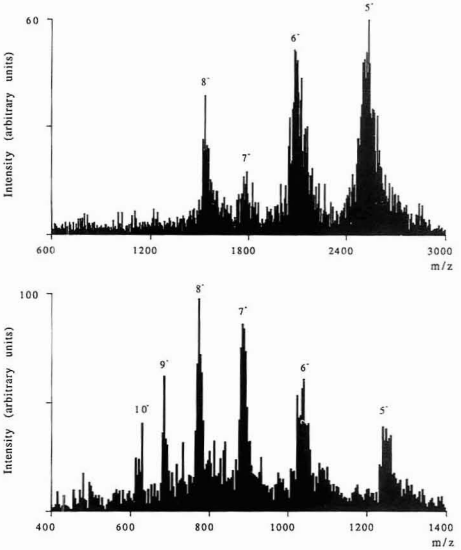

Figure 4. Electrospray mass spectrum of a ~10 μM aqueous solution of the 20-mer duplex consisting of the strands 5′-d(GAC AGG AAA GAC ATT CTG GC)-3′ and 5′-d(GCC AGA ATG TCT TTC CTG TC)-3′ (a, top) and the electrospray mass spectrum acquired for a 10 μM aqueous solution of the single-strand oligonucleotide 5′-d(GAC AGG AAA GAC ATT CTG GC)-3′ (b, bottom).

strand 20-mer 5′-d(GAC AGG AAA GAC ATT CTG GC)-3′ acquired using interface conditions similar to those used to acquire the spectrum of Figure 3a is shown in Figure 4b. The major peaks in the spectrum of Figure 4a are consistent with the 8⁻, 7⁻, 6⁻, and 5⁻ charge states of a 20-mer duplex.

A number of observations can be made upon examination of this spectrum. Perhaps the most convincing evidence that duplex ions give rise to at least some of the signal in the spectrum of Figure 4a comes from the peaks labeled as the 7⁻ and 5⁻ charge states. The 4⁻ and 3⁻ charge states of the single-strand 20-mers can at least nominally give rise to the peaks labeled as 8⁻ and 6⁻ for the duplex. However, the single-strand species cannot give rise to the odd-numbered charge states of the duplex because it would require a nonintegral number of charges to do so. A second observation is the unusual relative abundances of the peaks. Most ES mass spectra do not show irregular peak intensities as seen in Figure 4a in which the 7⁻ charge state is less abundant than both the 6⁻ and 8⁻ charge states. Most ES mass spectra appear like those of Figures 2, 3, and 4b in which the charge-state intensities fit a more or less smooth envelope. The origin of the irregular peak intensities cannot be determined from the data acquired for this system. However, it is probably noteworthy that irregular peak intensities were also observed in the original report of gaseous duplex DNA anions.[14]

Further evidence for the successful injection and storage of ionized duplex DNA molecules can be obtained from a tandem mass spectrometry experiment. The 5⁻ charge state of the 20-mer duplex discussed above would provide good candidate parent ions for confirmation of duplex ions by tandem mass spectrometry. However, high mass/charge multiply charged parent ions present practical difficulties with our ion trap instruments. We therefore chose to attempt to form a smaller duplex that might yield candidate parent ions of lower mass/charge values. A 10-mer duplex was formed by mixing 30 μM solutions of the complementary 10-mers 5′-d(ACA TTC TGG C)-3′ and 5′-d(GCC AGA ATG T)-3′ in 10 mM ammonium acetate and heating and cooling the solution as was done with the 20-mers. Figure 5a shows the electrospray mass spectrum acquired with this solution using interface conditions conducive to transmission of high mass/charge ions. Figure 5b shows the ES mass spectrum of one of the 10-mer single strands (5′-d(ACA TTC TGG C)-3′) for comparison. Figure 5a shows some signals at lower mass/charge that can clearly be attributed to ions derived from the single-strand molecules. These ions are indicated as the 5⁻ and 4⁻ charge states of single-strand (ss) species. The higher mass/charge peaks are labeled as 6⁻, 5⁻, and 4⁻ charge states of the duplex (ds). As noted above, the duplex ions with an odd number of charges cannot overlap in mass/charge with any ions derived from the single strands. In this case, the peak associated with the 5⁻ charge state is expected to be comprised solely of duplex ions, albeit with a mixture of counterions.

An ion trap tandem mass spectrometry experiment was performed on some of the ions making up the peak of the ds 5⁻ charge state, and the results are summarized in Figure 6. Low mass/charge and high mass/charge ions were ejected from the ion trap, leaving ions within a mass/charge range of roughly 1100–1300 in the ion trap. Such a wide range of

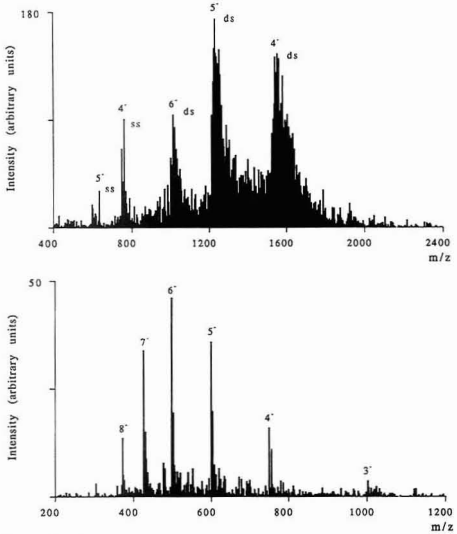

Figure 5. Electrospray mass spectrum of a 30 μM aqueous solution of the 10-mer duplex consisting of the strands 5′-d(ACA TTC TGG C)-3′ and 5′-d(GCC AGA ATG T)-3′ (a, top) and the electrospray mass spectrum acquired for a 30 μM aqueous solution of the single-strand oligonucleotide 5′-d(ACA TTC TGG C)-3′ (b, bottom).

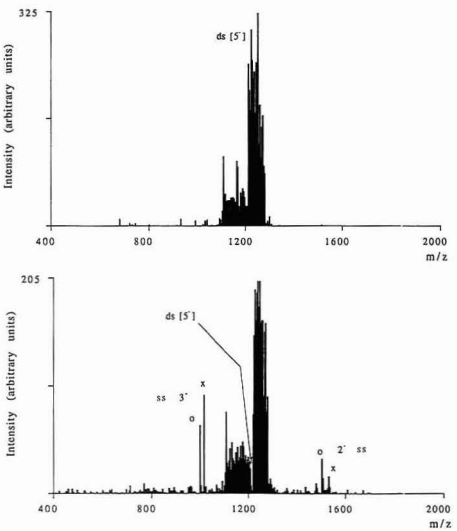

Figure 6. Electrospray mass spectrum of the duplex 10-mer (ds) after isolation of a range of mass/charge values encompassing the 5⁻ charge state prior to resonance excitation (a, top) and the MS/MS spectrum acquired after resonance excitation/ion activation (b, bottom). Ions derived from 5′-d(GCC AGA ATG T)-3′ are labeled o and ions derived from 5′-d(ACA TTC TGG C)-3′ are labeled x.

potential parent ions was isolated intentionally to avoid collisionally heating the ions of interest during the ion isolation period. Figure 6a shows the spectrum acquired after the ion

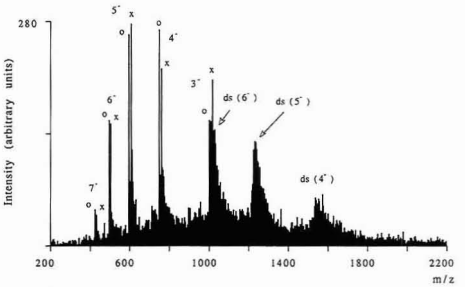

Figure 7. Electrospray mass spectrum of the duplex 10-mer acquired under a different set of interface conditions showing ions derived from single-strand molecules (o, x) as well as from the duplex (ds).

isolation procedure but prior to the collisional activation period. It is noteworthy that no fragmentation is noted in the absence of resonance excitation. This result shows that the isolated ions are kinetically stable in the presence of a bath gas under ion trap storage conditions for at least 100 ms (i.e., the length of time the ions remain trapped following parent ion isolation and prior to mass analysis). Figure 6b shows the spectrum acquired after resonance excitation of ions in the region of mass/charge 1220. Note that the width of the mass/charge range of ions subjected to ion activation is much narrower than that of the isolated ions as reflected in the relatively narrow range of ions removed by ion activation (see the arrow in Figure 6b). For this reason, the product ion peaks are much narrower than the signal associated with the isolated ions. The major products in this spectrum are two sets of complementary ions corresponding to the single strands. One set corresponds to the triply charged 10-mer of Figure 5b and its complement the doubly charged ion of the complementary 10-mer. The other set of ions correspond to the opposite situation in which the 10-mer of Figure 5b carries two charges and its complement carries three. The mass/charge range of this particular experiment precluded the observation of singly charged single strands, but the fact that the complementary quadruply charged strands are absent from the spectrum indicates that they were not formed in significant numbers. This experiment clearly indicates that the peak assigned as the 5⁻ charge state is comprised of the expected duplex.

All of the experiments just described for the 10-mer duplex were carried out on the same instrument. Electrospray mass spectra of the 10-mer duplex, acquired using the other electrospray/ion trap instrument, is shown in Figure 7. It is included here because it illustrates well several noteworthy points about observing and identifying duplex DNA ions. This spectrum was recorded using interface potentials of A1 = −100 V, AL1 = −100 V, and AL2 = −100 V. Note that either the transmission of higher mass/charge ions or greater dissociation of the duplex (or both) is enhanced under this set of conditions relative to those used to acquire the spectrum of Figure 5a. Ions derived from the single strands of both 10-mers are clearly apparent and are labeled as either o for 5′-d(GCC AGA ATG T)-3′ ions or x for 5′-d(ACA TTC TGG C)-3′ ions. The ions associated with the duplex are labeled ds. This spectrum therefore provides mass/charge information on the duplex as well as the component single

strands. Once again, the ions labeled as ds(6^-) might be attributed to the 3^- ions of the single strands. However, the significant high-mass tail associated with this peak compared with those of the lower mass/charge peaks would suggest that at least some of this signal is due to duplex DNA ions. It is also perhaps noteworthy that no identifiable signal attributable to the 7^- charge state of the duplex is apparent in either the spectrum of Figure 7 or the spectrum of Figure 5a. (Note that the 7^- ions of Figure 7 correspond to single-strand species.)

CONCLUSIONS

The results described here give strong evidence that duplex DNA molecules formed in solution can be observed as gaseous ions in the quadrupole ion trap operated in the presence of a bath gas at 1 mTorr. It has already been observed using other forms of mass spectrometry that electrospray can form these ions, that they can survive transport through the atmosphere/vacuum interface, and that they have lifetimes in the dilute gas phase of at least hundreds of microseconds. The data presented here suggest that they also have lifetimes of at least 100 ms in the presence of a thermalizing bath gas. This result suggests that the ions are kinetically stable at room temperature and perhaps at higher temperatures. It is also significant that they can survive the ion-trapping process, which involves the removal of ion kinetic energy via collisions with the bath gas. Inelastic collisions that occur during the cooling of ion translational motion can lead to fragmentation, but this apparently does not occur to a significant extent, at least for complexes as small as a 10-mer duplex. The mass analysis portion of the ion trap experiment also provides a mechanism for dissociation. Inelastic collisions during the resonance ejection process can lead to fragmentation. Under the resonance ejection conditions used in this study, no fragmentation during the mass analysis portion of the experiment was noted. Such a phenomenon would have been apparent during the tandem mass spectrometry study discussed above because the doubly charged single-strand products would have appeared in the spectrum of Figure 6a. However, an important question yet to be resolved is the extent to which the scan speed can be reduced before significant dissociation of the complex begins. Such a phenomenon might ultimately place a practical limitation on the mass resolution attainable with these species using the ion trap operated with conventional resonance excitation in the presence of a bath gas.

The present results are significant in that they indicate, along with the results recently reported for myoglobin ions, that the ion trap can be used in conjunction with electrospray to study physiologically important biological complexes. Both ion trap mass spectrometry and tandem mass spectrometry have been demonstrated. The ability to capture and store ionized biological complexes in the quadrupole ion trap adds impetus to develop further the ion trap for investigations of biological materials.

ACKNOWLEDGMENT

This work was supported by the Oak Ridge National Laboratory Director's Fund and by the National Institutes of Health under Grant GM45372. Oak Ridge National Laboratory is managed for the United States Department of Energy by Martin Marietta Energy Systems, Inc., under Contract DE-AC05-84OR21400. M.J.D. and S.H.-G. acknowledge support through an appointment to the Oak Ridge National Laboratory Postdoctoral Research Associates Program administered jointly by the Oak Ridge Institute for Science and Education and Oak Ridge National Laboratory.

Received for review April 11, 1994. Accepted June 17, 1994.®

® Abstract published in *Advance ACS Abstracts,* August 1, 1994.

Anal. Chem. **1994,** *66,* 3423–3430

Matrix-Assisted Laser Desorption/Ionization Using an Active Perfluorosulfonated Ionomer Film Substrate

Jian Bai, Yan-Hui Liu, Teresa C. Cain, and David M. Lubman*

Department of Chemistry, The University of Michigan, Ann Arbor, Michigan 48109-1055

The use of an active Nafion substrate is shown to enhance the performance of MALDI MS. The use of a Nafion substrate with certain matrices can significantly enhance the signals obtained over those observed with a stainless steel probe substrate. Analytes can often be observed with the use of the Nafion substrate that cannot be easily observed with the standard MALDI procedure, and usually a much wider range of peaks can be observed using MALDI from the Nafion substrate than with any single matrix on a stainless steel substrate. This enhancement of signal from the Nafion substrate is observed only with the sequential deposition of the sample and the matrix onto the Nafion film. If the analyte and matrix are premixed, then the effect is not observed. The use of the Nafion substrate has been shown to be particularly effective in analyzing real biological mixtures without prepurification. This has been demonstrated for various samples including the analysis of the products of chemical digests of proteins, protein profiling in milk and egg white samples, cell lysate analysis, and oligonucleotide detection.

Matrix-assisted laser desorption/ionization (MALDI)[1,2] has become a powerful tool in biological mass spectrometry. In particular, MALDI has been shown to be a valuable tool for characterizing proteins and peptides by mass spectrometry based upon the high achievable mass range where proteins of molecular mass greater than 200 000 u have been detected.[3] Other advantages of MALDI MS analysis include high sensitivity, which may be in the femtomole range, the simplicity of the sample preparation, and the capability to analyze mixtures,[4–6] often in the presence of biological interferences. Although initially developed mainly for peptide and protein analysis, various modifications of the technique have allowed its successful extension to other biopolymers such as oligosaccharides/carbohydrates,[7–12] gangliosides,[12] oligonucleotides[13–19] and synthetic organic polymers.[20] Initial results obtained with smaller oligonucleotides have also encouraged research on DNA screening and sequencing by MALDI MS.[14–19]

The success of MALDI experiments depends heavily on the choice of the UV-absorbing matrix material. Over 30 different matrices,[1,3,14,20–23] have been identified, mainly by trial and error. Although the matrices presently available often meet the need for protein analysis, characterization of suitable matrices still continues for other classes of molecules such as oligonucleotides and oligosaccharides. The development of new matrices, such as 3-hydroxypicolinic acid[14] or binary mixtures of common matrices with sugars,[5] has improved MALDI performance in these areas significantly. Despite the successes achieved by MALDI, the diversity of impurities in real biological samples presents real challenges for accurate analysis. Even analyzing mixtures containing several components in relatively pure form can be difficult due to the selectivity of certain matrices for producing ions for different analytes in the MALDI process. In such mixture analysis, often several MALDI experiments with different matrices are required to detect all the components.[6] In addition, the presence of contaminants may result in total loss of the ion signal, reduced signal intensity, or poor resolution, depending on the type and concentration of the contaminants and the properties of the analytes. The mechanisms by which different contaminants affect the MALDI experiment are not clearly understood. Water-soluble ionic surfactants appear to have the most harmful effect on the signal.[24] Sodium and potassium can easily form cationic attachment products with analytes during MALDI and act as a major peak-broadening source in the mass spectrum. Impurities such as glycerol tend to disturb the crystallization process of the matrix/analyte

(1) Karas, M.; Hillenkamp, F. *Anal. Chem.* **1988,** *60,* 2299–2301.
(2) Tanaka, K.; Waki, H.; Ido Y.; Yoshida Y.; Yoshida, T. *Rapid Commun. Mass Spectrom.* **1988,** *2,* 151–153.
(3) Beavis, R. C.; Chait, B. T. *Rapid Commun. Mass Spectrom.* **1989,** *3,* 432–435.
(4) Chevrier, M.; Cotter, R. J. *Rapid Commun. Mass Spectrom.* **1991,** *12,* 611–618.
(5) Billeci, T. M.; Stults, J. T. *Anal. Chem.* **1993,** *65,* 1709–1716.
(6) Perkins, J. R.; Smith, B.; Gallagher, R. T.; Jones, D. S.; Davis, S. C.; Hoffman, A. D. *J. Am. Soc. Mass Spectrom.* **1993,** *4,* 670–684.
(7) Mock, K. K.; Davey, M.; Cottrell, J. S. *Biochem. Biophys. Res. Commun.* **1991,** *177,* 644–651.
(8) Spengler, B.; Dolce, J. W.; Cotter, R. J. *Anal. Chem.* **1990,** *62,* 1731–1737.
(9) Harvey, D. J. *Rapid Commun. Mass Spectrom.* **1993,** *7,* 614–619.
(10) Siegel, M. M.; Hollander, I. J.; Hamann, P. R.; James, J. P.; Hinmann, L.; Smith, B. J.; Farnsworth, A. P. H.; Phipps, A.; King, D. J.; Karas, M.; Ingendolf, A.; Hillenkamp, F. *Anal. Chem.* **1991,** *63,* 2470–2481.
(11) Hurberty, M. C.; Vath, J. E.; Yu, W.; Martin, S. A. *Anal. Chem.* **1993,** *65,* 2791–2800.
(12) Juhasz, P.; Costello, C. E. *J. Am. Soc. Mass Spectrom.* **1992,** *3,* 785–796
(13) Currie, G. J.; Yates, J. R., III. *J. Am. Soc. Mass Spectrom.* **1993,** *4,* 955–963.
(14) Wu, K. L.; Steding, A.; Becker, C. H. *Rapid Commun. Mass Spectrom.* **1993,** *7,* 142–146.
(15) Schneider, K.; Chait, B. T. *Org. Mass Spectrom.* **1993,** *28,* 1353–1361.
(16) Tang, K.; Allman, S. L.; Chen, C. H.; Chang, L. Y.; Schell, M. *Rapid Commun. Mass Spectrom.* **1993,** *8,* 183–186.
(17) Fitzgerald, M. C.; Zhu, L.; Smith, L. M. *Rapid Commun. Mass Spectrom.* **1993,** *7,* 895–897.
(18) Tang, K.; Taranenko, N. I.; Allman, S. L.; Chang, L. Y.; Chen, C. H. *Rapid Commun. Mass Spectrom.*, in press.
(19) Bai, J.; Liu, Y.; Siemieniak, D.; Lubman, D. M. *Rapid Commun. Mass Spectrom.*, in press.
(20) Beavis, R. C.; Chaudhary, T.; Chait, B. T. *J. Org. Mass Spectrom.* **1992,** *27,* 156–158.
(21) Beavis, R. C.; Chait, B. T. *Rapid Commun. Mass Spectrom.* **1989,** *3,* 233–237.
(22) Juhasz, P.; Costello, C. E.; Biemann, K. J. *J. Am. Soc. Mass Spectrom.* **1993,** *4,* 399–409.
(23) Cornett, D. S.; Duncan, M. A.; Amster, I. J. *Anal. Chem.* **1993,** *65,* 2608–2613.
(24) Ling, V.; Guzzetta, A. W.; Canova-Davis, E.; Stults, J. T.; Hancock, W. S.; Covey, T. R.; Shushan, B. I. *Anal. Chem.* **1991,** *63,* 2909–2915.

0003-2700/94/0366-3423$04.50/0
© 1994 American Chemical Society

mixture, which is considered to be an important aspect of the sample preparation. Other contaminants seem to destroy the effectiveness of the matrix, either by dilution or by altering its photoactivity.[25] Even the cleanliness of the substrate or probe surfaces can affect the performance of MALDI.

A number of schemes have been used to enhance the performance of the MALDI process through sample preparation or the use of selective adsorption methods. A preliminary purification scheme often involves washing the final sample preparation with ice-cold water as described by Beavis and Chait.[26] This procedure has generally been limited to less water soluble matrices such as sinapinic acid to aid in removing more water soluble ionic contaminants. Rinsing the sample dried onto the probe tip before adding matrix allowed some hydrophobic analytes to be detected.[27] Immobilization/blotting of samples on poly(vinylidene difluoride) (PVDF) membrane and Nylon[28–30] has been used for the cleanup of more hydrophilic proteins and for interfacing MALDI MS with gel electrophoresis. Such membranes are routinely used for enhancing ion production in plasma desorption mass spectrometry.[30] More recently, Cottrell and co-workers[31] described immobilization protocols using nitrocellulose as a substrate for MALDI. Using this protocol it was shown that spectra could be obtained from low picomole quantities of protein in the presence of contaminants which did not inhibit the binding of the protein to the substrate. Other methods for improving the performance of MALDI developed by Hillenkamp and co-workers include an on-probe purification of DNA samples by ion exchange[32] and a novel sample preparation method using fine fibrous paper as the substrate for a liquid matrix.[33] More recently, Hutchens and Yip presented two new desorption strategies:[34] surface-enhanced neat desorption (SEND), in which energy-absorbing molecules are chemically bound to the polymeric layer of the sample presenting surface, and surface-enhanced affinity capture (SEAC), where the probe tip was chemically activated to selectively adsorb the analyte of interest. An important advantage of these schemes includes the elimination of external matrix and the resulting intensive signal of the matrix ions. In addition, the new probe surface can be exploited as a solid-phase reaction site enabling low-affinity molecular recognition events to be detected directly in situ and can be used for structural analysis through enzymatic modification of adsorbed analytes free from matrix interference.

In the present work, we have applied a Nafion film as an active substrate for MALDI MS. Nafion is a perfluorinated cation exchanger with sulfonic acid groups as the active sites and has been used as a substrate for PDMS.[35,36] Thin and homogeneous Nafion films can be easily prepared from liquid solutions. Nafion possesses a high surface activity and can selectively and effectively bind small cations as well as large organic cations, as demonstrated by PDMS studies.[35,36] Another unique property of the Nafion is that it has very limited solubility after drying when exposed to aqueous media. This makes it compatible with MALDI and other desorption techniques since water-soluble ionophores can have a deleterious effect on the desorption/ionization process. In this work, Nafion was used as an active substrate for MALDI detection of various macromolecules including mixtures such as a CNBr digest of cytochrome *c*, commercial milk, chicken egg white, *Escherichia coli* cell extract, and oligonucleotide samples. The improvement in detection and resolution using the Nafion substrate compared to an inert stainless steel probe tip is demonstrated.

EXPERIMENTAL SECTION

The TOF MS used in these studies was a modified Wiley–McLaren design[3,37] with the capability for high-voltage acceleration up to ±20 kV (manufactured by R. M. Jordan Co., Grass Valley, CA). The laser source was a DCR 11 Nd:YAG laser system (Spectraphysics, Mt. View, CA) which provided 266 and 355 nm radiation for desorption. The laser beam was focused onto the probe tip at a 45° angle to the probe surface with a single 12.5 in. focal length quartz lens. The detector was initially a dual microchannel plate (MCP), which is sufficient for detection of ions of less than m/z 10 000. For the detection of heavier ions, a triple MCP detector with a Cu/Be conversion dynode, designed for postacceleration capability up to ±15 kV, was used. The postacceleration stage enhances the efficiency for detection of heavy species, but at some expense to the resolution. Data was recorded using a Lecroy 9400 digital oscilloscope and were subsequently transferred to a 386 IBM PC /AT for processing.

Some commonly used matrix materials, including 2,5-dihydroxybenzoic acid (DHB), caffeic acid (CA), sinapinic acid (SPA), 3-hydroxypicolinic acid (HPA), and α-cyano-4-hydroxycinnamic acid (CHCA), were obtained from Aldrich Chemical Co. (Milwaukee, WI) and used without further purification. Near-saturated matrix solutions were prepared with 50% deionized water and 50% acetonitrile as solvents; 4–6 μL was applied to the probe tip. Two commonly used sample preparation methods were used, where one involves premixing the matrix with the sample and the second is the sequential application of the sample and matrix solutions. All sample deposits were air-dried.

Dairy milk and chicken egg were obtained from a local grocery store. The 5-mer ss-DNA oligomer was synthesized by the core facility of The University of Michigan Medical Center. Cyanogen bromide digest of cytochrome *c* (horse heart) and ss-DNA oligomers of 18-, 42-, 53-, and 69-mer were provided by Dr. Rachel Ogorzalek Loo and Mr. David Siemieniak of The University of Michigan Medical Center, respectively. *Escherichia coli* obtained from Carolina Bio-

(25) Ehring, H.; Karas, M.; Hillenkamp, F. *Org. Mass Sepctrom.* **1992**, *27*, 472–480.
(26) Beavis, R. C.; Chait, B. T. *Anal. Chem.* **1990**, *62*, 1836–1840.
(27) Hefta, S. A.; Stahl, D. C.; Mahrenholz, A. M.; Rutherford, S. M.; Lee, T. D. *Proceedings of the 39th Conference on Mass Spectrometry and Allied Topics*; Nashville, TN, ASMS, East Lansing, MI, 1992; p 1416.
(28) Vestling, M. M.; Fenselau, C. *Anal. Chem.* **1994**, *66*, 471–477.
(29) Strupat, K.; Karas. M.; Hillenkamp, F.; Eckerskorn, C.; Lottspeich, F. *Anal. Chem.* **1994**, *66*, 464–470.
(30) Lacey, M. P.; Keough, T. *Anal. Chem.* **1991**, *63*, 1482–1487.
(31) Mock, K. K.; Sutton, C. W.; Cottrell, J. S. *Rapid Commun. Mass Spectrom.* **1992**, *6*, 233–238.
(32) Nordhoff, E.; Ingendoh, A.; Cramer, R.; Overberg, A.; Stahl, B.; Karas, M.; Hillenkamp, F.; Crain, B. *Rapid Commun. Mass Spectrom.* **1993**, *6*, 771–776.
(33) Zhao, S.; Somayajula, K. V.; Sharkey, A. G.; Hercules, D. M.; Hillenkamp, F.; Karas, M.; Ingendoh, A. *Anal. Chem.* **1991**, *63*, 450–453.
(34) Hutchens, T. W.; Yip, T.-T. *Rapid Commun. Mass Spectrom.* **1993**, *7*, 576–580.
(35) Jordan, E. A.; Macfarlane, R. D.; Martin, C. R.; McNeal, C. J. *Int. J. Mass Spectrom. Ion Phys.* **1983**, *53*, 345–348.
(36) McNeal, C. J.; Macfarlane, R. D. *J. Am. Chem. Soc.* **1986**, *108*, 2132–2139.
(37) Wiley, W. C.; McLaren, I. H. *Rev. Sci. Instrum.* **1955**, *26*, 1150–1157.

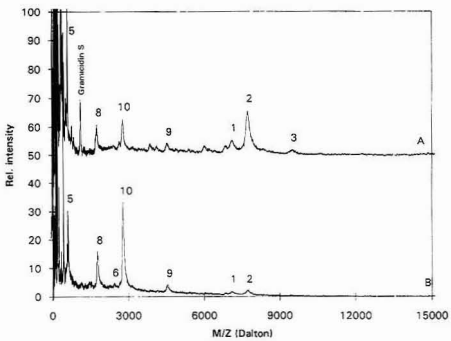

Figure 1. Positive ion MALDI mass spectra of the CNBr digest of cytochrome *c* with (A) CA matrix and (B) DHB matrix using 355 nm irradiation. The spectrum consists of 200 laser pulses averaged. Acceleration voltage, 18 kV.

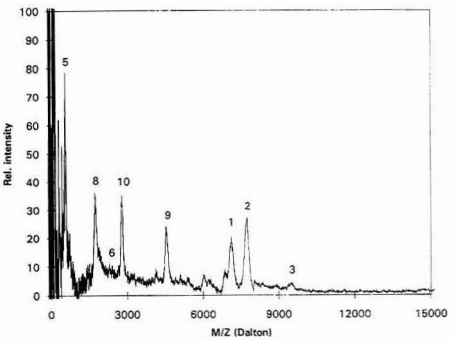

Figure 2. Positive ion MALDI mass spectrum of the CNBr digest of cytochrome *c* on the Nafion substrate with CA as the matrix using 355 nm irradiation. The spectrum consists of 200 laser pulses averaged. Acceleration voltage, 18 kV.

logical Supply Co. (Burlington, NC) was harvested at midlog phase (12 h growth) from trypticase soy broth by centrifugation and suspended in one-tenth the culture volume in 10 mM Tris buffer (pH 7.8). A cell extract was obtained by sonicating the cell suspension and centrifuging to remove any unbroken cells or cell fragments. Gramicidin S, Nafion, and polystyrene (MW 1800) were all obtained from Aldrich Chemical Co. and were used as provided. All samples were dissolved with deionized water. The sample probe tip was inserted through a vacuum lock and into the acceleration region such that the front end stainless steel surface was flush with the first acceleration plate.

Nafion Film and Polystyrene Film Preparation. Nafion is available in liquid form at a concentration of 5% in a mixture of 10% water and lower aliphatic alcohols. The pH of this solution was estimated with pH paper to be ~3. Approximately 5 μL of this solution was applied to the stainless steel probe tip (i.d. 5.6 mm) and air-dried, which generally produced a homogeneous film of ~12 mm^2 in size. Polystyrene film was prepared by applying a 5% solution in ethyl acetate to the stainless steel probe tip and air-drying. This solution tends to spread over the stainless steel probe tip during application, resulting in a larger and somewhat nonhomogeneous glassy deposit. Intensive heating of the deposit generated a more homogeneous yellowish layer and was used as an alternative for the preparation. Both forms of polystyrene film were tested and compared with Nafion films.

RESULTS AND DISCUSSION

CNBr Digest of Cytochrome *c* Analysis. In this work we demonstrate the capabilities of a Nafion surface for enhancing detection of components in mixtures. In particular, an important problem we examine is the analysis of the products of the CNBr digest of cytochrome *c*. Cytochrome *c* is a well-characterized protein with two methionine residues. Conventional methods such as electrophoretic analysis and HPLC with amino acid composition analysis have allowed the three major fragments and partial cleavage products to be identified after CNBr digestion. Figure 1 shows the MALDI mass spectra of the CNBr digest mixture obtained with DHB and CA as the matrix when the sample and matrix were mixed before application to the stainless steel probe tip. In all the spectra, expected cleavage products at methionine are obtained along with other minor peaks. Table 1 summarizes the possible cleavage products at methionine and tryptophan. The variations of the relative intensity of the different peaks reflect the enhancement or suppression effects of the matrices toward different analytes. A method where the sample was deposited directly onto the stainless steel probe tip before applying the matrix was also tested for this cytochrome *c* digest using several matrices, but produced basically the same result.

In order to enhance the detection of analytes by MALDI, Nafion, and polystyrene films were also tested as substrates for the MALDI analysis of cytochrome *c* digest. The various matrices used in these experiments included DHB, CA, and SPA. In the first set of experiments, the matrix and analyte were premixed and then applied to the probe surface coated with Nafion. This procedure produced mass spectra similar to those obtained in the MALDI experiment from the stainless steel probe as in Figure 1. However, a second set of experiments involved the sequential application of the sample and matrix to the Nafion film. A significant difference was obtained when the sample was deposited on the Nafion film and allowed to dry before adding CA as matrix. The mass spectrum of the CNBr digest of cytochrome *c* using this procedure is shown in Figure 2. It is apparent that a more homogeneous desorption of all the major components was obtained with the use of the Nafion surface and that the selectivity seen by the individual matrices is eliminated. Polystyrene surfaces were used instead of Nafion, but showed no improvement over the stainless steel probe. DHB on the Nafion surface showed minimal improvement. SPA was found to be unsuitable as a matrix when used with the Nafion film, as serious deterioration or total loss of the analyte signal was experienced. A visual inspection of the sample preparation revealed possible polymerization of the sinapinic acid, where the sample deposit turned into a foamy film during laser irradiation.

The molecular weight of the fragments detected from the CNBr digest compares favorably with the calculated values

Table 1. CNBr Digest Fragments of Cytochrome *c* and the Calculated and Measured Molecular Weight

frag. no.[a]	residues cleaved at C-terminal	fragment length	MW calc[b,c]	MW meas	error %
1	W(59)	G(1)–W(59)	7142	7138	0.06
2	M(65)	G(1)–HS(65)	7773		
	M(65)	G(1)–HSL(65)	7755	7754	0.01
3	M(80)	G(1)–M(65)–HS(80)	9567		
		G(1)–M(65)–HSL(80)	9549		
		G(1)–HS(65)–HS(80)	9537		
		G(1)–HS(65)–HSL(80)	9519	9528	0.09
4		G(1)–E(104)	12360	nd[d]	
5	W(59), M(65)	G(60)–HS(65)	649		
		G(60)–HSL(65)	631	627	0.63
6	W(59), M(80)	G(60)–M(65)–HS(80)	2442		
		G(60)–M(65)–HSL(80)	2424		
		G(60)–HS(65)–HS(80)	2412		
		G(60)–HS(65)–HSL(80)	2394	2400	0.25
7	W(59)	G(60)–M(65)–M(80)–E(104)	5235		
		G(60)–HS(65)–M(80)–E(104)	5205		
		G(60)–M(65)–HS(80)–E(104)	5205		
		G(60)–HS(65)–HS(80)–E(104)	5175	nd[d]	
8	M(65), M(80)	E(66)–HS(80)	1781		
		E(66)–HSL(80)	1761	1754	0.40
9	M(65)	E(66)–M(80)–E(104)	4574		
		E(66)–HS(80)–E(104)	4544	4550	0.13
10	M(80)	P(81)–E(104)	2781	2788	0.25

[a] Fragment number identical to the peak number in the mass spectra. [b] Cleavage at methionine produces C-terminal homoserine (HS) or homoserine lactone (HSL). [c] Side reaction at methionine (not cleaved) results in HS. [d] nd, not detected.

in Table 1. The mass calibration for the CNBr digest was done using internal standards including gramicidin S (*m/z* 1141) and substance P (*m/z* 1348). The *m/z* values obtained experimentally compared to those calculated are also compared in Table 1, where the percent difference may range from 0.01% to 0.63%. There is no significant difference between the mass values measured on the stainless steel probe tip and on the Nafion surface. The typical resolution of the peaks in these spectra is 40–50.

The expected cleavage products of the CNBr digest of cytochrome *c* dominate the spectrum; however, products due to incomplete cleavage at the two methionine amino acids were also detected and labeled as peaks 3 and 9. Peak 9 is one of the two components whose sensitivity was clearly improved on the Nafion surface. The other peak labeled as 1 is produced due to oxidative cleavage at the tryptophan site, which should produce two fragments of molecular weights 7142 and ~5200. A peak was not detected at molecular weight 5200 using MALDI on the stainless steel probe tip or with the Nafion surface. This would appear to indicate that this peak results from the cleavage of fragments 2 and/or 3 during sample handling/storage. Such cleavage should produce two additional products with molecular weights around 630 and 2400. The former peak was observed at 627 (peak 5) and the latter can be identified around 2400 (peak 6) in the MALDI spectrum obtained with the DHB matrix. In addition, a broad peak around 6100 was detected in all cases (except with the DHB matrix) which appeared as a doublet in the CA/Nafion spectra with molecular weights of 6050 and 6200. These two peaks could be the cleavage products at another site since their sum is close to the molecular weight of intact cytochrome *c*. In addition, the peak around 3840 in the CA MALDI spectrum may be the doubly charged species of peak 2.

CNBr digestion is a specific and valuable chemical cleavage method in protein characterization. MALDI MS in combination with the use of a Nafion substrate has shown that side products in addition to expected cleavage products are observed. The use of a Nafion substrate allows more uniform detection of the peaks present in the mixture than with the use of MALDI MS on a stainless steel probe. The identification of such peaks may provide additional structural information on the protein or on the chemical digestion reaction or may help identify the presence of impurity peaks. MALDI MS on a Nafion substrate provides a rapid means of screening such digestion reactions with identification of species not easily detected by the usual MALDI MS method.

Dairy Milk Analysis. The use of matrices more tolerant toward contaminants such as sinapinic acid has allowed direct analysis of complicated mixtures such as dairy milk with the identification of several proteins.[26] In this experiment, a 2% fat commercial milk sample was diluted 50-fold with deionized water. Mixing this diluted milk with DHB and SPA allowed us to obtain useful mass spectra under normal MALDI operation. The spectrum obtained with DHB is presented in Figure 3. Lactalbumin, lactoglobulin, and casein are tentatively identified and are labeled in all the mass spectra. Caffeic acid appears to be a less effective matrix for producing ions from this mixture and only one major peak was detected and identified as lactoglobulin. Application of sample onto the Nafion film substrate before adding matrices was also tested. Figure 4 shows the spectra obtained with CA as the matrix and with CA and sample deposited on the Nafion film. A pronounced improvement was achieved for caffeic acid using the Nafion substrate. The peaks detected with other matrices were present, along with the appearance of higher molecular weight species. A similar improvement was also observed for DHB used with the Nafion film. The higher molecular weight peaks could simply be the cluster ions or other higher molecular weight species in the milk, which are difficult to detect using MALDI with conventional matrices. SPA with Nafion film again failed to produce any useful spectra as before.

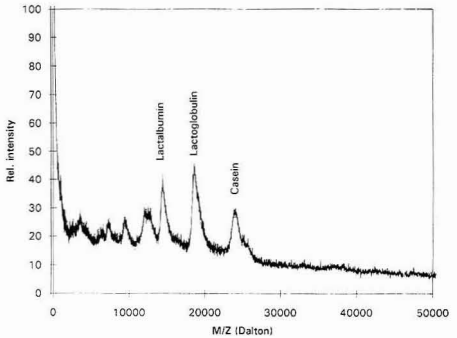

Figure 3. Positive ion MALDI mass spectrum of commercial milk with DHB as the matrix on the stainless steel probe using 355 nm irradiation. The spectrum consists of 200 laser pulses averaged. Acceleration voltage, 18 kV.

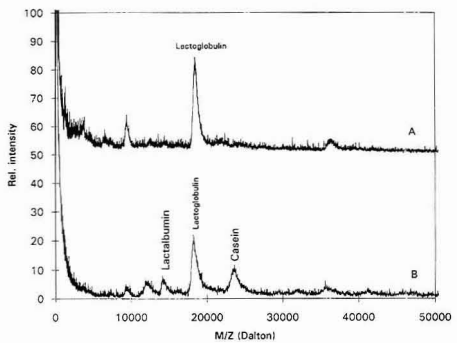

Figure 4. Positive mass spectra of commercial milk with CA matrix on (A) the stainless steel probe and (B) on the Nafion film using 355 nm irradiation. The spectrum consists of 200 shots averaged. Acceleration voltage, 18 kV.

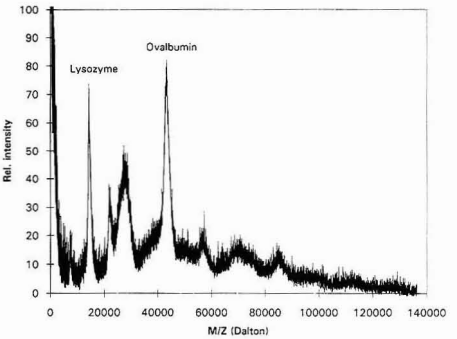

Figure 5. Positive ion MALDI mass spectrum of chicken egg white on Nafion film using CA as the matrix with 355 nm irradiation. The spectrum consists of 200 laser pulses averaged. Acceleration voltage, 20 kV.

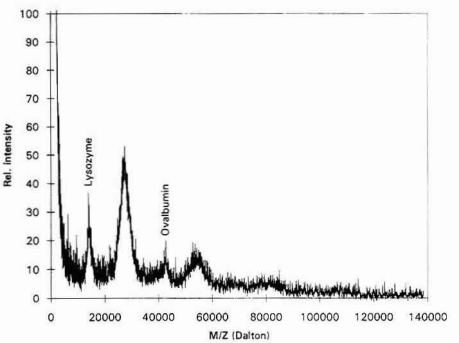

Figure 6. Positive ion mass spectrum of the aqueous layer from chicken egg white extract using CA as the matrix with 355 nm irradiation. The spectrum consists of 200 laser pulses averaged. Acceleration voltage, 20 kV.

Chicken Egg White Analysis. Chicken egg white, taken from a whole egg without disturbing the egg yolk, was diluted with deionized water and sonicated for 10 min. The final working mixture contains ~20 mg of egg white/mL. An attempt to analyze this mixture by MALDI using DHB, SPA, and CA matrices on the stainless steel probe by either premixing or sequential application of the sample and matrix did not generate any significant signal. However, excellent results for this sample were readily obtained with CA on the Nafion film. Massive components as large as 100 000 u were detected, as shown in Figure 5. Two of the peaks are tentatively identified as egg white lysozyme and ovalbumin.

The components of the egg white sample were further studied by use of a simple extraction procedure. Approximately 0.5 mL of 200 mg of egg white/mL was extracted into 1 mL of chloroform. The extract was sonicated for 7 min and allowed to settle for 20 min. Three separate layers were obtained from this procedure. After separation, the aqueous layer was analyzed by MALDI using DHB, SPA, and CA matrices without the Nafion substrate. As shown in Figure 6, the aqueous layer contains the unidentified component with the broad peak between m/z 25 000 and 30 000. The aqueous layer shows a slightly reduced level of lysozyme and ovalbumin. The precipitate obtained from the extraction procedure was washed with deionized water and was dissolved with 3 mL of a water/acetone/methanol (v/v/v 1:1:1) solution. The components of this mixture could also be detected using the standard MALDI procedure with DHB and SPA matrices. The Nafion substrate was unnecessary for detection in this case. The result shown in Figure 7 is basically the same spectrum obtained from the egg white sample on the Nafion substrate shown in Figure 5, with the broad peak at m/z ~25 000, which was extracted into the aqueous layer, considerably reduced.

The key point observed in the egg white extract experiment is that a simple procedure, i.e., using a Nafion film, enabled the major components in egg white to be detected with a standard MALDI procedure using a stainless steel probe, indicating that impurities or components of a real mixture may be a potential source of interferences in MALDI experiments. These impurities did not affect the MALDI mass spectrum obtained on a Nafion surface.

***Escherichia coli* Extract Analysis.** An important problem in which mass spectrometry can be particularly useful is the

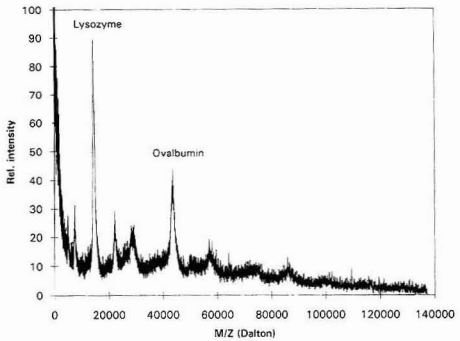

Figure 7. Positive ion mass spectrum of chicken egg white precipitate using DHB as the matrix with 355 nm irradiation. The spectrum consists of 200 laser pulses averaged. Acceleration voltage, 20 kV.

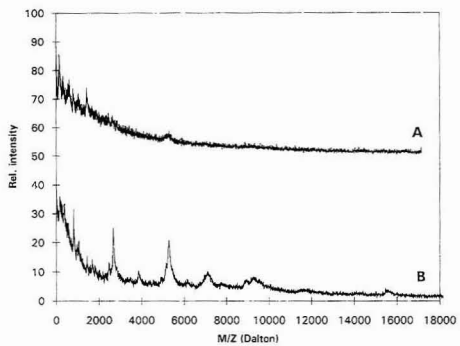

Figure 8. MALDI mass spectra of an *E. coli* extract with CA matrix (A) on the stainless steel probe and (B) on the Nafion substrate using 355 nm irradiation averaged for 250 laser pulses. Acceleration voltage, 20 kV.

rapid screening of cell contents. FAB MS has been used for the profiling of bacteria toward the development of a rapid method for the identification of bacteria.[38,39] In this work, a crude protein extract was obtained from the cell extract from disintegrated *E. coli* by precipitation with cold acetone. The precipitate was dispersed in deionized water for MALDI MS analysis using DHB, CA, SPA, and CHCA on the stainless steel probe tip and the Nafion substrate. CHCA gave the best result on the stainless steel, allowing the observation of several rather broad peaks. CA matrix on the stainless steel probe tip also allowed the detection of two components with *m/z* above 2000. Figure 8 shows the mass spectra of *E. coli* extract on the stainless steel and the Nafion substrate using CA matrix. As can be seen from Figure 8, the largest number of peaks were detected on the Nafion substrate with excellent sensitivity and signal-to-noise ratio. An interesting observation in this experiment is that, upon mixing CA with the sample and application of the mixture onto the stainless steel probe,

(38) Heller, D. N.; Fenselau, C.; Cotter, R. J.; Demirev, P.; Olthoff, J. K.; Honovich J.; Uy, M.; Tanaka, T.; Kishimoto Y. *Biochem. Biophys. Res. Commun.* **1987**, *142*, 194–199.
(39) Heller, D. N.; Cotter, R. J.; Fenselau, C.; Uy, O. M. *Anal. Chem.* **1987**, *59*, 2806–2809.

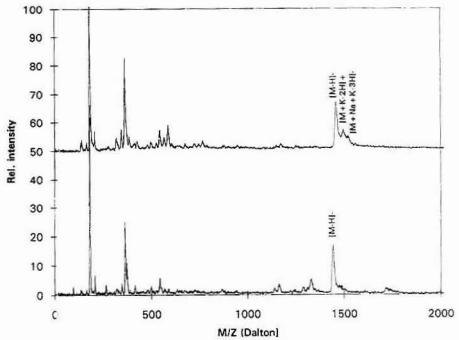

Figure 9. Negative ion mass spectra of a 5-mer ss-DNA oligomer (5′-CTT AA-3′) obtained on (A) a stainless steel probe and (b) Nafion film with CA as the matrix with 355 nm irradiation; ~20 pmol of sample loaded. The spectra consist of 100 laser pulses averaged. Acceleration voltage, −15 kV.

the sample deposit developed a black tint, indicating possible reactions which might interfere with the MALDI experiment. No such changes were observed when the sample and CA matrix were sequentially applied onto the Nafion substrate. Mass spectra from the MALDI process from the Nafion film using CHCA as the matrix showed an enhanced signal-to-noise ratio, but gave basically the same spectra as with CHCA on the stainless steel substrate. DHB did not generate any significant signals on either the stainless steel or the Nafion substrate.

Oligonucleotide Analysis. The analysis of oligonucleotides has proven to be particularly difficult because the MALDI process has been found to be very dependent on the matrix used. Various matrices have led to MALDI mass spectra which are base composition dependent[15] or result in fragmentation[15] or cation exchange.[32] Finding matrices of improved performance still constitutes a potential breakthrough in the area. The use of 3-HPA as a matrix has allowed oligonucleotide strands as long as 90 bases to be observed in MALDI MS,[14,16] and the use of a 3-HPA and picolinic acid matrix mixture has recently allowed the detection of DNA strands up to 500 base pairs long.[18] Purification procedures[32] and other sample preparation alternatives[13] have been shown to enhance the ability to obtain MALDI mass spectra of oligonucleotides.

In Figure 9 is shown the negative mass spectra of a single-stranded 5-mer obtained with CA matrix from the stainless steel probe and using a Nafion film substrate. The MH^- peak obtained using a CA matrix on a stainless steel probe shows several adduct peaks as is also observed for the HPA, DHB, and SPA matrices. These adduct peaks result from cation attachment. The intensity of these adducts depends on the matrix used and the concentration of the impurities present. These adduct peaks were effectively eliminated using the Nafion substrate. It appears that the Nafion effectively binds the inorganic cations to the anionic sites and eliminates these interferences during the MALDI process. DNA oligomers including an 18-, 42-, 53-, and 69-mer were also analyzed using the Nafion film. The observed mass spectra showed some improvement in sensitivity and signals that lasted over

an extended period of time. The improvement in signal for these relatively pure samples was found to be limited though, i.e., a factor of ~2. However, in more recent work,[19] DNA strands exceeding 200 base pairs in length obtained from restriction enzyme digests of plasmid DNA have been greatly enhanced by the Nafion surface. In this case though, the Nafion assists MALDI of a relatively impure biological sample.

Factors Affecting MALDI from a Nafion Film Substrate. In MALDI, as well as in other desorption processes which produce gas-phase ions from solid phases, impurities and strong interactions among large polar analytes are factors that affect the performance of the method. The introduction of matrix in MALDI partially relieves these strong interactions.[40] However, the presence of an active substrate can also effectively reduce the presence of impurities and their interactions with the analyte and/or matrix. The selective adsorption of impurities by active surfaces may result in the in situ purification of the sample. In the case of the Nafion film, small inorganic cations are adsorbed onto the surface and strongly bound, so that they are excluded from the analyte/matrix interactions. The procedure used in this work for applying the analyte and matrix to the surface may further enhance this effect. The sample is applied directly to the Nafion first, where it is in direct contact with the active polymer surface and the impurities can easily access the anionic sites in the Nafion and bind. The matrix is then applied to the sample, and sufficient analyte appears to interact with the matrix for MALDI to enhance the signal without involvement of the potential contaminants. If the matrix and sample are first mixed and then applied to the Nafion, then little effect is observed. It appears that the analyte and impurities do not easily access the active sites due to the large amount of matrix present under these conditions.

The use of active surfaces such as Nafion can allow removal of contaminants by selective adsorption provided they are either strongly or loosely adsorbed. If the contaminants are loosely adsorbed, then they can be washed away with water or other solvents. Such washing was performed with no obvious effect on the results. This leads us to believe that the impurities are strongly bound and do not interfere with the MALDI process.

The use of an active surface in the MALDI process may also involve other factors besides selective adsorption of contaminants. The analytes too may become strongly adsorbed on the surface and thus reduce the effectiveness of MALDI. This may be influenced by such factors as the counterions present in the Nafion surface, the solvent used, and the affinity of the matrix toward the analyte. The latter may explain the selectivity of a matrix toward enhancing the MALDI signal and explain the variation of the improvement observed in these experiments with different matrices with the use of the Nafion film. The crystallization process in MALDI may also be affected by the active surface. In these experiments, the presence of a small amount of liquid Nafion in DHB can totally destroy the effectiveness of this matrix. Thus, any solvent that dissolves dried Nafion films should be avoided.

In addition, an important factor to be considered is the capacity of the Nafion and the amount of salt impurity that can be tolerated. The capacity of the Nafion is estimated to be 0.9 mequiv/g (based on an equivalent molecular mass of 1100 Da). Loading of 5 μL of the Nafion (5%) corresponds to a theoretical capacity of ~0.2 μequiv. However, since the final form of the Nafion is a thin film, the effective capacity remains unknown and is complicated by factors such as the Nafion film thickness, the proportion of active sites on the surface available for ion exchange, whether ion exchange occurs due to ion transport/diffusion within the film, etc. The experimental evaluation of the actual capacity of the Nafion substrate is also complicated by (1) the MALDI process itself, which can tolerate moderate amounts of salt, and (2) the addition of (in)organic salts to the sample, which results in species due to ion exchange such as HCl, H_3PO_4, or acetic acid, if salts of those acids are added, which may affect the MALDI process. In these experiments, the loading of 0.25 μequiv of NaH_2PO_4 begins to degrade the MALDI spectrum of mixtures obtained on the stainless steel probe tip as compared to a loading of 0.35 μequiv of NaH_2PO_4 to reach a similar degradation using the Nafion substrate. However, further tests indicate that the CNBr digest of cytochrome *c*, for example, can still be observed upon loading of 1 μequiv of NaH_2PO_4 on the Nafion film.

The use of Nafion film for enhancing the observed signal is found to be particularly effective for impure samples. A dramatic enhancement is observed for egg white, *E. coli* lysate, and milk samples. The enhancement is these cases may be the difference between not observing a useful signal on the stainless steel probe to that of observing a strong signal intensity on the Nafion substrate. The signal enhancement in the case of the *E. coli* lysate appears to be greater than 100×. In the case of relatively pure samples such as the CNBr digest of cytochrome *c* or oligonucleotides, the enhancement effect is considerably smaller. For the CNBr digest, the Nafion was found to enhance components that could not be observed with specific matrices and provide a more general spectrum than any particular matrix. The overall intensity of the spectrum though was not enhanced significantly. The same was observed for synthesized oligonucleotides that were relatively pure, where little enhancement was observed using Nafion in the MALDI process.

CONCLUSION

This work has shown that active substrates such as Nafion can enhance considerably the performance of MALDI MS. The use of a Nafion substrate with certain matrices can significantly enhance the signals obtained over that observed with a stainless steel probe substrate. In addition, analytes that cannot be easily observed with the standard MALDI procedure can often be observed with the use of the Nafion substrate, and generally a much wider range of peaks can be observed using MALDI from the Nafion substrate than with any single matrix on the stainless steel substrate. The Nafion substrate can thus eliminate some of the matrix dependence of the MALDI process. The MALDI process from the Nafion substrate though is still very matrix dependent and often appears to work best with caffeic acid. In addition, the enhancement of signal from the Nafion substrate is observed only with the sequential application of the sample and the

(40) Karas, M.; Bahr, U.; Giessmann, U. *Rev. Mass Spectrom.* **1991**, *10*, 335–357.

matrix on the Nafion. If the analyte and matrix are premixed, the effect is not observed. This would seem to indicate that impurities in the sample that would normally inhibit the MALDI process are bound to active sites in the Nafion more tightly than the large analyte molecules. These impurities thus remain strongly bound during desorption and do not interfere with the MALDI process. The use of the Nafion substrate has been shown to be particularly effective in analyzing real biological mixtures without significant prepurification. This has been demonstrated for various samples ranging from chemical digests of proteins to cell lysates. The further development of substrates to enhance the MALDI process will no doubt continue to be an important area of investigation.

ACKNOWLEDGMENT

This work received support from the National Science Foundation under Grant BIR-9223677, the National Institutes of Health under the National Center for Human Genome Research Grant IR21H60068501A2, and the Environmental Protection Agency under Grant R-819605-01-0.

Received for review March 29, 1994. Accepted July 7, 1994.®

® Abstract published in *Advance ACS Abstracts*, September 1, 1994.

Anal. Chem. **1994,** *66,* 3431–3435

Chemical Characterization of Single Particles by Laser Ablation/Desorption in a Quadrupole Ion Trap Mass Spectrometer

John M. Dale,* Mo Yang, William B. Whitten, and J. Michael Ramsey
Analytical Chemistry Division, Oak Ridge National Laboratory, Oak Ridge, Tennesee 37831-6142

Particles are introduced into the center of the space surrounded by the hyperbolic electrode surfaces of a quadrupole ion trap mass spectrometer. Ions are desorbed or ablated from the surfaces of the particles with laser pulses from a Nd:YAG laser as the particles fall through the trap. The ions are trapped and subsequently mass analyzed using the mass-selective instability mode of operation of the ion trap. Desorption experiments were performed with ~100 μm silicon carbide particles with an average of a few nanograms of adsorbed trimethylphenylammonium chloride, tetraphenylphosphonium bromide, or 2,4,6-trinitrotoluene per particle. A conservative detection limit of 0.7 fm per particle was determined for tetraphenylphosphonium bromide. Ablation experiments were performed with ~50 μm nickel particles for isotope ratio measurements with good agreement between accepted and average experimental values.

Although instrumentation and techniques can be considered to be well-developed for the physical characterization of particles, there is still a need for instrumentation to chemically characterize these materials. Understanding the chemical nature of particles is important for a number of branches of science. The characterization of particles has become increasingly important in material science as new material synthesis processes rely on microparticulate precursors.[1] Particles in the form of aerosols play a central role in atmospheric studies and are important for understanding environmental issues.

The approaches currently used to chemically characterize particles have recently been reviewed by Niessner.[1] These methods can be classified as either optical techniques or vacuum techniques. The latter include various forms of mass spectrometry and photoelectron spectroscopy. Particles mounted on a substrate have been analyzed by secondary ion/neutral mass spectrometry using a quadrupole mass filter with special energy-selective ion optics.[2] Differentially-pumped, atmospheric-sampling, microparticle-beam generators have been used for the introduction of aerosol particles into the ionization region of quadrupole mass filters. The beam is produced by the expansion of the aerosol into the system vacuum through a capillary nozzle and skimmer. Individual particles contained in the beams have been volatilized and ionized sequentially for analysis by directing them either onto a hot filament[3-6] or into the path of a high-energy pulsed laser beam.[7] The use of a laser to produce ions from particles is an attractive approach. It provides the ability to either desorb molecules from the surface or vaporize an entire particle depending upon the energy of the laser pulse.

Although used extensively, the quadrupole mass filter severely limits the ability to perform chemical characterizations on a single particle basis because it does not monitor all of the ions from one sampling of the particle. Later work used a Matauch-Herzog mass spectrometer with an focal plane array detector to allow simultaneous multiple ion monitoring.[8] More recently, single particle analyses have been implemented using laser volatilization mass spectrometry and time-of-flight mass spectrometers.[9-13]

Laser desorption mass spectrometry has been demonstrated in a quadrupole ion trap with sample solutions that have been dried onto the end of a probe.[14-16] The probe is inserted through a hole in the central ring electrode in such a manner as to place the sample flush with the minimum radius of the electrode inner surface. The sample is vaporized with a pulsed laser beam entering the trap from the opposite direction. Multiple sampling can be made by rotating the probe.

The work described in this paper focuses on the ability to perform laser desorption experiments and mass analysis characterizations of particles which are sampled at the center of the quadrupole ion trap. The ion trap has interesting features that make it attractive for this type of analysis. When the mass-selective instability mode of operation[17] is used, ions of different masses generated in the ion trap from one

(1) Niessner, R. *Angew. Chem., Int. Ed. Engl.* **1991,** *30,* 466.
(2) Fichtner, M.; Lipp, M.; Goschnick J.; Ache, H. J. *Surf. Interface Anal.* **1991,** *17,* 151.
(3) Stoffels, J. *Int. J. Mass Spectrom.* **1981,** *40,* 217.
(4) Sinha, M. P.; Giffin, C. E.; Norris, D. D.; Estes, T. J.; Vilker, V. L.; Friedlander, S. K. *J. Colloid Interface Sci.* **1982,** *87,* 140.
(5) Allen, J.; Gould, R. K. *Rev. Sci. Instrum.* **1981,** *52,* 804.
(6) Sinha, M. P.; Platz, R. M.; Vilker, V. L.; Friedlander, S. K. *Int. J. Mass Spectrom. Ion Processes* **1984,** *57,* 125.
(7) Sinha, M. P. *Rev. Sci. Instrum.* **1984,** *55,* 886.
(8) Sinha, M. P. *Aerosols: Formation and Reactivity,* Proceedings of the 2nd International Aerosol Conference, Berlin, 1986; Pergamon: Oxford, 1986; p 875.
(9) McKeown, P. J.; Johnston, M. V.; Murphy, D. M. *Anal. Chem.* **1991,** *63,* 2069.
(10) Reents, W. D., Jr.; Swanson, A.; Downey, S.; Mujsce, A. M.; Muller, A. J.; Emerson, B.; Siconolfi, D. J.; Sinclair, J. D. Proceedings of the 41st ASMS Conference on Mass Spectrometry and Allied Topics, San Francisco, CA, 1993; p 640a.
(11) Hinz, K. P.; Daufmann, R.; Spengler, B. Proceedings of the 41st ASMS Conference on Mass Spectrometry and Allied Topics, San Francisco, CA, 1993; p 946a.
(12) Murray, K. K.; Russell, D. H. Proceedings of the 41st ASMS Conference on Mass Spectrometry and Allied Topics, San Francisco, CA, 1993; p 780a.
(13) Johnston, M. V.; Carson, P. G.; Neubauer, K. R.; Wexler, S. S. Proceedings of the 41st ASMS Conference on Mass Spectrometry and Allied Topics, San Francisco, CA, 1993; p 944a.
(14) Heller, D. N.; Lys, I.; Cotter, R. J. *Anal. Chem.* **1989,** *61,* 1083.
(15) Glish, G. L.; Goeringer, D. E.; Asano, K. G.; McLuckey, S. A. *Int. J. Mass Spectrom. Ion Processes* **1989,** *94,* 15.
(16) McLuckey, S. A.; Glish, G. L.; Kelley, P. E. *Anal. Chem.* **1987,** *59,* 1670.

0003-2700/94/0366-3431$04.50/0
© 1994 American Chemical Society

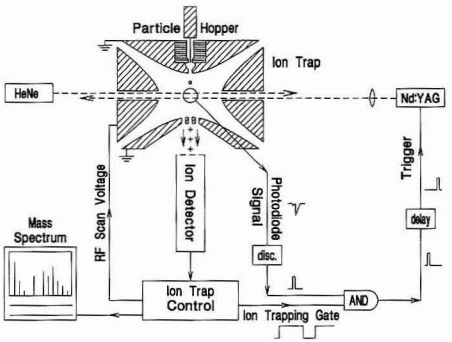

Figure 1. Schematic of the experimental setup for laser desorption mass spectroscopy of falling particles.

laser pulse sampling of the particle can be confined to the trap and subsequently mass analyzed. Energetic ions, if trapped, will be quickly cooled by collisions with the helium buffer gas in the trap. Consequently, these ions will not cause the mass resolution of the analysis to be limited as is the case when a time-of-flight mass spectrometer is used.

EXPERIMENTAL SECTION

The experimental work for this paper was performed with a Finnigan MAT Model 800 ion trap detector system (ITD). The standard ITD ion trap assembly consists of three cylindrically symmetric electrodes separated by ceramic spacers. The hyperbolic inner surfaces of the two end cap electrodes and the centrally located ring electrode define the volume of the trap. The minimum inner diameter of the ring electrode is 2.00 cm, and the axial distance between the end caps is 1.57 cm. The experimental setup as described below is shown schematically in Figure 1.

The ion trap was removed from the ITD vacuum chamber and modified by drilling four 3.18 mm holes on perpendicular axes through the central plane of the ring electrode. The trap was remounted in a 15.2 cm vacuum cube with its symmetry axis in the vertical position. The trap mounting assembly was designed so that the holes in the ring electrode were each perpendicular to a vacuum cube side port, three of which were fitted with 15.2 cm viewport flanges. The fourth backside port was connected to a vacuum tee which had the ITD turbo pump mounted on the vertical leg. The two window-accessible collinear holes in the ring electrode are for laser access to the center of the trap. The third hole, facing the frontside port, is for photodiode detection of light reflected from the particles as they pass through the center of the trap. The trapping radio frequency (rf) voltage is applied through a 3.18 mm brass rod that extends from the ITD autotransformer to a high-voltage vacuum feed-through and then through the vacuum tee to the remaining hole in the ring electrode. After the trap was installed in the vacuum cube, it was necessary to retune the autotransformer for resonance by moving the input tap on the rf coil.

(17) March, R. E.; Hughes, R. J. In *Quadrupole Storage Mass Spectrometry, Vol. 102, Chemical Analysis*; Winefordner, J. K., Ed.; Wiley-Interscience: New York, 1989.

A particle dropping device was made to fit in a hole on the topside of the top end cap electrode where the electron gun assembly normally resides. The body of the device is a 17.4 mm diameter brass cylindrical hopper with a 2.35 mm hole that extends through the center of the hopper and terminates in a 0.56 mm hole at the bottom. A 0.46 mm diameter drill bit attached to an 8 mm diameter rod rests inside the hopper such that the end of the drill bit is flush with the bottom of the hopper. The bottom of the hopper is 12.2 mm above the center of the trap. A slot in the top of the 8 mm rod fits a mating piece that is attached to the shaft of a rotary vacuum feed-through. Particles of interest are loaded into the hopper and made to fall into the trap through a 1.2 mm hole in the center of the top cap electrode by rotating the vacuum feed-through either by hand or with a stepping motor. A freely falling particle will reach the center of the trap in about 50 ms with a velocity of ~0.5 mm/ms and will be observable through the holes in the ring electrode for about 6 ms.

The second harmonic 532 nm radiation from a Quanta-Ray DCR-2A pulsed Nd:YAG laser is used to desorb or ablate and ionize material from particles as they fall through the center of the trap. The pulse for triggering the Nd:YAG laser is synchronized so that the laser fires as the particle passes through its beam path. The onset of the trigger is generated by light scattered from the particle as it passes through the beam of a 4 mW HeNe laser. The two beam paths are coplanar and propagate through the trap from opposing side ports with the HeNe beam parallel to and about 2 mm above the Nd:YAG beam. A falling particle traverses the distance between the two beams in about 4 ms. As the particle falls through the HeNe laser beam, the scattered radiation is detected by a photodiode, and the output is converted to a TTL pulse. When this pulse is coincident with an ion trapping gate from the ion trap control of the ITD, a TTL pulse is generated by the AND gate. The output of the AND gate, after passing through an adjustable delay generator, is used to trigger the Nd:YAG laser. The Nd:YAG laser fires about 3 ms after it is triggered. The displacement between the HeNe beam path and the Nd:YAG beam path is made a little larger than the distance that the particles fall during this 3 ms period. The additional distance allows the trigger to be delayed by an adjustable amount until the particles are consistently intercepted by the Nd:YAG pulses. This condition is determined by monitoring the Nd:YAG radiation scattered from the particles with the photodiode. The magnitude of the photodiode pulse provides a measure of the degree to which the beam intercepted the particle and also shows a qualitative correlation to the total number of ions produced. Particles are consistently intercepted by the 10 ns pulse of the Nd:YAG laser after proper beam alignment and trigger delay adjustment.

A Galileo Electro-Optics Corp. Channeltron electron multiplier with conversion dynode, Model 4773, is mounted below the trap to detect ions as they are ejected through the holes in the bottom cap electrode. The perpendicular axis through the center of the entrance grid of the multiplier is aligned to be collinear with the symmetry axis of the ion trap. In this position, the vertical projection of the grid is intercepted by the conversion dynode, which is mounted at an angle below the grid. The channeltron is mounted adjacent to the open

face side of the conversion dynode. This configuration prevents any particle that might fall through one of the holes in the bottom cap electrode from dropping directly into the channeltron. Electrical connections for the high-voltage input, the signal output, the grid potential, and the conversion dynode potential are made through vacuum feed-throughs in the top flange of the vacuum cube where the rotary vacuum feedthrough is mounted. For positive ion detection, the grid was maintained at −500 V, and the conversion dynode was at ground. For negative ion detection, the grid was at +800 V, and the dynode was at +3000 V. The channeltron was set at −1600 V. A 10.2 cm diameter by 5.1 cm long cap welded to a 15.2 cm flange is mounted on the bottom port of the vacuum cube to provide additional space for the electron multiplier. A helium supply from an adjustable leak valve is connected to the cap to maintain a helium pressure of 0.13 Pa inside the vacuum cube. Helium atoms collide with the ions in the trap to provide increased resolution and sensitivity by dampening the ion trajectories.[18] The ITD is tuned throughout the full mass range of the instrument using ions generated from perfluorotributylamine ($(C_4F_9)_3N$) so that adjacent peaks differing by 1 amu are resolved. Peak broadening may occur, however, if a particular laser desorption produces an ion population that is sufficiently high to generate a space charge. In this case, the leading and trailing edges of a major peak may be interpreted as separate masses by the ITD electronics and will not be distinguishable from true masses adjacent to the peak.

The compounds used for the particle desorption experiments were trimethylphenylammonium chloride, tetraphenylphosphonium bromide, and 2,4,6-trinitrotoluene. The particles were made of silicon carbide that had been produced originally for use as an abrasive. A size distribution analysis of the particles showed that sizes from 98 to 120 μm accounted for the middle 60% of the particles by weight, with a median size of 112 μm. The surface area was 0.113 m^2/g. The particles were coated with a quaternary salt by dissolving a weighed amount in methanol, combining the solution with a weighed quantity of particles, and evaporating the solvent. Acetone was used to dissolve the 2,4,6-trinitrotoluene. The average quantity of material adsorbed per particle in each case was a few nanograms or a few tens of picomoles. This corresponds to about 10 monolayers on the surface of a particle based upon the surface area measurements.

Nickel particles with cross-sectional diameters of ~50 μm were used for the ablation experiments. The objective of these mass spectral measurements was to investigate the possibility for using laser ablation mass spectroscopy to perform isotopic analyses on individual particles in the ion trap.

RESULTS AND DISCUSSION

The mass spectrum shown in Figure 2 is a composite of results obtained from two trimethylphenylammonium chloride coated silicon carbide particles, each irradiated with a single 10 ns pulse from the Nd:YAG laser. Due to the characteristics of the ITD electronics, the full mass range of ions ablated from one particle with one laser pulse cannot be covered with a single mass scan of the ion trap. In this case, an m/z scan from 20 to 99 was taken for one particle and from 100 to 160 for a second particle. The consecutive m/z scans were then combined to provide the mass range displayed. The peak intensities are expressed as the digitized values of an integrated analog voltage which is proportional to the output of the electron multiplier detector. The parent cation for trimethylphenylammonium chloride, $(CH_3)_3(C_6H_5)N^+$, is observed at m/z 136. The loss of a methane molecule accounts for the peak at m/z 120. The low mass peaks at m/z 23 and 39 are due to impurities of sodium and potassium, respectively, which seem to be omnipresent. The m/z values obtained in the manner described above with the ITD are reproducible from particle to particle, but the relative intensities are not because of the variables involved with each laser desorption, as described later. The more recent Finnigan MAT ITMS electronic ion trap controller provides for single scans from m/z 20 to 650 and will allow the acquisition of the true relative intensities of all of the ions from one particle with one laser pulse.

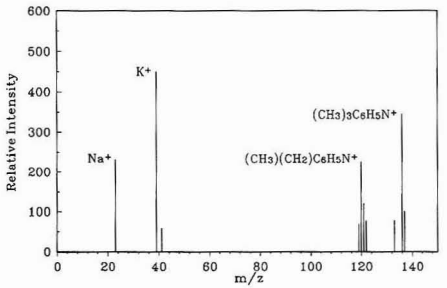

Figure 2. Quadrupole ion trap laser desorption mass spectrum of trimethylphenylammonium chloride adsorbed on silicon carbide particles.

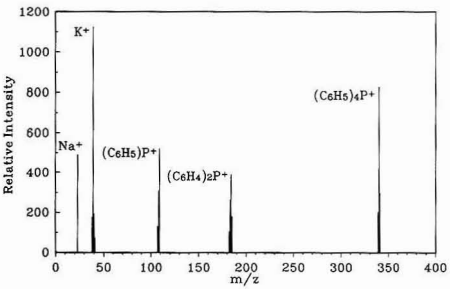

Figure 3. Quadrupole ion trap laser desorption mass spectrum of tetraphenylphosphonium bromide adsorbed on silicon carbide particles.

The most satisfactory spectra for the coated particles were acquired with pulse energies of about 2 mJ (10^9 W/cm^2). Higher pulse energies overloaded the ion trap and resulted in a decrease in the quality of the mass spectra. This is apparently due to space charge effects.

The mass spectrum shown in Figure 3 is a composite of results from three tetraphenylphosphonium bromide coated silicon carbide particles obtained from m/z scans of 20–99, 100–249, and 250–400. The parent cation, $(C_6H_5)_4P^+$, is observed at m/z 339. Peaks are also observed that correspond

(18) Stafford, G. C.; Kelly, P. E.; Syka, J. E. P.; Reynolds, W. E.; Todd, J. F. J. *Int. J. Mass Spectrom. Ion Processes* **1984**, *60*, 85.

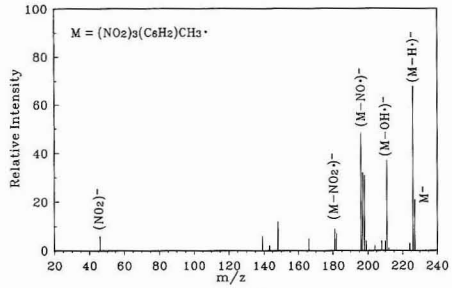

Figure 4. Quadrupole ion trap laser desorption mass spectrum of 2,4,6-trinitrotoluene adsorbed on silicon carbide particles.

to the loss of two benzene units at m/z 183 and the loss of three phenyl groups at m/z 108. The loss of a single phenyl group results in an odd electron ion and is occasionally observed in low abundance. The loss of two benzene groups instead of two phenyl groups was confirmed by secondary ion mass spectrometric analysis of the coated silicon carbide particles. The low mass peaks are again due to sodium and potassium.

The mass spectrum shown in Figure 4 is a composite of results from two 2,4,6-trinitrotoluene coated silicon carbide particles obtained from m/z scans of 20–99 and 100–240. The parent molecular anion, $(NO_2)_3(C_6H_2)CH_3^{\bullet -}$, is observed at m/z 227. Entity losses from the parent anion correspond to the loss of a $H^\bullet$ at m/z 226, $OH^\bullet$ at m/z 210, $NO^\bullet$ at m/z 197, and $NO_2^\bullet$ at m/z 181. The NO_2^- anion is observed at m/z 46.

To obtain an estimate for the detection limit of tetraphenylphosphonium bromide, experiments were performed with particle samples prepared as described previously with decreasing amounts of the salt until mass analysis of the particles no longer detected the parent ion peak. It is difficult to establish the accuracy of the value obtained for the detection limit. This is due to the combined uncertainties of the amount of material that is adsorbed on a particular particle, the uniformity of the adsorption, the permanence of the adsorbed layer prior to analysis, the size and shape of the particle, the rotational position of the particle when it is struck by the laser pulse, the intensity of the laser pulse, and the position of the particle within the intensity profile of the pulse. The particles that we use have different sizes and angular shapes, and the particular surface of the particle that happens to be facing the oncoming laser pulse will be some unknown fraction of the total surface of the particle. In light of these qualifications, a conservative estimate of 0.7 fm per particle was made for the detection limit. The estimate assumes that all of the particles were 112 μm diameter spheres and that all of a 0.3 nm sample of tetraphenylphosphonium bromide was adsorbed with equal proportions on each of the estimated 0.4×10^6 particles of the 1 g sample.

The 0.7 fm per particle detection limit is smaller by 4 orders of magnitude compared to earlier work for similar species evaporated onto a probe inserted up to the minimum radius of the ring electrode.[15] It is equivalent to more recent results reported for biological molecules using a probe and matrix-assisted laser desorption (MALD).[19] It is interesting to speculate on possible improvements in the sensitivity of MALD experiments by applying the technique to particles laser sampled at the center of the trap.

We believe that further improvement in the sensitivity for particle analysis is possible. Our detection limit represents about 10^9 molecules per particle. The laser beam should easily illuminate 10^8 of these molecules. We are detecting, however, only about 100 ions at this level of loading on the particle. We have shown in earlier work that ions generated by resonance enhanced multiphoton ionization of gas phase species can be trapped and mass analyzed with a 5–50% efficiency.[20] For 100 ions detected, this represents 2000–200 ions produced, respectively. The 5–6 orders of magnitude difference between the number of molecules on the particle illuminated by the laser beam and the number of ions produced must, therefore, be explained by some combination of desorption, ionization, and trapping efficiencies. It has been concluded in earlier work that thermal ionization of quaternary ammonium salts is a qualitatively efficient soft ionization process.[21] It is possible in the current work that the trapping efficiency is adversely affected by the presence of the particle in the trap causing possible perturbation of the trapping field. We are exploring further the significance of the various efficiencies involved and the implication of the particle's presence within the trap confines for some portion of the trapping period.

The mass spectra presented for salts desorbed from falling particles are representative of the better spectra observed and compare favorably with the spectra obtained for the probe mounted samples[15,16] and secondary ion mass spectroscopy data for the same particles. Spectra of this quality are observed with about 50% of the particles that are hit with the Nd:YAG laser. The other 50% of the experiments are either of low ion yield due to poor overlap of the Nd:YAG laser beam with the particle or of too high an ion yield, which overloads the ion trap and results in poor mass resolution from space charge effects.

We have also shown that isotope ratios can be estimated from single particle, single laser shot measurements. A spectrum for a $\sim$50 μm nickel particle irradiated with a 10 ns pulse from the Nd:YAG laser is shown in Figure 5. The experimental isotope intensities (solid lines) for nickel and potassium are compared to the expected intensities (broken lines) obtained from the product of the total experimental count for each metal ion and the percent natural abundance for each isotope.[22] A summary of the results for the isotopic analyses of 36 nickel particles is given in Table 1. Although the experimental average percent abundances found are reasonably close to the accepted values, it would be desirable to determine if the experimental conditions could be adjusted in some way to produce better statistics.

CONCLUSIONS

We have demonstrated laser desorption mass spectroscopy for particles in an ion trap for both positive and negative ions.

(19) Chambers, D. M.; Goeringer, D. E.; McLuckey, S. A.; Glish, G. L. *Anal. Chem.* **1993**, *65*, 14.
(20) Goeringer, D. E.; Whitten, W. B.; Ramsey, J. M. *Int. J. Mass Spectrom. Ion Processes* **1991**, *106*, 175.
(21) Glish, G. L.; Smith, D. H. *Int. J. Mass Spectrom. Ion Phys.* **1983**, *50*, 143.
(22) De Bievre, P.; Taylor, P. D. P. *Int. J. Mass Spectrom. Ion Processses* **1993**, *123*, 149.

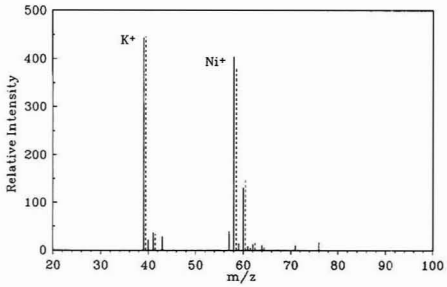

Figure 5. Isotope intensities for potassium 39 and 41 and nickel 58, 60, 61, 62, and 64 ablated from a nickel particle. Natural abundance, - - -; experimental, —.

It has also been shown that isotopic analysis of particles is possible by laser ablation mass spectroscopy in an ion trap. Improvements in the current apparatus promise to yield higher sensitivities for materials on the surface of particles. Combining particle levitation with ion trapping may allow multiple desorption experiments to be performed on a single particle and thus permit signal averaging. We have developed a laser desorption mass spectroscopy system for the analysis of single levitated particles in the quadrupole ion trap. Spectra have been obtained for single laser shot desorption and ionization. The results of this work will be described in a later paper.

Table 1. Nickel Isotope Analysis Summary

isotope	natural abundance, %	abundance found, %	standard deviation
58	68.1	68.7	4.4
60	26.2	25.3	3.0
61	1.1	1.8	2.0
62	3.6	3.5	1.1
64	0.9	0.7	0.6

ACKNOWLEDGMENT

The authors express their appreciation to W. H. Christie and T. M. Rosseel for obtaining SIMS data on the particles investigated, to P. J. Todd for interpretation of some of the mass spectra, and to G. L. Glish and D. D. Goeringer for suggesting and providing the quaternary salts and the trinitrotoluene.

Received for review April 7, 1994. Accepted July 6, 1994.®

® Abstract published in *Advance ACS Abstracts,* September 1, 1994.

Anal. Chem. **1994,** *66,* 3436–3446

Improvement in Detection Limits for the Determination of Paralytic Shellfish Poisoning Toxins in Shellfish Tissues Using Capillary Electrophoresis/Electrospray Mass Spectrometry and Discontinuous Buffer Systems

S. J. Locke and P. Thibault*

Institute for Marine Biosciences, National Research Council, 1411 Oxford Street, Halifax, Nova Scotia, Canada B3H 3Z1

The application of on-column sample preconcentration with capillary isotachophoresis (CITP) and discontinuous buffer systems prior to CZE separation has been investigated for the analysis of paralytic shellfish poisoning (PSP) toxins. A judicious choice of leading and terminating electrolytes for the preconcentration step has provided an improvement of the concentration detection limit of at least 2 orders of magnitude over that obtainable using the conventional CZE format. Such improvements in sample loadings now enable identification and quantitation of PSP toxins present in dinoflagellate and shellfish extracts using capillary electrophoresis. This preconcentration technique was found to be entirely compatible with electrospray mass spectrometry (ESMS) and permitted the analysis of scallop extracts containing submicromolar levels of PSP toxins. In situations where higher levels of selectivity are required for unambiguous identification of individual PSP toxins, CITP/CZE was combined with tandem mass spectrometry. The ease of operation, flexibility, selectivity, and short analysis time of CITP/CZE/ESMS make this technique an attractive method for the monitoring of PSP toxins.

Paralytic shellfish poisoning (PSP) is caused by a group of related toxins produced by marine dinoflagellates, most of which are members of the genus *Alexandrium*.[1] When shellfish such as scallops and clams feed on these dinoflagellates, PSP toxins accumulate mostly in the digestive glands of the filter-feeding organisms without causing any apparent harm to the shellfish. However, this group of toxins represents some of the most potent biological poisons known to man (LD_{50}, 6–40 $\mu g/kg$[2,3]), and consumption of contaminated shellfish results in a variety of neurological symptoms that can lead to death, depending on the toxin levels.

Toxins associated with PSP such as saxitoxin (STX), neosaxitoxin (NEO) and the gonyautoxins (GTXs) are characterized by a five-membered ring fused on a perhydropurine skeleton[1] (Figure 1). At present, the official analytical procedure for detecting shellfish toxins responsible for PSP is the mouse bioassay.[3,4] Although this method provides adequate sensitivity for detection of "total PSP toxin content" in shellfish extracts (0.8 ppm in shellfish meat[5]), its narrow dynamic range, its inherent variability, and the social pressure to ban animal bioassays are presently increasing the demand for alternative methods of analysis. Over the past decade numerous instrumental and immunological procedures have been investigated for the detection of PSP toxins. One of the most attractive techniques developed thus far involves separation by liquid chromatography (LC) and conversion of the PSP toxins into fluorescent derivatives using a postcolumn oxidation procedure.[6] Recently, an alternative LC technique was reported,[7–9] involving precolumn oxidation of the toxins followed by reversed-phase gradient elution and fluorescence detection of the oxidized products. The latter technique provides remarkable sensitivity (detection limit of 0.3 ng/mL for STX[9]) and can be applied for screening analysis of PSP toxins in contaminated shellfish extracts. In spite of these remarkable advances, some of the drawbacks of the latter technique[7–9] come from the variability of the fluorescence yields associated with the formation of the oxidation products and the conversion of different PSP toxins into common fluorescent derivatives, thus preventing unambiguous determination of toxin profiles. Furthermore, identification of complex biological extracts of novel toxins or of oxidation products with low fluorescent yields can be difficult. Sensitive and selective instrumental methods enabling identification of native toxins would thus be preferable.

The development of analytical methods for native PSP toxins has provided a significant challenge due to the highly polar nature of these compounds and their lack of a useful chromophore for sensitive UV absorption or fluorescence detection. Recently capillary zone electrophoresis (CZE) methods combined with either UV[10] or mass spectral detection[11–13] were described for the analysis of native PSP

(1) Shimizu, Y. In *Handbook of Natural Toxins*; Tu, T., Ed.; Dekker, M.: New York, 1988; Vol. 3, pp 63–85.
(2) Carmichael, W. W. In *Advances in Botanical Research*; Callow, E. A., Ed.; Academic: London, 1986; Vol. 12, pp 47–101.
(3) *Official Methods of Analysis*, 14th ed.; Association of Official Analytical Chemists: Arlington, VA, 1984; section 18.086–18.092.
(4) *Recommended Procedures for Examination of Sea Water and Shellfish*, 4th ed.; American Public Health Association: New York, 1970; pp 61.
(5) Boyer, G. L.; Fix-Wichmann, C.; Mosser, J.; Schantz, E. J.; Schnoes, H. K. In *Toxic Dinoflagellate Blooms*; Taylor, D. L., Seliger, H. H., Eds.; Elsevier: Amsterdam, The Netherlands, 1979; pp 373–376.
(6) Sullivan, J. J.; Iwaoka, W. T. *J. Assoc. Off. Anal. Chem.* **1983,** *66,* 297–303.
(7) Lawrence, J. F.; Menard, C.; Charbonneau, C. F., Hall S. *J. Assoc. Off. Anal. Chem.* **1991,** *74,* 404–409.
(8) Lawrence, J. F.; Menard, C. *J. Assoc. Off. Anal. Chem.* **1991,** *74,* 1006–1012.
(9) Janecek, M.; Quilliam, M. A.; Lawrence, J. F. *J. Chromatogr.* **1993,** *644,* 321–331.
(10) Thibault, P.; Pleasance, S.; Laycock, M. V. *J. Chromatogr.* **1991,** *542,* 483–501.
(11) Pleasance, S.; Thibault, P.; Kelly, J. F. *J. Chromatogr.* **1992,** *591,* 325–339.
(12) Pleasance, S.; Ayer, S. W.; Laycock, M. V.; Thibault, P. *Rapid Commun. Mass Spectrom.* **1992,** *6,* 14–24.

0003-2700/94/0366-3436$04.50/0
Published 1994 by the American Chemical Society

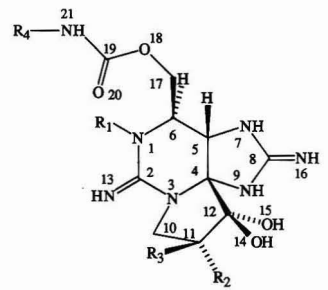

R_1	R_2	R_3	R_4	Toxin	Molecular mass (Da)
H	H	H	H	STX	299
H	H	H	SO_3H	B_1	379
H	OSO_3H	H	H	GTX_2	395
H	H	OSO_3H	H	GTX_3	395
H	OSO_3H	H	SO_3H	C_1	475
H	H	OSO_3H	SO_3H	C_2	475
OH	H	H	H	NEO	315
OH	H	H	SO_3H	B_2	395
OH	OSO_3H	H	H	GTX_1	411
OH	H	OSO_3H	H	GTX_4	411
OH	OSO_3H	H	SO_3H	C_3	491
OH	H	OSO_3H	SO_3H	C_4	491

Figure 1. Structures and molecular masses of the major toxins associated with paralytic shellfish poisoning.

toxins in extracts from toxic dinoflagellates. The presence of readily ionizable functionalities makes these compounds ideal candidates not only for separation techniques based on ionic mobilities in aqueous buffers but also for mass spectral ionization techniques such as electrospray. The high resolution capability of CZE provides high separation efficiencies for PSP toxins ($N > 150\,000$) and enables separation of closely related isomers such as the epimeric GTXs.[11,13] In order to achieve such a high resolution, the widths of the analyte zones have to be much smaller than the width attributed to diffusional processes taking place during the separation. As a result of these constraints, injection sizes are usually confined to less than 2% of the capillary volume in order to maintain high separation efficiencies. Although the mass detection limit thus achieved is in the low picogram level using either CZE/UV[10] or CZE/MS,[11] the small injection volume amenable to CZE only provides concentration detection limits in the order of 3–10 μM (1–4 μg/mL) for most PSP toxins. When translated into weight equivalent of shellfish tissue, this concentration detection limit represents 1–4 ppm of a typical extract obtained through the extraction procedure described by the Association of Official Analytical Chemists (AOAC).[3] Consequently, the CZE technique is of limited practical value for the monitoring of toxins in shellfish extracts at concentrations close to the regulatory level.

Such difficulties in obtaining submicromolar detection limits for underivatized analytes using a conventional CZE format are not atypical, and various approaches using improved detection systems or enhanced sample loadings have been proposed to alleviate this problem.[14–18] In the former case, enhancement in zone detectability is achieved using improved UV detector cell designs and extending the optical path length of the detector flow cell.[14] Investigations using an optimized Z-cell with a path length of 3 mm have provided a 5–10-fold increase in sensitivity for STX, NEO, and $GTX_{2,3}$ compared to that using the conventional configuration.[19] However, more substantial improvements in detection limits can be obtained using on-column analyte concentration. Various strategies including sample stacking,[16–18] field amplification,[15,20] capillary isotachophoresis (CITP),[21–23] and chromatographic concentration[24] have been described, and this subject was reviewed recently.[14]

One of the main objectives of the present study was to develop simple preconcentration techniques compatible with the CZE format that permit the injection of larger sample volumes of PSP toxin extracts without degradation of separation performance. Such techniques should also be compatible with the use of a mass spectrometric detection system in order to provide the selectivity and sensitivity required for unambiguous identification of trace levels of PSP toxins in complex biological extracts. Previous investigations have reported the successful coupling of CITP to CZE with electrospray mass spectrometry (ESMS) by use of either a coupled column system[25] or a single capillary with a discontinuous buffer system.[26] The applicability of such techniques has been demonstrated for the analysis of anthracyclines[25] and proteins.[26] When compared to CZE/ESMS, such CITP preconcentration procedures have shown an improvement in

(13) Pleasance, S.; Thibault, P. In *Capillary Electrophoresis Theory and Practice*; Camillieri, P., Ed.; CRC Press: Boca Raton, FL, 1993; pp 484–487.
(14) Albin, M.; Grossman, P. D.; Moring, S. E. *Anal. Chem.* **1993**, *65*, 489A–497A.
(15) Chien, R. L.; Burgi, D. S. *Anal. Chem.* **1992**, *64*, 1046–1050.
(16) Schwer, C.; Lottspeich, F. *J. Chromatogr.* **1992**, *623*, 345–355.
(17) Gebauer, P.; Thormann, W.; Bocek, P. *J. Chromatogr.* **1992**, *608*, 47–57.
(18) Aebersold, R.; Morrison, H. D. *J. Chromatogr.* **1990**, *516*, 79–88.
(19) Moring, S. E.; Pairaud, C.; Albin, M.; Thibault, P.; Locke, S. J.; Tindall, G. W. *Am. Lab.* **1993**, *11*, 32–36.
(20) Chien, R. L.; Burgi, D. S. *Anal. Chem.* **1992**, *64*, 489A–496A.
(21) Foret, F.; Sustacek, V.; Bocek, P. *J. Microcolumn Sep.* **1990**, *2*, 299–303.
(22) Stegehuis, D. S.; Irth, H.; Tjaden, U. R.; van der Greef, J. *J. Chromatogr.* **1991**, *538*, 393–402.
(23) Foret, F.; Szoko, E.; Karger, B. L. *J. Chromatogr.* **1992**, *608*, 3–12.
(24) Debets, A. J. J.; Mazereew, M.; Voogt, W. H.; van Iperen, D. J.; Lingeman, H.; Hupe, K.-P.; Brinkman, U. A. T. *J. Chromatogr.* **1992**, *608*, 151–158.
(25) Tinke, A. P.; Reinhoud, N. J.; Niessen, W. M. A.; Tjaden, U. R.; van der Greef, J. *Rapid Commun. Mass Spectrom.* **1992**, *6*, 560–563.
(26) Thompson, T. J.; Foret, F.; Vouros, P.; Karger, B. L. *Anal. Chem.* **1993**, *65*, 900–906.

concentration detection limits of at least 2 orders of magnitude.[25,26]

The present study reports results on the use of CITP/CZE, with both UV and mass spectrometric detection, for the analysis of PSP toxins in shellfish tissues. Different buffer systems were investigated with respect to their suitability as separation buffers and to their compatibility with mass spectrometric detection based on electrospray ionization. The judicious choice of electrolytes has decreased the concentration detection limits of PSP toxins to the low nanomolar range, thus making this technique an attractive option for screening suspected contaminated samples. The combination of this CITP preconcentration procedure with ESMS has proved to be particularly well suited to analysis of trace levels of toxins in complex scallop extracts, with minimal cleanup requirements. The improvement in sample loadings has also permitted unambiguous identification of PSP toxins using full mass scan acquisition and tandem mass spectrometric analyses.

EXPERIMENTAL SECTION

Preparation of PSP Toxins. Samples of STX, NEO, and GTX_{1-4} were purified from cultured algal cells of *Alexandrium excavatum* and *Alexandrium minutum* according to a procedure described earlier.[27] All toxins were dissolved in 0.1 M acetic acid. These toxins can also be obtained through the Marine Analytical Chemistry Standards Program (Institute for Marine Biosciences, Halifax, NS, Canada) as individual calibration solutions. Saxitoxinol (STXol) was prepared by mild reduction of STX in sodium borohydride to produce the 12-deoxysaxitoxin.[28] Decarbamoyl STX (dc-STX) was produced by heating a solution of saxitoxin in 6 N HCl in a sealed, evacuated glass ampule for 3 h at 110 °C.[27] The solution was dried in a vacuum desiccator, redissolved in 0.1 M acetic acid, and passed through a LC-18 Sep Pak extraction cartridge (Waters, Milford, MA).

Biological Extracts. Homogenized scallop liver tissue samples (15 g) were extracted at room temperature in 15 mL of 0.1 M acetic acid and centrifuged at 10000*g* for 20 min. The supernatant was filtered using a 0.22 μm nylon membrane (Millipore, Bedford, MA), 0.5 mL of the filtrate was passed through a reversed phase LC-18 octadecylsilica solid phase extraction cartridge (Waters) and eluted with 1 mL of 0.1 M acetic acid. The cartridges have been preconditioned with 2 mL each of methanol, water, and 0.1 M acetic acid.

Capillary Electrophoresis. All experiments were performed using a Beckman P/ACE 2100 system (Beckman Instruments, Fullerton, CA). Uncoated fused silica columns were obtained from Polymicro Technologies (Phoenix, AZ). Unless otherwise specified, dimensions were typically 75 or 50 μm i.d., 360 μm o.d. columns, and 97 cm length (90 cm to UV detector). The inner wall of the capillary surface was coated with linear polyacrylamide[29] to eliminate the electroosmotic flow within the capillary. Separations were conducted in constant-voltage mode by applying +30 kV at the injector end of the capillary. Samples were introduced by pressurizing the vial with either low (0.5 psi) or high (20 psi) pressure injection. The volume of sample introduced into the capillary was regularly measured by determining the time taken by the sample to reach the detector under continuous pressure. Separations using UV detection were monitored at 200 nm. Unless otherwise specified, the CZE background electrolyte (BGE), which also acted as the leading electrolyte, was 35 mM morpholine in water adjusted to pH 5.0 with formic acid. The CITP terminating electrolyte was 10 mM formic acid. All buffer chemicals were purchased from Sigma Chemical Co., St. Louis, MO.

Mass Spectrometer and Interface. All mass spectrometric experiments were performed using a Perkin-Elmer SCIEX API/III$^+$ triple quadrupole mass spectrometer (Thornhill, ON, Canada) equipped with an atmospheric pressure ionization (API) source operated in nebulizer-assisted electrospray (ion spray) mode. The interface was constructed from a fully articulated IonSpray source and is based on a coaxial column arrangement,[30] which was subsequently modified in our laboratory.[11] In this configuration two zero-dead-volume tees were mounted within the fully articulated interface, one providing the make-up solution (25% methanol, 0.2% formic acid) necessary for the maintenance of good electrical continuity during the electrophoretic separation, while the other is used to introduce the nebulizing gas. The electrospray needle (23 gauge stainless steel) was maintained at 5 kV and extended through both tees, thus allowing the introduction of the make-up solution. Electrical contact between this solution and the CZE electrolyte was made at the tip of the electrospray needle, thus eliminating postcolumn band broadening. The make-up solution was delivered by a syringe pump (Applied Biosystems, Santa Clara, CA) via a submicroliter injection valve (Valco) with a 0.1 μL loop. This injector provides a postcolumn means of rapidly optimizing the interface and calibrating the mass spectrometer.

CZE/ESMS and CITP/CZE/ESMS analyses used the same CE system as that described above except that the current monitoring function of the Beckman P/ACE 2100 instrument was disabled to permit normal CZE operation once the cathodic end of the capillary was connected to the CE-ESMS interface. In order to minimize the length of the CZE column, the cartridge was modified so that the capillary exited from the top left corner of the cartridge. Mass spectral acquisition was performed using dwell times of 3 ms per step of 1 Da in full mass scan mode or 100 ms per channel for selected ion monitoring experiments. Fragment ion spectra obtained from combined CITP/CZE/MS/MS analyses were achieved by selecting the appropriate precursor m/z values in the first quadrupole and using collisional activation with argon target gas in the second (rf-only) quadrupole equipped with a high-pressure collision cell (API/III+, SCIEX). Collision energies were typically 20 eV in the laboratory frame of reference, and collision gas thickness was 3.50×10^{15} atoms/cm^2 as measured from the Baratron pressure sensor upstream of the cell. Tandem mass spectra were acquired using dwell times of 3 ms per step of 0.5 Da in full-scan mode or 80 ms per channel monitored in multiple reaction monitoring (MRM) experiments. A MacIntosh Quadra 950 computer was used for instrument control, data acquisition, and data processing.

(27) Laycock, M. V.; Thibault, P.; Ayer, S. W.; Walter, J. A. *Nat. Toxins* **1994**, *2*, 175–183.
(28) Koehn, F. E.; Ghazorossian, V. E.; Schantz, E. J.; Schnoes, H. K.; Strong, F. M. *Bioorg. Chem.* **1981**, *10*, 412–428.
(29) Huang, M.; Vorkink, W. P.; Lee, M. L. *J. Microcolumn Sep.* **1992**, *4*, 233–238.
(30) Smith, R. D.; Olivares, J. A.; Nguyen, N.; Udseth, H. R. *Anal. Chem.* **1988**, *60*, 436–441.

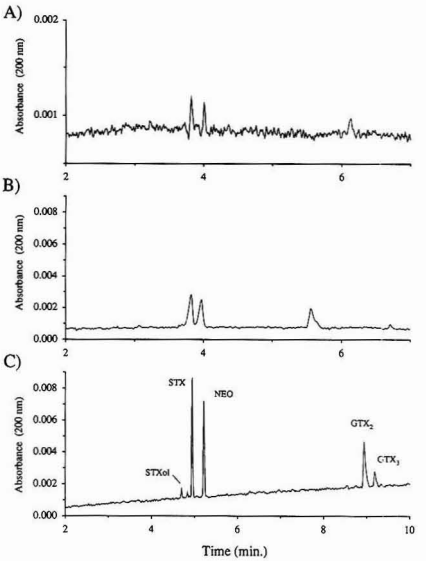

Figure 2. CZE/UV analysis of PSP standards. CZE separation corresponding to the injection of 20 (A) and 250 nL (B) of sample on a bare fused silica column. Combined CITP/CZE/UV separation (C) for the injection of 250 nL of PSP standards on a polyacrylamide-coated column. Conditions: PSP standard solution (dissolved in 0.1 M acetic acid) containing STX and NEO (1.4 μg/mL each), GTX_2 (1.2 μg/mL), and GTX_3 (0.29 μg/mL); terminating electrolyte, 10 mM formic acid (CITP duration, 30 s); background electrolyte, 35 mM morpholine pH 5 buffer; 20 kV; 57 cm × 50 μm i.d. column for all separations.

RESULTS AND DISCUSSION

Development of Separation Conditions for the Analysis of PSP Toxins by CITP/CZE/UV. Preliminary experiments using CZE/UV were performed using uncoated fused silica capillaries in order to determine the practical limits in terms of both sample loadings and separation efficiencies for the analysis of PSP toxin standards. These studies also offer a basis for comparison with subsequent experiments using the various preconcentration methods developed here. Analyses of PSP toxins using CZE/UV are shown in panels A and B of Figure 2 for the injection of 20 nL (2% of the capillary volume) and 250 nL (25% of the capillary volume), respectively, on a 50 μm i.d. × 57 cm column. A field strength of 260 V/cm was used for the separations shown in Figure 2. All PSP toxins were prepared in 0.1 M acetic acid at a concentration of 1.4 mg/mL for STX and NEO, 1.2 mg/mL for GTX_2, and 0.29 μg/mL for GTX_3. Dissolution of these toxins in acidic buffers is required to maintain their long-term stability. The lower sample loading (Figure 2A) represents the typical injection volume used in CZE. The signal-to-noise ratios (S/N) for this analysis (Figure 2A) are 3:1 for STX and NEO and 2:1 for GTX_2. Under such electrophoretic conditions, the concentration detection limit for most PSP toxins is approximately 1 μg/mL or 3 μM. Separation efficiencies, calculated from peak widths at half-height, were in excess of 80 000 theoretical plates for STX and NEO. In view of the fact that the PSP toxins are dissolved in a low ionic strength buffer, improved detectability can be obtained through sample stacking using larger injection volumes. Figure 2B illustrates this point where as much as 12 times more sample volume than that used to obtain Figure 2A was introduced into the capillary. Although a better S/N ratio was obtained for the 250 nL injection, substantial degradation of the resolution and separation efficiencies resulted from this larger sample loading. Preparation of the PSP toxins in higher acidity or lower ionic strength buffers did not significantly improve the overall performance of this separation. Plate counts calculated from STX and NEO peaks were of the order of 20 400, whereas the other two toxins were poorly resolved, as indicated by the broad peak at 5.5 min. In order to maintain adequate resolution of the PSP toxins, especially for GTX_2 and GTX_3, sample loadings had to be kept below 10% of the capillary volume (100 nL at most) in this particular capillary configuration. Improved detectability can also be obtained by using larger internal diameter columns although separation efficiencies are reduced substantially. Another problem associated with the use of uncoated fused silica columns is the variability of electroosmotic flow from one run to another. This in turn gives rise to irreproducible migration times and makes peak assignments difficult unless mobility markers are used. These variations are even more severe when samples containing high salt concentrations, such as those from biological extracts, are injected on the capillary. These adverse effects thus limit the practical use of such simple CZE/UV procedures for the analysis of PSP toxins in extracts of either shellfish tissues or plankton.

In order to obtain better performance in terms of both sample loadings and separation efficiencies, it is important to minimize dispersion effects associated with the injection of a large sample volume. Using a single-capillary arrangement, a large sample plug can be focused into very narrow analyte zones of high concentration by use of an isotachophoresis preconcentration step prior to the CZE separation. Stacking conditions leading to proper preconcentration necessitate the choice of an adequate electrolyte system, with due consideration to mobility and p*K* values of the constituents and lengths of the sample plug.[16-23]

The electrophoretic mobilities of STX and NEO in morpholine buffer, at pH values below 6, are 32×10^{-9} and 28×10^{-9} $m^2 V^{-1} s^{-1}$, respectively. Other sulfated PSP toxins such as GTXs have much smaller mobility values and range from 15×10^{-9} to 18×10^{-9} $m^2 V^{-1} s^{-1}$. An effective means of obtaining suitable isotachophoretic conditions is to select a leading electrolyte with a higher effective mobility than any of the sample ions. Preconcentration is achieved by using a terminating electrolyte of lower mobility than the sample components. However, when the counterion of the leading electrolyte is a weak acid, the migrating front of hydrogen ions can be used as a universal terminator.[23,31] Under such conditions, the highly mobile H^+ ions are slowed by recombination reactions taking place at the boundary with the leading electrolyte. Proper stacking conditions also require that a gradient of pH be established, ranging from high to low between the leading, sample, and terminating buffers. Once the ions have been stacked into sharp bands in order of their

(31) Bocek, P.; Deml, M.; Gebauer, P.; Dolnik, V. *Analytical Isotachophoresis*; Radola, B. J., Ed.; VCH: Weinheim, Germany, 1988; pp 177–202.

electrophoretic mobilities, the isotachophoresis step is halted and the terminator is changed such that sample ions can be separated by zone electrophoresis.

The selection of the leading electrolyte for CITP, which can also be used as background electrolyte (BGE) during the subsequent CZE separation, can be made by comparing the electrophoretic mobilities of the analytes with those found in published tables.[32] During the course of this study, different leading electrolytes, including β-alanine, triethylamine, and morpholine, were evaluated. Although all of these buffers had the desired characteristics required for them to act as both leading and background electrolytes, the choice was also motivated by considerations affecting the sensitivity for mass spectral detection. Suitable buffers for CZE separation must also be volatile and compatible with the electrospray processes taking place prior to mass spectrometric analysis. For reasons that will be outlined in the following section, morpholine appears to provide adequate characteristics as an electrolyte for the CITP/CZE separation while providing limited chemical noise in the mass spectrometric analysis.

The combined CITP/CZE/UV analysis of PSP toxins, with an injection volume (250 nL) identical with that used to obtain Figure 2B, is shown in Figure 2C. This analysis used 35 mM morpholine pH 5 as the leading electrolyte. Isotachophoresis was conducted on a polyacrylamide-coated capillary for 30 s, using 10 mM formic acid as terminating electrolyte. It is noteworthy that the use of discontinuous buffer system unavoidably gave rise to longer migration times, although the sample is stacked further along the capillary. This delay comes from the reduced electroosmotic flow, and from the period required for the pH gradient to dissolve and the electrophoretic mobilities to adjust before any destacking of the analyte bands can take place. As indicated in Figure 2C, significant improvements in CZE resolution, separation efficiencies, and signal detectability are obtained using a CITP preconcentration step when compared to a similar CZE separation performed using an uncoated column (Figure 2B). Separation efficiencies were usually in excess of 100 000 plates for all four toxins, with that for STX reaching 213 000 plates on this 57 cm length column.

The ability to manipulate a relatively large sample volume with enhanced resolution also facilitates the identification of minor toxin contaminants such as that observed at 4.7 min in Figure 2C. This peak was found to migrate at the same position as STXol obtained by the reduction of STX using sodium borohydride and conversion to its 12-deoxy derivative.[28] Further confirmation of this peak as STXol was obtained using CITP/CZE in combination with ESMS as described later. During the purification procedures leading to the preparation of PSP standards from a highly toxic strain of *A. excavatum*,[27] STXol was found to coelute with STX on preparative ion-exchange chromatography. The presence of STXol in these extracts was unexpected and suggests that this PSP toxin derivative can also be produced naturally by the dinoflagellate. Conversion of STXol to a fluorescent derivative using periodate oxidation was found to be relatively slow, thus resulting in low reaction yields and weak response in HPLC with postcolumn oxidation and fluorescence detection.[33] This poor conversion yield, coupled with the coelution of STXol with STX using reversed phase HPLC,[6] could account for the relatively few reports documenting its occurence in dinoflagellate or shellfish extracts.

For a given pH, the concentration of morpholine can have a significant influence on the peak widths and resolution. When the morpholine concentration was raised to 75 mM, plate counts were generally higher by 25% compared to those observed at a concentration of 35 mM. However, the improved peak resolution thus obtained for all PSP toxins resulted in migration times approximately 30% longer than those observed using the 35 mM buffer. Variation of pH of the BGE also resulted in variation of the separation performance. For a 20 mM morpholine buffer at pH 4, tailing and poor resolution of the PSP toxins was observed. Raising the pH to 6 provided sharper peaks except for NEO, which displayed an unusual peak broadening probably reflecting a change in its electrophoretic mobility since the buffer pH is approaching that of its first pK_a at 6.75.[34] Optimum separation conditions providing baseline resolution of all PSP toxins, including all four GTXs, were obtained using a 35 mM morpholine/formate buffer at pH 5.

Increases in the length of the preconcentration period, and in the acidity of the terminating electrolyte, also provided better separation efficiencies. However, both of these effects resulted in the introduction of larger quantities of H^+ ions into the column and thus in correspondingly longer destacking periods. It is noteworthy that, since the sample is dissolved in acetic acid, preconcentration can be effected without the use of a terminating electrolyte. The preconcentration CITP step was found necessary to improve the resolution of analytes of lower mobilities such as the GTXs. Separation of all PSP toxins, within 30 min on a 80 cm column, was achieved by using a stacking period of 1.5 min with a constant voltage of 30 kV and a 10 mM formic acid terminating electrolyte.

In order to determine the loading capacity of this mode of sample preconcentration, replicate injections were performed on a 50 μm i.d. × 80 cm polyacrylamide-coated column for different sample volumes (injection volume of 150–900 nL, or 10–60% of the capillary volume). For samples dissolved in 0.1 M acetic acid, separation efficiencies decreased progressively with the volume loaded on the column. For example, separation efficiencies observed for STX were in excess of 500 000 for injection volumes of less than 300 nL. However, plate counts rapidly declined to less than 200 000 for injections corresponding to more than 50% of the total capillary volume. The peak width of the injection band could be maintained with minimal loss of efficiency for injections of less than 450 nL or 30% of the total capillary volume.

The sample loading capacity and signal detectability can be improved further using larger diameter columns. On a 100 cm × 75 μm i.d. column, the injection of 2.2 μL (50% of the capillary volume) of a solution containing STX, NEO, and $GTX_{2,3}$, each at concentrations similar to those used in Figure 2, provided plate counts of 487 000, 380 000, 180 000, and 247 000, respectively. On-column CITP preconcentration has also been reported previously by Foret et al.[35] for the

(32) Pospichal, J.; Gebauer, P.; Bocek, P. *Chem. Rev.* **1989**, *89*, 419–430.

(33) Cembella, A.; Uher, T. J., unpublished results.

(34) Shimizu, Y.; Hsu, C.; Fallon, W. E.; Oshima, Y. *J. Am. Chem. Soc.* **1978**, *100*, 6791–6793.

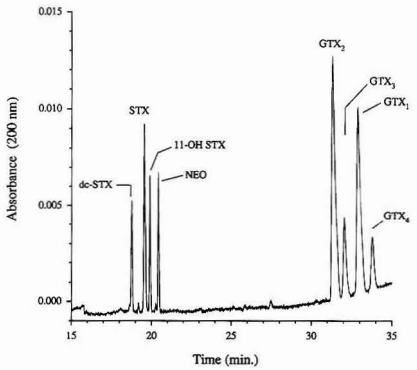

Figure 3. CITP/CZE/UV analysis of a mixture of eight PSP standards. Injection of 2.2 μL of a solution containing 500 ng/mL $GTX_{1,2}$ and 200 ng/mL for all other toxins. Experimental conditions as for Figure 2 except that a 107 cm × 75 μm i.d. coated column was used, CITP duration was 90 s, and applied voltage was 30 kV.

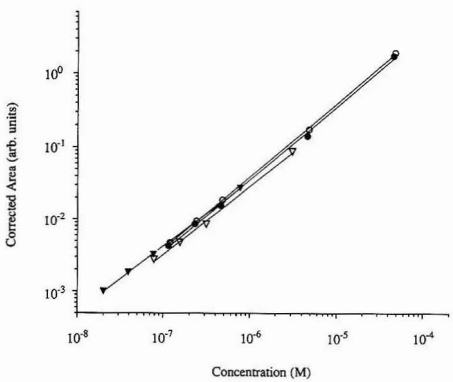

Figure 4. Calibration plots of concentration vs corrected peak areas for STX (open circles) $r^2 = 0.9999$, NEO (closed circles) $r^2 = 0.9994$, GTX_2 (open triangles) $r^2 = 0.9984$, and GTX_3 (closed triangles) $r^2 = 0.9998$. Separation conditions as for Figure 3.

separation of basic proteins using a sample volume of up to 50% of that of the 75 μm i.d. separation column. The present study indicated that smaller losses in separation efficiencies were generally obtained for a correspondingly larger sample loading when the 75 μm i.d. column was used as compared to that of a 50 μm i.d. column of similar length. The enhanced performance observed for the 75 μm i.d. capillary could possibly reflect the ease of preparing and adequately covering the surface of the larger diameter fused silica column with a linear polyacrylamide coating.

The CITP/CZE separation of a mixture of eight PSP standards, performed using a 107 cm × 75 μm i.d. column with 35 mM morpholine as leading electrolyte, is presented in Figure 3 for a 2.2 μL sample injection. With the exception of GTX_1 and GTX_2 for which the concentrations were 500 ng/mL, all other PSP toxins were present at a level of 200 ng/mL. Sulfated and nonsulfated PSP toxins appear as sharp bands migrating in two distinct groups. It is interesting to note that, in comparison with other nonsulfated toxins, the peak width of STX is unusually broad. In fact, a close inspection of this peak reveals a shoulder on the trailing edge of the STX peak. The extra component, migrating just after STX, is actually one of the two epimeric isomers of 11-OH STX. Similarly, the reduction of GTX_2 and GTX_3 to form their corresponding hydroxyl derivatives gives rise to two isomers (α and β) which can be separated from one another by CZE. Unfortunately the electrophoretic mobilities of STX and 11-OH STX (β) are too similar, which prevents their resolution under the present CZE conditions.

The dependence of peak area on sample concentration was examined next for a fixed injection volume of a mixture of STX, NEO, and $GTX_{2,3}$. Figure 4 shows typical calibration curves for these four PSP toxins. Corrected peak areas (peak area/migration time) are presented over the concentration range of 10^{-8}–10^{-4} M. Similar UV responses were obtained for all toxins after correction of the peak areas by their respective migration times. In all cases, good linearity with correlation coefficients $r^2 > 0.998$ was found over the concentration range examined. The concentration detection limits (S/N 3:1) were determined as 10 nM for STX and NEO and 20 nM for $GTX_{2,3}$. The limit of detection obtained using this CITP/CZE/UV technique represents an improvement of 300-fold compared to that using conventional CZE separation. At a concentration higher than 10 μM, baseline resolution of the GTX toxins could no longer be obtained, and this precludes any reliable quantitation beyond this point. In comparison, detection limits obtainable on the 50 μm i.d. column were found to be approximately 3 times higher than that for the 75 μm i.d. capillary. This reflects both the smaller optical path length and the fact that smaller sample volume can be injected on the 50 μm i.d. column. The ratio of column diameters would yield a difference of 1.5 in optical path length between the two capillaries, whereas a factor of 4 is expected from the sample loadings (0.5 and 2 μL injection for the 50 and 75 μm i.d. capillaries, respectively).

Reproducibilities of migration times and of peak areas obtainable by this CITP/CZE/UV method were investigated using a mixture of the four PSP toxin standards. Replicate injections ($n = 5$) of 100 ng/mL solutions yielded relative standard deviations (rsd) of corrected peak areas typically less than 5%. The reproducibility of migration times was better than 0.5% rsd for all toxins examined.

The application of this isotachophoresis preconcentration technique was evaluated for the analysis of a contaminated scallop extract. At present, the extraction procedure commonly used[3] in PSP toxin monitoring programs involves hydrolysis of the shellfish tissues with boiling 0.1 N HCl. This method converts the predominant C toxins into more potent toxins such as GTXs and STX, so that these severe hydrolysis conditions do not permit the acquisition of a native PSP toxin profile. A mild acid extraction procedure was thus developed to enable the identification of native PSP toxins in scallop homogenates. Less acidic extraction also minimizes the problems associated with longer analysis times in the CITP/CZE method, as described above. Alternatively, it is possible to dilute the extracts obtained from HCl hydrolysis prior to

(35) Foret, F.; Szoko, E.; Karger, B. L. *Electrophoresis* **1993**, *14*, 417–428.

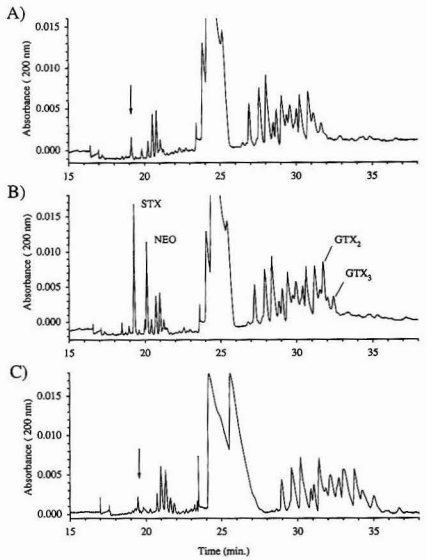

Figure 5. Analysis of a contaminated scallop liver extract using CITP/CZE/UV for the injection of 2.2 μL of a mild acid extract on a 107 cm × 75 μm i.d. coated column (A) and for the same sample spiked with 650 pg of STX, NEO, and $GTX_{2,3}$ (B). Injection of 490 nL of the scallop extract on a 107 cm × 50 μm i.d. coated column (C). Arrow indicates the STX peak in the native extract. Separation conditions as for Figure 3.

their analysis. Homogenized scallop liver tissues (15 g) were extracted with 15 mL of 0.1 M acetic acid, centrifuged, filtered, and subsequently cleaned up using C_{18} solid phase extraction cartridges.

The analysis of scallop liver tissues using CITP/CZE/UV is presented in Figure 5. The profile shown in Figure 5A correspond to a scallop extract diluted 20-fold with 0.1 M acetic acid. When the 75 μm i.d. column was used, dilution of the extract was necessary to improve the resolution and enable proper peak identification. STX, which migrates at 19.3 min under these electrophoretic conditions, is indicated by an arrow on Figure 5A. Unfortunately other PSP toxins such as the GTXs could not be unambiguously identified due to the presence of comigrating components. Confirmation of the peak identity was made by spiking known amounts of STX, NEO, and $GTX_{2,3}$ into the extract. Figure 5B shows the corresponding analysis when 650 pg of each of these four toxins was mixed with the sample plug. The concentration of STX found in this diluted extract was 52 ng/mL and corresponds to an equivalent of 1.4 ppm in the original scallop homogenate.

The analysis of biological extracts which contain a high concentration of salt often requires adjustment of the preconcentration conditions. Highly mobile alkali ions present in the extract form a leading zone during the isotachophoresis step and can influence the migration of the other analyte zones during the zone electrophoresis separation.[35] A high salt concentration can lead to sharp peaks with limited resolution as the sample zones migrate in the isotachophoresis stack. It is possible to improve the resolution by increasing the electric charge transported by the analyte ions by use of a higher BGE concentration. Unfortunately this also increases the separation current and can impose considerable limitations on instruments with no temperature regulation or on analyses conducted with mass spectrometric detection.

Undiluted extracts can be analyzed directly on the 75 μm i.d. column provided the sample loading is reduced to less than 500 nL, or 20% of the total capillary volume. Such analyses can also be performed using a smaller diameter column with an equivalent volume of sample. Figure 5C shows the separation of an undiluted scallop extract, using a 50 μm i.d. capillary and an injection of 490 nL of sample. STX is indicated by an arrow in Figure 5C and has a migration time comparable to that observed on Figure 5A. With the exception of late-migrating peaks, the resolution obtainable with the 50 μm column was similar to that achieved previously using the larger diameter column (Figure 5A). More importantly, the possibility of directly analyzing shellfish extracts with minimal sample treatment and without sacrifying the performance of the analysis are attractive features of this method. Smaller size columns also offer practical advantages when used in conjunction with mass spectrometry since lower associated currents and chemical background noise are generated during the separation.

Analysis of PSP Toxins in Shellfish Extracts by CITP/CZE/ESMS. From a practical point of view, the analysis of complex biological extracts using UV detection has limited capability for identification of targeted species since the presence of comigrating analytes often precludes unequivocal assignment. More sensitive, selective, and structurally informative detection methods are thus required for unambiguous confirmation of PSP toxins in shellfish or plankton extracts. To this end, the coupling of CZE to mass spectrometry provides advantageous features which offer the potential for detecting specific analytes using selected ion monitoring (SIM) and for identifying unknowns present in complex matrices by tandem mass spectrometry (MS/MS).

The coupling of the CITP/CZE technique with ESMS is not without its own difficulties, and judicious selection of electrolyte systems has to be made to avoid compromising the overall performance of the analysis. Suitable buffers, compatible with the operation of ESMS, must also carry relatively low currents, be sufficiently volatile to prevent any accumulation of residue on the orifice plate, and have low proton affinity to minimize the level of chemical background noise. During the study involving CITP/CZE with UV detection, buffers such as β-alanine, triethylamine, and morpholine all provided adequate electrophoretic characteristics as leading electrolyte and support buffer. However, the same buffers gave very different performances when used in conjunction with the mass spectrometer. Both triethylamine and β-alanine gave strong cluster ions in the range m/z 150–500, thereby reducing the sensitivity in both SIM and full mass scan acquisition. Furthermore, β-alanine was found to be of limited volatility as it forms a film on the orifice sampling cone after several column washes. Morpholine appears to offer the most accommodating properties and was used for all subsequent analyses.

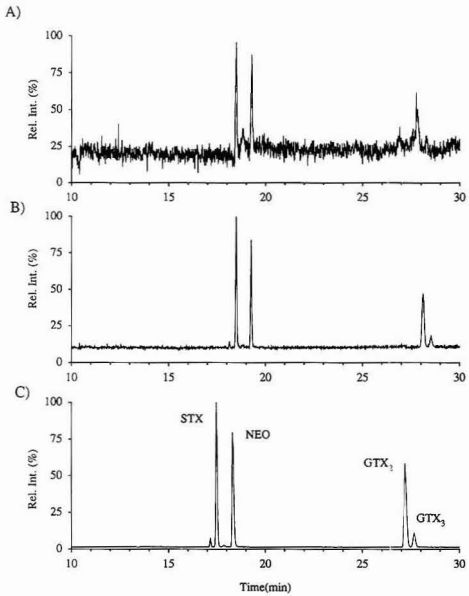

Figure 6. CITP/CZE/ESMS analysis of PSP toxin standards in SIM acquisition mode for a dilution series of a solution containing 1.4 μg/mL STX and NEO, 1.2 μg/mL GTX_2, and 0.29 μg/mL GTX_3. TIC profiles for $\sum MH^+$ ions at m/z 300, 316, and 396 for dilution of 1:100 (A), 1:10 (B), and neat solution (C). Separation conditions: Injection of 475 nL on a 95 cm × 50 μm i.d. coated capillary; terminating electrolyte, 10 mM formic acid (CITP duration, 90 s); BGE, 35 mM morpholine pH 5, sheath flow of 25% methanol/0.2% formic acid; 8 μL/min flow rate.

The sensitivity of the CITP/CZE/ESMS combination for the analysis of PSP toxins was first investigated using SIM and recording only the ions corresponding to the protonated molecules (MH^+) of each analyte. Figure 6 shows the total ion current (TIC) for the sum of all MH^+ obtained for a dilution series of a mixture of STX, NEO, and $GTX_{2,3}$. This analysis used an injection of 475 nL on a 95 cm × 50 μm i.d. column. The concentrations for the lowest level of this mixture of toxin standards (Figure 6A) correspond to 14, 14, 12, and 2.9 ng/mL of STX, NEO, GTX_2, and GTX_3, respectively. The limits of detection in SIM, with a S/N ratio of 3:1, were observed at a level of 16 nM for STX and NEO but at approximately 30 nM for $GTX_{2,3}$. Calibration curves obtained for serial dilutions of these toxins showed good linearity over 3 orders of magnitude from 15 nM to 30 μM, with correlation coefficient $r^2 \geq 0.998$. Deviation from linearity was however obtained for the highest concentration of STX and NEO, where 14 pmol was loaded on the column. Another interesting feature observed in Figure 6 is the maintenance of peak width over the entire concentration range. For example, the peak width at half-height for STX in Figure 6A is 4.5 s whereas a value of 5.2 s is obtained in Figure 6C. Degradation of the separation performance due to column overloading was not observed up to a concentration level of 1.4 μg/mL of any individual toxin. For a concentration of approximately 1.4 μg/mL of each toxin (Figure 6C), separation efficiencies of 219 000, 239 000, 209 000, and 215 000 were obtained for STX, NEO, GTX_2, and GTX_3, respectively. Bearing in mind the inherent variability in the preparation of different polyacrylamide-coated columns, these values compare well with those obtained previously using UV detection. This observation confirms that the coaxial capillary interface gives good separation performance with minimal postcolumn peak broadening.

Capillaries with internal diameters larger than 50 μm were also investigated in an attempt to increase the sample loading. On 75 and 100 μm i.d. columns, up to 2.2 and 3.9 μL (50% of the total volume), respectively, can be injected on the capillary while adequate resolution is maintained for a toxin solution of 500 ng/mL. When compared to the 50 μm i.d. column, these loadings are higher by a factor of 5–8 for the same length of capillary. Although lower detection limits would be expected using these larger columns, experiments performed using CITP/CZE/ESMS with either a 75 or a 100 μm i.d. capillary demonstrated that, under SIM acquisition, the lowest detection limit obtainable was 47 nM for STX. This value is approximately 3 times higher than that achieved previously with the smaller size column. Using the present configuration, the poorer performance obtained for the 75 and 100 μm i.d. capillaries is explicable by the higher separation currents associated with these columns. The fact that a larger proportion of the ionic species is derived from the buffer itself can suppress the analyte signal, as the background chemical noise is dominated by more intense cluster ions arising from ion–molecule reactions between morpholine and water. In view of the enhanced performance obtainable with the 50 μm i.d. column, this capillary size was preferred over the larger size columns for all CITP/CZE/MS studies, in spite of the occasional difficulties in preparing the polyacrylamide coating.

An example of mass spectra, obtained during the CITP/CZE/ESMS analysis of PSP standards, is presented in Figure 7. This analysis corresponds to the injection of a solution of approximately 200 ng/mL for GTX_2, 50 ng/mL for GTX_3, and 500 ng/mL for all other toxins. For this injection volume (475 nL), good S/N ratios are obtained for all toxins, as indicated in the extracted ion current profile corresponding to the sum of all protonated molecules (Figure 7A). The background-subtracted spectra for STX, 11-OH (β) STX, and GTX_2, are shown in Figure 7B–D, respectively. For the nonsulfated toxins, all spectra were dominated by a strong MH^+ ion signal, but the GTX toxins were also found to form adduct ions with morpholine $(MH+87)^+$. Under the present ionization conditions, protonated GTX toxins readily dissociate in the orifice/skimmer region of the mass spectrometer to form a fragment ion corresponding to the loss of sulfate from the protonated molecule, as indicated in Figure 7D. It is interesting to note that although STX and 11-OH (β) STX migrate closely to one another, no cross-talk was observed in their extracted mass spectra as shown in panels B and C of Figure 7.

Previous investigations conducted in our laboratory indicated that under the conventional CZE format the lowest concentration detection limits for STX with SIM and full-scan acquisition were 3 and 30 μM, respectively.[11,13] The present preconcentration technique has led to an improvement in detection limits of 2 orders of magnitude, for each of these two modes of acquisition. The capability of obtaining lower

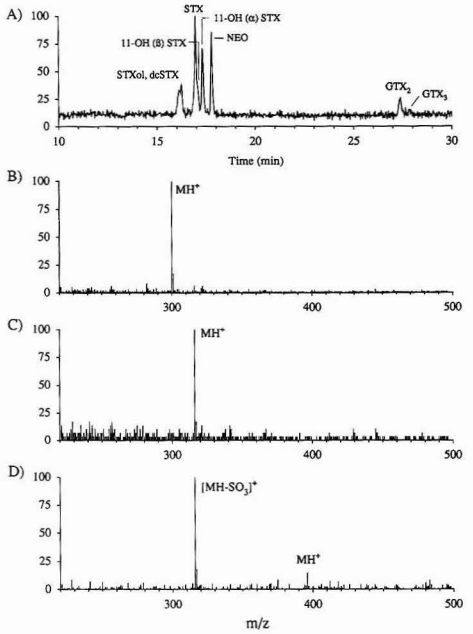

Figure 7. CITP/CZE/ESMS analysis of PSP toxin standards using full mass scan acquisition (m/z 220–500). Extracted ion current profile for $\sum MH^+$ ions at m/z 257, 284, 300, 316, and 396 (A). Background-subtracted mass spectra for the peaks at 16.9 (B), 17.0 (C), and 27.3 min (D). Separation conditions same as for Figure 6. PSP standards solution containing 200 ng/mL GTX_2, 50 ng/mL GTX_3, and 500 ng/mL for all other toxins.

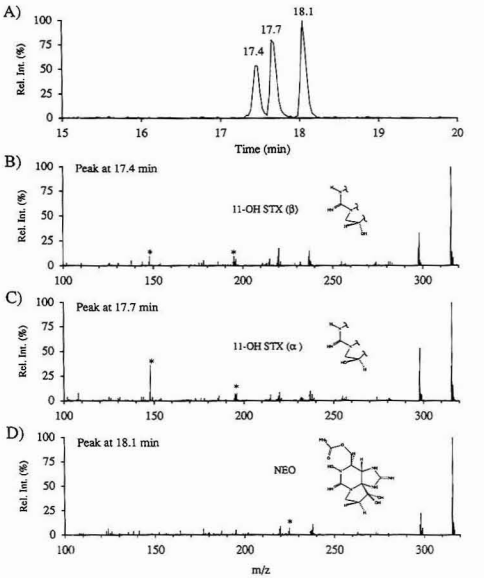

Figure 8. Product ion scan of m/z 316 using CITP/CZE/MS/MS. TIC profile for all fragment ion generated during the separation (A), extracted MS/MS spectra for peaks at 17.4 (B), 17.7 (C), and 18.1 min (D). Separation conditions same as for Figure 6 except that 475 nL of a standard solution containing 500 ng/mL of each toxin was used. Collisional activation was obtained using argon at a target gas thickness of 3.5×10^{15} atoms/cm^2 with collision energy of 20 eV (laboratory frame of reference).

concentration limits with either SIM or full mass scan acquisition now makes this technique more practical for the analysis of mollusc extracts. Furthermore, it is also possible to obtain structural information for low concentration levels of toxins using this separation technique combined with tandem mass spectrometry. This latter possibility was explored for the analysis of common PSP toxin standards. An example of a CITP/CZE/MS/MS analysis is shown in Figure 8 for NEO and two of its isomers, α and β 11-OH STX. This analysis was obtained for the injection of 475 nL of a solution of 500 ng/mL of each toxin. Since these three toxins migrate within less than 1 min of one another, the acquisition of all spectra in one run was only possible using a continuum mode. Despite the time constraints and the relatively low sample loading (750 fmol), it was possible to average four or five scans for each analyte and obtain intense fragment ion spectra for all three toxins as observed in Figure 8B–D. This mode of acquisition also permits the extraction of specific fragment ion profiles to enable identification of fragment ions characteristic of each isomer. As observed in panels B and C of Figure 8, the two 11-OH STX isomers gave almost superimposable MS/MS spectra. The only significant difference between these two spectra was the relative intensities of the fragment ions at m/z 148, 196, and 220. Characteristic fragment ions for the three MH^+ precursor ions (m/z 316) are indicated by an asterisk in Figure 8B–D. The MS/MS spectrum of NEO (Figure 8D) was similar to that of the 11-OH STX isomers with the exception of a characteristic fragment ion at m/z 225, which was virtually nonexistent for the other two isomers. This fragment ion possibly arises from the consecutive or concomitant losses of the C(17) side chain plus the hydroxyl group on N(1) (Figure 1). Such dissociation would lead to the formation of a conjugated double bond between N(1) and C(6), providing additional stability to the resultant fragment ion. However, in the case of the 11-OH STX, the carbamoyl side chain is stabilized through interaction with the hydroxyl group on C(11), in a fashion similar to that described for $GTX_{2,3}$,[12] thus preventing the formation of the m/z 225 ion.

A list of fragment ions and relative intensities for MS/MS spectra of toxin standards, obtained using CITP/CZE/MS/MS experiments similar to that described above, are listed in Table 1. The intent of the present study was to investigate the feasibility of using MS/MS at low concentration levels, and no rationalization of the fragment ions observed is provided here. Rather, this list of ions is meant to be used as a guide to selection of relevant fragment ions characteristic of a given analyte. The practical application of these structure-related ions lies in the possibility of using MS/MS in a MRM mode, where both sensitivity and selectivity are utilized in a nonmutually exclusive manner.

The real benefit of mass spectral detection comes from its unique selectivity at high sensitivity, a particular advantage

Table 1. Characteristic Fragment Ions (*m/z* Values) Observed in CITP/CZE/MS/MS Experiments

toxins	MH^+	major fragment ions and relative intensitie[a]
dc-STX	257	126 (100), 138 (57), 156 (43), 180 (57), 198 (45), 222 (75), 239 (95)
STX	300	144 (27), 186 (36), 204 (73), 221 (55), 240 (18), 258 (18), 282 (100)
11-OH STX (α)	316	148 (55), 196 (20), 220 (15), 237 (13), 298 (100)
11-OH STX (β)	316	148 (42), 196 (33), 220 (67), 237 (50), 298 (100)
NEO	316	187 (22), 220 (30), 225 (26), 238 (35), 298 (100)
GTX_1	412	314 (8), 332 (100)
GTX_2	396	196 (2), 220 (2), 237 (4), 298 (10), 316 (100)
GTX_3	396	196 (5), 220 (3), 237 (3), 298 (100), 316 (12)
GTX_4	412	314 (100), 332 (23), 394 (8)
B_1	380	300 (100), 282 (12), 221 (10)

[a] Numbers in parentheses indicate intensity relative to the most abundant fragment ion (indicated as 100%).

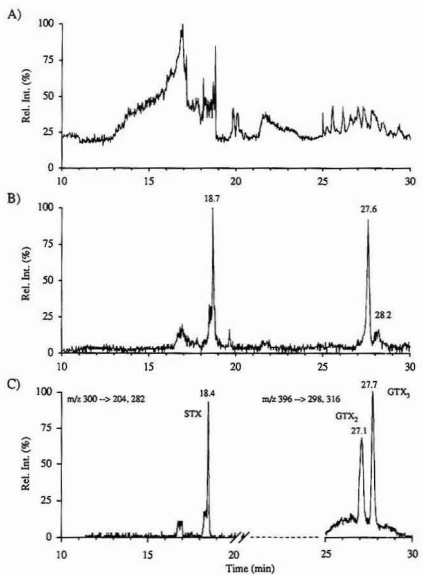

Figure 9. Analysis of a contaminated scallop liver extract using CITP/CZE/ESMS. TIC profile for *m/z* 220–500 obtained under full mass scan acquisition (A); extracted ion current profile for $\sum MH^+$ ions at *m/z* 300, 316, and 396 (B) extracted from the analysis shown in (A). CITP/CZE/MS/MS using MRM acquisition mode (C), for the reaction channels *m/z* 300 → 204, 282 (10–20 min) and *m/z* 396 → 298, 316 (25–30 min). Experimental conditions same as for Figure 8.

that becomes apparent when extracts from biological sources are analyzed. An example of such an application is presented in Figure 9 for the analysis of a contaminated scallop liver extract obtained from the same sample as that used to obtain Figure 5. The TIC corresponding to the full mass scan analysis (*m/z* 220–500) is presented in Figure 9A. With the exception of the large UV-transparent salt fronts observed at 13–17 min, this profile is qualitatively similar to that presented in Figure 5C. Another striking difference was also noted for several unidentified peaks migrating at 22–24 min which gave a much weaker response when compared to that of the same peaks at 24–27 min in Figure 5C.

The summed ion current profile for ions at *m/z* 300, 316, and 396 extracted from the same data set is shown in Figure 9B. In contrast to the same analysis obtained with UV detection, Figure 9B clearly shows characteristic peaks at 18.7, 19.7, 27.6, and 28.2 min corresponding to STX, NEO, GTX_2, and GTX_3, respectively. Mass spectra extracted for each of these peaks clearly showed MH^+ and fragment ions characteristic of each of these four toxins including NEO, which was present at a level of only 120 ng/mL in this extract. Unfortunately it was not possible to detect any C toxins under the present conditions since these compounds would not be positively charged at this pH. It is noteworthy that no significant signal was observed for any of the other commonly encountered toxins such as $B_{1,2}$ or $GTX_{1,4}$. This extract was obtained from contaminated scallops harvested on the northeastern coast of Canada, where blooms of toxic strains of *A. excavatum* are often encountered. The toxin profiles associated with these dinoflagellates typically contain a high proportion of STX, $GTX_{2,3}$, and $C_{1,2}$,[36] and results obtained in the present study are consistent with these earlier observations.

Quantitative analyses (n = 3), performed using SIM acquisition mode, have indicated that STX, NEO, GTX_2, and GTX_3 were present at concentration levels of 0.52 ± 0.01, 0.12 ± 0.01, 0.82 ± 0.01, and 0.30 ± 0.03 μg/mL, respectively, in this scallop extract. When converted in terms of weight equivalent of shellfish tissues, these concentrations represent 1.04 ± 0.02, 0.12 ± 0.01, 0.82 ± 0.01, and 0.60 ± 0.06 ppm, respectively. It is noteworthy that the concentration of STX obtained in this experiment agrees remarkably well with that calculated from the UV analysis (Figure 5), described in the previous section.

The potential of tandem mass spectrometry was also explored with a view to providing additional selectivity for the analysis of contaminated shellfish extracts. In the present case, this analysis was performed in MRM mode by selecting precursor and fragment ions characteristic of STX and $GTX_{2,3}$. Since the migration times of these two groups of analytes are separated by several minutes, the mass spectrometer was set to record the first reaction channels (300 → 204, 282) between 10 and 20 min and the second reaction channnel (*m/z* 396 → 298, 316) between 25 and 30 min. The results of the CITP/CZE/MS/MS analysis performed under these conditions is shown in Figure 9C. The toxins previously detected in the full mass scan analysis are here unambiguously identified using this mode of acquisition. The peak corresponding to STX is observed at 18.4 min with a small fronting peak characteristic of an incomplete destacking. Such a situation is typically encountered for analytes migrating close to the salt front and can be corrected by decreasing the volume loaded on the column. It is interesting to note that the signal corresponding to GTX_3 is more intense than that of GTX_2 although the concentration of the latter toxin is higher in the actual extract. This arises from the lower abundance of the precursor ion of GTX_2, which is more susceptible to dissociation in the orifice/skimmer region of the mass spectrometer prior to mass selection and collisional activation in the rf-only quadrupole collision

(36) Cembella, A. D.; Sullivan, J. J.; Boyer, G. L.; Taylor, F. J. R.; Andersen, R. J. *Biochem. Syst. Ecol.* **1986**, *15*, 171–186.
(37) Sullivan, J. J.; Wekell, M. M.; Kentala, L. L. *J. Food Sci.* **1985**, *50*, 26–29.

cell. While Figure 9C clearly demonstrates the application of CITP/CZE/MS/MS to selective identification of trace levels of PSP toxin contaminants in shellfish extracts, this type of analysis also provides remarkable sensitivity. This combination is of particular importance when unrelated isobaric ions comigrate with the analyte of interest or when the background chemical noise interferes with the ion monitored.

CONCLUSION

PSP toxins present at low concentration levels in contaminated shellfish extracts can be analyzed directly by capillary electrophoresis, with either UV or mass spectrometric detection, by use of a simple preconcentration procedure on a single capillary arrangement. The enhancement in signal detectability is achieved by introducing larger injection sizes than those typically used in the conventional CZE format and focusing the analytes into narrow bands prior to their zone electrophoresis separation. For analysis of PSP toxin standards and extracts from contaminated shellfish using mass spectral detection, best separation performance was obtained using linear polyacrylamide-coated capillaries of 50 μm i.d. and morpholine as leading electrolyte. Analyses performed in selected ion monitoring mode provided detection limits (S/N 3:1) of 16 nM for STX and NEO and 30 nM for GTX toxins. Mass spectral detection provided enhanced selectivity compared to UV detection, and meaningful spectra were generally obtained for toxins present at levels as low as 100 nM in extracts of contaminated scallop liver tissues. When combined with MS/MS, this isotachophoresis preconcentration procedure enables access to valuable structural information and facilitates the identification of low levels of isomeric toxins such as NEO and the α and β epimers of 11-OH STX.

The present method thus provides concentration detection limits comparable to those of HPLC/FLD but does not require conversion to fluorescent derivatives. More importantly, CZE gives remarkable separation efficiencies (N > 150 000/m) with resolution of most PSP toxins in less than 30 min. The only exception in this regard is for the neutral C toxins, which could not be mobilized properly under the present conditions.

ACKNOWLEDGMENT

The authors thank Dr. M. V. Laycock and R. Richards for providing several of the PSP standards used in the present study, P. K. S. Blay for technical assistance, and Dr. R. K. Boyd for valuable discussions.

Received for review March 15, 1994. Accepted July 5, 1994.®

® Abstract published in *Advance ACS Abstracts*, September 1, 1994.

Anal. Chem. **1994,** *66,* 3447–3448

Postionization Chemical Separation: A Mass Spectrometric Technique for Isotopic Analysis of Mixtures

Karl K. Irikura,*,† Edmund H. Fowles,‡ and J. L. Beauchamp

Arthur Amos Noyes Laboratory of Chemical Physics, California Institute of Technology, Pasadena, California 91125

Mass spectrometric analysis of isotopic mixtures is difficult when isotopes of different elements possess nearly the same mass and cannot be resolved. A new strategy, in which gaseous reagents induce selective "chemical shifts" in the mass spectrum, is proposed for resolving such mass interferences. This application of ion–molecule chemistry is demonstrated for the separations of $^{187}Re^+$ and $^{187}Os^+$ and of $^{186}Os^+$ and $^{186}W^+$.

Distinguishing different ions of the same mass is one of the major challenges in mass spectrometry. For polyatomic ions, a number of fragmentation techniques have become relatively common, most notably collision-induced dissociation.[1] Atomic ions cannot, of course, be analyzed by fragmentation. Although some progress has been made toward in situ analysis,[2] elements of similar mass are typically separated prior to mas spectrometric analysis.[3,4] This conventional approach exploits the different bulk chemistry of elements to achieve their separation. We propose, instead, that the chemical separation be postponed until after the sample has been ionized in the mass spectrometer. Thus, gas-phase ion chemistry can be substituted for tedious and difficult preparative work.

EXPERIMENTAL SECTION

A solid solution of osmium and rhenium in iron was prepared by fusion of compressed powders in an induction furnace. Electron microprobe analysis indicated atom fractions of 1.9% for Os and 0.8% for Re, with reasonable homogeneity (Os/Re = 2.30, σ = 0.06). The sample was mounted in the wall of the cell of a Fourier-transform mass spectrometer which was equipped with a conventional electromagnet and ionized by excimer laser ablation (308 nm). Reagent gases were admitted through variable leak valves. Dynamic range problems were avoided by resonant ejection of Fe^+ for a period of several milliseconds that included the laser pulse.

RESULTS AND DISCUSSION

To demonstrate the feasibility of postionization chemical separation (PICS), we consider the separation of ^{187}Re and ^{187}Os. This is of interest because the β decay of ^{187}Re to ^{187}Os (half-life = 4.23×10^{10} years[5]) constitutes a clock for dating geological samples.[6] An appropriate PICS reagent is methane, since Os^+ reacts readily with methane ($k = 3 \times 10^{-10}$ cm^3 s^{-1}) but ground-state Re^+ does not ($k < 1.4 \times 10^{-15}$ cm^3 s^{-1}).[7]

$$Os^+ + CH_4 \rightarrow OsCH_2^+ + H_2 \quad (1)$$

$$Re^+ + CH_4 \rightarrow \text{no reaction} \quad (2)$$

Tungsten is occasionally problematic because of the isobaric ^{186}W and ^{186}Os isotopes.[8] We have found that CO_2 reacts with W^+ ($k = 6 \times 10^{-11}$ cm^3 s^{-1}) but not with ground-state Os^+ or Re^+, so carbon dioxide is an appropriate reagent for separating tungsten ions.

$$W^+ + CO_2 \rightarrow WO^+ + CO \quad (3)$$

$$Os^+, Re^+ + CO_2 \rightarrow \text{no reaction} \quad (4)$$

The selective chemistry is given by eqs 1–4. WO^+ reacts readily with both CH_4 and CO_2.[7] A pulse of CO_2 followed by one of CH_4 will therefore separate a mixture of Re^+, Os^+, and W^+ into Re^+, $OsCH_2^+$, and heavier species $WO_nC_mH_{2m}^+$ ($n \leq 2, m \leq 3$). Note that $^{12}CH_4$ may be used as the reagent gas to avoid a contribution at $m/z = 201$ due to $^{186}Os^{13}CH_2^+$.

The sample ionization process, such as laser ablation, may produce atomic ions in excited states.[9] Excited ions often react more vigorously than their ground-state counterparts,[10–13] thereby degrading the chemical selectivity. Good selectivity

† Permanent address: Chemical Kinetics and Thermodynamics Division, National Institute of Standards and Technology, Gaithersburg, MD 20899.

‡ Permanent address: Laporte Research & Development, P.O. Box 51, Moorfield Rd., Widnes, WA 8 OFE, U.K.

(1) Cooks, R. G., Ed. *Collision Spectroscopy*; Plenum: New York, 1978.
(2) Creaser, R. A.; Papanastassiou, D. A.; Wasserburg, G. J. *Geochim. Cosmochim. Acta* **1991**, *55*, 397–401.
(3) Völkening, J.; Walczyk, T.; Heumann, K. G. *Int. J. Mass Spectrom. Ion Processes* **1991**, *105*, 147–159.
(4) (a) Russ, G. P., III; Bazan, J. M.; Date, A. R. *Anal. Chem.* **1987**, *59*, 984–989. (b) Walker, R. J. *Anal. Chem.* **1988**, *60*, 1231–1234. (c) Roth, E.; Poty, B., Eds. *Nuclear Methods of Dating*; Kluwer Academic: Dordrecht, 1989. (d) Morgan, J. W.; Walker, R. J. *Anal. Chim. Acta* **1989**, *222*, 291–300. (e) Horan, M. F.; Morgan, J. W.; Walker, R. J.; Grossman, J. N. *Science* **1992**, *255*, 1118–1121. (f) Suzuki, K.; Qi-Lu; Shimizu, H.; Masuda, A. *Geochim. Cosmochim. Acta* **1993**, *57*, 1625–1628.
(5) Lindner, M.; Leich, D. A.; Russ, G. P.; Bazan, J. M.; Borg, R. J. *Geochim. Cosmochim. Acta* **1989**, *53*, 1597–1606.
(6) (a) Luck, J.-M.; Allègre, C. J. *Nature* **1983**, *302*, 130–132. (b) Luck, J.-M. In *Nuclear Methods of Dating*; Roth, E., Poty, B., Eds.; Academic: Dordrecht, 1989; Chapter 4.
(7) Irikura, K. K.; Beauchamp, J. L. *J. Phys. Chem.* **1991**, *95*, 8344–8351.
(8) Teng, R. T. D.; Fehn, U.; Elmore, D.; Hemmick, T. K.; Kubik, P. W.; Gove, H. E. *Nucl. Instrum. Methods Phys. Res.* **1987**, *B29*, 281–285.
(9) (a) Kang, H.; Beauchamp, J. L. *J. Phys. Chem.* **1985**, *89*, 3364–3367. (b) Wiedeman, L.; Helvajian, H. *J. Appl. Phys.* **1991**, *70*, 4513–4523. (c) Haglund, R. F., Jr.; Affatigato, M.; Arps, J. H.; Tang, K.; Niehof, A.; Heiland, W. *Nucl. Instrum. Methods B* **1992**, *65*, 206–211.
(10) (a) Freas, R. B.; Ridge, D. P. *J. Am. Chem. Soc.* **1980**, *102*, 7129–7131. (b) Halle, L. F.; Armentrout, P. B.; Beauchamp, J. L. *J. Am. Chem. Soc.* **1981**, *103*, 962–963.
(11) Armentrout, P. B. *Annu. Rev. Phys. Chem.* **1990**, *41*, 313–344.
(12) (a) Hanton, S. D.; Noll, R. J.; Weisshaar, J. C. *J. Phys. Chem.* **1990**, *94*, 5655–5658. (b) Sanders, L.; Hanton, S. D.; Weisshaar, J. C. *J. Chem. Phys.* **1990**, *92*, 3498–3518.
(13) Oriedo, J. V. B.; Russell, D. H. *J. Am. Chem. Soc.* **1993**, *115*, 8376–8381.

0003-2700/94/0366-3447$04.50/0
© 1994 American Chemical Society

can be restored by adding gases that complement the primary PICS reagents. Thus, CH_4 and H_2 are used in combination, and CO_2 and CO are used as a pair. Products of excited-state chemistry such as $ReCH_2^+$ and OsO^+ are then converted back to their precursor atomic ions by processes such as reactions 5 and 6. An alternative to reagent pairing is to allow excited atomic ions to relax in an inert buffer gas before the reagents are introduced.[14]

$$ReCH_2^+ + H_2 \rightarrow Re^+ + CH_4 \quad (5)$$

$$OsO^+ + CO \rightarrow Os^+ + CO_2 \quad (6)$$

Figure 1a shows the initial mass spectrum of the laser-ablated ions. The small $^{187}Os^+$ peak is buried beneath the much larger $^{187}Re^+$ peak. Figure 1b illustrates the separation of Re^+ from Os^+ achieved by PICS. Any of the hot product $ReCH_2^+$ that may form undergoes a secondary reaction with CH_4 with $k = 1.6 \times 10^{-10}$ cm^3 s^{-1}.[7] Based upon reactions of methane alone, the steady-state ratio of $ReCH_2^+$ to Re^+ will therefore be less than 1:100 000. If hydrogen is also present, the ratio will be even smaller. Thus, the chemical selectivity of the separation easily exceeds 10^5. Selectivity of >250 has been obtained by negative thermal ion mass spectrometry. A selectivity of $\geq 10^3$ has been obtained both by three-color resonant ionization of sputtered Os atoms[15] and by accelerator mass spectrometry.[16]

CONCLUSIONS

Postionization chemical separation is a viable technique for separating isobaric isotopes of Re^+, Os^+, and W^+. The procedure can probably be extended to separations relevant to other isotopic dating schemes and to other applications in atomic mass spectrometry.[17] Recent improvements in Fourier-transform mass spectrometers, such as external ion sources,[18] raise the exciting possibility of in situ analysis. Since sample material may be limited and one often wishes to apply a number of dating methods, it is desirable to avoid tedious sample preconcentration. Analyzing the different elements and isotope ratios in a single, small sample would be a simple matter of selecting reagent gas mixtures.

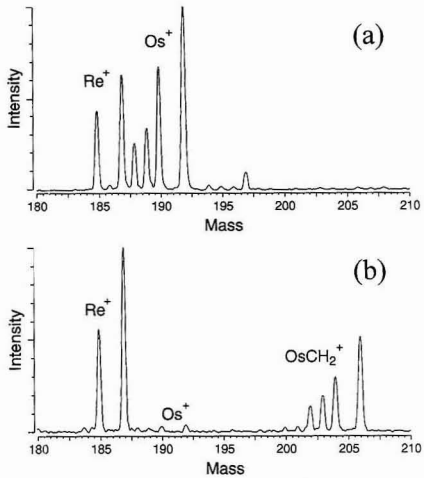

Figure 1. (a) Mass spectrum of laser-ablated Re^+ and Os^+. (b) Same, but after 100 ms in a mixture of methane (1.3×10^{-4} Pa) and hydrogen (4.3×10^{-3} Pa). $OsCH_2^+$, but no $ReCH_2^+$, is produced. In the upper spectrum, the small peaks at m/z 194–197 are due to Pt^+ and Au^+ impurities in the source region.

ACKNOWLEDGMENT

We thank G. J. Wasserburg for bringing this subject to our attention. Funding was provided by the National Science Foundation (Grant CHE-9108318) and the Caltech Consortium in Chemistry and Chemical Engineering (founding members, E. I. duPont de Nemours and Co.; Eastman Kodak Co.; Minnesota Mining and Manufacturing Co.; and Shell Development Co.). K.K.I. is grateful for fellowship support from the Department of Education. This article is contribution 8374 from the Arthur Amos Noyes Laboratory of Chemical Physics.

Received for review April 5, 1994. Accepted July 7, 1994.®

® Abstract published in *Advance ACS Abstracts,* September 1, 1994.

(14) Elkind, J. L.; Armentrout, P. B. *J. Phys. Chem.* **1987**, *91*, 2037–2045.
(15) Blum, J. D.; Pellin, M. J.; Calaway, W. F.; Young, C. E.; Gruen, D. M.; Hutcheon, I. D.; Wasserburg, G. J. *Anal. Chem.* **1990**, *62*, 209–214.
(16) Fehn, U.; Teng, R.; Elmore, D.; Kubik, P. W. *Nature* **1986**, *323*, 707–710.
(17) Koppenaal, D. W. *Anal. Chem.* **1990**, *62*, 303R–324R.
(18) (a) Smalley, R. E. *Anal. Instrum.* **1988**, *17*, 1–21. (b) Alford, J. M.; Williams, P. E.; Trevor, D. J.; Smalley, R. E. *Int. J. Mass Spectrom. Ion Processes* **1986**, *72*, 33–51. (c) Lebrilla, C. B.; Amster, I. J.; McIver, R. T., Jr. *Int. J. Mass Spectrom. Ion Processes* **1989**, *87*, R7–R13. (d) Kofel, P.; McMahon, T. B. *Int. J. Mass Spectrom. Ion Processes* **1990**, *98*, 1–24. (e) Marcus, R. K.; Cable, P. R.; Duckworth, D. C.; Buchanan, M. V.; Pochkowski, J. M.; Weller, R. R. *Appl. Spectrosc.* **1992**, *46*, 1327–1330.

Anal. Chem. **1994,** *66,* 3449–3457

Analytical Applications and Implications of Intramolecular Micelle-Mimetic Ionene Aggregates

Willie L. Hinze,* Bernardo Moreno,† Frank H. Quina,‡ Yasuzo Suzuki,§ and Hong Wang‖

Department of Chemistry, Laboratory for Analytical Micellar Chemistry, Wake Forest University, P.O. Box 7486, Winston-Salem, North Carolina 27109

The synthesis and relevant properties of some cationic polyelectrolytes of the [*x*,*y*]-ionene type (i.e., molecules consisting of dimethylammonium charge centers interconnected by alternating alkyl chain segments containing *x* and *y* methylene groups) are described. Such hydrophobic ionenes can form intramolecular aggregates and function as micelle-mimetic agents since they mimic the key properties of traditional surfactant micelles (such as hexadecyltrimethylammonium bromide) in many respects. However, the ionenes possess certain important advantages over surfactant micelles. For example, aqueous ionene-containing solutions exhibit much less foaming and analyte molecules can be extracted and recovered from their solutions by use of organic solvents. In this work, some applications of the ionenes in analytical chemistry, such as their use as mobile phase additives for thin-layer chromatographic and capillary electrophoretic separations, as fluorescence enhancement agents, and as a means to catalyze slow spectroscopic derivatization reactions are demonstrated. In addition, other potential advantages concerning the utilization of the micelle-mimetic ionenes in chemical analysis applications are mentioned.

As summarized in a recent review article, the utility of micelles in analytical chemistry has grown tremendously since the mid-1970s.[1] As illustrated in a monograph devoted to this topic, they have been successfully utilized in almost every facet of chemical analysis and separation science with demonstrated benefits.[2] In a great majority of the applications reported to date, anionic sodium dodecyl sulfate (NaLS or SDS) or cationic hexadecyltrimethylammonium bromide or chloride (CTAB or CTAC) micellar systems have been employed. However, despite the numerous successful applications of such micellar media in analytical methodology, difficulties which limit their utility or diminish their general effectiveness arise in certain situations.

Thus, for example, an important practical experimental inconvenience encountered when working with any aqueous micelle-containing solution is the problem of foam formation (sudsing or frothing). Great care and patience is often requiredin order to prepare and/or dilute such solutions accurately for analytical applications. Additionally, the problem of foam formation is magnified whenever it becomes necessary to deoxygenate such micellar solutions by purging with nitrogen gas, as is sometimes required in electrochemical or luminescence applications. While special sample cells for degassing[3] or facile chemical means for deoxygenation[4] of surfactant solutions have been reported for luminescence applications, these can be somewhat time-consuming, tedious, inconvenient, and/or suffer from other chemical problems.[5]

In separation science applications, another serious drawback of micellar media stems from the fact that it is difficult to recover and isolate the analyte of interest from the surfactant solution following the separation step.[6] This has severely hampered utilization of micelles in preparative or process-level separation schemes. Although this complication can be overcome by precipitating out the surfactant in some insoluble form[7] or by the use of so-called "destructable" surfactants,[8] these approaches are either time-consuming or costly and ordinarily not a very convenient alternative.

There are also limitations with respect to the amount of organic cosolvent(s) that can be employed when micellar solutions are used since micelle formation is precluded in most instances once the percentage of organic additive is ~30–40% or greater. In addition the amount of surfactant required for the onset of micelle formation, i.e., the critical micelle concentration (cmc), is very dependent upon the exact experimental conditions employed. Last, the potential analytical utility of micelles is limited by the dynamic nature of the aggregation process. Since micelles are in equilibrium with free surfactant monomer, they cannot be immobilized on solid supports. This restricts their utilization to solution applications.

In this paper, we detail the synthesis and some analytical applications of water-soluble polymeric materials that retain the important fundamental features of micellar systems while circumventing many of the aforementioned difficulties encountered with conventional surfactant micelles. Thus, it has been shown that certain linear cationic polyelectrolytes of the

† Present address: Departamento de Quimica Analitica, Nutricion y Bromatologia Facultad de Quimica, Universidad de Salamanca, 37008 Salamanca, Spain.
‡ Present address: Instituto de Quimica, Universidade de Sao Paulo, Sao Paulo, Brazil.
§ Present address: National Institute of Materials and Chemical Research, Tsukuba, Japan.
‖ Present address: Pioneer/Eclipse Corp., Box 909, Sparta, NC 28675.

(1) McIntire, G. L. *CRC Rev. Anal. Chem.* **1990,** *21,* 257–278.
(2) Pfuller, U. *Mizellen, Vesikel, Mikroemulsionen: Tensidassoziate und ihre Anwendung in Analytik und Biochemie,* 1st ed.; Veb Verlag: Berlin, 1986.
(3) Buell, S. L.; Demas, J. N. *Rev. Sci. Instrum.* **1982,** *53,* 1298–1299.
(4) Diaz-Garcia, M. E.; Sanz-Medel, A. *Anal. Chem.* **1986,** *58,* 1436–1440.
(5) Nugara, N. E.; King, A. D. *Anal. Chem.* **1989,** *61,* 1431–1435.
(6) Hinze, W. L. In *Ordered Media in Chemical Separations*; Hinze, W. L., Armstrong, D. W., Eds.; ACS Symposium Series 342; American Chemical Society: Washington, DC, 1987; Chapter 1.
(7) Jaeger, D. A.; Robertson, R. E. *J. Org. Chem.* **1977,** *42,* 3298–3301.
(8) Jaeger, D. A.; Finley, C. T.; Walter, M. R.; Martin, C. A. *J. Org. Chem.* **1986,** *51,* 3956–3959.

0003-2700/94/0366-3449$04.50/0
© 1994 American Chemical Society

[x,y]-ionene type (dimethylammonium charge centers interconnected by alternating chain segments containing x and y methylene groups, respectively; see structure **I**) can function

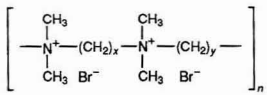

x,y ionene bromide

I

as micelle-mimetic agents in aqueous solutions.[9–11] Namely, ionenes with $x = 3$ and $y > 14$ were shown to exhibit properties that resemble those of micelles in many important respects. For example, they retain the characteristic ability of micelles to bind both amphiphilic and hydrophobic molecules in solution. In addition, the degrees of counterion binding, counterion-exchange selectivity, substrate solubilization, and catalytic rate enhancements were found to be comparable in magnitude to those observed for conventional micelles, such as CTAB.[10]

However, in contrast to micellar media, such ionenes are macromolecular species and they possess no critical aggregation concentration since the micellelike domains are formed intrapolymerically. Compared to micelles, they exhibit much less foaming, allowing, as demonstrated here, bound analytes to be easily recovered by simple extraction of aqueous ionene solutions with organic solvents. The potential utility of such micelle-mimetic ionenes in other selected analytical applications, e.g., as luminescence enhancement agents and as a mobile phase in pseudophase liquid chromatography, will also be demonstrated.

EXPERIMENTAL SECTION

Apparatus. Fluorescence spectra (uncorrected) and measurements were made on an Aminco Bowman recording spectrophotofluorometer equipped with a Xe lamp source, 1P21 PM tube detector, and J10-222A PM microphotometer using 1.0 cm quartz cells with the fluorometer entrance, exit, and detector slits all set at 1.0 mm. Absorption measurements and spectra were obtained on an IBM 346 spectrophotometer using 1.0 cm optical path length cuvettes.

Materials. 1,3-Dibromopropane (**I**) and *N,N,N′,N′*-tetramethyl-1,6-hexanediamine (**V**) (Aldrich Chemical Co.) were vacuum distilled just prior to use. Tetrahydrofuran (THF), chloroform, toluene, and dimethylacetamide were all distilled from calcium hydride. 1,16-Hexadecanediol, hexadecanedioic acid (thapsic acid), and docosanedioic acid were all obtained from Aldrich. The other solvents were all reagent grade materials and used without further purification. The water utilized was HPLC grade (Fisher Scientific Co.). The analytes employed included nystatin (Sigma Chemical Co.), dansyl amino acids (Sigma or Pierce Chemical Co.), *N*-phenyl-1-naphthylamine and pyrene (Aldrich), anthranilic acid (i.e., *o*-aminobenzoic acid) and *m*-aminobenzoic acid (Eastman Kodak Co.), and *p*-aminobenzoic acid (Merck & Co.).

Table 1. Summary of Reaction Conditions Employed in the Preparation of the Different Ionenes

run no.	ionene	halide[a] (g)	amine[a] (g)	solvent (mL)	time, h	yield, g (%)
1	[3,16]	**I** (2.0234)	**III** (3.1295)	MeOH (10)	48	4.46 (86.6)
2	[3,16]	**I** (3.8050)	**III** (5.8845)	MeOH (10)	48	9.28 (95.7)
3	[3,22]	**I** (1.0134)	**IV** (1.9913)	MeOH (5)	48	2.69 (89.5)
4	[3,22]	**I** (0.2482)	**IV** (0.4841)	THF (5)	96	0.64 (87.3)
5	[16,16]	**II** (1.9652)	**III** (1.5985)	MeOH (5)	48	3.20 (89.9)
6	[3,6]	**I** (2.0739)	**V** (1.7695)	MeOH (10)	48	2.73 (71.0)

[a] Key: **I**, 1,3-dibromopropane; **II**, 1,16-dibromohexadecane; **III**, *N,N,N′,N′*-tetramethyl-1,16-hexadecanediamine; **IV**, *N,N,N′,N′*-tetramethyl-1,22-docosanediamine; **V**, *N,N,N′,N′*-tetramethyl-1,6-hexanediamine.

Ionenes. The [3,y]- or [x,y]-ionenes employed in this work were prepared by reacting the appropriate 1,x-bis(dimethylamino)alkane with an equimolar quantity of 1,3-dibromopropane (or 1,y-dibromoalkane) using modified literature procedures.[9–13] The following polymerization reaction procedure for the preparation of [3,16]-ionene serves to illustrate the typical conditions employed for the preparation of the other ionenes.

[3,16]-Ionene. Equimolar quantities of the reactants, *N,N,N′,N′*-tetramethyl-1,16-hexadecanediamine (3.1296 g, 10 mmol) and 1,3-dibromopropane (2.0434 g, 10 mmol), were dissolved in 10 mL of methanol, and the solution stirred for 48 h at 40 ± 1 °C. The resulting viscous solution was added dropwise to dry ethyl ether (100 mL) from which the [3,16]-ionene separated as a viscous oil. After decanation of the original ethyl ether, fresh ethyl ether was added; the mixture was cooled in an ice bath and stirred ~1 h to crystallize the ionene in the form of a powder. The material was filtered and dried over phosphorus pentoxide under vacuum to give 4.46 g of [3,16]-ionene (86.6% yield). The other ionenes were prepared in a similar fashion. The specific conditions employed in the preparation of these ionenes and yields obtained are summarized in Table 1. It should be noted that the [3,6]-ionene is also commercially available from Aldrich under the name hexadimethrine bromide (Polybrene).

The different dihalo- and bis(diamino)alkanes required for the preparation of these ionenes (Table 1) were synthesized as follows:

1,16-Dibromohexadecane (II). Triphenylphosphine (7.68 g, 29 mmol) was gradually added to a stirred mixture of hexadecanediol (1.34 g, 5.17 mmol) and carbon tetrabromide (6.97 g, 21 mmol) in 50 mL of dry ethyl ether. The reaction was allowed to proceed overnight at room temperature, after which the precipitated triphenylphosphine oxide was removed by filtration. The solvent was removed from the filtrate by rotary evaporation and the crystalline residue washed with an aqueous 60% (v/v) ethanol solution to remove any remaining triphenylphosphine oxide and then dried. The synthesis yielded 1.39 (70% yield) of the dibromide **II**, mp 56–57 °C (lit.[12] mp 50–52 °C; lit.[14] mp 56–57 °C; lit.[15] mp 55–56 °C).

(9) Nieves, V. E.; Ribaldo, E. J.; Baround, R.; Quina, F. H. *J. Polym. Sci., Polym. Lett. Ed.* **1982**, *20*, 433–437.
(10) Soldi, V.; Erismann, N. M.; Quina, F. H. *J. Am. Chem. Soc.* **1988**, *110*, 5137–5143.
(11) Suzuki, Y.; Tazuke, S. *J. Polym. Sci., Polym. Lett. Ed.* **1982**, *20*, 259–264.
(12) Kunitake, T.; Tsuge, A.; Takarabe, K. *Polym. J. (Tokyo)* **1985**, *17*, 633–640.
(13) Rembaum, A.; Noguchi, H. *Macromolecules* **1972**, *5*, 261–269.
(14) Chunit, P.; Hausser, J. *Helv. Chim. Acta* **1929**, *12*, 850–859.
(15) Cipiciani, A.; Fracassini, M. C.; Germani, R.; Savelli, G.; Bunton, C. A. *J. Chem. Soc., Perkin Trans. 2* **1987**, 547–551.

N,N,N′,N′-Tetramethyl-1,16-hexadecanediamine (III). 1,16-Hexadecanedioic acid (8.04 g, 28.1 mmol) was refluxed with 30 mL of thionyl chloride for 5 h, after which the excess thionyl chloride was removed by vacuum distillation and the corresponding acid chloride obtained in the form of brown crystals. A chloroform solution of the acid chloride was then added to a well-chilled, vigorously stirred aqueous solution of dimethylamine (40% (v/v), 20 mL) containing 1.8 g of sodium hydroxide. After a 30 min reaction time, the chloroform layer was collected and washed with water. Evaporation of the chloroform solution yielded 6.19 g of the crude diamide product. The original aqueous layer was concentrated and the precipitated diamide filtered. The crude diamide was combined, recrystallized from a mixture of 3:4 (v/v) ethyl acetate–hexane, and dried to give 8.43 g (88% yield) of the diamide, mp 91–92 °C.

Next, the diamide (8.23 g, 24.2 mmol) was added (in successive 1 g portions) with stirring to a mixture of lithium aluminum hydride ($LiAlH_4$) (3.09 g, 81.5 mmol) in 150 mL of THF and the resultant mixture was refluxed. After 8 h, another 80 mL of THF and 0.5 g (13.2 mmol) of $LiAlH_4$ were added and the solution was refluxed for another 7 h. The excess of $LiAlH_4$ was destroyed by the careful addition of ethyl acetate. After addition of 250 mL of ethyl ether, a few milliliters of water were added until the white precipitate settled to the bottom of the flask when the stirring was stopped. The precipitate was filtered and the filtrate dried over anhydrous magnesium sulfate. The solvent was removed from this solution by evaporation and the crude, oily diamine product (**III**) thus obtained dissolved in aqueous hydrochloric acid and then neutralized with aqueous ammonium hydroxide. The diamine thus precipitated was filtered and dried under vacuum, giving 6.90 g (92%) of **III**, mp 40 °C.

N,N,N′,N′-Tetramethyl-1,22-docosanediamine (IV). 1,22-Docosanedioic acid (purity 85%, 5.03 g, 11.5 mmol) was refluxed with ~30 mL of thionyl chloride for 5 h. After this reaction, excess thionyl chloride was removed by vacuum distillation and the acid chloride obtained as brown crystals. An ethyl ether solution (30 mL) of the acid chloride was added with vigorous stirring to a well-chilled aqueous solution of dimethylamine (40%, 10 mL) containing 3 g of sodium hydroxide. After 1 h reaction time, chloroform was added to this reaction mixture and the organic layer collected. This organic phase was dried over magnesium sulfate, and the solvents were removed by evaporation. The crude diamide thus obtained was recrystallized from ethyl acetate to give 4.18 g (86% yield) of the diamide, mp 99–100 °C (lit.[10] mp 99–100 °C).

Next, 1 g portions of the diamide (total of 4.09 g, 9.62 mmol) were added stepwise to a mixture containing $LiAlH_4$ (2.12 g, 55.9 mmol) and 150 mL of THF, and the total mixture was refluxed for 18 h. The excess $LiAlH_4$ was destroyed by addition of ethyl acetate and 300 mL of ethyl ether to the reaction mixture. A few milliliters of water were added until the white precipitate settled to the bottom of the flask when the stirring was stopped. The precipate was filtered and the filtrate solution dried over magnesium sulfate. The solvents were removed from the filtrate by evaporation, and the diamine **IV** was obtained as white crystals. The crystals were dissolved in 100 mL of hydrochloric acid, and the solution was neutralized by addition of aqueous ammonium hydroxide solution. The precipitated diamine was filtered and dried under vacuum to yield 3.37 g (88% yield) of **IV**, mp 47–48 °C (lit.[10] mp 48–48.5 °C).

Procedures. *Fluorescence Measurements.* To a series of volumetric flasks were added appropriate measured volumes of the [*x*,*y*]-ionene stock solutions and an approprite amount of a standard solution of the test analyte, nystatin, such that the final nystatin concentration was constant (9.10×10^{-6} M), and the flasks were completed to the final volume using distilled water. The fluorescence signal of nystatin (excitation and emission wavelengths of 306 and 404 nm, respectively) as a function of the added ionene concentration was measured versus a background blank solution.

Thin-Layer Chromatography. Aqueous solutions of varying ionene concentration were prepared and utilized as the mobile phases in TLC experiments with polyamide (Brinkmann Instruments or Baker Chemical Co.) or cellulose-F (Baker) stationary phase sheets. The standard test solutes were prepared by dissolving 1–10 mg of the solid in ~10 mL of spectral grade methanol, acetone, or dimethyl sulfoxide. Typically, about 0.5–1.0 μL of the standard solution was spotted on the polyamide (or cellulose) TLC sheets with a Hamilton microsyringe, and after evaporation of the solvent, the sheets placed in an air-tight rectangular development chamber (Analtech). After development, the components were detected as fluorescence-quenched dark spots against the brightly fluorescencing background when illuminated at either 254 or 366 nm with a Model UVSL-25 Mineralight hand lamp. The R_f factors were determined in the usual manner.

Capillary Electrophoresis (CE) Separation. CE experiments were performed using a capillary electrophoresis System I (Dionex Corp., Smyrna, GA), which was equipped with a 254 nm lamp and a 75 μm × 55 cm fused silica capillary. The electrophoretic solutions were 25 mM phosphate buffer (pH 7.0, Fisher Scientific Co.) containing 2.4 mg/mL [3,22]-ionene and 20% (v/v) methanol. The run voltage was 20 kV for all experiments, which were carried out at ambient temperature (~25 °C).

Extractive Recovery of Analytes from Aqueous Ionene Solutions. The extraction procedure consisted of addition of 2.00 mL of the aqueous ionene solution containing the test analyte (*N*-phenyl-1-naphthylamine) to a conical test tube followed by addition of 2.00 mL of the organic solvent under consideration. The test tube was vigorously shaken for 1 min and then left to stand undisturbed for several minutes in order to allow for separation of the two phases. For those systems that yielded clear aqueous and organic phases, aliquots of the organic phase were then taken using a microsyringe and the fluorescence intensity of the *N*-phenyl-1-naphthylamine test analyte was measured at the optimum fluorescence excitation and emission wavelengths versus a reference obtained by performing a blank extraction (i.e., identical experimental conditions, but no analyte present).

Foam Test Procedure. In order to determine the extent of foaming of ionene solutions upon purging with gases relative to that of a typical surfactant micellar medium such as CTAB, the following semiquantitative experiment was performed. A 2.00 mL aliquot of the ionene (or CTAB) containing solution was introduced into a 25.00 mL buret. Next, nitrogen gas

Table 2. Reaction Conditions and Yields for the Preparation of *N,N,N′,N′*-Tetramethyl-1,16-hexadecanediamide and *N,N,N′,N′*-Tetramethyl-1,22-docosanediamide

n[a]	acid, g	solvent (mL)	dimethylamine,[b] mL	NaOH, g	time, h	yield, g (%)
16	0.88	benzene (7)	5	0.00	0.70	0.53 (51.0)
16	5.72	benzene (16)	10	1.30	1.5	5.48 (73.0)
16	8.04	chloroform (20)	20	1.90	0.50	8.43 (88.0)
16	10.1	chloroform (20)	30	5.00	2.0	9.97 (83.0)
22	5.03[c]	ethyl ether (30)	10	3.10	1.0	4.18 (86.0)

[a] *n* value for the compounds given in eq 1. [b] The dimethylamine concentration was 40 wt %. [c] The purity of the acid used was 85%.

was passed through the buret at a constant flow rate for specified amounts of time, and the foam height in the buret column was measured 1 min after interruption of the gas flow for the two systems.

Solubility Measurements. The solubility of *N*-phenyl-1-naphthylamine was determined in the following manner: a series of solutions was prepared in test tubes such that all contained the same volume of an aqueous ionene- or CTAB-containing solution in which the ionene or CTAB concentration was successively increased. After addition of an excess of the solid analyte, each test tube was vigorously shaken and then allowed to stand for 48 h at 20 °C. The amount of *N*-phenyl-1-naphthylamine that had been solubilized by the ionene- or CTAB-containing solutions was then determined by spectrofluorometry (using excitation and emission wavelengths of 340 and 444 nm, respectively).

Viscosity Measurements. Relative viscosity measurements were made with an Ostwald viscometer with water as the reference liquid in the usual manner.

RESULTS AND DISCUSSION

Preparation and Properties of the Ionenes. *Synthesis.* The α,ω-ditertiary amines required for the ionene synthesis were prepared in quite good yield, as shown by eq 1, where x = 16

$$\mathrm{HOOC(CH_2)_{x-2}COOH} \xrightarrow[\text{(2) aq } (CH_3)_2NH]{\text{(1) } SOCl_2} \mathrm{(CH_3)_2NCO(CH_2)_{x-2}CON(CH_3)_2} \xrightarrow{\text{(1) } LiAlH_4} \mathrm{(CH_3)_2N(CH_2)_xN(CH_3)_2} \quad (1)$$

or 22, utilizing procedures similar to those previously reported in the literature.[9,10,12] However, in the synthesis of the intermediate amides, we employed aqueous dimethylamine (Schotten–Baumann reaction[16]) rather than gaseous dimethylamine because aqueous dimethylamine is easier to handle and less expensive. The specific reaction conditions and yields obtained for the amide and amine intermediates are summarized in Tables 2 and 3, respectively.

The 1,16-dibromohexadecane required for the synthesis of the [3,16]- and [16,16]-ionenes was prepared from 1,16-hexadecanediol. Attempts were made to use phosphorus tribromide and thionyl bromide to convert 1,16-hexadecanediol to the dibromo analog, but the yield and purity obtained were

(16) Sandler, S. H.; Kalo, W. *Organic Functional Group Preparations*; Academic Press: New York, 1968; p 299.

Table 3. Summary of Reaction Conditions and Yields for the Preparation of *N,N,N′,N′*-Tetramethyl-1,16-hexadecanediamine and *N,N,N′,N′*-Tetramethyl-1,22-docosanediamine

n[a]	amide, g	$LiAlH_4$, g	solvent (mL)	refluxing time, h	yield, g (%)
16	0.81	0.64	THF (50)	7.0	0.67 (93)
16	8.23	3.09	THF (150)	15.0	7.28 (96)
16	9.97	3.09	THF (150)	22.0	8.66 (95)
22	4.09	2.12	THF (100)	18.0	3.37 (88)

[a] *n* value for the compounds given in eq 1.

Table 4. Summary of Conditions and Yields for the Preparation of 1,16-Dibromohexadecane from the Corresponding Diol

run	diol, g	CBr_4, g	triphenylphosphine, g	reaction time, h	yield, % (g)
1	0.51	2.84	2.05	4.5	45 (0.34)
2	1.79	9.17	7.25	6.5	48 (1.23)
3	1.39	6.97	7.68	5.5	70 (1.39)

not satisfactory. However, the conversion was successful when the phosphorus ylid reaction (eq 2)[17] was employed (see Table 4 for conditions and yields).

$$\mathrm{Ph_3P + CBr_4 \rightarrow Ph_3P^+BrC^-Br_3} \xrightarrow{\text{(1) HO-R′-OH}} \mathrm{Br(CH_2)_{16}Br + Ph_3PO + HCBr_3} \quad (2)$$

The yields of the ionenes obtained via the polymerization reaction of the dibromoalkanes with the diamines (eq 3) are

$$\mathrm{CH_3N(CH_2)_xNCH_3\,CH_3} + \mathrm{Br(CH_2)_yBr} \longrightarrow \left[\mathrm{-N^+(CH_3)_2(CH_2)_x-N^+(CH_3)_2(CH_2)_y-}\right]_n \quad (3)$$

summarized in Table 1. Although it is known that this Menschutkin reaction is fastest in dipolar aprotic solvents,[13,18] we carried out most of the reactions in methanol because all the ionenes exhibited excellent solubility in methanol. After workup, the product ionenes were all obtained in the form of powders. Complete removal of the dibromide and diamine starting materials from the final ionene products was confirmed by thin-layer chromatography and infrared measurements. Thus, the requisite ionenes can be prepared fairly easily and in good yield from readily available starting materials, which should facilitate their use in chemical analysis and separation science applications.

Solution Conformation. On the basis of available literature work, the preferred ionene conformation in aqueous solution can range from extended or rodlike in the case of the more hydrophilic [3,6]-ionene to "micellelike" or globular in the more hydrophobic [3,16]- and [3,22]-ionenes.[9-12] These latter two ionenes are thought to undergo intramolecular aggregation in aqueous solution by folding up in an accordion-like manner (see Figure 1A). A vesicle and/or lamellar-like structure

(17) Hooz, J.; Gilani, S. S. H. *Can. J. Chem.* **1968**, *46*, 86–87.
(18) Suzuki, Y.; Tazuke, S. *Macromolecules* **1980**, *13*, 25–30.

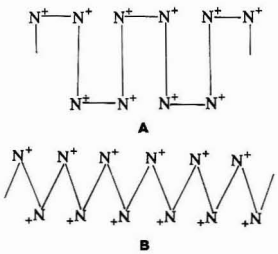

Figure 1. Schematic artistic illustration of the conformations of the intramolecular aggregate species formed in aqueous solution by the hydrophobic (A) [3,16]- and [3,22]-ionenes[9-12] and (B) [16,16]-ionene.[12,19]

Table 5. Solubility of the Polymeric Ionenes in Different Solvents[a]

	[x,y]-ionene			
solvent	[3,6]	[3,16]	[3,22]	[16,16]
water	++	++	++	–(+)
aqueous KBr (0.4 M)	++	–	–	–
methanol	++	++	++	++
DMSO	–	++	+	+
DMF	–	++	+	+

[a] Key: ++, soluble at room temperature, +, soluble only upon heating; –, insoluble.

(Figure 1B) has been postulated in the case of the [16,16]-ionene.[12,19] These structures closely resemble that of a surfactant micelle or vesicle except that it is a macromolecule. Thus, unlike conventional micelles, the structure would be expected to retain its cohesion over the entire range of concentrations and in a greater variety of solvents. The intrapolymeric aggregates formed in these latter three ionene aggregate systems can mimic micelle functions since they possess a hydrocarbon–water interface (or surface) of high charge density and a hydrophobic inner region. One would thus expect them to function in a manner akin to micelles of a cationic surfactant such as CTAB or CTAC, but without some of the problems associated with these latter micellar systems (vide supra).

Solution Properties of Ionenes. Table 5 summarizes the relative solubilities of the ionenes in different solvents. The reduced viscosities of aqueous ionene solutions are summarized in Table 6. All ionene polymers were found to be highly soluble in methanol, and all but the [16,16]-ionene were also very soluble in water. With the exception of the [3,16]-ionene, the other ionenes were found to be insoluble or only sparingly soluble in organic solvents such as DMF and DMSO. The fact that these ionenes are stable and soluble in water–methanol mixtures (from 0 to 100% MeOH) renders them particularly suitable for use in those analytical applications requiring relatively large percentages of organic modifiers (as in HPLC or CZE). For comparison, the use of the sodium 10-undecylenate oligomer, a polymer which also forms intramolecular micellar-like aggregates, was restricted to solutions containing less than 60% methanol due to its diminished solubility.[20]

(19) Kunitake, T.; Nakashima, N.; Takarake, K.; Nagai, M.; Tsuge, A.; Yanagi, H. *J. Am. Chem. Soc.* **1981**, *103*, 5945–5947.

Table 6. Reduced Viscosity of the Ionenes[a]

	$\eta_{sp/c}$	
ionene	in water	in aq 0.40 M KBr
[3,6]	0.97 (0.502)[b]	0.137 (0.474)[b]
[3,16]	0.161 (0.376)[b]	0.011[c] (0.431)[b,c]
[3,22]	0.218 (0.384)[b]	*d*
[16,16]	*d*	*d*

[a] Viscosity measurements made at 30.0 °C. [b] Value in parentheses represents the ionene concentration (g/100 mL) at which the viscosity measurement was made. [c] Viscosity measurement made using saturated solution of the [3,16]-ionene. [d] Reduced viscosity could not be measured due to a lack of solubility of the ionene.

The surface tension of aqueous [3,16]- and [3,22]-ionene-containing solutions is similar to that of water provided that the diamide and dibromide starting materials required in their preparation are completely removed. This is in agreement with literature reports that ionene or polysoap solutions exhibit a continuous decrease of surface tension with increasing concentration, if they are surface active at all.[21,22] No break point resembling a cmc is observed in plots of surface tension with concentration for intramacromolecular (or single molecule) micelles or similar polysoaps, in contrast to low molecular weight surfactants.[21,22] As a consequence, in comparison to aqueous solutions of surfactant micelles, aqueous ionene solutions exhibit significantly less foaming. For example, a 20 cm high foam column was observed after purging an aqueous 0.03 M CTAB solution contained in a buret, as compared to only a 0.20 cm foam column for an aqueous [3,16]-ionene solution (1.0 mg/mL). Thus, relative to micellar solutions, ionene-containing solutions facilitate and accelerate the preparation stage as well as any deoxygenation or degassing steps. Most importantly, the lack of foam allows one to dilute such ionene solutons accurately. Low-foaming characteristics have also been reported for other polymer surfactant systems.[23]

Solubilization and Extraction of Solutes from Ionene Solutions. The solubility of *N*-phenyl-1-naphthylamine in water as a function of the concentration of added [3,16]-ionene is given in Table 7, together with data for the solubility of this solute as a function of added hexadecyltrimethylammonium bromide. In the case of CTAB, the solubility of the solute remains low and essentially constant below the cmc (9.2×10^{-4} M) of CTAB. In the case of the [3,16]-ionene, however, the solubility of *N*-phenyl-1-naphthylamine increases even at very low concentrations of added ionene, with no indication of a threshold concentration for the onset of solubilization. This reflects the fact that the micellelike aggregates of the ionene are formed within the polymer molecule by aggregation of several of its repeating surfactant-like subunits (Figure 1). Similar behavior has previously been reported for the polymeric sodium undec-10-enyl sulfate

(20) Palmer, C. P.; Khaled, M. Y.; McNair, H. M. *J. High Resolut. Chromatogr.* **1992**, *15*, 756–762.
(21) Piirma, I. *Polymeric Surfactants*; Marcel Dekker: New York, 1992; p 59.
(22) Anton, P.; Koberle, P.; Laschewsky, A. *Makromol. Chem.* **1993**, *194*, 1–27.
(23) Yokota, K.; Ichihara, A.; Shinike, H. *Spec. Publ.—R. Soc. Chem.* **1992**, *No. 107*, 29–48.

Table 7. Solubility of *N*-Phenyl-1-naphthylamine in Aqueous Ionene and CTAB Solutions at 22.0 °C

[3,16]-Ionene,[a] mg/mL	solubility,[b] mg/mL	CTAB,[c] M	solubility,[b] mg/mL
0.10	0.0015	1.0×10^{-5}	0.0013
0.20	0.0016	5.0×10^{-5}	0.0013
0.40	0.002	1.0×10^{-4}	0.0013
0.80	0.006	5.0×10^{-4}	0.0014
6.0	0.14	1.0×10^{-3}	0.023
8.0	0.29	5.0×10^{-3}	0.20
10.0	0.40	1.0×10^{-2}	0.59

[a] Ionene concentration expressed in milligrams per milliliter. [b] Refers to the solubility of the *N*-phenyl-1-naphthylamine solute in milligrams per milliliter. [c] CTAB surfactant concentration given in molar units.

Table 8. Summary of Data for the Extraction of *N*-Phenyl-1-naphthylamine from an Aqueous [3,16]-Ionene Solution with Different Organic Solvents[a]

organic solvent	aqueous phase[b]	organic phase[b]	% recovery
cyclohexane	C	T	
chloroform	C	T	
carbon tetrachloride	C	C	97.4
hexane	C	T	
heptane	C	T	
1-octanol	T	T	
petroleum ether	C	T	
benzene	C	T	
isooctane	T	T	
ethyl acetate	C	C	94.1
ether	C	C	110[c]
1-pentanol	T	T	

[a] Refer to the Experimental Section for the conditions. [b] C, clear, transparent; T, turbid. [c] Ionene concentration was 1.0 mg/mL.

"unimolecular" micellar system.[24] In terms of solubilization capacity, a 10.0 mg/mL ionene solution solubilizes as much of the *N*-phenyl-1-naphthylamine solute as does a ~8.0 mM CTAB (3 mg/mL) solution, indicating that the [3,16]-ionene functions about as effectively as micellar CTAB. Thus, the hydrophobic ionenes can be utilized as solubilization enhancement agents in analytical chemistry just as surfactant micelles have previously been employed.[25] Unlike surfactant micelles, in which dilution of the surfactant solution below the cmc will lead to a deposition of the solubilizates contained, this problem does not exist for ionenes. The ionenes are capable of solubilization at any concentration due to their intramolecular aggregation state.

A significant limitation with conventional surfactant micellar media in separation science applications (particularly on preparative or process scales) is the problem of recovery of the analyte from the surfactant media and subsequent recycling of the surfactant.[6] In the case of surfactant micelles, attempts to extract with conventional organic solvents typically result in troublesome emulsion formation during the recovery step. In this work, we examined the recovery of the test analyte, *N*-phenyl-1-naphthylamine, from an aqueous 0.10 mg/mL [3,16]-ionene solution via extraction with 12 organic solvents. The results are tabulated in Table 8. In all but three cases, either the aqueous or organic phase (or both) became cloudy or turbid upon mixing and shaking together equal volumes of the organic solvent and the ionene solution. However, with carbon tetrachloride, ether, or ethyl acetate as the extractive organic solvents, both the organic and aqueous ionene phases were transparent following mixing, shaking, and spontaneous phase separation. Nearly quantitative recovery of the test analyte, *N*-phenyl-1-naphthylamine, in the extractant organic phase was achieved with each of these latter three organic solvents (Table 8). Similar results were obtained in the extraction of this analyte from aqueous [3,22]- or [16,16]-ionene solutions when ethyl ether was used as the organic solvent. In contrast, attempted extraction of the analyte from an aqueous 0.03 M CTAB solution using ethyl ether resulted in formation of an emulsion. Thus, a significant advantage of the use of aqueous solutions of these hydrophobic ionene aggregates is that solutes can be subsequently recovered from them by extraction using conventional organic solvents.

Table 9. R_f Values of *o*-, *m*-, and *p*-Aminobenzoic Acids Chromatographed on Polyamide TLC Sheets and Developed with Aqueous [3,16]-Ionene Solutions

	R_f values at different [3,16]-ionene concns[a]			
compound	0.00	5.0	10.0	20.0
o-aminobenzoic acid	0.09	0.33	0.47	0.66
m-aminobenzoic acid	nd[b]	0.44	0.60	0.76
p-aminobenzoic acid	0.12	0.18	0.40	0.52

[a] Ionene concentrations in milligrams per milliliter. [b] Not determined.

Some Specific Analytical Applications. *Separation Science.* Surfactant micelles have been employed with success in numerous separation science applications.[1,2] In this work, we briefly investigated the feasibility of utilizing some of the hydrophobic ionenes in an analogous manner as the pseudophase in thin-layer chromatography.[26,27] Aqueous solutions of the [3,16]-ionene proved to be an effective mobile phase when organic compounds such as positional isomers of disubstituted benzene were chromatographed on polyamide thin-layer sheets. Table 9 and Figure 2 illustrate data obtained for the TLC separation of *o*-, *m*-, and *p*-aminobenzoic acids on polyamide using aqueous solutions of [3,16]-ionene as the mobile phase. These compounds moved as distinct spots (Figure 2), and their R_f values were dependent on the concentration of the ionene used. The greater the concentration of the ionene, the greater the R_f value (Table 9). Cellulose stationary phases were of little use for the separation of the isomeric aminobenzoic acids with ionene-containing mobile phases because they bind the acids too weakly.

Thus, it appears that aqueous ionene-containing solutions can be used in a manner akin to surfactant micelles in chromatography. As with micelles, the highly selective partitioning of many solutes to the ionene intramolecular aggregates cannot be duplicated by any pure or mixed solvent system.[28,29] To change the "apparent polarity" of the ionene mobile phase, one simply alters the concentration of the ionene in solution, just as in micellar or pseudophase chromatography. An important advantage of ionene mobile phases compared to micelles is that analytes can be extracted and recovered from aqueous ionene-containing solutions, as previously mentioned.

(24) Boyer, B.; Lamaty, G.; Leydet, A.; Roque, J. P.; Sama, P. *New J. Chem.* **1992**, *16*, 883–886.
(25) Hinze, W. L. In *Solution Chemistry of Surfactants*; Mittal, K. L., Ed.; Plenum Publishing Corp.: New York, 1979; Vol. 1, pp 79–127.
(26) Armstrong, D. W.; Terrill, R. Q. *Anal. Chem.* **1979**, *51*, 2160–2163.
(27) Armstrong, D. W. *Sep. Purif. Methods* **1985**, *14*, 213–304.

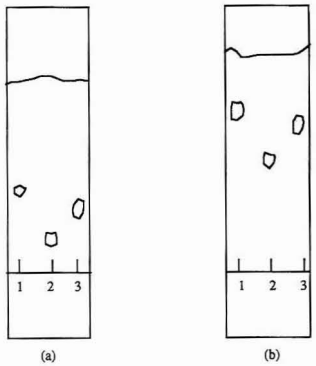

Figure 2. Tracing of developed chromatograms. The chromatograms show the separation of (1) *m*-aminobenzoic acid, (2) *p*-aminobenzoic acid, and (3) *o*-aminobenzoic acid on polyamide stationary phases developed with aqueous (a) 5.0 and (b) 20.0 mg/mL [3,16]-ionene-containing solutions as the mobile phase.

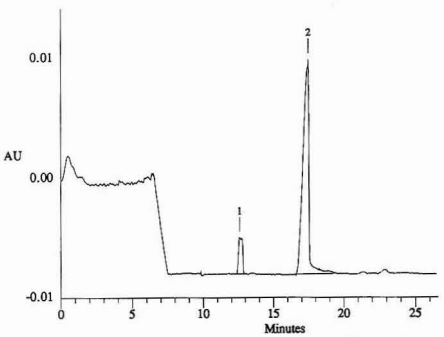

Figure 3. Electropherogram showing the CE separation of fluorene (1) and naphthalene (2) achieved via use of a background electrolyte containing 2.4 mg/mL [3,22]-ionene, 25 mM phosphate buffer (pH 7.0), and 20% (v/v) methanol. UV detection (254 nm) was used. See Experimental Section for further details.

Some preliminary experiments were conducted in order to determine whether ionenes could be successfully utilized in capillary electrophoretic separations in a manner akin to that of micelles. Figure 3 shows an electropherogram for the separation of a mixture of two polycyclic aromatic hydrocarbons (PAHs), naphthalene and fluorene, which was obtained with a 25 mM phosphate buffer solution (pH 7.0) containing 2.4 mg/mL [3,22]-ionene and 20% (v/v) methanol. As in the cases previously reported for cationic CTAB surfactant or poly(diallyldimethylammonium) chloride (PDDAC) polyelectrolyte molecules,[30-33] when [3,22]-ionene is used in the electrolyte buffer medium, the positively charged ionene is adsorbed on the negatively charged surface of the fused silica walls, giving a hydrophobic, positively charged wall. As a result, the bulk ionene solution is electroosmotically driven toward the positive electrode (anodal electroosmotic flow). Although the ionene itself appears to migrate from the positive to the negative electrode, the two neutral PAHs were detected at the positive end, because the electroosmotic flow is faster than the electrophoretic migration of the bulky ionene polymeric molecule. The potential at the injection end of the capillary was accordingly changed from positive to negative to ensure that the PAHs would migrate past the detector.

It appears that the PAH that interacts most weakly with the ionene migrates faster than the one that interacts more strongly. As a result, the migration order is the same as that observed with anionic sodium dodecyl sulfate micelles in micellar electrokinetic chromatography, however, the migration direction is reversed. A similar trend has been reported when CTAB is used in MEKC.[33] Use of ionene pseudostationary phases in CZE could be potentially advantageous because they are soluble and stabe in solutions containing very high percentages of organic modifiers (such as methanol). Thus, they may prove useful in the CZE separation of very hydrophobic compounds, as has been reported for an anionic polymeric micellar system.[20] Of course, much more work is required in order to determine the advantages and limitations of employing ionenes in capillary electrophoretic separations.

Chiral ionenes have been reported in the literature,[28] which suggests that these intramolecular materials may also be employed for chiral CZE and/or TLC separations. We have previously noted that such ionenes can be utilized as the chiral discrimination agent for membrane-based enantiomeric separation processes.[29]

Spectroscopy. Micellar solutions have been employed to enhance the luminescence output of a number of analytes relative to that in water alone.[1,2,34] On the basis of previous luminescence probe studies of such media,[10,11,28,35] one would expect similar behavior in the presence of ionenes. Indeed, addition of either [3,16]- or [3,22]-ionene to aqueous solutions of several typical analytes resulted in significant shifts in emission wavelength maximum and enhanced fluorescence intensity (Table 10) compared to water. Thus, for example, upon increasing the ionene concentration, the fluorescence emission maxima of dansylated amino acids, such as dansylglycine and dansylvaline, progressively shift toward shorter wavelengths (from 550 nm in water to ~520 nm in aqueous ionene solutions). Concomitantly, the fluorescence intensity of these peaks increases significantly (Table 10). Depending upon the ionene employed and its concentration, fluorescence enhancements of from 10 to 15 are observed for dansylated amino acids. These observations suggest that the dansylamino acids sense a microenvironment of lower polarity than water upon binding to the ionene intramolecular aggregate. The luminescence shifts upon adding ionenes, and the observed enhancements are very similar to those found using surfactant micelles such as CTAB or CTAC[36] (Table 10). Intensity enhancements comparable to those achieved using cationic CTAB or CTAC micellar media were also obtained with the

(28) Suzuki, Y.; Tazuke, S. *Makromol. Chem.* **1984**, *185*, 521–526.
(29) Hinze, W. L.; Williams, R. W.; Fu, Z. S.; Suzuki, Y.; Quina, F. H. *Colloids Surfaces* **1990**, *48*, 79–94.
(30) Terabe, S.; Isemura, T. *Anal. Chem.* **1990**, *62*, 650–652.
(31) Ramsey, R. S.; Kerchner, G. A.; Cadet, J. J. *High Resolut. Chromatogr.* **1994**, *17*, 4–8.
(32) Crosby, D.; El Rassi, Z. *J. Liq. Chromatogr.* **1993**, *16*, 2161–2187.
(33) Yashima, T.; Tsuchiya, A.; Morita, O.; Terabe, S. *Anal. Chem.* **1992**, *64*, 2981–2984.
(34) Hinze, W. L.; Singh, H. N.; Baba, Y.; Harvey, N. G. *Trends Anal. Chem.* **1984**, *3*, 193–199.
(35) Tazuke, S.; Suzuki, Y. *J. Polym. Sci.: Polym. Lett. Ed.* **1978**, *16*, 223–228.
(36) Singh, N. H.; Hinze, W. L. *Analyst* **1982**, *107*, 1073–1080.

Table 10. Fluorescence Enhancement Data for Organic Solutes in Different Organized Assemblies

analyte	conditions[b]	fluorescence enhancement factor[a] [3,6]-ionene	[3,16]-ionene	[3,22]-ionene	0.03 M CTAB	6.3 mM CTAC	10.0 mM β-CD
nystatin	306/304	1.0–0.5[g]	18.3[c]	41.7[d]	35.0		2.4
p-aminobenzoic acid	305/334		1.2[e]		1.2		1.3
dansylglycine	338/521	1.1–1.2[g]	9.5[f]	11.3[c]	12.3	13.3	9.8
dansylvaline	360/520	1.1–1.4[g]	13.0[h]		16.0	17.0	5.6

[a] Enhancement factor in indicated medium relative to that observed in water alone under otherwise identical experimental conditions. [b] The numbers refer to the excitation and emission wavelengths, respectively, for the indicated analyte. [c] Ionene concentration was 1.0 mg/mL. [d] Ionene concentration was 0.06 mg/mL. [e] Ionene concentration was 0.3 mg/mL. [f] Ionene concentration was 5.0 mg/mL. [g] Ionene concentration ranged from 1.0 to 20.0 mg/mL. [h] Ionene concentration was 22.4 mg/mL.

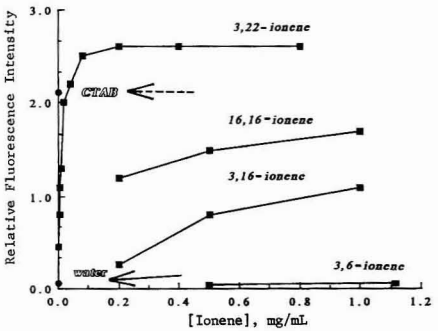

Figure 4. Dependence of the relative fluorescence intensity of nystatin as a function of the ionene concentration. The solid and dashed arrows indicate the relative intensity observed in the presence of bulk water alone and in 30 mM CTAB, respectively. The excitation and emission wavelengths were 306 and 404 nm, respectively.

[3,16]- and [3,22]-ionenes for the analytes *p*-aminobenzoic acid and nystatin (Table 10). In almost all cases, the fluorescence enhancements in the presence of the hydrophobic ionenes were greater than those obtainable using β-cyclodextrin solutions (Table 10) to improve sensitivity.

The magnitude of the enhancement observed in the presence of the ionenes was found to depend on ionene concentration. As illustrated in Figure 4 for the polyene antibiotic nystatin, the typical fluorescence intensity–ionene concentration behavior is a progressive increase in the intensity with increasing concentration up to a maximum plateau value. Similar profiles were obtained for the other analytes examined. In general, the [3,22]-ionene gave greater fluorescence enhancement factors at lower concentrations than the [16,16]- or [3,16]-ionene. This appears to parallel the order of relative hydrophobicities at the surface of the intramolecular aggregates of these ionenes[10]. As expected, the hydrophilic [3,6]-ionene did not function well as a fluorescence enhancement agent, with the fluorescence intensity values of the different analytes being only comparable to that achieved in water alone (see Table 10 and Figure 4). This is due to the fact that this ionene has an extended structure rather than a micellar-like hydrophobic domain, as previously noted. Thus, the [3,6]-ionene cannot appreciably bind analyte molecules and protect their excited states from quenchers.

It is known that when ester hydrolysis is performed in the presence of the [3,22]-ionene, the resultant catalytic rate enhancement is comparable to that obtained using surfactant CTAB micelles.[9,10] Thus, in addition to their use as luminescence enhancement agents, the ionenes can be employed to speed up otherwise slow analytical derivatization reactions. A cogent example is the spectrophotometric method for the determination of cyanide based on the reaction of the cyanide ion with Ellman's reagent, 5,5′-dithiobis(2-nitrobenzoic acid), to give the 2-nitro-5-thiobenzoate (TNB) anion.[37] The main disadvantage of this method is the relatively slow rate of the analytical reaction (eq 4) at the low concentrations employed

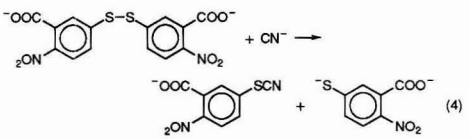

(4)

(110 min in aqueous pH 9.8 buffer). In the presence of the [3,16]-ionene (>0.20 mg/mL), however, the reaction was complete within 2 min in aqueous buffer (pH 8.0) solution. The high positive charge density of the ionene attracts and concentrates both Ellman's reagent and the negatively charged cyanide ion at the ionene surface, thus enhancing the reaction rate. Linear Beer's law plots for cyanide were obtained for this modified procedure (molar absorptivity 12 300 M^{-1} cm^{-1}), the wavelength maximum of the absorbing TNB anion being shifted from 412 nm in water to 436 nm in the presence of the [3,16]-ionene, comparable to the value of 435 nm in micellar CTAB.[38] This wavelength shift is consistent with the transfer of TNB anion to a much less polar environment upon binding to the [3,16]-ionene.

On the basis of the above results, intramolecular ionenes should prove useful as catalytic enhancers in reaction rate methods.[39,40]

CONCLUDING REMARKS

Compared to conventional surfactant micelles, the ionenes have other unique features that can be exploited in future analytical applications. Unlike micelles, ionenes can be immobilized on silica or solid supports[10] or transformed into insoluble films by means of cross-linking reactions, further facilitating the isolation of substrates and recycling of the ionene itself. Furthermore, the relatively facile synthesis of the requisite monomer building blocks should permit the tailor-

(37) Humphrey, R. E.; Hinze, W. L. *Talanta*, **1971**, *18*, 491–497.
(38) Fendler, J. H.; Hinze, W. L. *J. Am. Chem. Soc.* **1981**, *103*, 5439–5447.
(39) Bendito, D. P.; Rubio, S. *Trends Anal. Chem.* **1993**, *12*, 9–18.
(40) Gonzalez, V.; Moreno, B.; Sicilia, D.; Rubio, S.; Bendito, D. P. *Anal. Chem.* **1993**, *65*, 1897–1902.

made synthesis of ionenes possessing a variety of functionalities useful for specific analytical applications.

Acknowledgment is made to the Donors of The Petroleum Research Fund, administered by the American Chemical Society (PRF Grant 20162-AC7 to W.L.H.), the National Science Foundation (NSF Grant INT-9203011 to W.L.H.), and Brazilian CNPq Grant (to F.H.Q.) for the support of this research. In addition, F.H.Q. acknowledges research support from FAPESP and PADCT, and B.M. acknowledges financial support in the form of a fellowship from the DGICYT of Spain. The authors acknowledge Chris Maple and Bill Marsh (Dionex Corp.) for their assistance with the electrophoretic measurements.

Received for review February 4, 1994. Accepted June 24, 1994.®

® Abstract published in *Advance ACS Abstracts,* August 15, 1994.

Anal. Chem. **1994,** *66,* 3458–3465

Selectivity in Micellar Reversed-Phase Liquid Chromatography: C-18 and C-8 Alkyl Bonded Phases

Barry K. Lavine,* Sumar Hendayana, and Jonathan Tetreault
Department of Chemistry, Clarkson University, Potsdam, New York 13699-5810

Employing a set of six vanillin compounds as retention probes, the role of the surfactant-modified stationary phase in the micellar liquid chromatographic (MLC) separation process was investigated. Specifically, the effect of surfactant adsorption on retention and selectivity in MLC was evaluated by comparing the retention behavior of the vanillin compounds in different micellar media. Surfactant adsorption was found to produce distinct changes in the selectivity of the stationary phase. In fact, differences in selectivity between cetyltrimethylammonium bromide (CTAB) and sodium dodecyl sulfate (SDS) micellar reversed-phase liquid chromatography were found to be due to the differing nature of the SDS and CTAB bonded phase association. For SDS, the hydrophobic tail is associated with the bonded alkyl phase, with the sulfate head group oriented away from the alkyl bonded phase surface. Adsorption of SDS in the manner described would lead to the formation of a hydrophilic layer on C-18 and C-8, which would explain the superior resolution achieved with SDS for the vanillin compounds, which are also hydrophilic. For CTAB adsorbed on C-18, the nitrogen head group is probably incorporated partially or wholly into the bonded phase because of hydrophobic interactions between the methyl nitrogens and the bonded phase. Incorporation of CTAB in the manner described would ensure that much of the hydrophobic character of the original bulk phase is retained, which could also explain the longer retention time of the vanillin compounds with CTAB micellar mobile phases.

The field of micellar liquid chromatography (MLC) has experienced unprecedented growth since the first report on the use of aqueous micellar solutions as mobile phase in reversed-phase liquid chromatography (RPLC) by Armstrong and Henry in 1980.[1] Interest in MLC can be attributed to the unique selectivities exhibited by micellar mobile phases.[2,3] Micelles can organize and compartmentalize solutes at various sites within a surfactant assembly;[4] the location of the solute in the assembly is determined by the nature of the solute and the surfactant system used. Each solubilization site in/on the micelle is unique, i.e., the properties of fluidity, acidity, and polarity vary from one site to the next and are distinctly different from those of the bulk solvent.

The ability of micelles to selectively solubilize and interact with solute molecules is believed to be the basis of separation in MLC.[5] However, surfactant molecules readily adsorb on bonded stationary phases, e.g., C-18, C-8, or cyanopropyl. Because many stationary phase properties are altered by the process of surfactant adsorption,[6,7] the modification of the stationary phase by adsorbed surfactant can have profound implications with regard to retention and selectivity in MLC.

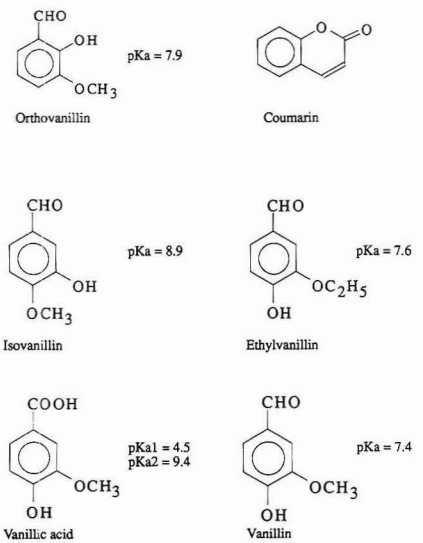

Figure 1. Vanillin test mixture. The pK_a values are from ref 8.

Employing a set of six vanillin compounds as retention probes (see Figure 1), the role of the surfactant-modified stationary phase in the MLC separation process was investigated. Specifically, the effect of surfactant adsorption on retention and selectivity in MLC was evaluated by comparing the retention behavior of the vanillin compounds in different micellar media. Surfactant adsorption was found to produce distinct changes in the selectivity of the stationary phase. Adsorption of sodium dodecyl sulfate (SDS) imparted a more hydrophilic character to the C-18 and C-8 reversed-phase material, whereas cetyltrimethylammonium bromide (CTAB)

(1) Armstrong, D.; Henry, S. J. *J. Liq. Chromatogr.* **1980**, *3*, 657–662.
(2) Armstrong, D. W.; Hinze, W. L.; Bui, K. H.; Singh, H. N. *Anal. Lett.* **1981**, *14*, 1659–1667.
(3) Weinberger, R.; Yarmchuk, P.; Cline-Love, L. J. *Anal. Chem.* **1982**, *54*, 1552–1558.
(4) Hinze, W. L.; Singh, H. N.; Baba, Y.; Harvey, N. G. *Trends Anal. Chem.* **1984**, *3*, 193.
(5) Hinze, W. L. In W. L. Hinze and D. W. Armstrong (Editors), *Ordered Media in Chemical Separations*; ACS Symposium Series 342; American Chemical Society: Washington, DC, 1987; pp 2–82.
(6) Berthod, A.; Roussel, A. *J. Chromatogr.* **1989**, *449*, 349–360.
(7) Borgerding, M. F.; Hinze, W. L.; Stafford, L. D.; Fulp, G. W.; Hamlin, W. C. *Anal. Chem.* **1989**, *61*, 1353–1358.
(8) Kortum, G.; Vogel, W.; Andrussow, W. *Dissociation Constants of Organic Acids in Aqueous Solutions*; Butterworth: London, 1961.

0003-2700/94/0366-3458$04.50/0
© 1994 American Chemical Society

adsorption on C-18 produced a more bulk hydrophobic stationary phase. Models depicting the structure of the SDS and CTAB surfactant-coated stationary phases are proposed from the retention data, and these models are in good agreement with solid state NMR data[9] on SDS- and CTAB-modified C-18.

EXPERIMENTAL SECTION

The vanillin compounds were obtained from Aldrich and were used as received. Stock solution of the test solutes were prepared in methanol and then diluted to the appropriate working concentration (550 μg/mL) using 50% methanol in water. The surfactants, sodium dodecyl sulfate (SDS) and cetyltrimethylammonium bromide (CTAB), were purchased from BDH Chemicals, Ltd., and prior to chromatographic use were purified using Kratohvil's procedure,[10] i.e., the surfactant was dissolved in ethanol and then activated charcoal was added to the ethanolic solution. After the charcoal was separated from the mother liquor by filtration, the surfactant was recrystallized from the ethanol and dried in an oven at 65 °C.

The micellar solutions were prepared in HPLC grade distilled water (J. T. Baker). The methanol–water mobile phases were also prepared with HPLC grade solvents. Both the micellar solutions and the methanol–water mobile phase solutions were filtered twice with a 0.45 μm Nylon membrane filter (Rainin Instruments, Woburn, MA) to remove particulate matter. Prior to use, the solutions were degassed and the pH was adjusted to 3 with hydrochloric acid to prevent ionization of the polar solutes in the mobile phase solutions.

All high-performance liquid chromatographic (HPLC) measurements were made with a Rainin 81–20 M analytical HPLC system which incorporates two Rainin HP pumps (Rainin Instruments), an Apple Macintosh SE computer as the controller, a Model 7125 Rheodyne injection valve, and a Rainin Dynamax mixer. The detector was a Knauer variable-wavelength UV–visible spectrometer (Berlin, Germany). The analytical column was either an Apex I 5-μm C-18 (10 cm × 4.6 mm i.d.) or an Apex I 5-μm C-8 (10 cm × 4.6 mm i.d.). The C-18 and C-8 columns used in this study were purchased from Jones Chromatography (Golden, CO) and were made from the same 5 μm silica support. The analytical column and mobile phase reservoir were water jacketed and temperature controlled. A silica precolumn (Rainin Instruments) placed between the injector and the pump saturated the mobile phase with silicates to minimize dissolution of the analytical column packing. Separate columns were used for cationic and anionic surfactants (as well as the methanol–water mobile phases) because of the strong and irreversible adsorption of these surfactants on the stationary phase of the C-18 and C-8 columns.

The dead volume of the system was determined by injecting different solutions such as methanol, methanol–water, or water onto the Jones columns. This volume, approximately 1.0 mL, was used for all k' calculations. k' values determined in this study were averages of at least triplicate determinations.

(9) Lavine, B. K.; Cooper, W. T.; He, Y.; Hendayana, S.; Han, J. H.; Tetreault, J. *J. Colloid Interfac. Sci.* **1994**, *165*, 497–504.

(10) Hsu, W. P. Micellar Growth in Solutions of Synthetic and Biological Surfactants. Ph.D. Thesis. Clarkson University, Potsdam, NY, 1985.

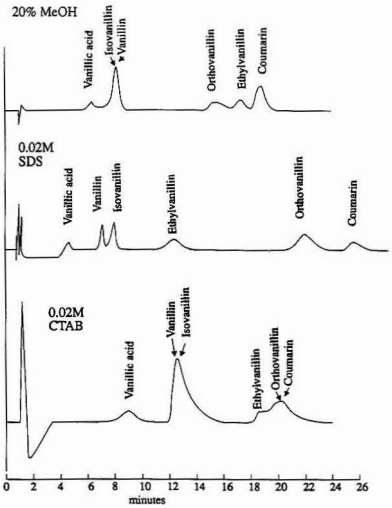

Figure 2. Chromatograms of the test mixture on Apex I C-18 with the following mobile phases: (a) 20% methanol in water, (b) 0.02 M SDS, and (c) 0.02 M CTAB. Flow rate was 1.0 mL/min; pH of each mobile phase was 3; the temperature of the column was 25 °C for methanol–water and SDS, 30 °C for CTAB. The chromatograms were reproduced using Corel 3.0.

Deviations in individual capacity factor values were never greater than 5%. All k' measurements were made at a flow rate of 1.0 mL/min. The k' values were measured at 25 °C for SDS and 30 °C for CTAB. (Since the Kraft point of CTAB is 23 °C, it was necessary to carry out the CTAB studies at higher temperature.)

RESULTS AND DISCUSSION

A series of chromatograms were run to illustrate some of the advantages associated with micellar mobile phases. The test mixture consisted of six compounds: vanillin, the principal flavor component in vanilla extract, and isomers or analogues of vanillin. Food chemists have long been interested in isolating and quantifying these compounds in a variety of sample matrices which, in part, was our motivation in choosing these compounds to study via MLC.

Figure 2 shows the separation of the mixture on Apex I C-18 with the following mobile phases: methanol–water, 0.02 M SDS, and 0.02 M CTAB. The acidified 20% methanol/80% water mobile phase has been recommended for the separation of vanillin from the other compounds in extract of vanilla on C-18 by Supelco.[11] For the anionic surfactant, the optimum separation is achieved with a 0.02 M SDS mobile phase. For the cationic surfactant, 0.02 M CTAB does not yield the optimum separation. However, it is representative of the type of separation which can be obtained for the test mixture using CTAB micellar mobile phases and is shown here for comparative purposes.

Several things are apparent from an examination of the data. First, the test mixture is completely separated by the

(11) Supelco. Technical Report, Vol. XI, No. 4, 1992; pp 15–16.

Table 1. Variation of Efficiency[a] and Asymmetry[b] with Mobile Phase on C-18 Column

	20/80 CH_3OH/H_2O (pH = 3)		0.02 M SDS (pH = 3)		0.02 M CTAB (pH = 3)	
compound	N	B/A	N	B/A	N	B/A
vanillic acid	684	1.25	528	2.19	169	4.31
vanillin	1113	0.80	576	2.38	289	4.12
orthovanillin	106	6.00	206	3.80	11	7.87
ethylvanillin	3897	1.00	561	2.08	514	2.97
isovanillin	834	0.46	578	3.34	394	4.30
coumarin	2559	1.00	271	3.50	147	4.34

[a] The Foley–Dorsey method[12] was used to compute N and determine the asymmetry of each peak. [b] Plate count values reported in this study were the averages of at least triplicate determinations.

SDS micellar mobile phase but not by the hydroorganic or CTAB mobile phase. Second, the efficiency of the chromatographic process is poor for all three mobile phases (see Table 1), and this implies that the variability in the resolution of the test mixture among the three mobile phases is due to differences in selectivity. Third, the retention time of four of the six vanillin compounds is greater with 0.02 M CTAB (cmc of CTAB is 0.9 mM at 30 °C in distilled water) than that with 0.02 M SDS (cmc of SDS is 8 mM at 25 °C in distilled water), even though the CTAB mobile phase contains significantly more micelles, which suggests that the interaction between each of these four compounds and the stationary phase is greater with CTAB-modified C-18 than that with SDS-modified C-18.

To better understand the reasons for the differences in selectivity among the three mobile phases, we first measured k' on Apex I C-18 for the vanillin compounds using five different SDS mobile phases: (1) 0.01 M SDS, (2) 0.02 M SDS, (3) 0.03 M SDS, (4) 0.04 M SDS, and (5) 0.05 M SDS. Next, k' was correlated to surfactant concentration using the equation developed by Cline-Love and Arunyanart:[13]

$$1/k' = [M]K_2/\Theta[L_s]K_1 + 1/\Theta[L_s]K_1 \quad (1)$$

where [M] is the concentration of surfactant, K_2 is the solute–micelle binding constant per monomer of surfactant, Θ is the chromatographic phase ratio, $[L_s]$ is the concentration of ligate on the stationary phase, and K_1 is the solute–stationary phase binding constant. A plot of $1/k'$ versus [M] should result in a straight line. In fact, excellent linearity was observed for all six compounds, i.e., $r^2 > 0.98$. A similar study with CTAB was undertaken, and again the agreement between $1/k'$ and [M] was very good, i.e., $r^2 > 0.98$. K_2 and $\Theta[L_s]K_1$ (the reciprocal of the intercept) for the six vanillin compounds are listed for SDS in Table 2 and for CTAB in Table 3. (K_2 is obtained by dividing the slope by the intercept.)

For the hydroorganic mobile phase, the interaction of the vanillin compounds with the mobile and the stationary phase was evaluated using the following linear relationship:

$$\ln k' = \ln k_w - B\Phi \quad (2)$$

$\ln k_w$ is the natural logarithm of the capacity factor of a solute in a purely aqueous medium and is a measure of the interaction of the solute with the stationary phase. Φ is the volume percentage of organic modifier (i.e., methanol) in the mobile phase. B is directly related to the solvent strength of the organic modifier but is used here as a measure of the strength of interaction between the solute and the mobile phase. For C-18 alkyl bonded phases, this equation[14] is valid when the modifier content is in the range of 10–50%.

Retention data for the vanillin compounds were generated using methanol–water mobile phases containing 10–50% methanol. The data were fitted to eq 2. Over this range of modifier content, reasonably good linear retention behavior was observed ($r^2 > 0.98$) for the vanillin compounds. Table 4 lists the values of K_w and B for each compound.

In Tables 2–4, the vanillin compounds are listed in the order that they elute from the C-18 column. For SDS (see Table 2), elution order clocks $\Theta[L_s]K_1$, implying that solute–stationary interactions define the selectivity of the separation. (If the micelle–solute binding constant defined the selectivity of the separation, K_2 would be expected to decrease as the retention time of the compounds increased, which is not the

Table 2. K_2 and $\theta[L_s]K_1$ for the Vanillin Compounds in Sodium Dodecyl Sulfate on C-18[a]

compound	$\theta[L_s]K_1$	K_2
vanillic acid	4.2 ± 0.18	28.9 ± 2.07
vanillin	9.6 ± 0.92	39.5 ± 6.12
isovanillin	10.5 ± 0.99	37.6 ± 4.75
ethylvanillin	17.5 ± 1.23	45.7 ± 3.65
orthovanillin	31.2 ± 1.95	41.3 ± 3.0
coumarin	41.7 ± 3.13	59.0 ± 4.60

[a] Determined on an Apex I C-18 column (10 cm × 4.6 mm i.d.); flow rate of 1.0 mL/min; pH = 3. Uncertainties in $\Theta[L_s]K_1$ and K_2 were determined from the statistical parameters of the least-squares fitting and from propagation of error.

Table 3. K_2 and $\Theta[L_s]K_1$ for the Vanillin Compounds in Cetyltrimethylammonium Bromide on C-18[a]

compound	$\Theta[L_s]K_1$	K_2
vanillic acid	16.9 ± 1.43	58.6 ± 5.23
vanillin	17.2 ± 1.18	32.7 ± 2.73
isovanillin	17.4 ± 1.21	29.7 ± 2.70
orthovanillin	26.5 ± 1.40	31.7 ± 2.31
ethylvanillin	36.0 ± 2.59	58.8 ± 4.47
coumarin	29.5 ± 3.48	37.3 ± 5.30

[a] Determined on an Apex I C-18 column (10 cm × 4.6 mm i.d.); flow rate of 1.0 mL/min; pH = 3. Uncertainties in $\Theta[L_s]K_1$ and K_2 were determined from the statistical parameters of the least-squares fitting and from propagation of error.

Table 4. K_w and Slope for the Vanillin Compounds in Methanol–Water Mobile Phase on C-18[a]

compound	K_w	slope
vanillic acid	31.8 ± 2.5	–0.035 ± 0.002
isovanillin	36.8 ± 1.5	–0.035 ± 0.001
vanillin	35.4 ± 1.4	–0.033 ± 0.001
orthovanillin	70.9 ± 2.1	–0.034 ± 0.001
ethylvanillin	101 ± 4.0	–0.037 ± 0.001
coumarin	103 ± 2.1	–0.035 ± 0.001

[a] Determined on an Apex I C-18 column (10 cm × 4.6 mm i.d.); flow rate of 1.0 mL/min; pH = 3. Uncertainties in K_w and the slope were determined from the statistical parameters of the least-squares fitting and from propagation of error.

(12) Foley, J. P.; Dorsey, J. G. *Anal. Chem.* **1983**, *55*, 730–737.
(13) Arunyanart, M.; Cline-Love, L. J. *Anal. Chem.* **1984**, *56*, 1557–1561.
(14) Kaliszan, R.; Osmialowski, K. *J. Chromatogr.* **1986**, *352*, 141–150.

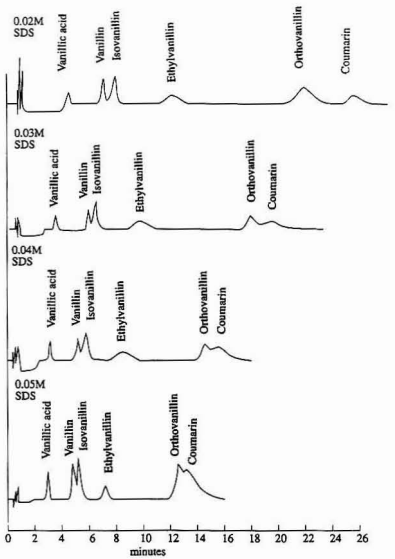

Figure 3. Chromatograms of the test mixture on Apex I C-18 with the following micellar mobile phases: 0.02 M SDS, 0.03 M SDS, 0.04 M SDS, and 0.05 M SDS. Flow rate was 1.0 mL/min; pH of each mobile phase was 3; column temperature was 25 °C. The chromatograms were reproduced using Corel 3.0.

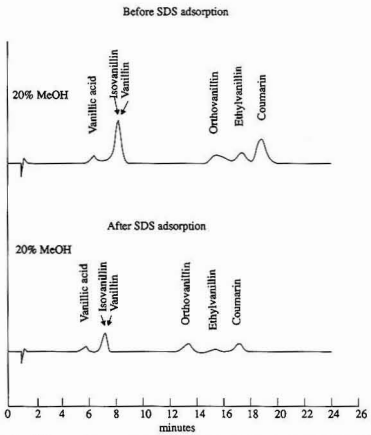

Figure 4. Chromatograms of the test mixture on an Apex I C-18 column using a 20% methanol in water mobile phase (pH = 3, 25 °C, flow rate of 1.0 mL/min) prior to and after separations with SDS micellar mobile phases. Since it is generally accepted that retention of all solutes in RPLC decreases as the polarity of the stationary phase increases, the decrease in retention time is probably due to an increase in the polarity of the C-18 phase as a result of SDS adsorption. The chromatograms were reproduced using Corel 3.0.

case.) Solute–stationary phase interactions also appear to play an important role in the separation process with the methanol–water mobile phase (see Table 4). (If solute–mobile phase interactions defined the selectivity of the separation, the slope would be expected to decrease as the retention time of the compound increased, which is not the case.) For CTAB, the elution order can be correlated to changes in both $\Theta[L_s]K_1$ and K_2 (see Table 3), which suggests that it is a combination of the interaction of the micelles and the surfactant-modified stationary phase with the solute that defines the selectivity of the separation of the test mixture on C-18 when a CTAB mobile phase is used.

Although SDS adsorption enhances the selectivity of the stationary phase toward the vanillin compounds, SDS micelle–solute interactions also contribute to the selectivity of this separation. For example, SDS micelles interact more strongly with vanillin than with isovanillin, as evidenced by the greater K_2 value for vanillin, and this interaction is responsible, at least in part, for the 6σ or base line resolution of these two compounds. Nevertheless, the successful separation of the vanillin compounds with the 0.02 M SDS mobile phase is primarily due to solute–stationary phase interactions, which is also the reason why the separation of the vanillin test mixture is more favorable at lower SDS concentrations (see Figure 3). At higher SDS concentrations, there are more micelles in the mobile phase, and the net result is that micelle–solute interactions play a greater role (which is not altogether beneficial) in the separation of the vanillin compounds. [Note that surfactant stationary phase interactions are independent of micelle concentration because the amount of surfactant adsorbed on the stationary phase remains constant once the concentration of surfactant in the mobile phase is above the cmc.[15]]

The observed differences in selectivity between CTAB and SDS micellar RPLC can be explained by the differing nature of the SDS and CTAB bonded phase association. In the case of SDS, it appears that the hydrophobic alkyl tail of the surfactant is associated with the C-18 bonded phase, with the sulfate group oriented away from it.[9] SDS incorporated into the bonded phase in the manner described, i.e., with its polar head group projecting away from the C-18 bonded phase toward the mobile phase, would greatly affect the polarity of the bonded phase (see Figure 4 and Table 5) and would also lead to the formation of a hydrophilic layer, which would explain the superior resolution achieved by SDS for the vanillin compounds, which probably undergo some type of selective hydrogen-bonding interaction with the layer. The increase in polarity of the C-18 bonded phase as a result of SDS adsorption is evident from an examination of Figure 4, which shows chromatograms of the test mixture on C-18 using a 20% methanol in water mobile phase prior to and after separations involving SDS micellar mobile phases. The shorter retention times of the vanillin compounds on the SDS-modified C-18 are due to an increase in the polarity of the stationary phase that has occurred as a result of surfactant adsorption. In addition, the correlation coefficient, r, for log $K_{1(SDS)}$ and log of the octanol–water partition coefficient or log P (which is a well-known index of hydrophobicity) is 0.166 (see Table 5), which is substantively smaller than the correlation coefficient for log K_w vs log P. Clearly, the smaller log P correlation coefficient suggests that a decrease in the hydrophobicity of the bonded phase has occurred as a result of surfactant adsorption.

(15) Hung, C. T.; Taylor, R. B. *J. Chromatogr.* **1981**, *209*, 175–190.

Table 5. Solute Hydrophobicity as Represented by the log[a,b] of the Octanol–Water Partition Coefficient (log *P*) versus log K_w or log K_1 for the Vanillin Compounds on C-18

compound	log *P*	log K_w[c]	log $K_{1(SDS)}$[d]	log $K_{1(CTAB)}$[e]
isovanillin	0.97	1.57	1.02	1.24
vanillin	1.21	1.55	0.98	1.24
orthovanillin	1.37	1.85	1.49	1.42
coumarin	1.39	2.01	1.62	1.47
vanillic acid	1.43	1.50	0.62	1.23
ethylvanillin	1.88	2.00	1.24	1.56

[a] log *P* is a well-known index of hydrophobicity. [b] log *P* values were obtained from the CLOGP Program, Medicinal Chemistry Project, Pomona College, Claremont, CA. [c] The correlation coefficient for log *P* and log K_w is 0.638. [d] The correlation coefficient for log *P* and log $K_{1(SDS)}$ is 0.188. The decrease in *r* is not surprising since SDS adsorption imparts significant hydrophilic character to the C-18 bonded phase. [e] The correlation coefficient for log *P* and log $K_{1(CTAB)}$ is 0.758. The high correlation between log *P* and log $K_{1(CTAB)}$ is not altogether surprising since incorporation of CTAB into the bonded phase in the manner described would ensure that much of the hydrophobic character of the original bulk C-18 phase is retained.

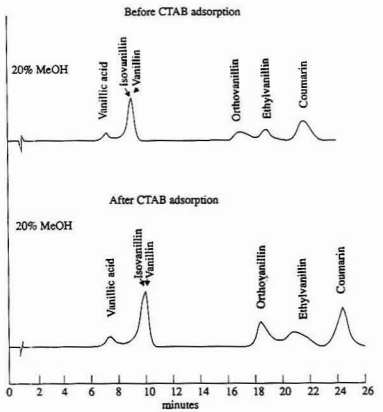

Figure 5. Chromatograms of the test mixture on an Apex I C-18 column using a 20% methanol in water mobile phase (pH = 3, 25 °C, flow rate of 1.0 mL/min) prior to and after separations with CTAB micellar mobile phases. The increase in retention time is probably due to an increase in the hydrophobicity of the C-18 phase as a result of CTAB adsorption. The chromatograms were reproduced using Corel 3.0.

The hydrophilic layer that is formed on the stationary phase would also affect the penetration depth of the vanillin compounds into the bonded phase because of strong hydrogen-bonding interactions between these compounds and the layer. The expected result would be a decrease in hydrophobic interactions between the vanillin compounds and the C-18 stationary phase. Clearly, this is part of the answer as to why the retention time of the vanillin compounds is greater with 0.02 M CTAB than with 0.02 M SDS or 0.03 M SDS. (The concentration of micelles in the 0.02 M CTAB solution is approximately the same as that in the 0.03 M SDS solution using the cmc and aggregation number data on page 224 of ref 5.)

This simplified model of the SDS-modified C-18 bonded phase has also been used by Armstrong and Berthod[16] to explain poor stationary phase mass transfer in MLC. According to Armstrong, a hydrophobic solute has to traverse the hydrophilic boundary layer formed by the sulfate head groups, ions, and associated waters in order to gain access to or to leave the stationary phase. This boundary layer can, therefore, obstruct mass transfer between the bulk solvent and the bonded phase. Furthermore, both the thickness and the viscosity of the polar layer can be increased by adsorption of more surfactant onto the bonded phase. Any or all of these factors can contribute to poor stationary phase mass transfer in SDS micellar RPLC.

For CTAB, the nitrogen head group is probably oriented closer to the silica surface due to hydrophobic interactions between the N-methyl groups and the bonded phase.[9] In fact, the nitrogen head group of CTAB is probably incorporated partially or wholly into the bonded phase, giving rise to a modified bulk phase that is significantly denser. Incorporation of CTAB in the manner described would ensure that much of the hydrophobic character of the original bulk stationary phase is retained. This conclusion is reinforced by Figure 5, which shows chromatograms of the test mixture on C-18 using a 20% methanol in water mobile phase prior to and after separations involving CTAB micellar mobile phases. The longer retention times of the vanillin compounds on the CTAB-modified C-18 suggests that an increase in the hydrophobicity of the bonded phase has occurred as a result of surfactant adsorption. We believe that a small amount of CTAB adsorbs "head-first" on the bonded phase. (The technique of solid state NMR which was used in a previous study[9] to examine the nature of surfactant bonded phase associations in MLC is probably not sufficiently sensitive to pick up the signal generated by the small amount of CTAB monomer which is adsorbed head-first on C-18.) The CTAB that is adsorbed head-first is probably irreversibly adsorbed on C-18. Hence, it is conceivable that a sizable fraction of CTAB irreversibly sorbed on the C-18 exists in the so-called head-first orientation, which would explain the greater retention time of the vanillin compounds with a 20% methanol in water mobile phase after, rather than prior to, separations involving CTAB micellar mobile phases because of the decrease in the silanol activity of the bonded phase. In other words, the decrease in silanol activity due to head-first adsorption by some CTAB monomers might compensate for the increase in the polarity of the C-18 phase due to the presence of N-alkyl head groups at the surface of the stationary phase, which would explain the observed differences in retention times for the chromatograms shown in Figure 5.

The correlation coefficient for log *P* and log $K_{1(CTAB)}$ is 0.758, whereas *r* is 0.638 for log K_w and log *P* (see Table 5). However, the correlation coefficients are small enough that we judge them to be approximately equal, which reinforces our conclusion that much of the hydrophobic character of the original bulk phase is retained because of the manner in which CTAB is adsorbed onto the bonded phase. Models that depict the structure of CTAB- and SDS-modified C-18 are shown in Figure 6.

Our studies of the modification of bonded alkyl phase by the adsorption of SDS or CTAB monomers were not limited to C-18 alkyl bonded phases. In Figure 7, the separation of the vanillin test mixture on Apex I C-8 is shown with the same

(16) Armstrong, D. W.; Ward, T. J.; Berthod, A. *Anal. Chem.* **1986**, *58*, 579–582.

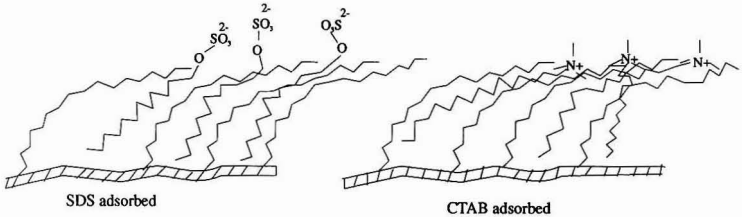

Figure 6. Models depicting the structures of SDS- and CTAB-modified C-18.

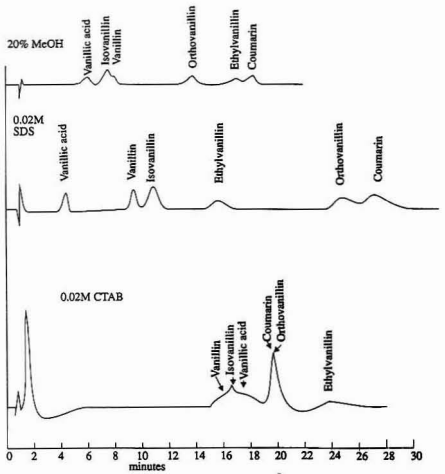

Figure 7. Chromatograms of the test mixture on Apex I C-8 with the following three mobile phases: 20% methanol in water, 0.02 M SDS, and 0.02 M CTAB. Flow rate was 1.0 mL/min; pH of each mobile phase was 3; column temperature was 25 °C for methanol–water and SDS, 30 °C for CTAB. The chromatograms were reproduced using Corel 3.0.

Table 6. K_2 and $\Theta[L_s]K_1$ for the Vanillin Compounds in Sodium Dodecyl Sulfate on C-8[a]

compound	$\Theta[L_s]K_1$	K_2
vanillic acid	4.4 ± 0.4	21.2 ± 2.9
vanillin	12.5 ± 1.6	41.1 ± 8.1
isovanillin	14.2 ± 2.0	37.9 ± 7.8
ethylvanillin	24.1 ± 0.6	58.9 ± 1.6
orthovanillin	40.5 ± 1.6	66.6 ± 2.9
coumarin	49.8 ± 1.2	86.0 ± 2.4

[a] Determined on an Apex I C-8 column (10 cm × 4.6 mm i.d.); flow rate of 1.0 mL/min; pH = 3. Uncertainties in $\Theta[L_s]K_1$ and K_2 were determined from the statistical parameters of the least-squares fitting and from propagation of error.

three mobile phases used in the C-18 study: 0.02 M SDS, 0.02 M CTAB, and 20% methanol in water.

Several things are apparent from an examination of the data. First, the test mixture is completely separated by the SDS micellar mobile phase but not by the hydroorganic mobile phase. As with C-18, solute–stationary phase interactions again appear to play an important role in the separation of the test mixture with these two mobile phases (see Tables 6 and 7). Second, the retention time of the vanillin compounds with the 0.02 M SDS mobile phase is longer on C-8 than on

Table 7. K_w and Slope for the Vanillin Compounds in 20% Methanol in Water on C-8[a]

compound	K_w	slope
vanillic acid	15.7 ± 1.6	−0.030 ± 0.004
isovanillin	21.1 ± 0.42	−0.030 ± 0.0005
vanillin	20.7 ± 0.41	−0.029 ± 0.0007
orthovanillin	41.2 ± 1.2	−0.030 ± 0.0008
ethylvanillin	54.7 ± 1.1	−0.033 ± 0.0007
coumarin	59.7 ± 1.8	−0.032 ± 0.0008

[a] Determined on an Apex I C-8 column (10 cm × 4.6 mm i.d.); flow rate of 1.0 mL/min; pH = 3. Uncertainties in K_w and slope were determined from the statistical parameters of the least-squares fitting and from propagation of error.

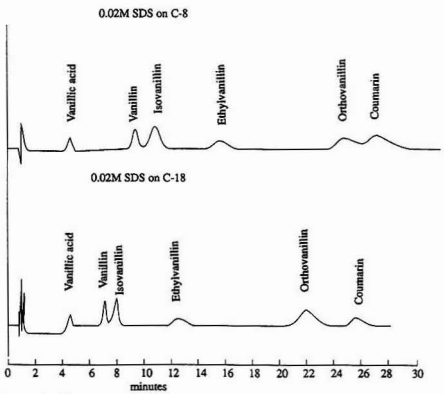

Figure 8. Chromatograms of the test mixture on a C-18 and C-8 Apex I column with a 0.02 M SDS mobile phase. Flow rate was 1.0 mL/min; pH of each mobile phase was 3; column temperature was 25 °C. The chromatograms were reproduced using Corel 3.0.

C-18 (see Figure 8), even though the C-18 phase has a higher carbon loading. (According to the manufacturer, the carbon loading of Apex I C-18 is 13.3%, whereas it is only 9.0% for Apex I C-8.) Since the C-18 and C-8 columns used in this study were the same except for the bonded phase, the longer retention time of the vanillin compounds on C-8 can probably be attributed to lower SDS sorption on octylsilane because of the higher bonding chain density of the C-8 phase used in this study. (Berthod, Ginnard, and Gonnet have also reported that significantly more SDS adsorbs on C-18 than on C-8 alkyl bonded phases.[17]) Lower SDS sorption would result in a more hydrophobic phase. Since the hydrophilic layer formed by sorbed SDS is responsible for the superior resolution

(17) Berthod, A.; Girard, I.; Gonnet, C. *Anal. Chem.* **1986**, *58*, 1356–1361.

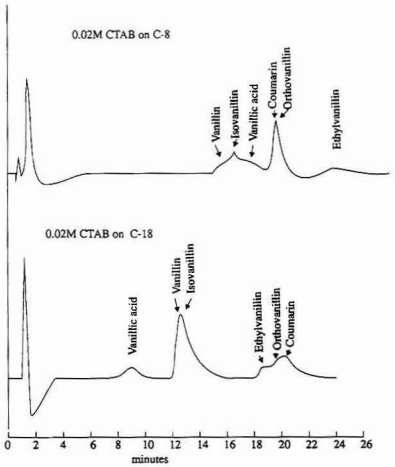

Figure 9. Chromatograms of the test mixture on a C-18 and C-8 Apex I column with a 0.02 M CTAB mobile phase. Flow rate was 1.0 mL/min; pH of each mobile phase was 3; column temperature was 30 °C. The chromatograms were reproduced using Corel 3.0.

achieved by the 0.02 M SDS micellar mobile phase for the vanillin test mixture, the decrease in the resolution of the polar test mixture which occurs when a C-8 column is used (see Figure 8) can probably be attributed to lower SDS sorption on octylsilane as well. Third, there is a change in elution order when an Apex I C-8 column is used, in lieu of an Apex I C-18 column, with the 0.02 M CTAB mobile phase (see Figure 9). The retention time of the vanillin compounds with the 0.02 M CTAB mobile phase is also longer on C-8 than on C-18. On the basis of these two effects, reversals in elution order and longer retention times, we can conclude that differences in the selectivity of CTAB-modified C-18 and C-8 alkyl bonded phases toward the vanillin compounds are due to the differing nature of the CTAB monomer C-18 and C-8 bonded phase association. In all likelihood, small surfactant aggregates form within the C-8 stationary phase, and these aggregates are responsible for the longer retention times and reversals in elution order of the polar test mixture. (We define the stationary phase in MLC as a ternary combination of silica substrate, bonded organic moiety, and adsorbed surfactant.) These aggregates are probably similar in nature to the surfactant clusters that form in the presence of water-soluble polymers, e.g., poly(ethylene oxide) or poly(vinyl pyrrolidone) in aqueous media.[18]

Our previous studies[19] in MLC have shown that CTAB aggregates exhibit strong selectivity toward phenols and other compounds containing acidic functional groups. This selectivity can be attributed to a secondary chemical equilibrium process involving the transfer of a proton from the ionogenic solute to water molecules in the Stern region of the surfactant aggregate. In fact, a decrease of 0.5–3.0 in the pK_a value of a dissociable amphiphile can occur upon incorporation of the guest molecule into a cationic micelle.[20]

Table 8. K_2 and $\Theta[L_s]K_1$ for the Vanillin Compounds in Cetyltrimethylammonium Bromide on C-8[a,b]

compound	$\Theta[L_s]K_1$	K_2
vanillin	20.4 ± 0.8	46.4 ± 2.3
isovanillin	21.2 ± 3.2	41.3 ± 7.5
vanillic acid	37.9 ± 7.2	126.2 ± 24.2
coumarin	25.1 ± 0.6	43.9 ± 1.3
orthovanillin	27.3 ± 2.2	36.5 ± 3.6
ethylvanillin	38.6 ± 1.5	69.0 ± 2.9

[a] Determined on an Apex I C-8 column (10 cm × 4.6 mm i.d.); flow rate of 1.0 mL/min; pH = 3. Uncertainties in $\Theta[L_s]K_1$ and K_2 were determined from the parameters of the least-squares fitting and from propagation of error. [b] The correlation between $\Theta[L_s]K_1$ and elution order for the vanillin compounds is stronger on C-8 than it is on C-18. (If vanillic acid is removed from the table, the correlation between $\Theta[L_s]K_1$ and elution order is very strong.)

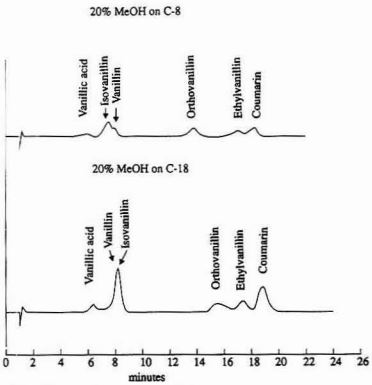

Figure 10. Chromatograms of the test mixture on a C-18 and C-8 Apex I column with a 20% methanol in water mobile phase. Flow rate was 1.0 mL/min; pH of each mobile phase was 3; column temperature was 25 °C. The chromatograms were reproduced using Corel 3.0.

The aforementioned acid–base effect would explain the strong interaction of vanillic acid with the CTAB-modified C-8 phase (see Table 8). In other words, a decrease in the pK_a of the vanillic acid probably occurs as a result of its incorporation into the CTAB aggregates that we postulate to exist within the C-8 bonded phase. The existence of surfactant aggregates within the C-8 stationary phase would also explain the longer retention times and the differences in elution order between C-18 and C-8 bonded phases which occur when CTAB micellar mobile phases are used. The importance of solute–stationary phase interactions in the separation of the polar test mixture on C-8 with CTAB micellar mobile phases (see Table 8) further reinforces this conclusion. Although lower CTAB sorption on the C-8 bonded phase could also be responsible for the longer retention time of the vanillin compounds, it cannot be the cause of the reversals in the elution order of the test mixture.

Because of the greater silanol activity of the C-8 phase, the possibility that silanol groups are responsible for the reversals through their interactions with the vanillin compounds was also considered. If the silanol groups were responsible for the

(18) Goddard, E. D. *Colloids Surf.* **1986**, *19*, 255–300; 301–329.
(19) Lavine, B. K.; White, A. J.; Han, J. H. *J. Chromatogr.* **1991**, *542*, 29–40.
(20) Underwood, A. L. *Anal. Chim. Acta* **1982**, *140*, 89–97.

reversals, then there would be a marked difference in the retention behavior of the vanillin compounds on C-18 and C-8 with a methanol in water mobile phase. However, the vanillin compounds on C-18 and C-8 exhibit similar retention behavior with a 20% methanol in water mobile phase (see Figure 10), as well as with other methanol–water mobile phases, e.g., 30%, 40%, or 50% methanol in water solvent mixture. Hence, the reversals in the elution order of the test mixture must be due to the differing nature of the CTAB monomer C-18 and C-8 bonded phase association.

CONCLUSION

Solute–stationary phase interactions in MLC are very important. The differing nature of the SDS and CTAB bonded phase association is largely responsible for the observed differences in selectivity between CTAB and SDS micellar reversed-phase liquid chromatography. Perhaps some of the reported differences[21,22] in selectivity between MLC and reversed-phase HPLC with hydroorganic mobile phases are also due in some measure to the modification of the stationary phase by adsorbed surfactant.

(21) Khaledi, M. G. *Anal. Chem.* **1988**, *60*, 876–887.
(22) Khaledi, M. G.; Peuler, E.; Ngwainbi, J. N. *Anal. Chem.* **1987**, *59*, 2738–2747.

ACKNOWLEDGMENT

This work was supported by a grant from the Reynolds Tobacco Company. Jonathan Tetreault acknowledges the generous support of the National Science Foundation (NSF-REU awardee), and Sumar Hendayana acknowledges the financial support of the Ministry of Education of Indonesia. Critical discussions on amphiphilic association structures and surfactant adsorption with Stig Friberg, Petr Zuman, and Josip Kratohvil of the Chemistry Department of Clarkson University are also acknowledged.

Received for review February 10, 1994. Accepted June 30, 1994.®

® Abstract published in *Advance ACS Abstracts*, August 15, 1994.

Anal. Chem. **1994,** *66,* 3466–3471

Modification of the Electrophoretic Mobility of Neutral and Charged Polysaccharides

Morgan Stefansson and Milos Novotny*
Department of Chemistry, Indiana University, Bloomington, Indiana 47405

Suitable buffer additives can either induce or reduce the electrophoretic mobility of certain polysaccharides during capillary electrophoresis. With water-soluble cellulose derivatives, adsorption of detergents on the analyte molecules governs the migration rates. Different types of adsorption sites, including multilayer formation, were found to be present on the cellulose-derived polymers. For highly charged polysaccharides (heparins), the electrophoretic mobility can be controlled by the use of ion-pairing reagents. The concentration and number of cationic charges appear useful in optimizing the separation selectivity. Migration models based on secondary thermodynamic equilibria are presented and evaluated for different polysaccharides.

The area of glycoconjugate analysis has recently been advanced by various methodological developments in capillary zone electrophoresis (CZE).[1-9] In particular, the combination of CZE with laser-induced fluorescence detection allows ultrasensitive detection of oligosaccharides cleaved from glycoproteins[2] as well as detection of polysaccharides labeled fluorescently at the reducing end of a molecule.[3] The separation media utilized in such analyses include higher concentrated gels,[4] entangled polymer matrices,[5] and free-buffer media.[6,7] Buffer additivies can further aid selectivity, as exemplified by chiral recognition based on sugar–sugar interactions.[8]

An additional important role of buffer additives in the CZE of carbohydates involves assisting electrophoretic migration through addition of charged moieties. The complexation of vicinal hydroxy groups in a sugar molecule with borate[9] is the most well-known example, although additional anions[10] and even cations[11,12] can also complex with carbohydrates. In CZE experiments using spectroscopic detection of sugar derivatives, the choice of a tag with charged moieties additionally affects electrophoretic mobility.[8] The borate complexation does not appear uniform throughout the length of a heterogenous oligosaccharide chain due to differences in the stability constants for various sugar structures, and further optimization of the separation of complex oligomeric mixtures is feasible by affecting various secondary-equilibrium processes (use of additional buffer additives).

Using certain buffer additivies, we were successful in optimizing the separation of a variety of complex oligosaccharide mixtures, including dextrans, amylose, laminarin, and amylopectin fragments.[8,13] Such separations in CZE are essentially governed by differences in the charge-to-mass ratios among the oligomers, and the number of charges on the fluorescent tag and concentration of boric acid are the primary means of optimizing the separation selectivity and analysis time for α- and β-glucans.[8,13] Notable exceptions causing problems in electrophoresis are two classes of very important polysaccharides: chemically modified celluloses and heparins. Due to the lack of sufficient hydroxyl groups in their molecules, chemically modified celluloses do not complex readily with borate and thus cause problems with migration in electric fields. Heparins, on the other hand, are totally ionized throughout the entire pH range due to their abundance of sulfate groups. Consequently, their electrophoretic mobility is high, resulting in comigration of different polymeric species. For representative structures of modified celluloses and heparins, see Figure 1.

Celluloses are perhaps the most abundant biopolymers in nature (wood, plants, seaweed, etc.). They are highly polydisperse materials, characterized by different degrees of polymerization and low water solubility. Through chemical modification of their hydroxy groups, a variety of chemical and physical properties can be imposed on the cellulose molecules: water solubility, gel strength, viscosity, stability toward enzymatic degradation, etc. Modified celluloses are important materials for extensive use in food and pharmaceutical industries. During isolation and chemical modification of cellulose, heterogeneities often arise due to incomplete substitution, side reactions, depolymerization, oxidation, etc.[14] Incomplete reactions may result in products of questionable uniformity. Yet, such variations may present difficulties for drug formulation, release, and uptake in the human body during various pharmaceutical applications. Analytical characterization of the cellulose-derived materials has thus far been in a fairly primitive stage, confined mostly to gross measurements of average molecular weight and bulk physical properties. Alternatively, polymer hydrolysis is performed, followed by measurements of derivatized, small fragments by chromatographic methodologies.[14] A more detailed analysis of intact polymers would clearly improve the prospects of

(1) Honda, S.; Makino, A.; Suzuki, S.; Kakehi, K. *Anal. Biochem.* **1990,** *191,* 228–236.
(2) Liu, J.; Shirota, O.; Wiesler, D.; Novotny, M. *Proc. Natl. Acad. Sci. U.S.A.* **1991,** *88,* 2302–2306.
(3) Liu, J.; Shirota, O.; Novotny, M. *Anal. Chem.* **1991,** *63,* 413–417.
(4) Liu, J.; Shirota, O.; Novotny, M. *Anal. Chem.* **1992,** *64,* 973–975.
(5) Sudor, J.; Novotny, M. *Proc. Natl. Acad. Sci. U.S.A.* **1993,** *90,* 9451–9455.
(6) Stefansson, M.; Novotny, M. *Anal. Chem.* **1994,** *66,* 1134–1140.
(7) Chiesa, C.; Horvath, C. *J. Chromatog.* **1993,** *645,* 337–352.
(8) Stefansson, M.; Novotny, M. *J. Am. Chem. Soc.* **1993,** *115,* 11573–11580.
(9) Novotny, M.; Sudor, J. *Electrophoresis* **1993,** *14,* 373–389.
(10) Bourne, E. J.; Searle, F.; Weigel, H. *Carbohydr. Res.* **1971,** *16,* 185–187.
(11) Honda, S.; Yamamoto, K.; Suzuki, S.; Ueda, M.; Kakehi, K. *J. Chromatogr.* **1991,** *588,* 327–333.
(12) Stefansson, M.; Westerlund, D. *J. Chromatogr.* **1993,** *632,* 195–200.
(13) Stefansson, M.; Novotny, M. *Carbohydr. Res.* **1994,** *258,* 1–9.
(14) Yalpani, M. *Polysaccharides: Synthesis, Modifications, and Structure/Property Relations*; Elsevier: Amsterdam, 1988; Chapter 6.

0003-2700/94/0366-3466$04.50/0
© 1994 American Chemical Society

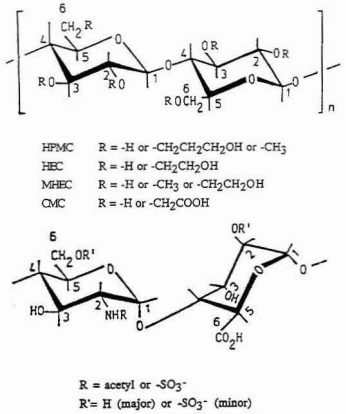

Figure 1. Structures of (top) chemically modified celluloses and (bottom) heparins.

both cellulose modification processes and applications of such modified materials.

Heparins constitute another important class of polysaccharides due to the variety of biological activities they exhibit. They are highly charged, sulfated structures with an average molecular weight of 5000–40 000.[15] Heparins also display a high degree of polydispersity, rendering the analysis and characterization of such compounds difficult.

The main purpose of this communication is to demonstrate that the above-mentioned, hard-to-analyze classes of polysaccharides can be successfully dealt with through CZE. With respect to modified celluloses, the relative hydrophobicity of such compounds is being utilized in binding conventional ionic detergents that provide the needed charge for electromigration. Conversely, highly charged polysaccharides can be modified by other suitable buffer additives. Simple migration models, based on secondary thermodynamic equilibria (ion-pairing and adsorption interactions), are also presented. Examples of optimized separations will be demonstrated as based on this approach.

EXPERIMENTAL SECTION

Chemicals. All chemicals used in this study were received from Sigma (St. Louis, MO), except for boric acid (Malinkrodt, Inc., Paris, KY) and sodium cyanoborohydride (Aldrich, Milwaukee, WI). Acrylamide and ammonium persulfate were purchased from Bio-Rad Laboratories (Hercules, CA). The celluloses used were carboxymethyl- (CMC), hydroxypropylmethyl- (HPMC 300 and 60), hydroxyethyl- (HEC), and methylhydroxyethyl (MHPC) cellulose, where the designations 300 and 60 on HPMC refer to the average relative molecular weights (300 000 and 60 000, respectively). The samples were kindly donated by Prof. Jörgen Vessman (Astra Hässle AB, Mölndal, Sweden).

Column Preparation. Various lengths of fused silica capillaries (Polymicro Technologies, Phoenix, AZ) of 50 μm i.d. (187 μm o.d.) were used as the separation columns. They were coated with a layer of linear polyacrylamide according to a slightly modified version of the Hjertén method.[16] First, the new capillary was treated with 0.1 M NaOH for 1 h and rinsed with 20 mM acetic acid and methanol. The silica wall was activated by coupling of (γ-methacryloxy)propyl)-trimethoxysilane (10 μL dissolved in dichloromethane containing 0.02 M acetic acid) to the inner surface during a 60-min treatment performed under nitrogen pressure. The capillary was then rinsed with methanol and water. Subsequently, a 4% (w/w) acrylamide solution, containing 1 μL/mL of *N,N,N′,N′*-tetramethylethylenediamine (TEMED) and 1 mg/mL ammonium persulfate, was passed through the capillary under nitrogen pressure for 30 min. Finally, the capillary was rinsed with water and dried under a stream of nitrogen.

Sample Preparation. The polysaccharides were converted to fluorescent derivatives using the CBQCA reagent.[3] The reducing ends of the polysaccharide molecules were reductively aminated by adding an aliquot containing 1 M ammonium sulfate and 0.2 M sodium cyanoborohydride and heating the mixture at 100 °C for 90 min. Thereafter, the samples were desalted by precipitation, using a large excess of ethanol, reconstituted in 20 mM potassium cyanide containing 10 mM CBQCA reagent, and left at room temperature for 60 min. The samples were stable when stored at −20 °C before analysis. The hydrodynamic technique of sample introduction was employed.

Apparatus. Our home-made instrumental setup for capillary electrophoresis/laser-induced fluorescence has been described earlier.[17] A high-voltage power supply (Spellman High Voltage Electronics, Plainview, NY) capable of delivering 0–40 kV was employed. On-column fluorescence detection was accomplished with a Model 4112-50 helium/cadmium laser (Omnichrome, Chino, CA) as the excitation source, operating at 442 nm, while fluorescence was measured at 550 nm.

RESULTS AND DISCUSSION

Migration Models. *Uncharged Solutes.* In order to impose electrophoretic migration, μ_{ep}, on a neutral or uncharged analyte, C, it is necessary to induce complex formation or adsorption of a charged species, S, on the solute. This can be described by the mass-balance equation, C + S = CS, and the apparent stability constant is expressed accordingly:

$$K_{app} = [CS]/[C][S] \quad (1)$$

Assuming that the molecular weight of S is negligible compared to that of C, μ_{ep} becomes proportional to the amount of S complexed to C, i.e., the adsorption isotherm for S. When all sites on C are occupied, the migration velocity reaches a maximum, μ_{max}, in accord with Langmuirian adsorption behavior.[18,19] The magnitude of μ_{max} will be determined by the number of sites on the solute (capacity). The electro-

(15) Oegema, T. R., Jr.; Kraft, E. L.; Jourdian, G. W.; Van Valen, T. R. *J. Biol. Chem.* **1984**, *259*, 1720–1726.

(16) Hjertén, S. *J. Chromatogr.* **1985**, *347*, 191–198.
(17) Liu, J.; Hsieh, Y.-Z.; Wiesler, D.; Novotny, M. *Anal. Chem.* **1991**, *63*, 408–412.
(18) Horejsi, V. *J. Chromatogr.* **1979**, *178*, 1–13.
(19) Bog-Hansen, T. C. *Anal. Biochem.* **1973**, *56*, 480–486.

phoretic migration velocity will consequently be governed by the degree of complexation/adsorption at a given concentration of S, which can be expressed as

$$\mu_{ep} = \mu_{max}[CS]/([CS] + [C]) = \mu_{max}K_{app}[S]/(1 + K_{app}[S]) \quad (2)$$

A linear relationship is obtained by inverting eq 2:

$$1/\mu_{ep} = 1/\mu_{max} + 1/(\mu_{max}K_{app}[S]) \quad (3)$$

where μ_{max} and K_{app} can be obtained from the intercept and the slope, respectively.

If more than one molecule S is complexed/adsorbed to the same site, i.e., a multilayer formation is achieved, the equilibrium situation can be expressed by the cumulative apparent constant K_n:

$$K_n = [CS_n]/[C][S]^n \quad (4)$$

where n is the number of S molecules (assuming that $K_n[S]^n \gg K_{(n-1)}[S]^{(n-1)}$). The expression for μ_{ep} is

$$\mu_{ep} = \mu_{max}K_n[S]^n/(1 + K_n[S]^n) \quad (5)$$

and through linearization by rearrangement and use of a logarithm, it becomes

$$\log(\mu_{ep}/\mu_{max} - \mu_{ep}) = \log K_n + n \log [S] \quad (6)$$

Charged Solutes. The reduction in μ_{ep} for a charged analyte, H, by complexation with a species, S, of opposite charge, can similarly be expressed. In the absence of S, the solute migrates with maximum velocity, μ_{max}. If S is added to the system and complexes to H, the effective charge will decrease; hence, the electrophoretic mobility will decrease. The quantity μ_{ep} can be considered to be a direct function of the degree of μ_{max} present at a given concentration of S, once again assuming that the molecular weight contribution of S is negligible. The electrophoretic mobility for the charged solute at a given concentration of S can similarly be expressed as the fraction of free analytes according to:

$$\mu_{ep} = \mu_{max}[H]/([H] + [HS]) = \mu_{max}/(1 + K_{app}[S]) \quad (7)$$

The linearized expression for μ_{ep} then becomes

$$1/\mu_{ep} = (1/\mu_{max}) + K_{app}[S]/\mu_{max} \quad (8)$$

The advantage of using this approach in deriving the migration models presented above is that no knowledge of the complexation mechanism(s) involved is needed in describing the relationship between electrophoretic migration and concentration of a complexing agent. Furthermore, the constants (K_{app} and μ_{max}) needed in evaluation of the models can easily be obtained experimentally.

Chemically Modified Celluloses. Electrophoretic mobility, caused solely by a charged and fluorescent tag covalently bound to an uncharged cellulose molecule, will be extremely low due to the high molecular weight of the analyte (low charge-to-mass ratio). Furthermore, as most hydroxyl groups have been chemically modified, complexation with boric acid is negligible. During chemical modification of celluloses, oxidation of functional (hydroxyl) groups might also occur, resulting in the formation of carboxylates.[14] No electrophoretic peaks were observed when the samples were run at pH 2.85, using 0.1 M acetic acid as the electrolyte. However, some of the polymeric species started to migrate as the pH was increased to 6.0 (50 mM morpholinoethanesulfonate (MES) and 25 mM tris(hydroxymethyl)aminomethane (Tris)), as can be seen for HPMC 60 in Figure 2. This was most likely due to the presence of carboxylate groups. Only minor changes were caused by a further increase of pH to 8.65, and with the use of 0.2 M borate–Tris as a buffer. It must be emphasized that only some of the sample components migrated under these conditions. Additionally, polysaccharides that lack the reducing end (due to modification) will not undergo derivatization with CBQCA, and, consequently, they will not be observed in the electropherograms.

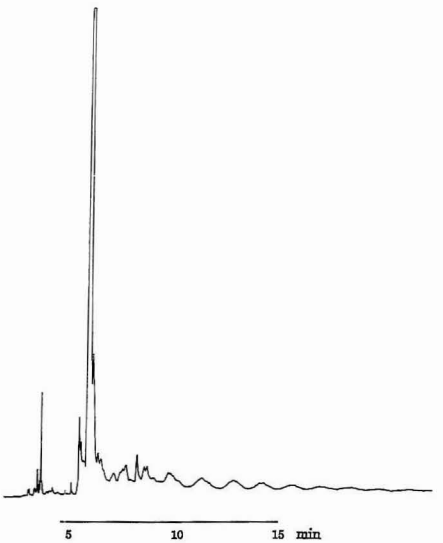

Figure 2. Electropherogram of HPMC 60. Conditions: −350 V/cm (18 μA) using 50 mM MES, 25 mM Tris, and 20 mM sodium acetate (pH 6.0) as the electrolyte. The effective length of the separation capillary was 25 cm.

Due to the high water solubility and multiple hydroxyl groups, polysaccharides are routinely considered to be extremely hydrophilic molecules. The amphiphilic behavior of polysaccharides has, however, been reported in the literature[20] and can, perhaps, most easily be exemplified by the complexation between hydrophobic guest molecules and cyclodextrins or amyloses (dextrins).[21]

(20) Balasubramanian, D.; Raman, B.; Sundari, C. S. *J. Am. Chem. Soc.* **1993**, *115*, 74–79.
(21) Aoyama, Y.; Otsuki, J.; Nagai, Y.; Kobayashi, K.; Toi, H. *Tetrahedron Lett.* **1992**, *33*, 3775–3779.

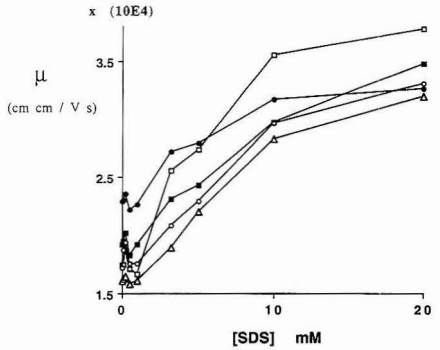

Figure 3. Effects of SDS concentration on the electrophoretic mobility of selected polymers from chemically modified cellulose samples. □, HPMC 60; ■, HEC; ○, MHEC; ●, HPMC 300; △, CMC. The ionic strength was kept constant by addition of sodium acetate. Applied voltage, −350 V/cm.

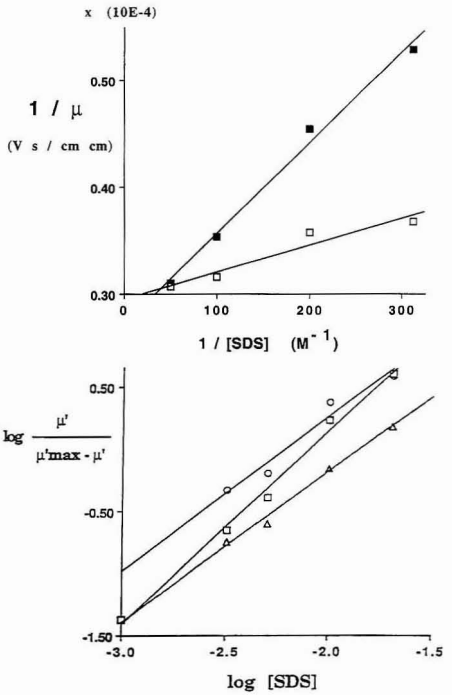

Figure 4. Plots of the electrophoretic migration data in Figure 3 according to the migration models: (A, top) monolayer or (B, bottom) multilayer formation of SDS on the different modified cellulose polymers. Symbols in A: ■, CMC; □, HPMC 300. Symbols in B: ○, HPMC 60; □, MHEC; △, HEC.

Sodium dodecyl sulfate (SDS) has been known for some time to complex with proteins.[22] In fact, this property is being extensively utilized in the size separation of hydrophobic and hydrophilic proteins by gel electrophoresis and size-exclusion chromatography.[23,24] Recently, SDS has also been shown to bind to poly(ethylene glycol)s.[25] Noting the presence of more or less hydrophobic chemical modifications in our cellulose derivatives and the polyalkylene-like backbone (glycosidic and acetal oxygen atoms) of polysaccharides, we utilized here different hydrophobic and charged compounds as electrolyte additives. Our aim was to induce electrophoretic migration for all components in a sample. Such a process is apparently governed by dynamic secondary equilibria, allowing μ_{ep} to be regulated by a type and concentration of an additive.

The influence of SDS concentration on μ_{ep} (randomly choosing one of the larger peaks in the electropherogram of an injected cellulose sample) is shown in Figure 3. This procedure was employed, as no individual standards are commercially available. While the electrophoretic mobility for a given sample component may or may not be representative for the overall sample, it should be useful in evaluation of the migration models. The electrolyte contained 50 mM MES and 25 mM Tris at pH 6. The ionic strength was kept constant through additive of sodium acetate. The mobilities increased with an increasing SDS concentration and seemed to asymptotically approach a maximum value, which is typical for a Langmuir-like adsorption process, and the leveling-off at higher concentrations is due to saturation of the binding sites. The interactions between SDS and different celluloses (measured by the change in mobility for a respective peak) were evaluated, using the linear relationships in eqs 3 and 6, for the two migration models. A monolayer of SDS seemed to be formed on the chosen HPMC 300 and CMC peaks (Figure 4A), and the apparent stability constants, K_{app} (obtained from the slope and the intercept), were on the order of 1180 and 320 M^{-1}, respectively. HPMC 60, MHEC, and HEC contained sites where multilayers could be readily formed (Figure 4B). The slopes in the plots were 1.25, 1.56, and 1.22, respectively, indicating that most of the sites adsorbed only one molecule of SDS. Information on the exact character of the different sites cannot be obtained, but the elucidation of the migration behavior could be an important tool in quality control. The electrophoretic mobilities were corrected for the migration due to the carboxylic groups present on the polymers, as indicated in the plots by primed mobilities. An electropherogram of the MHEC sample is displayed in Figure 5. As most components migrate very fast in the electric field due to adsorbed SDS, relatively low resolution is obtained (optimized separation conditions will be demonstrated later in this text). No evidence of complexation could be seen in the electropherograms when 50 mM of sodium octylsulfonate was utilized (instead of SDS) in the MES–Tris buffer, probably indicating the importance of a hydrophobic chain. This was further supported by the use of dodecylamine as an additive; using this approach, all components migrated fast but in the opposite direction, i.e., to the cathode (caution should be observed when adding hydrohobic cations to the electrolyte, as many anionic polysaccharides are known to precipitate under such conditions.[26] Consequently, hydrophobicity seems to be the fundamental parameter in the complex formation,

(22) Dunker, A. K.; Rueckert, R. R. *J. Biol. Chem.* **1969**, *244*, 5074–5080.
(23) Weber, K.; Osborn, M. In *The Proteins*, 3rd ed.; Neurath, H., Hill, R. L., Eds.; Academic Press: New York, 1975; pp 179–223.
(24) Mascher, E.; Lundahl, P. *J. Chromatogr.* **1989**, *476*, 147–158.
(25) Maltresh, C.; Somasundaran, P. *Langmuir* **1992**, *8*, 1926–1930.

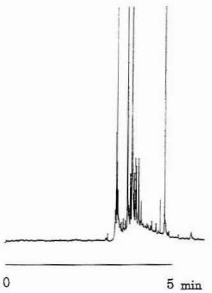

Figure 5. Separation of a MHEC sample. Conditions: 50 mM MES, 25 mM Tris, and 20 mM SDS at pH 6.0. The effective capillary length was 25 cm using −350 V/cm (14 μA).

supporting the Langmuir adsorption mechanism, as suggested by the migration models.

Heparins. Polysulfonated glucosaminoglycans, like heparin, heparan, and keratan, are highly charged polymers that can be extracted from various organs, tissues, and cells. Heparins have been used in different pharmaceutical preparations for half a century due to its potent biological activities, although its structures have not been fully elucidated. The separation and analysis of these types of polymers are especially important for characterization and purity determination of a sample, as they often occur as contaminating mixtures.[27] The currently used separation techniques involve polyacrylamide gel electrophoresis[28] and anion-exchange chromatography.[29]

Relatively small and hydrophilic cations with different numbers of charges were investigated as electrolyte additives, keeping in mind the possibility of precipitating the solutes. The concept for separation, based on eq 7, is a charge-dependent complexation between the heparins and the cations by ion-pairing, where differences in charge distribution between the polymers might be manifested in the stability constants. The effects of Tris, ethylenediamine (EDA), and spermine on μ_{ep} are shown in Figure 6. pH was kept constant by sodium hydroxide. The value of μ_{ep} was calculated from the peak maximum of the injected sample. The mobility for heparin decreased strongly with increasing charge and concentration of the cations, and there was no direct relationship between the "concentration" of cationic charges added, indicating that the stability constants differ greatly. Plots of the data according to the migration model are shown in Figure 7. The apparent stability constant/μ_{max} ratios for Tris, EDA, and spermine were 22 400, 279 000, and 1 324 000, respectively. A polycation can bind to one or several of the sulfate groups, thus determining the number of charges left on the heparin to be complexed by further ion-pairing. Spermine seemed to "compress" the heparin sample components into one narrow peak, whereas EDA interacted more selectively, and a partial separation is shown in Figure 8, revealing the complexity of such a sample.

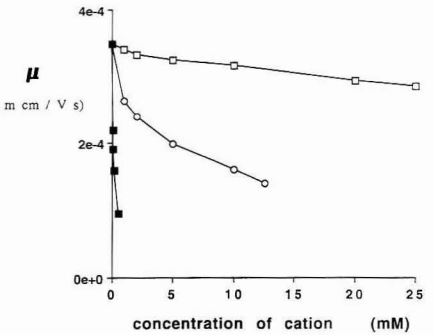

Figure 6. Electrophoretic mobility of heparin as a function of the concentration and charge using Tris (□), ethylenediamine (○), and spermine (■) as different cationic buffer additives.

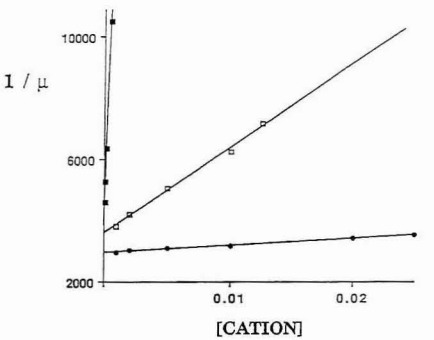

Figure 7. Electrophoretic mobilities of heparin in Figure 6, plotted according to the migration model. ■, Spermine; □, EDA; ●, Tris.

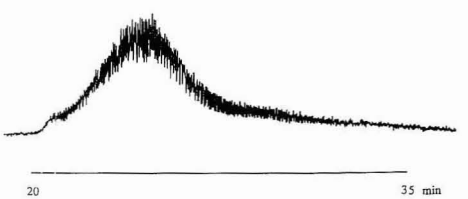

Figure 8. Partial separation of heparins using 50 mM MES and 12.5 mM ethylenediamine (pH 6.0) as the electrolyte. The effective capillary length was 65 cm using −400 V/cm (22 μA).

Modulation of Electrophoretic Mobility by Competing Additives. Attempts were made to further improve the separation of modified celluloses. Since the components migrate as SDS complexes at a relatively high velocity, competing agents were added to the electrolyte buffer in order to slow them down and, preferably, also to introduce a greater separation selectivity. Basically, two different approaches became apparent. First, the amount of SDS adsorbed onto a cellulose derivative molecule can be displaced by a neutral and hydrophobic additive. This is similar to the common use of organic solvents or specific competitor molecules in reversed-phase liquid chromatography. Second, an ion-pairing reagent, as investigated in the heparin study, can be utilized for reduction of the number of charges on the solute.

(26) Fishman, M. M.; Miller, R. S. *J. Colloid Sci.* **1960**, *15*, 232–235.
(27) Volpi, N. *Carbohydr. Res.* **1993**, *247*, 263–278.
(28) Edens, R. E.; Al-Hakim, A.; Weiter, J. M.; Rethwisch, D. G.; Fareed, J.; Linhardt, R. J. *J. Pharm. Sci.* **1992**, *81*, 823–827.
(29) Linhardt, R. J.; Rice, K.; Kim, Y. S.; Lohse, D. L.; Wang, H.-M.; Loganathan, D. *Biochem. J.* **1988**, *254*, 781–787.

If the secondary equilibria of competing additives (S, T, ..., Z) are included in the migration model

$$\mu_{ep} = \mu_{max}[C]/([C] + [CS] + [CT] + \cdots [CZ]) \quad (9)$$

the apparent stability constants ($K_{CS}, K_{CT}, ..., K_{CZ}$) for a given additive can also be determined by keeping the concentration of the others constant. The linearized form is

$$\mu'_{max}/\mu_{ep} = 1 + K_{CS}[S] + K_{CT}[T] + \cdots + K_{CZ}[Z] \quad (10)$$

where μ'_{max} denotes the new maximum velocity in the presence of additives. Using different, specific additivies (pharmaceuticals being one example) and studying their influences on the solute migration could provide further means of characterizing the polymers.

Many bases are incompatible with SDS micelles and will precipitate as hydrophobic and insoluble complexes. Nevertheless, low concentrations of spermine could be solubilized, resulting in improved separations, as demonstrated with representative samples of HPMC 60 and CMC in Figure 9A and B, respectively. The possibility of employing more specific interactions could also prove useful in future work to further increase the separation selectivity of such complex mixtures.

CONCLUSIONS

We have shown that the electrophoretic migration of neutral and highly charged polysaccharides, exemplified by chemically modified celluloses and heparins, can be regulated by secondary thermodynamic equilibria using buffer additives in open-tubular capillary electrophoresis. Induced electrophoretic migration of otherwise uncharged, chemically modified celluloses was obtained by adsorption of hydrophobic and charged detergents onto the analyte components, and the processes could be described by Langmuir adsorption isotherms. Different polymers were found to contain different kinds of adsorption sites, including multilayer formation.

Reduction of a high electrophoretic mobility was obtained by the addition of ion-pairing reagents to the electrolyte buffer. The concentration and number of charges were important parameters, influencing both migration velocity and selectivity.

Both types of processes could be expressed by simple migration models, allowing the determination of the apparent stability constants. Optimized separations of the chemically modified celluloses were obtained by using several competing agents added to the main buffer electrolyte.

ACKNOWLEDGMENT

This work was supported by Grant No. 24349 from the National Institute of General Medical Sciences, U.S. Department of Health and Human Services, and a grant-in-aid from Astra/Hässle (Mölndal, Sweden). One of us (M.S.) has been a recipient of fellowships from the Sweden-American Foundation, the Foundation "Stiftelsen Blanceflour Boncampagni-Ludovisi, född Bildt", and the Swedish Academy of Pharmaceutical Sciences.

Received for review January 3, 1994. Accepted July 6, 1994.*

* Abstract published in *Advance ACS Abstracts,* August 15, 1994.

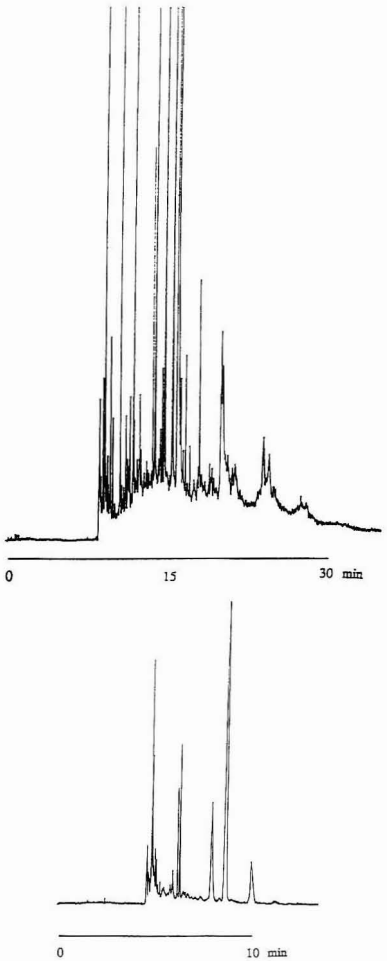

Figure 9. Optimized separations of (A, top) HPMC 60 and (B, bottom) CMC. Conditions: 25 mM MES, 12.5 mM Tris, 20 mM SDS, 1.0 mM spermine, and 5% tetrahydrofuran (pH 6.0). The effective capillary length was 65 cm using −400 V/cm (14 μA).

Anal. Chem. **1994,** *66,* 3472–3476

Microchip Capillary Electrophoresis with an Integrated Postcolumn Reactor

Stephen C. Jacobson, Lance B. Koutny, Roland Hergenröder, Alvin W. Moore, Jr., and J. Michael Ramsey*

Chemical and Analytical Sciences Division, Oak Ridge National Laboratory, P.O. Box 2008, Oak Ridge, Tennessee 37831-6142

A glass microchip with a postcolumn reactor was fabricated to conduct postseparation derivatization using *o*-phthaldialdehyde as a fluorescent "tag" for amino acids. This miniaturized separation device was constructed using standard photolithographic, wet chemical etching, and bonding techniques. Effects of the reagent stream on separation efficiency were investigated. In addition, a novel gated injector was demonstrated which maintains the integrity of the analyte, buffer, and reagent streams.

For capillary separation systems, the small band volumes can limit the number of viable detection schemes. Fluorescence detection remains one of the most sensitive detection techniques for capillary electrophoresis.[1] When incorporating direct fluorescence detection into a system that does not have naturally fluorescing analytes, derivatization of the analyte must occur either pre- or postseparation. When the fluorescent "tag" is short lived or the separation is hindered by preseparation derivatization, postcolumn addition of derivatizing reagent becomes the method of choice. A variety of postcolumn reactors have been demonstrated for capillary electrophoresis.[2-7] However, the ability to construct a postcolumn reactor with extremely low volume connections to minimize band distortion has been difficult. We have taken the approach of fabricating a microchip device for electrophoretic separations with postcolumn reactions using standard microchip fabrication techniques. The injector, separation column, and reaction column can be coupled in a single monolithic device, enabling extremely low volume exchanges between individual column functions. This microfabrication approach is a part of the continuing effort toward micromachining of miniaturized instrumentation for chemical separations which includes devices for gas chromatography,[8] liquid chromatography,[9,10] and capillary electrophoresis.[11-16]

In this paper, we describe a first generation postcolumn reactor on a microchip. Broadening of the analyte band due to conventional mechanisms including injection plug length, detector observation length, and axial diffusion and the added influence of combining of the separation effluent and reagent stream of the fluorescent tag, *o*-phthaldialdehyde (OPA),[17] are studied. In addition, a new approach to analyte injection was developed to isolate the analyte, running buffer, and reagent streams. Previous flow designs used for electrophoretic sample loading and separation on microchip devices for capillary electrophoresis[11,14,15] are difficult to implement with a postcolumn reactor. The operating conditions and benefits of the new injection scheme are discussed.

EXPERIMENTAL SECTION

The microchip was fabricated using standard photolithographic, wet chemical etching, and bonding techniques. A photomask was fabricated by sputtering chrome (50 nm) onto a glass slide and ablating the column design (Figure 1) into the chrome film via a CAD/CAM laser machining system (Resonetics, Inc., Nashua, NH). The column design was then transferred onto the substrates using a positive photoresist (Shipley 1811, Newton, MA). The channels were etched into the substrate in a stirred, dilute HF/NH_4F bath for 20 min. To form the separation column, a coverplate was bonded to the substrate over the etched channels using a direct bonding technique.[15] The surfaces were hydrolyzed in dilute NH_4OH/H_2O_2 solution, rinsed in deionized, filtered H_2O, joined, and then annealed at 500 °C. Cylindrical glass reservoirs were affixed on the substrate using RTV silicone (General Electric, Waterford, NY). Platinum electrodes provided electrical contact from the power supply (Spellman CZE1000R, Plainview, NY) to the solutions in the reservoirs. The dimensions of the columns on the microchip are labeled in Figure 1. Because the substrate is glass and the channels are chemically wet etched, an isotropic etch occurs, i.e., the glass etches uniformly in all directions, and the resulting channel geometry is trapezoidal. The channel cross section has dimensions of 5.2 μm deep, 57 μm wide at the top, and 45 μm wide at the bottom. The dimensions were obtained using a profilometer (Alpha-Step 200, Tencor Instruments, Mountain View, CA) after etching of the substrate and prior

(1) For example, see: Kuhr, W. G.; Monnig, C. A. *Anal. Chem.* **1992,** *64,* 389R.
(2) Pentoney, S.; Huang, X.; Burgi, D.; Zare, R. *Anal. Chem.* **1988,** *60,* 2625.
(3) Tsuda, T.; Kobayashi, Y.; Hori, A.; Matsumoto, T.; Suzuki, O. *J. Chromatogr.* **1988,** *456,* 375.
(4) Rose, D. J., Jr.; Jorgenson, J. W. *J. Chromatogr.* **1988,** *447,* 117.
(5) Nickerson, B.; Jorgenson, J. *J. Chromatogr.* **1989,** *480,* 157.
(6) Rose, D. J., Jr. *J. Chromatogr.* **1991,** *540,* 343.
(7) Albin, M.; Weinberger, R.; Sapp, E.; Moring, S. *Anal. Chem.* **1991,** *63,* 417.
(8) Terry, S. C.; Jerman, J. H.; Angell, J. B. *IEEE Trans. Electron Devices* **1979,** *26,* 1880.
(9) Manz, A.; Miyahara, Y.; Miura, J.; Watanabe, Y.; Miyagi, H.; Sato, K. *Sens. Actuators* **1990,** *B1,* 249.
(10) Jacobson, S. C.; Hergenröder, R.; Koutny, L. B.; Ramsey, J. M. *Anal. Chem.* **1994,** *66,* 2369.
(11) Manz, A.; Harrison, J.; Verpoorte, E. M. J.; Fettinger, J. C.; Paulus, A.; Lüdi, H.; Widmer, H. M. *J. Chromatogr.* **1992,** *593,* 253.
(12) Harrison, D. J.; Manz, A.; Fan, Z.; Lüdi, H.; Widmer, H. M. *Anal. Chem.* **1992,** *64,* 1926.
(13) Seiler, K.; Harrison, D. J.; Manz, A. *Anal. Chem.* **1993,** *65,* 1481.
(14) Harrison, D. J.; Fluri, K.; Seiler, K.; Fan, Z.; Effenhauser, C. S.; Manz, A. *Science* **1993,** *261,* 895.
(15) Jacobson, S. C.; Hergenröder, R.; Koutny, L. B.; Warmack, R. J.; Ramsey, J. M. *Anal. Chem.* **1994,** *66,* 1107.
(16) Jacobson, S. C.; Hergenröder, R.; Koutny, L. B.; Ramsey, J. M. *Anal. Chem.* **1994,** *66,* 1114.
(17) Roth, M. *Anal. Chem.* **1971,** *43,* 880.

0003-2700/94/0366-3472$04.50/0
© 1994 American Chemical Society

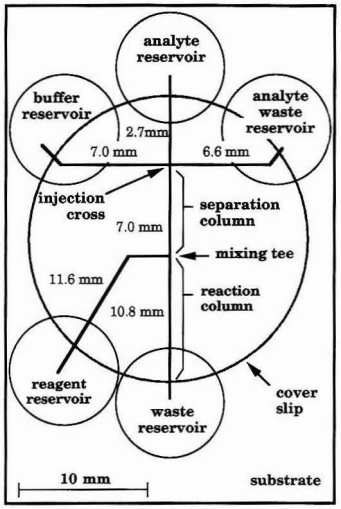

Figure 1. Schematic of the microchip with postcolumn reactor.

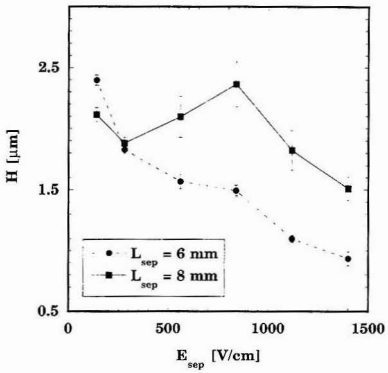

Figure 2. Variation of plate height (H) with the separation field strength (E_{sep}) for rhodamine B with L_{sep} = 6 (●) and 8 mm (■). Error bars are $\pm\sigma$.

to bonding of the coverplate. The profilometer uses a stylus to provide a one-dimensional depth profile of the substrate surface.

Column performance and separations were monitored on-microchip via fluorescence using an argon ion laser (351.1 nm for amino acid/OPA, 10 mW, and 514.5 nm for rhodamine B, 50 mW; Coherent Innova 90, Palo Alto, CA) for excitation. The fluoresence signal was collected with a photomultiplier tube (PMT; Oriel 77340, Stratford, CT) for point detection and a charge coupled device (CCD; Princeton Instruments, Inc. TE/CCD-512TKM, Trenton, NJ) for imaging a region of the microchip.[15] The compounds used for the experiments were rhodamine B (Exciton Chemical Co., Inc., Dayton, OH), arginine, glycine, threonine, and *o*-phthaldialdehyde (Sigma Chemical Co., St. Louis, MO). A sodium tetraborate buffer (20 mM, pH 9.2) with 2% (v/v) methanol and 0.5% (v/v) β-mercaptoethanol was the buffer in all experiments. The concentrations of the amino acid, OPA, and rhodamine B solutions were 2 mM, 3.7 mM, and 50 μM, respectively. Several run conditions were utilized for microchip diagnostics and will be described as needed.

RESULTS AND DISCUSSION

Because several separation lengths were used to study different aspects of the microchip performance, the efficiencies will be reported primarily using the plate height (H). The contributions to the plate height are[18,19]

$$H = H_{diff} + H_{inj} + H_{det} = \frac{2D_m}{u} + \frac{l_{inj}^2}{12L_{sep}} + \frac{l_{det}^2}{12L_{sep}} \quad (1)$$

where H_{diff}, H_{inj}, and H_{det} are the contributions of axial diffusion, injection plug length, and detector observation length to the plate height, respectively. D_m is the diffusion coefficient of the analyte in the buffer, u is the linear velocity of the analyte, l_{inj} is the injection plug length, l_{det} is the detector observation length, and L_{sep} is the separation length. The effects of Joule heating were not considered because the power dissipation was below 1 W/m for all experiments.[20] The contribution from the axial diffusion is time dependent, and the contributions from the injection plug length and detector observation length are time independent. In electrophoretic separations, the linear velocity of the analyte, u, is equal to the product of the effective electrophoretic mobility, μ_{ep}, and the electric field strength, E.

To test the band broadening effects of reagent addition at the mixing tee, a fluorescent laser dye, rhodamine B, was used as a probe. Efficiency measurements calculated from peak widths at half-heights were made using the point detection scheme at distances of 6 and 8 mm from the injection cross, or 1 mm upstream and 1 mm downstream from the mixing tee. The results are plotted in Figure 2 as the plate height versus the electric field strength in the separation column (E_{sep}). Rhodamine B was injected onto the column using the pinched sample loading method[15] to ensure that the contribution of the injection plug length to the plate height remained constant over the measurements (H_{inj} = 0.23 and 0.17 μm for the separation lengths of 6 and 8 mm, respectively). Single point detection was used, and the column length observed by the detector is equal to the laser spot size, $\approx$60 μm (H_{det} = 0.05 and 0.04 μm for the separation lengths of 6 and 8 mm, respectively). The time-independent contributions are small relative to the total plate height for these experiments.

The electric field strengths in the reagent column and the separation column were approximately equal, and the field strength in the reaction column was a factor of 2 higher. This voltage configuration provided approximately a 1:1 volume ratio of reagent stream to effluent from the separation column. As the field strengths increase, the degree of turbulence at the

(18) Giddings, J. C. *Dynamics of Chromatography, Part I: Principles and Theory*; Marcel Dekker: New York, 1965; Chapter 2.
(19) Sternberg, J. C. *Adv. Chromatogr.* **1966**, *2*, 205.
(20) Monnig, C. A.; Jorgenson, J. W. *Anal. Chem.* **1991**, *63*, 802.

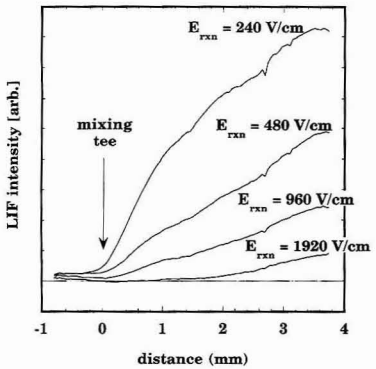

Figure 3. Variation of laser-induced fluorescence (LIF) intensity with distance downstream from the mixing tee for glycine derivatized with *o*-phthaldialdehyde with E_{rxn} = 240, 480, 960, and 1920 V/cm.

mixing tee appears to increase. At the separation distance of 6 mm (1 mm upstream from the mixing tee), the plate height data decrease as expected, i.e., with the inverse of the linear velocity of the analyte (eq 1). At the 8-mm distance (1 mm downstream from the mixing tee), the plate height decreases as the field strength increases from 140 to 280 V/cm as expected but increases in the 280–840 V/cm range. This behavior is abnormal (eq 1) for typical capillary electrophoresis experiments and demonstrates a band broadening phenomenon or turbulence for converging electroosmotically pumped streams. The geometry of the mixing tee was not optimized to minimize this band distortion. Above the separation field strength of 840 V/cm, the system stabilizes, and again the plate height decreases with increasing linear velocity. For E_{sep} = 1400 V/cm, the plate height at the 8-mm distance is 60% greater than that at 6 mm. Efficiency losses at typical field strengths used in capillary electrophoresis (<250 V/cm) appear to be minimal.

Following the combining of the two streams at the mixing tee, the intensity of the fluorescence signal generated from the reaction of the OPA with an amino acid was tested by continuously pumping glycine down the column as a frontal electropherogram to mix with the OPA at the mixing tee. The fluorescence signal from the OPA/amino acid reaction was collected using a CCD camera as the reaction occurred downstream from the mixing tee (Figure 3). Again, the relative volume ratio of the OPA and glycine streams was ≈1:1. OPA has a typical half-time of reaction with amino acids of 4 s.[21] In Figure 3, the average residence times of an analyte molecule in the window of observation (0–4 mm) are 4.68, 2.34, 1.17, and 0.58 s for the electric field strengths in the reaction column (E_{rxn}) of 240, 480, 960, and 1920 V/cm, respectively. The relative intensities of the fluorescence correspond qualitatively to this 4-s half-time of reaction. As the field strength increases in the reaction column, the slope of the intensity of the fluorescence decreases because the glycine and OPA are swept away from the mixing tee faster with higher field strengths. The fluorescence signal has a positive slope from the mixing tee to the waste reservoir because the amino acids continue to react as they travel down the column. In the observation window, the residence time of the product is 8 times longer at the field strength of 240 V/cm than at 1920 V/cm. Only a 5-mm region of the reaction column was observed to ensure even illumination of the microchip by the expanded laser beam and efficient collection of the fluorescence signal by the CCD. Ideally, the observed fluorescence from the product would have a step function for a response following the mixing of the separation effluent and derivatizing reagent. However, the kinetics of the reaction and a finite rate of mixing dominated by diffusion prevent this from occurring.

A different injection scheme was developed for the post-column reactor microchip in order to keep the analyte, buffer, and reagent streams isolated. For the postcolumn reaction separations, the microchip was operated in a continuous sample loading/separation mode whereby the sample was continuously pumped from the analyte reservoir through the injection cross toward the analyte waste reservoir. Buffer was simultaneously pumped from the buffer reservoir toward the analyte waste and waste reservoirs to deflect the analyte stream and prevent the sample from migrating down the separation column. To inject a small aliquot of sample, the potentials at the buffer and analyte waste reservoir are simply floated for a short period of time (≈100 ms), allowing sample to migrate down the separation column as in an electrokinetic injection.[22] To break off the injection plug, the potentials at the buffer and analyte waste reservoir are reapplied. A shortfall of this method is that the composition of the injected plug has an electrokinetic bias whereby the faster migrating compounds are introduced preferentially into the separation column over slower migrating compounds. The schematic in Figure 4a shows the electric potential distributions used when 1 kV is applied to the entire system. With this voltage configuration, the electric field strengths in the separation column (E_{sep}) and the reaction column (E_{rxn}) are 200 and 425 V/cm, respectively. This allows the combining of 1 part separation effluent with 1.125 parts reagent at the mixing tee. A sample introduction system such as this, with or without postcolumn reaction, allows a very rapid cycle time for multiple analyses.

In Figure 4b–d, the gated injection at the injection cross is imaged by the CCD camera with the potential configuration in Figure 4a. The analyte being pumped through the microchip was rhodamine B (shaded area), and the orientation of the CCD images of the injection cross is the same as in Figures 1 and 4a. Figure 4b shows the analyte being pumped through the injection cross prior to the injection. Between Figures 4b and 4c, the potentials at the buffer and analyte waste reservoirs are floated for 100 ms. At this point, the analytes migrate down the separation column according to their electrophoretic mobilities. The potentials at the buffer and analyte waste reservoirs are reapplied prior to the CCD image taken in Figure 4c. Figure 4c catches the analyte plug being broken away from the analyte stream and being injected into the separation column. Figure 4d shows the analyte plug moving away from the injection cross after an injection plug has been completely introduced into the separation column. By Figure 4d, the

(21) Butchner, E. C.; Lowry, O. H. *Anal. Biochem.* **1976**, *76*, 502.

(22) Jorgenson, J. W.; Lukacs, K. D. *Anal. Chem.* **1981**, *53*, 1298.

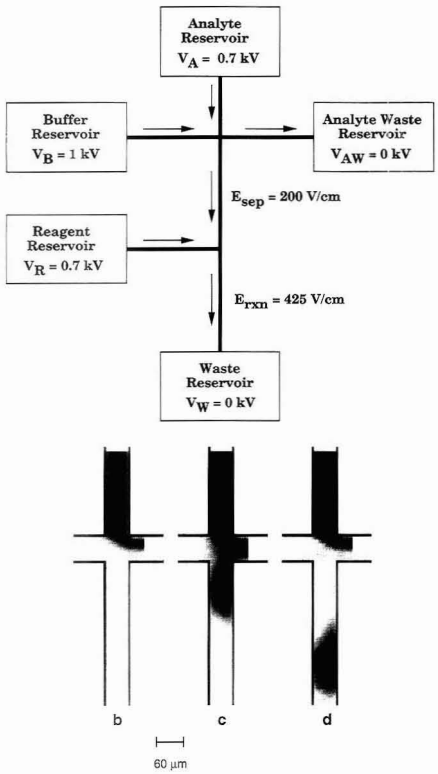

Figure 4. (Top, a) Schematic of flow pattern for gated injector (arrows depict direction of flow). (Bottom) CCD image of gated injector using rhodamine B (b) prior to injection, (c) during injection of analyte plug, and (d) after injection into separation column with E_{sep} = 200 V/cm.

loading/separation mode has resumed, and a clean injection plug with a length of 142 μm has been introduced into the separation column. As seen below, the gated injector contributes only a minor fraction to the total plate height. The injection plug length is a function of the time of the injection and the electric field strength in the column. The shape of the injected plug is skewed slightly because of the directionality of the cleaving buffer flow.

This gated injector differs from the pinched sample loading on several counts. With the gated injector, the sample migrates electrophoretically down the separation column and is cleaved by restoring the flow of buffer from the buffer reservoir. The pinched sample loading pumps the sample through the injection cross, and the plug which is injected onto the separation column is the sample which resides in the injection cross. With the pinched sample loading, the amount introduced onto the separation column is time independent and has no electrophoretic bias. The gated sample injector is both time dependent and electrophoretically biased. Presently, the pinched sample loading cannot be run in a continuous sampling mode, whereas the gated injector can.

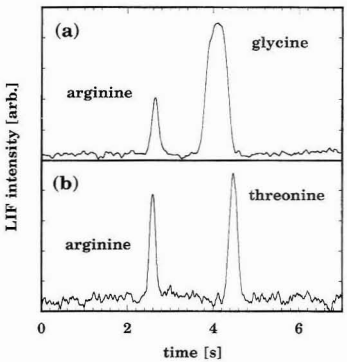

Figure 5. Electropherograms of (a) arginine and glycine and (b) arginine and threonine using postcolumn derivatization with *o*-phthaldialdehyde with E_{sep} = 800 V/cm and L_{sep} = 13.5 mm.

Table 1. Retention and Efficiency Data for Electropherograms in Figure 5

compd	t_R (s)	N	H (μm)
	Figure 5a		
arginine	2.64	1320	10.2
glycine	4.11	329	41.0
	Figure 5b		
arginine	2.59	1300	10.4
threonine	4.47	2460	5.5

The electropherograms in Figure 5 demonstrate the separation of two pairs of amino acids. The voltage configuration is the same as in Figure 4a, except the total applied voltage is 4 kV, which corresponds to an electric field strength of 800 V/cm in the separation column (E_{sep}) and 1700 V/cm in the reaction column (E_{rxn}). The injection times were 100 ms for the experiments which correspond to estimated injection plug lengths of 384, 245, and 225 μm (H_{inj} = 0.91, 0.37, and 0.31 μm) for arginine, glycine, and threonine, respectively. The injection volumes of 102, 65, and 60 pL correspond to 200, 130, and 120 fmol injected for arginine, glycine, and threonine, respectively. The point of detection is 6.5 mm downstream from the mixing tee, which gives a total column length of 13.5 mm for the separation and reaction, and H_{det} equals 0.02 μm for a 60-μm laser spot size. Again, the time-independent contributions to the total plate height are small (Table 1). The efficiencies for the separations involving the postcolumn reactions are much lower than those for the rhodamine B (H = 1.8 μm for E_{sep} = 840 V/cm and L_{sep} = 8 mm in Figure 2). The plate heights for arginine, glycine, and threonine were 6, 23, and 3 times those of rhodamine B, respectively.

The reaction rates of the amino acids with the OPA are moderately fast but not fast enough on the time scale of these experiments. An increase in the band distortion is observed, presumably because the mobilities of the derivatized compounds are different from those of the pure amino acids. Until the reaction is complete, the zones of unreacted and reacted amino acid will move at different velocities, causing a broadening of the analyte zone. As evidenced in Figure 5a, glycine shows significant broadening with the postcolumn

labeling. To ensure that the excessive band broadening was not a function of the migration time, threonine was also tested. Threonine has a slightly longer migration time than the glycine (Figure 5); however, the broadening is not as extensive as that for glycine.

CONCLUSION

The use of micromachined postcolumn reactors can improve the power of postseparation reactions as an analytical tool by minimizing the volume of the extracolumn plumbing, especially between the separation and reagent columns. This microchip design (Figure 1) was fabricated with modest lengths for the separation (7 mm) and reaction columns (10.8 mm) which were more than sufficient for this demonstration. Longer separation columns can be manufactured on a similar size microchip using a serpentine geometry[15] to perform more difficult separations. There are a number of potential improvements to increase the performance of this initial demonstration device. Examples include variation of the reagent/effluent flow rates and the separation/reaction channel widths to reduce flow rates in the reaction channel and modification of column geometry to improve mixing efficiency. In addition, detection sensitivity can be improved by fabrication on fused silica substrates rather than on glass. These improvements are presently being explored in our laboratory.

ACKNOWLEDGMENT

This research was sponsored by U.S. Department of Energy (DOE), Office of Research and Development. Oak Ridge National Laboratory is managed by Martin Marietta Energy Systems, Inc., for the U.S. Department of Energy under contract DEAC05-84OR21400. Also, this research was sponsored in part by an appointment for S.C.J. to the Alexander Hollaender Distinguished Postdoctoral Fellowship Program sponsored by the U.S. DOE, and for L.B.K., A.W.M., and R.H. to the ORNL Postdoctoral Research Associate Program. These programs are administered by the Oak Ridge Institute for Science and Education and ORNL.

Received for review April 5, 1994. Accepted June 17, 1994.®

® Abstract published in *Advance ACS Abstracts*, August 1, 1994.

Anal. Chem. **1994,** *66,* 3477–3484

Maltooligosaccharides as Chiral Selectors for the Separation of Pharmaceuticals by Capillary Electrophoresis

Helena Soini, Morgan Stefansson,† Marja-Liisa Riekkola,‡ and Milos V. Novotny*
Department of Chemistry, Indiana University, Bloomington, Indiana 47405

Complexation between the linear maltodextrin oligosaccharides and certain enantiomeric compounds of pharmaceutical interest in buffered solutions can lead to an analytically desirable chiral recognition. Different maltodextrins were assessed in their capacity to cause enantiomeric separations under various conditions of capillary electrophoresis. The mechanism of chiral recognition has been probed through electrophoretic mobility and selectivity measurements for different buffer solutions and organic solvent additives. A differential interaction of chiral solutes with the maltodextrin helical entities emerges as the basis of such enantioselectivity. This notion is further supported by ^{1}H- and ^{13}C-NMR experiments. Optimized separations of simendan, ibuprofen, warfarin, and ketoprofen enantiomers are demonstrated together with a chiral determination of ibuprofen in a blood serum sample at the therapeutic level.

Oligosaccharides, both linear and cyclic, are endowed with the capability of complexation to various classes of compounds.[1] The host–guest complexation is the most common interaction of this kind. Some of these complexations may play a role in the biological functions of polysaccharides and proteoglycans at the level of surface recognition in cell membranes. Additionally, chemically modified cyclodextrins (CDs), also displaying the host–guest behavior, have been used as model media for enzymatic reactions.[2] During the last decade, cyclodextrins (cyclomaltooligosaccharides) have found a very significant utilization in separation science. Besides various chromatographic applications, CDs are quite effective as chiral selectors in high-performance capillary electrophoresis (HPCE).[3–11]

In spite of the structural versatility of CDs, such as their variation in cavity size and the feasibility of preparing different derivatives, these cyclic "bucket-like" host molecules occasionally fail to achieve desirable separations of certain enantiomers. Recently, a search for suitable chiral selectors for acidic pharmaceuticals has led[12] to consideration of linear maltooligosaccharides (maltodextrins or amyloses). Both CDs and linear maltodextrins (MDs) consist of D-(+)-glucose units which are connected through Glu-(1–4)-α-D-Glu linkages. Hydrolysis of starch yields a mixture of amyloses which can further be hydrolyzed into shorter oligosaccharides. Linear MDs are characterized by their degrees of polymerization (DP), corresponding to the number of glucose residues in the molecule. The use of MDs with high DP in aqueous solutions is limited by their solubility, which decreases with molecular size. Isolation of the individual MD oligosaccharides from hydrolysis reaction mixtures is obviously a difficult task. The highest oligomer commercially available is maltoheptaose (DP = 7), while typical MDs are sold and used as complex oligomeric mixtures. A mixture is typically defined by its dextrose equivalent (DE) number. The higher the DE number, the higher is the extent of starch hydrolysis and, consequently, the shorter are the oligomeric chains present in a mixture.

In our study of MDs as chiral selectors, we initially followed the work of D'Hulst and Verbeke,[12] who screened a variety of commercial MD mixtures, corn syrups, and some individual oligomers for their capacity of chiral resolution with several acidic pharmaceuticals (such as non-steroid inflammatory drugs and coumarins). Using HPCE, they found differences in the chiral recognition properties among various commercial products. Chiral recognition with the aid of linear MDs has been a somewhat obscure albeit analytically useful type of host–guest complexation. Consequently, we decided to explore further and in more general terms the chiral recognition mechanisms with MDs. Both acidic and basic pharmaceuticals were included as model solutes. The studies presented here take into account the conformation (random coil/helix transitions) of MDs with respect to complexing molecules. Using simendan, ibuprofen, warfarin, and ketoprofen as model compounds, we demonstrate the effects of zwitterionic buffers and organic solvent modifiers on chiral separations. A series of ^{1}H- and ^{13}C-NMR spectroscopic complexation studies have been conducted for selected compounds to elucidate the chiral recognition mechanisms involved. Additionally, an MD-based chiral recognition system has been utilized here to measure ibuprofen enantiomers in blood serum spiked at the therapeutic level.

EXPERIMENTAL SECTION

Capillary Electrophoresis. Home-built CE instruments were used in all measurements. The high-voltage power supply (0–60 kV) was from Spellman High Voltage Electronics

† Permanent address: Department of Analytical Chemistry, P.O. Box 531, Uppsala University, S-75121 Uppsala, Sweden.
‡ Permanent address: Department of Analytical Chemistry, P.O. Box 6, University of Helsinki, FIN-00014 Finland.

(1) Ring, S. G.; Whittam, M. A. *ACS Symp. Ser.* 1991, *No. 458,* 272.
(2) Bender, M. L.; Komiyama, M. *Cyclodextrin Chemistry*; Springer Verlag: Berlin, 1978.
(3) Fanali, S. *J. Chromatogr.* **1991,** *545,* 437.
(4) Snopek, J.; Soini, H.; Novotny, M. V.; Smolkova-Keulemansova, E.; Jelinek, I. *J. Chromatogr.* **1991,** *559,* 215.
(5) Prunoñosa, J.; Obach, J.; Diez-Cascón, A.; Gouesclou, L. *J. Chromatogr.* **1992,** *574,* 127.
(6) Soini, H.; Riekkola, M.-L.; Novotny, M. V. *J. Chromatogr.* **1992.** *608,* 265.
(7) Belder, D.; Schomburg, G. *J. High Resolut. Chromatogr.* **1992,** *15,* 686.
(8) Gareil, P.; Gramond, J. P.; Guyon, F. *J. Chromatogr.* **1993,** *615.* 317.
(9) Stefansson, M.; Novotny, M. V. *J. Am. Chem. Soc.* **1993,** *115,* 11573.
(10) Rawjee, Y. Y.; Staerk, D. U.; Vigh, G. *J. Chromatogr.* **1993,** *635,* 291.
(11) Nielen, M. W. F. *J. Chromatogr.* **1993,** *637,* 81.
(12) D'Hulst, A.; Verbeke, N. *J. Chromatogr.* **1992,** *608,* 275.

0003-2700/94/0366-3477$04.50/0
© 1994 American Chemical Society

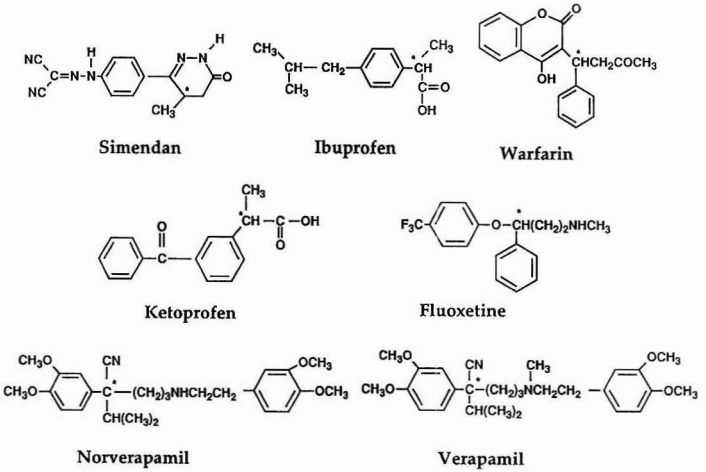

Figure 1. Chemical structures of the model solutes.

(Plainview, NY). The applied voltages were 18–26 kV (positive or negative ground). For the on-column UV absorbance detection, Jasco UVIDEC-100-IV or UVIDEC-100-V (Tokyo, Japan) was set at the wavelength of 220 nm (0.005 AUFS). The on-column fluorescence detection of fluorescently tagged oligosaccharides[13] was accomplished with a Model 4112-50 helium/cadmium laser (Omnichrome, Chino, CA) as the excitation source operating at 442 nm. Emission was measured at 550 nm. Capillaries of 50 and 75 μm i.d. (180 μm o.d.) and various lengths were received from Polymicro Technologies (Phoenix, AZ). The separation capillaries were used uncoated or coated with a linear polyacrylamide.[14] Sample injection was performed in the hydrodynamic mode.

Materials. Zwitterionic buffers CHES (2-(*N*-cyclohexylamino)ethanesulfonic acid), TAPS (3-[*N*-[tris(hydroxymethyl)methyl]amino]propanesulfonic acid), Tricine (*N*-[tris(hydroxymethyl)methyl]glycine), MES (2-(*N*-morpholino)ethanesulfonic acid), and Trizma base (Tris) were purchased from Sigma (St. Louis, MO). Sigma was also a source of pure maltooligosaccharides (triose, tetraose, pentaose, hexaose, and heptaose). Phosphoric acid (85%, HPLC grade), ammonium sulfate, and acetonitrile (HPLC grade) were received from Fisher Scientific (Fair Lawn, NJ). (*R*)-(–)-2-Butanol, (*S*)-(+)-ibuprofen, cyanoborohydride, and poly(vinylpyrrolidone) (average MW of 360 000) were obtained from Aldrich (Milwaukee, WI). (*R*)-(–)-Ibuprofen was from Research Biochemicals International (Natick, MA). Maltodextrins (Dextrin 20, Dextrin 15, and Dextrin 10, with DE 20, 15, and 10, respectively), were purchased from Fluka Chemie (Buchs, Switzerland). Maltrin M040 (DE 5) was a gift from Grain Processing Corp. (Muscatine, IA). Ethanol (absolute grade) was from McCormick (Weston, MO). Methanol and 2-propanol (Photrex) as well as *n*-hexane were from J. T. Baker (Phillipsburg, NJ). Potassium cyanide and boric acid were supplied by Mallinckrodt (Paris, KY). A fluorogenic reagent, CBQCA (3-(4-carboxybenzoyl)-2-quinolinecarboxaldehyde), was synthesized in our laboratory.[15]

Pharmaceuticals (racemic simendan, (*R*)-(–)-simendan, (*S*)-(+)-simendan, racemic ibuprofen, warfarin, ketoprofen, verapamil, norverapamil (desmethyl verapamil), and (*S*)-(+)-naproxen) were a gift from Orion-Farmos Pharmaceuticals (Espoo, Finland). Fluoxetine was donated by Eli Lilly Research Laboratories (Indianapolis, IN). The solutions of pharmaceuticals were prepared in methanol at concentrations of 100–200 μg/mL. The structures of these model solutes are shown in Figure 1. Maltodextrins Dextrin 10, 15, and 20 and Maltrin MO40 were tagged with the fluorogenic reagent CBQCA after reductive amination. This method is described elsewhere.[13]

Equations. Resolution (R_s) was calculated from $R_s = 2(t_{2migr} - t_{1migr})/(w_1 + w_2)$, where t_{1migr} and t_{2migr} are apparent migration times of enantiomers 1 and 2, respectively, and w_1 and w_2 are the corresponding widths at the peak base. Selectivities (α) were calculated using the equation $\alpha = (t_{2migr} - t_0)/t_{1migr} - t_0)$, where t_0 represents electroosmosis.

Serum Sample Preparation. Human serum was donated by a healthy volunteer and stored at –20 °C. A 0.5 mL aliquot of thawed serum was spiked with 4.25 μg (8.5 μg/mL) of the racemic ibuprofen, and 4.2 μg of (*S*)-(+)-naproxen was added as an internal standard. Additions were made in 25 μL of methanol. After the sample was mixed, 100 μL of 2 M HCl was added to acidify it. The ibuprofen enantiomers were extracted into 3.0 mL of *n*-hexane with 0.1% (v/v) 2-propanol by shaking the probe gently for 10 min. After centrifugation, 2.5 mL of the organic layer was evaporated to dryness under nitrogen flow. The residue was redissolved in 50 μL of methanol.

(13) Liu, J.; Shirota, O.; Wiesler, D.; Novotny, M. *Proc. Natl. Acad. Sci. U.S.A.* **1991**, *88*, 2302.
(14) Hjerten, S. *J. Chromatogr.* **1985**, *347*, 191.
(15) Liu, J.; Hsieh, Y.-Z.; Wiesler, D.; Novotny, M. *Anal. Chem.* **1991**, *63*, 408.

NMR Spectroscopy. The ^1H- and ^{13}C-NMR spectra were recorded with a Bruker AM 500 MHz NMR spectrometer (Karlsruhe, Germany) in deuterium oxide. ^{13}C-NMR spectra were one-dimensional, proton decoupled recordings, referenced to TPS (trimethylsilyl)propanesulfonic acid) signal. The spectra were obtained after 256 scans at 25 °C. Deuterium oxide (D 99.9%) and deuteriomethanol (D 99.8%) were purchased from Cambridge Isotope Labs (Noburn, MA). TPS (sodium salt) was from E. Merck (Darmstadt, Germany).

In the complexation studies, maltoheptaose and Maltrin M040 (DE 5) were dissolved at concentration of 5% (w/w) (44 mM maltoheptaose) in deuterium oxide containing TPS (8 mM) and 10 mM Tris, which was added for pH adjustment and to imitate the conditions used in CE. The selected pharmaceuticals were added separately in 30 μL of deuteriomethanol, mixed for 15 min, and left equilibrating for an additional 30 min before the measurement. Concentrations in the samples were 4 mM for simendan (limited solubility) and 30 mM for ibuprofen.

RESULTS AND DISCUSSION

Complexation of the maltodextrin (MD) oligosaccharides with the optical isomers appears crucial to their successful separation. The conformational change from the flexible coil to a helix in the presence of complexing molecules and buffer salts is also believed to be essential in such selective interactions. The helical structure is hydrophobic inside, much like the cavity of cyclodextrins (CDs), but MDs represent a considerably more flexible entity than CDs, leading to less restriction toward a steric approach of an interacting solute. Similarities between CD and amylose complexation behaviors have been noted previously.[1] Amyloses bind small molecules, such as iodine, fatty acids,[16,17] linear and branched alcohols,[18] dimethyl sulfoxide,[19] and naphthyl and phenolic derivatives.[9,20] Crystalline complexes with amyloses are known as V-amyloses, in which adjacent turns of a helix are in contact with each other in the form of a collapsed helix.[21] In some circumstances, extended helical forms can be generated.[22] The general preferable properties of the molecules complexing with amylose include a hydrophobic core to which yet another nonpolar substituent is attached together with a more polar group.[1]

In our earlier studies[9] on resolving D- and L-monosaccharides (fluorescently labeled with a naphthyl moiety), we were successful in using both CDs and dextrins as the buffer additives. In a series of maltooligosaccharides, we noticed increased selectivity with increasing molecular weight and postulated that the helical structure (formed in a borate buffer) mimicking a CD cavity was responsible for chiral recognition. In the study by D'Hulst and Verbeke,[12] various commercial MD preparations were differently effective in resolving some acidic pharmaceuticals. Consequently, the effectiveness of MD types and their concentrations had to be related to the composition of these ill-defined MD mixtures and various solvating conditions. A series of electrophoretic and NMR measurements, described below, probe further the mechanisms of these selective interactions.

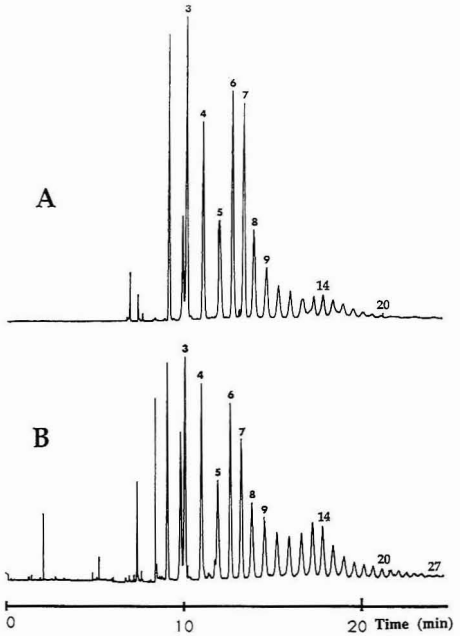

Figure 2. Oligosaccharide profiles from (A) Dextrin 10 (DE 10) and (B) Maltrin MO40 (DE 5) after reductive amination and fluorescent tagging with CBQCA. Detection, fluorescence, using He/Cd laser at 442 (excitation) and 550 (emission) nm wavelengths; separation capillary, linear polyacrylamide coated, 75 μm i.d. × 40 cm (25 cm effective length); run buffer, 0.1 M Tris/borate; pH 8; run voltage, 16 kV (positive ground). Peak numbers indicate the number of glucose residues in oligosaccharides.

Maltodextrin Type and Concentration. The maltodextrin mixtures were characterized by HPCE combined with the laser-induced fluorescence detection of their CBQCA derivatives. The HPCE profiles of Dextrin 10 and Maltrin MO40 revealed that the larger peaks range from three residues (triose) to seven residues (heptaose), but oligomers with a polymerization degree (DP) of as high as 27 were present as minor peaks in Maltrin MO40 (DE 5), as seen in Figure 2.

When the Dextrin 15 (DP = 8–16) and Dextrin 20 (DP = 8–13) mixtures were analyzed by HPCE (results not shown), higher oligomers were also visible but to a lesser extent than with Dextrin 10 and Maltrin M040. According to our experience, the higher oligomers are particularly effective as chiral selectors. Their quantities are not particularly small, as the later peaks are broader and the relative weights of the later-appearing components increase with increasing molecular size. (CBQCA labels a sugar molecule only at its reducing end.)

Dextrin 10 was used further in demonstrating the effect of its concentration on enantiomeric separation. Using a constant buffer composition (TAPS/Tris, with 4% ethanol addition) and uncoated capillaries, the Dextrin 10 concentra-

(16) Mikus, F. F.; Hixon, R. M.; Rundle, R. E. *J. Am. Chem. Soc.* **1946**, *68*, 1115.
(17) Yamamoto, M.; Sano, T.; Yasunaga, T. *Bull. Chem. Soc. Jpn.* **1982**, *44*, 1886.
(18) Kowblansky, M. *Macromolecules* **1987**, *18*, 1776.
(19) Simpson, T. D.; Dintzis, F. R.; Taylor, N. W. *Biopolymers* **1972**, *11*, 2591.
(20) Aoyama, Y.; Otsuki, J.; Nagai, Y.; Kobayashi, K.; Toi, H. *Tetrahedron Lett.* **1992**, *33*, 3775.
(21) French, A. D.; Murphy, V. G. *Cereal Foods World* **1977**, *22*, 61.
(22) Sarko, A.; Biloski, A. *Carbohydr. Res.* **1980**, *79*, 11.

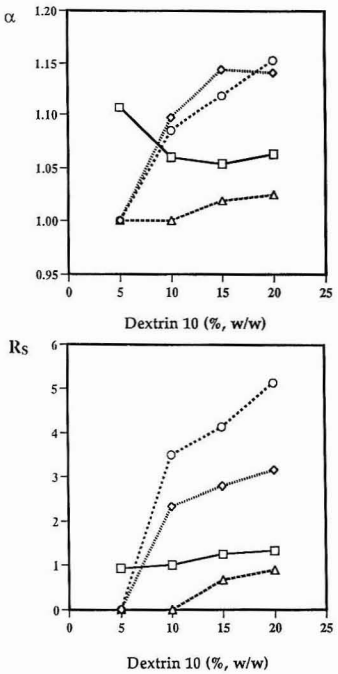

Figure 3. (A, top) Selectivity (α) and (B, bottom) resolution (R_s) of simendan (□), ibuprofen (◊), warfarin (O), and ketoprofen (Δ) enantiomers as a function of Dextrin 10 concentration. Buffer, 20 mM TAPS/6.5 mM Tris/4% (v/v) ethanol, pH 7.7; uncoated capillary, 50 μm i.d. × 60 cm (44 cm effective length); UV detection at 220 nm; run voltage, 26 kV.

tion was varied from 5 to 20% (w/w). The simendan enantiomers were partially separated already at 5% MD concentration, while ibuprofen and warfarin necessitated at least 10% concentration and ketoprofen isomers at least 15%. Figure 3 shows the selectivity (α-values) and resolution (R_s) plotted against concentration of Dextrin 10 in the buffer solution. Ibuprofen, warfarin, and (to a lesser degree) ketoprofen show increasing α-values and resolution with Dextrin 10 concentration. An anomalous situation is observed for the simendan enantiomers, which show more favorable α-values at lower concentration and a partial loss of selectivity at higher oligosaccharide concentrations. Differential behavior of the simendan enantiomers from the other test solutes might be explained through the presence of polar nitrogen groups in the molecule which may exhibit hydrogen-bonding abilities in the enantiospecific complexation with the maltooligosaccharides. It is presently unclear whether the sugar–sugar interactions[23] at higher concentration compete with the enantiomer complexation in this particular case. The effective mobilities (an average of three measurements) of the four acidic pharmaceuticals are plotted against Dextrin 10 concentrations in Figure 4. Once again, simendan appears here different from the other model solutes, which is likely due to

(23) Aoyama, Y. *Trends Anal. Chem.* **1993**, *12*, 23.

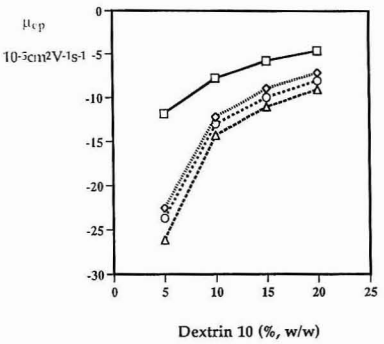

Figure 4. Electrophoretic mobilities (μ_{ep}) of simendan (□), ibuprofen (◊), warfarin (O), and ketoprofen (Δ) for the first eluted enantiomer. Analytical conditions as in Figure 3. (Results are an average over three runs.)

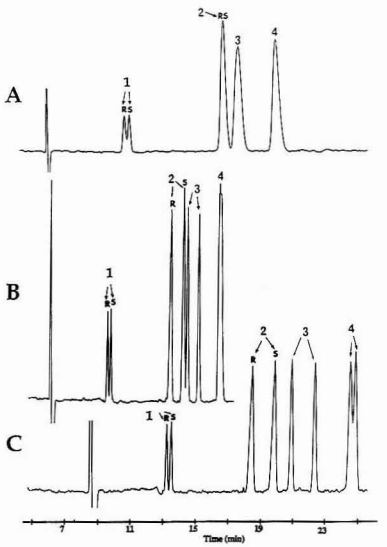

Figure 5. Electropherograms of the acidic model compounds with Dextrin 10 concentrations (w/w) (A) 5%; (B) 10%; (C) 15%. Solutes: peaks 1, R = (*R*)-(−)-simendan, S = (*S*)-(+)-simendan; peaks 2, R = (*R*)-(−)-ibuprofen, S = (*S*)-(+)-ibuprofen. Peaks 3, warfarin enantiomers. Peaks 4, ketoprofen enantiomers. Analytical conditions as in Figure 3.

the larger complexation constant or the changed complexation mechanism with the maltooligosaccharides. Since these model solutes exhibit different migration times, the example electropherograms for three different maltodextrin concentrations are demonstrated in Figure 5. The general enhancement of enantioseparation with the increase of MD concentration is clearly indicated. The role of electroosmosis is less important, as documented at 5% (Figure 5A) and 10% (Figure 5B). Dextrin concentrations had quite similar electroosmotic properties; the respective enantioseparations were considerably improved.

The effects of single maltodextrins in concentrations of 2–6% (w/w) were tested for simendan, ibuprofen, and warfarin with coated capillaries under the negligible electroosmotic flow. Maltoheptaose in a buffer of pH 6.7 separated the enantiomers of simendan and ibuprofen but not warfarin. The hint of separation for ibuprofen was first observed at the concentration of 3% (w/w). Severe peak-tailing, observed particularly with the later-migrating enantiomers (stronger binding), indicated slow equilibration of the binding process. Maltohexaose was effective in chiral recognition for simendan only, starting at the concentration of 2% (w/w) and showing only a partial enantiomer separation. This observation is consistent with the earlier observations on simendan at low Dextrin 10 concentrations. Maltopentaose, maltotetraose, and maltotriose (5% w/w concentration) lacked the enantioseparation ability for all solutes at pH 6.7 and 7.7 when coated capillaries were used. Furthermore, maltotetraose up to 15% (w/w) did not separate the enantiomers of ibuprofen and simendan. The success in chiral recognition with higher oligomers is probably due to the ability of pentaose and higher oligosaccharides to overcome an induced-fit conformation change depending on the size of a complexing molecule.[20] The oligomers with a DP higher than 7 thus seem most suitable for the separation process.

Solvation Effects. With uncoated capillaries, aminopropane- and aminoethanesulfonic acids (TAPS, CHES) and Tricine zwitterions had important effects on resolution, selectivity, and separation times for the enantiomers of acidic pharmaceuticals. The buffer systems Tricine/Tris (pH 7.4), TAPS/Tris (pH 7.8), and CHES/Tris (pH 8.5) were primarily used. With increasing hydrophobicity near the zwitterion's cationic group (e.g., cyclohexyl group in the CHES molecule), the electroosmotic velocity decreased and migration times increased, resulting in improved resolution of the enantiomeric pairs. The separated zone broadened, but the peak shapes remained symmetrical. Apparently, interactions of the wall-adsorbed zwitterions and the analytes were increased. The enantiomers of ketoprofen were separated with TAPS- and CHES- but not with Tricine/Tris buffers. The migration times with CHES buffer were prolonged to more than 1 h.

Decreasing the zwitterion concentration increased both the resolution and the selectivity (α), but also the migration times were increased due to a slower electroosmotic velocity. Limited availability of zwitterions for both the capillary wall and dynamic complexation with dextrins and analytes may influence certain complexation equilibria at the wall. The presence of the analytes and dextrins close to the capillary surface has obviously changed the magnitude of electroosmosis. The four-component test mixture of racemic compounds, simendan, ibuprofen, warfarin, and ketoprofen, listed in their migration order, was used in these experiments. The enantiomeric separation of warfarin (best resolution) and ketoprofen (worst resolution) using a series of dilutions with the TAPS/Tris buffers is shown in Figure 6. The resolution of ibuprofen was not increased in the same way as with the other solutes because of a pronounced band-broadening effect (asymmetrical fronting edge) observed with a decreasing ionic strength. This band-broadening has been assumed to be a sign of multiple complexation of the ibuprofen enantiomers with dextrins differing in their rate constants. Either association or dissociation of some of the complexes is slow, while the material competing for the available sites has been diminished. The ^{13}C-NMR studies, described below, at least partially support this assumption. Among the test solutes, the ibuprofen molecular structure featured the highest flexibility; therefore, also the least geometrical restrictions for interactions with the maltooligosaccharides were expected.

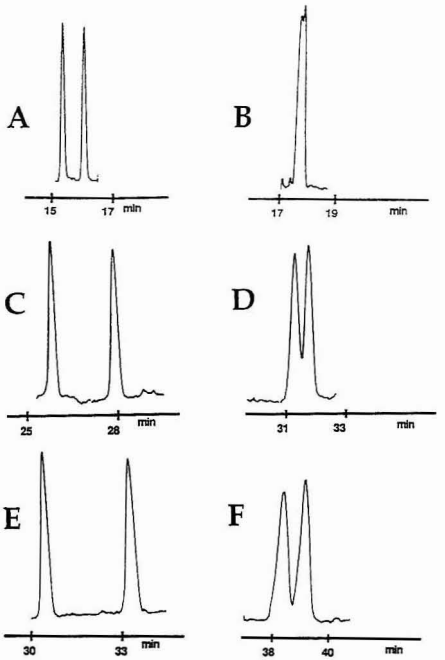

Figure 6. Effect of buffer concentration on the enantiomeric separation of warfarin (A, C, E) and ketoprofen (B, D, F). A, B: 120 mM TAPS/40 mM Tris. C, D: 40 mM TAPS/13 mM Tris. E, F: 20 mM TAPS/6.5 mM Tris. Uncoated capillary, 50 μm i.d. × 60 cm (44 cm effective length); additive, Dextrin 10, 20% (w/w), pH 7.7; UV detection at 220 nm; run voltage, 24 kV.

The organic solvent additives such as methanol, ethanol, (*R*)-(–)-2-butanol, and acetonitrile used at concentrations of 0.5–5% (v/v) were studied in Tricine/Tris (pH 7.4). Addition of organic solvents to CHES/Tris or TAPS/Tris buffer systems was found to be impractical due to excessive analysis times. On the basis of a reported complexation of alcohols[18] and other small molecules with amyloses, the added solvents were responsible for yet another set of competing equilibria in the buffer solution. Ethanol and acetonitrile had the most pronounced effect on the resolution of enantiomeric pairs but only a slight effect on selectivity. In general, the electroosmotic velocity decreased, peaks became broader, and the analysis times increased due to organic solvent additives.

The initially untreated capillaries were dynamically coated with poly(vinylpyrrolidone) (PVP) (average MW 360 000) during the separation of simendan enantiomers with Dextrin 20. Electroosmosis was negligible under such conditions. A base line separation due to reduced electroosmosis was achieved

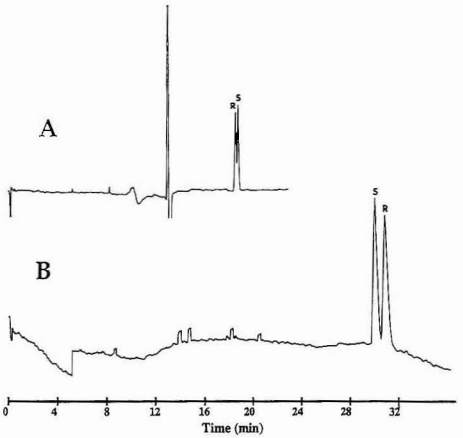

Figure 7. Separation of simendan enantiomers without polymer additive (A, buffer, 20 mM Tris/80 mM Tricine; Dextrin 20, 25% (w/w), *n*-propanol 2%, pH 7.4; voltage, +26 kV) and with PVP polymer additive (B, buffer, 10 mM Tris/40 mM Tricine pH 7.4; Dextrin 20, 12.5% (w/w), 1% (v/v) *n*-propanol, 0.1% (w/w) poly(vinylpyrrolidone) (MW 360 000); voltage, −26 kV. Other analytical conditions as in Figure 6. R = (*R*)-(−)-simendan, S = (*S*)-(+)-simendan.

for this analyte, which had previously not been separated under electroosmosis with a similar type of buffer system (Figure 7). The maltooligosaccharides were compatible in solution with PVP. A similar compatibility of two polymers and enhancement of enantioselectivity was observed earlier in this laboratory with poly(ethylene oxide) and cyclodextrins.[24]

Basic Pharmaceuticals. With uncoated capillaries, the basic solutes (fluoxetine, verapamil, and norverapamil) migrated under electroosmosis in relatively sharp but asymmetric tailing zones. To eliminate the electroosmotic flow, the polyacrylamide coated capillaries[14] were used to study such chiral separations. In the pharmaceuticals examined in the separation system, a position of the chiral center next to the aromatic ring was found necessary for chiral recognition. The enantiomers of basic pharmaceuticals fulfilling this requirement were easily separated, as demonstrated in Figure 8. In comparison, the same compounds could be separated in our previous study using trimethylated β-cyclodextrin containing buffers.[16] Single maltodextrins, from pentaose to heptaose (up to 6%, w/w), added in the same buffer system did not separate any of the three basic enantiomers (structures shown in Figure 1), suggesting that a beneficial chiral interaction must be due to the oligomeric chains longer than seven residues.

Serum Samples. In the analysis of racemic ibuprofen extracted from a spiked serum, an interference-free background was first ascertained through UV detection at 220 nm, using an uncoated capillary (Figure 9B). The levels of 8.5 μg/mL (4.25 μg/mL of each enantiomer) were within the concentration range reported after a single dose of 400 mg of racemic ibuprofen.[25] Maltrin MO40 (96% content of oligosaccharides longer than pentaose) was beneficial in 5% (w/w) concentration for the separation of equal amounts of enantiomers. Using (*S*)-(+)-naproxen as an internal standard, precision of peak–height ratios for each ibuprofen enantiomer and the internal standard was 1.0% (RSD, n = 5). The migration time stability was 1.3% (RSD, n = 5). (*R*)-(−)-Ibuprofen eluted as the first peak under electroosmotic conditions. When electroosmosis was suppressed with the use of a coated capillary, the elution order changed, showing

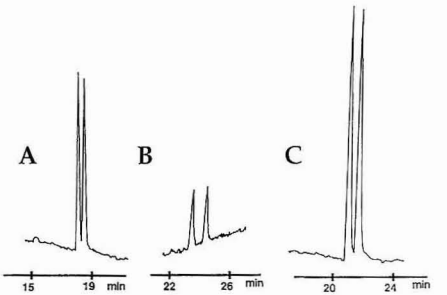

Figure 8. Separation of the basic drugs (A) verapamil, (B) norverapamil, and (C) fluoxetine with Dextrin 10, 20% (w/w) in 25 mM Tris/phosphoric acid buffer, pH 3.4. Coated capillary, 50 μm, i.d. × 60 cm (44 cm effective length); UV detection at 220 nm; run voltage, 22 kV (negative ground).

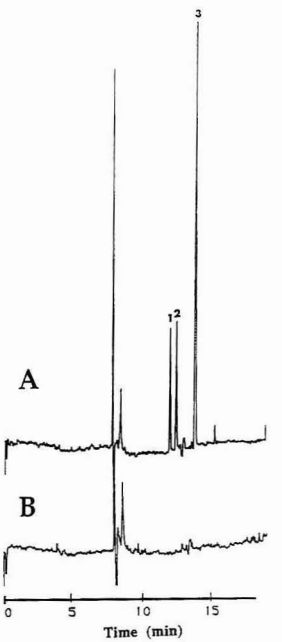

Figure 9. Electropherograms of (A) spiked serum sample (racemic ibuprofen, 8.5 μg/mL) and (B) blank serum after extraction with hexane/2-propanol. Separation buffer, Maltrin MO40 5% (w/w) in 30 mM TAPS/10 mM Tris, pH 7.8; run voltage, 24 kV. Other analytical conditions as in Figure 6. Peak 1, (*R*)-(−)-ibuprofen; peak 2, (*S*)-(+)-ibuprofen; peak 3, (*S*)-(+)-naproxen as an internal standard.

(24) Soini, H.; Riekkola, M.-L.; Novotny, M. V. *J. Chromatogr.*, in press.
(25) Lemko, C. H.; Caillé, G.; Foster, R. T. *J. Chromatogr.* **1993**, *619*, 330.

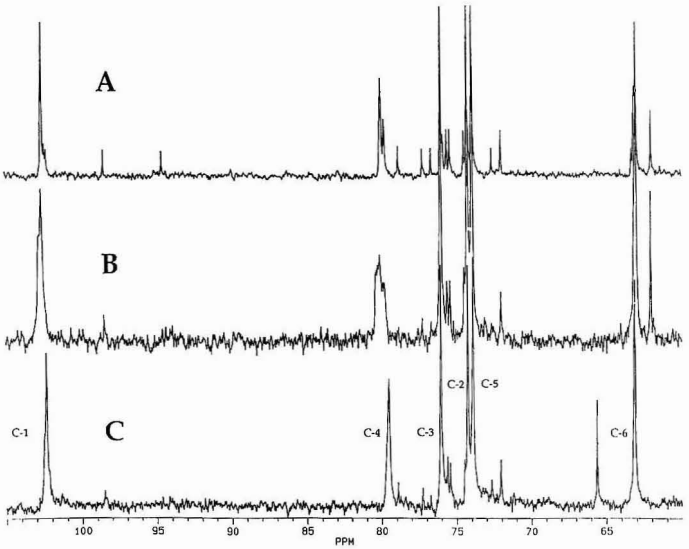

Figure 10. ^{13}C-NMR spectra for complexation of (A) racemic ibuprofen and maltoheptaose (DP = 7); (B) racemic ibuprofen and Maltrin MO40 (DP = 3–27); and (C) maltoheptaose (DP = 7) without solute. The solutions contained D_2O/Tris/TSP. ^{13}C-NMR signals (500 MHz) were proton decoupled and referenced to TSP proton signal (not shown).

(*R*)-(−)-ibuprofen binding more strongly with maltodextrins under the analytical conditions used. In comparison, the selective interaction was stronger for (*R*)-(−)-simendan than for (*S*)-(+)-simendan.

NMR Measurements. There is ample documentation of the usefulness of ^{1}H- and ^{13}C-NMR techniques in elucidating the nature of complexation between complex carbohydrates and smaller molecules, as well as in some other aspects of the advanced structures. Jane et al.,[26] investigating complexation of amyloses with dimethylsulfoxide and α-naphthol by ^{13}C-NMR, found characteristic downfield shifts on C-1 and C-4. In their interpretation, the magnitude of the shift change ratio was found to reflect compactness of the polymer helices. Similar downfield shifts of ^{13}C-NMR signals were also observed during complexation of 3–0-methyl-α-(1–4)-mannan with acyl-CoA[27] and triiodine complexes with maltodextrins of DP = 1–20.[28] In linear maltooligosaccharides, C-1 and C-4 participate in the glycosidic bond. For the proposed process of helix formation, the glycosidic bonds bend into an energetically favored conformation, in which the adjacent turns of the helix are in contact with each other. A helical arrangement of the short-chain maltodextrins during complexation with derivatized monosaccharides in a borate buffer was also suggested by the ^{1}H-NMR and fluorescence measurements in our laboratory.[9]

In agreement with the earlier studies,[26] our ^{13}C-NMR measurements registered identical spectra for maltoheptaose and Maltrin MO40 (DE 5) in the absence of chiral molecules. After ibuprofen was added, large downfield shifts were observed for both maltoheptaose and Maltrin MO40. Line broadening and peak splitting were pronounced for Maltrin MO40 (DP = 3–27) in the presence of the pharmaceutical, while for the identical experiment with maltoheptaose, the peak at about 80 ppm was split (Figure 10). A similar splitting behavior was seen with the racemic ibuprofen and the two pure enantiomers (measured individually). One can assume that the ratios of chemical shift changes correspond to a compact helical form (0.6–0.7) and the linear, extended form (1.7) of maltodextrin.[26] The two forms are at equilibrium, which is slow at the time scale of NMR measurements. The spectra for maltotriose (DP = 3) and maltotriose plus ibuprofen were also registered for the sake of comparison. In this case, the chain bending is expected to be minimal, yielding the chemical shifts for C-1 and C-4 as useful comparative values. Furthermore, if interactions of ibuprofen or buffer molecules with maltotriose were to occur, they should be considerably less pronounced with the oligosaccharides smaller than maltopentaose. (Stability constants of molecules complexing with DP = 6–12 were reported[28] relatively unchanged.) In Table 1, we show the chemical shifts for C-1 and C-4 and the characteristic ratios of shift changes, $\Delta\delta$(C-1)/$\Delta\delta$(C-4), for the solutes complexing with various maltooligosaccharides.

The observed shift change ratios (0.6–0.7) for ibuprofen complexation with DP = 7 and DP = 3–27 maltodextrins seem to support a notion of a relatively tight helix form. The broadened signal bands with DP = 3–27 also suggest multiple complexations with varying equilibrium constants, which is in agreement with the above-mentioned electrophoretic experiments, showing asymmetrical peaks. In our ^{1}H-NMR experiments with the same solutions, we observed no significant

(26) Jane, J.-L.; Robyt, J. F.; Huang, D.-H. *Carbohydr. Res.* **1985**, *140*, 21.
(27) Maggio, J. E. *Proc. Natl. Acad. Sci. U.S.A.* **1980**, *77*, 2582.
(28) Vetter, D.; Thorn, W. *Starch/Stärke* **1992**, *44*, 271.

Table 1. Chemical Shifts and Ratios of Shift Changes C-1 and C-4 Registered with Proton Decoupled ^{13}C-NMR Spectroscopy

complexation system	δ(C-1) ppm	δ(C-4) ppm	Δδ(C-1)/Δδ(C-4)
DP 3	3	102.167	79.538
(+)-ibuprofen/DP 3	102.378	79.636	2.153
(±)-ibuprofen/DP 7	102.550	80.013	0.806
		79.780	1.583
(+)-ibuprofen/DP 7	102.444	79.935	0.688
		79.700	1.685
(–)-ibuprofen/DP 7	102.440	79.923	0.709
		79.696	1.728
(±)-ibuprofen/DP 3–27	102.612	80.070[a]	0.836
(+)-ibuprofen/DP 3–27	102.485	79.988[a]	0.707
(–)-ibuprofen/DP 3–27	102.499	80.055[a]	0.642
(–)-simendan/DP 7	102.295	79.673	1.422
(±)-simendan/DP 3–27	102.538	79.839	1.233

[a] Broad signal band.

shift changes but a clear broadening of all proton signals. The signal broadening was also more extensive for (*R*)-(–)-ibuprofen compared to (*S*)-(+)-ibuprofen, supporting the previously observed electrophoretic migration behavior that suggested a stronger complexation of the *R*-isomer.

For simendan, both ^{1}H- and ^{13}C-NMR spectra suggested interaction with a relatively extended form of the dextrin polymer. All proton signals were broadened, but the ratios of carbon shift changes were 1.2–1.4, showing little support for bending at the glycosidic bond.[26] In this respect, a higher separation selectivity at lower concentrations of Dextrin 10 observed during capillary electrophoresis could be explained by a higher stability of complex with the extended chains. Complexation at higher Dextrin concentrations might involve less beneficial side reactions for the chiral recognition of simendan, such as 1:2 complexation, which would be negligible at lower Dextrin concentrations.

The helix formation of linear maltodextrins in the presence of various complexing compounds is extensively documented, but the exact mechanisms of complexation remain uncertain. Most likely, there are different mechanisms, depending on a momentary structure of the guest molecule. Electrostatic dipole–dipole[16] and CH-π interactions as well as multiple hydrogen bonding are obviously important parameters in the binding processes.[20] There has been evidence for some complexing molecules located inside the helix cavity in several studies.[17,26] However, partial inclusion[29] and complexation between helical structures[30] have been under consideration as well. Additionally, complexation and a chirally specific complexation may sometimes be two separate processes. Our evidence for the importance of the location of a chiral center between the aromatic moiety and the negative or positive charge in the chiral recognition is consistent with the observations of the stabilizing effects of a negative charge in complexation.[18]

Through a combination of electrophoretic and NMR measurements, we have gained some valuable insights into how various chiral molecules interact with linear oligosaccharides. Similar techniques can potentially be utilized in probing additional interactions with various carbohydrate molecules. Optimization of the analytical separations of acidic pharmaceuticals have been a practically important highlight of our investigation.

(29) Wulff, G.; Kubik, S. *Carbohydr. Res.* **1992**, *237*, 1.
(30) Booy, F. P. *Biopolymers* **1979**, *18*, 2261.

ACKNOWLEDGMENT

This research was supported by Grant GM 24349 from the National Institute of General Medical Science, U.S. Department of Health and Human Services. We also appreciate additional funds from the Jenny and Antti Wihuri Foundation, the Emil Aaltonen Foundation, and a fellowship conferred by the Finnish Academy of Sciences to H.S. Special thanks are due to Robert E. Addleman and Dr. Mark D. Pagel for running the ^{1}H- and ^{13}C-NMR experiments and helping with spectral interpretation. Also, we are grateful to Dr. Timo Lotta (Orion-Farmos Pharmaceuticals, Espoo, Finland) for donating pure enantiomers of simendan.

Received for review April 5, 1994. Accepted July 6, 1994.[⊗]

[⊗] Abstract published in *Advance ACS Abstracts*, September 1, 1994.

Anal. Chem. **1994,** *66,* 3485–3491

Electroosmotic Pumping and Valveless Control of Fluid Flow within a Manifold of Capillaries on a Glass Chip

Kurt Seiler, Zhonghui H. Fan, Karl Fluri, and D. Jed Harrison*

Department of Chemistry, University of Alberta, Edmonton, Alberta, Canada T6G 2G2

Fluid flow was driven within a network of intersecting capillaries integrated on a glass chip using electroosmotic pumping. Potentials could be applied to several capillaries simultaneously to quantitatively control the amount of each reagent stream delivered to an intersection of capillaries. An example of a simple dilution of sample with buffer is shown. Kirchhoff's rules for resistive networks were found to predict the currents and fluid flow within the capillaries. Leakage of sample from one channel to another at an intersection was shown to arise from both diffusive and hydrodynamic effects. Application of potentials to the intersecting channels could fully arrest such leakage. These phenomena were evaluated both qualitatively from photomicrographs of the fluid flow in the channels and quantitatively from measurements of electrophoretic separations of amino acids and fluoresceins.

Electroosmotic flow can be used as a pumping mechanism within a capillary.[1-3] We have shown that multiple, intersecting capillaries can be integrated on a planar device to form a manifold of flow channels in which capillary electrophoresis can be used for separation of sample components.[4-8] Flow injection style sample handling can also be effected within the manifold.[3] Separations on a time scale of seconds or even milliseconds can be achieved in such devices.[9] It is also possible to control the flow of liquids at the intersection of channels with electric fields rather than valves or pumps, so that fluidic systems with no moving parts can be realized.[3-5] The potential applications of such systems include miniaturized analytical systems that could compete with bench-top instruments or chemical sensors in terms of performance, analysis time, or durability.[3-11]

To practically realize the use of electroosmotic pumping in a complex manifold of channels, it is necessary to develop an understanding of the factors that control flow within such systems, particularly at the intersection of two channels containing different solutions. One of the best ways to achieve this is to visually image the flow process within the channels.[3] In addition, the quantitative study of flow rates and study of the ability to control the direction of solvent flow using applied fields are required. In this report we present both images and quantitative studies of diffusional and convective mixing of solutions at channel intersections. We also show that judicious application of voltages to multiple channels within a manifold can be used to control such mixing and direct the flow of solvent and sample in the desired manner. This control can be used to reduce or eliminate unwanted leakage effects[3-5] and to provide controlled delivery of solutions and reagents within a complex manifold of intersecting capillaries, as might be required in flow injection analysis systems. When the electrolyte resistivities in each channel are either the same or known and the electroosmotic flow rates are the same in all channels, it is possible to quantitatively calculate the potential required to control the flow directions using a simple resistance network model of the channels.

EXPERIMENTAL SECTION

Device Fabrication. Figure 1a shows the layout and dimensions of the principal glass device studied, which consisted of three capillary channels intersecting at right angles to form a T junction. It is referred to as COCE. The channels were 10 μm deep and 30 μm wide where shown as a single line width in the figure and 220 μm wide where shown as a heavier line. A cover plate, with 1.5-mm-diameter holes drilled ultrasonically or with a diamond bit, provided channel access points. It was thermally bonded to a glass plate in which channels were etched. A second device, Jet-1, is shown in Figure 1b; the narrow lines are for channels 10 μm deep and 30 μm wide, while the heavier lines represent channels 300 μm wide. Devices were fabricated in Corning 7740 Pyrex glass at the Alberta Microelectronic Centre (AMC) using a modification of bulk silicon micromachining methods described elsewhere.[11]

Apparatus. A computer-controlled system was used to apply and switch the potentials on the device reservoirs and is described in detail elsewhere.[4,11] Labview programs (National Instruments Corp., Austin, TX) written locally were used for data acquisition and instrument control. A 488-nm argon ion laser (Uniphase/Ionics Model 2011) was used to excite fluorescence after being focused to about a 40-μm spot size in the device channel. The fluorescent emission was collected with a 10:1 microscope objective and directed onto a photomultiplier tube through a 1-mm pinhole at the image plane and an optical band pass filter (508–533 nm), as described elsewhere. For imaging the channels, the laser beam

(1) Manz, A.; Fettinger, J. C.; Verpoorte, E.; Lüdi, H.; Widmer, H. M.; Harrison, D. J. *Trends Anal. Chem.* **1991**, *10*, 144–149.
(2) *Capillary Electrophoresis: Theory and Practice*; Grossman, P. D., Colburn, J. C., Eds.; Academic Press: New York, 1992.
(3) Harrison, D. J.; Fluri, K.; Seiler, K.; Fan, Z.; Effenhauser, C. S.; Manz, A. *Science* **1993**, *261*, 895–897.
(4) Seiler, K.; Harrison, D. J.; Manz, A. *Anal. Chem.* **1993**, *65*, 1481–1488.
(5) Harrison, D. J.; Manz, A.; Fan, Z.; Lüdi, H.; Widmer, H. M. *Anal. Chem.* **1992**, *64*, 1926–1932.
(6) Manz, A.; Harrison, D. J.; Verpoorte, E. M. J.; Fettinger, J. C.; Paulus, A.; Lüdi, H.; Widmer, H. M. *J. Chromatogr.* **1992**, *593*, 253–258.
(7) Harrison, D. J.; Glavina, P. G.; Manz, A. *Sens. Actuators* **1993**, *B10*, 107–116.
(8) Harrison, D. J.; Fan, Z.; Seiler, K.; Manz, A.; Widmer, H. M. *Anal. Chem.* **1993**, *283*, 361–366.
(9) Effenhauser, C. S.; Manz, A.; Widmer, H. M. *Anal. Chem.* **1993**, *65*, 2637–2642.
(10) Manz, A.; Harrison, D. J.; Verpoorte, E.; Widmer, H. M. In *Advances in Chromatography*; Brown, P. R., Grushka, E., Eds.; Marcell Dekker: New York, 1993; Chapter 1, pp 1-65.
(11) Fan, Z.; Harrison, D. J. *Anal. Chem.* **1994**, *66*, 177–184.

0003-2700/94/0366-3485$04.50/0
© 1994 American Chemical Society

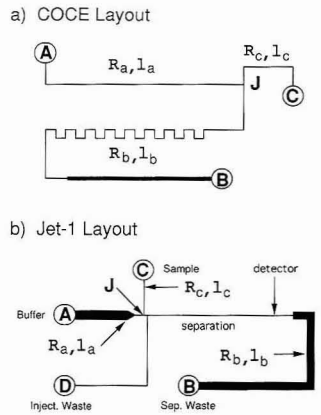

Figure 1. (a) Device COCE layout with reservoir labels, channel lengths (l_a), and resistances, (R_a) indicated. Values are given in Table 1. Overall dimensions were 2.8 × 7.0 cm. (b) Device Jet-1 layout with various labels. Values are in Table 1.

was expanded slightly and directed onto the device. The device was mounted on a stage under an Olympus BH-2 microscope using a 5:1 magnification, a long working distance objective, and a 10:1 eyepiece.[3] Photos were taken with a camera adaptor and an Olympus OM-2 camera body, while potentials were applied to the channels. Exposures were about 1.5 s long.

The current in the channels was monitored from the potential drop across a 10-kΩ resistor located between the channel reservoir and the power supply ground and recorded on a strip chart recorder.

Materials and Reagents. Amino acids, fluorescein, and fluorescein 5-isothiocyanate (FITC) were used as received (Sigma). Amino acids were labeled with FITC.[3-5,12] Several pH 9.1 buffer solutions were used, including solutions 10, 30, or 64 mM in carbonate ion or 10 mM in $Na_2B_4O_7{\cdot}10H_2O$. The carbonate stock solution was prepared from a solution of 0.054 M $NaHCO_3$ and 0.0096 M Na_2CO_3. All chemicals were reagent grade; deionized, doubly-distilled water was used for all solutions. Solutions were filtered using 0.22-μm pore size Millipore-GV sterile filter units (Millipore, Bedford, MA) before being injected into the capillaries on the chip in the manner previously described.[4,5,11]

RESULTS AND DISCUSSION

Two devices were prepared with networks of intersecting channels in order to study the effect of applying potentials to multiple channels simultaneously on the behavior of fluid transport in the channel networks. The device COCE shown in Figure 1 consisted of three channels intersecting in a T configuration in which simple mixing experiments were performed, while Jet-1, also shown in Figure 1, had a slightly more complex geometry and was used for sample injection and separation. A labeling scheme is shown that is used to identify the channel resistances and lengths (R and l) by subscripts associated with the channel segment between the intersection J and each of the reservoirs. Values of R and l are reported in Table 1 for both devices.

Three intersecting channels with potentials applied to the solvent reservoirs of all three channels can be modeled as a simple network of three resistors, as illustrated in Figure 2. With two voltage sources and a near-ground potential connected to the channels, the current in each channel and the potential at the intersection are readily expressed using Kirchhoff's rules[13] to give eqs 1–4,

$$I_3 = V_J/R_3 \tag{1}$$

$$I_1 = (V_1 - V_J)/R_1 \tag{2}$$

$$I_2 = (V_2 - V_J)/R_2 \tag{3}$$

$$I_3 = I_1 + I_2 \tag{4}$$

where the assumed directions of the currents I_1, I_2, and I_3 are shown in Figure 2. The 10-kΩ resistor has been omitted in eq 1, as it is much smaller than R_3 in our applications. Solving for V_J and I_3 gives eqs 5 and 6,

$$V_J = (V_1R_2R_3 + V_2R_1R_3)/(R_1R_2 + R_2R_3 + R_1R_3) \tag{5}$$

$$I_3 = [V_1R_2 + V_2R_1]/(R_1R_2 + R_2R_3 + R_1R_3) \tag{6}$$

While in general the potentials V_1 and V_2 can have any polarity, in this study V_1 was always positive and V_2 always negative. Equation 6 shows that a plot of I_3 versus V_1 will be linear when V_2 is held constant; however, I_3 may be positive or negative depending on the potentials applied and the resistance of each channel. Note that a switch in sign of the current will also mean a change in the direction of electroosmotic flow. During the course of experimentation, the polarity of potentials applied to each of the device reservoirs was varied. The correlations of device channel resistances with the values in eqs 5 and 6 are provided in the text or figure captions.

Electrical Characteristics. Table 1 gives the measured lengths and resistances between each pair of reservoirs identified in Figure 1 for both devices. The ratios of these values to those for the reservoir pair A–B or the channel length l_a are also given for the two different devices. The resistance of each channel should be proportional to the length of the channel and its cross-sectional area, as well as the electrolyte resistivity.[14] Some segments were either 220 or 300 μm wide, while the standard channels were 30 μm wide at the top surface, so that the segment resistances varied along their length. For convenience an equivalent length (l_{eq}) was calculated for the wider segments using the formula

$$l_{eq} = l_{true}A_{30}/A_{true} \tag{7}$$

where A_{30} and A_{true} are the cross-sectional areas of the 30-μm and the wider channels, respectively. It is these equivalent lengths that are given in Table 1. The resistances and their

(12) Sweedler, J. V.; Shear, J. B.; Fishman, H. A.; Zare, R. N.; Scheller, R. H. *Anal. Chem.* **1991**, *63*, 496–502.

(13) Halliday, D.; Resnick, R. *Physics*; J. Wiley and Sons: New York, 1960.

(14) The relationship between R and geometry is $R = \rho l/A$, where ρ depends on a given electrolyte's resistivity and l and A are the channel's length and cross sectional area, respectively.

Table 1. Comparison of Channel Lengths and Experimentally Determined Resistances for Devices COCE and JET-1[a]

	A–B[b]	A–C	C–B	A	B	C
			Device COCE			
distance (mm, ±0.05 mm)	138.3	53	101.3	45	93.3	8
resistance (MΩ)[c]	1035 ± 2	396 ± 4	797 ± 9	320 ± 20	720 ± 20	79 ± 8
distance ratio to A–B	1	0.383 ± 0.010	0.732 ± 0.013			
resistance ratio to A–B	1	0.382 ± 0.005	0.770 ± 0.011			
distance ratio to l_a				1	2.07 ± 0.03	0.18 ± 0.01
resistance ratio to R_a				1	2.3 ± 0.2	0.25 ± 0.08
			Device Jet-1[d]			
distance (mm, ±0.05 mm)	30.85	4.7	29.35	3.1	27.75	1.6
resistance (MΩ)[c,d]	526 ± 3	81.4 ± 0.5	502 ± 3	53 ± 2	473 ± 2	29 ± 2
distance ratio to A–B	1	0.152 ± 0.002	0.951 ± 0.002			
resistance ratio to A–B	1	0.155 ± 0.001	0.954 ± 0.008			
distance ratio to l_a				1	9.0 ± 0.1	0.52 ± 0.06
resistance ratio to R_a				1	8.9 ± 0.3	0.55 ± 0.04

[a] Errors (standard deviation) in resistance between reservoirs are determined from least-square fits of current–voltage curves, while errors in lengths are ±0.05 mm based on an estimate of probable alignment errors. All other errors are calculated using error propagation analysis. [b] Labels A, B, and C and A–B, etc. refer either to the individual channels originating from the reservoirs and terminating at the intersection or to the channel lengths between the indicated reservoir pairs, respectively. See Figure 1A for the reservoir labels. [c] The resistance of a given channel segment and its length are given. Ratios are given relative to the length or resistance of the segment between reservoirs A and B or between A and the intersection point, as indicated. [d] For Jet-1, no calculations were performed using the resistance of channel D, so those data are omitted for brevity (note l_d = 20.3 mm).

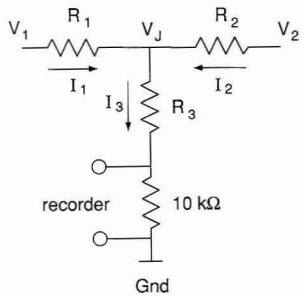

Figure 2. Equivalent circuit for intersection of three channels with controlled potentials.

standard deviations were determined from the slopes of linear current–voltage curves obtained with a potential applied between each reservoir pair. Table 1 also gives the lengths, l_a, l_b, and l_c, and the corresponding resistances, R_a, R_b, and R_c, for each of the channel segments measured from the intersection point to each reservoir. The error in the channel lengths arises from the error in positioning the reservoir access holes in the cover plate over the channels and is taken as ±0.5 mm, although this may be an overestimate.

The data show that the resistances R_a, R_b, and R_c are indeed proportional to the equivalent channel lengths within experimental error. This would be expected providing there is no defect in the bonding of the glass cover plate to the etched piece. The results are consistent with our previous observations with other devices.[4-8,11]

The behavior of COCE with potentials applied to all three channels was evaluated according to the scheme indicated in the inset of Figure 3. The current was measured from the potential drop across a 10-kΩ resistor between ground and reservoir C, with V_1 and V_2 applied to reservoirs A and B, respectively. In this configuration, the resistances for eqs 1–6 were $R_1 = R_a$, $R_2 = R_b$, and $R_3 = R_c$. The current was indeed linear in V_1 when V_2 was held constant. Figure 3 shows the data obtained for three different values of V_2. It was possible to calculate the current using eq 6 and the measured channel

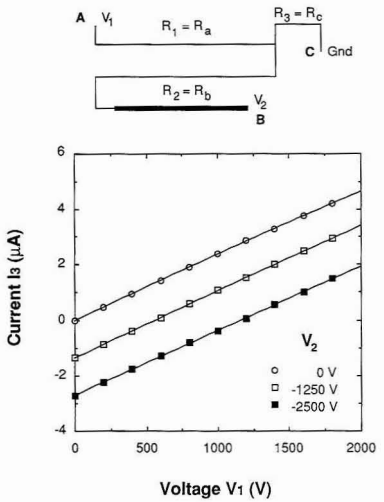

Figure 3. Current as a function of V_1 applied to reservoir A, with the indicated values of V_2 applied to reservoir B. Symbols are for experimental data; solid lines are for current calculated from eq 6 using the data in Table 1. The inset shows the applied potential scheme.

resistances given in Table 1, and the calculated response is shown as the solid lines in Figure 3. The very good agreement illustrated between theory and experiment shows that the model is accurate. It can be used to determine potentials and currents within a complex network of capillaries when several voltage sources are applied simultaneously.

A practical limitation of most high-voltage power supplies should be noted here. The high-tension terminal of a power supply presents a very high impedance path to ground, so current will not normally flow into this terminal when there is an alternate route to ground. For example, if both V_1 and V_2 in Figure 2 were positive supplies, then the potential at the junction would be positive. If V_2 was set sufficiently large, the intersection potential V_J would exceed the value of V_1.

This would demand that V_1 act as a sink for current, but since the resistance network provides a path to ground the power supply would usually not. Consequently, no current would flow in resistance (i.e., channel) 1, and V_1 would no longer control the potential along that channel. This puts limitations on the design of networks that can be utilized and may define where the ground terminal can be located.

Mixing of Solutions Using Voltage Control. When electroosmotic flow is present in a capillary, the linear flow velocity, v, is given by eq 8,

$$v = (\mu_{eo} + \mu_{ep})E \tag{8}$$

where μ_{eo} and μ_{ep} are the electroosmotic and electrophoretic mobilities, respectively, and E is the electric field applied.[15] The overall mobility, μ, is the vector sum of these two mobilities, and μ_{eo} is generally larger than μ_{ep} in absolute terms. In the following discussions it is helpful to note that with negatively charged capillary walls, the direction of electroosmotic flow of the solvent will be in the same direction as the current flow. This is the case for glass at pH 9. The velocity of species i in each of the channels is given by eqs 9–11,

$$v_{i,1} = \mu_i(V_1 - V_J)/l_1 \tag{9}$$

$$v_{i,2} = \mu_i(V_2 - V_J)/l_2 \tag{10}$$

$$v_{i,3} = \mu_i V_J/l_3 \tag{11}$$

where V_J is given by eq 5, and the various v_i refer to the velocity of species i in each channel of length l. The subscripts 1, 2, and 3 refer to the velocity and channel length associated with the potential sources V_1, V_2, and ground, respectively. These expressions indicate that controlled mixing of solutions should be possible at the intersection of the three channels by adjustment of the potentials V_1 and V_2. This phenomenon was explored both quantitatively and qualitatively, as described below.

Equations 9–11 express the electrokinetically driven flow. Since the channel cross sections are equal at the intersection, the sum of v_1 and v_2 for the linear flow rate of the solvent must equal v_3 in order to have mass balance. Substitution of μ_{eo} for μ_i in eqs 9–11 shows that the mass balance condition will be met by electroosmotic flow alone only when μ_{eo} is the same in each channel. This will require that the ionic strength and pH be the same in each channel. If this is not the case, then the excess electroosmotic flow in the channel with the highest μ_{eo} will induce additional flow in the other channels so that mass balance will occur. In this work, the pH and ionic strength were the same in all channels.

The COCE device was mounted under a microscope equipped with a camera, and the region near the intersection was illuminated with 488-nm light. Any striations visible in the fluorescent dye stream seen in Figure 4 and later photos are due to nonuniformity in the illumination or collection efficiences, as it is the tendency of the intensity to fade at the edges of the photos. The exposures were about 1.5 s long and so capture the steady-state flow of the fluid stream. Following

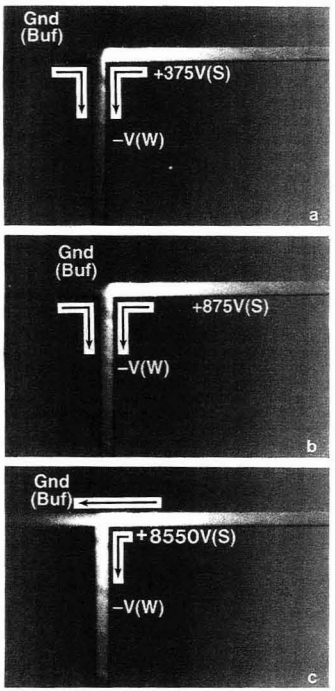

Figure 4. Photomicrographs with arrows showing the direction of flow during controlled mixing of 10 mM carbonate buffer, pH 9.1, and 100 μM fluorescein in the same buffer. Channels are 30 μm wide and provide the scale for the photo. The buffer reservoir (Buf) was at grounded, and the sample reservoir (S) had the indicated positive potentials applied, while the waste reservoir (W) was at –3.75 kV.

application of the voltages, it usually required a few seconds or less for the steady-state flow to be established.

Figure 4 shows the dye stream when the buffer reservoir (Buf) was maintained at ground and the waste reservoir (W) at -3.75 kV, while the potential on the sample reservoir (S) varied from +325 to +8550 V. The potentials applied to the three reservoirs of COCE drove 10 mM carbonate buffer, pH 9.1, from the left (marked GND(Buf)) of Figure 4a and 100 μM fluorescein sample (S) from the right (+375 V(S)) toward the waste reservoir (–V(W)). Figure 4a shows the mixing of the two streams as they move downstream of the intersection point in the direction of the arrows.

Figures 4b and c establish that increasing the potential on the sample reservoir increases the amount of dye relative to buffer downstream of the intersection. However, Figure 4c also illustrates that the direction of flow in the channel connected to ground can be reversed as the potential at the channel junction, V_J, changes from negative to positive. Figure 4c captures this change in flow direction within 5 s of increasing the potential to 8550 V. The potential V_1 required for such a reversal of the buffer flow was calculated using eq 5, with $R_1 = R_b$, $R_2 = R_a$, and $R_3 = R_c$ for the COCE device. The potential V_J is predicted to be negative when the sample channel potential V_1 is less than 8400 V, causing flow from the buffer

(15) Jorgenson, J. W.; Lukacs, K. D. *Anal. Chem.* **1981**, *53*, 1298–1302.
(16) Lauer, H. H.; McManigill, D. *Anal. Chem.* **1986**, *58*, 166–170.

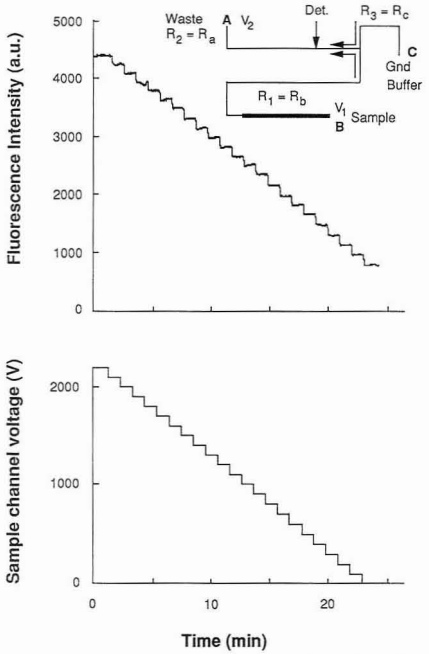

Figure 5. Fluorescence intensity downstream of the T intersection as a function of time, while the potential on the sample reservoir was decreased in −100 V steps every 60 s. Polarities are indicated in the inset and are the same as those for Figure 4 with $V_2 = -2$ kV (30 mM carbonate, pH 9.1 buffer, and 10 μM fluorescein sample in the same buffer).

reservoir towards the junction, while V_3 should be +5 V when V_1 is 8550, causing dye to flow into the buffer channel, as was observed in Figure 4c.

A similar experiment was performed in a quantitative fashion using a detector located about 1 cm downstream of the mixing intersection. The potentials were applied with the same polarity as in Figure 4 and are shown in the inset of Figure 5. The intensity of the focused laser beam was reduced to the point where photobleaching of fluorescein did not occur, so the intensity of the signal was not a function of the solution velocity. Figure 5 shows the intensity decreased in a stepwise fashion as the potential applied to the sample reservoir was decreased; however, there was a lag time of about 10 s. The decreased intensity arose from the decreased amount of dye relative to buffer downstream of the intersection. The lag time is in agreement with the expected transit time between the intersection point and the detector, confirming that the decrease in signal is due to dilution of the dye.

Imaging of Leakage. We have previously discussed leakage effects at the intersection of channels.[3-5,11] In particular, if a side channel is left floating while a potential is applied to cause flow in the main channel, there will be leakage of solution from the side channel, contaminating the main channel. We have indirectly shown that both hydrodynamic and diffusion effects contribute to this mixing or leakage effect at the

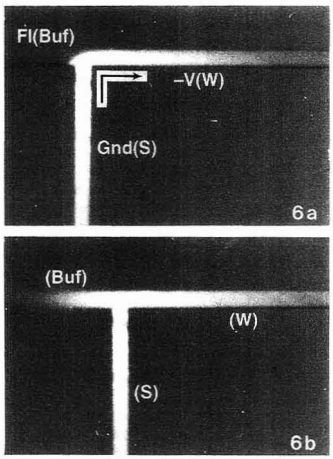

Figure 6. (a) Photomicrograph showing flow of dye around a corner with no potential applied (Fl) to the buffer reservoir (Buf) (10 mM carbonate, pH 9.1). The sample reservoir (S) was grounded (100 μM fluorescein in the same buffer), and the sample was driven toward the waste reservoir (W) at −10 kV. Arrows show the flow direction, and the channels were 30 μm wide. (b) Effect of disconnecting all potentials for 15 s after the profile in part a was established.

intersection.[11] In previously studied devices with various layouts, the concentration of sample leaking into the main channel was about 1–3% of that in the sample channel.[4,5,11]

Figures 6 and 7 illustrate the leakage effect at the intersection in COCE. In Figure 6, sample (S) was directed from the grounded reservoir (GND(S)) toward the negative waste reservoir (–V(W)), while the remaining reservoir which contained buffer (Buf), was left floating (Fl). Figure 6a shows that the sample turned the corner at the intersection without significantly spreading back into the buffer channel. All reservoirs were then left floating (i.e., with no applied potentials) for 15 s to allow diffusion to occur, creating the dye distribution seen in Figure 6b. This illustrates the significant extent of diffusion that occurs at the uncontrolled intersection and exemplifies the diffusion effects discussed by Dose and Guiochon.[17] However, when the sample was flowing, as in Figure 6a, the dye distribution was quite sharp. This must mean that buffer was drawn out of its channel and swept the diffusing dye downstream, leading to the sharp distribution observed at the corner. This flow of the buffer likely arises from the viscous drag of the flowing dye stream on the stagnant solution within the buffer channel.[18] It is equivalent in nature to the forces causing aspiration.

A more graphic demonstration of the leakage phenomenon in COCE is shown in Figure 7. In this case, the grounded buffer solution (GND(Buf)) was driven toward the negative waste reservoir (–V(W)), while the dye sample reservoir was left floating (Fl(S)). The flow of dye into the intersection from the side channel and subsequent mixing downstream are

(17) Dose, E. V.; Guiochon, G. *Anal. Chem.* **1992**, *64*, 123–128.
(18) (a) Gerhart, P. M.; Gross, R. J. *Fundamentals of Fluid Mechanics*; Addison-Wesley: Reading, MA, 1985. (b) Jeppson, R. W. *Analysis of Flow in Pipe Networks*, Ann Arbor Science Pub.: Ann Arbor, MI, 1976.

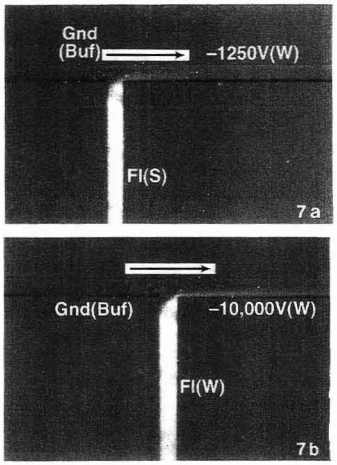

Figure 7. Leakage of sample dye solution (S) from a floating side channel (Fl) when flow was directed from the grounded buffer reservoir (Buf) to the waste reservoir (W) with (a) −1.25 kV applied and (b) −10 kV applied to W. Solutions were the same as in Figure 6. Arrows show the flow direction, and the channels were 30 μm wide.

very clearly seen. The flow velocity increased with increasing potential, and this increased both the extent of leakage and the distance of travel required for mixing downstream of the intersection, as seen in Figure 7. This demonstrates that hydrodynamic flow effects lead to leakage, in addition to any diffusion-driven transport.

In comparing the leakage effects observed within COCE, Jet-1, and other devices[4,5,11] studied previously, it became clear that the magnitude of the effect can vary greatly: from 1 to 3% in some layouts and up to 21% in COCE. The principal difference in the layouts was the relative lengths of the intersecting channels. When a separation channel was much longer than a side channel, leakage was more pronounced. This is presumably related to the resistance to flow associated with a channel's geometry and a need to balance these resistances. We do not yet have a clear picture of the factors governing leakage, but it is clearly desirable to eventually put our present understanding on a more quantitative basis.

Leakage Control. Control of the leakage at an intersection can be achieved by controlling the potential of three channels simultaneously. Figure 8 shows that dye can be forced to sit at the intersection in COCE without leaking into the flowing channel with the appropriate choice of potentials. The dye appeared immobilized for over 60 s, and then buffer slowly crept into the sample channel over several minutes. For this experiment, the potential was adjusted to achieve stasis, but it is possible to calculate the required values with reasonable accuracy, as illustrated quantitatively below for device Jet-1.

Figure 9 shows data obtained in device Jet-1 with the layout and reservoir labeling indicated in Figure 1. The separation of fluorescein isothiocyanate (FITC)-labeled arginine (Arg) and tyrosine (Tyr) is shown. For these experiments, sample solution (S) was present in reservoir C, which was held at ground. As shown in the diagram at the top of Figure 9,

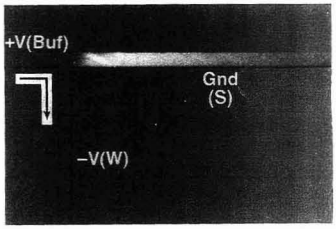

Figure 8. Immobilization of sample dye solution (S) at an intersection by the application of potential to all three channels. The buffer reservoir (Buf) was at 525 V, the sample reservoir (S) was at ground, and the buffer flowed toward the waste reservoir (W) at a potential of −3.75 kV. Solutions were the same as in Figure 6. Arrows show the flow direction, and the channels were 30 μm wide.

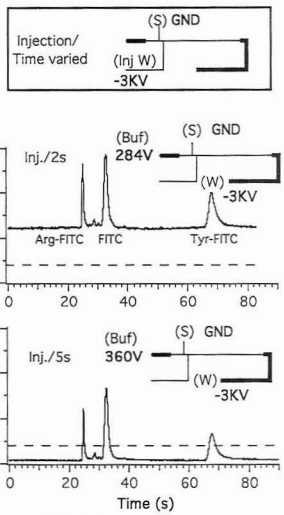

Figure 9. Separation of 20 μM Arg-FITC and 40 μM Tyr-FITC in 0.064 M carbonate buffer, pH 9.1, with potentials applied to three reservoirs of device Jet-1. The injection procedure is shown at the top, and separations with two different values of V_1 applied to the buffer reservoir are shown. The dashed lines indicate the background level when the sample channel was instead left floating during separation.

samples were injected across a "double T" injector[9] from (S) toward the injection waste reservoir (inj W), which was at −3 kV. This created a sample plug in the separation channel defined by the offset of the double T geometry, about 150 μm in length.

To evaluate the ability to control leakage during a separation we applied potentials to three reservoirs simultaneously. The voltages of the buffer (Buf), sample (S), and separation waste (W) reservoirs (A, C, and B, respectively, in Figure 1) were controlled, while the injection waste reservoir was left floating (i.e., no electrical contact), as shown in the insets of Figure 9. In the first electropherogram of Figure 9, V_1 = 284 V was applied to the buffer reservoir during the separation. This resulted in a high background fluorescence compared to the background seen when the sample channel was instead left floating (dashed line). The potential at the sample to separation channel intersection, V_3, was calculated to be −17

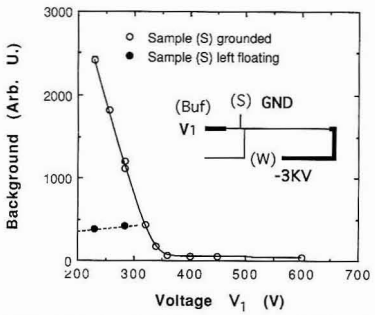

Figure 10. Effect of control of three voltages as in Figure 9 on the background level, shown as a function of V_1, the potential applied to the buffer reservoir, with other conditions as in Figure 9.

± 12 V using eq 5 and the measured resistances of the channels in Table 1, with $R_1 = R_a$, $R_2 = R_b$, and $R_3 = R_c$. Since the sample channel was at ground, the result should have been a net flow out of the sample channel during the separation and an increased background, as was observed. With V_1 = 360 V and the sample channel grounded, the background fluorescence dropped well below the level observed when the sample channel was left floating (dashed line in Figure 9). The potential V_J was calculated to be 8 ± 10 V, indicating that buffer would flow into the sample channel during the separation or the sample would be held stagnant at the intersection, either way preventing leakage of the dye. The decrease in background in Figure 9 confirms that the flow in the sample channel was either stagnant or reversed. The longer injection times required as the separation potential V_1 was increased to 360 V indicate a need to compensate for backflow into the sample channel during separation and demonstrate that sample flow was reversed.

Figure 10 shows the intensity of background fluorescence during separation as a function of the buffer potential. About 350 V was required on the buffer reservoir to prevent leakage from the side channel. This compares favorably with the value of 334 ± 14 V that is predicted to be needed to stop flow from the sample channel, given the measured channel resistances. The slight discrepancy between these numbers is most likely experimental error, although it may reflect any additional voltage required to reduce leakage from the side channel that arises from the effects of diffusion and the viscous drag caused by flow in the main channel.

For the scheme described above and shown in Figure 9, leakage from the injection waste channel, i.e., from reservoir D, could still occur. The length of the waste channel (20.3 mm) relative to the sample (1.6 mm) and buffer (3.1 mm) channels meant it had a comparatively high resistance to flow. Consequently, leakage from the injection waste channel was expected to be much smaller than that from the sample channel. The low background levels achieved show that this was the case, further confirming that the resistance of a channel to flow is a significant design parameter in controlling leakage effects. However, the data also show that applied potentials can be used to actively control leakage and that the values required can be predicted quantitatively from a simple impedance network.

CONCLUSIONS

These experiments show that simultaneous control of the potential of multiple channels in a manifold is possible. The channels behave as resistors in terms of their electrical characteristics, so the potential at any point within a channel can be estimated by application of Kirchhoff's rules if the channel geometries are known and the solution resistivity is the same in all channels or the resistivities are known. This makes it possible to predict the direction and magnitude of solvent flow at intersections. The applied voltages can be used to control the flow, so that a truly valveless fluidic control system can be achieved. The demonstration of sample dilution presented here shows that the addition of reagents for pH adjustment, derivatization, complexation or masking of interferences, as would be performed in flow injection analysis, can be achieved within a chip.

The behavior of flow within a manifold can be qualitatively understood. The images clearly show that both hydrodynamic and diffusional effects contribute to mixing and leakage at intersections. However, not all of the behavior is completely understood, and it will be necessary to develop a more quantitative description of the influence of the resistance to flow of intersecting channels on phenomena such as leakage or mixing at intersections. Qualitatively, when a short side channel feeds into a long main channel, there will be a relatively high induced flow from the side channel when flow is present in the main channel. When the intersecting channels have similar flow resistances, the hydrodynamically induced leakage will be substantially reduced. These results and the ability to image the flow processes in situ will aid greatly in the design of channel manifolds.

ACKNOWLEDGMENT

We thank the Natural Sciences and Engineering Research Council of Canada and Ciba-Geigy, Basel, Switzerland, for support of this research. We thank the Alberta Microelectronic Centre (AMC) for use of their facilities and assistance in device fabrication. Z. F. thanks AMC for a graduate stipend.

Received for review November 11, 1993. Accepted June 17, 1994.®

® Abstract published in *Advance ACS Abstracts*, August 1, 1994.

Anal. Chem. **1994,** *66,* 3492–3499

Interpretation of the Retention Mechanism of Transition-Metal Cations in Ion Interaction Chromatography

Sergio Zappoli* and Chiara Bottura

Dipartimento di Chimica Industriale, University of Bologna, Viale Risorgimento 4, 40136 Bologna, Italy

A retention model is proposed for the prediction of the retention factors of metals eluted on a reversed-phase column, using an eluent containing an organic acid and an alkanesulfonate. The prediction equation offers both a qualitative and a quantitative description of the retention behavior of metals in such conditions. Metals are eluted primarily by the action of an alkali cation which exerts a "pushing" action on the analyte. The cation exchange, which governs the action of the alkali cation, occurs at the anionic sites of the alkanesulfonate adsorbed on the stationary phase. The number of sites is regulated by the amount of alkanesulfonate adsorbed, which, in turn, depends on the ionic strength of the eluent. The organic acid permits the chromatographic resolution of the metals, accelerating the rate of elution by the formation of neutral complexes which subtract the metal from the primary ionic exchange equilibrium. The application of the model and its prediction ability are discussed.

In recent years, the application of chromatographic techniques for the determination of metals has been greatly increased. Robards et al.[1] have summarized and discussed several kinds of analytical strategies for separating and detecting metal ions by liquid chromatography.

Among the analytical approaches used to determine metals and rare earths in liquid chromatography, the ones entailing an anionic surfactant as ion interaction reagent (IIR) and a weak organic ligand are proving particularly effective[2-6] for the direct separation of metals cations on reversed-phase (RP) chromatographic supports. In these techniques, the separation is achieved by establishing secondary chemical equilibria (SCE), such as complex and ion-pair formation, which modify the partition of the analyte between the stationary and the mobile phases. The advantage of SCE chromatography lies mainly in the easy control of the retention by direct modification of the eluent composition.

The use of anionic surfactants for the separation of metals and rare earths was firstly proposed by Cassidy et al.[7] Metals were chromatographated both on reversed-phase columns permanently coated with long-chain alkyl sulfates (C_{20}) and on reversed-phase columns dyamically coated with short chain alkyl- and alkanesulfonates (C_6, C_8, and C_{12}). Cassidy and co-workers subsequently developed theoretical treatments in order to explain the retention behavior of analytes. They adopted the use of a relative ion-exchange constant ($K_{IEX,R}$) to evaluate of the relative changes in selectivity for a given set of eluent conditions. It is important to note that this constant depends on the retention factor (k) and on the capacity of the stationary phase.[8] The authors found that the $K_{IEX,R}$ for inorganic analytes does not remain constant and is affected by IIR loading and ionic strength.

Recently Stulik et al.[9] proposed a retention mechanism for alkaline earths and some heavy metals eluted on a C-18 column permanently coated with sodium dodecyl sulfate and a mobile phase containing Cu^{2+} or Ce^{3+}. They suggested that retention is governed mainly by an ion-exchange mechanism, although side reactions of complexation can accelerate the elution. Secondary chemical equilibria were used by Sevenich and Fritz[10] to separate heavy metals on a low-capacity cation-exchange column. In their experiments, the eluent was a solution of tartaric acid and ethylenediamine at pH 3.5–4.0. The authors postulated that the mechanism governing the elution is the combination of a "pushing" effect of the cationic species and a "pulling" effect of the ligand.

Increasing the surfactant IIR concentration above the critical micelle concentration (cmc) leads into the field of micellar chromatography, where micelles act as a new phase added to the chromatographic system. Okada[11-13] extensively investigated the micellar chromatography of inorganic anions and cations, developing, on the basis of a previous paper by Armstrong and Nome,[14] an interesting model for partitioning of metals in such system. In the presence of micelles in the mobile phase, retention is controlled by two partition coefficients for the analyte between (i) the bulk mobile phase and the micelle and (ii) the bulk mobile phase and the stationary phase. The resulting equations permit a good prediction of retention times over the pH range and an optimization of elution conditions.

The main purposes of the present paper were (i) to investigate the retention behavior of heavy metals in reversed-phase liquid chromatography, using octanesulfonate as IIR at a concentration far below the cmc and a mild organic complexing agent, and (ii) to propose a mathematical relationship to predict the retention factors of heavy metals under different elution conditions.

(1) Robards, K.; Starr, P.; Patsalides, E. *Analyst* **1991**, *116*, 1247–1273.
(2) Barkley, D. J.; Blanchette M.; Cassidy, R. M.; Elchuk, S. *Anal. Chem.* **1986**, *58*, 2222–2226.
(3) Adachi, M.; Oguma, K.; Kuroda, R. *Chromatographia* **1990**, *29*, 579–582.
(4) Schuster, G; Hampel, W. A. *Anal. Chim. Acta* **1992**, *258*, 275–280.
(5) Sarasawaty, R.; Desikan, N. R.; Athavale, S. V.; Rao, T. H. *Anal. Chim. Acta* **1990**, *237*, 325–328.
(6) O'Dea, P.; Shearan, P.; Dunne, S.; Smyth, M. R. *Analyst* **1988**, *113*, 1791–1794.
(7) Cassidy, R. M.; Elchuk, S. *Anal. Chem.* **1982**, *54*, 1558–1583.
(8) Bailey, R.; Cassidy, R. M. *J. Chromatogr.* **1991**, *546*, 17–25.
(9) Janos, P.; Stulik, K.; Pacakova, V. *Talanta* **1992**, *39*, 29–34.
(10) Sevenich, G. J.; Fritz, J.. S. *Anal. Chem.* **1983**, *55*, 12–16.
(11) Okada, T. *Anal. Chem.* **1988**, *60*, 1511–1516.
(12) Okada, T. *Anal. Chem.* **1988**, *60*, 2116–2119.
(13) Okada, T. *Anal. Chem.* **1992**, *54*, 589–594.
(14) Armsrong, D. W.; Nome F. *Anal. Chem.* **1991**, *53*, 1662–1666.

0003-2700/94/0366-3492$04.50/0
© 1994 American Chemical Society

EXPERIMENTAL SECTION

Apparatus. The HPLC system consisted of an isocratic pump (Waters Model 501), a Rheodyne injector valve (Model 7125 metal free), and a variable-wavelength absorbance detector (Waters Model 484). The detector signal was monitored at 510 nm and the raw chromatographic data were acquired and analyzed with a computer program (Maxima 820, Dynamic Solution). The eluted metal ions were detected with a postcolumn derivatization system (Waters Delivery System Module). The postcolumn reagent was a solution of 4-(2-pyridylazo)resorcinol (PAR), 2×10^{-4} M, prepared according to the literature.[7] The PAR and the eluent flow were kept at the same value of 1 mL/min. The chromatographic column was kept at constant temperature with a glass water jacket connected to a thermostat (Haake). All the experiments were performed at 30 °C. Breakthrough experiments were performed by connecting the column end to a conductivity detector Waters Model 431 and recording the signal with a pen recorder AMEL Model 868 (Milan).

Reagents and Materials. All chemical used were of analytical grade purity from Aldrich Chemical (Milwaukee, WI). All standard metal solutions were prepared from atomic absorption standard solution 1000 ppm (Titrisol, Merck). All solutions were prepared with water purified with a Milli-Q apparatus (Waters). Eluents were prepared by dissolving the appropriate amount of reagents in water, adjusting the pH with NaOH if necessary, and filtering through a 0.22-μm filter. The reversed-phase used was 5-μm silica-based Spherisorb RP-C18 (HPLC Technology). The concentration of octanesulfonate in the eluent was maintained at 2 mmol/L in all the chromatographic runs.

THEORETICAL BACKGROUND

To describe the retention behavior of metals in our system, we followed the basic approach proposed by Sevenich and Fritz[10] and by Okada.[13]

Firstly, the chromatographic ability to separate metals is due to the adsorption of the IIR on the stationary RP-C18 phase:

$$O_w + R \rightleftharpoons OS_sR \qquad (1)$$

where OS is the IIR adsorbing on the stationary phase, R represents the stationary phase, and subscripts s and w indicate stationary and mobile phases, respectively; the amount of IIR adsorbed provides a value for the exchange capacity.

This dynamic modification of the stationary phase[7] allows the subsequent ionic exchange equilibrium to take place:

$$Na_yOS_sR + M_w^{y+} \rightleftharpoons yNa_w^{+} + MOS_sR \qquad (2)$$

which is governed by the ionic exchange constant K_{IE},

$$K_{IE} = [Na_w^{+}]^y[MOS_sR]/[M_w^{y+}][Na_yOS_sR] \qquad (3)$$

where $[Na_w^{+}]$ represents the concentration of the exchanged alkaline cation, typically the counterion of the surfactant or of the strong base added to reach the desired pH. The number of cations, y, involved in the equilibria has been left indeterminate because, in our approach, this value can be experimentally determined. From the same reasoning, the metal species actually exchanging (M^{y+}) remains indeterminate in the equation and can be defined only after collection of chromatographic data. In addition, given the relative complexity of the system, it is useful not to make any a priori assumption about the kind of compounds actually participating in the equilibrium described by eq 2 and to consider the term y as the average number of exchanged charges.[15]

The main equilibria established between the metal and the ligands present in the eluent are

$$M^{2+} + L^{2-} \overset{\beta_L}{\rightleftharpoons} ML \qquad \beta_L = [ML]/[M^{2+}][L^{2-}] \qquad (4)$$

$$M^{2+} + HL^{-} \overset{\beta_{HL}}{\rightleftharpoons} MHL^{+} \qquad \beta_{HL} = [MHL]/[M^{2+}][HL^{-}] \qquad (5)$$

where β_L and β_{HL} are the complex formation constants as tabulated by Martell.[16]

Finally, one must consider the dissociation of the acidic ligand as described by the two equilibria:

$$H_2L \overset{K_1}{\rightleftharpoons} HL^{-} + H^{+} \qquad K_1 = [HL^{-}][H^{+}]/[H_2L] \qquad (6)$$

$$HL^{-} \overset{K_2}{\rightleftharpoons} L^{2-} + H^{+} \qquad K_2 = [L^{2-}][H^{+}]/[HL^{-}] \qquad (7)$$

where K_1 and K_2 are the acidic dissociation constants of the ligand.

In the ionic exchange equilibrium (eq 2), one must take into account that the free metal is subtracted from the equilibrium by binding with the ligand (eqs 4 and 5). Therefore, it is necessary to introduce a term for the masking effect due to secondary equilibria between the metal ion and the ligands. An easy way to do this is to express the concentration of the metal ion using the side reaction coefficient, α_M:

$$\alpha_M = \frac{[M^{y+}]}{C_M} = \frac{1}{1 + \beta_{HL}[HL^{-}] + \beta_L[L^{2-}]} \qquad (8)$$

where C_M is the total concentration of the metal in the mobile phase.

Substituting the value of $[M^{y+}]$ in eq 3 and considering $[NaOS_sR]$ equal to the concentration of IIR adsorbed on the stationary phase ($[OS_sR]$), one has

$$K_{IE} = \frac{[Na_w^{+}]^y}{[OS_sR]^y} \frac{1 + \beta_{HL}[HL^{-}] + \beta_L[L^{2-}]}{C_M} [MOS_sR] \qquad (9)$$

In this expression, the term $[MOS_sR]/C_M$ can be seen as a partition factor (K) for the metal (M) between the stationary and the mobile phases. Strictly speaking, the term $[MOS_sR]/C_M$ is a conditional partition coefficient, given that the term

(15) Karcher, B. D.; Krull, I. S. In *Trace Metal Analysis and Speciation*; Krull, I. S., Ed.; Elsevier: Amsterdam, 1991; p 123.
(16) Martell, A. E. *Critical Stability Constants. Vol. 3. Other Organic Ligands*; Plenum Press: New York, 1977.

C_M comprises all the possible forms in which M could be present in solution, in addition to the free ion. It is possible to write the retention factor, k, as the product of the partition coefficient ($[MOS_sR]/C_M$) and the phase ratio Φ. Substituting $\Phi[MOS_sR]/C_M$ for k in eq 9 and converting to the logarithmic form, one obtains

$$\log k = \log(K_{IE}/\Phi) + y \log [OS_sR] - y \log [Na^+] - \log\{1 + \beta_{HL}[HL^-] + \beta_L[L^{2-}]\} \quad (10)$$

It is possible to simplify eq 10 by using equilibria 6 and 7, expressing $[HL^-]$ and $[L^{2-}]$ in term of the ionization fraction values α_1 and α_2, and including Φ in the K_{IE} term. The following equation is obtained:

$$\log k = \log K_{IE} + y \log [OS_sR] - y \log [Na^+] - \log\{1 + (\beta_{HL}[H^+]/K_2 + \beta_L)\alpha_2 C_{HT}\} \quad (11)$$

where C_{HT} is the analytical concentration of the complexing agent present in the eluent solution. The fourth term on the right side of eq 11 represents the effect of a complexing agent on the retention of a metal and can be considered as a masking factor. This factor should include the β constants for all possible side reactions. As it will be shown below, with a weak complexing agent, such as tartaric acid, at relatively high concentration in the eluent, the masking factor is due mainly to this organic ligand. However, if the concentration of the main ligand decreases below a certain value, the effect of other complexing agents, e.g., the anion of an added salt, could become relevant. Moreover, complexing with HL^- is not common;[16] therefore, for the precision required in our final model, the term, which depends on β_{HL}, will be ignored.

From eq 11 it is possible to predict the general behavior of the retention factors on the basis of the variation of the various analytical parameters. In particular, it is possible to identify two variables that increase the retention time: the concentration of octanesulfonate in the stationary phase and the value of the exchange constant K_{IE}. It is also possible to identify two variables that exert the opposite effect of reducing the retention time: the alkaline ion concentration and the masking factor.

Equation 11 is formally consistent with the models describing retention mechanisms proposed for ion-exchange phases[10] and for micellar chromatography.[13] Equation 11 gives a good qualitative description of the retention behavior of metals when the stationary phase is dynamically modified with an IIR. Nevertheless, when eq 11 is applied for the prediction of metal retention factors (k) under a large range of ionic strength values, some inaccuracy arises, due to the fact that the value of $[OS_sR]$ is a function of eluent composition and cannot be considered a constant. In particular, we observed an effect of salt concentration on the amount of IIR adsorbed on the stationary phase. At present, such a salt effect is not quantitatively accounted for by any theoretical equation, and, therefore, it has to be empirically defined. This observation led us to the development of a new retention model which includes an empirical relationship derived from experimental data.

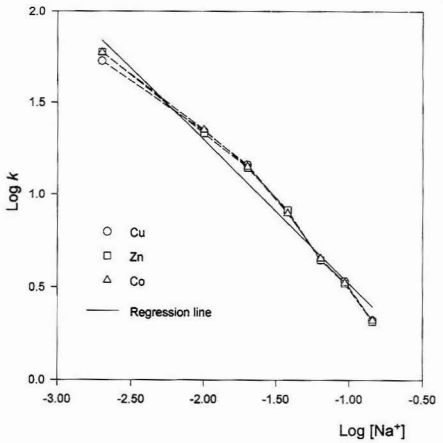

Figure 1. Logarithms of the retention factors of copper, zinc, and cobalt plotted against the logarithm of the concentration of sodium in the eluent. Eluent was 2 mM octanesulfonate in water containing various concentrations of sodium nitrate. For chromatographic conditions, see text.

RESULTS

Ionic Strength Effects. In secondary chemical equilibria chromatography the ionic concentration of the eluent plays a relevant role in the retention time of analytes. A general description of the effect of ionic strength can be found in Karger et al.[17]

We were able to identify four different phenomena related to the saline concentration of the eluent: (1) a direct effect on the rate of metal ions elution, (2) an effect of the salt cation, (3) an effect on the degree of adsorption of the IIR on the stationary phase, and (4) an effect of the different complexing strength of the salt anion. Of these we looked into only the first three.

(1) The effect of saline concentration in accelerating the elution of metals was investigated using the eluent solution at different sodium nitrate concentrations without tartaric acid. The results of this set of experiments confirm that increasing the ionic strength of the eluent causes a reduction of k. It is also possible to observe a loss of chromatographic resolution due to the absence of the ligand in the eluent. Moreover, when the logarithms of k are plotted against the logarithm of sodium concentration, it is possible to see that the linearity typical of the ion exchange mechanism is not respected (Figure 1). This fact suggests that there are other effects driving the retention process in addition to ionic exchange, such as a change in the effective capacity of the modified phase due to a variation of IIR adsorption on the stationary phase. Figure 2 shows that even a low concentration of the complexing agent ([HT] = 10 mM) causes a discrimination effect on the retention times of the various metals, which barely persist at relatively high sodium concentrations. The effect of ionic strength on metal retention was further investigated using different sodium salts. The

(17) Karger, B. L.; LePage, J. N.; Tanaka, N. In *HPLC: Advances and Perspectives*; Horvath, C., Ed.; Academic Press: New York, 1980; pp 113–208.

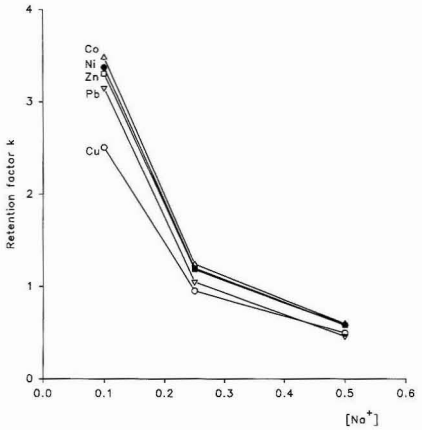

Figure 2. Dependence of the retention factors of copper, lead, zinc, nickel, and cobalt on the concentration of sodium salt in presence of 10 mM tartaric acid in the eluent.

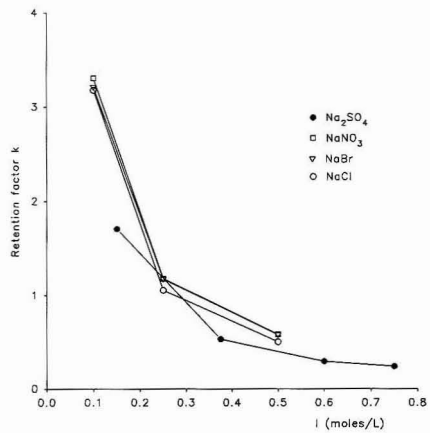

Figure 3. Dependence of the retention factor of zinc on the ionic strength of the eluent with different sodium salts.

retention behavior was similar for all the metals. Figure 3 shows the trend for zinc. Ionic strength is plotted instead of sodium concentration in order to normalize the sulfate concentration. As one can see, a salt with a stronger coordinative anion brings about a reduction on the retention time by increasing the value of the masking factor.[18]

(2) The influence of the size of alkaline cation on the retention was also studied. Chromatographic runs were carried out at salt concentration of 0.05 M, using an eluent containing octane sulfonate and tartaric acid at concentrations of 2 and 10 mM, respectively. The pH of the eluent was left at the value (around 2.50) due to the added tartaric acid. The salts used in these experiments were LiCl, NaCl, KCl, and CsCl.

(18) Martell, A. E; Smith, R. M. *Critical Stability Constants. Vol. 4. Inorganic Complexes*; Plenum Press: New York, 1976.

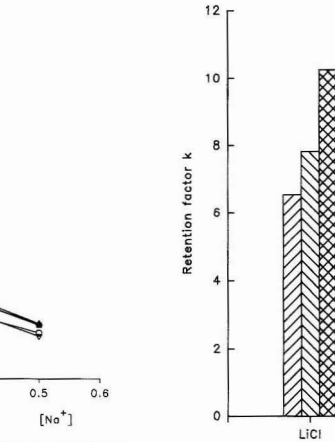

Figure 4. Effect of cation size on the retention factors of metals. Eluent composition was 2 mM octanesulfonate, 10 mM tartaric acid, and 0.5 mM chloride salt.

Table 1. Effect of Sodium Ion Concentration on the Amount of Octanesulfonate Adsorbed on the Stationary Phase (Spherisorb RP18 5 μm)[a]

[Na+], mM	corrected breakthrough volume	OS, mmol
0	22.0	0.044
0.01	37.5	0.075
0.05	59.0	0.118
0.07	66.5	0.133
0.10	73.0	0.146

[a] These values were used to calculate the parameters *a* and *b* of eq 12

In Figure 4, it is possible to observe the very strong dependence of the retention factor on the size of the cation, indicating the presence of an ion-exchange driving force in the chromatographic process. Moreover, the eluent strength follows the order Cs > K > Na > Li, which is the common selectivity order for an ionic exchange governed by the free energy of hydration of the cation.

(3) Ionic strength also has an effect on the adsorption efficiency of the IIR on the stationary phase; in particular, we observed that an increase in the saline concentration increases the amount of octanesulfonate adsorbed on the stationary phase. This phenomenon is in accord with the general surfactant's adsorption behavior,[19] with the experimental findings of Liu and Cantwell[20,21] on the adsorption of tetrabutylammonium and *p*-nitrobenzenesulfonate on a C-18 reversed-phase, and with the retention behavior of IIR on RP.[22] It is possible to simply assess the amount of surfactant adsorbed on the stationary phase by measuring the breakthrough point of 2 mM octanesulfonate solution at different sodium concentrations. The results are reported in Table 1.

(19) Rosen, M. J. *Surfactants and Interfacial Phenomena*, 2nd ed.; Wiley: New York, 1989.
(20) Liu, H.; Cantwell, F. F. *Anal. Chem.* **1991**, *63*, 993–1000.
(21) Liu, H.; Cantwell, F. F. *Anal. Chem.* **1991**, *63*, 2032–2037.
(22) Zhou, D.; Pietrzyk, J. P. *Anal. Chem.* **1992**, *64*, 1003–1008.

The amount of the adsorbed octanesulfonate was calculated by multiplying the corrected breakthrough volume (breakthrough volume minus void volume) for the concentration of octanesulfonate in the eluent (2 mM).

The amount of octanesulfonate adsorbed on the stationary phase, q_{OS}, exhibits a multiplicative dependence on sodium concentration. The fitting equation is

$$q_{OS} = 0.31[Na^+]^{0.353} \qquad (R = 0.9999) \qquad (12)$$

One therefore observes a contrasting action of added salt. On the one hand, increasing the salt concentration increases the amount of surfactant adsorbed on the stationary phase, thus improving the retention factors of metals (eq 11); on the other, it causes a shift to the left of the equilibrium exchange between cation and metal (eq 2) and, consequently, an acceleration of metals elution. The dependence on ionic strength of the degree of octanesulfonate adsorption means that assuming a constant number of exchangeable sites on the phase is valid only under the condition of constant ionic strength. Moreover, it is highly plausible that similar behavior would be observed if other parameters influencing the adsorption ability of surfactants were modified. For example, the addition of an organic modifier to the eluent solution should be effective. Therefore, the dynamic coating of the stationary phase is strongly affected by changes in the eluent solution. In other words, a modification in eluent composition is effective both in changing the rate of elution and in modulating the exchange surface characteristic.

In order to take into account the dependence of the amount of octanesulfonate adsorbed on the stationary phase on sodium concentration, eq 11 was modified:

$$\log k = \log K_{IE} + y \log\{(a[Na^+]^b)/A_s[Na^+]\} - \log\{1 + (\beta_{HL}[H^+]/K_2 + \beta_L)\alpha_2 C_{HT}\} \quad (13)$$

where A_s is the surface area of the stationary phase and a and b are coefficients that depend on both the kind of stationary phase and the IIR used. The empirical values of these coefficients for our system were $a = 0.31 \pm 0.01$ and $b = 0.353 \pm 0.003$. Omitting the term $\beta_{HL}[H^+]/K_2$ and rearranging eq 13, this final expression is obtained:

$$\log k = \gamma + y(b-1) \log [Na^+] + B \log(1 + \beta_L \alpha_2 C_{HT}) \qquad (14)$$

where

$$\gamma = \log K_{IE} + y \log(1/A_s) + y \log a \qquad (15)$$

and B is an adjustable parameter whose chemical significance will be described in the Discussion section. It is important to note that in the model that we propose (eq 14), the exchange capacity does not explicitly appear. This variable would be defined for each IIR by the two empirical parameters, a and b, and by the alkaline ion concentration.

Moreover, it turns out that all the factors defining the term γ (eq 15) are related to parameters directly governing the exchange process, namely, ionic exchange constants, total surface area, amount of surface area available for the surfactant, and number of exchangeable charges. These parameters are actually constants of the system for each IIR and establish that γ is a constant term.

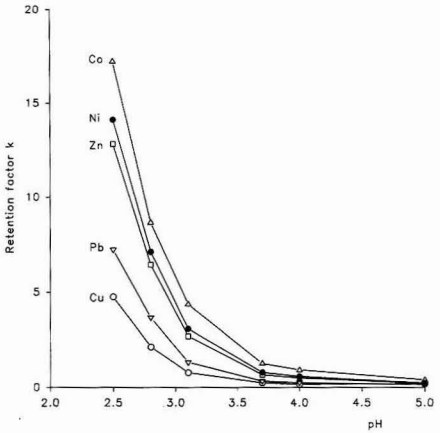

Figure 5. Dependence of the retention factors of metals on the eluent pH. Eluent composition was 2 mM octanesulfonate and 60 mM tartaric acid.

A secondary consequence of the increase in the octanesulfonate adsorption with salt concentration (or ionic strength) is the lowering of the void volume of the column. This phenomenon approximately follows the increase in ionic strength of the eluent and is undoubtedly due to the augmented fraction of stationary-phase surface covered by the IIR.

Data Collection and Model Validation. To collect data to validate eq 14, the dependence of the retention factor on the concentration of the ligand (tartaric acid) and the pH of the eluent was investigated. The experimental parameters and the retention data are available from the authors on request. The concentrations of Na^+, when added as sodium hydroxide, and of tartrate (L^{2-}) were calculated using the distribution coefficients of the acid, α_1 and α_2. The values of the acid constants were corrected for the effect of ionic strength with the Davis equation.[23] In the calculation of the total sodium ion concentration, we always took into account the contribution of the dissociation of the sodium octanesulfonate in the eluent.

As is known, the species distribution of a weak organic acid depends on the pH of the solution. Therefore, from eq 11, we should expect a reduction of retention time as the concentration of the more complexing form ($L^{2-} = \alpha_2 C_{HT}$) increases, i.e., when the pH, the C_{HT}, or both increase.

The observed retention times of the metals follow the general behavior predicted by eq 14, i.e., an increase in pH and [HT] reduces the retention time.

In Figure 5 is reported the effect of eluent pH on the retention factor at a 60 mM concentration of tartaric acid. The role of the concentration of the organic ligand in the retention behavior of metals was investigated using an eluent solution at pH 3.4, where there is a good buffer capacity. The results are shown in Figure 6.

(23) Stumm, W.; Morgan, J. J. *Aquatic Chemistry*, 2nd ed.; Wiley-Interscience: New York, 1981; p 136.

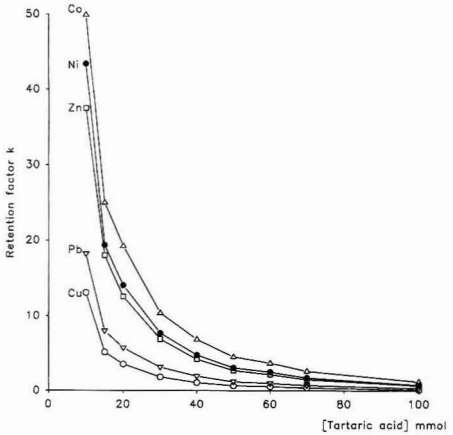

Figure 6. Dependence of the retention factors of metals on the concentration of tartaric acid in the eluent. Eluent composition was 2 mM octanesulfonate at pH 3.40.

Table 2. Calculated Parameters, γ, y, and B for Cu, Pb, Zn, Ni, and Co Obtained from the Multiple Regression Performed with Eq 14[a]

metal	γ	y	B	MAE	R_{sqa}
Cu	−0.46 ± 0.09	1.51 ± 0.06	−0.79 ± 0.03	0.07	0.982
Pb	−0.55 ± 0.09	1.42 ± 0.05	−0.66 ± 0.05	0.08	0.979
Zn	−0.60 ± 0.07	1.66 ± 0.04	−0.73 ± 0.03	0.07	0.985
Ni	−0.61 ± 0.08	1.65 ± 0.05	−1.06 ± 0.06	0.08	0.980
Co	−0.62 ± 0.08	1.72 ± 0.05	−0.80 ± 0.05	0.07	0.984

[a] The associated error for each parameter is the standard error. To calculate the confidence limits, one should multiply the standard error for the t value of 2.04. MAE is the mean absolute error, which is the average error expected in a prediction. R_{sqa} is the regression coefficient adjusted for the degrees of freedom.

By running a multiple regression analysis on the entire set of data, it was possible to calculate the best fit for the parameters of eq 14 (Table 2). Figure 7 shows the plots of the observed data against the predicted values of retention factors for the metals, attesting to a good prediction ability of our proposed retention model.

DISCUSSION

Some considerations can be made from the calculated parameters. First of all, the value of parameter y, which represents the number of charges involved in the ionic exchange, are around 1.5. This value, points out that, in our system, the metal is not completely exchanged in its bivalent form and that some exchange reaction involving a monovalent form of the metal (for example, MHL^+) is taking place.

The absolute value of parameter γ increases following the elution order. As we have shown (eq 15), parameter γ is a collection of constant terms, including the exchange constant K_{IE}. From eq 15, it is possible to see that $\log K_{IE} = \gamma/y$, if the constant term a/A_s, which is independent of the kind of metal, is ignored. One can observe that the differences in the magnitude of $\log K_{IE}$ among the different metals are not very significant, confirming that, although the exchange equilibrium

Table 3. Comparison of Experimental Values of Retention Factors with Calculated Values (in Parentheses)[a]

[HM], mM	k(Cu)	k(Pb)	k(Zn)	k(Ni)	k(Co)
5	3.7 (4.3)	68.6 (34.1)	72.9 (50.3)	60.6 (41.9)	73.2 (57.6)
10	1.1 (1.5)	31.7 (18.4)	34.9 (26.2)	28.3 (19.9)	35.4 (29.1)
15	0.6 (0.7)	17.5 (12.0)	20.3 (16.7)	14.9 (11.7)	20.8 (18.2)
20	0.4 (0.5)	9.8 (8.6)	13.3 (11.7)	8.7 (7.6)	13.7 (12.5)
30	0.2 (0.2)	5.1 (5.1)	6.7 (6.8)	4.4 (3.9)	6.8 (7.1)
40	0.2 (0.1)	3.8 (3.4)	5.0 (4.5)	3.3 (2.3)	5.2 (4.5)
50	0.2 (0.1)	2.7 (2.5)	3.6 (3.1)	2.3 (1.5)	3.6 (3.1)
60	0.2 (0.06)	2.0 (1.9)	2.6 (2.3)	1.7 (1.0)	2.7 (2.3)
70	0.2 (0.04)	1.6 (1.5)	2.1 (1.8)	1.4 (0.7)	2.2 (1.7)

[a] Eluent containing malonic acid (HM) at pH 3.97 and octanesulfonate, 2 mM.

is the driving force of the chromatographic process, it is not able to discriminate among the different eluting species. It is important to note that the term γ, hence the K_{IE} value, actually remains constant, independent of the eluent conditions. This is an effect of substituting of the capacity of the phase with its sodium-dependent function (eq 12). If the exchange capacity of the derivatized stationary phase is considered constant and then included in the term γ, a shift in the value of K_{IE} would be observed, resulting in a failure of the model to fit the experimental data, more evident at high sodium concentrations.

The expected value of parameter B should be close to 1, given that no multiplicative coefficient is involved in the model. It must be observed that the masking factor includes all the secondary chemical equilibria which the metal may undergo during the chromatographic process. Therefore, the parameter B accounts for a number of equilibria which cannot be explicitly expressed or which are difficult to quantitize, such as the complexation with HL^-. Moreover, parameter B includes all possible effects that may influence the value of the complexation constants (ionic strength, surfactant concentration, etc.). A value less than 1 of B means that some reduction in the expected efficiency of complexing agent has taken place. This is the case for all the metals except nickel. A better understanding of the variation of parameter B needs further investigation. A closer look at values of k obtained from eq 14 demonstrates that a lack of fit appears mainly at low pH and at low HT concentrations. This is probably due to the difficulties in estimating a reliable value of the sodium ion concentration in the mobile phase, the value being dependent on the amount of octanesulfonate adsorbed on the stationary phase. In fact, the assumption that all the sodium ions are able to interact freely in the mobile phase is a rough approximation that is valid only when sodium added to the eluent solution reaches a certain value (approximately 0.02/0.03 M). This approximation does not hold when the concentration of sodium in the mobile phase is close to the concentration of octanesulfonate, because a relevant part of the sodium is fixed to the surfactant, showing a minor exchange ability. In other words, the system acts as if it were of a lower sodium concentration than the calculated one. A more precise evaluation of the effect of the IIR counterion at low counterion concentrations is in progress.

Application of the Model. The calculated parameters (Table 2) were used to predict the retention times of metals eluted using malonic acid instead of tartaric acid. The only

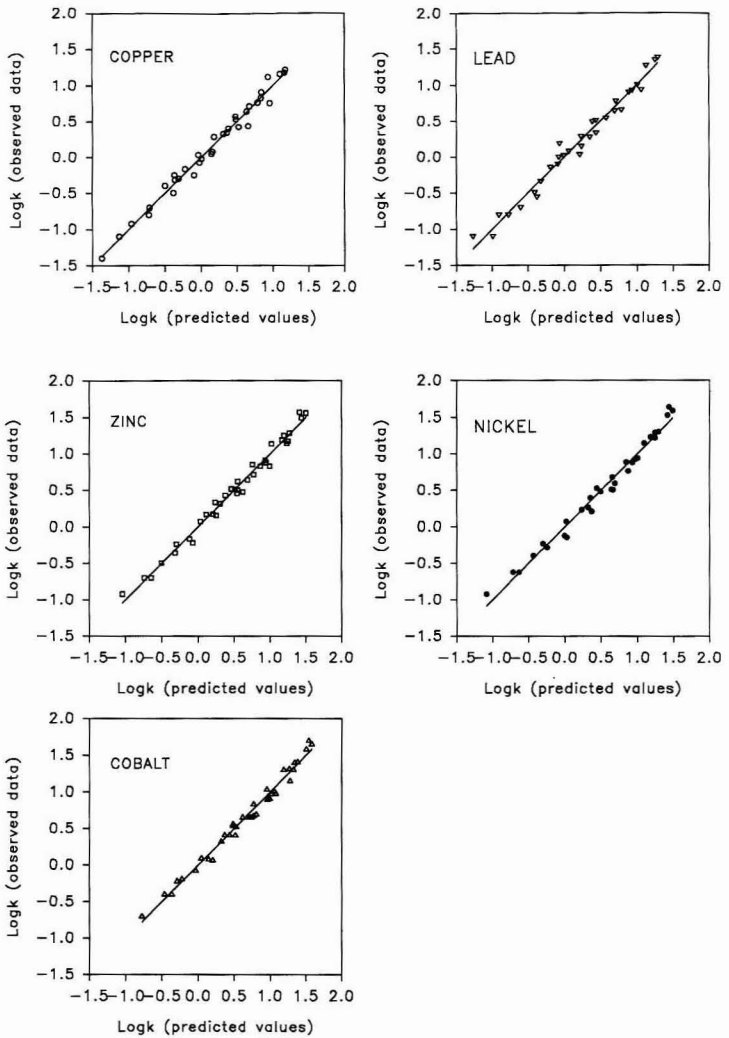

Figure 7. Relationship between the predicted and observed log k of the investigated metals. Predicted values were calculated using the parameters of Table 2.

difference in the system was due to the different complexing ability of malonic acid with respect to the tartaric acid, which produces a completely different elution pattern (Figure 8).

The retention factors of the metals obtained at pH 3.97, with an eluent containing octanesulfonate (2 mM) and a concentration of malonic acid ranging from 5 to 70 mM, are reported in Table 3 and are compared to the retention factors calculated from eq 14. The agreement between calculated and experimentally measured retention factors is not the same for all the investigated metals but is fairly good, considering the completely different elution order of metals when malonic acid is used. As already remarked above, at low sodium concentrations it is possible to observe a severe lack of fit, which confirms the difficulty in estimating the amount of sodium actually participating in the ionic exchange. Another factor that could reduce the goodness of the fit is parameter B. The magnitude of this parameter is related to the coordinative ability of the ligand, which, in turn, is affected by the composition of the eluent solution. It is possible that B differs slightly for different ligands used and that this difference could alter the prediction of the retention factor. In any case, the model gives good predictions for retention times in the range 20–50 mM of malonic acid concentrations, which is the usual working condition.

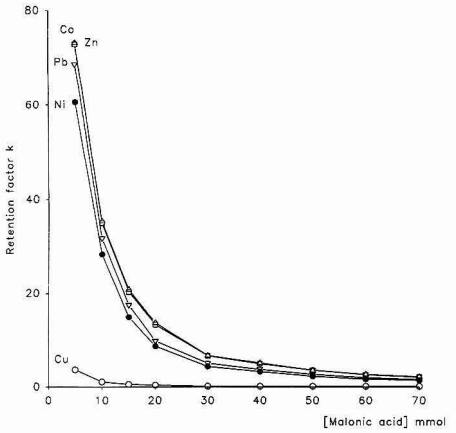

Figure 8. Dependence of the retention factors of metals on the concentration of malonic acid in the eluent. Eluent composition was 2 mM octanesulfonate at pH 3.97.

CONCLUSION

The model proposed with eq 14 contributes to an understanding of the mechanisms acting in the retention of charged species in ion interaction chromatography.

From the model and the data obtained, it was possible to describe the mechanisms governing the retention of metals in ion interaction chromatography. The elution of the metals is brought about by the primary "pushing" action on the analyte exerted by an alkali cation, usually the surfactant counterion. The role of the organic ligand is to control the chromatographic resolution of the metals, modifying the rate of elution through the formation of neutral complexes, which subtract the metal from the primary ionic exchange equilibria. Cation exchange governing the action of the alkali cation occurs on the anionic sites of the alkanesulfonate adsorbed on the stationary phase. The number of sites on the stationary phase depends on the amount of alkanesulfonate adsorbed, whose logarithm depends linearly on the logarithm of the ionic strength of the eluent (or sodium concentration if one uses a 1:1 salt). This relationship allows one both to evaluate the number of sites for each ionic strength of the eluent and to obtain stable values for the ionic exchange constants, K_{IE}, at the different elution conditions used. From eq 14, it is also possible to obtain satisfactory predictions of retention factors in a wide range of elution conditions and using different organic ligands.

ACKNOWLEDGMENT

The authors wish to thank Prof. Pietro Lanza, Dr. Carlo Tomba, and Simonetta Tunesi, Ph.D., for their comments to the paper. This work was supported, in part, by the Progetto Strategico Metalli Pesanti nelle Deposizioni Meteoriche-CNR.

Received for review February 4, 1994. Accepted June 30, 1994.[⊕]

[⊕] Abstract published in *Advance ACS Abstracts,* August 1, 1994.

Correspondence

Anal. Chem. **1994,** *66,* 3500–3502

Subfemtomole Detection of Catecholamine with Interdigitated Array Carbon Microelectrodes in HPLC

Hisao Tabei,*,† Masaya Takahashi,‡ Satoshi Hoshino,†,§ Osamu Niwa,†,§ and Tsutomu Horiuchi†,§

NTT Basic Research Laboratories, Nippon Telegraph and Telephone Corporation, Tokai, Ibaraki 319-11, Japan, and NTT Interdisciplinary Research Laboratories, Nippon Telegraph and Telephone Corporation, Musashino, Tokyo 180, Japan

An IDA carbon microelectrode for HPLC was fabricated by photolithographic techniques from the carbon film of pyrolyzed 3,4,9,10-perylenetetracarboxylic dianhydride on thermally oxidized silicon wafers. The IDA electrode consisted of 300 pairs, the finger widths and gaps were 5 μm, and each finger was 2 mm long. The electrode in a small-volume thin-layer cell incorporated in a microbore HPLC system achieved a low detection limit for dopamine due to current enhancement by redox cycling and low background noise at the carbon IDA microelectrode. The detection limit of 0.5 fmol of dopamine can be realized because of the low noise level and high current density.

Microbore high-performance liquid chromatography (HPLC) has received much attention because a small volume sample can be analyzed and the low dispersion in the column increases the sensitivity.[1–4] These characteristics make it suitable for the analysis of trace solutes in a sample which is usually determined by microdialysis in neurotransmitter research. In this situation, an electrochemical detector is expected to play an important role with regard to high sensitivity. A microelectrode array is a good candidate for the electrode in a flow-cell detector, and carbon microelectrodes are especially well suited for measurement because of their high signal-to-noise ratio and high current density. These characteristics have already been reported for random and linear arrays of carbon microelectrodes in flowing streams.[5,6]

A metal film-based interdigitated array (IDA) microelectrode has been shown to be a highly sensitive electrochemical detector in HPLC due to a high mass-transfer flux resulting from redox cycling at the IDA.[7] With IDA electrodes, a product generated at one band electrode collects at one of the adjacent band electrodes and reverts to its initial state when the potential of the adjacent band electrode is sufficient for the reverse reaction. Then, having reverted to its initial state, the species collects again at the first electrode. As this redox cycle repeats, the currents of both the anodic and cathodic electrodes are increased.[8,9] However, current enhancement by redox cycling is less effective in a flow stream than in a stationary solution. This is because a rapid flow stream interferes with the redox cycling.

Microbore columns are frequently used for biological analysis because very small samples must be analyzed. The combination of a microbore column and an IDA carbon microelectrode is expected to improve sensitivity because an HPLC system with a microbore column operates at a slower flow rate than one with an ordinary size column. In addition, an IDA carbon microelectrode is expected to have an excellent signal-to-noise ratio since it has a wider potential window and larger overpotential[9,10] for oxygen reduction and hydrogen evolution than previously reported metal-based IDAs.[11]

In this paper, we demonstrate the high current response of catecholamine measured with an IDA carbon microelectrode incorporated in a microbore HPLC system and the subfemtomole detection of dopamine.

EXPERIMENTAL SECTION

IDA Carbon Microelectrode Fabrication. The IDA carbon microelectrode was fabricated by photolithographic techniques from the carbon film of pyrolyzed 3,4,9,10-perylenetetracarboxylic dianhydride on thermally oxidized silicon wafers as reported previously.[9,10] The IDA electrode consisted of 300 pairs, the finger widths and gaps were 5 μm and each finger was 2 mm long. A carbon IDA was used without pretreatment, since the peak separation of catecholamine is even smaller than that at a well-polished GC electrode. This is because the plasma reactive etching method applied at the

† NTT Basic Research Laboratories.
‡ NTT Interdisciplinary Research Laboratories.
§ Present address: NTT Basic Research Laboratories, Morinosato Wakamiya, Atsugi, Kanagawa 243-01. Japan.

(1) Goto, M.; Nakamura, T.; Ishii, D. *J. Chromatogr.* **1981**, *226*, 33.
(2) Durkin, T. A.; Caliguri, E. J.; Mefford, I. N.; Lake, D. M.; Macdonald, I. A.; Sundstrom, E.; Jonsson, G. *Life Science* **1985**, *37*, 1803.
(3) Kendrick, K. M. *Curr. Sep.* **1990**, 9, 136.
(4) Cheng, F. C.; Kuo, J. S.; Shin, Y.; Lai, J. S.; Ni, D. R.; Chia, L. G. *J. Chromatogr., Biomed. Appl.* **1993**, *615*, 225.
(5) Magee, L. J., Jr.; Osteryoung, J. *Anal. Chem.* **1989**, *61*, 2124.
(6) Wang, J.; Brennsteiner, A.; Sylwester, A. P. *Anal. Chem.* **1990**, 62.
(7) Takahashi, M.; Morita, M.; Niwa, O.; Tabei, H. *J. Electroanal. Chem.* **1992**, *335*, 253.
(8) Aoki, K.; Morita, M.; Niwa, O.; Tabei, H. *J. Electroanal. Chem.* **1988**, *256*, 269.
(9) Tabei, H.; Morita, M.; Niwa, O.; Horiuchi, T. *J. Electroanal. Chem.* **1992**, *334*, 25.
(10) Niwa, O.; Tabei, H. *Anal. Chem.* **1994**, 66, 285.
(11) Niwa, O.; Morita, M.; Tabei, H. *Anal. Chem.* **1990**, 62, 447.

0003-2700/94/0366-3500$04.50/0
© 1994 American Chemical Society

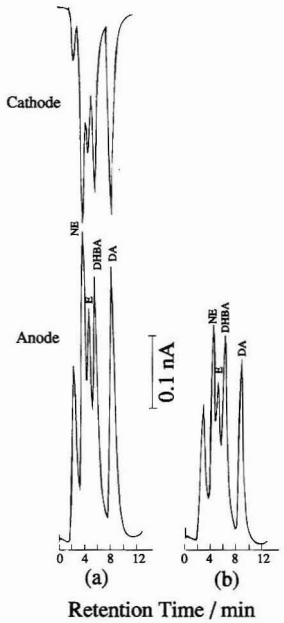

Figure 1. Typical chromatograms of catecholamine measured with the IDA carbon microelectrode: (a) dual mode and (b) single mode. The cell thickness is 12 μm, volume flow rate is 0.05 mL/min, and injection volume is 5 μL.

end of the fabrication process may remove surface contamination.

Reagents. A standard catecholamine solution was obtained from Katayama Chemical Industry (Osaka). It contained 10 mM each of epinephrine (E), norepinephrine (NE), dopamine (DA), and L-dopa. An internal standard solution was also obtained from Katayama Chemical Industry, which contained 10 mM of dihydroxybenzylamine (DHBA). These reagents were used as received. The mobile phase consisted of 0.85 M sodium acetate, 0.09 M tartaric acid, 0.5 mM ethylenediaminetetraacetic acid disodium salt, 0.8 mM 1-octanesulfonic acid sodium salt, and 5.5% acetonitrile.

Apparatus and Procedure. The liquid chromatography system used to characterize this electrode consisted of an 880-PU pump (Japan Spectroscopic Co., Tokyo) and a CC-4 HPLC system incorporating an LC-4B amperometric detector from Bio Analytical Systems (BAS), West Lafayette, IN. The thickness of the cell channel was 12 μm, and a 100-mm × 1-mm (i.d.) SepStick reversed-phase column (BAS) was employed. The column was kept at 30 °C using a BAS LC-22A system. To obtain the amperometric response for catecholamine, the potential of the anodic array of the IDA electrode was held at +0.6 V vs Ag/AgCl and that of the cathodic array was held at –0.005 V.

RESULTS AND DISCUSSION

Figure 1 shows typical chromatograms of catecholamine measured with an IDA carbon microelectrode in which both

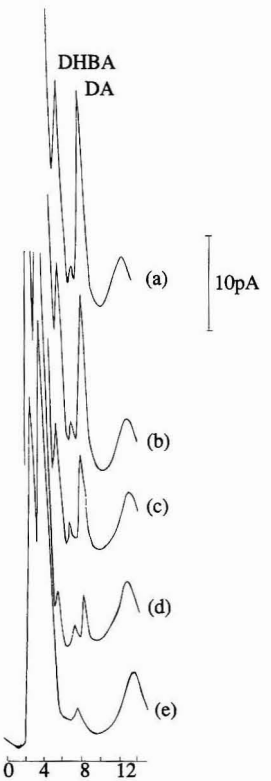

Figure 2. Anodic chromatograms of low-concentration samples in a dual mode: (a) 3.5 fmol (700 pM), (b) 2.5 fmol (500 pM), (c) 1.5 fmol (300 pM), (d) 0.5 fmol (100 pM), and (e) background chromatogram for mobile phase.

the anodic and cathodic arrays are potentiostated (dual mode). The injected sample was a 5-μL solution which contained 10 nM of catecholamine and DHBA. The flow rate was 0.05 mL/min. A large front peak, generated by the sample solution used as the mobile phase, was observed at retention times of 2.5 and 3.5 min. In addition, gentle background noise peaks generated by the solvent were observed at about 7 and 14 min (shown in Figure 2). The L-dopa peak cannot be distinguished because it overlaps the front peak observed at about 2.5 min.

The collection efficiency which is defined as the ratio of cathodic to anodic current at the IDA increases when the redox cycling number increases.[11] As a result, a higher peak current is expected through the use of the IDA electrode. The collection efficiency was 70% for DA in HPLC. However, the collection efficiency for E was 60% which was lower than that of other analytes. Since E is not stable after electrochemical oxidation and changed to the indole form as a result of the cyclization reaction, some of the E molecules may be chemically changed before reaching the cathode array

electrode after electrochemical oxidation.[12]

The collection efficiency of aq-ferrocene is more than 90%[11] and that of dopamine is at least 80%[13] in a stationary solution. These values are greater than that in a flow cell, suggesting that the flow stream reduces the collection efficiency. In our flow-cell experiment we used an IDA which had a 5-μm band width and gap. The above values are higher than those obtained in this work. This lower collection efficiency is due to the flowing stream and may also be due to the fact that part of the product at one band electrode is collected not only by the adjacent band electrodes but also by the auxiliary electrode which faces the IDA electrode in a cell with a narrow gap. Although the value of 70% is not as high as anticipated, it can be expected that redox cycling will increase the peak current. The peaks of chromatogram (b) were measured with the same IDA in which only the anodic array was potentiostated (single mode). As expected, the dual mode chromatogram exhibits a higher current peak than in the single mode. These high current values are due to the redox cycling of analytes at the anode and cathode electrode arrays in a flowing stream. However, the current peak in the dual mode was only 1.4 times higher than that in the single mode. It is considered that redox cycling occurred effectively between the anodic array and the auxiliary electrode even in the single mode because the thickness of the cell channel was 12 μm, which is not very different from the IDA gap of 5 μm. The current density of the single mode must be higher than that in an ordinary flow-cell detector with a thick channel because the current peaks in the single mode are already enhanced by redox cycling between the anode and the auxiliary electrode. Similar phenomena have also been reported for the microtip electrode of a scanning electrochemical microscope and in a voltammetric measurement using a narrow gap micro–macro twin electrode in a stationary solution.[14,15] Therefore, the amplification factor which is the ratio of the peak current measured in the dual mode to that measured in the single mode is not very high.

The peak current density corresponding to 100 nM DA, which was 12 nA/cm^2, was measured with a commercially available glassy carbon (GC) disk electrode for a 12-μm-thick cell in the single mode.[16] On the other hand, the current density of the DA at the carbon based IDA was 9 times higher than that at the GC electrode, and we could obtain a larger peak current than with the GC electrode.

Figure 2 shows anodic chromatograms of catecholamine and DHBA obtained using an IDA electrode operating in a dual mode for low concentration samples. A chromatogram without a catecholamine sample is also illustrated in Figure 2. The injected moles are (a) 0.5 fmol (100 pM), (b) 1.5 fmol (300 pM), (c) 2.5 fmol (500 pM), (d) 3.5 fmol (700 pM), and (e) 0 fmol (injected only mobile phase solution). Although L-dopa, NE, and E are also included in the injected sample, their peaks overlap the front peaks in this low concentration range. In contrast, the current peaks of DA and DHBA can be distinguished from baseline noise in such a low concentration sample. Although the noise peak generated by the injected sample solution appears at 7 min between the DHBA and DA peaks, both peaks can be distinguished even in the 0.5 fmol (100 pM) sample, and they are proportional to the sample concentration. The noise level of the GC detector was 6 pA,[7] whereas the noise level observed using the IDA carbon microelectrode was less than 1 pA which is a little lower than that of an ordinary GC disk electrode.

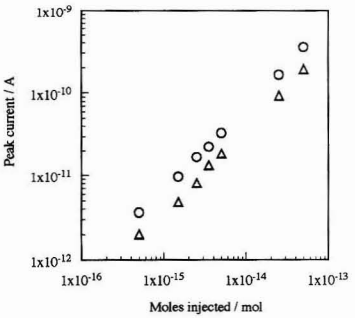

Figure 3. Calibration curves for dopamine and dihydoxybenzylamine measured with the IDA electrode: (○) dopamine; (△) dihydroxybenzylamine.

As the injected sample volume is 5 μL and the lowest concentration is 100 pM in this experiment, a dopamine detection limit of 0.5 fmol can be achieved because of the low noise level and high current density. Figure 3 shows the calibration curves for DA and DHBA. The plot shows good linearity from 0.5 to 50 fmol.

In summary, an IDA carbon microelectrode for HPLC was fabricated by photolithographic techniques from the carbon film of pyrolyzed 3,4,9,10-perylenetetracarboxylic dianhydride on thermally oxidized silicon wafers. The electrode in a small-volume thin-layer cell incorporated in a microbore HPLC system achieved a low dopamine detection limit of 0.5 fmol due to current enhancement by redox cycling and low background noise at the carbon IDA electrode. Other catecholamines such as E and NE may be detected with high sensitivity by shifting their retention time by changing the mobile phase. A lower detection limit can be expected if an IDA carbon microelectrode is used which has a smaller pattern size.

Received for review November 5, 1993. Accepted June 15, 1994.®

® Abstract published in *Advance ACS Abstracts,* August 1, 1994.

(12) Hawley, M.; Tatawawadi, S.; Adams, R. N. *J. Am. Chem. Soc.* **1967**, *89*, 447.
(13) Niwa, O.; Morita, M.; Tabei, H. *Electroanalysis* **1991**, 3, 163.
(14) Bard, A. J.; Fan, F.-R. F.; Kwak, J.; Lev, O. *Anal. Chem.* **1989**, 61, 132.
(15) Horiuchi, T.; Niwa, O.; Morita, M.; Tabei, H. *J. Electrochem. Soc.* **1991**, *138*, 3549.
(16) Takahashi, M.; Morita, M.; Niwa, O.; Tabei, H. *Sensors Actuators B* **1993**, *13–14*, 336.

Anal. Chem. **1994,** *66,* 3503–3504

Comment on Wet Effluent Denuder Coupled Liquid/Ion Chromatography Systems: Annular and Parallel Plate Denuders

Franco De Santis

CNR—Istituto Inquinamento Atmosferico, Area della Ricerca di Roma, Via Salaria Km. 29,300, CP 10, 00016 Monterotondo Stazione, Roma, Italy

Simon and Dasgupta (Simon, P. K.; Dasgupta, P. K. *Anal. Chem.* 1993, *65,* 1134–1139) have reported on the design and characterization of high-efficiency wetted denuders of parallel plate and annular geometries. On the basis of laboratory results evaluated according to a theoretical treatment which refers to previous literature, they found that a "supertheoretical" collection efficiency was exhibited by the parallel plate denuder. It was found that a factor of 2 should be taken into account in the expression which describes the diffusion-based collection efficiency. By using the correct formula, the parallel plate denuder shows an excellent agreement to the theoretical efficiency curve. Discrepancies noted in the paper for the annular denuder and possible explanations for them have also been discussed.

In a recent paper in this journal, Simon and Dasgupta[1] described an interesting instrumental application of denuder technology. They reported on the design and characterization of high-efficiency wetted denuders of parallel plate (PPD) and annular (AD) geometries.

I feel that some reflections on this and earlier papers could be useful for defining better the issue of collection efficiency of denuders.

On the basis of the laboratory results evaluated according to a theoretical treatment reported by Ali et al.,[2] which refers to a paper of Gormley,[3] Simon and Dasgupta found that "... a supertheoretical collection efficiency was exhibited by the parallel plate denuder...". This anomalous behavior has a simple explanation. In their paper, they assume that the collection efficiency (f) for a PPD is expressed by

$$1 - f = 0.91 \exp(-3.77\alpha DL/Q) \qquad (1)$$

where D is the diffusion coefficient of the gas, L is the length of the tube, and Q is the volumetric flow rate. For a PPD, the parameter α is given by

$$\alpha = b/a \qquad (2)$$

where b is the long dimension of the denuder cross section.

The correct value for a, as deduced from the original paper of Gormley[3] or from Fuchs,[4] corresponds to the half-depth of the rectangular channel and not, as Simon and Dasgupta (following Ali et al.[2]) erroneously assume, to its depth. Therefore, a factor of 2 should be taken into account in the expression which describes the diffusion-based collection efficiency. Following Ali et al.,[2] Simon and Dasgupta also assume that this equation is valid for the annular denuder with the provision that α be defined as

$$\alpha = \pi(d_o + d_i)/(d_o - d_i) \qquad (3)$$

where d_o and d_i are the outer and inner diameters defining the annulus, respectively. From the original paper of Gormley[3] it can be deduced that the equation for the annular denuder is the following:

$$1 - f = 0.91 \exp\left[-7.54\frac{\pi(d_o + d_i)}{(d_o - d_i)}\frac{DL}{Q}\right] \qquad (4)$$

The correct formulas 1 and 4 have been applied to the evaluation of the PPD and AD denuders by using the data set obtained from Figure 6 of the Simon and Dasgupta paper. The results are shown in Figure 1. Now the PPD shows an excellent agreement to the theoretical efficiency curve, whereas the AD shows a systematic negative deviation, especially at higher flow rates.

Simon and Dasgupta advance some hyphotheses related to the practical aspects of the PPD geometry, such as formation of dry spots, or of "oscillating waves" in the liquid film, that can alter the theoretical performance of the denuder. These hyphotheses can also be considered viable in the case of the AD geometry.

In particular Simon and Dasgupta point out that the hydraulic cross section of the AD is substantially lower than that of the PPD. This results in a corresponding higher flow velocity which can cause the efficiency to be significantly underestimated because of channeling and dry spot formation.

It should be stressed that theoretical predictions simply establish an upper limit which can be reached or not, depending on the characteristics of the denuder (in particular on the reactivity of the coating).

In general, if we are interested in the behavior of a denuder, be it a cylindrical, annular, or parallel plate, the determination of the collection efficiency can be calculated by the Winiwarter equation,[5] a solution of Fick's diffusion equation which holds at any geometry of the denuder. Following this approach, the fractional penetration of a pollutant inside a denuder can be expressed as a function of the parameter $k = d_i/d_o$ by means

(1) Simon, P. K.; Dasgupta, P. K. *Anal. Chem.* **1993**, *65*, 1134–1139.
(2) Ali, Z.; Thomas, C. L. P.; Alder, J. F. *Analyst* **1988**, *114*, 759–769.
(3) Gormley, P. G. *Proc. R. Ir. Acad. Sec. A* **1938**, *45*, 59–63.
(4) Fuchs, N. A. *The Mechanics of Aerosols*; Pergamon Press: Oxford, England, 1964; p 206.
(5) Winiwarter, W. *Atmos. Environ.* **1989**, *23*, 1997–2002.

0003-2700/94/0366-3503$04.50/0
© 1994 American Chemical Society

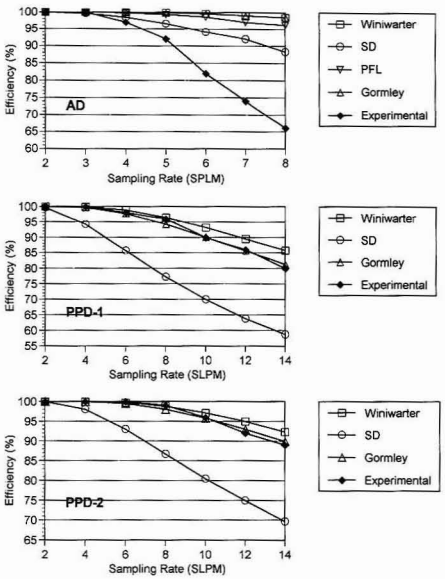

Figure 1. Collection efficiency of wet denuders for Simon and Dasgupta's data.

of the formula

$$C/C_o = B_{(k)} \exp(-\beta^2_{(k)} X) \tag{5}$$

with

$$X = (2LD)/d^2 v_m$$

where d is the hydrodynamic equivalent diameter and v_m the mean flow velocity. The $B_{(k)}$ and $\beta_{(k)}$ values are obtained by numerical integration.

Parallel plate and cylindrical geometry represents an upper ($k = 1$) and lower ($k = 0$) limit, respectively, whereas the annular denuder employed in the Simon and Dasgupta paper is characterized by $k = 0.7$. The solutions in the case of the parallel plate ($(C/C_o)_{pp}$), and annular denuder ($(C/C_o)_{ad}$), derived from Table 1 and by graphical interpolation from Figure 2 of the Winiwarter paper, assuming laminar flow and that every collision to the wall results in uptake, are given by

$$(C/C_o)_{pp} = 0.91 \exp(-3.883^2 X) \tag{6}$$

$$(C/C_o)_{ad} = 0.91 \exp(-3.874^2 X) \tag{7}$$

In the units employed by Gormley these equations are (for the PPD denuder)

$$1 - f = 0.91 \exp\left[-15.08 \frac{DL(2a + b)^2}{4Qab}\right] \tag{8}$$

(for the AD denuder)

$$1 - f = 0.91 \exp\left[-15.01 \frac{\pi DL(d_o + d_i)}{2Q(d_o - d_i)}\right] \tag{9}$$

If we assume that $b \gg a$, eq 8 becomes the expression used by Gormley.[3] As an example of the application of the Winiwarter equation and of the limits imposed by the nature of the coating, we might consider a paper of Possanzini et al.[6] These authors adapted the well-known Gormley–Kennedy equation for cylindrical denuders[7] to annular geometry and suggested an empirical equation on the basis of the sampling efficiency of annular denuders coated with tetrachloromercurate for the collection of SO_2. In the same units as above their equation is

$$(C/C_o)_{ad} = 0.85 \exp(-3.36^2 X) \tag{10}$$

The comparison with the Winiwarter theoretical solution ($B_{(k)}$ and $\beta_{(k)}$ values calculated for $k = 0.75$) shows that the theory values are significantly higher than the experimental values (B is 0.91 and β is 3.878). Winiwarter contended that a better agreement between the two expressions can be achieved by adaptation of one parameter and suggested an optimized diffusion coefficient $D = 0.107$ cm^2/s. This procedure has no physical meaning as in the expression 6 the values for $B_{(k)}$ and $\beta_{(k)}$ arise from the channel geometry and reactivity of the wall, respectively. A simple explanation for the observed discrepancy is that the theoretical equation assumes, as stated above, complete retention of the pollutant upon contact with the coated surface (the wall should be a "perfect sink"). Apparently, this is not verified in the case of tetrachloromercurate and SO_2. A better sink for SO_2 is sodium carbonate, a coating species which has subsequently been adopted by the same authors.[8] The Possanzini et al.[6] equation (PFL in the figure) and the Winiwarter equation have also been applied to the data of Simon and Dasgupta for the annular denuder. The experimental values are much lower than theoretical predictions.

In conclusion, if we compare the experimental behavior of the PPD and the AD denuders, we can state that the surface coating used by Simon and Dasgupta presents the characteristics of a perfect sink (i.e., the PPD follows exactly the theoretical prediction) whereas the poor performance of the AD seems likely to be due to its design. It may be theoretically interesting to know why the AD behaves as it does. For instance, this could be done by examining AD denuders of different cross sections.

Received for review April 12, 1994. Accepted June 27, 1994.®

® Abstract published in *Advance ACS Abstracts,* August 1, 1994.

(6) Possanzini, M.; Febo, A.; Liberti, A. *Atmos. Environ.* **1983**, *17*, 2605–2610.
(7) Gormley, P. G.; Kennedy, M. *Proc. R. Ir. Acad. A* **1949**, *52*, 73, 163–169.
(8) Allegrini, I.; De Santis, F.; Di Palo, V.; Febo, A.; Perrino, C.; Possanzini, M.; Liberti, A. *Sci. Total Environ.* **1987**, *67*, 1–16.

Anal. Chem. **1994,** *66,* 3505–3511

Determination and Characterization of Unreacted Hydroxyl Groups in a Cross-Linked Poly(ortho ester)

John D. Stong* and Leonore C. Witchey-Lakshmanan
Merck Research Laboratories, West Point, Pennsylvania 19486

A method is presented for the identification and quantitative determination of unreacted hydroxyl groups in a cross-linked poly(ortho ester) derived from the diketene acetal 3,9-bis-(ethylidene-2,4,8,10-tetraoxaspiro[5.5]undecane), (±)-1,2,6-hexanetriol, 1,6-hexanediol, and tetraethylene glycol. This method involves exhaustive derivatization of unreacted hydroxyl groups in the intact polymer in advance of mild hydrolysis followed by gradient HPLC analysis. Each of the derivatized polymer components was synthesized and characterized, and evidence is presented demonstrating that exhaustive derivatization has occurred.

Bioerodible implants based on polymeric ortho esters have shown great promise and, indeed, utility in sustained drug delivery. Controlled release of an incorporated drug is most desirably achieved through surface erosion of the polymer, which results in a steady zero-order release of drug.[1–5] The advantages of such a delivery device have prompted considerable work in recent years, especially with regard to the synthesis of new polymers and the design of the delivery device and its behavior in vivo and in vitro.[1]

Both linear and cross-linked poly(ortho esters) (POE) derived from 3,9-bis(ethylidene-2,4,8,10-tetraoxaspiro[5.5]-undecane) (DETOSU) and di- and trifunctional alcohols have been described for use as bioerodible matrices for the delivery of bioactive compounds. The difunctional alcohols serve as monomers and chain ends, while the trifunctional alcohols can also serve as branch points. Variation of polymer structure (with associated variations in physical and chemical properties) can be achieved by varying the types of alcohols and their stoichiometry.[6]

The alcohols used to prepare the poly(ortho ester) that is the subject of this work are 1,6-hexanediol (HD), tetraethylene glycol (TEG), and (±)-1,2,6-hexanetriol (HT). (Henceforth it will be understood that the hexanetriol used in this work is a racemic mixture, and the (±) designation will be dropped.) Presented in Figure 1 is a schematic representation of the reactions between the alcohols and DETOSU and the structure of a hypothetical POE segment, together with a representation of the present analytical method for the determination and identification of the unreacted hydroxyl groups in this hypothetical segment.

We would like to obtain as much information as possible concerning the chemical microstructure of these poly(ortho esters). This will provide more detailed correlations of such factors as reaction conditions, stoichiometry, drug loading, physical properties, and in vivo performance with chemical structure and polymerization kinetics.

Presented in this paper is an analytical procedure for the determination of the quantity and identity of unreacted hydroxyl groups in this class of poly(ortho esters). The method presented here is based on a method for the determination of cross-linking developed by Shih et al.[7] These methods afford a measurement of the degree of cross-linking by reporting on the number of moles per sample of trifunctional monomer incorporated as a branch point. The present method also reports on the number and identity of chain ends and the relative reactivities of the individual hydroxyl groups. A brief mathematical formalism is presented together with some calculated properties which we define in the Appendix of this paper.

EXPERIMENTAL SECTION

Materials. 1,6-Hexanediol, 1,2,6-hexanetriol, tetraethylene glycol, and dibutyltin diacetate were all from Aldrich and were distilled under reduced pressure. They were stored in vacuo over P_2O_5. Triethylamine (Aldrich) was distilled and stored over P_2O_5. Phenyl isocyanate (Aldrich) was distilled and stored over $CaCl_2$. DETOSU was obtained from Merck and Co. and was stored in sealed 1-L bottles at −15 °C. 1,4-Diazabicyclo[2.2.2]octane (DABCO) was from Aldrich and was used as received. All other reagents and solvents were used as received.

Apparatus. The analytical HPLC equipment consisted of a Hewlett-Packard 1090M solvent delivery system equipped with a Hewlett-Packard 1040A diode array detector, a Shimadzu SIL-6A autoinjector, and a Rainin Model III

(1) Heller, J.; Fritzinger, B. K.; Ng, S. Y.; Penhale, D. W. H. *J. Controlled Release* **1985,** *1,* 233.
(2) Shih, C.; Higuchi, T.; Himmelstein, K. J. *Biomaterials* **1984,** *5,* 237.
(3) Sparer, R. V.; Shih, C.; Ringeisen, C. D.; Himelstein, K. J. *J. Controlled Release* **1984,** *1,* 23.
(4) Heller, J.; Ng, S. Y.; Penhale, D. W.; Fritzinger, B. K.; Sanders, L. M.; Burns, R. A.; Gaynon, M. G.; Bhosale, S. S. *J. Controlled Release* **1987,** *6,* 217.
(5) Heller, J.; Penhale, D. W. H.; Helwing, R. F. *J. Polym. Sci., Polym. Lett. Ed.* **1980,** *18,* 619.
(6) Heller, J.; Penhale, B. K.; Fritzinger, B. K.; Rose, J. E.; Helwing, R. F. *Contracept. Deliv. Syst.* **1983,** *4,* 43.
(7) Shih, C.; Waldron, N.; Traugott, C. Q. *J. Appl. Polym. Sci.* **1993,** *49,* 2221.

0003-2700/94/0366-3505$04.50/0
© 1994 American Chemical Society

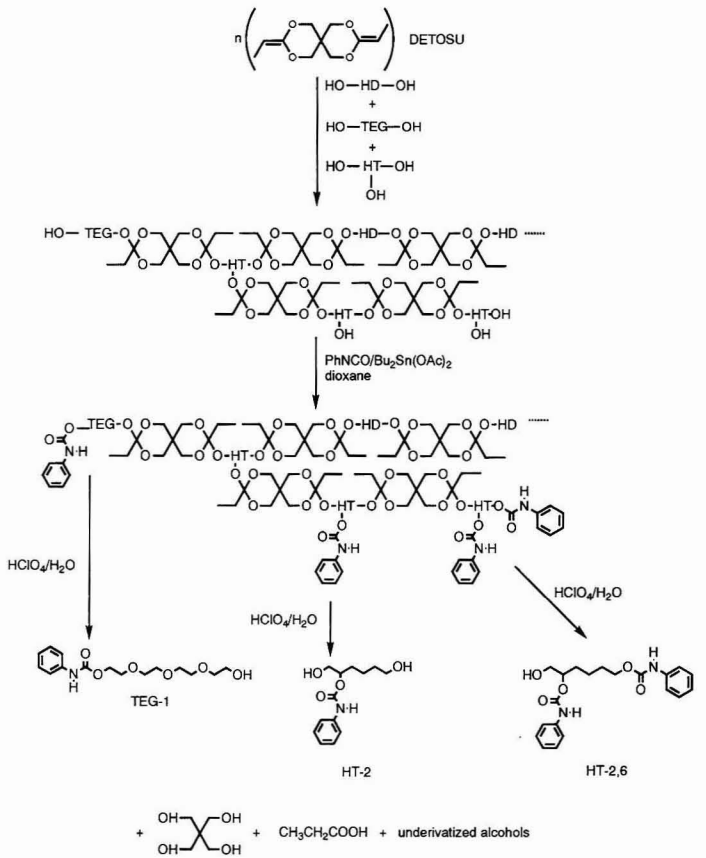

Figure 1. Schematic representation of the reaction of DETOSU with 1,6-hexanediol (HD), tetraethylene glycol (TEG), and 1,2,6-hexanetriol (HT) and the structure of a hypothetical poly(ortho ester) fragment. Schematic representation of the derivatization scheme of this fragment is also shown.

column oven. Absorption spectra were measured with a Hewlett-Packard HP8450 diode array spectrophotometer. A preparative HPLC system controlled by a DEC MINC-11 computer was constructed and used for the isolation of several compounds.

Syntheses and Isolation of Qualitative Standards. The basic principle of the derivatization is the reaction of the isocyanate with hydroxyl groups remaining unreacted after the polymerization of the poly(ortho ester). The polymer is then hydrolyzed, and the carbamate derivatives are analyzed via HPLC. In order to identify and quantitate these derivatives, qualitative standards were prepared by reacting the monomers with the phenyl isocyanate.

The synthetic procedures used to make the qualitative standards were intended to be the most direct and obvious methods for the production of amounts sufficient for structure determination and identification of the derivatized POE hydrolysate. No attempt was made to maximize yields of these standards, which were very small (probably less than 1%) for 1,2,6-hexanetriol (HT) mono- and disubstituted derivatives and 1,6-hexanediol (HD) and tetraethylene glycol (TEG) monosubstituted derivatives to about 75–90% for the completely substituted derivatives of HT, HD, and TEG.

For simplicity, the following acronyms will be used to indicate the various derivatives: 1-(*N*-phenylcarbamoyl)-hexane-2,6-diol (HT-1); 2-(*N*-phenylcarbamoyl)hexane-1,6-diol (HT-2); 6-(*N*-phenylcarbamoyl)hexane-1,2-diol (HT-6); 1,2-bis(*N*-phenylcarbamoyl)hexan-6-ol (HT-1,2); 2,6-bis(*N*-phenylcarbamoyl)hexan-1-ol (HT-2,6); 1,6-bis(*N*-phenylcarbamoyl)hexan-2-ol (HT-1,6); 1-(*N*-phenylcarbamoyl)hexan-6-ol (HD-1); 1-(*N*-phenylcarbamoyl)tetraethylene glycol (TEG-1); 1,2,6-tris(*N*-phenylcarbamoyl)hexane (HT-1,2,6); 1,6-bis(*N*-phenylcarbamoyl)hexane (HD-1,6); 1,8-bis(*N*-phenylcarbamoyl)tetraethylene glycol (TEG-1,8).

The monosubstituted *N*-phenylcarbamates of 1,2,6-hexanetriol, 1,6-hexanediol, and tetraethylene glycol are most conveniently prepared by carefully titrating an excess of the alcohol with small amounts of phenyl isocyanate using DABCO

as catalyst. The various derivatives are subsequently examined by HPLC analysis of an aliquot of the reaction mixture. At low concentrations of phenyl isocyanate, a single peak (for HD and TEG) or a group of three early-eluting peaks (for HT) is seen. The total area of these peaks increases with increasing phenyl isocyanate concentration. As the phenyl isocyanate concentration is increased even further, the areas of the early-eluting HPLC peaks begin to decrease, with a concomitant increase in the areas of late-eluting peaks. These peaks are the disubstituted HD and TEG derivatives or the di- and trisubstituted HT derivatives.

It is most convenient to isolate the HT, HD, and TEG monosubstituted derivatives by preparative HPLC. The HT-1,6 derivative can be synthesized and isolated directly by taking advantage of the fact that secondary alcohols react much more slowly with phenyl isocyanate than primary alcohols, in the absence of a catalyst. The inclusion of a catalyst such as DABCO and an excess of phenyl isocyanate, however, afford an almost quantitative yield of the disubstituted derivatives of HD and TEG and of the trisubstituted derivative of HT.

The 1,2- and 2,6-disubstituted derivatives of HT are more difficult to prepare. It is necessary to block the C6 or C1 OH group, respectively, prior to reaction with phenyl isocyanate. As would be expected, HT will react with other nucleophiles (including benzoyl and silyl chlorides) exactly as it does with phenyl isocyanate. Thus, addition of a small amount of *tert*-butyldimethylsilyl chloride to a solution of HT will yield predominantly the monosilyl ethers, which can then be reacted further at the remaining hydroxyl groups with phenyl isocyanate and then hydrolyzed under mild conditions. The hydrolysis removes the silyl ethers, resulting in a mixture of HT-1,2, HT-1,6, and HT-2,6. These are then purified by preparative HPLC. Proton NMR and mass spectral data were entirely consistent with the assigned structures of all the compounds.

Preparation of Standards and Determination of Accuracy and Linearity. The *N*-phenylcarbamate derivatives of methanol (ME-1), 1-hexanol (HX-1), 2-propanol (PR-2), and isobutyl alcohol (BU-i) were prepared by well-known methods.[8] Each was recrystallized from hexane. HT-1, HT-6, HT-1,6, TEG-1,8, HD-1,6, and HT-1,2,6 were prepared as described above and were recrystallized from acetonitrile. These compounds were dried for 4 days in vacuo at 40 °C. Accurately prepared solutions of PR-2, HX-1, HT-1, HT-6, HT-1,6, TEG-1,8, HD-1,6, and HT-1,2,6 were used to determine the molar absorptivity per *N*-phenylcarbamate group. Concentrations of the standards (ME-1 and BU-i) were then determined spectrophotometrically using the absorptivity determined as described above, $\epsilon = (1.676 \pm 0.033) \times 10^4\ M^{-1}\ cm^{-1}$.

The linearity of instrument response was checked over a large range of concentrations that spanned the concentration range of *N*-phenylcarbamate derivatives found in the samples. Linearity of representative compounds included ME-1 (0.03–3.4 μmol/mL), HT-1 (0.01–1.0 μmol/mL), HT-1,6 (0.006–0.6 μmol/mL), and HT-1,2,6 (0.005–0.45 μmol/mL). Plots of HPLC peak area vs concentration were linear, with $r^2 \geq 0.999$.

(8) Shriner, R. L.; Fuson, R. C.; Curtin, D. Y. *The Systematic Identification of Organic Compounds*; John Wiley and Sons: New York, 1964, p 246.

Accuracy of the method was estimated by chromatographically determining the concentrations of known solutions of HT-1, HT-6, HT-1,6, TEG-1,8, HD-1,6, and HT-1,2,6 relative to the external standard (ME-1), using the conditions of the present method.

Preparation of Poly(ortho ester) Pellets. Poly(ortho ester) pellets measuring 0.5 in. diameter × 1.0 in. were prepared in a glovebox under nitrogen. Into a jacketed beaker maintained at 40 °C was added 7.73 g (39.8 mmol) of tetraethylene glycol, 2.80 g (20.9 mmol) of 1,2,6-hexanetriol, and 0.05 mL (0.36 mmol) of triethylamine, each from a separate tared syringe. In addition, 4.69 g (39.7 mmol) of 1,6-hexanediol was added as a solid. The mixture was stirred at 40 °C until all the HD dissolved. The temperature was then lowered to 25 °C and 23.03 g (108.5 mmol) of DETOSU was added rapidly with stirring from a tared 60-mL syringe. The mixture became cloudy upon addition of DETOSU and was stirred at 25 °C until it cleared (about 15 min).

The clear viscous solution was then transferred to a Teflon mold containing 12 equally spaced holes (0.5 in. diameter × 1.0 in.) in two rows of 6. The bottom of the mold was a sheet of Teflon 0.25 in. thick and was held in place and sealed by silicone caulk. After filling, the top (also 0.25-in. Teflon sheet) was placed over the mold and secured with equally spaced (3 in. on center) C-clamps. The assembled mold was removed from the glovebox and placed in an oven at 65 °C for curing. Cure time was 72 h. After being cooled to room temperature, the mold was opened and the pellets were removed. The individual pellets were placed in 25-mL vials and stored in a vacuum desiccator over P_2O_5.

Preparation of Samples. The poly(ortho ester) pellets were cut into slices of varying thickness with a fine-tooth saw and a small aluminum miter box, and the "sawdust" produced by this procedure was also collected. The thickness of each slice was measured with calipers, weighed, and placed into 25-mL vials equipped with Teflon/silicone rubber seals.

Analytical Procedure. Five milliliters of dry dioxane containing 0.2 g (0.57 mmol) of dibutyltin diacetate/mL was added to each polymer sample, and 0.125 mL (1.14 mmol) of phenyl isocyanate was added. The vials were sealed and the derivatization reaction was allowed to proceed for various times at room temperature. The reaction was quenched by the addition of 0.25 mL (1.59 mmol) of 1-octanol at the desired times. This reaction was allowed to proceed overnight in an attempt to eliminate completely any traces of phenyl isocyanate occluded within the polymer matrix. After the quench, the samples were hydrolyzed by addition of 0.15 mL of 3% perchloric acid, and were then placed on a rotary shaker (New Brunswick Scientific) at 250 rpm. Complete dissolution of the polymer occurred within 2–4 h. After the samples were completely hydrolyzed, 0.50 mL of the internal standard solution (isobutyl *N*-phenylcarbamate, 54.07 μmol/mL) was added and the samples were carefully transferred to 50-mL volumetric flasks and diluted to volume with acetonitrile. The internal standard is used to identify the locations of the analyte peaks by comparing retention times relative to that of the internal standard. HPLC analyses were performed using a Zorbax Rx C8, 4.6 mm × 250 mm column at 50 °C and a double gradient, beginning with 0% acetonitrile/2.5% methanol/97.5% water, going to 20% acetonitrile/0% methanol/

Table 1. Equivalent Absorptivities for Several *N*-Phenylcarbamates

compd	$10^{-4}e/N$ (M^{-1} cm^{-1}/N)[a]	compd	$10^{-4}e/N$ (M^{-1} cm^{-1}/N)[a]
HT-1	1.721	HD-1,6	1.639
HT-6	1.708	HT-1,2,6	1.662
HT-1,6	1.690	PR-2	1.645
TEG-1,8	1.640	HX-1	1.699

[a] *N*, number of *N*–phenylcarbamates groups per molecule.

20% water in 25 min, and then to 100% acetonitrile in 50 min. Flow rate was 1.00 mL/min, and the reequilibration time was 14 min. Detection was at 233 and 269 nm. The external standard was run as a bracketed standard after every third sample.

The content of the *i*th POE derivative in micromoles per gram is given by

$$C_i = \frac{A_i}{A_{ES}} \frac{C_{ES}}{n_i} \frac{V_S}{w}$$

where A_i is the chromatographic peak area of the *i*th derivative, C_{ES} is the concentration (μmol/mL) of the external standard solution, V_S is the volume (mL) of the sample, A_{ES} is the chromatographic peak area of the external standard, n_i is the ratio of the number of *N*-phenylcarbamate groups on the *i*th derivative to the number of *N*-phenylcarbamate groups on the external standard, and w is the weight (g) of the polymer sample.

RESULTS

Listed in Table 1 are the equivalent absorptivities (molar absorptivity per *N*-phenylcarbamate group) measured for several *N*-phenylcarbamates. The average value obtained was $(1.676 \pm 0.033) \times 10^4$ M^{-1} cm^{-1}/N, rsd = 1.97%.

The 75-min double gradient produced resolution of all the derivatized POE components and the internal standard. Chromatograms of a mixture of the pure derivatives and the hydrolysate of a derivatized sample are shown in Figure 2. Identification of the derivatives in the POE sample is facilitated by comparing relative retention times of the analytes in a reference solution with those of the sample by use of the internal standard retention time as reference. Moreover, it was found that the relative retention times were very consistent from run to run and from column to column. The relative retention times for all of the POE–phenyl isocyanate derivatives are provided in Table 2. Also presented in Table 2 is a comparison of the apparent recoveries obtained for solutions of HT-1, HT-6, HT-1,6, TEG-1,8, HD-1,6, and HT-1,2,6 using the external standard (methyl *N*-phenylcarbamate). The mean recovery for these compounds is 101.4 ± 4.4%. It is assumed that this is representative for all of the components in the sample.

The results from the analysis of the POE pellet slices are tabulated in Table 3a for the monosubstituted derivatives and in Table 3b for the di- and trisubstituted derivatives. The average values for the reaction times and each corresponding content of each derivative are listed and compared with the component content for the "sawdust" measured at the same time. These data are summarized in Figure 3a, in which the content of the monosubstituted components is presented as a function of time, and in Figure 3b, in which this relationship is presented for the di- and trisubstituted derivatives. For clarity, only the most abundant derivative content from the sawdust is shown in this figure.

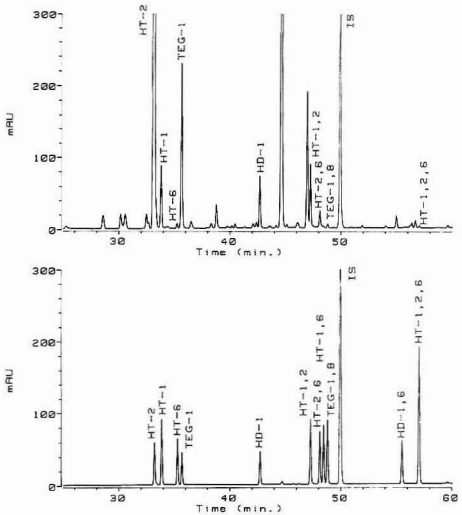

Figure 2. HPL chromatograms of a mixture of pure phenyl isocyanate derivatives (bottom) and of derivatized POE hydrolysate (top). IS, internal standard. Note that in this derivatized POE sample, as in most, HT-1,6 and HD-1,6 are not present in detectable amounts.

Table 2. Relative Retention Times for the POE–Phenyl Isocyanate Derivatives, with Internal Standard t_r(Bu-I) = 1.000, and Recoveries of some POE–Phenyl Isocyanate Derivatives

compd	mean rel retention time (min)	std dev (min)	% rsd	rec (%)
HT-2	0.662	0.005	0.735	nd[a]
HT-1	0.675	0.005	0.721	99.6
HT-6	0.704	0.004	0.544	95.8
TEG-1	0.718	0.002	0.307	nd
HD-1	0.860	0.002	0.249	nd
HT-1,2	0.953	0.003	0.339	nd
HT-2,6	0.968	0.002	0.197	nd
HT-1,6	0.975	0.001	0.131	103.8
TEG-1,8	0.978	0.002	0.164	99.7
HD-1,6	1.117	0.002	0.203	100.8
HT-1,2,6	1.148	0.003	0.235	108.7

[a] nd, not determined.

DISCUSSION

The chemistry of this method is based upon the well-known reaction of phenyl isocyanate with alcohols to form a *N*-phenylcarbamate (phenylurethane):

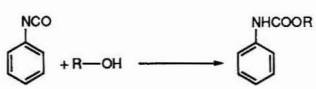

These derivatives are hydrolytically stable and can therefore

Table 3. Results from Derivatization Analysis of Poly(ortho ester) Pellets

(a) Monosubstituted Derivatives

	thickness (mm)	reaction time (h)	derivative content (μmol/g) HT-2	HT-1	HT-6	TEG-1	HD-1
group 1							
mean (n = 6)	2.92	2.91	165	6.45	0.605	17.8	5.58
std dev	0.59	0.21	44	1.79	0.138	7.21	1.27
group 1 sd[a]	0.00	2.83	297	10.7	0.950	37.5	9.63
group 2							
mean (n = 4)	3.55	16.33	302	12.6	1.000	31.6	10.5
std dev	0.29	0.27	9	2.0	0.126	4.19	1.6
group 2 sd[a]	0.00	16.23	298	12.1	0.908	35.7	9.60
group 3							
mean (n = 3)	3.87	45.08	299	12.2	0.908	30.0	9.93
std dev	0.23	0.12	4	0.3	0.030	0.8	0.34
group 3 sd[a]	0.00	45.17	297	11.6	0.879	39.5	10.3
group 4							
mean (n = 4)	3.58	144.51	317	11.1	0.986	32.1	10.1
std dev	0.08	0.32	20	1.5	0.046	2.9	1.1
group 4 sd[a]	0.00	144.78	293	10.7	1.036	37.4	10.4

(b) Disubstituted and Trisubstituted Derivatives

	thickness (mm)	reaction time (h)	derivative content (μmol/g) HT-1,2	HT-2,6	HT-1,6	TEG-1,8	HD-1,6	HT-1,2,6
group 1								
mean (n = 6)	2.92	2.91	3.04	1.04	0.000	0.329	0.092	0.130
std dev	0.59	0.21	0.79	0.25	0.000	0.110	0.080	0.041
group 1 sd[a]	0.00	2.83	4.86	1.88	0.000	0.558	0.000	0.309
group 2								
mean (n = 4)	3.55	16.33	4.52	1.96	0.000	0.752	0.259	0.248
std dev	0.29	0.27	2.80	0.28	0.000	0.608	0.518	0.259
group 2 sd[a]	0.00	16.23	5.31	2.26	0.000	0.515	0.000	0.257
group 3								
mean (n = 3)	3.87	45.08	5.60	1.97	0.048	0.370	0.024	0.129
std dev	0.23	0.12	0.22	0.02	0.083	0.024	0.042	0.024
group 3 sd[a]	0.00	45.17	5.25	1.60	0.000	0.417	0.000	0.302
group 4								
mean (n = 4)	3.58	144.51	5.74	2.07	0.196	0.420	0.135	0.155
std dev	0.08	0.32	0.62	0.21	0.024	0.079	0.096	0.033
group 4 sd[a]	0.00	144.78	5.44	2.00	0.000	0.418	3.17	1.66

[a] sd, indicates the sample prepared from the fine powders recovered from the cutting of the polymer samples.

be subjected to conditions that will completely and quickly hydrolyze the poly(ortho ester). The over-all chemistry of the method is presented schematically in Figure 1. At this point it is necessary to explicitly distinguish between the POE–phenyl isocyanate derivatives that are actually determined by the present method and the corresponding POE structural elements they represent. It is seen in Figure 1 that HT-2, for instance, represents 1,2,6-hexanetriol in the original polymer, which remained unreacted at the 2 position. The derivative content, therefore, refers to the number of moles per unit weight of the polymer of monomer unreacted in the indicated position (e.g., HT-2 is 1,2,6-hexanetriol unreacted in the 2 position, HT-1,2 is 1,2,6-hexanetriol unreacted in the 1 and 2 positions, etc.).

Practical considerations lead us to examine the possibility of using a small number of easily prepared standards for the quantitation of the POE–phenyl isocyanate derivatives. The lengthy synthetic procedures for many of the POE derivatives themselves, and the difficulty in purifying them in quantity, make it very impractical to use these compounds as standards. The requirements for quantitative standards include equivalent instrument responses for analytes and standards. The N-phenylcarbamate of methanol was found to be suitable, and the recoveries appear satisfactory. The N-phenylcarbamate of isobutyl alcohol was found to elute in a clear region and was chosen as an internal marker for the determination of relative retention times.

Another concern in developing the method is that exhaustive derivatization of all the unreacted hydroxyl groups has occurred. There are two reasonable limiting factors: the rate at which phenyl isocyanate reacts with primary and secondary hydroxyl groups (in the presence and absence of neighboring substituents) and the diffusion rate of phenyl isocyanate into the polymer matrix. Among the most efficient catalysts known for the reaction of phenyl isocyanate with alcohols is dibutyltin diacetate.[9,10] For example, HT dissolved in dioxane was completely derivatized within 1–2 h using this catalyst. Therefore, the rate-limiting step for this derivatization procedure would most likely be the diffusion of phenyl isocyanate into the polymer. By comparing the results as a function of time of the derivatization of a group of polymer slices about 3–4 mm thick with those of the sawdust powder obtained in the cutting process, the amount of time necessary for complete derivatization can be determined. The fine powder was found to swell immediately upon addition of the

(9) Saunders, J. H.; Frisch, K. C. *Polyurethanes, Chemistry and Technology; Part I, Chemistry*; Interscience Publishers: New York, 1962, p 166.
(10) Hostettler, F.; Cox, E. F. *Ind. Eng. Chem.* **1960**, *52*, 609.

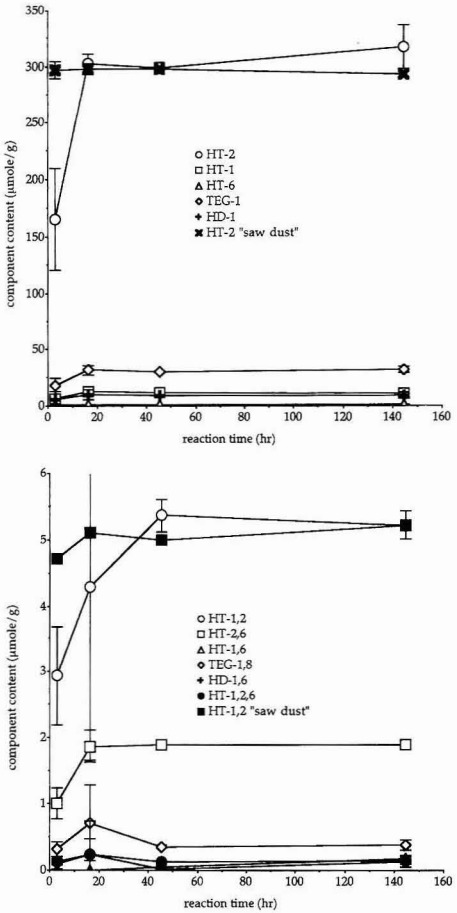

Figure 3. (a, top) Monosubstituted POE–phenyl isocyanate derivative content as a function of derivatization reaction time for POE pellet slices up to 4.13 mm thick. The content of HT-2 from the powder is shown for comparison, indicating the maximum probable yield per unit weight of that derivative. (b, bottom) Di- and trisubstituted POE–phenyl isocyanate derivative content as a function of derivatization reaction time for POE pellet slices up to 4.13 mm thick. The sawdust content of HT-1,2 is shown for comparison, indicating the maximum probable yield per unit weight of that derivative.

derivatizing solution, indicating that diffusion of the solvent throughout the polymer had occurred relatively quickly. Indeed, full formation of the phenyl isocyanate derivatives was achieved in the powder samples during the earliest stages of the experiment, while about 20 h was required for the thicker slices to reach limiting values. Moreover, the limiting values attained by the powder and the slices were identical for each derivative. In addition, the data also indicate that full derivatization has taken place and that no significant decomposition of either the polymer or of the derivatives has occurred, since these values did not change with longer reaction times.

In addition to the kinds of information briefly described here, this method applied to this polymer system should be capable of providing detailed information on rates of polymerization (including linear polymerization and rate of cross-linking) and information concerning rates of cross-linking of preformed polymers. These issues will be the topic of later research.

APPENDIX

The analytical concentrations of the reactants (i.e., the concentration of each reactant in the reaction mixture) are given by C_1^0, analytical concentration of HT (μmol/g); C_2^0, analytical concentration of HD (μmol/g); C_3^0, analytical concentration of TEG (μmol/g); and C_4^0, analytical concentration of DETOSU (μmol/g).

These quantities are related by the expression

$$2C_4^0 = 3C_1^0 + 2C_2^0 + 2C_3^0$$

which relates the total number of hydroxyl groups to the total number of ketene acetal double bonds.

Let the content of each of the derivatized components be represented by the subscripted variables: c_1, HT-2 content (μmol/g); c_2, HT-1 content (μmol/g); c_3, HT-6 content (μmol/g); c_4, HT-2,6 content (μmol/g); c_5, HT-1,6 content (μmol/g); c_6, HT-1,2 content (μmol/g); c_7, HD-1 content (μmol/g); c_8, TEG-1 content (μmol/g).

And also let c_1' equal the amount of HT (μmol/g) fully incorporated into polymer, c_2' equal the amount of HD (μmol/g) fully incorporated into polymer, and c_3' equal amount of TEG (μmol/g) fully incorporated into polymer.

These values of fully incorporated monomer are then calculated from the following expressions:

$$c_1' = C_1^0 - \sum_{i=1}^{6} c_i$$

$$c_2' = C_2^0 - c_7$$

$$c_3' = C_3^0 - c_8$$

The following properties can now be calculated. The degree of cross-linking is defined as the fraction of trifunctional monomer (1,2,6-hexanetriol, in this case) that is incorporated into the polymer by bonding through all three hydroxyl groups. This is given by

$$\alpha = (C_1^0 - \sum_{i=1}^{6} c_i)/C_1^0$$

The ratio of chain carriers to branch points gives a measure of the average number of monomers between branch points:

$$R_0 = (\sum_{i=1}^{3} C_i' + \sum_{i=1}^{3} c_i)/(C_1^0 - \sum_{i=1}^{6} c_i)$$

Using the data from Table 3a,b at $t = 45.08 \pm 0.12$ h we obtain the following values for these quantities:

$$\alpha = 0.415 \pm 0.022$$

$$R_0 = 11.4 \pm 0.6$$

In addition to these structurally related parameters we note that c_7 and c_8 represent the number (per gram) of HD and TEG molecules, respectively, incorporated as chain ends. We further note that

$$R_1 = c_8/c_7 = 3.02 \pm 0.19$$

which indicates that under the conditions used here to prepare the poly(ortho ester), TEG is approximately 3 times as likely to be incorporated as a chain end as is HD.

We note in closing that the experimentally accessible structural parameters measured by the present method can be expressed as a vector, the components of which are the POE component contents:

$$\hat{V} = (c_i)$$

This formalism should be useful in describing the effects of initial reaction conditions, stoichiometry, etc., on the structure of the polymer and the effects of these parameters on physical and chemical properties.

Received for review March 3, 1994. Accepted June 3, 1994.*

* Abstract published in *Advance ACS Abstracts,* July 15, 1994.

Anal. Chem. **1994,** *66,* 3512–3518

Analysis of Human Cerebrospinal Fluid by Capillary Electrophoresis with Laser-Induced Fluorescence Detection

Jonas Bergquist,[†] S. Douglass Gilman,[‡] Andrew G. Ewing,*[,‡] and Rolf Ekman[†]

Department of Clinical Neuroscience, Section of Psychiatry and Neurochemistry, Göteborg University, Mölndal Hospital, S-431 80 Mölndal, Sweden, and Department of Chemistry, 152 Davey Laboratory, Penn State University, University Park, Pennsylvania 16802

Capillary electrophoresis with laser-induced fluorescence detection is used to analyze 10 μL samples of human cerebrospinal fluid. Primary amine-containing compounds in untreated cerebrospinal fluid are labeled with 3-(4-carboxybenzoyl)-2-quinolinecarboxaldehyde prior to analysis, producing fluorescent isoindoles. Electropherograms containing approximately 50 peaks are obtained in less than 35 min from cerebrospinal fluid samples. Ten peaks in the electropherograms have been identified and quantitated: arginine, glutamine, threonine, valine, γ-amino-*n*-butyric acid, serine, alanine, glycine, glutamic acid, and aspartic acid. Detection limits for these 10 amino acids range from 0.29 nM for γ-amino-*n*-butyric acid to 100 nM for threonine, and separation efficiencies as high as 190 000 theoretical plates are obtained for these analytes. Electropherograms of cerebrospinal fluid samples from patients with Alzheimer's disease and from children with different neurological disorders are compared to those of healthy controls. Differences in individual amino acid levels are observed between the patient groups, and these differences appear to be disease and age related. These results indicate that analysis of cerebrospinal fluid by capillary electrophoresis will be useful as a selective, rapid, and sensitive tool for both diagnosis of central nervous system disorders and for study of the mechanisms of these disorders.

Capillary electrophoresis offers several advantageous characteristics for the analysis of biological fluids, and its emergence as an effective tool for clinical analysis has been the subject of recent reviews.[1-4] The high separation efficiencies obtained with capillary electrophoresis result in large peak capacities, high resolving power, and very short analysis times. Analysis of substances in biological fluids requires high selectivity in order to quantitate particular analytes without interference from other species, and large peak capacities are desirable in order to analyze many species of interest simultaneously. The small sample volumes required for capillary electrophoresis (femtoliter to nanoliter), along with the ability of capillary electrophoresis to determine multiple analytes, reduce the amount of sample consumed, leaving more sample for other types of analysis. Also, analysis of biological fluids with capillary electrophoresis often requires minimal sample processing before injection, and many biological samples can be directly injected into the capillary without adverse effects.[1-4] Finally, the short analysis times obtained with capillary electrophoresis and the ease of automation of the technique can save valuable time and labor.

One potential disadvantage of the small volumes used with capillary electrophoresis is that concentration sensitivity for detection is compromised by extremely small detection volumes. This is particularly true for optical detection methods such as UV absorbance and refractometric detection where the short optical path length provided by the capillary results in poor concentration sensitivity relative to larger volume techniques. While the sensitivity offered by UV detectors commonly used with capillary electrophoresis is sufficient to detect a variety of analytes, many important species present in biological fluids are found in only trace quantities or do not absorb strongly enough and will go undetected.

Laser-induced fluorescence (LIF) detection is one of the most successful methods used to overcome concentration detection insensitivity for capillary electrophoresis. Concentration detection limits on the order of 10^{-12} M can be obtained with LIF detection of fluorescently labeled analytes using a number of detector configurations.[5-8] Native fluorescence with UV lasers can also be used to obtain very low detection limits for a variety of analytes;[9-12] however, many interesting analytes are not natively fluorescent, and most reports of LIF detection with capillary electrophoresis involve the use of visible lasers and labeling of analytes with fluorescent functional groups.

One derivatization reagent successfully used with capillary electrophoresis and LIF detection is 3-(4-carboxybenzoyl)-2-quinolinecarboxaldehyde (CBQCA), which has recently been developed by Novotny and co-workers.[13] When allowed to react with a suitable nucleophile and compounds containing

† Göteborg University.
‡ Penn State University.

(1) Chen, F.-T. A.; Liu, C.-M.; Hsieh, Y.-Z.; Sternberg, J. C. *Clin. Chem.* **1991,** *37,* 14–19.
(2) Guzman, N. A.; Gonzalez, C. L.; Hernandez, L.; Berck, C. M.; Trebilcock, M. A.; Advis, J. P. In *Capillary Electrophoresis Technology*; Guzman, N. A., Ed.; Marcel Dekker, Inc.: New York, 1993; Chapter 22.
(3) Shihabi, Z. K. *Ann. Clin. Lab. Sci.* **1992,** *22,* 398–405.
(4) Thormann, W.; Molteni, S.; Caslavska, J.; Schmutz, A. *Electrophoresis* **1994,** *15,* 3–12.
(5) Sweedler, J. V.; Sheer, J. B.; Fishman, H. A.; Zare, R. N.; Scheller, R. H. *Anal. Chem.* **1991,** *63,* 496–502.
(6) Hernandez, L.; Escalona, J.; Joshi, N.; Guzman, N. *J. Chromatogr.* **1991,** *559,* 183–196.
(7) Wu, S.; Dovichi, N. J. *Talanta* **1992,** *39,* 173–178.
(8) Amankwa, L. N.; Albin, M.; Kuhr, W. G. *Trends Anal. Chem.* **1992,** *11,* 114–120.
(9) Lee, T. T.; Yeung, E. S. *J. Chromatogr.* **1992,** *595,* 319–325.
(10) Milofsky, R. E.; Yeung, E. S. *Anal. Chem.* **1993,** *65,* 153–157.
(11) Chan, K. C.; Janini, G. M.; Muschik, G. M.; Issaq, H. J. *J. Liq. Chromatogr.* **1993,** *16,* 1877–1890.
(12) Nie, S.; Dadoo, R.; Zare, R. N. *Anal. Chem.* **1993,** *65,* 3571–3575.
(13) Liu, J.; Hsieh, Y.-Z.; Wiesler, D.; Novotny, M. *Anal. Chem.* **1991,** *63,* 408–412.

0003-2700/94/0366-3512$04.50/0
© 1994 American Chemical Society

primary amines, CBQCA forms highly fluorescent isoindole products in a manner analogous to the behavior of *o*-phthaldialdehyde and naphthalene-2,3-dicarboxaldehyde.[14] There are several important advantages realized by the use of CBQCA, including detection limits in the nanomolar range, excellent linearity, compatibility with micellar electrokinetic capillary chromatography, fast reaction time, and good product stability.[13] Background fluorescence is minimal because CBQCA itself does not fluoresce, and, therefore, no purification of CBQCA derivatives is required prior to analysis. Also, CBQCA can be used with both HeCd (442 nm) and argon ion lasers (488 nm) which are available with commercial capillary electrophoresis-LIF instruments. Because CBQCA is readily available, is easy to use, and provides very low detection limits for primary amines, it is an excellent precolumn derivatization reagent for biological fluids.

Cerebrospinal fluid is secreted in the brain, primarily by the choroid plexus, and cerebrospinal fluid is in a steady state with the extracellular fluid surrounding brain cells. Cerebrospinal fluid plays a critical role in providing a constant chemical environment for neurons and glia, and it is the body fluid most likely to reflect disturbances of the central nervous system. The molecules found in cerebrospinal fluid cover a wide spectrum including primary amine-containing species such as amino acids, amino sugars, short peptide fragments, neuropeptides, and larger proteins. Using HPLC, ion-exchange chromatography, and isotachophoresis in large capillaries, changes in amino acid levels in cerebrospinal fluid have been found for a number of diseases including chronic schizophrenia,[15] multiple sclerosis,[16] Parkinson's syndrome,[17] Alzheimer's disease (AD),[18] and other important central nervous system disorders.[19–24] These reports emphasize the need for the development of simple and rapid techniques for the study of primary amine-containing compounds in cerebrospinal fluid. Analysis by HPLC and ion-exchange chromatography are very effective tools for cerebrospinal fluid analysis, but separations can be time consuming, and substantial sample treatment is often used prior to analysis.[15–17,20–23] Isotachophoresis in large capillaries has been used to determine only one amino acid quantitatively in cerebrospinal fluid.[24] If suitable methods were available, patients with a variety of neurological disorders could be more rapidly diagnosed, and the roles of particular molecules in these diseases could be more easily studied. As discussed earlier, capillary electrophoresis with LIF detection is well suited to the analysis of biological fluids, including cerebrospinal fluid. A few reports on the analysis of human cerebrospinal fluid by capillary electrophoresis using UV detection[1,2] and LIF detection[25] have been published, but very few peaks in the resulting electropherograms have been identified, and little or no quantitative data have been presented in these studies. Capillary electrophoresis has been used to quantitatively determine compounds in dialysates of cerebrospinal fluid from rats using UV detection,[26] electrochemical detection,[27] and LIF detection.[28]

In this paper we present data from a quantitative, sensitive, and rapid analysis of human cerebrospinal fluid obtained using capillary electrophoresis with LIF detection and precolumn CBQCA derivatization. Ten of the approximately 50 peaks obtained in separations of these cerebrospinal fluid samples have been identified and quantitated. Separation efficiencies, detection linearity, and detection limits are reported for the identified peaks. Values obtained for amino acids in cerebrospinal fluid from healthy adult patients, patients with Alzheimer's disease, healthy elderly patients, and children with different neurological disorders are compared. These results are used to assess the potential of this method as a diagnostic tool for neurological disorders and for the study of the mechanisms of these central nervous system disturbances.

EXPERIMENTAL SECTION

Apparatus and Separation Conditions. A P/ACE 2100 instrument (Beckman Instruments; Fullerton, CA) equipped with a P/ACE-LIF detector was used to obtain all capillary electrophoresis separations. The LIF detector used an argon ion laser for excitation at 488 nm (4 mW), and a 560 ± 40 nm band-pass filter provided with the LIF detector was used to reject scattered laser light for fluorescence detection. Fused silica capillary (75 μm i.d., 360 μm o.d.) was obtained from Polymicro Technologies (Phoenix, AZ), and all separations were performed in 57 cm lengths (50 cm to detector) of untreated capillary.

The separation buffer consisted of 50 mM borate and 30 mM sodium dodecyl sulfate (SDS) in ultrapure water (Milli-Q UF Plus; Millipore Corp., Milford, MA). The pH was adjusted to 9.0 by addition of sodium hydroxide, and dimethyl sulfoxide (DMSO) was added to this solution (20% DMSO vol/vol) to form the final separation buffer. The instrument was programmed to rinse the capillary with 0.1 M NaOH at high pressure for 2.0 min and then with separation buffer at high pressure for 3.0 min prior to each injection in order to obtain consistent migration times from run to run. Samples were injected automatically by pressure injection for 1.0 s (5.9 nL volume). A separation potential of 20 kV was used, and the capillary was held at 25 °C. The electrophoretic current was typically 33 μA.

Data Collection and Analysis. Data collection, processing, and analysis were performed using the System Gold software package (Beckman). Data were collected at a sampling rate of 5 Hz. Peaks were identified by spiking cerebrospinal fluid samples with standard solutions of amino acids. Amino acids

(14) Roach, M. C.; Harmony, M. D. *Anal. Chem.* **1987**, *59*, 411–415.
(15) Korpi, E. R.; Kaufmann, C. A.; Marnela, K.-M.; Weinberger, D. R. *Psychiatry Res.* **1987**, *20*, 337–345.
(16) Qureshi, G. A.; Baig, M. S. *J. Chromatogr.* **1988**, *459*, 237–244.
(17) Gjessing, L. R.; Gjesdahl, P.; Dietrichson, P.; Presthus, J. *Eur. Neurol.* **1974**, *12*, 33–37.
(18) Basun, H.; Forssell, L. G.; Almkvist, O.; Cowburn, R. F.; Eklöf, R.; Winblad, B.; Wetterberg, L. *J. Neural Transm.* **1990**, *2*, 295–304.
(19) Perry, T. L.; Krieger, C.; Hansen, S.; Eisen, A. *Ann. Neurol.* **1990**, *28*, 12–17.
(20) Hagberg, H.; Thornberg, E.; Blennow, M.; Kjellmer, I.; Lagercrantz, H.; Thiringer, K.; Hamberger, A.; Sandberg, M. *Acta Paediatr.* **1993**, *82*, 925–929.
(21) Manyam, B. V.; Giacobini, E.; Ferraro, T. N.; Hare, T. A. *Arch. Neurol.* **1990**, *47*, 1194–1199.
(22) Kaakkola, S.; Marnela, K.-M.; Oja, S. S.; Icén, A.; Palo, J. *Acta Neurol. Scand.* **1990**, *82*, 225–229.
(23) Halawa, I.; Baig, S.; Qureshi, G. A. *Biomed. Chromatogr.* **1991**, *5*, 216–220.
(24) Hiraoka, A.; Miura, I.; Tominaga, I.; Hattori, M. *Clin. Biochem.* **1989**, *22*, 293–296.
(25) Jansson, M.; Roeraade, J.; Laurell, F. *Anal. Chem.* **1993**, *65*, 2766–2769.
(26) Tellez, S.; Forges, N.; Roussin, A.; Hernandez, L. *J. Chromatogr.* **1992**, *581*, 257–266.
(27) O'Shea, T. J.; Weber, P. L.; Bammel, B. P.; Lunte, C. E.; Lunte, S. M.; Smyth, M. R. *J. Chromatogr.* **1992**, *608*, 189–195.
(28) Hernandez, L.; Escalona, J.; Verdeguer, P.; Guzman, N. A. *J. Liq. Chromatogr.* **1993**, *16*, 2149–2160.

were quantitated using linear calibration curves based on peak area. Each calibration curve contained data points at a minimum of six different concentrations, and each curve spanned the range of concentrations found in cerebrospinal fluid samples. Somatostatin (3-6) was used as an internal standard. Because the internal standard contains two primary amine groups due to the presence of a lysine residue, two peaks are observed after derivatization with CBQCA. Peak areas were normalized to the combined area of the two peaks, and this was experimentally determined to give consistent values over a large number of injections. All errors are reported as the standard error of the mean. Linearity was assessed using standard least-squares analysis of peak area vs concentration plots. Detection limits were estimated at 2 times the peak to peak noise by extrapolation from plots of peak height vs concentration. Separation efficiencies were calculated using peak widths at 10% of the peak height. Comparisons of amino acid levels in different samples were made using the standard two-tailed t test.

Derivatization Procedures. Untreated human cerebrospinal fluid was directly derivatized for capillary electrophoresis-LIF analysis. One microliter of internal standard [somatostatin (3-6), 198 μM in H_2O], 5 μL of CBQCA (3 mg/mL in MeOH), and 2 μL of KCN (50 mM in 50 mM borate buffer, pH 9.0) were added to 10 μL of cerebrospinal fluid in 100 μL plastic vials provided for use with the capillary electrophoresis instrument. The vial housings were filled with H_2O in order to reduce solvent evaporation during the reaction time. Solutions were left to react for 2.0 h at room temperature before direct injection from the reaction vial without purification of the reaction products. Solutions containing standards were made in H_2O and were derivatized under conditions identical to those used for cerebrospinal fluid samples. Samples used for examination of amino acid recoveries from cerebrospinal fluid samples were derivatized as described for other cerebrospinal fluid samples except that 5 μL of a standard solution of amino acids was added to 5 μL of cerebrospinal fluid (from CCSF), and 5 μL of H_2O was added to the control cerebrospinal fluid sample (5 μL from CCSF). These solutions were allowed to equilibrate for 15 min at room temperature before addition of CBQCA and KCN.

Chemicals. All chemicals were used as received. Atto-Tag CBQ amine derivatization kit (CBQCA) was purchased from Molecular Probes, Inc. (Eugene, OR). Amino acid standards and γ-amino-n-butyric acid (GABA) were obtained from Sigma Chemical Co. (St. Louis, MO). The synthetic peptide fragment used as an internal standard [somatostatin (3-6), H-Cys-Lys-Asn-Phe-OH] was a gift from Professor Vécsei, Department of Neurology and Psychiatry, Szent-Györgi University Medical School, Szeged, Hungary. All other chemicals used were from E. Merck (Darmstadt, Germany).

Human Cerebrospinal Fluid Samples. The investigation was approved by the Human Ethics Committee at the Faculty of Medicine, Göteborg University, Sweden. All patients gave their informed consent to participate in these studies after the nature of the procedure was fully explained. Lumbar punctures were performed in the L3-4 or L4-5 interspace in the morning and with the patient in a recumbent position. The first 12 mL of the cerebrospinal fluid (3 mL for children) was collected in plastic tubes and gently mixed to avoid gradient effects. Blood samples were collected at the same time. Samples of cerebrospinal fluid and serum were stored at –20 °C until analysis. Quantitative determination of albumin in cerebrospinal fluid and serum was performed by rocket immunoelectrophoresis.[29] The albumin ratio [cerebrospinal fluid albumin (in mg/L) divided by serum albumin (in g/L)] was used as a measure of blood–brain barrier function[30] in order to exclude samples from patients with pathologically increased levels of compounds from serum in their cerebrospinal fluid.

A pooled control sample (pool CCSF) consisted of a pool of 80 human cerebrospinal fluid samples sent to the laboratory for protein analysis. These samples did not exhibit pathological values for albumin or immunoglobulins G and M. All samples in the pool were from individuals over 15 years of age.

The AD age-matched healthy control pool (pool AMCCSF) consisted of five samples (four males and one female; 66–70 years of age; mean age, 67.4 ± 0.7 years) from patients admitted for minor surgery involving spinal anesthesia. None of these patients had histories, symptoms, or signs of psychiatric or neurological disease or systematic disorders. The cognitive status of each patient was evaluated using the Mini-Mental State examination.[31] Individuals with scores below 28 were excluded.

The Alzheimer's type I patient pool (pool ADCSF) consisted of five samples (two males and three females; 60–68 years of age; mean age, 62.8 ± 1.6 years; duration of dementia, mean, 5.8 ± 1.5 years). All patients underwent thorough clinical investigation, including a medical history, physical examination, neurological and psychiatric examinations, screening laboratory tests, electrocardiography, chest roentgenography, electroencephalography, and computer tomography of the brain. Patients with a history of psychiatric or neurological disorders, alcoholism, or major head trauma were excluded, as were those patients with other manifest or suspected primary causes and secondary causes of dementia. Patients with a history of transient ischemic attacks or stroke episodes or occurrence of pronounced vascular factors or with computed tomographic scan findings of infarcts were also excluded. Thus, the diagnosis of "probable AD" was made in accordance with the NINCDS-ADRDA criteria.[32] All of the AD patients belonged to the subgroup AD type I.[33]

Four cerebrospinal fluid samples were obtained from children admitted for investigation of suspected neurological disease. All four children were determined to have normal blood–brain barrier function, and no pathological values were found for routine protein or monoamine metabolite analysis of each child. Patient A was a 4-year-old female with undiagnosed muscular pain. She showed no oligoclonal bands or change in IgG index for her cerebrospinal fluid. No pathological values for albumin, IgG, or IgM were found in her cerebrospinal fluid. She had normal values for β-endorphin and neuropeptide Y. She may suffer from a brain stem lesion.

(29) Laurell, C.-B. *Scand. J. Clin. Lab. Invest.* **1972**, *29*, Suppl. 124, 21–37.
(30) Link, H.; Tibbling, G. *Scand. J. Clin. Lab. Invest.* **1977**, *37*, 391–396.
(31) Folstein, M. F.; Folstein, S. E.; McHugh, P. R. *J. Psychiatry Res.* **1975**, *12*, 189–198.
(32) McKhann, G.; Drachman, D.; Folstein, M.; Katzman, R.; Price, D.; Stadlan, E. M. *Neurology* **1984**, *34*, 939–944.
(33) Blennow, K.; Wallin, A. *J. Geriatr. Psychiatry Neurol.* **1992**, *5*, 106–113.

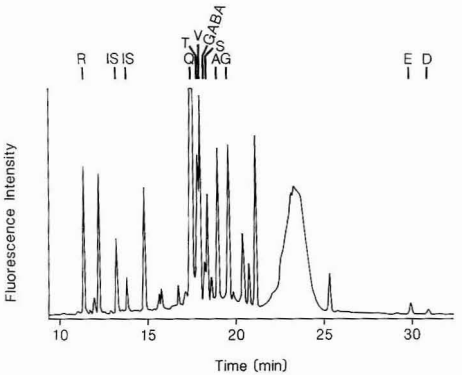

Figure 1. Electropherogram of a CBQCA-derivatized human cerebrospinal fluid sample from a pool of healthy adults (pool CCSF). Peaks that have been identified are R, arginine; Q, glutamine; T, threonine; V, valine; GABA; S, serine; A, alanine; G, glycine; E, glutamic acid; D, aspartic acid. The internal standard (IS) is somatostatin (3-6).

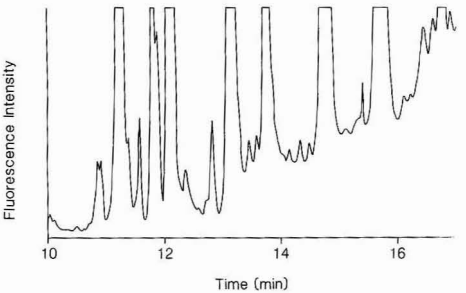

Figure 2. Expanded view of the electropherogram in Figure 1 showing some of the smaller peaks from CBQCA-derivatized human cerebrospinal fluid (pool CCSF).

Patient B was a 3-year-old female diagnosed with progressive epilepsy. She exhibited no intrathecal production of IgG, and no oligoclonal bands were found in her cerebrospinal fluid. She might, however, suffer from some neuroimmunological/neurodegenerative disturbance. Patient C was a 7-year-old female with suspected infantile autism and mental retardation. Patient D was a 9-year-old male who suffered from a headache and a swollen forehead. He exhibited normal values for IgG, β-endorphin, neuropeptide Y, and somatostatin. He had high values for eosinophile cells and IgE in his blood and was diagnosed as having a parasitic infection. Based on these examinations, patients A and D were determined to be "brain healthy."

RESULTS AND DISCUSSION

Separation and Detection of Human Cerebrospinal Fluid. An electropherogram of cerebrospinal fluid from a pool of 80 healthy humans is shown in Figure 1. The sample has been derivatized with CBQCA for LIF detection, and the separation is performed in uncoated fused silica capillaries using a separation buffer consisting of 20% DMSO and 80% 30 mM SDS, 50 mM borate, pH 9.0. Sodium dodecyl sulfate is used in the buffer to enhance the electrophoretic separation by formation of a micellar pseudostationary phase,[34] and the organic modifier, DMSO, is added to increase peak capacity by reduction of electroosmotic flow.[35] Ten amino acid peaks in the electropherogram have been identified by spiking small aliquots of the cerebrospinal fluid sample with the individual amino acids. Figure 2 shows an expanded view of a small region of the electropherogram shown in Figure 1. A large number of smaller peaks and shoulders are apparent in this view of the separation, and approximately 50 peaks are present in the electropherogram in the time window from 10 to 35 min.

Buffer modification with an organic additive has been used to improve peak capacity in the separation, leading to the ability to separate a large number of analytes in a short time period; however, reduction of electroosmostic flow does result in increased analysis time. The final composition of the separation buffer represents a compromise between the amount of information obtained from the separation and the total analysis time. Initial separations using borate buffer at pH 9.0 resolved only a few species with an analysis time of 15 min. Addition of 30 mM SDS to the buffer has been found to greatly enhance the separation of CBQCA-derivatized cerebrospinal fluid, and, as expected, the elution order of the peaks in the separation changed dramatically. Modification of this buffer with DMSO has been found to increase the peak capacity for the separation without dramatically altering the separation selectivity. The final DMSO concentration used (20%) allows a large number of peaks to be resolved in a reasonably short period of time (35 min). The selectivity and analysis time of this separation can be optimized for specific applications by modification of the buffer pH, the micellar phase composition, the organic modifier concentration, and the potential field strength.

An electropherogram of a standard solution of the 10 amino acids identified in the cerebrospinal separation and the internal standard, somatostatin (3-6), is shown in Figure 3. All 10 amino acids, with the exception of GABA and serine, are separated with near base line resolution in less than 35 min. Separation efficiencies obtained range from 120 000 theoretical plates for glutamic acid and aspartic acid up to 190 000 theoretical plates for arginine (Table 1). Concentrations of amino acids in this electropherogram range from 0.2 μM for GABA to 140 μM for threonine. Detection sensitivity varies significantly with amino acid structure as described previously.[13] Detection limits for these 10 amino acids range from 0.29 nM for GABA to 100 nM for threonine as shown in Table 1.

The final derivatization time of 2.0 h has been chosen after examination of reaction times for cerebrospinal fluid samples between 5 min and 7 h. The reaction of amino acids with CBQCA should be nearly complete in 1 h at room temperature,[13] but cerebrospinal fluid contains a large number of different amine-containing compounds at a wide range of concentrations. Structurally different primary amines should react with CBQCA at different rates, and reaction rates for a specific compound will change as the concentration of that

(34) Terabe, S. In *Capillary Electrophoresis Technology*; Guzman, N. A., Ed.; Marcel Dekker, Inc.: New York, 1993; Chapter 2.
(35) Schwer, C.; Kenndler, E. *Anal. Chem.* **1991**, *63*, 1801–1807.

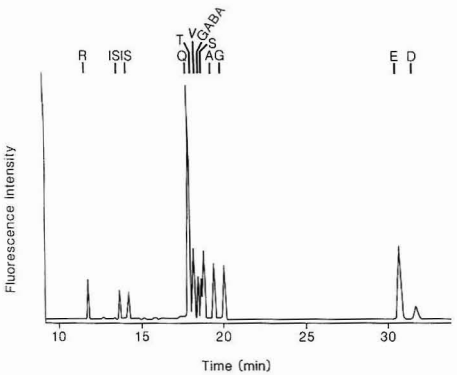

Figure 3. Electropherogram of a standard solution containing the 10 CBQCA-labeled amino acids identified in cerebrospinal fluid samples. Peak identities are as in Figure 1. Analyte concentrations (in μM) are arginine, 6.0; glutamine, 65; threonine, 140; valine, 30; GABA, 0.2; serine, 20; alanine, 20; glycine, 2.5; glutamic acid, 65; aspartic acid, 14; internal standard, 11.

Table 1. Separation Efficiencies, Detection Limits, and Linear Correlation Coefficients for CBQCA-Labeled Amino Acid Standard Solutions

amino acid	separation efficiency, theoretical plates	detection limit (nM), 2 × peak to peak noise	linear correlation coefficient, r
Arg	190 000	68	0.999
Gln	150 000	10	0.999
Thr	150 000	100	0.983
Val	180 000	4.3	0.999
GABA	160 000	0.29	0.999
Ser	140 000	19	0.999
Ala	160 000	16	0.971
Gly	180 000	5.2	0.999
Glu	120 000	58	0.998
Asp	120 000	1.1	0.999

compound changes. Individual peaks in the cerebrospinal fluid electropherogram have been observed to slowly change throughout derivatization times from 5 min to 7 h. The final time of 2.0 h has been chosen because at this time, the response for the 10 peaks that have been identified is sufficiently stable for quantitative analysis. As additional peaks in the cerebrospinal fluid electropherograms are identified and targeted for more detailed analysis, the reaction times for these species will have to be assessed.

Calibration curves have been obtained for standard samples of each of the 10 identified amino acids in order to quantitate these species in human cerebrospinal fluid samples. The curves have been constructed by derivatizing amino acid standards at each concentration and normalizing the corresponding peak areas to the total area of the internal standard peaks. As shown in Table 1, correlation coefficients of 0.971 or greater are obtained over concentration ranges spanning the range of values found for each amino acid determined in human cerebrospinal fluid. The internal standard, somatostatin (3-6), contains two labeling sites due to the presence of lysine and gives two peaks in the electropherogram. Although this internal standard is not ideal, the total area of the two peaks has been found experimentally to give a consistent response for repeated derivatization and injection, and the two peaks

Table 2. Amino Acid Values[a] in Pooled Samples of Human Cerebrospinal Fluid

amino acid	pool CCSF	pool AMCCSF	pool ADCSF
Arg	27.0 ± 5.7	14.6 ± 1.5	18.1 ± 2.2
Gln	670 ± 140	391 ± 43	375 ± 50
Thr	151 ± 46	45.7 ± 8.7	88 ± 34
Val	37 ± 12	10.18 ± 0.74	11.1 ± 4.6
GABA	0.1045 ± 0.0077	0.0919 ± 0.0025	0.0396 ± 0.0053
Ser	36.7 ± 5.3	21.52 ± 0.41	23.1 ± 2.1
Ala	59.3 ± 8.2	45.1 ± 4.2	43.6 ± 4.0
Gly	20.5 ± 4.6	9.53 ± 0.94	19.0 ± 1.9
Glu	8.3 ± 1.5	14.7 ± 1.7	19.9 ± 2.3
Asp	0.127 ± 0.023	0.172 ± 0.018	0.162 ± 0.043

[a] In μmol/L ± SEM, $N = 3$.

are well separated from any major peaks in the cerebrospinal fluid electropherograms. The precision of the 1.0 s pressure injection has also been assessed by making repeated injections of 5×10^{-7} M fluorescein, and a relative standard deviation of 6.3% has been obtained for five injections. Five 5.0 s injections of the same sample give a relative standard deviation of 1.9%, indicating that the precision of the analysis can be improved by increasing the injection time from 1.0 s.

Amino Acid Levels in Different Patient Groups. Amino acid levels have been determined for pools of cerebrospinal fluid from three different patient groups, and the results are shown in Table 2. Pool CCSF consists of cerebrospinal fluid samples from 80 healthy individuals, all more than 15 years of age. Pool AMCCSF consists of cerebrospinal fluid from five healthy individuals showing no signs of dementia and aged 66–70. Pool ADCSF consists of cerebrospinal fluid from five individuals aged 60–68 and diagnosed with Alzheimer's disease. The amino acid levels reported for pool CCSF are similar to values obtained previously for adult human cerebrospinal fluid controls by ion-exchange chromatography and HPLC.[22,23,36,37] The values of threonine and alanine for pool CCSF are considerably higher than those previously reported, and valine and glycine levels are higher than some previously reported values. Threonine and valine are poorly resolved in the cerebrospinal fluid separations, which may lead to inaccurate quantitation, but glycine and alanine appear to be well separated from other large peaks. A wide range of control values has been reported previously for amino acids in cerebrospinal fluid.[37]

Recoveries of amino acids from human cerebrospinal fluid samples have been examined by spiking cerebrospinal fluid samples (from CCSF) with the 10 amino acids that have been identified and quantitated in this study (data not shown). Standard solutions of amino acids have been allowed to equilibrate for 15 min with cerebrospinal fluid prior to addition of CBQCA and KCN, and the amino acid peaks in the electropherograms from these samples have been compared to control samples of cerebrospinal fluid and to samples of amino acid standards. Glutamine, alanine and glycine recoveries are within 5% of 100% recovery. The recovery for glutamic acid is 107%, and recoveries for threonine, valine,

(36) McGale, E. H. F.; Pye, I. F.; Stonier, C.; Hutchinson, E. C.; Aber, G. M. *J. Neurochem.* **1977**, *29*, 291–297.
(37) Spink, D. C.; Swann, J. W.; Snead, O. C.; Waniewski, R. A.; Martin, D. L. *Anal. Biochem.* **1986**, *158*, 79–86.

GABA, serine, and aspartic acid range from 74% to 87%. It is difficult to determine the significance of these results. The reduced recoveries of amino acids may be due to adsorption to other molecules in the cerebrospinal fluid, reaction with other molecules in the samples, or incomplete reaction with CBQCA. Levels of a number of amino acids measured in cerebrospinal fluid including glutamine, GABA, glutamic acid, and aspartic acid have been shown to change with time as a result of storage at room temperature and deproteinization with sulfosalicyclic acid.[37-39] It is clear that a number of different factors can alter recoveries of amino acids in the analysis of cerebrospinal fluid, and uniform sample storage, sample preparation, and sample derivatization are critical in order for comparisons to be made using values determined for amino acids in different samples.

γ-Amino-*n*-butyric acid determination in cerebrospinal fluid has been particularly challenging in the past due to both the instability of GABA levels in cerebrospinal fluid over time and the low level at which this neurotransmitter is found. Degradation of homocarnosine has been shown to cause increases in free GABA levels when untreated cerebrospinal fluid is stored at room temperature,[38] and a very wide range of GABA levels has been reported in human cerebrospinal fluid.[39] The GABA levels reported here fall in the lower end of the range of previously reported values. The ability to determine an amino acid involved in neurotransmission at nanomolar levels in cerebrospinal fluid emphasizes the sensitivity advantage gained by using LIF detection with capillary electrophoresis.

Several differences in amino acid levels are observed between the three different pooled human cerebrospinal fluid samples. The most interesting differences are between the Alzheimer's patient pool and its age-matched control pool, ADCSF and AMCCSF, respectively. Figure 4 shows electropherograms from these two pools. Substantially lower levels of GABA are found in the Alzheimer's pool ($P < 0.001$), and glycine levels are increased in the Alzheimer's pool compared to AMCCSF ($P < 0.02$); however, the glycine level in ADCSF is similar to that for the younger pool CCSF. Basun et al. have reported decreased levels of valine, glycine, and leucine in cerebrospinal fluid from Alzheimer's patients relative to controls, but they did not examine GABA levels.[18] Our results do not agree with those of Basun et al., and it is unclear why this is so. Comparison of the pool of healthy elderly patients (AMCCSF) with the control pool (CCSF) shows significant differences in levels of serine (decreased in AMCCSF, $P < 0.05$) and glutamic acid (increased in AMCCSF, $P < 0.05$). These differences in amino acid levels may be age related, but these age correlations have not been found in other studies.[17,22,36]

Table 3 shows amino acid levels found in the cerebrospinal fluid of four children. The amino acid levels for these children agree very well with recently reported values for cerebrospinal fluid from children with the exception of GABA, which is found at much lower levels in our study.[20] Other reports of GABA levels for children agree with our results.[40] Levels of

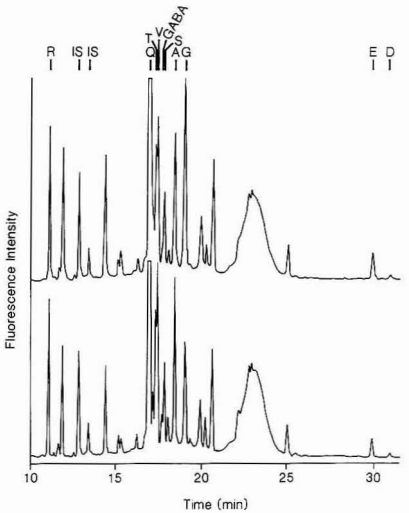

Figure 4. Comparison of electropherograms obtained from separations of CBQCA-derivatized cerebrospinal fluid from a pool of Alzheimer's patients (pool ADCSF, top) and from an age matched control pool (pool AMCCSF, bottom).

each amino acid appear to be similar for each child with the exception of patient D. This patient is a 9-year-old male suffering from a headache and a swollen forehead and has been diagnosed as having a parasitic infection. Compared to the other three children, patient D shows significantly reduced levels of glutamine ($P < 0.05$ for D vs A, B, C, and $\sum$A–C) and threonine ($P < 0.02$ vs A, B, C, and $\sum$A–C). Patient C seems to have an amino acid profile similar to the apparent norms for the other three children. Patients A and B exhibit relatively unexceptional amino acid levels in their cerebrospinal fluid; however, patient A exhibits elevated levels of serine ($P < 0.01$ for A vs B, C, D, and $\sum$B–D), and patient B has relatively low levels of alanine ($P < 0.05$ for B vs A, C, D, and $\sum$A,C,D).

Comparison of amino acid values in adult and elderly cerebrospinal fluid pools to the values obtained for children reveals more age related differences. Alanine levels are lower in cerebrospinal fluid from the children compared to those of the adult pools ($P < 0.02$ for CCSF vs A, B, C, D, and $\sum$A–D, and for AMCCSF vs A, B, C, D, and $\sum$A–D). The levels of aspartic acid are lower in the children relative to those in the elderly control pool ($P < 0.01$ for AMCCSF vs A, B, C, D, and $\sum$A–D), and glutamic acid levels are considerably lower in the samples from children relative to those of both adult cerebrospinal fluid pools ($P < 0.01$ for CCSF vs A, B, C, D, and $\sum$A–D, and for AMCCSF vs A, B, C, D, and $\sum$A–D). Figure 5 shows an unidentified peak which exhibits a strong age dependence for five different cerebrospinal fluid samples. Compared with the cerebrospinal fluid samples from elderly and control patient pools, this peak is highly elevated in the samples from four children ($P < 0.01$ for $\sum$A–D vs CCSF, for $\sum$A–D vs AMCCSF, and for $\sum$A–D vs ADCSF). Relative peak areas found are CCSF, 1.0 ± 0.2; AMCCSF, 1.3 ± 0.1; ADCSF, 0.8 ± 0.2; patients A–D, 14.5. ± 2.7.

(38) Grove, J.; Schechter, P. J.; Tell, G.; Rumbach, L; Marescaux, C.; Warter, J.-M.; Koch-Weser, J. *J. Neurochem.* **1982**, *39*, 1061–1065.
(39) Schechter, P. J.; Sjoerdsma, A. *Neurochem. Res.* **1990**, *15*, 419–423.
(40) Jaeken, J.; Casaer, P.; Haegele, K. D.; Schechter, P. J. *J. Inherited Metab. Dis.* **1990**, *13*, 793–801.

Table 3. Amino Acid Values[a] in Cerebrospinal Fluid from Children

amino acid	patient A	B	C	D
Arg	24.2 ± 3.0	24.3 ± 1.3	21.8 ± 1.4	14.8 ± 2.5
Gln	786 ± 103	411 ± 21	707 ± 51	254 ± 42
Thr	97 ± 16	122.0 ± 5.5	96.2 ± 3.5	28.3 ± 2.2
Val	12.1 ± 3.3	14.8 ± 1.4	18.8 ± 2.3	4.57 ± 0.99
GABA	0.117 ± 0.014	0.0575 ± 0.0097	0.061 ± 0.026	0.059 ± 0.011
Ser	58.1 ± 4.4	26.15 ± 0.42	36.7 ± 2.5	22.4 ± 0.88
Ala	33.4 ± 3.4	20.56 ± 0.35	26.6 ± 1.3	30.7 ± 3.2
Gly	12.2 ± 1.3	8.57 ± 0.44	12.71 ± 0.61	7.38 ± 0.90
Glu	1.22 ± 0.28	1.56 ± 0.39	2.13 ± 0.11	1.610 ± 0.052
Asp	0.094 ± 0.031	0.047 ± 0.015	0.0973 ± 0.0055	0.0671 ± 0.0055

[a] In μmol/L ± SEM, $N = 3$.

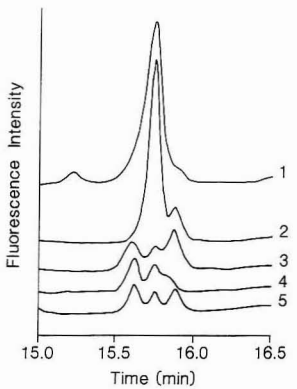

Figure 5. Expanded portions of five electropherograms showing three unidentified peaks. The middle peak appears to be age dependent. Electropherograms: 1, patient A; 2, patient B; 3, pool ADCSF; 4, pool AMCCSF; 5, pool CCSF. Electropherograms for patients C and D are similar to those for patients A and B for these three peaks.

CONCLUSION

Capillary electrophoresis with LIF detection has been used to analyze small molecules in human cerebrospinal fluid samples. This method takes advantage of the separation and sampling capabilities of capillary electrophoresis and the sensitivity of LIF detection. The high peak capacities and short analysis times available with capillary electrophoresis are used to obtain electropherograms containing approximately 50 peaks in less than 35 min. The ability of capillary electrophoresis to analyze relatively unclean samples with few adverse effects allows untreated cerebrospinal fluid to be directly injected after CBQCA derivatization. Use of untreated cerebrospinal fluid is also advantageous because trace analytes such as small peptides are not lost or hydrolyzed during extraction steps or protein precipitation steps prior to analysis. Because capillary electrophoresis uses extremely low volume injections, small amounts of sample are consumed, and in this study only 10 μL of untreated cerebrospinal fluid was used for each separation. Additionally, only small amounts of derivatization reagents are required for analysis of each sample. Precolumn derivatization with CBQCA and laser-induced fluorescence detection are shown to be capable of determining primary amine-containing compounds in cerebrospinal fluid both sensitively and quantitatively, and derivatization with CBQCA does not require product purification prior to analysis.

Preliminary studies of cerebrospinal fluid from Alzheimer's patients and children with different neurological disorders indicate that capillary electrophoresis-LIF analysis of cerebrospinal fluid may be useful for diagnosis of diseases in a clinical setting and study of central nervous system related diseases in the research laboratory. Most of the sample pools used in this study are small, and considerably more samples will have to be analyzed carefully in order to use capillary electrophoresis-LIF to make specific conclusions about neurological disorders such as Alzheimer's disease. However, differences in amino acid levels are clearly observed among the patients and patient pools examined in this study, indicating that disease related differences in cerebrospinal fluid chemical profiles can be examined effectively by capillary electrophoresis-LIF.

ACKNOWLEDGMENT

This work was supported, in part, by grants from the Swedish Medical Research Council (07517), the Faculty of Medicine, Göteborg University, Sweden, Bohuslandstinget, Sweden, the United States National Science Foundation, and the National Institutes of Health, USA. Andrew G. Ewing is a Camille and Henry Dreyfus Teacher-Scholar. The authors want to thank Kaj Blennow and Arne Akefeldt for providing cerebrospinal fluid samples. The authors would also like to thank Beckman Instruments, Göteborg and Stockholm, Sweden for providing the LIF detector used in this study.

Received for review March 24, 1994. Accepted June 27, 1994.[⊗]

[⊗] Abstract published in *Advance ACS Abstracts*, August 1, 1994.

Anal. Chem. **1994,** *66,* 3519–3520

Fabrication of Patterned Sensor Arrays with Aryl Azides on a Polymer-Coated Imaging Optical Fiber Bundle

Karen S. Bronk and David R. Walt*

Max Tishler Laboratory for Organic Chemistry, Department of Chemistry, Tufts University, Medford, Massachusetts 02155

Arrays of sensing regions are photodeposited on the distal tip of a single imaging optical fiber. First, the distal surface of the fiber is spin-coated with a thin film of poly(hydroxyethyl methacrylate). The fluorophor is then derivatized with a photoreactive group and subsequently immobilized in a finite area of the film by discrete illumination. Dye incorporation occurs only in the illuminated areas, creating distinct regions of analyte-sensitive fluorescent dye at the fiber's distal end. This paper describes both the chemistry and the manipulations required to make an optical microarray and demonstrates the technique with pH sensors. The fabrication of a four-sensor array is described along with performance data.

There is presently a tremendous interest in preparing microstructures and arrays for optical storage and sensors. Information storage based on site-selective, photoinduced charge trapping in a thin film of photoconductive material has been developed using photolithographic techniques.[1] Photolithography has also been used to spatially direct the covalent attachment of biomolecules to a glass surface for the formation of biosensor arrays.[2] Site-selective immobilization of biomolecules has also been accomplished using azide derivatives. Aryl azides have been used as cross-linking reagents to study biological macromolecules.[3] Heterobifunctional photolabeling and photocross-linking reagents are being developed to probe ligand binding sites present in biological systems. The cross-linker is first conjugated to the ligand by a thermal reaction. After the ligand binds to its receptor, the photoactive portion of the cross-linker is activated with UV light and reacts with the receptor. Recently, perfluorophenyl azides were used to produce micrometer-scale structures by deep-UV lithography.[4] In this case, a polymeric surface was derivatized site selectively with *N*-hydroxysuccinimide-functionalized perfluorophenyl azides, followed by incorporation of an amine-containing dye or biomolecule. We report here a combination of the two ideas presented above for the production of sensor arrays.

The distal surface of an optical imaging fiber[5] is silanized using 3-(trimethoxysilyl)propyl methacrylate to functionalize the surface with a polymerizable acrylate which facilitates adhesion of the polymer to the glass fiber substrate. A thin layer of poly(hydroxyethyl methacrylate) is then polymerized[6,7] at the distal tip using photochemical polymerization in conjunction with spin coating methods. The monomer solution is prepolymerized to form a viscous oligomer, after which a drop is placed on the tip of a functionalized imaging fiber. The fiber is spun to spread the material uniformly across its surface and is subsequently illuminated with ultraviolet light to complete polymerization and bonding to the fiber.[8] The polymer coating is on the order of 5–10 μm thick.

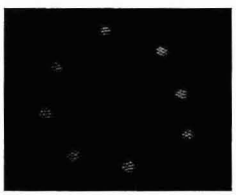

Figure 1. Fluorescence image of an array containing eight pH sensing regions.

5-Azidofluorescein was prepared from 5-aminofluorescein using a literature procedure.[9] The pH-sensitive fluorescein moiety is immobilized within the polymer matrix via azide decomposition to the nitrene.[10] The coated distal surface of the imaging bundle is soaked in a solution of azidofluorescein (2.5 mg/mL in THF), removed, and allowed to dry. A discrete area is then photolyzed by illuminating a small circular area of the 350-μm fiber. Light from a xenon–mercury arc lamp is focused through a precision pinhole and imaged on the proximal surface of the fiber with the appropriate optics. The fiber is held by an *xy*-micropositioner that allows for the translation of the illuminated region across the surface of the fiber. For this study, a 100-μm pinhole and a 15× objective were used to selectively illuminate a 15-μm circular area of

(1) Liu, C.; Pan, H.; Fox, M. A.; Bard, A. J. *Science* **1993,** *261,* 897–899.
(2) Rozsnyai, L. F.; Benson, D. R.; Fodor, S. P. A.; Schultz, P. G. *Angew. Chem., Int. Ed. Engl.* **1992,** *31,* 759–761.
(3) Kamata, M.; Schuster, G. B. *J. Org. Chem.* **1993,** *58,* 5323–5328.
(4) Yan, M.; Cai, S. X.; Wybourne, M. N.; Keana, J. F. J. *Am. Chem. Soc.* **1993,** *115,* 814–816.
(5) Fiber-optic imaging bundles are comprised of thousands of individual fibers melted and drawn together in a coherent manner and are capable of carrying and maintaining an image from one end to the other.
(6) Munkholm, C.; Parkinson, D. R.; Walt, D. R. *J. Am. Chem. Soc.* **1990,** *12,* 2608.
(7) The stock polymerization solution consisted of 10 mL of hydroxyethyl methacrylate (HEMA, opthalmic grade) and 200 μL of ethylene glycol dimethacrylate (EGDMA). Individual solutions are prepared with 1.0 mL of stock and 60 mg of benzoin ethyl ether. The solution is bubbled with N_2 for 15 min before each use.
(8) Into a 6 × 50 mm test tube is placed 100 μL of stock polymerization solution. The solution is stirred and prepolymerized with 366-nm light for 45 s. The resulting oligomer is then dropped onto a fiber and spun at 2000 rpm for 20 s. The fiber is illuminated (366-nm light) for 1.5 min.
(9) Fluoresceinamine was derivatized according to a procedure analogous to that found in: Vanin, E. F; Ji, T. J. *Biochemistry* **1991,** *20,* 6754. The presence of product was verified by TLC and FTIR (N_3, 2140 cm^{-1}).
(10) Irradiation of aryl azides generates either an intermediate dehydroazepine by ring expansion or the nitrene. The former reacts rapidly only with nucleophilic groups. The latter reacts slowly with unactivated hydrogen atoms if it is a triplet nitrene or rapidly inserts into C–H bonds if it is a singlet nitrene.

0003-2700/94/0366-3519$04.50/0
© 1994 American Chemical Society

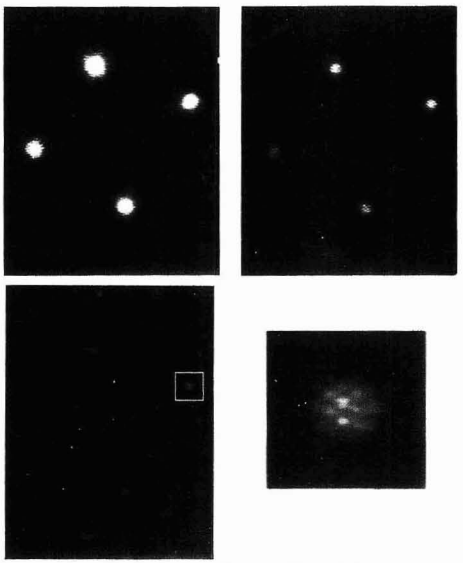

Figure 2. Panels A (top left), B (top right), and C (bottom left): fluorescence images of a four-spot sensor in pH 9.0, 6.5, and 4.5 phosphate buffer, respectively. Panel D (bottom right): enlarged section of panel C showing the individual fibers in the imaging bundle. Each fiber is 3–4 μm in diameter.

the imaging fiber. The circular region is positioned, and the area is illuminated for 10 s with approximately 3-μW white light. The fiber is then repositioned and illuminated at a different location (without further soaking). After immobilization is complete, the fiber tip is soaked in ethanol, followed by phosphate buffer to wash out any unbound dye. Figure 1 shows the resulting pattern observed using our

(11) Instrumentation for fluorescence measurements and imaging is a modified Olympus fluorescence microscope. The microscope has been converted from a vertical to a horizontal configuration. White light from a 75-W xenon lamp is collimated, passed through a 490-nm excitation filter, reflected 90° by a dichroic, and focused on the proximal end of the imaging fiber with a 20× microscope objective. The imaging fiber is held in an *xy*-micropositioner (Spindler and Hoyer) on the microscope stage, which allows for fine focusing. Excitation light is transmitted down the fiber and illuminates the sensing layer, which fluoresces in proportion to analyte concentration. The returning fluorescence light is passed through the dichroic, filtered at the appropriate emission wavelength, and detected by the CCD camera. Ratiometric measurements are obtained by monitoring fluorescence at 530 nm while switching between two excitation filters, 490 and 440 nm, using a computer-controlled filter wheel. The Philips CCD camera contains a 256 × 256 photosensitive element and is coupled to an electronic intensifier, which is connected to a Macintosh Quadra 950 having a video graphic card and image processing software that digitizes and processes the video image. Illumination for imaging purposes is achieved by illuminating the object at the distal end of the fiber with an independent source.

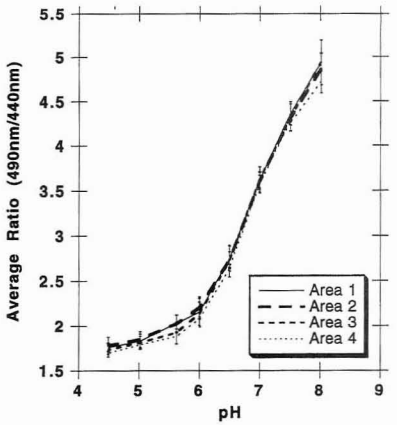

Figure 3. pH titration curves for four pH sensing regions. Each reading is an average of five measurements.

fluorescence imaging instrument.[11] Eight sensing regions of dye were immobilized sequentially on a 350-μm imaging bundle. Figure 2 depicts images of a four-spot sensor in pH 9.0, 6.5, and 4.5 (panels A, B, and C, respectively), showing that photoimmobilization does not destroy fluorescein's pH sensitivity. There is slight blooming occurring during photolysis, probably due to crosstalk between adjacent fibers in the bundle, which is noticeable when examining the pH 9.0 image in which the fluorescent area is larger than 15 μm. The true size of the illuminated area is most closely represented by the pH 4.5 image. The enlarged section (Figure 2, panel D) shows the individual fibers in the imaging bundle; each fiber is 3–4-μm in diameter. The pH titration curves for these four areas are shown in Figure 3. The correlation between the regions is excellent, all having a pK_a of approximately 6.8 pH units.

The technique has many potential applications. A number of different dyes or biomolecules may be derivatized with photoactivatable cross-linkers and subsequently immobilized in a polymer matrix to form a multianalyte sensor array.

ACKNOWLEDGMENT

We gratefully acknowledge the National Institutes of Health (GM-48142) for financial support of this work and Polaroid for instrumentation support. We wish to thank Gerard Barki (Stortz) for the imaging fibers.

Received for review May 27, 1994. Accepted June 27, 1994.®

® Abstract published in *Advance ACS Abstracts,* August 1, 1994.

Anal. Chem. **1994,** *66,* 3521–3524

Solvent Extraction of Radium with Crown Ether Carboxylic Acids

M. K. Beklemishev, Sadik Elshani, and C. M. Wai*

Department of Chemistry, University of Idaho, Moscow, Idaho 83843

The capabilities of a series of 11 crown ether carboxylic acids with different hydrocarbon substituents have been evaluated for solvent extraction of radium in aqueous solutions. The extraction of radium proceeds from alkaline media into chloroform solutions of the crown ethers. The extraction requires no specific counteranions and is reversible with respect to pH. Substitution of *tert*-butyl groups in the benzene rings of *sym*-dibenzo-16-crown-5-oxyacetic acid increases the lipophilicity of the macrocyclic compound and enhances the extraction efficiency for radium. Radium forms a RaL_2-type complex with this *tert*-butyl-substituted crown ether carboxylic acid with a binding constant of $(4.2 \pm 0.7) \times 10^8$.

Crown ethers are a class of selective ligands that form stable complexes with metal ions based primarily on the ionic radius–cavity size compatibility concept.[1] Although numerous reports exist in the literature regarding crown ether extraction of alkaline earth metals, few of them are related to radium. McDowell reported the extraction of radium with dicyclohexano-21-crown-7 in the presence of organocarboxylic acids as counteranions.[2-4] The possibility of transporting radium through a liquid membrane with dicyclohexano-18-crown-6 was also described in a patent.[5] To our knowledge, no other crown ethers have been studied for solvent extraction of radium. Recently, proton ionizable crown ethers with attached carboxylate groups have been shown to effectively extract alkali metals,[6-9] alkaline earth metals,[10,11] and lanthanides.[12] The extraction requires no specific counteranions and is reversible with respect to pH. Thus, metal ions extracted into an organic solvent can be stripped with an acid to regenerate the ligand. There is no report in the literature regarding solvent extraction of radium with ionizable crown ethers.

In this paper, we report the results of extraction of radium (^{226}Ra, $t_{1/2}$ = 1622 y) by a series of crown ether carboxylic acids. The relationships between the extraction efficiency of radium and the structure of the macrocyclic compounds are discussed. The binding constant of Ra^{2+} with a selected crown ether carboxylic acid is also reported. Since radium is a radioactive element, it is not possible to obtain macroamounts of its complexes for stability constant measurements. The partition method, which is one of the appropriate methods for radioisotope binding studies, is used in this investigation.

EXPERIMENTAL SECTION

Reagents and Instruments. A standard Ra^{2+} solution (101.3 μg of ^{226}Ra in 5 M hydrochloric acid solution) was obtained from NIST. Other chemicals used were as follows: chloroform and HCl (Fisher Chemical), glacial acetic acid and boric acid (J. T. Baker), and lithium hydroxide (EM Industries). Macrocyclic compounds **1**, **9**, and **10** were synthesized in our laboratory according to ref 13, compound **8** according to ref 14. The derivatives of dibenzo-16-crown-5-oxyacetic acid were prepared from corresponding *sym*-hydroxydibenzo-16-crown-5 by reactions with corresponding bromo-substituted carboxylic acids in tetrahydrofuran in the presence of NaH. The total yields of these synthetic processes were 60–80%. The compounds were recrystallized four times from hexane. The detailed description of the synthetic procedure, including spectral data, will be given elsewhere.

The solutions were prepared using deionized water obtained from a Milli-Q reagent water system. Measurements of pH were made with an Orion Research Model 701A pH meter with an Orion 91-03 glass semimicroelectrode. Absorption spectra of the reagents were measured with a Perkin-Elmer Lambda 4C UV–visible spectrophotometer. Radium concentrations were measured by γ spectrometry using a high-resolution Ge(Li) detector (EG&G Ortec) with a multichannel analyzer, the data from which were processed by an IBM computer software (EG&G Ortec).

Procedures. For solvent extraction experiments, 1.5 mL of a chloroform solution containing a crown ether and 1.5 mL of the aqueous phase containing radium (0.031 mg/L) and buffer solution were placed in stoppered glass vials (20 mL in volume). Buffers used were lithium borate or lithium acetate (concentration of lithium in the aqueous phase was kept at 0.02 M). Samples were shaken vigorously by hand at room temperature (21 ± 2 °C) for a few minutes, which was shown to give sufficiently constant values of distribution coefficients (D). After phase equilibration, aliquots of 1.0 mL of each

(1) Pedersen, C. J. *Science* **1988,** *241,* 536.
(2) McDowell, W. J.; Case, G. N.; Aldrup, D. W. *Sep. Sci. Technol.* **1983,** *18,* 1483.
(3) McDowell, W. J. *Sep. Sci. Technol.* **1988,** *23,* 1251.
(4) McDowell, W. J.; Arndston, B. A.; Case, G. N. *Solvent Extr. Ion Exch.* **1989,** *7,* 1377.
(5) Rollat, A.; Sabot, J. L.; Burgard, M.; Delloye, T. Eur. Pat. Appl. EP 188394 A1 860723, 1987; *Chem. Abstr.* **1987,** *106,* 35491v.
(6) Walkowiak, W.; Charewicz, W. A.; Kang, S. I.; Yang, I.-W.; Pugia, M.J.; Bartsch, R. A. *Anal. Chem.* **1990,** *62,* 2018.
(7) Walkowiak, W.; Kang, S. I.; Stewart, L. E.; Ndip, G.; Bartsch, R. A. *Anal. Chem.* **1990,** *62,* 2022.
(8) Bartsch, R. A. *Solvent Extr. Ion Exch.* **1989,** *7,* 829.
(9) Bartsch, R. A.; Kim, J. S.; Olsher, U.; Purkiss, D. W.; Ranesh, V.; Dalley, K. N.; Hayashita, T. *Pure Appl. Chem.* **1993,** *65,* 399.
(10) Uhlemann, E.; Geyer, H.; Gloe, K.; Muhl, P. *Anal. Chim. Acta* **1986,** *185,* 279.
(11) Uhlemann, E.; Bukowsky, H.; Dietrich, F.; Gloe, K.; Muhl, P.; Mosler, H. *Anal. Chim. Acta* **1989,** *224,* 47.
(12) Wood, D. W.; Elshani, S.; Du, H. S.; Natale, N. R.; Wai, C. M. *Anal. Chem.* **1993,** *65,* 1350.
(13) Charewicz, W. A.; Heo, G. S.; Bartsch, R. A. *Anal. Chem.* **1982,** *54,* 2094.
(14) Bartsch, R. A.; Heo, G. S.; Kang, S. I.; Liu, Y.; Strzelbicki, J. *J. Org. Chem.* **1982,** *47,* 457.

0003-2700/94/0366-3521$04.50/0
© 1994 American Chemical Society

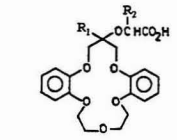

R_1	R_2	Crown
H	H	**1**
Phenyl	H	**2**
n-Decyl	H	**3**
n-Octadecyl	H	**4**
H	n-Dodecyl	**5**
H	n-Tetradecyl	**6**
H	n-Hexadecyl	**7**

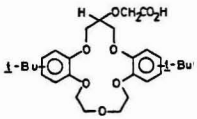

Crown **8**

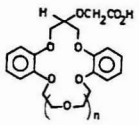

n	Crown	Cycle type
0	**9**	13C4
1	**1**	16C5
2	**10**	19C6
3	**11**	22C7

Figure 1. Structures of the macrocyclic reagents tested for Ra^{2+} extraction.

phase were taken by pipets and placed into 10-mL polyethylene vials for radioactivity measurements. The area of the peak corresponding to ^{226}Ra (186 keV) was taken as the measure of its concentration. Typical standard deviation of the radioactivity measurements was about 10%. After counting, the pH of the aqueous phase was measured.

For reagent partition studies, 2 mL of 0.001 M crown solution in chloroform was shaken in a separatory funnel for 15 min with 20 mL of 0.02 M buffer (lithium acetate or lithium borate, depending on pH). After phase separation and appropriate dilution, the organic solutions were measured at 276.5 nm against chloroform. Standard chloroform solutions of the crown were used for calibration. The aqueous phase was extracted with 4 mL of chloroform with subsequent measurement of absorption to determine the quantity of crown ether in aqueous phase.

RESULTS AND DISCUSSION

The first group of compounds studied was derived from *sym*-dibenzo-16-crown-5-oxyacetic acid with different substitution groups at the pivot position and at the α position of the pendant carboxylate group as shown in Figure 1. For an initial evaluation of crown ether extraction capability, the distribution coefficients of radium (D_{Ra}) at a fixed pH (9.2) were obtained for a series of macrocyclic compounds (1×10^{-3} M in $CHCl_3$). For the substituent R_1 varied at the pivot position (R_2 = H), the following results were observed, indicating that lipophilic substitution enhances the D value of radium significantly:

substituent R_1	H	phenyl	*n*-decyl	*n*-octadecyl
crown no.	**1**	**2**	**3**	**4**
D_{Ra}	0.1	0.5	2.0	0.9

For the substituent in R_2 position of the pendant arm (R_1 = H everywhere), the lipophilic effect is of the same order of magnitude as for R_1:

substituent R_2	H	*n*-dodecyl	*n*-tetradecyl	*n*-hexadecyl
crown no.	**1**	**5**	**6**	**7**
D_{Ra}	0.1	1.1	1.1	2.8

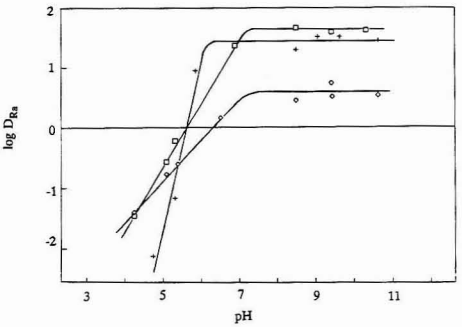

Figure 2. Radium(2+) extraction versus pH with 0.01 M solutions of reagents **8** (□), **7** (+), and **11** (◇) in $CHCl_3$. Aqueous phase contains 0.02 M Li^+ introduced as solutions of buffers: acetate (pH <7) and borate (pH 7–10), and as LiOH (pH >10).

For comparison, stearic acid (n-$C_{16}H_{33}COOH$) was studied as an extractant for radium under the same conditions. With 0.001 M of stearic acid in $CHCl_3$, the D_{Ra} value at pH 9.2 was 0.01, about 2 orders of magnitude less than that observed for crown ether carboxylic acid **7**. The result indicates that the macrocyclic structure is important for binding Ra^{2+} in this system.

Another way of amplifying the lipophilicity is to attach substituents such as *tert*-butyl groups to the benzene rings of the macrocycle host as shown in reagent **8**. This crown ether provides a D value of Ra equal to 23 ± 4 (0.001 M **8** in $CHCl_3$, pH 9), which indicates that this way of enlarging of lipophilicity is preferable with regard to radium extraction than substitution in R_1 or R_2 positions. Crown ether carboxylic acid **8** appears to be highly lipophilic and the most effective extractant for Ra^{2+}.

The effect of cavity size on Ra^{2+} extraction is illustrated by the following results:

ring size	13C4	16C5	19C6	22C7
crown no.	**9**	**1**	**10**	**11**
D_{Ra}	0.1	0.1	0.1	0.5

Crown **11** appears to give a higher D_{Ra} value than the others. It is possible that the 22-crown-7 may provide a more appropriate ring size for Ra^{2+} complexation. We are currently preparing a series of lipophilic crown ether carboxylic acids with 22-crown-7 ring for further investigation.

According to the results of this survey, we have selected three of the crown ether carboxylic acids, including crown **8**, for pH-dependence studies (Figure 2). For all crown reagents,

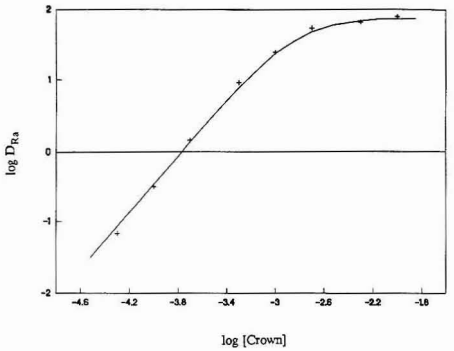

Figure 3. Radium extraction with reagent **8** versus reagent concentration at pH 9.1 (0.02 M lithium borate buffer). Dots are experimental data, and the line is calculated by use of the stability constant K_{12} value, obtained according to eq 15.

extraction of Ra^{2+} from acidic solutions does not occur. The D_{Ra} values begin to increase rapidly in the pH range 4–7. Above pH 8, the D_{Ra} values become almost constant. The results suggest an interesting possibility of regenerating and reusing the crown reagents after radium extraction by stripping the metal with acid. For this purpose, it was necessary to find out whether the crown reagents are lipophilic enough to be kept in the organic phase for repeated use. This appears to be the case for reagent **8**, since its partition coefficient (D_L) between chloroform and water determined by spectrophotometry at 276.5 nm are >160 at pH <5 and 29 at pH 9.1. According to these D_L values, crown ether carboxylic acid **8** dissolves only slightly in basic solutions at pH ~9.

A plot of log D_{Ra} versus log crown **8** concentration at a fixed pH (9.1) is shown in Figure 3. The initial slope of the plot at low crown concentrations is close to 2, suggesting a RaL_2-type complex for Ra^{2+} and crown **8** (L = ionized crown). At high crown concentrations the slope approaches zero. These results allow us to make some attempts to reveal the equilibria taking place within the extraction system. We assume the minimal number of processes that should be taken into account in this system are as follows: complex formation (eqs 1 and 2), complex partition (eq 3), reagent partition (eq 4), and reagent dissociation (eq 5). In the following equations, species with no subscripts refer to aqueous phase and those with the subscript o refer to organic phase.

$$Ra^{2+} + L^- = RaL^+ \quad K_1 \tag{1}$$

$$RaL^+ + L^- = RaL_2 \quad K_2 \tag{2}$$

$$RaL_{2,o} = RaL_2 \quad K_D \tag{3}$$

$$HL_o = HL \quad K_L \tag{3}$$

$$HL = H^+ + L^- \quad K_a \tag{5}$$

It can be shown by use of the approach described below that this set of equilibria leads to a system of n equations with $n + 1$ unknowns. If we are interested in determining stability constants, we have to use optimization procedures instead of a direct solving of the system of equations. To avoid this, we have proposed to regard complex formation as a one-step process:

$$Ra^{2+} + 2L^- = RaL_2 \quad K_{12} \tag{6}$$

Based on this assumption, all of the equilibrium constants (for processes 3–6) are expressed by equations 7–10. The distribution ratio of the metal and equations of material balance for the metal (M) and reagent are given in eqs 11–13, considering that the total concentration of the metal C_M is far less than that of the reagent C_L, pH is much greater than pK_a, and volumes of the aqueous and organic phases are equal:

$$K_D = [ML_2]_o/[ML_2] \tag{7}$$

$$K_L = [HL]_o/[HL] \tag{8}$$

$$K_a = [H^+][L^-]/[HL] \tag{9}$$

$$K_{12} = [ML_2]/[M^{2+}][L^-]^2 \tag{10}$$

$$D_M = [ML_2]_0/([ML_2] + [M^{2+}]) \tag{11}$$

$$C_M = [ML_2]_o + [ML_2] + [M^{2+}] \tag{12}$$

$$C_L = [HL]_o + [L^-] \tag{13}$$

The plateau part of the plot in Figure 3 can be attributed to exhausting complexation of radium and therefore $D_M = K_D$ for $C_L > 0.001$ M. This enables us to evaluate the distribution constant of the complex ($K_D = 75$). Instead of K_L and K_a (i.e., eqs 8 and 9), we may use the expression for the partition coefficient of the crown reagent determined experimentally:

$$D_L = [HL]_o/[L] = K_L[H]/K_a = 29 \tag{14}$$

Thus, we have obtained a system of six equations (7 and 10–14) with six unknowns (equilibrium concentrations and K_{12}). Solving these equations, we obtained the following expression for K_{12}:

$$K_{12} = [(1 + D_L)^2 D_M]/[C_L^2(K_D - D_M)] \tag{15}$$

For stability constant estimation, we may use the five left points of the plot in Figure 3. The points on the plateau, where D_M is close to K_D, cannot be used in the calculation since they imply that K_{12} is approaching infinity according to eq 15. Calculating K_{12} for each point with $D_M < 0.001$ M, we obtain the median value of $K_{12} = (4.2 \pm 0.7) \times 10^8$. This value should be considered as the apparent stability constant at pH 9.1 in 0.02 M lithium borate buffer. For comparison, an analogue of reagent **5** with a shorter alkyl chain binds calcium with $K_{12} = 10^{5.15}$

The proposed minimal set of equilibria for the Ra^{2+}–crown **8** extraction system looks reasonable, and no other noticeable

(15) Bukowsky, H.; Uhlemann, E.; Gloe, K.; Muhl, P. *Polyhedron* **1991**, *10*, 1591.

processes appear to take place in the system. This is supported by the calculation of D_M using the obtained binding constant K_{12} as shown by the solid line in Figure 3. The calculated D_M values agree well with the experimental data. Crown ether carboxylic acid **8** appears to be a strong ligand for extraction of radium from alkaline media.

ACKNOWLEDGMENT

This work was supported by the U.S. Department of Energy under Contract DE-AC06-76RLO 1830 with Pacific Northwest Laboratory at Richland, WA. Pacific Northwest Laboratory is operated for the Department of Energy by Battelle Memorial Institute. We thank Dr. Darrell Fisher at Pacific Northwest Laboratory for his support of this study and for many helpful discussions.

Received for review April 29, 1994. Accepted June 29, 1994.[⊗]

[⊗] Abstract published in *Advance ACS Abstracts,* August 1, 1994.

Anal. Chem. **1994,** *66,* 3525–3527

Diffusion Denuder Method for Sampling Vapor-Phase Nicotine in Mainstream Tobacco Smoke

David A. Lewis, Ian Colbeck,* and Derek C. Mariner

Institute for Environmental Research, University of Essex, Wivenhoe Park, Colchester, CO4 3SQ, U.K.

The partition of nicotine between the vapor and the particulate phases of mainstream tobacco smoke leaving the butt of a cigarette has been determined. Greater than 99% of the nicotine was found to be initially associated with the particles using a technique that draws mainstream tobacco smoke through cylindrical denuders coated with oxalic acid. The rate at which nicotine diffuses from undiluted mainstream tobacco smoke was found to be 38 ± 13 times less than the diffusion rate of nicotine vapor.

Tobacco smoke is a heterogeneous condensation aerosol containing at least 3875 chemical compounds.[1] As soon as the smoke is generated, these compounds are subject to continuous and rapid changes due to reaction and particle effects such as coagulation, dilution, evaporation, and diffusion. To aid fundamental understanding in this field, a technique has been developed and evaluated for investigating the evaporation of nicotine from mainstream tobacco smoke. The technique uses a diffusion denuder which selectively collects diffusing vapor-phase nicotine, while the particulate-phase nicotine is collected by a filter at the exit of the denuder. Diffusion from a vapor flowing through a cylindrical tube has previously been described.[2] Studies of evaporation using denuder tubes are limited, and there is currently no published source describing the kinetics of the evaporation and diffusion of a species from an aerosol flowing through a cylindrical tube. Harrison et al.[3] determined the evaporation rates of ammonium chloride and ammonium nitrate aerosols using denuders. However, an unknown kinetic constraint is reported, and evaporation rates measured were found to be "remarkably low" compared with existing theories of aerosol evaporation. This paper describes the use of denuder techniques to determine the initial percentage of nicotine in the vapor phase and the apparent diffusion coefficient of nicotine after evaporating from the particulate phase of mainstream tobacco smoke.

EXPERIMENTAL SECTION

The diffusion denuders were thin-walled Pyrex tubes, 1.5 m in length. The internal surface of the denuders was coated with oxalic acid[4] by "wetting" the internal surface with a 10% (w/v) solution of oxalic acid in methanol and by drying with filtered air. A coating of approximately 4 mg/cm of denuder was applied, allowing collection of up to 7.4 mg/cm of nicotine, assuming an equimolar reaction. Deionized water was used to remove the coating from a length L at the entrance of the denuder, to ensure that laminar flow had been established before collection could begin. L is given by Ferm[4] to be $L \geq 0.05d(Re)$, where d is the internal diameter of the denuder and Re the Reynolds number. This gives a value for L of greater than or equal to 2.1 cm when sampling is done at a flow rate of 5 $cm^3 s^{-1}$. Denuders were chosen with an internal diameter of 0.78 cm because this ensured a tight fit of a cigarette in the denuder entrance. Denuders of a range of radii have been shown to produce consistent results when normalized with respect to the sampling flow rate and the total sampling time.[5]

The sampling procedure drew mainstream tobacco smoke from a cigarette through a denuder by means of a pump attached to the exit of the denuder. Some of the variability between commercially available cigarettes was eliminated by using cigarettes selected to be ±10% of the mean weight and impedance and conditioning them at standard temperature and humidity. The desired rate was achieved and monitored by means of a needle valve and a bubble-type flow meter positioned in-line between the denuder and the pump. Smoke particulate leaving the denuder was collected by a glass fiber filter. Gravitational sedimentation of the mainstream tobacco smoke particles was eliminated by orienting the denuder vertically. The maximum collection of particulate-phase (rather than vapor-phase) nicotine by the denuder was determined to be less than 0.5% (in agreement with Gormley and Kennedy's equation[2]) by comparing the mass of solanesol (a very low volatility constituent of tobacco smoke) collected by the denuder and by the filter. Nicotine loss by evaporation from the filter at the exit of the denuder tube was found to be less than 0.05% of the nicotine mass on the filter using XAD-4 sample tubes (SKC Ltd., Dorset, U.K.) positioned downstream of the filter.[6]

Following sampling of the mainstream tobacco smoke, the extraction of nicotine from the denuder wall was achieved by dividing the denuder into 5-cm sections. Each section was placed in a glass-stoppered test tube and shaken for 1 min with 5 cm^3 of sodium hydroxide (5 M) and 1 cm^3 of dichloromethane containing an internal standard of quinoline. The organic phase of each sample was removed with a micropipet and stored in 2-cm^3 autosampler vials. Nicotine was extracted from the filters by shaking for 30 min in 20 cm^3 of 2-propanol, containing an internal standard of quinoline.

Gas Chromatography. The nicotine concentration in each extract was determined by gas chromatography using a

(1) Dube, M. F.; Green, C. R. *Recent Adv. Tob. Sci.* **1982,** *8,* 42–102.
(2) Gormley, P. G.; Kennedy, M. *Proc. R. Ir. Acad., Sect. A* **1949,** *52,* 163–169.
(3) Harrison, R. M.; Sturges, W. T.; Kitto, A.-M. N.; Yuanqian, L. *Atmos. Environ.* **1990,** *24,* 1883–1888.
(4) Ferm, M. *Atmos. Environ.* **1979,** *13,* 1385–1393.
(5) Lewis, D. A. Ph.D. Thesis, University of Essex, Colchester, U.K., 1994; Chapter 4.
(6) Ogden, M. W. *J.-Assoc. Off. Anal. Chem.* **1989,** *72,* 1002–1006.

0003-2700/94/0366-3525$04.50/0
© 1994 American Chemical Society

Table 1. Results from Nine Experiments at Three Sampling Flow Rates

sampling rate, $cm^3\ s^{-1}$	total nicotine entering the denuder, μg	nicotine initially in the vapour phase, %	apparent diffusion coefficient of evaporating nicotine, $cm^2\ s^{-1}$	R^2
5.11 ± 0.02	2115 ± 10	0.6 ± 0.1	0.0011 ± 0.0018	0.993
	1867 ± 10	0.6 ± 0.1	0.0030 ± 0.0009	0.997
	2000 ± 10	0.9 ± 0.1	0.0032 ± 0.0005	0.990
3.33 ± 0.01	1344 ± 10	0.9 ± 0.3	0.0021 ± 0.0003	0.983
	1501 ± 10	0.5 ± 0.1	0.0019 ± 0.0003	0.995
	1227 ± 10	0.7 ± 0.4	0.0017 ± 0.0003	0.930
1.79 ± 0.01	846 ± 10	1.2 ± 0.7	0.0012 ± 0.0004	0.971
	986 ± 10	1.5 ± 0.8	0.0018 ± 0.0004	0.982
	1174 ± 10	1.2 ± 1.8	0.0013 ± 0.0005	0.932

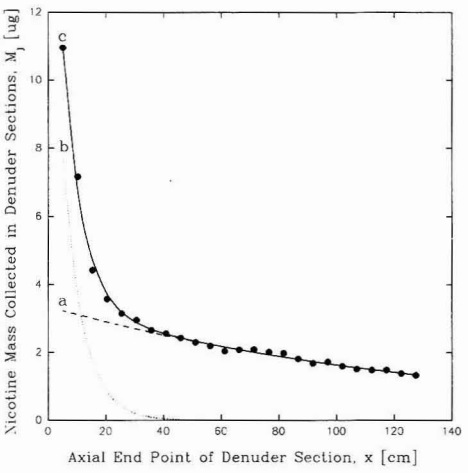

Figure 1. Nicotine mass collected by denuder as a function of distance along the denuder: (a) mass collected due to the diffusion of nicotine originally in the particulate phase; (b) mass collected due to the diffusion of nicotine originally in the vapor phase; (c) total nicotine mass collected (a + b).

Hewlett-Packard 5880A with a nitrogen–phosphorous detector (detector temperature, 250 °C). A 1-μL aliquot of each sample was injected, using a cold, on-column injection, onto a 10-m × 0.53-mm CP-sil-5-CB capillary column (Chrompak, London, U.K.). The gas flow rates were hydrogen, 3 cm^3/min; helium (carrier gas), 3 cm^3/min; helium (make-up), 20 cm^3/min; and air, 100 cm^3/min. The oven temperature program was as follows: initial temperature of 40 °C for 1 min, increasing at 15 deg/min to 200 °C, which was held for 3 min. The detection limit was 0.1 $\mu g\ cm^{-3}$, and the recoveries from denuder and filter extracts were 98 ± 1.5% and 99.8 ± 0.5%, respectively.

RESULTS AND DISCUSSION

Figure 1 shows the nicotine mass collected in denuder sections at increasing axial distances from the entrance of the denuder. Mainstream tobacco smoke from three consecutive cigarettes was sampled by a single denuder, with a sampling flow rate of 5.11 ± 0.02 $cm^3\ s^{-1}$. Variations in the temperature and humidity of the mainstream tobacco smoke were minimized by sampling from only the first 2 cm of each cigarette, which also ensured that the smoke was at ambient temperature before entering the denuder.[7] The partition of nicotine between the vapor phase and the particulate phase of the mainstream tobacco smoke was calculated by fitting to experimental data the sum of two forms of an equation given by Durham and Stockburger,[8] which each calculate the mass of diffusing vapor collected in a sectioned denuder. The mass reactive vapor collected by the jth denuder section can be written as

$$m_j = k \exp\left(\frac{-11.49Dx}{Q}\right) \quad (1)$$

where D is the diffusion coefficient of the vapor in $cm^2\ s^{-1}$, x is the axial distance of the end point of the jth denuder section from the entrance of the reactive denduer tube in cm, Q is the volumetric flow rate through the denuder in $cm^3\ s^{-1}$, and k is given by

$$k = 0.819 m_T\left(-1 + \exp\left(\frac{11.49D\delta x}{Q}\right)\right) \quad (2)$$

where δx is the length of each discrete section in cm and m_T is the total amount of the reactive vapor entering the denuder.

Preliminary diffusion denuder experiments using a particulate-free nicotine vapor source found that most of the nicotine vapor (>99.8%) was collected when $x/Q < 8$ and that nicotine vapor had a diffusion coefficient of 0.065 ± 0.002 $cm^3\ s^{-1}$, which compares favorably with the value (0.065 ± 0.006 $cm^2\ s^{-1}$) given by Eatough et al.[9] The nicotine mass in the denuder sections, for $x/Q > 8$, must therefore be exclusively due to diffusing nicotine vapor which has evaporated from the mainstream tobacco smoke particles. This mass can be represented by eq 3,

$$m_j = k_A \exp\left(\frac{-11.49D_A x}{Q}\right) \quad (3)$$

which is analogous to eq 1. D_A is the apparent nicotine diffusion coefficient and represents the rate at which nicotine diffuses from the surface of the smoke particles to the wall of the denuder, dependent upon the partial pressure of nicotine at the surface of the particles and the immediate environment of the particles. k_A is dependent upon the initial rate of nicotine evaporation for the surface of the particles. The total nicotine mass collected on the wall of the denuder is the sum of eqs 1 and 3; D_A and k_A can be determined by the line that best

(7) Gyatt, A. R.; Baldry, A. G. *Beitr. Tabakforsch.* **1988**, *14*, 119–126.
(8) Durham, J. L.; Stockburger, L. *Atmos. Environ.* **1986**, *20*, 559–563.
(9) Eatough, D. J.; Benner, C. L.; Bayona, J. M.; Richards, G.; Lamb, J. D.; Lee, M. L.; Lewis, E. A.; Hansen, L. D. *Environ. Sci. Technol.* **1989**, *23*, 679–687.

fits the data for $x/Q > 8$, D is the vapor equivalent nicotine diffusion coefficient (0.065 ± 0.002 cm^2 s^{-1}), and k is determined by the line that best fits the data (with eq 3 subtracted) for $x/Q < 8$. Equations 1 and 3 and their sum (correlation coefficient, $R^2 = 0.990$) are illustrated in Figure 1.

The nicotine entering the denuder in the vapor phase, m_T, and the apparent diffusion coefficients, D_A, for nine experiments are given in Table 1. The nicotine initially in the vapor phase, m_T, is represented as a proportion of the total nicotine entering the denuder (the sum of the nicotine collected by the denuder and the filter at the end of the denuder). Results at three flow rates are given, showing the tendency for the percentage of nicotine in the vapor phase to decrease with increasing sample flow rates. The total nicotine mass entering the denuder was determined by summation of the mass collected by the denuder and the filter. The correlation coefficient, R^2, representing the fit of the sum of eqs 1 and 3 to the data, is given for each experiment.

The averaged value for the percentage of nicotine entering the denuder in the vapor phase for these experiments was 0.9 ± 0.3%, and the apparent diffusion coefficient was 0.0019 ± 0.0007 cm^3 s^{-1}, which is 38 ± 13 times less than the diffusion coefficient of nicotine vapor.

Received for review February 10, 1994. Accepted June 30, 1994.®

® Abstract published in *Advance ACS Abstracts*, August 1, 1994.

Anal. Chem. **1994,** *66,* 3528–3532

Reactivation and Stability of Pyrolytic Carbon Film Electrodes on Macor Substrates

Jill K. Clark, William A. Schilling, Charles A. Wijayawardhana, and Paula R. Melaragno*

Ebaugh Laboratories, Denison University, Granville, Ohio 43023

The stability of pyrolytic carbon film electrodes based on Macor substrates was evaluated. Electrode activity, estimated via cyclic voltammetry of ferricyanide, was virtually unchanged after 120 min in solution (k° = 0.018 cm/s). The response decayed by less than 40% after 20 h in solution. Electrodes were deactivated by air exposure but could be restored to good levels of performance via electrode anodization (to k° = 0.005 cm/s). Other reactivation methods were evaluated. Heat treatment in an Ar atmosphere and an acetone wash were nearly as effective as anodization but were less reliable. Polishing was relatively ineffective.

Pyrolytic carbon films (PCFs) are potentially quite useful electrode surfaces. Rates of electron transfer equivalent to or even better than those obtained at conventionally polished glassy carbon (GC) electrode can be obtained without electrode pretreatment.[1-4] Electrode capacitance (and thus the level of residual current) is ordinarily quite low, on the order of 10 μF/cm^2.[1,2]

PCF electrodes based on Macor substrates are among those which display good charge transfer characteristics, although the capacitance is somewhat larger and more variable than that reported for other substrates.[4] And *unlike* the quartz and GC substrates typically employed for film work, Macor can be machined using ordinary high-speed tools. Therefore, PCF electrodes based on this substrate should be uniquely well-suited for construction of electrodes of unusual size and shape. However, routine use of this type of electrode required that we address two additional concerns.

The first issue was electrode activity over long periods of time in solution. Ideally, the initial response would be maintained over several h, which would facilitate process monitoring and detector applications. In this paper, we demonstrate that for Macor-based films, performance is maintained for longer than 21 h.

The second issue was that of film reactivation. Although the PCF can be completely removed from the substrate by heating in air and can then be replaced by fresh film, this is a time-consuming procedure. We evaluated other convenient methods of electrode reactivation, including electrochemical anodization, heating in an inert atmosphere, an acetone "wash", and, finally, polishing. Electrochemical anodization was found to be the most effective of these methods, restoring films to activity levels comparable to that reported for conventionally polished GC electrode.[5]

EXPERIMENTAL SECTION

Chemicals. All chemicals were reagent grade. Nanopure water was used in preparation of solutions. Ferricyanide solutions were 0.5–1.0 mM in 1.0 M KCl. Macor was obtained from AstroMet Associates Inc. (Cincinnati, OH) in rods $^1/_8$ in. in diameter which were cut to desired lengths using ordinary high-speed tools and a water soluble coolant. Natural gas was taken from the common laboratory line and used without further purification. The composition was 95.24% methane, 2.43% ethane, 0.50% propane, 0.10% isobutane, 0.10% *n*-butane, 0.04% isopentane, 0.03% *n*-pentane, 0.14% hexanes and higher order hydrocarbons, 0.45% N_2, 0.96% CO_2 and 0.10% *tert*-butanethiol. Argon was of 99.4% purity.

Pyrolysis. All films were fabricated at temperatures of 926 °C for a time of 3 h. The procedure was the same as described earlier[4] except for the following two changes. First, gas flow rates were controlled via a two tube proportioner (Matheson, Model 7392T). Second, pyrolysis was intentionally performed in a "dirty" furnace liner, i.e., a liner which contained residual film left over from previous pyrolyses. Films made in the presence of residual film were much more reliable than those made in clean quartz liners. Reliability of performance was gauged by the range of ΔE_p observed for the ferri-/ferrocyanide redox couple. For clean liners, the range was 65–104 mV (N = 10). For "dirty" liners the range was 64–77 mV (N = 23).

Electrochemistry. Two coats of black Dennison marker were used to insulate the sides of the Macor-based film such that only the bottom planar disk was exposed to solution. Use of this type of insulation in aqueous solution has been described previously.[6] A flat current base line was obtained when the entire film surface was coated (including the bottom planar disk) in the presence of ferricyanide. This verified that the insulation was sufficient.

Care was taken to minimize film exposure to air prior to analysis. The minimum exposure was fixed by the time required to insulate the sides of the electrode, 2–6 min. No significant differences in performance were observed over this time range. Significant loss of performance was observed when films were exposed to air for longer than 6 min.

A Cypress Systems Model CS1090 electrochemical analyzer was used for cyclic voltammetry. The reference was a BAS Ag/AgCl, 3 M NaCl electrode, and a Pt wire served as the auxiliary. A scan rate of 0.100 V/s was used throughout this work. The system software was used to determine $k^\circ/\sqrt{D}$ from the separation between the anodic and cathodic

(1) Beilby, A.; Carlsson, A. *J. Electroanal. Chem.* **1988,** *248,* 283–304.
(2) Eriksson, A.; Norekrans, A.; Carlsson, J. *J. Electroanal. Chem.* **1992,** *324,* 291–305.
(3) McFadden, C.; Melaragno, P.; Davis, J. *Anal. Chem.* **1990,** *62,* 742–746.
(4) McFadden, C.; Russell, L.; Melaragno, P.; Davis, J. *Anal. Chem.* **1992,** *64,* 1521–1527.
(5) McCreery, R. L. In *Electroanalytical Chemistry*; Bard, A. J., Ed.; Marcel Dekker, Inc.: New York, 1991; Vol. 17, pp 221–374.
(6) Sternitzke, K.; McCreery, R. *Anal. Chem.* **1990,** *62,* 1339–1344.

0003-2700/94/0366-3528$04.50/0
© 1994 American Chemical Society

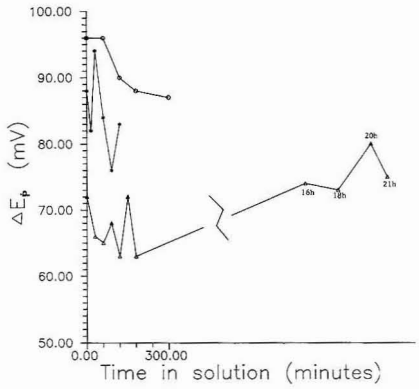

Figure 1. ΔE_p for ferri-/ferrocyanide as a function of time in solution at GC (*) and PCF when fresh (Δ) and when reactivated via ECT (O).

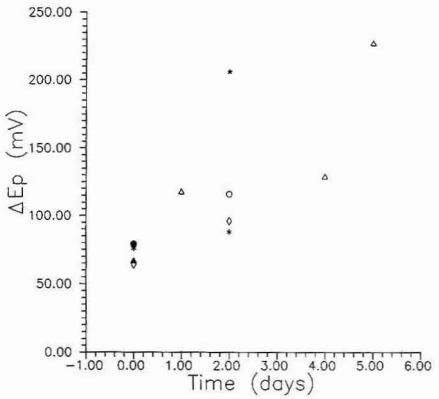

Figure 2. ΔE_p for ferri-/ferrocyanide at five PCF electrodes as a function of number of days of air exposure. Symbols *, O, Δ, ★, ◊ designate different electrodes.

peaks as described by Nicholson.[7] The diffusion coefficient used for ferricyanide was 0.677×10^{-5} cm²/s.[8] All electrochemical measurements were made at room temperature.

Electrode Treatment. Electrochemical treatment (ECT) consisted of a 90 s anodization at potentials in the range of 1.0–1.8 V followed by cathodization for ca. 30 s at –0.100 V. The solvent was 1 M KNO_3. Heat treatment consisted of heating the films in the tube furnace at ca. 600 °C for 2 h under an argon atmosphere. Polishing was done by hand, using 0.05 μM alumina (Beuler) on glass covered with a polishing cloth. In a few cases, the polishing cloth was not used. Polishing was ordinarily followed by ultrasonication in or copious rinsing with nanopure water.

RESULTS/DISCUSSION

Electrodes were evaluated by comparing ΔE_p obtained via cyclic voltammetry for the ferri-/ferrocyanide redox couple. This parameter can be related to $k°$, the standard rate constant which governs the heterogeneous electron transfer, after the method of Nicholson.[7] Although this particular redox couple may not be the best choice for evaluating ease of electron transfer,[9] it has been the most widely used and continues to serve as a useful means of comparing different electrodes.

Film Stability. The stability of fresh films in solution was excellent. As can be seen in Figure 1, over 120 min of continuous exposure to ferricyanide solution, ΔE_p for the ferri-/ferrocyanide redox couple varied over a range of only 10 mV. We observed slightly more variation for a conventionally polished GC electrode, and these results are also shown in Figure 1. As a point of comparison, very active GC electrodes ($k°$ ca. 0.2 cm/s) are also quite stable in solution, with less than 10% decrease in $k°$ over 200 min in Nanopure electrolyte.[10] It is important to note, in this case at least, that the PCF electrode exhibited a faster rate of electron transfer than the GC electrode at all times.

After 21 h in solution, ΔE_p did increase but only slightly. The maximum value observed (at 20 h) was 80 mV, which corresponds to $k°$ of 0.011 cm/s. This compares quite well to the initial value for this particular PCF electrode (0.018 cm/s). Semiintegral analysis of the CVs showed no evidence of ferricyanide adsorption.[11]

Films based on Macor were much more stable than those described by Erikkson et. al., who report that $k°$ for films on prepolished GC substrates decreased to 15% of the original value in just 300 min of continuous exposure, with much of that occurring in the first 100 min.[2] These authors attribute the dramatic change to a surface rearrangement process which increases the proportion of basal to edge plane carbon. Perhaps in the case of Macor substrate, the film adheres more tightly to the rougher, machined surface, preventing such a rearrangement.

Films were much less stable with respect to air exposure and in most cases were deactivated overnight. Deactivation was indicated by two voltammetric features: an increase in ΔE_p of 20 mV or more and a marked decrease in peak current.

In Figure 2, ΔE_p for several PCF electrodes is tracked for up to 5 days of air exposure. All five electrodes exhibit ΔE_p of <79 mV ($k°$ ca. 10^{-2}) initially. After 48 h of air exposure, ΔE_p had increased in all cases to more than 88 mV, corresponding to a $k°$ on the order of 10^{-3} cm/s. The rate of deactivation is not reproducible, even when the electrodes exhibit essentially the same initial activity. For example, note O and ★ at 0 and 2 days.

The change in appearance of the CV itself upon deactivation can be seen in Figure 3, by comparison of the initial CV (solid line) and that obtained after prolonged air exposure (dash-dot line). The decrease in i_{pa} and i_{pc} combined with the increase in ΔE_p results in an extended, less well defined voltammetric wave.

Reactivation. The question of reactivation has not been systematically addressed for carbon films on any substrate. However, "preconditioning" via electrode anodization,[1,12]

(7) Nicholson, R. *Anal. Chem.* **1965**, *37*, 1351.
(8) Arvia, A. J.; Bazan, J. C.; Carrozza, J. S. W. *Electrochim. Acta.* **1968**, *13*, 81–90.
(9) Kneten, K.; McCreery, R. *Anal. Chem.* **1992**, *64*, 2518–2524.
(10) Poon, M.; McCreery, R. *Anal. Chem.* **1986**, *58*, 2745–2750.
(11) Bowling, R.; McCreery, R. *Anal. Chem.* **1988**, *60*, 605–608.

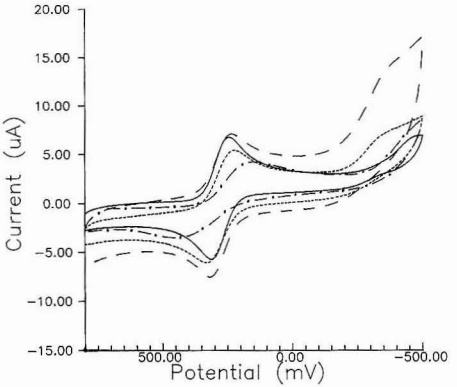

Figure 3. CV of ferricyanide at fresh PCF electrode (—), deactivated (– · –), and after anodization at 1.5 (—) and 1.65 V (– – –).

Table 1

treatment	N^a	ΔE_p (mV)^b	RSD (%)^c	$k°$ (cm/s)^d
ECT	6	101	9.9	0.005
HT	4	130	2.5	0.003
acetone	4	122	16	0.003
polish	6	220	32	0.001
fresh films	23	72	5.5	0.018

[a] Number of electrodes. [b] Average ΔE_p for ferri/ferrocyanide at scan rate of 0.100 V/s. [c] Relative standard deviation. [d] Corresponding to average ΔE_p.

potential cycling,[13] or an organic solvent "wash" [14] has been used to improve the *initial* performance of some films.

In this work, several methods of reactivating "aged" films were investigated. These included electrochemical treatment (ECT), heat treatment in an inert atmosphere (HT), polishing, and an acetone wash. The first three of these methods are commonly used to reactivate GC surfaces,[5] so they were obvious choices here. The acetone effect was actually observed by accident during the course of this work. However, in retrospect, this should not have been a surprise, since Lundstrom routinely washed with an organic solvent (CH_2Cl_2/ethanol) *prior* to analysis, ostensibly to activate the surface.[14]

In general, films were considered to be "aged" and thus good candidates for reactivation when ΔE_p for the ferri-/ferrocyanide couple was 200 mV or greater. By chance, the electrodes which underwent heat treatment were an exception to this rule, exhibiting an average ΔE_p prior to reactivation of 143 mV. Without exception, all electrodes chosen for treatment exhibited extended, poorly defined voltammetric waves characteristic of deactivated electrodes.

Table 1 contains average values of ΔE_p obtained after each reactivation method along with the relative standard deviation (RSD). Also given is $k°$ corresponding to each average ΔE_p. Values obtained for fresh films are given here for comparison. These are similar to those obtained previously.[4]

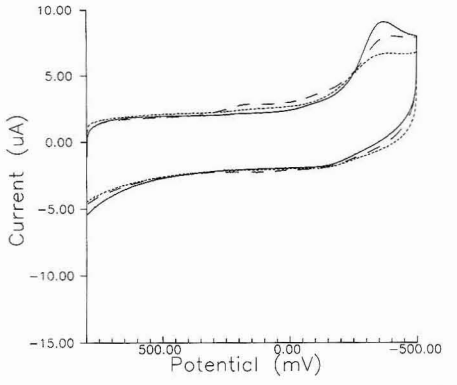

Figure 4. Residual current at fresh PCF, initial (—) and second potential scan (—) and after 6 min of air exposure (– – –). Solvent was 1 M KCl.

Electrochemical Treatment (ECT). This method was the most effective and reliable means of restoring electrode activity, as can be seen by inspection of the data in Table 1. ECT yielded ΔE_p values closest to those for fresh films, with the smallest RSD. The original activity was not totally regained, as $k°$ was reduced by a factor of 3.5. However, $k°$ was identical to the value most often quoted for conventionally polished GC.[5] In other words, reactivated films were comparable to conventionally polished GC, at least for the ferri-/ferrocyanide redox couple.

The degree of reactivation depended upon the anodization voltage. Voltages in the range of 1.0–1.8 V were investigated. At 1.0 V or less, essentially no activation occurred. At anodization voltages of 1.7 V or greater, the increase in background current was prohibitively large. The best compromise between activation and increased background current was obtained for anodization voltages of 1.65 V.

The extent of reactivation is evident in Figure 3, where the CV for the deactivated electrode (dash-dot line) is shown with that obtained after anodization at 1.5 (dotted line) and 1.65 V (dashed line). Kinetically, the result after 1.5 V was a little sluggish in comparison to that obtained when the film was fresh (the solid line in Figure 3). The increase in background was slight, except at potentials negative of –300 mV. After anodization at 1.65 V, the same film showed improved kinetics but increased background over the entire potential range.

The background peak in the vicinity of –300 mV evident in Figure 3 after anodization was characteristic of electrochemically treated films and was frequently observed for fresh films as well. In the case of treated films, it can be attributed to reduction of a surface oxide produced during the anodization step. It was not present prior to ECT, as can be seen from Figure 3. And indeed, the formation of such oxides during anodization is well documented for other carbon materials like GC and HOPG.[5] In the case of fresh films, the surface oxide would seem to be the product of air oxidation. This is demonstrated by the series of CVs in Figure 4. This particular film exhibited an unusually pronounced cathodic peak at –310 mV after just 3 min of air exposure (solid line). The peak height decreased upon the second potential scan (dotted line)

(12) Rojo, A.; Rosenstratten, A.; Anjo, D. *Anal. Chem.* **1986**, *58*, 2988–2991.
(13) Blaedel, W.; Mabbott, G. *Anal. Chem.* **1978**, *50*, 933–936.
(14) Lundstrom, K. *Anal. Chim. Acta* **1983**, *146*, 97–108.

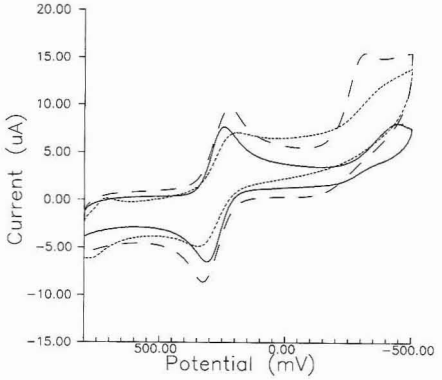

Figure 5. CV of ferricyanide at PCF electrode, fresh (—), deactivated (—), and reactivated via HT (– – –).

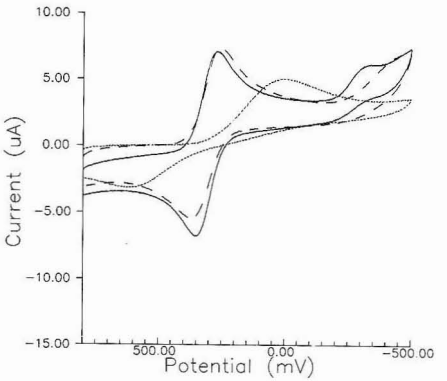

Figure 6. CV of ferricyanide at PCF electrode when fresh (—), after 20 days of storage in air (—), and after restoration via acetone wash (– – –).

but increased again upon several min more exposure to air (dashed line). It is important to emphasize that no correlation between film activity and the magnitude of the cathodic peak in the background was observed.

Films reactivated via ECT exhibited good stability in solution over at least 300 min, as can be seen from the data included in Figure 1. In addition, after ECT, films were less sensitive to air effects. For example, ΔE_p increased by only about 10 mV for one film after 3 days storage in air. After an additional anodization, virtually no decline in performance was observed after 5 days of air exposure. The same effect has been noted for GC in solution[15] and was attributed to the formation of an "oxide" layer which presumably affords some protection against adsorption of organic materials. The same effect may be important here.

Films could be reactivated via ECT several times but with a concomitant increase in current background. One film was reactivated five times. Each time, $k°$ returned to a value of 0.005 cm/s, but the background gradually increased until the peaks were nearly obscured.

We found that initial rates of electron transfer were not improved by ECT. This was surprising because it contradicted an earlier report[1] in which rates of electron transfer as fast as 0.1 cm/s were observed after anodization at 1.65 V. However, these authors also note that the PCF film appeared to be at least partially removed by anodization. Therefore, their result is probably due to activation of the underlying prepolished GC substrate. No film loss was observed for Macor-based films, even upon multiple anodization. Again, this may reflect better adherence between the film and the relatively rough Macor surface.

Other Treatment Methods. Heat treatment (HT) in an argon atmosphere was less effective and reliable than ECT, as can be seen from the average ΔE_p and RSD given in Table 1. In addition, residual current increased significantly upon HT, as shown in Figure 5. The cathodic peak in the vicinity of –300 mV was quite pronounced relative to that observed when the film was fresh and after the film was deactivated by air exposure. Finally, some film loss was visible after the HT process. These last two points are consistent with film oxidation, which would occur during HT if trace O_2 was present in the system.

An acetone wash was a surprisingly effective means of restoring film activity. This can be seen from ΔE_p and RSD values given in Table 1. A significant advantage of this reactivation method was that residual current levels were not significantly increased upon the wash, either prior to the ferricyanide reduction peak or in the vicinity of –300 mV. This can be seen by inspection of the CVs in Figure 6.

Surface cleansing would seem to be the obvious explanation for acetone activation. And, as noted earlier, an organic wash solvent has been used prior to initial analysis for this express purpose.[14] However, this mechanism is inconsistent with two experimental observations. First, the acetone wash was effective only once. When films were allowed to degrade after an initial acetone treatment and were then retreated, the results were quite unimpressive, with average ΔE_p of 327 mV (RSD of 36%, $N = 4$). Second, an acetone wash *deactivated* fresh films. For two fresh films, ΔE_p values of 626 and 804 mV were obtained, values well outside the ordinary range of results. These results indicate that more than simple surface cleansing is involved.

Polishing was the least effective and reliable reactivation method (Table 1). Polishing without a polishing cloth gave similarly poor results. In addition, without the cloth, some film was removed upon polishing. Residual current levels increased only slightly with respect to the inactive film.

CONCLUSIONS

Macor-based PCF electrodes are viable alternatives to GC for routine analysis and should be particularly useful in applications requiring an electrode of unique size and shape. These electrodes display initial rates of electron transfer which are quite good, and these are maintained over long periods of solution exposure. Once films become inactive, they can be successfully reactivated via ECT. ECT is a convenient in situ method which does not require mechanical or optical access

(15) Wang, J.; Tuzhi, P. *Anal. Chem.* **1986**, *58*, 1787–1790.

to the surface like polishing or laser ablation, which is an important consideration for some geometries, particularly flow-through types.

One disadvantage of using Macor-based PCF electrodes is that residual current levels are somewhat higher than those observed at comparable electrode materials. As previously reported,[4] residual currents on the order of 1 μA are typically obtained at a $^1/_8$ in. diameter disk. This translates into a capacitance of 126 $\mu F/cm^2$, which is 3–6 times that generally observed at GC and as much as 15 times larger than that reported for PCFs on prepolished GC substrates. This may be due, in part, to the relatively rough machined surface of the Macor substrate. However, preliminary results obtained in our laboratory indicate that the purity of the pyrolysis gas may be a more important factor. And, indeed, there is significant room for improvement here, as the natural gas used in this work to prepare films contained significant amounts of other components (see Experimental Section). It may be possible to decrease film capacitance through use of higher purity pyrolysis gases.

Surface oxides are produced by ECT as well as air oxidation. Although this is typical of carbon materials in general, this poses a problem for routine analysis. Reduction of the surface oxide produces a peak in the region of −300 mV which can be quite pronounced and thus limits utility in this region.

Since ECT does not improve *initial* rates of electron transfer, it is tempting to conclude that 0.02 cm/s represents an upper limit on the rate constant for ferri-/ferrocyanide at PCF electrodes. Results in this range have been measured independently by three different groups[1–4] on both GC and Macor substrates. However, vacuum heat treatment[16] or laser ablation,[10] the two most effective methods for activating GC, might yield faster rates. The first of these would afford rigorous exclusion of O_2 during treatment, which was probably not provided by the experimental arrangement employed in this work. The advantage of the second method is that it is an in situ method which does not produce surface oxides.[17]

ACKNOWLEDGMENT

This work was supported by a William and Flora Hewlett Foundation Award of Research Corporation and by the Denison University Research Fund and the Anderson Endowment Program of Denison University.

Received for review March 10, 1994. Accepted July 4, 1994.®

® Abstract published in *Advance ACS Abstracts,* September 1, 1994.

(16) Fagan, D.; Hu, I.; Kuwana, T. *Anal. Chem.* **1985**, *57*, 2759–2763.
(17) Rice, R.; Pontikos, N.; McCreery, R. *J. Am. Chem. Soc.* **1990**, *112*, 4617–4622.

Anal. Chem. **1994,** *66,* 3533–3539

Performance of a Novel Silica T-Tube Interface for the AAS Detection of Arsenic and Selenium Compounds in HPLC Column Eluate

Georges-Marie Momplaisir, Tian Lei, and William D. Marshall*

Department of Food Science and Agricultural Chemistry, Macdonald Campus of McGill, 21111 Lakeshore Road, Ste-Anne-de-Bellevue, Québec, Canada, H9X 3V9

An improved interface design for the *on-line* AAS detection of arsenic and selenium compounds in HPLC column eluate is described. Analyte contained in either an aqueous or a polar organic mobile phase is combusted in the hydrogen/oxygen atmosphere of a heated pyrolysis chamber contained within an expanded section of the lower portion of the fused silica T-tube device. Products are entrained into an unheated optical tube by the expanding gases. The interface provides approximately equivalent responses to different analyte–element oxidation states which result in low to subnanogram chromatographic limits of detection for As oxyanions, arsonium cations, Se anions and Se amino acids in an aqueous or methanolic mobile phase. Nascent As anions and As cations are conveniently coextracted from aqueous solution or from fish muscle by phenol extraction and quantified in the same chromatographic run. This method was applied to a standard reference sample of freeze-dried dogfish muscle.

A major constraint in the use of atomic absorption spectrometry (AAS) detection for As and Se analytes is that the principal resonance lines for these elements (189.0, 193.7, and 197.2 nm for As and 196.0 nm for Se) lie in the vacuum ultraviolet region where all conventional premixed flames absorb an appreciable portion of the incident radiation[1] (some 60% at 193.7 nm). In consequence, nonflame atomization devices provide much lower limits of detection as well as extended linear ranges for these elements. Several designs for "flame in tube" devices have been described for atomizing volatile analytes containing arsenic or selenium within the optical beam of an AAS. For gaseous streams containing the analytes or their volatile derivatives, the use of silica tubes as both an atomization cell and an atom keeper/retarder has been well established for hydride generation techniques. When combined with cold-trapping methods which (1) preconcentrate mixtures of arsines and then (2) separate the components by selective revolatilization upon controlled rewarming of the trap, a very sensitive chemical speciation technique is achieved.

By contrast to other atomic spectroscopic techniques (MIP, ICP, and ICPMS), there have been relatively few reports of the use of silica tubes for directly interfacing flowing streams of liquids with AAS. Yet the use of HPLC as a separatory technique offers many advantages for the determination of nonvolatile and/or ionic As and Se analytes. One successful approach to speciation analysis of As or Se compounds has been to couple HPLC separation with *on-line* hydride generation.[2–6] Once formed, the volatile product hydrides are purged from the liquid effluent of the postcolumn reactor and swept up into a silica T-tube mounted within the optical beam of the spectrometer. However, not all As analytes are readily reduced by BH_4^-/H^+ to form volatile products. Several arsonium and selenonium compounds do not react under postcolumn reaction conditions unless they have been predigested (base,[7] acid persulfate,[8] or photolytic oxidation[9]) to liberate hydrolysis products which could, in theory at least, be reacted *on-line*.

As an alternate HPLC-AAS interface,[10] a slotted tube atom trap (STAT) mounted over a hydrogen–argon-entrained air flame provided limits of detection for As oxyanions (arsenate, arsenite, methyl arsonate, and dimethyl arsinate) and arsonium cations (arsenobetaine, arsenocholine, and tetramethylarsonium) which ranged between 0.5 and 1.5 μg/for 100 μL injections. The oxyanion analytes were separated from each other and from coinjected As cations on an anion-exchange column. Alternately, the arsonium analytes were resolved from each other and from coinjected As oxyanions using a cation-exchange stationary phase.

Recently, we described an all-silica interface which permitted the on-line AAS detection of arsonium and selenonium compounds in HPLC column eluate.[11,12] In operation, a predominantly methanolic mobile phase was transferred by thermospray nebulization into a pyrolysis chamber and combusted in an oxygen atmosphere. The pyrolysis products were converted to their hydrides in a hydrogen-rich atmosphere in the downstream portion of the chamber and then atomized as they passed through a second microflame maintained just upstream from the unheated optical tube. For Se analytes, trapping experiments dem-

(1) Brooks, R. B.; Ryan, D. E.; Zhang, H. *Anal. Chim. Acta* **1981**, *131*, 1–16.
(2) Ricci, G. R.; Shepard, L. S.; Colovos, G.; Hester, N. E. *Anal. Chem.* **1981**, *53*, 610–613.
(3) Maitani, T.; Uchiyama, S.; Saito, Y. *J. Chromatogr.* **1987**, *391*, 161–168.
(4) Comber, S. D. W.; Howard, A. G. *Anal. Proc.* **1989**, *26*, 20–22.
(5) Crecelius, E. A.; Bloom, N. S.; Cowan, C. E.; Jenne, E. A. *Speciation of Selenium and Arsenic in Natural Waters and Sediments*; Arsenic speciation, EPRI; Battelle Northwest Laboratories: Washington, 1986; Vol. 2.
(6) Hakala, E.; Pyy, L. *J. Anal. At. Spectrom.* **1992**, *7*, 191–196.
(7) Kaise, T.; Yamauchi, T.; Hiragama, T.; Fukui, S. *J. Appl. Organomet. Chem.* **1988**, *2*, 339–347.
(8) Gunn, A. M. Technical Report TR169; Research Center Medmenham: 1981.
(9) Stringer, G. E.; Atterp, M. *Anal. Chem.* **1979**, *51*, 731–734.
(10) Hansen, S. H.; Larsen, E. H.; Pritzl, G.; Cornett, C. *J. Anal. At. Spectrom.* **1992**, *7*, 629–634.
(11) Blais, J. S.; Momplaisir, G. M.; Marshall, W. D. *Anal. Chem.* **1990**, *62*, 1161–1166.
(12) Blais, J. S.; Huyghues-Despointes, A.; Marshall, W. D. *J. Anal. At. Spectrom.* **1991**, *6*, 225–232.

0003-2700/94/0366-3533$04.50/0
© 1994 American Chemical Society

onstrated the formation of appreciable quantities of H_2Se whether SeO_2 or $(CH_3)_3SeI$ served as the reactant but only in the presence of H_2. If He replaced H_2 in the pyrolysis chamber, only derivatives of Se(IV) were detected. The prototype was described as a thermochemical hydride generation (THG) interface.

The principal limitation of the THG device was the requirement for a predominantly methanolic mobile phase (>60% CH_3OH) to support the combustion process which, in turn, placed severe constraints on the HPLC separatory modes which could be used to resolve ionic analytes. In contrast to equivalent detector responses to As analytes [As(V), As(III), and $(CH_3)_4As^+$], the response to SeO_4^{2-} was only 20% of the response to SeO_3^{2-} or $(CH_3)_3Se^+$.

The advantages of the THG design were that (1) the luminosity associated with the combustion and atomization processes was removed from the optical beam and (2) the optical tube was unheated, which further reduced background spectral emissions. The objective of the current studies was to develop an HPLC-AAS interface which would function efficiently with conventional flow rates of either aqueous or methanolic mobile phases containing volatile buffers. This device was then to be evaluated for the determination of anions containing arsenic or selenium in natural matrices.

EXPERIMENTAL SECTION

HPLC-AAS Chromatography. The instrument consisted of a Varian Star 9000 HPLC pump, a manual HPLC injector fitted with a 50-μL injection loop, a silica T-tube interface, and a Philips Model PU 9100 atomic absorption spectrometer (AAS) equipped with a deuterium background corrector and fitted with arsenic or selenium hollow cathode lamps (Super Lamps, Photron Pty., Victoria, Australia). Chromatograms were developed with an anion-exchange column (7.5 × 0.46 cm, IC PAK HR (Millipore Waters Chromatography, Montréal, Québec) or a 15 × 0.46 cm, PL-SAX, 8 μm (Polymer Laboratories, Amhearst, MA)) or with a cyanopropyl bonded phase column (15 × 0.46, 5 μm Supelcosil LC CN, Supelco, Oakville, Ontario, Canada) and recorded with either a Hewlett-Packard Model 3390A recording integrator or a chromatographic data reduction software package (Turbochrome-3, Perkin-Elmer Corp., Montréal, Québec, Canada).

Interface Design. The two-component, all-quartz interface (Figure 1A) was a modified T-tube design consisting of an upper optical tube (a, 12 cm × 0.9 cm i.d.) mounted within the AAS optical beam and a lower sample introduction tube (total length, 13 cm). Liquid column eluate, contained in a 25 cm × 0.05 mm i.d. capillary silica transfer line (f), was nebulized by thermospray effect into a pyrolysis chamber (b, 4.5 cm × 0.9 cm i.d.). The capillary line was supported by a guide tube (g, 0.32 cm o.d.) which extended concentrically inside the thermospray tube [c, 6 cm × 0.64 cm (4 mm i.d.)] past the coil of high-resistance heating wire (eight turns of 22-G Kanthal A-1 wire, 4 Ω/m). The positioning of the guide tube (g) within the thermospray tube (c) and of the tip of the transfer line within the guide tube was fixed with 0.64–0.32 and 0.32–0.16 stainless steel Swagelok reducing union, respectively, and made gas-tight with nuts (i, Figure 1B) and Vespel ferrules (k, Figure 1B; Chromatographic Specialties, Brockville, Ontario, Canada). The pyrolysis was supported

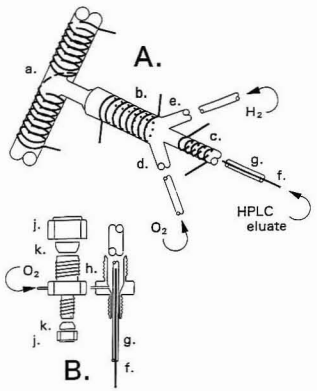

Figure 1. (A) Silica interface T-tube consisting of an optical tube (a) and a lower sample tube containing a pyrolysis chamber (b) surrounded by a 10-turn coil of high-resistances heating wire; a thermospray tube (c) surrounded by an 8-turn coil of high-resistances heating wire; gas inlet ports for O_2 (d) and H_2 (e); a fused silica capillary transfer line (f); and a 0.32-cm o.d. guide tube (g). (B) Close-up and cross sectional views of the 0.64–0.32 stainless steel reducing union (h) which was made gas-tight with ferrules (k) and nuts (j) and modified to accept a 0.16 o.d. stainless steel tube which served as the entry port for supplementary O_2.

by O_2 and H_2 added via separate gas entry ports [d and e, respectively, 6 cm × 0.64 cm (4 mm i.d.)] which met the pyrolysis chamber at an angle of approximately 45°. These gases were added to the interface via flow controllers (0–500 mL and 0–2.5 L capacity, respectively, Matheson, Whitby, Ontario, Canada) connected to quartz insert tubes (8 × 0.16 cm o.d.) which extended inside the gas entry ports to the pyrolysis chamber. The insert tubes were constricted to a 2-mm orifice at the exit end, positioned within the entry ports with Swagelok 0.64–0.32 reducing unions, and made gas-tight with Vespel ferrules. If a predominantly methanolic mobile phase was used, a portion of the O_2 was redirected to the interface via a 0.64–0.32 Swagelok reducing union (Figure 1B) which had been drilled out so as to form a collar around the guide tube. A stainless steel tube (3 × 0.16 mm i.d.) was silver soldered into a 3-mm-diameter hole which had been drilled into the side of this fitting to provide a gas entry port. The supplementary flow of O_2 was thus directed to the pyrolysis chamber via the gas-tight channel between the guide tube (g) and the thermospray tube (c).

The pyrolysis chamber was heated with a 10-turn coil of the same heating wire which served to superheat the liquid column eluate contained in the capillary transfer line. The heating coils were separately energized by an alternating current rectified by a variable transformer (Variac). The heating coils were energized with a current of 4 A (2 A on standby), wrapped with insulating wool (Fibrefax, Carborundum Co., Niagara Falls, NY), and encased in shaped firebrick as previously described.[11,13] The unheated optical tube was positioned within the optical beam of the spectrometer with a hinged aluminum cradle[13] which was attached to the positioning platform of the instrument to facilitate alignment within the optical beam of the instrument.

(13) Forsyth, D. S.; Marshall, W. D. *Anal. Chem.* **1985**, *57*, 1299–1305.

To initiate the operation of the interface, the pyrolysis chamber and the thermospray tube were heated to their normal operating temperatures. The H_2 flow rate was increased to 700 mL/min and ignited with an open flame held sequentially to each exit to the optical tube. The flow rate of O_2 was then increased gradually until autoignition occurred (typically at approximately 50 mL/min) and then increased further to attain the normal operating flow rate. Subsequently, the H_2 flow rate was decreased until the visible flames receded into the pyrolysis chamber (typically at about 150 mL/min) and then again increased to the normal operating flow rate. The transfer line was positioned within the guide tube, and the flow of mobile phase was ramped rapidly from 0 to the desired flow rate. Once operational, portions (as necessary) of the O_2 flow were redirected to the supplementary gas entry port on the modified reducing union. To extinguish the diffused flame within the pyrolysis chamber, the flow of the mobile phase was stopped and the capillary line was withdrawn from the guide tube. The flows of O_2 (to the pyrolysis chamber and to the thermospray tube) were stopped. Finally, the H_2 flow was interrupted, and the interface was permitted to cool to room temperature.

Caution! The operator should be protected from possible injury caused by explosion-induced shattering of the interface. The order of the procedural steps for igniting and extinguishing the pyrolysis should be followed rigidly. The interface should be positioned directly below an efficient hood capable of venting the exit gases directly to the outside.

Interface Optimization. The initial characterization of the operation of the interface was performed using a response surface methodology with the system operated in a flow injection mode (absence of a column). The AAS transient signal (peak area) resulting from the injection of 30 ng of Se analyte was recorded as a function of the flow rates of O_2 and H_2 to the interface and of the mobile phase. A cuboctahydron experimental design was employed in which the peak area responses to three replicate injections of selenate and separately of selenomethionine under each of 12 flow rate combinations (plus three replicates of the center point) were recorded following a random order. The results were fitted to a second-order model (including cross products) using the RSREG procedure (least-squares multiple regression) of the SAS statistical software (SAS Institute, Cary, NC). In preliminary trials, the approximate center of the design had been defined, and it had been established that heating the thermospray tube and the pyrolysis chamber above critical levels had only a minor and detrimental influence on the response. Arbitrarily, a potential of 20 V was applied to the heating coil of the pyrolysis chamber.

Extraction of As Analytes from DORM-1. Lyophilized dogfish muscle (DORM-1, National Research Council of Canada, Ottawa, Ontario, Canada), 0.500 g, was suspended in 10 mL of 9:1 (v/v) methanol–water, vortexed at high speed for 30 s, and then centrifuged at 1500*g* for 3 min. The supernatant liquid was removed, and the residue was reextracted twice with the same solvent. The combined extracts (30 mL) were evaporated nearly to dryness, and the residue was resolubilized in 15 mL of 10% (v/v) aqueous acetic acid and then reextracted three times with 5 mL of liquified phenol. The combined phenolic extracts diluted with 75 mL of diethyl ether and back-extracted four times with 10 mL of distilled water. The aqueous fractions were combined and evaporated to dryness, and the residue, dissolved in 1–10 mL of distilled water, was analyzed by HPLC-AAS. Quantitation was performed by monitoring the increase in analyte peak area resulting from the addition of an aqueous solution of analytical standard directly to the lyophilized powder (method of standard additions).

Table 1. Optimized Flow Rates of O_2 and H_2 for the Detection[a] of As Analyte Contained in Different Mobile Phases Delivered to the Interface at 0.6 mL/min

	O_2 (mL/min)		H_2 (mL/min)	
mobile phase	to PC[b]	to TT[c]	to PC	to TT
water	170	0	2050	0
methanol	20	350	2050	0
acetonitrile	170	0	1520	1520

[a] Working standard (50 μL, containing 30 ng of As analyte), prepared by diluting aqueous stock solution with the test mobile phase, was determined in the flow injection mode. [b] PC, pyrolysis chamber. [c] TT, thermospray tube.

RESULTS AND DISCUSSION

The current interface design (Figure 1) represents a configurational modification and a simplification of the previous prototype. The pyrolysis chamber in the new configuration (Figure 1, c) has been moved from a separate side arm to become an extension of the lower sample introduction tube. In operation, liquid column eluate is nebulized by thermospray effect and mixed with O_2 and H_2 in the pyrolysis chamber. Additionally, the atomization, which was previously effected by passing the combustion products through a small O_2-supported analytical flame maintained just upstream from the optical tube (tip of tube b, Figure 2), is combined with the pyrolysis process in the current design.

The initial characterization of the operating parameters of the interface was performed in a flow injection mode using distilled deionized water as the sample carrier. As had been observed previously with the THG interface, equivalent responses were obtained for equimolar injections of arsenate (AsO_4^{3-}), arsonite (AsO_3^{2-}), and tetramethylarsonium [$(CH_3)_4As^+$] ions. Although it is recognized that these species are at least partially protonated in most media, the convention of referring to these anions without regard to the degree of ionization is followed in this discussion. Maximum response to As analytes in aqueous carrier was achieved with O_2 flow rates which were diminished some 5-fold (170 mL/min) relative to optimal operating conditions for the THG interface (800–850 mL/min) while retaining H_2 flow rates of 2 L/min. The interface operating parameters which resulted in maximum detector response were somewhat dependent on the composition of the mobile phase (Table 1).

For selenium analytes, an appreciable improvement in the detection efficiency for Se(VI) analyte was evidenced by equivalent molar responses obtained for selenomethionine [$CH_3Se(CH_2)_2CH(NH_2)CO_2H$] and selenate ($SeO_4^{2-}$). Moreover, response surface analyses of the integrated detector signal (resulting from 30 ng as Se) as a function of flow rates of O_2, H_2, and the mobile phase to the interface (Figure 2) indicated that the net nebulization/atomization/detection

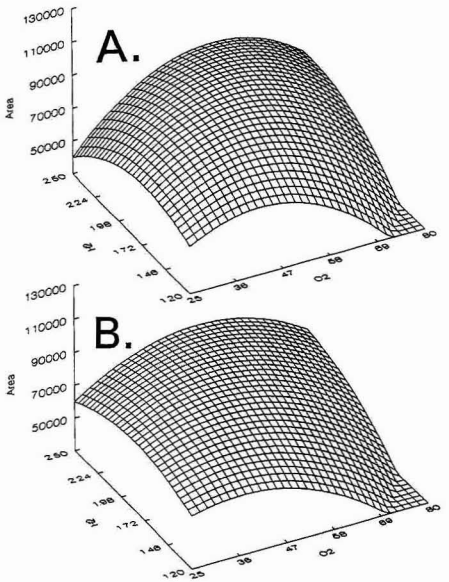

Figure 2. Predicted response surfaces for peak area resulting from 30 ng of Se as SeO_4^{2-} (A) or as selenomethionine (B) as a function of flow rates of O_2 and H_2 delivered to the pyrolysis chamber. Energy inputs to the thermospray and pyrolysis chamber coils were maintained constant, the optical tube was unheated, and the aqueous mobile phase was delivered to the interface at 0.8 mL/min.

process was only moderately sensitive to changes in these interface operating parameters (less than 50% variation in response over the wide range of H_2 and O_2 flow rates).

Three chromatographic approaches to the separation of As oxyanions have been popular. For reversed-phase packings and neutral to slightly acidic mobile phases containing quaternary ammonium ions $[(C_4H_{10})_4N^+$ or $(C_7H_{16})_4N^+]$, the order of elution was arsonite (AsO_3^{2-}), dimethyl arsinate $[(CH_3)_2AsO_2^-]$, methyl arsonate ($CH_3AsO_3^{2-}$), and arsenate (AsO_4^{3-}),[14-16] although the order of elution of the first two analytes was apparently dependent on the buffer concentration.[16] A second approach has involved the use of a reverse-phase C_{18} column and dilute sulfuric acid as eluent. With these conditions, the observed order of elution was arsenate, methyl arsonate, arsenite, and dimethyl arsinate.[17] For anion-exchange chromatography, typically with resin-based quaternary ammonium functional groups and carbonate or carbonate/bicarbonate mobile phases, the order of elution was AsO_3^{2-}, $(CH_3)_2AsO_2^-$, $CH_3AsO_3^{2-}$, and AsO_4^{3-}.[2,10,18] The separation of these four analytes together with trimethylarsine oxide $[(CH_3)_3AsO]$ was readily achieved by ion exchange (Figure 3A). A sixth component, methyl arsonite ($CH_3AsO_2^-$), when present in mixtures of the other analytes, was characterized by only moderate stability and was not investigated further.

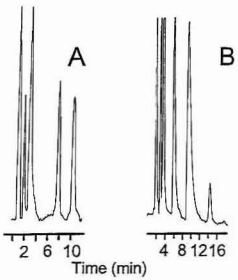

Figure 3. HPLC-AAS chromatograms of (A) As oxyanions containing approximately 30 ng each (as As) of trimethylarsine oxidase (t_R, 1.57 min), dimethyl arsinate (t_R, 2.23), arsonite (t_R, 3.84), methyl arsonate (t_R, 8.02), and arsenate (t_R, 11.24) separated on the IC PAK HR column with 0.1 M $(NH_4)_2CO_3$ (pH 9) delivered at 0.6 mL/min and (B) arsenate (t_R, 1.90), methyl arsonate (t_R, 2.97), arsenite (t_R, 3.66), dimethyl arsinate (t_R, 6.17), phosphorylarsenocholine (t_R, 9.63), and arsenobetaine (t_R, 14.25) separated on the cyanopropyl column with 0.6% HAc delivered at 0.7 mL/min.

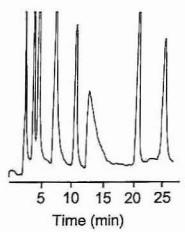

Figure 4. HPLC-AAS chromatogram of arsenate (t_R, 2.36 min), methyl arsonate (t_R, 3.65), arsenite (t_R, 4.42), dimethyl arsinate (t_R, 7.16), arsenobetaine (t_R, 10.64), phosphorylarsenocholine (t_R, 13.09), arsenocholine (t_R, 21.12), and tetramethylarsonium ion (t_R, 25.50). Analytes were separated on the cyanopropyl column using a solvent program which varied linearly from 0.01% (v/v) acetic acid to 1% acetic acid plus 0.075% (v/v) tetramethylammonium hydroxide over 10 min.

Previous success with a cyanopropyl bonded phase packing for the separation of arsonium analytes prompted an investigation of the suitability of this phase for separating As oxyanions as well. The chromatogram of Figure 3B presents the separation of four oxyanions together with phosphorylarsenocholine $[(CH_3)_3AsCH_2CH_2OPO_3^{2-}]$ and arsenobetaine $[(CH_3)_3AsCH_2CO_2^-]$. Interestingly, the order of elution of the As oxyanions is reversed in the two chromatograms of this figure. The versatility of the interface coupled with the cyanopropyl stationary phase is demonstrated by the separation of nascent anions and cations in the same chromatographic run (Figure 4) using a solvent program which included increasing amounts of tetramethylammonium ion. As anticipated for a reversed-phase separation, the protonated As oxyanions are apparently eluted in order of their decreasing relative polarities, and the cationic species are subsequently displaced by the tetramethylammonium mobile phase additive (ion competition mechanism). The presence of these additives in the mobile phase did not cause a perceptible change in the response to these analytes.

(14) Brinckmann, F. E.; Jewett, K. L.; Iverson, W. P.; Irgolic, K. W.; Ehrhardt, K. C.; Stockton, R. A. *J. Chromatogr.* **1980**, *191*, 31–46.
(15) Cullen, W. R.; Dodd, M. *Appl. Organomet. Chem.* **1989**, *3*, 401–409.
(16) Hakala, E.; Pyy, L. *J. Anal. At. Spectrom.* **1992**, *7*, 191–196.
(17) Ebdon, L.; Walton, A. P.; Ward, R. W. *Analyst (London)* **1988**, *113*, 1159–1165.
(18) Spall, W. D.; Lynn, J. G.; Andersen, J. L.; Valdez, J. G.; Gurley, L. R. *Anal. Chem.* **1986**, *58*, 1340–1344.

Table 2. Chromatographic Limits of Detection for Arsenic and Selenium Analytes in HPLC Eluate

analyte	mobile phase[a] composition	t_R (min)	LOD[b]
$(CH_3)_3AsCH_2CO_2^-$	A	5.62	0.7
$(CH_3)_3AsCH_2CH_2OH$	A	7.30	0.6
$(CH_3)_4As^+$	A	8.01	0.9
$(CH_3)_3AsCH_2CO_2^-$	B	6.10	0.6
$(CH_3)_3AsCH_2CH_2OH$	B	8.00	0.6
$(CH_3)_4As^+$	B	10.3	0.7
AsO_3^{2-}	C	3.95	0.7
AsO_4^{3-}	C	1.96	1.0
$CH_3AsO_3^{2-}$	C	2.95	1.0
$(CH_3)_2AsO_2^-$	C	6.90	0.8
$CH_3SeCH_2CH_2CH(NH_2)CO_2H$	D	6.68	1.0
$[-SeCH_2CH(NH_2)CO_2H]_2$	D	5.20	1.0
$C_2H_5SeCH_2CH_2CH(NH_2)CO_2H$	D	8.45	1.0
SeO_4^{2-}	E	6.95	2.0
SeO_3^{2-}	E	4.74	2.0

[a] Mobile phase A consisted of 1% (v/v) methanolic HAc containing 0.075% TMAH delivered to the CNPr column at 0.6 mL/min; B contained 0.075% tetramethylammonium hydroxide in 1% (v/v) aqueous acetic acid delivered at 0.6 mL/min to the CNPr column; C contained 0.01% (v/v) aqueous HAc delivered att 0.6 mL/min to the CNPr column; D contained 0.04% (v/v) acetic acid in water delivered at 0.5 mL/min to the CNPr column; and E contained 0.1% (w/v) $(NH_4)_2CO_3$ in 0.01 M aqueous ammonia delivered at 0.6 mL/min to the PL-SAX column. [b] LOD $= 3[s_B^2 + s_i^2 + (i/S)^2 s_S^2]^{1/2}/S$, where s_B is the standard deviation of the peak-to-peak base line noise/5 (recorded over 10 min) and S, i, s_S, and s_i are the slope, intercept, and their respective standard deviations of the calibration plot (obtained by linear regression). If LOD $= 3s_B/S$ is used, the magnitude of the estimates is reduced approximately 7-fold.

To maximize the response to As analytes in a methanolic mobile phase, it was necessary to redirect a portion of the gas flows to the interface. For a methanolic mobile phase, it proved to be more effective (Table 1) to direct a portion of the flow of O_2 (or the H_2 for a mobile phase containing acetonitrile) axially through the channel between the thermospray tube and the guide tube using Swagelok reducing modified with a gas entry port (Figure 1B). By changing the flow rates of fuel and oxidant gases to the interface, it was possible to compensate for the deleterious influence of the mobile phase composition on the detection process. Identical system responses and similar retention times on the cyanopropyl column for arsenobetaine, arsenocholine, and tetramethylarsonium ion were achieved with either 1% aqueous acetic acid (HAc) containing 0.075% tetramethylammonium hydroxide (TMAH) or 1% methanolic HAc containing 0.075% TMAH delivered at 0.7 mL/min.

The chromatographic limits of detection for the four arsenic oxyanions and separately for the three arsonium compounds were calculated (first-order error propagation model with base line noise normally distributed) from their calibration curves under optimal detection conditions as described previously.[19,20] The linear models were highly correlated ($r > 0.997$) over the range of concentrations studied (5–100 ng). Estimates of the chromatographic limits of detection ranged from 0.7 to 1.5 ng (as As) for the oxyanions and from 0.6 to 0.9 ng for the cationic species (Table 2). For the arsonium analytes, this represents approximately a 10-fold improvement over the THG interface.[11]

Given the feasibility of separating anionic and cationic species containing arsenic in the same chromatographic run,

(19) Foley, J. P.; Dorsey, J. G. *Chromatographia* **1984**, *18*, 503–512.
(20) Blais, J. S.; Marshall, W. D. *J. Anal. At. Spectrom.* **1989**, *4*, 641–645.

Table 3. Arsenic Compounds in Lyophilized Dogfish Muscle (DORM-1) Reference Material

analyte	concn, μg/g (as As) ± 1 RSD[a] (this work)	literature values ref 24	ref 22	ref 25
AsO_4^{3-} [As(V)]	0.21 ± 11.5	0.60		<0.05
$CH_3AsO_3^{2-}$ [MMA]	1.33 ± 11.8			<0.05
$(CH_3)_2AsO_2^-$	0.39 ± 7.6		0.47 ± 0.02	NA[a]
$(CH_3)_3As^+CH_2CO_2^-$	13.77 ± 3.1	15.65	15.7 ± 0.8	14.14
$(CH_3)_3As^+CH_2CH_2OH$	0.038 ± 5.4	ND[a]	0.11 ± 0.05[b]	0.019
$(CH_3)_4As^+$	0.36 ± 10.0	0.46		0.39
unknown(s)[c]	0.31 ± 4.8	0.41		0.41[c]
sum As(V), As(III), and MMA			0.18 ± 0.04	
total extractable As (μg/g)	16.58[d]	17.2 ± 0.9[e]	16.3 ± 0.6[f]	16.62[g]

[a] RSD, relative standard deviation, in %; NA, not analyzed; ND analyzed but not detected. [b] The identity of this analyte has been questioned. [c] The quantities of unknown(s) are not comparable, having been detected in chromatograms developed with different stationary and mobile phases. [d] Estimate, by FI–quartz tube–AAS, of the As content in the water–methanol fraction to be chromatographed. [e] Estimate, by ICP-OES, of the As content in the methanol–water fraction to be chromatographed. [f] Estimate, by GFAAS, of the As content in the methanol–water fraction to be chromatographed. [g] Estimate, by ICPMS, of the As content in the methanol–water fraction to be chromatographed.

it was of interest of develop/optimize an extraction procedure for these analytes from marine soft tissues known to contain appreciable quantities of arsenobetaine. A procedure involving the sequential partitioning of the analytes from aqueous solution into liquified phenol and subsequent recovery back into water after diluting the combined phenol phases with diethyl ether had been previously optimized for arsonium analytes (arsenobetaine, arsenocholine, and tetramethylarsonium ions).[21] Initial trials with the four As oxyanions in aqueous solution were promising. To our knowledge, no standard reference material is available which is certified regarding arsenic speciation; however, DORM-1, a lyophilized powder of dogfish muscle (National Research Council of Canada), has been studied with respect to the levels of constituent arsenic compounds.[22–25] A simplification of the previous method involved three sequential water–methanol extractions of the powder. Rather than subjecting the crude extract to filtration through an anion exchanger, the combined aqueous extracts were evaporated, the residue was dissolved in dilute acetic acid, and the analytes were partitioned into liquified phenol. Analytes were recovered from the diluted phenol phase into water, concentrated virtually to dryness, resolubilized in distilled water phase, and analyzed. Relative to the chromatography of standards, coextractive(s) from the dogfish powder changed the retention times of certain As analytes but did not have a perceptible influence on the detector response to these analytes. In addition to arsenobetaine, the reference material was found to contain arsenate, methyl arsonate, dimethyl arsinate, arsenocholine, tetramethylarsonium ion, and an unknown, which were separately quantified by the method of standard additions (Table 3, Figures 5 and

(21) Momplaisir, G. M.; Blais, J. S.; Quinteiro, M.; Marshall, W. D. *J. Agric. Food Chem.* **1991**, *39*, 1448–1451.
(22) Beauchemin, D.; Bednas, M. E.; Berman, S. S.; McLaren, J. W.; Siu, K. W. N.; Sturgeon, R. E. *Anal. Chem.* **1988**, *60*, 2209–2212.
(23) Beauchemin, D.; Siu, K. W. N.; McLaren, J. W.; Berman, S. S. *J. Anal. At. Spectrom.* **1989**, *4*, 285–289.
(24) Shibata, Y.; Morita, M. *Anal. Chem.* **1989**, *61*, 2116–2118.
(25) Larsen, E. H.; Pritzl, G.; Hansen, S. H. *J. Anal. At. Spectrom.* **1993**, *8*, 1075–1084.

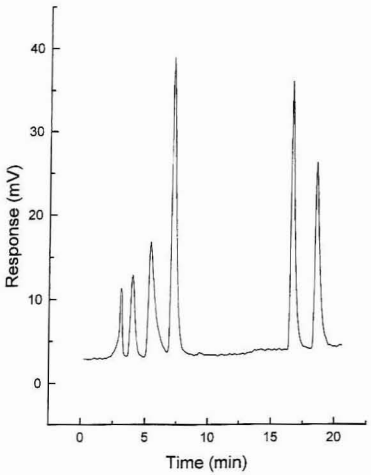

Figure 5. Gradient elution of HPLC–AAS chromatogram of a 50-μL injection of the 10-mL final extract from 0.50 g of lyophilized dogfish muscle (DORM-1) which had been spiked with 5 μg each of arsenate (t_R, 3.06), methyl arsonate (t_R, 3.96), dimethyl arsinate (t_R, 5.37), and arsenobetaine (t_R, 7.04) and 12.5 μg each of arsenocholine (t_R, 16.38) and tetramethylarsonium ion (t_R, 18.27). Analytes were separated on the cyanopropyl column using a solvent program which varied linearly from 0.01% (v/v) acetic acid to 1% acetic acid plus 0.15% (v/v) tetramethylammonium hydroxide over 10 min.

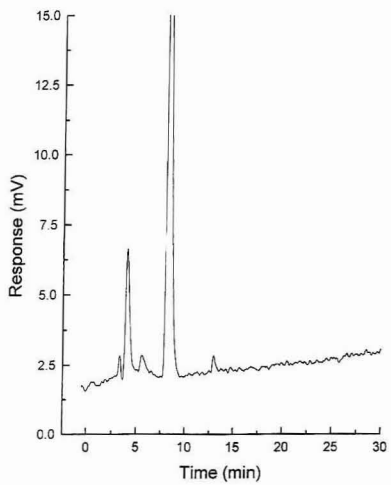

Figure 6. Isochratic elution HPLC-AAS chromatogram of a 50-μL injection of the 10-mL final extract from 0.50 g of DORM-1, indicating the presence of arsenate (t_R, 3.38 min), monomethyl (t_R, 3.96), dimethyl arsinate (t_R, 5.50), arsenobetaine (t_R, 7.35), and an unknown As compound (t_R, 11.06). Mobile phase, 10% (v/v) aqueous acetic acid, was delivered to the cyanopropyl bonded phase column at 0.6 mL/min.

6). Several of these analytes have been detected in seaweed[3] and have been quantified in DORM-1 by HPLC-ICPMS.[22,24,25] The certified total content of As in this reference material is 17.7 ± 2.1 μg/g. There was good qualitative agreement concerning the identities of the As species present in DORM-1

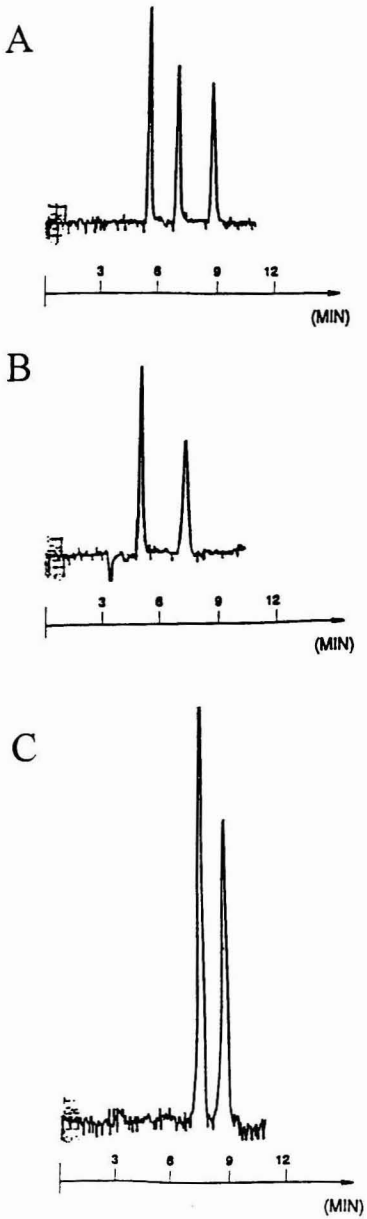

Figure 7. HPLC-AAS chromatograms of a mixture of (A) 10 ng each (as Se) of selenocystine (t_R, 5.20 min), selenomethionine (t_R, 6.68), and selenoethionine (t_R, 8.45) eluted with 0.04% (v/v) aqueous acetic acid delivered at 0.5 mL/min to the cyanopropyl column; (B) 20 ng each (as Se) of selenite (t_R, 4.74) and selenate (6.95) eluted with 1.1 mM $(NH_4)_2CO_3$ (adjusted to pH 9.0) delivered at 0.6 mL/min to the PL-SAX column; and (C) 50 ng each (as Se) of methaneselenic (t_R, 7.21) and methaneselenonic (t_R, 8.44) acids eluted with 0.02% (w/v) $(NH_4)_2CO_3$ delivered at 0.6 mL/min to the PL-SAX column.

and good agreement on the levels of arsenobetaine and total As which was extracted from this matrix. However, different extraction procedures and different HPLC chromatographic modes (different stationary and mobile phases) apparently result in appreciably different estimates of the levels of some of the minor As constituents. Additionally, one[22] and two[25] unknown compounds have been reported in the crude extracts of this material. Although somewhat speculative, it seems likely that the oxyanions result, at least in large part, from postmortem changes in the tissue. Several of these analytes were also observed in cod fillet which had been stored frozen for 18 months.

That the interface can also be useful for selenium speciation studies (Figure 7) is suggested by the separations of a synthetic mixture of selenoamino acids {selenocystine [(–$SeCH_2CH(NH_2)CO_2H)_2$], selenomethionine ($CH_3SeCH_2CH_2CH(NH_2)CO_2H$), and selenoethnionine ($C_2H_5SeCH_2CH_2CH(NH_2)CO_2H$)}, a mixture of selenite (SeO_3^{2-}) and selenate (SeO_4^{2-}), and a mixture of methyl seleninate ($CH_3SeO_2^-$) and methyl selenonate ($CH_3SeO_3^-$). Estimates of the chromatographic limits of detection for these analytes are recorded in Table 2.

CONCLUSIONS

The principal advantage of the current interface design for arsenic and selenium detection remains its compatibility with both aqueous and organic mobile phases and the relative insensitivity of the response process to the presence of mobile phase modifiers. Thus, it is feasible to exploit a variety of different separatory modes inherent in different stationary phases and to optimize separations by solvent programming. In addition to an increased ease of operation, this interface design has proven to be relatively robust. Interface tubes have been in continuous operation for up to 9 months without an appreciable loss of response (less than 50%). A somewhat unexpected benefit is the moderately improved limits of detection observed for both Se and As analytes. The repeatability of the quantitation process for different As analytes in DORM-1 extracts as measured by the replicate determinations of Table 3 suggests that the operation of this interface does not degrade the precision of the results to any greater extent than do other chromatographic detectors.

In total, this interface provides an efficient link between HPLC and AAS and results in a cost-effective system which can be competitive in terms of sensitivities with other optical atomic spectroscopic techniques.

ACKNOWLEDGMENT

Financial support from the Natural Science and Engineering Research Council of Canada (NSERC) is gratefully acknowledged.

Received for review February 17, 1994. Accepted June 18, 1994.[⊗]

[⊗] Abstract published in *Advance ACS Abstracts,* August 1, 1994.

Anal. Chem. **1994,** *66,* 3540–3542

Real-Time Measurement Capabilities Using Aerosol Time-of-Flight Mass Spectrometry

T. Nordmeyer and K. A. Prather*
Department of Chemistry, University of California, Riverside, California 92521

This note describes the recent development of a new technique, aerosol time-of-flight mass spectrometry, that allows for real-time analysis of single particles. We report here the first results demonstrating the utility of this technique for real-time analysis of polydisperse systems of aerosols, determining both size and composition. Future calibration studies will follow, enabling complete analysis of complex atmospheric systems, determining particle size distributions and, more importantly, the corresponding compositional variations for each particle size.

Real-time aerosol analysis, determining the size and chemical composition of individual particles, has been an elusive goal for aerosol researchers since the early 1970s.[1,2] We recently reported a method for accomplishing this goal using aerosol time-of-flight mass spectrometry (ATOFMS), a technique which combines aerodynamic particle sizing and time-of-flight mass spectrometry.[3] In that paper, we described an electronic logic circuit that was under development which would allow us to correlate particle size and composition measurements in the real-time analysis of individual particles. This external circuit has now been added, completing the initial stage of development of the system, which is now capable of highly efficient aerosol analysis. To our knowledge, this is the first analytical technique capable of determining the size and complete mass spectrum of an individual particle in real time. This paper presents details of the real-time capability of this system.

The electronic circuit serves as a crucial link between the particle sizing and composition analysis regions of the system by tracking the individual aerosol particles through the system while providing the logic and timing necessary for efficient particle analysis.[3] The implications of analysis using ATOFMS are far reaching, potentially changing the direction of aerosol research by allowing the first *direct* investigations of a multitude of atmospherically relevant processes in real time. Although techniques exist for determination of both size and composition of single particles, these techniques are not in situ, and therefore sample integrity is often in question. As a result, many atmospheric researchers have opted to use computer models to simulate real systems because of the lack of adequate analytical techniques which could provide such information.[4] The ATOFMS system described herein will ultimately allow establishment of the key correlation between particle composition and size.

In a previous paper, preliminary results and details of the total ATOFMS system were presented, so only a summary of the experimental details will be given here. A block diagram of the experimental setup is shown in Figure 1. Particles of known size and composition are generated using a commercially available aerosol generator, whereupon they are dried, neutralized, and then directed to the inlet of a particle interface. After they are admitted into the interface, particles pass through a capillary and supersonically expand through three differentially pumped regions separated by three skimmers to form a narrow particle beam. This beam of particles travels under vacuum through two low-power laser beams used to track the particles into the ionization region of the mass spectrometer. The signal from the tracking lasers is sent to a custom electronic circuit used to measure the particle velocity and also to synchronize the arrival of the particle in the exact center of the ionization region of the mass spectrometer. A pulsed high-powered Nd:YAG and/or CO_2 laser is then fired at the appropriate time to intercept the particle with the desorption/ionization pulse. Ions formed in the laser desorption/ionization process are accelerated into the time-of-flight drift region where they separate by mass-to-charge ratio. The complete mass spectrum is obtained on a digital oscilloscope interfaced to a personal computer. We are currently modifying a data acquisition program which will allow each particle's mass spectrum to be stored with the corresponding aerodynamic particle velocity, which later will be converted to particle size.

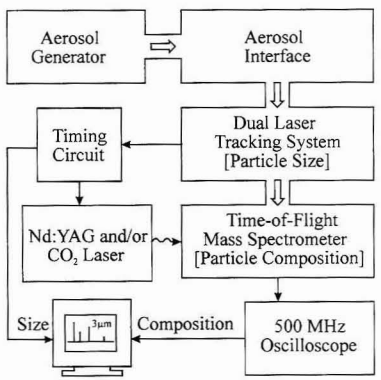

Figure 1. Block diagram of the aerosol time-of-flight mass spectrometer.

Earlier attempts at determination of particle size and composition showed some success. However, these techniques utilized a quadrupole mass analyzer and thus were unable to provide the entire mass spectrum for an individual particle.[5,6]

(1) Myers, R. L.; Fite, W. L. *Environ. Sci. Technol.* **1975,** *9,* 334–336.
(2) Davis, W. D. *Environ. Sci. Technol.* **1977,** *11,* 587–592.
(3) Prather, K. A.; Nordmeyer, T.; Salt, K. *Anal. Chem.* **1994,** *66,* 1403–1407.
(4) Hanson, D. D.; Ravishankara, A. R.; Solomon, S. *J. Geophysical Res.* **1994,** *99,* 3615–3629.

0003-2700/94/0366-3540$04.50/0
© 1994 American Chemical Society

In addition, the timing schemes for laser desorption/ionization in these experiments were based on a fixed delay and were not suitable for polydisperse aerosol systems in which particles assume a range of velocities upon expansion into vacuum. Other researchers have incorporated time-of-flight mass spectrometry for single particle composition analysis; however, these methods have either been off-line or incapable of determining the size and composition of single particles simultaneously. One method involves firing a high-powered laser at high repetition rates, randomly desorbing those particles that happen to be in the path of the laser at the time of firing.[7] This method, in addition to being extremely inefficient,[8] does not allow for determination of particle size and therefore has limited utility. Other methods utilize a single low-powered continuous wave visible laser to detect an individual particle in the source region of the mass spectrometer.[9,10] Upon detection, a high-powered laser is instantly fired to desorb the particle and obtain the mass spectrum. Determination of particle size from such experiments is difficult because the Mie scattering intensity is a complex function of particle size, index of refraction, and the angle of detection. In addition, laser beam inhomogeneity in single laser systems can yield misleading results, because particles of the same size possess unique trajectories and sample different portions of the beam, resulting in different scattering intensities. In our experiment, we utilize two low-powered continuous wave lasers separated by a fixed distance, determining particle size by measuring the transit time of the particle between the two lasers. The correlation between transit time and aerodynamic particle size can be established experimentally using particles of known size and composition. This method for particle sizing was first introduced by Dahneke in 1973.[11] Substantial research in this area has led to the commercialization of instruments designed to measure transit time using a dual tracking laser approach. In Figure 2, we show the measured relationship of transit time as a function of aerodynamic particle size for $(NH_4)_2SO_4$ particles in the 1–10 μm size range. The error bars in this figure (one standard deviation) represent the distribution of velocities imparted to particles of the same size during the expansion process into vacuum.[12] Ammonium sulfate particles of known density (1.8 g/cm^3) were chosen initially for use in calibration studies because of this species's ubiquitous presence in the atmosphere. The advantage of determining both aerodynamic size and composition simultaneously is that each particle can be associated with a particular group or class of particles with a known density. This knowledge of particle density allows for conversion from aerodynamic particle size to geometric particle size.

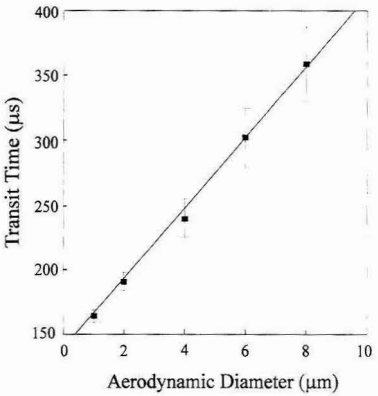

Figure 2. Transit time vs aerodynamic diameter for individual ammonium sulfate particles. The error bars represent one standard deviation.

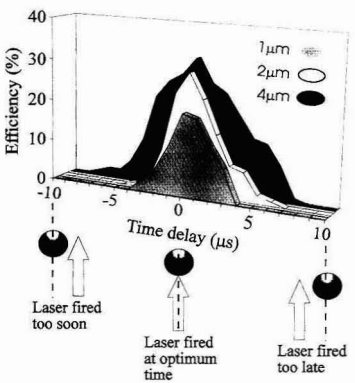

Figure 3. Graph showing desorption efficiency as a function of time delay between the particle arrival in the center of the source and Nd:YAG desorption pulse for three different particles sizes.

The efficiency of the timing circuit in determining the arrival of a particle to coincide with the Nd:YAG pulse is demonstrated for 1.0, 2.0, and 4.0 μm 2,4-dihydroxybenzoic acid particles in Figure 3. Particles that pass through both tracking beams are fired upon at the calculated arrival time, $t = 0$. The percentage of particles sized and tracked by the circuit for which a corresponding mass spectrum was obtained is shown as a function of the delay time, which is the delay between the predicted arrival of the particle in the center of the source of the mass spectrometer and the Nd:YAG pulse. It should be noted that as the Nd:YAG pulse is delayed either before or after the arrival of the particle, the probability for ionization decreases because the particles pass out of the "interception zone" defined by the overlap between the projected volume from the tracking lasers and the volume of the Nd:YAG laser beam. The fact that the optimum time delay is the same for both large and small particles demonstrates the ability of this technique to analyze polydisperse samples; if the interception time were calculated incorrectly, the peak center would shift with particle size, i.e., particle

(5) Sinha, M. P.; Giffen, C. E.; Norris, D. D.; Estes, T. J.; Vilker, V. L.; Friedlander, S. K. *J. Coll. Inter. Sci.* **1982**, *87*, 140–153.
(6) Sinha, M. P. *Rev. Sci. Instrum.* **1984**, *55*, 886–891.
(7) Reents, W. D.; Swanson, A.; Downey, S.; Mujsce, A. M.; Muller, A. J.; Emerson, B.; Siconolfi, D. J.; Sinclair, J. D. Proceedings of the ASMS Conference on Mass Spectrometry, San Francisco, CA, May 30–June 4, 1993; Abstr. 640a.
(8) We have experimentally measured a 10 000-fold increase in the number of mass spectra obtained when using our method of particle tracking as opposed to the random fire mode of operation.
(9) McKeown, P. J.; Johnston, M. V.; Murphy, D. M. *Anal. Chem.* **1991**, *63*, 2069–2073.
(10) Thomson, D. S.; Murphy, D. M. *Appl. Opt.* **1993**, *32*, 6818–6826.
(11) Dahneke, B. *Nat. Phys. Sci.* **1973**, *244*, 54–55.
(12) The error in the flight time of each individual particle is less than 2%.

velocity. Note that larger particles travel more slowly and remain in the zone longer and therefore yield a longer time window for particle desorption/ionization. The fact that fewer than 100% of all particles tracked by the circuit are desorbed can be explained by the dispersive nature of the particle beam. This is further supported by the greater dispersion (less percentage ionization) seen for smaller particles. These results are typical for particle beams undergoing supersonic expansion through a capillary and will be studied in more detail to determine the optimum conditions for our system.[13,14]

In the current mode of operation, we obtain both the complete mass spectrum and size information for approximately 300 single particles in 1 min, using initial (i.e., before expansion through capillary nozzle into particle interface) particle concentrations of approximately 10^2–10^3 cm^{-3}. We have observed desorption/ionization efficiencies up to 50%, meaning one out of two particles that pass through both scattering lasers results in mass spectra. The total efficiency of analysis using ATOFMS is ultimately determined by the fraction of particles admitted to the particle interface which produce both mass spectra and size information. Several factors important in determining this efficiency are being explored. The final results will be presented in a full paper. Among those factors under study are the following: (1) particle transfer efficiency, (2) transmission efficiency through the particle interface, (3) spatial overlap of particles with tracking lasers, (4) projected overlap between the tracking lasers and the ionizing laser, (5) threshold levels used to discriminate between particles and background noise, (6) coincidence errors in the timing circuit resulting from multiple particle triggers, and (7) dead time in the timing circuit due to limitations of laser repetition rate (approximately 50%). Current plans for study of these factors include construction of x–y positioners for the tracking laser optics to allow real-time optimization of the particle/scattering laser overlap and projected particle beam overlap with the ionization laser. In addition, the dispersion of the particle beam for various particle sizes is being studied for different capillary and nozzle designs.

In summary, we have combined the techniques of aerodynamic particle sizing with time-of-flight mass spectrometry and have shown the ability of this system to properly determine both size and composition for a range of particle sizes. The implications are numerous because now, for the first time, there is a method that can provide, in real time, both the size *and* the chemical composition of individual particles. In addition, the ability to determine these properties for polydisperse systems has also been demonstrated. Such analytical capability opens new areas for research in atmospheric studies, both for field sampling and for analytical studies of heterogeneous reactions. These types of studies will lead to improved models for atmospheric processes that are currently not well understood, such as ozone depletion. This method may also be adapted for on-line particle sampling in combustion processes such as diesel and gas engine emissions. Now that ATOFMS has proven to be a highly efficient method for single particle analysis, the next stage of development will involve performing calibration experiments using particles of varying size and chemical composition while optimizing the system for real-time particle analysis.

Received for review May 16, 1994. Accepted July 5, 1994.[⊗]

(13) Estes, T. J.; Vilker, V. L.; Friedlander, S. K. *J. Colloid Interface Sci.* **1983**, *93*, 84–94.
(14) Cheng, Y. S.; Dahneke, B. E. *J. Aerosol Sci.* **1979**, *10*, 257–274.

[⊗] Abstract published in *Advance ACS Abstracts,* August 15, 1994.

Anal. Chem. **1994,** *66,* 3543–3551

Simple Fiber-Optic Interface for On-Line Supercritical Fluid Extraction Fourier Transform Infrared Spectrometry

Daniel L. Heglund and David C. Tilotta*

Department of Chemistry, University of North Dakota, Grand Forks, North Dakota 58202

Steven B. Hawthorne and David J. Miller

Energy & Environmental Research Center, University of North Dakota, Grand Forks, North Dakota 58202

A simple and inexpensive fiber-optic interface for coupling a supercritical fluid extractor to a FT-IR spectrometer is described. The interface, based on chalcogenide (AsSeTe) fiber optics and a stainless steel union cross, is rugged up to pressures of 400 atm, has a spectral window from 5000 to 800 cm^{-1}, and is relatively easy to clean. It is shown that the SFE-FT-IR interface allows qualitative and quantitative information to be obtained from the extracts of real-world samples (caffeine in coffee and total petroleum hydrocarbons in soil, respectively) without the use of either a flow restrictor or a collection solvent. The determination of total petroleum hydrocarbons (TPH) in soils by static on-line SFE-FT-IR yields values in good agreement with both off-line SFE and Soxhlet extraction. The detection limit for TPH, using a 48-s scan time, was determined to be 1.6 ppm (wt TPH/wt sample). The linear dynamic range of calibration for the TPH determinations was greater than 3 orders of magnitude.

Supercritical fluid extraction (SFE) has been shown to be an excellent alternative to conventional solvent extraction for the removal of organic compounds from solid samples.[1-3] Generally, SFE is fast (<30 min) and uses nontoxic fluids as extraction solvents (usually CO_2). In addition, a typical SFE uses about the same amount of CO_2 per minute as the average adult exhales per minute (assuming the average adult human exhales ca. 240 mL CO_2/min).[4] Thus, SFE is an efficient and essentially nonpolluting means of extracting analytes from solid matrices.

To date, the majority of SFEs have been performed in the off-line mode, i.e., the extracted material is collected from flowing CO_2 (dynamic) after depressurization into a solvent or onto a sorbent trap prior to further analytical processing. The depressurization step is normally achieved by passing the supercritical CO_2 through a flow restrictor, which has the disadvantage that it often becomes plugged during the extraction.[3,5] In addition, collection of many analytes can be difficult because of the high gaseous flow rate of CO_2 that results from the depressurization.[3,6] On-line SFE methods, which involve directly coupling the supercritical fluid extractor to a second analytical instrument (e.g., SFE-GC), are most often performed by depressurizing the supercritical fluid through a flow restrictor and cryogenically trapping the extract.[3,7] As is the case for off-line SFE, the collection of more volatile analytes is greatly complicated by the high flows of gaseous CO_2 that occur after depressurization.

An ideal on-line SFE method would be capable of measuring the extracted analytes without the need for depressurization of the extraction fluid. Such a completely closed SFE system would eliminate the need for collection solvents and eliminate the loss of any extracted volatiles. The second major advantage of such an on-line SFE system is that if no flow restrictor is used, then the plugging problems associated with the restrictor are also eliminated.

Infrared (IR) spectroscopy is a very useful detector for SFE since it is a proven analytical method superior to fluorescence and ultraviolet/visible (UV/vis) spectroscopy in its ability to provide information on molecular structure. Previous attempts at interfacing supercritical fluid systems to FT-IR spectrometers employed either mobile-phase elimination devices[8-13] or high-pressure flow cells.[11,12,14-22] The mobile-phase elimination approach is used extensively in supercritical fluid chromatography and involves depressurizing the CO_2 through a flow restrictor and collecting the separated analytes on a substrate. Mobile-phase elimination interfaces have not yet been applied to SFE but probably would yield

(1) Camel, V.; Tambuté, A.; Caude, M. *J. Chromatogr.* **1993**, *642*, 263.
(2) Janda, V.; Bartle, K. D.; Clifford, A. A. *J. Chromatogr.* **1993**, *642*, 283.
(3) Hawthorne, S. B. *Anal. Chem.* **1990**, *62*, 633A.
(4) McMurray, J.; Castillion, M. E. *General, Organic, and Biological Chemistry*; Prentice Hall: Englewood Cliffs, NJ, 1992; p 243.
(5) Burford, M. D.; Hawthorne, S. B.; Miller, D. J.; Braggins, T. *J. Chromatogr.* **1992**, *609*, 321.
(6) Langenfeld, J. J.; Burford, M. D.; Hawthorne, S. B.; Miller, D. J. *J. Chromatogr.* **1992**, *594*, 297.
(7) Greibrokk, T. *J. Chromatogr.* **1992**, *626*, 33.
(8) Griffiths, P. R.; Haefner, A. M.; Norton, K. L.; Fraser, D. J. J.; Pyo, D.; Makishima, H. *J. High Resolut. Chromatogr. Chromatogr. Commun.* **1989**, *12*, 119–122.
(9) Shafer, K. H.; Pentoney, S. L., Jr.; Griffiths, P. R. *Anal. Chem.* **1986**, *58*, 58–64.
(10) Pentoney, S. L., Jr.; Shafer, K. H.; Griffiths, P. R. *J. Chromatogr. Sci.* **1986**, *24*, 230–235.
(11) Jinno, K. *Chromatographia* **1987**, *23*, 55–62.
(12) Bartle, K. D.; Raynor, M. W.; Clifford, A. A.; Davies, I. L.; Kithinji, J. P.; Shilstone, G. F.; Chalmers, J. M.; Cook, B. W. *J. Chromatogr. Sci.* **1989**, *27*, 283–292.
(13) Fuoco, R.; Pentoney, S. L., Jr.; Griffiths, P. R. *Anal. Chem.* **1989**, *61*, 2212–2218.
(14) Shafer, K. H.; Griffiths, P. R. *Anal. Chem.* **1983**, *55*, 1939–1942.
(15) Ikushima, Y.; Saito, N.; Hatakeda, K.; Ito, S.; Arai, M.; Arai, K. *Ind. Eng. Chem. Res.* **1992**, *31*, 568–574.
(16) Olesik, S. V.; French, S. B.; Novotny, M. *Chromatographia* **1984**, *18*, 489–495.
(17) Kirschner, C. H.; Taylor, L. T. *Anal. Chem.* **1993**, *65*, 78–83.
(18) Hughes, M. E.; Fasching, J. L. *J. Chromatogr. Sci.* **1985**, *24*, 535–540.
(19) Jordan, J. W.; Taylor, L. T. *J. Chromatogr. Sci.* **1986**, *24*, 82–88.
(20) Hellgeth, J. W.; Jordan, J. W.; Taylor, L. T.; Khorassani, M. A. *J. Chromatogr. Sci.* **1986**, *24*, 183–188.
(21) Johnson, C. C.; Jordan, J. W.; Taylor, L. T.; Vidrine, D. W. *Chromatographia* **1985**, *20*, 717–723.
(22) Wiebolt, R. C.; Kempfert, K. D.; Later, D. W.; Campbell, E. R. *J. High Res. Chromatogr.* **1989**, *12*, 106–111.

0003-2700/94/0366-3543$04.50/0
© 1994 American Chemical Society

few advantages over conventional off-line SFE methods because of their mechanical complexity and reliance on flow restrictors. In contrast, flow cell interfaces allow the direct coupling of the supercritical fluid system to the infrared spectrometer. In this manner, the analytes are detected in the CO_2 matrix in a completely closed system (i.e., a system without a flow restrictor). Flow cells use thick, optically transparent windows (e.g., ZnSe, IRTRAN, and CaF_2) to allow transmission of infrared radiation. These windows, however, suffer from a number of drawbacks including expense ($100–400/window), poor optical transmission properties, and difficult replacement if contaminated or damaged.

Although fiber-optic interfaces have been developed for coupling UV/vis spectroscopy with supercritical processes,[23–25] none have been developed yet to couple IR spectroscopy with SFE. Fiber optics are advantageous over windows from the standpoint of cost, ease of replacement if dirtied or damaged, and ease of cleaning. Infrared optical fibers are available in a number of different materials (e.g., chalcogenide, silver halide, etc.) and core diameters and, when used as light guides in a high-pressure flow cell, offer the advantage of a truly "windowless" SFE-FT-IR interface. The optical fibers used in this study are based on chalcogenide glass (AsSeTe), are inexpensive ($2.00/cm), and have excellent optical transmission properties in the 5000–800-cm^{-1} spectral region. In addition, chalcogenide optical fibers are chemically inert and do not degrade on exposure to oxygen or water.

In this work, we report the development of an inexpensive fiber-optic-based interface (<$150 for all components) for coupling IR spectroscopy with SFE that allows routine working pressures at least up to 400 atm. The fiber-optic-based interface for SFE-FT-IR is used to provide either qualitative or quantitative information about specific analytes in real-world samples without the use of a flow restrictor, a collection solvent, or intermediate trapping. In this work, the samples are extracted statically (i.e., no CO_2 flow once the SFE cell is filled), and then the extract is directly transferred to the fiber-optic IR flow cell. Preliminary results indicate that SFE-FT-IR has sensitivity in the low-to-sub-parts per million (wt analyte/wt sample) range and a linear dynamic range of calibration greater than 3 orders of magnitude.

EXPERIMENTAL SECTION

Fiber Optics. The fiber-optic cables (Amorphous Materials, Garland, TX) used for this work were commercially available chalcogenide (AsSeTe) core cables, and both glass-clad and plastic-clad fibers were evaluated. Although available in any length, the fibers were purchased in 1-m lengths for ease of handling. The outside diameters for the glass-clad and the plastic-clad fibers were 0.047 in. (1.19 mm) and 0.041 in. (1.04 mm), respectively, and each fiber had a 750-μm core diameter, the largest available commercially.

The fibers were cleaved to 7.5-cm lengths with a razor blade, and the ends were polished with wet/dry sandpaper and commercial glass cleaner (Windex). Coarse and fine polishing were performed respectively with 1000- and 1500-grit sandpaper (3M Co., St. Paul, MN). Once the large shards were removed, the fiber was further polished using first 1.0-μm and second 0.3-μm sandpaper (Buehler, Lake Bluff, IL) to achieve a shiny, glasslike surface.

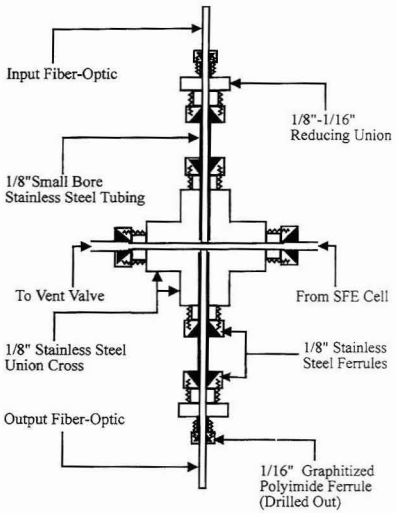

Figure 1. Schematic diagram of fiber-optic SFE-FT-IR interface. Components are described in the text.

Construction of SFE-FT-IR Interface. The fiber-optic SFE-FT-IR interface is diagrammed in Figure 1 and consists of a 1/8-in. stainless steel union cross, small inside diameter (0.059 in., 1.50 mm), 1/8-in. o.d. stainless steel tubing; fiber optics; 1/16-in. graphitized polyimide and 1/4-in. stainless steel ferrules; and 1/8-in. × 1/16-in. reducing unions. The stainless steel union cross and stainless steel ferrules were purchased from the Parker Hannifin Corp. (Huntsville, AL). The graphitized polyimide ferrules (M-2A; Supelco, Bellefonte, PA) were drilled out to a drill index number of 55 (0.052 in., 1.32 mm). All stainless steel tubing for cell construction and transfer lines was cut using a Dremel Moto-Tool 275 (Racine, WI) with attached cutting wheel.

A drill press with a no. 30 bit (0.128 in., 3.25 mm) was used to enlarge the center of the 1/8-in. stainless steel union cross (opposing arms, see Figure 1) to facilitate the insertion of the small inside diameter, 1/8-in. o.d. stainless steel tubing used as a sheath for the fiber optics. The 1.50-mm i.d. of the 1/8-in. stainless steel tubing was selected to be just large enough to allow the optical fiber to pass through it so that the fibers would be centered opposite one another once the interface was assembled. Also, the narrow inside diameter allowed the dead volumes around the fibers to be minimized. This allowed the IR cell to be easily cleaned between samples as discussed below.

To assemble the interface, one side of the narrow-bore 1/8-in. o.d. tubing was placed in the drilled-out cross until its edge was visible from one of the perpendicular legs. The stainless steel pressure fitting (using the stainless steel ferrules

(23) Zagrobelny, J.; Li, M.; Wang, R.; Betts, T. A.; Bright, F. V. *Appl. Spectrosc.* **1992**, *46*, 1895–1897.
(24) Fjeldsted, B. E.; Richter, W. P.; Jackson, W. P.; Lee, M. L. *J. Chromatogr.* **1983**, *423*, 279.
(25) Howdle, S. M.; Stanley, K.; Popov, V. K.; Bagratashvili, V. N. *Appl. Spectrosc.* **1994**, *48*, 214–218.

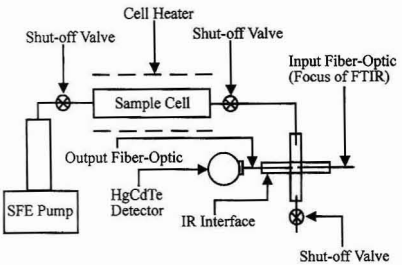

Figure 2. Schematic diagram of on-line SFE-FT-IR instrumentation.

provided with the cross) was then tightened to join the cross to the tubing. The other end of the tubing was reduced to 1/16 in. with a stainless steel reducing union, and the fiber was inserted into the exposed, 1/16-in. male fitting until the fiber was just visible inside the cross. The predrilled graphitized polyimide ferrule and 1/16-in. nut was then tightened around the fiber-optic cable. The same procedure was repeated for the other half of the cross, resulting in pressure-tight seals around the fibers.

The fiber-optic cable was connected on the 1/16-in. side of the reducing union with a graphitized polyimide ferrule. The fiber runs the entire length of the leg, flush with the stainless steel tubing, inside the stainless steel union cross, and the other end protrudes about 1 cm from the 1/16-in. nut. The total length of the cell was 15 cm, including the union cross and plumbing fittings. A shut-off valve attached to the union cross (opposite leg from the SFE cell) was opened when the extraction was complete for venting and cleaning.

The separation between the fiber ends inside the union cross (the optical path length) was adjusted to 4 mm. Although a longer optical path would be preferred (from Beer's law considerations), this separation maximizes the optical path without leading to a serious loss in radiation collection (due to the expanding acceptance/transmission cone of the fiber optics). The dead volume of the IR cell was determined by capping one end of the union cross and introducing water into the cell and was found to be 50 μL. The volume between the fibers, assuming a 4-mm optical path length and a 750-μm core diameter, was calculated to be 1.8 μL.

For the analytical determinations, the IR interface was held at room temperature. However, for the supercritical fluid spectra obtained at 100 and 250 atm, the IR interface was heated to 40 °C by fixing a low-wattage (40 W) soldering iron to the body of the union cross. The temperature of the soldering iron was adjusted by varying its voltage with a Variac to maintain the temperature as monitored by a thermocouple attached to the body of the stainless steel cross.

FT-IR Spectrometer. All spectra were acquired on a Bio-Rad FTS-40 (Cambridge, MA) FT-IR spectrometer equipped with a narrow-range, liquid nitrogen-cooled mercury–cadmium–telluride (MCT) detector. Figure 2 shows a schematic diagram of the experimental arrangement. A simple cell stage was made in-house from 1/4-in. plate aluminum to allow for reproducible and stable placement of the IR cell. A slot was milled in the stage and its top plate fastener to hold the union cross tightly and prevent it from moving. Holes were drilled in the top plate and the stage to allow the opposing plumbing legs (SFE cell connection and venting valve) of the union cross to protrude through the stage. The stage was fastened to the optical bench of the FT-IR spectrometer sample compartment with silicone sealant.

In order to minimize the expense of the fiber-optic interface, beam-condensing optics were not utilized in the FT-IR instrument. The detector focusing mirror was removed, and the output fiber optic from the IR cell was placed immediately in front of the MCT face (as shown in Figure 2). The focusing mirror was removed because the light exiting the output fiber-optic cable has a diameter approximately equivalent to that of the detector, and the most convenient optical design (without beam-condensing optics) is to place the detector as close as possible to the exiting radiation from the fiber. The output fiber-optic cable was placed at the focus, where the sample is usually placed in the normal configuration of the FT-IR spectrometer. Stray radiation was eliminated by winding black electrical tape around the output fiber-optic stainless steel tubing. Because of the placement of the MCT detector, the protruding liquid nitrogen plug interfered with the closure of the cover. Thus, the main cover for the FT-IR spectrometer was open for all experiments unless otherwise stated.

All IR spectra were collected as similarly as possible. The scan speed of the FT-IR spectrometer was set at 10 kHz (1.33 scans/s) with an electronic filtering frequency of 4.5 kHz and a resolution of 4 cm^{-1}. In addition, the FT-IR spectrometer used a triangular apodization function, 2× zero-filling, and a *k*-factor of 2. The background for all spectra, unless otherwise stated, was obtained through the atmospheric pressure, fiber-optic IR cell prior to the SFE. All spectra were the sum of 64 coadded scans with the exception of those of the caffeine reference (in CH_2Cl_2) on KBr salt plates (16 scans).

SFE Apparatus. The SFE syringe pump was a commercially available ISCO 260D pump (Lincoln, NE) with a liquid CO_2 capacity of 260 mL. A 6.94-mL SFE cell rated to 340 atm (Keystone Scientific, Bellefonte, PA) was used for all experiments. Liquids were introduced into the SFE cell using either a 0.5- or a 10-μL syringe. The extraction cell was heated to 77–80 °C with heat tape. For the supercritical experiments, the stainless steel plumbing interconnecting the IR cell and the SFE cell was heated to 40 °C with heat tape. The temperature of the SFE cell and IR cell was monitored using a digital thermometer (HH 81; Omega, Stamford, CT).

Reagents and Samples. SFC/SFE grade CO_2 (Air Products, Allentown, PA) was used for the extraction experiments. Caffeinated and decaffeinated coffee were purchased locally. Reagent grade caffeine (Aldrich Chemical Co., Milwaukee, WI) was used for identification of the caffeine absorption bands. The quantitative reference standard used in the total petroleum hydrocarbon (TPH) study consisted of a 2:3:3 v/v mixture of reagent grade chlorobenzene, *n*-hexadecane, and isooctane (Aldrich), i.e., the same calibration standard to be used in the proposed EPA method for off-line SFE-IR determinations of TPH from soil.[26,27] Soil samples contami-

(26) Lopez-Avila, V.; Bendicto, J.; Dodhiwala, N. S.; Young, R. *J. Chromatogr. Sci.* **1992**, *30*, 355.
(27) Lopez-Avila, V.; Young, R.; Kim, R.; Beckert, W. *J.-Assoc. Off. Anal. Chem.* **1993**, *76*, 555.

nated with various fuel types were obtained by sampling adjacent to fuel tanks on local farm sites as previously described.[28] No sample pretreatment other than sieving to 1/4 in. to remove rocks and sticks was performed prior to analysis. Standard 20–30 mesh Ottawa sand (Fisher Scientific, Fairlawn, NJ) was used as purchased for the detection limit determinations.

SFE Procedures. The procedure for the coffee extraction was typical for a static, on-line SFE-FT-IR experiment. The coffee sample (1.0 g plus 0.1 mL of water as a modifier) was placed in the SFE cell. The volume of CO_2 in the pump was noted (after a zero flow was obtained upon pressurization of the pump), and the SFE cell was then pressurized to 185 atm (with the SFE cell outlet valve shut). After flow equilibrium was obtained (i.e., the pump registered a flow of <0.05 mL/min), the SFE cell inlet valve was shut, and the volume of CO_2 was again noted to determine the volume of CO_2 used for the extraction (i.e., the void volume in the sample cell). The extraction cell was heated to 77–80 °C, bringing the SFE cell pressure to ca. 340 atm. (Note that the pressure limit in this system was based on the 340 atm safety limit of the extraction cell. The fiber-optic cross was reliable at least up to 400 atm.) The static extraction was performed for 30 min, and then the valve between the SFE cell and the IR cell was opened (Figure 2) to fill the IR cell with the SFE extract. Opening the valve caused the expansion of the supercritical CO_2 into the IR cell, cooling the CO_2 by about 10 °C; thus, the cell was heated until the temperature was 77–80 °C. When the SFE cell reached thermal equilibrium (2–3 min), the valve separating the SFE and IR cells was closed during the IR scan. The final pressure of the IR cell after equilibrium was ca. 250 atm. Note that the full extraction pressure, 340 atm, could easily have been transferred to the IR cell by opening the valve between the pump and SFE cell during the transfer step. However, this procedure could possibly lead to contamination of the pump. Therefore, since no advantage in sensitivity was observed by this procedure, the valve between the pump and the SFE cell was typically left closed after initial pressurization of the SFE cell, and the pressurization of the IR cell was achieved using the pressure from the SFE cell as described above.

For the TPH determinations, soil samples (0.050 or 0.50 g for soils contaminated with diesel fuel or gasoline, respectively) were extracted in triplicate using the procedure described previously (CO_2 at 340 atm; however, without modifiers). Calibration of the on-line SFE-FT-IR TPH determinations was accomplished with the EPA reference oil. Aliquots of 1, 5, 10, 15, and 20 μL were added to the SFE cell with a 10-μL syringe to yield concentrations of 111, 554, 1109, 1663, and 2217 ppmv (parts per million by volume), respectively. The aliquots were treated to the same extraction conditions as the soil samples. After the absorption data were acquired, a five-point calibration plot of TPH concentration versus corrected absorbance was constructed from the data taken at 2932 cm^{-1}. Since the dead volume of the SFE system with a sample present was known from the pump displacement information, the concentration of TPH was first calculated in ppmv and then converted to ppm (wt TPH/wt soil), as discussed in the Results and Discussion section.

(28) Hawthorne, S. B.; Miller, D. J.; Hegvik, K. M. *J. Chromatogr. Sci.* **1993**, *31*, 26–30.

The TPH in the soil samples was determined prior to this study by the proposed EPA method using off-line SFE with CO_2 and a standard 4-h Soxhlet extraction using 150 mL of Freon-113.[28] Both the off-line SFE and the Soxhlet methods use IR for the quantitative determinations of TPH in the extracts.

IR Cell Cleaning. Typically, the IR cell was cleaned on-line by simply flushing it with five void volumes of liquid CO_2 (the IR cell did not require disassembly for cleaning). The SFE cell was first pressurized to 185 atm, and then the valve separating the cells was opened to pressurize the IR cell. The valve between the cells was then closed and the vent opened, allowing the IR cell to be vented without depressurizing the SFE cell. This venting and repressurizing of the IR cell was repeated five times before the CO_2 in the SFE cell was exhausted. Generally, filling the SFE cell five times, yielding 25 total flushes of the IR cell, was sufficient to bring the C–H absorption to approximately that of background (<1 ppm, wt solute/wt sample). Total cleaning time between samples was on the order of 3 min. However, after extraction of the coffee samples, the carry-over concentration in the IR cell was on the order of 40 ppmv, which required an additional flushing with about 20 void volumes of CO_2 for removal.

RESULTS AND DISCUSSION

IR Interface. The fiber-optic transmission cell functioned extremely well as an SFE-FT-IR interface for the 6-month duration of these experiments. On-line SFE-FT-IR spectra were easily acquired at a temperature of 40 °C and pressures up to 400 atm without fiber degradation or seal (ferrule) failure. In fact, the upper pressure limit for the SF extractions was governed by the SFE cell rather than the IR interface.

Initially, two types of chalcogenide fiber optics were tested for use in the interface, glass-clad and plastic-clad, to determine the appropriate fiber for this application. Both cables had a core diameter of 750 μm and differed only in their cladding. The plastic-clad cables had an outer cladding layer of polyamide plastic. The cladding of the glass-clad cable was similar in crystal structure to that of the core but with a different refractive index (to cause total internal reflection). According to the manufacturer's specifications, both cables can be used at temperatures of up to 136 °C (the glass-transition temperature).

Because the plastic-clad cable had absorption bands in the infrared (due to the polyamide plastic), radiation transmission through these cables was significantly less than that for the glass-clad cables. Thus, the plastic-clad fibers were abandoned for the superior transmission properties of the glass-clad cables. Figure 3 shows an infrared transmittance spectrum of a 15-cm length of the glass-clad fiber-optic cable. Because of the difficulty involved in obtaining a single-beam background spectrum through a 750-μm pinhole (corresponding to the core diameter), the ordinate has been normalized to the highest transmittance. With the exception of the H_2Se band at 2174 cm^{-1}, the glass-clad cable is essentially featureless over its useable range of 5000–800 cm^{-1}. This spectral window is ideal for detecting analytes in subcritical or supercritical CO_2 since CO_2 itself is not transparent below 800 cm^{-1}.[18]

CO_2 Spectra. The top and bottom spectra shown in Figure 4 are supercritical CO_2 at 40 °C and 250 atm and at 40 °C

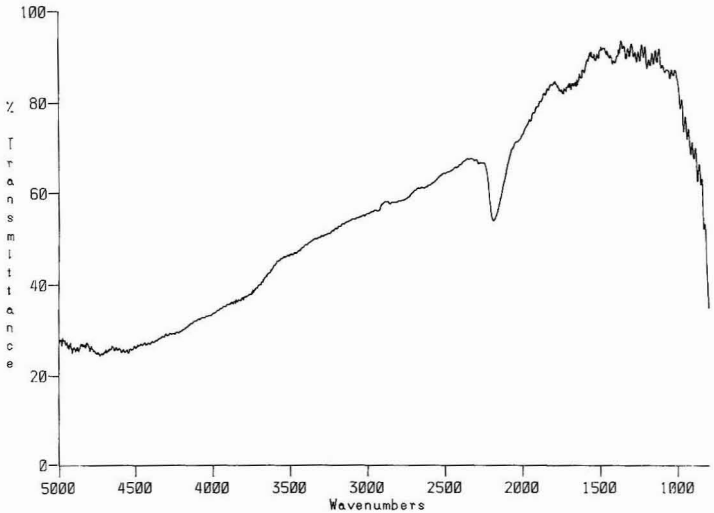

Figure 3. Transmittance spectrum of a 15-cm length of chalcogenide (AsSeTe) fiber-optic cable.

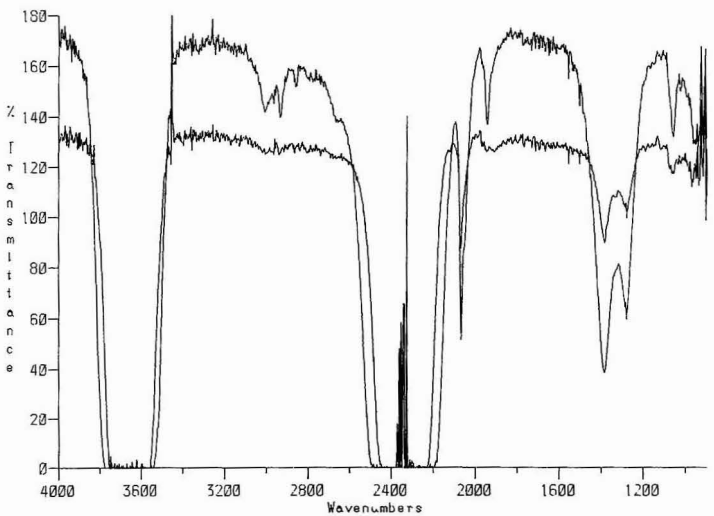

Figure 4. Transmittance spectra of supercritical CO_2 obtained with the fiber-optic interface. Upper spectrum: CO_2 at 250 atm and 40 °C. Lower spectrum: CO_2 at 100 atm and 40 °C.

and 100 atm, respectively. Air at 1 atm in the interface was used to obtain the reference single-beam background spectra. Liquid and supercritical CO_2 have two major IR bands that absorb all incident radiation occurring in the regions from 3800 to 3500 cm^{-1} and from 2500 to 2150 cm^{-1}. Because these two absorption bands are quite strong, no information may be gathered about an analyte in these regions. The "lines" appearing in the center of the strong CO_2 absorption band at 2260 cm^{-1} are artifacts and arise because both the single-beam sample spectrum and the single-beam background spectrum (both obtained with the instrument cover open) have virtually zero responses in this region (i.e., no radiation transmission due to the CO_2 in the IR cell and the CO_2 in the atmosphere, respectively). Thus, the transmittance spectrum in this region is a ratio of two very small numbers and yields very large transmittances. The absorptivities of other bands of liquid and supercritical CO_2, including the Fermi resonance bands in the region of 1200–1400 cm^{-1}, are not as large as those of the two major bands. Thus, with the exception of the two large absorption bands, the supercritical or subcritical CO_2 matrix is reasonably IR transparent. Of course, as Figure 4 demonstrates, the absorptivities of all the bands of super-

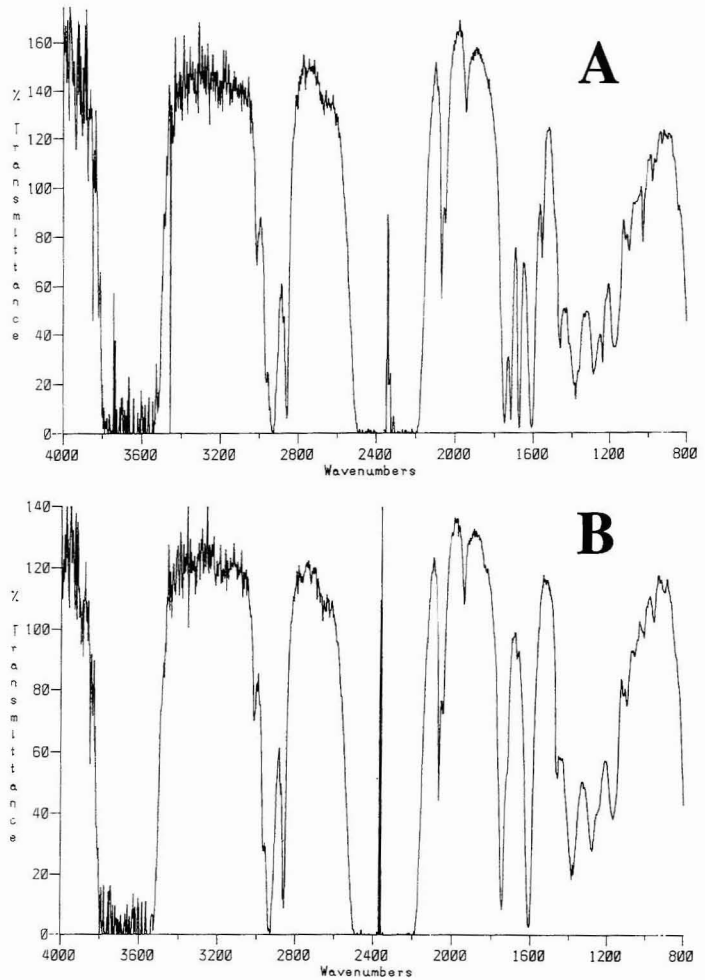

Figure 5. On-line infrared spectra of (A) caffeinated coffee SFE extract and (B) decaffeinated coffee SFE extract. SFE conditions: 340 atm and 77–80 °C for 30 min.

critical CO_2 (including the Fermi resonance bands) are pressure dependent and increase with increasing pressure (or density).

Typically, transmittance spectra of liquid or supercritical CO_2 as obtained with our IR cell produce base lines that exceed the theoretical maximum of 100% transmittance. This higher than normal transmittance is due to the higher refractive index of the liquid or supercritical CO_2 (versus the air background, which has a refractive index of ca. 1.0) which effectively increases the numerical aperture of the fiber-optic cable. It is well known that the refractive index of a substance is proportional to its density.[29] Since the density of CO_2 increases with increasing pressure, the CO_2 acts as beam-condensing optics (decreases the acceptance/transmission cone) at high pressure and allows better transfer of radiation from one fiber to the other. Therefore, the amount of radiation increases for the sample spectrum over the background spectrum and gives a higher than usual percent transmittance. In fact, an approximately 20% increase in interferogram magnitudes was seen for the sample spectra at 100–300 atm over the background spectra at 1 atm.

Background Normalization. The base line shift due to the refractive index change made the quantitative interpretation of the spectra difficult. If an absorption band was interpreted without some background correction, negative absorbances would be obtained at low analyte concentrations ($T > 100\%$) and positive absorbances would be obtained at high analyte concentrations ($T < 100\%$). Although these absorbances are

(29) Hecht, E. *Optics*; Addison-Wesley Publishing: Reading, MA, 1990; p 60.

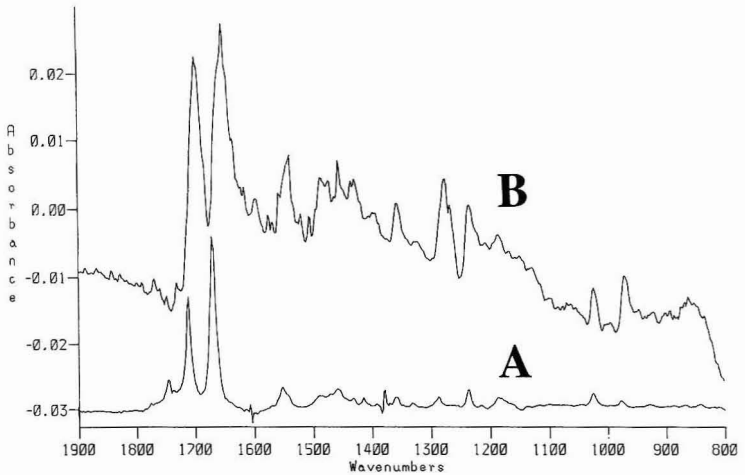

Figure 6. Infrared absorbance spectra of caffeine obtained (A) by subtraction of on-line spectrum of decaffeinated coffee SFE extract from on-line spectrum of caffeinated coffee SFE extract and (B) in CH_2Cl_2. The spectra have been offset for clarity.

proportional to analyte concentration (and can be used quantitatively as long as the calibration is performed under the same experimental conditions), they are sensitive to variations in the pressure or temperature of the SFE-IR system. Thus, the experimentally obtained absorbance values were converted to corrected absorbance values by spectral normalization. The procedure used here is similar to other methods developed to normalize diffuse reflectance spectra for calibration plots.[13] Specifically, the transmittance spectrum is normalized to 100% transmittance using a region of the spectrum where neither the analyte nor the matrix absorbed radiation. The actual transmittance of a band that absorbs was then a fraction of the original value. For example, if the uncorrected transmittance at a specified nonabsorbing wavenumber was 140% and that of a C–H stretching band was presented as 70%, then the computed "corrected" transmittance is (70/140) × 100, or 50% corrected transmittance. This transmittance spectrum was then converted to a "corrected" absorbance spectrum for quantitation. For this work, the nonabsorbing transmittance value was obtained at 2755 cm^{-1}.

Spectral Subtraction. Spectral subtraction is useful in SFE in order to remove spectral interferences arising from both the CO_2 matrix and the coextracted compounds (assuming that spectral information concerning these coextracted compounds can also be obtained). Of course, in order to eliminate the bands of the CO_2 matrix, the spectra must be acquired under similar pressure and temperature conditions. An on-line SFE-FT-IR spectrum of caffeinated coffee after 30 min of SFE is shown in Figure 5A in the region from 4000 to 800 cm^{-1}. The infrared bands shown in this spectrum are due to caffeine, natural oils and aromas, the CO_2 background, and the water modifier (ca. 1600 cm^{-1}). Figure 5B shows an on-line SFE-FT-IR spectrum of decaffeinated coffee in the same spectral region. Notice that many of the bands present in the caffeinated coffee spectrum are also present in the decaffeinated coffee spectrum. The caffeine bands in the caffeinated coffee spectrum can be spectrally isolated by subtracting the decaffeinated coffee spectrum from the caffeinated coffee spectrum. The resultant subtraction spectrum is shown in Figure 6A and has been plotted in the 1900–800-cm^{-1} region. (The C–H stretching region is not shown in Figure 6A because of subtraction artifacts arising from the strong absorption of the coffee oils and aromas.) For comparison, Figure 6B shows an IR spectrum of caffeine in CH_2Cl_2. Note that the caffeine spectrum is nearly cleanly recovered by spectrally subtracting the two SFE coffee extract spectra (in fact, the SFE-FT-IR spectrum of caffeine has a nearly straight base line as compared with the sloping base line of the caffeine reference spectrum). The subtle differences in the band positions of caffeine in the CO_2 matrix have been reported previously and do not arise from the subtraction process.[17]

Determination of TPH in Soil by On-Line SFE-FT-IR Spectroscopy. The ability to obtain quantitative information with the fiber-optic SFE system was tested by determining TPHs in soils. A totally static extraction (no CO_2 flow once the SFE cell was filled) at 340 atm and 77–80 °C was utilized to remove the TPH components from the samples. Transfer of the extracted organics into the IR cell was facilitated by holding the IR cell at atmospheric pressure until the extraction was complete. Following extraction, the valve separating the SFE cell from the IR cell was opened, and the extracted components were transferred as the CO_2 depressurized to about 250 atm.

Examples of the raw infrared spectra of the SFE extracts (i.e., without transmittance correction or subtraction of the CO_2 background) are shown in Figure 7. These spectra were obtained at an interface pressure and temperature of 250 atm and 25 °C, respectively. Figure 7A shows an infrared spectrum of the gasoline-contaminated soil extract after 30 min of SFE,

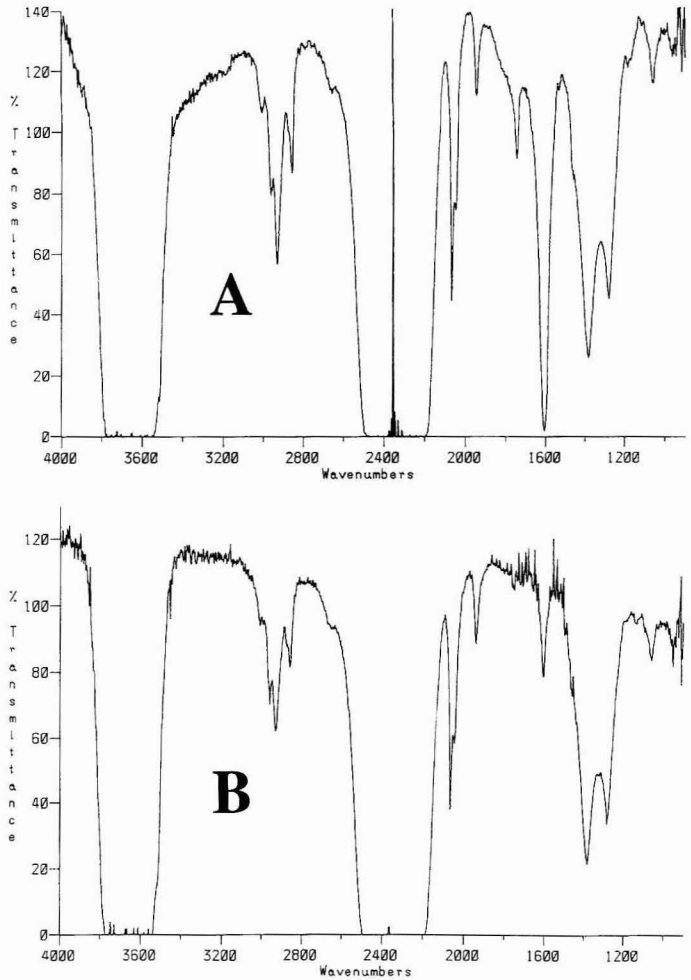

Figure 7. On-line infrared spectra of (A) gasoline-contaminated soil SFE extract and (B) diesel fuel-contaminated soil SFE extract. SFE conditions: 340 atm and 77–80 °C for 30 min.

and Figure 7B shows an infrared spectrum of the diesel fuel-contaminated soil extract after 30 min of SFE. Both spectra show strong C–H stretching vibrations in the region of 3000 cm^{-1}. In addition, it should be noted that both spectra show the presence of water. The spectrum in Figure 7A shows both the broad O–H stretching vibration at ca. 3400 cm^{-1} (which overlaps the strong CO_2 absorption at 3700 cm^{-1}) and the bending vibration at ca. 1600 cm^{-1}. The spectrum in Figure 7B, which was obtained from a sample with a lower concentration of water, shows only the bending vibration at ca. 1600 cm^{-1}.

Quantitation was accomplished by monitoring the 2932-cm^{-1} C–H stretching absorption (with base line correction, as described above) and employing a slightly unconventional application of Beer's law. Strict application of Beer's law employs units of concentration that are dependent upon the volume or mass of the solution (e.g., molarity or ppm). However, when using a variable density solvent such as CO_2, conventional concentration units are awkward because changes in pressure (at constant cell volume) change the volume or mass of the solvent (and hence, the volume of solution) in the cell. In order to simplify the on-line experimental procedure, the TPH was determined in units of ppmv using the system dead volume (the entire system volume less the volume occupied by the sample) rather than the mass or volume of the CO_2. When the dead volume of the system is utilized rather than the volume of the CO_2 solvent, the concentration of the solute is independent of the system temperature or pressure. Parts per million by volume is converted to ppm (wt solute/wt sample) with

$$C_{ppm} = \frac{C_{ppmv} D V_d \times 1000}{W}$$

where C_{ppm} is the concentration in $\mu g/g$ of soil, C_{ppmv} is the concentration in $\mu L/L$, D is the density of the EPA reference oil (0.83 g/mL), V_d is the dead volume of the system (in L), and W is the weight of the soil sample. The factor of 1000 in the numerator is used for unit conversion.

The total dead volume (the volume of the system with a sample in the SFE cell) was determined at room temperature using the volume information on the control panel of the ISCO pump. First, the initial (empty) volume of the system was determined by measuring the amount of CO_2 at 185 atm that was needed to fill the entire system. This volume is needed in order to determine the dead volume of the IR cell and the interconnecting plumbing between the SFE and IR cell. The outflow of CO_2 from the pump was deemed to be at equilibrium when the CO_2 flow rate (according to the pump readout) was <0.05 mL/min, which generally required 1–3 min. (Note that temperature equilibration would be faster if the water jacket available with the 260D pump was utilized.) Next, the IR cell was sealed-off from the SFE cell, and the dead volume of the empty SFE cell was determined. The two dead volumes were then subtracted (the dead volume of the empty system less the dead volume of the SFE cell) to yield the dead volume of the IR cell and interconnecting plumbing. Since this volume is constant for a given experimental arrangement, this measurement needs to be performed only once and noted.

Next, the dead volume of the SFE cell with sample was determined. This was accomplished by simply noting the amount of CO_2 at 185 atm required to fill the SFE cell with a sample in it. Finally, the total dead volume was obtained by adding the dead volume of the IR cell and interconnecting plumbing to the dead volume of the SFE cell with sample.

This procedure for determining the system dead volume was verified using the known volume of a series of glass beads (determined by water displacement). A plot of the volume of the glass beads determined by water displacement versus the volume of the glass beads determined by CO_2 displacement yielded a straight line ($y = 0.205 + 0.986x$) and a regression coefficient (r) of 0.995. The reproducibilities of the volume measurements performed in this fashion were typically <4% (relative standard deviation).

Calibration of the on-line SFE-FT-IR TPH determinations was accomplished by constructing working curves (corrected absorbance at 2932 cm^{-1} vs concentration) using the EPA reference oil. The calibration curve for the determination of the TPH by on-line SFE-FT-IR was linear over the concentration range of our calibration standards (111–2217 ppmv), with an equation of $y = 0.018 + 0.00065x$ and $r^2 = 0.9995$. Overall calibration linearity is from the detection limit to ca. 2200 ppmv.

Results for the determination of TPH by several analytical methods for two "real-world" soil samples are shown in Table 1. It can be seen in Table 1 that the TPH determined by on-line SFE-FT-IR agrees remarkably well with both the standard Soxhlet procedure and the off-line SFE-IR method. The major cause of the large standard deviations in the measurements is likely the heterogeneity (e.g., small rocks) in the small soil samples employed. Because it was necessary to keep the total TPH concentration under about 2200 ppmv (with a 4-mm path length as used in this IR cell), the soil samples were of low weight (50 mg for the diesel-contaminated soil and 500 mg for the gasoline-contaminated soil).

Table 1. Comparison of On-Line SFE-FT-IR with Off-Line SFE-IR and Soxhlet Extraction Determinations of Total Petroleum Hydrocarbons for Selected Soil Samples

	TPH, ppm (RSD, %)[b]		
sample	off-line SFE-IR[a]	on-line SFE-FT-IR	Soxhlet[a]
farm diesel	31 000 (3)	38 041 (24)	38 500 (11)
farm gasoline	6240 (5)	6538 (17)	5840 (3)

[a] Off-line SFE was performed for 30 min with collection in 5 mL of Freon-113. The Soxhlet extraction was performed for 4 h using 150 mL of Freon-113. Results are adapted from ref 28. [b] TPH results shown are average values from triplicate determinations.

The detection limit of TPH for this system, defined as the concentration of the reference oil where the absorbance is equal to twice the peak-to-peak base line noise, was determined by extracting 0.2-μL spikes of the reference oil from clean sand (12-g quantities). Triplicate extractions yielded average corrected absorbances approximately 18× the base line noise absorbance. Thus, a 48-s scan time (64 coadded scans) yielded a detection limit of 1.6 ppm (wt TPH/wt sand). Assuming a 1.8-μL volume between the fiber ends, this concentration corresponds to a mass detection limit of 22 ng. Longer scan times yield lower detection limits (e.g., a 15-min scan time yields a detection limit of ca. 360 ppb or ca. 5 ng).

CONCLUSIONS

An inexpensive fiber-optic interface for coupling a supercritical fluid extractor to a FT-IR spectrometer has been developed. This interface, based on chalcogenide fiber optics, has been demonstrated to provide both qualitative and quantitative measurements of real-world supercritical fluid extracts in an on-line fashion without the need for flow restrictors and collection solvents or sorbents required by off-line SFE. The interface is physically rugged up to 400 atm and can be quickly cleaned by a simple pressurization/venting procedure. Analysis of real-world soil samples for TPH by on-line SFE-FT-IR gives results in good agreement with Soxhlet extraction and off-line SFE. Although the system is not optimized for sensitivity, detection limits for the present system are in the low-to-sub-parts per million range (wt hydrocarbon/wt soil).

ACKNOWLEDGMENT

The partial financial support from Chevron Oil Co. and U.S. EPA (EMSL, Las Vegas, NV), instrument loans from ISCO, and the gift of CO_2 from Air Products are gratefully acknowledged. The authors would also like to thank Greg Whaley at Amorphous Materials for the initial gift of the fiber-optic cables and for many useful discussions. This paper was presented, in part, at the 1994 Pittsburgh Conference on Analytical Chemistry and Applied Spectroscopy as Nos. 514P and 77.

Received for review April 25, 1994. Accepted June 27, 1994.®

® Abstract published in *Advance ACS Abstracts,* August 1, 1994.

Author Index

Baechtel, F. S., 3303
Bai, J., 3423
Beauchamp, J. L., 3447
Beklemishev, M. K., 3521
Bergquist, J., 3512
Booksh, K. S., 3328
Bottura, C., 3492
Bronk, K. S., 3519
Burgess, L. W., 3328, 3337, 3345

Cain, T. C., 3423
Chen, E. T., 3318
Clark, J. K., 3528
Colbeck, I., 3525
Colton, R., 3394
Currie, L. A., 3303

Dale, J. M., 3431
De Santis, F., 3503
Doktycz, M. J., 3416
Duewer, D. L., 3303

Ebdon, L., 3400
Ekman, R., 3512
Elshani, S., 3521
Evans, E. H., 3400
Ewing, A. G., 3512

Fan, Z. H., 3485
Fluri, K., 3485
Fowles, E. H., 3447

Gilman, S. D., 3512
Guevremont, R., 3289

Habibi-Goudarz, S., 3416
Harrison, D. J., 3485
Hawthorne, S. B., 3543
Heglund, D. L., 3543
Hendayana, S., 3458
Henshaw, J. M., 3328, 3337, 3345
Hergenröder, R., 3472
Hinze, W. L., 3449
Hobbs, S. E., 3371
Horiuchi, T., 3500
Hoshino, S., 3500
Houck, K., 3379

Hu, J., 3384

Irikura, K. K., 3447

Jacobson, S. C., 3472
Jannasch, H. W., 3352
Johnson, K. S., 3352

Karube, I., 3297
Koutny, L. B., 3472
Kowalski, B. R., 3328, 3337, 3345

Lavine, B. K., 3458
Le Blanc, J. C. Y., 3289
Lei, T., 3533
Leigh, S. D., 3303
Lewis, D. A., 3525
Liu, H. K., 3303
Liu, Y.-H., 3423
Locke, S. J., 3436
Lubman, D. M., 3423

Mariner, D. C., 3525
Marriott, P. J., 3394
Marshall, W. D., 3533
McCormick, M. J., 3394
McLuckey, S. A., 3416
Melaragno, P. R., 3528
Miller, D. J., 3543
Mitsubayashi, K., 3297
Momplaisir, G.-M., 3533
Moore, A. W., Jr., 3472
Moreno, B., 3449
Mudd, J. L., 3303

Niwa, O., 3500
Nordmeyer, T., 3540
Novotny, M., 3466
Novotny, M. V., 3477

Olesik, J. W., 3371

Pardue, H. L., 3318
Pemberton, J. E., 3362
Prather, K. A., 3540
Pretorius, W., 3400

Quina, F. H., 3449

Ramsey, J. M., 3431, 3472
Reeder, D. J., 3303
Riekkola, M.-L., 3477
Rowland, S., 3400

Sakamoto, C. M., 3352
Schilling, W. A., 3528
Seiler, K., 3485
Sherrard, K. B., 3394
Siu, K. W. M., 3289
Smilde, A. K., 3337, 3345
Smith, G., 3394
Soini, H., 3477
Stedman, D. H., 3384
Stefansson, M., 3466, 3477
Stokes, D. L., 3379
Stong, J. D., 3505
Suzuki, Y., 3449

Tabei, H., 3500
Takahashi, M., 3500
Takeuchi, T., 3297
Tauler, R., 3337, 3345
Tetreault, J., 3458
Thibault, P., 3436
Thompson, W. R., 3362
Tilotta, D. C., 3543

Van Berkel, G. J., 3408
Vo-Dinh, T., 3379

Wai, C. M., 3521
Walt, D. R., 3519
Wang, H., 3449
Weigl, B. H., 3323
Whitten, W. B., 3431
Wijayawardhana, C. A., 3528
Witchey-Lakshmanan, L. C., 3505
Wolfbeis, O. S., 3323

Yang, M., 3431
Yokoyama, K., 3297

Zappoli, S., 3492
Zhou, F., 3408

BOTTOM LINE:

The more you read the higher you go.

Success for your company and your career means having the right information at the right time. And that's where *C&EN* comes in.

Week after week, *C&EN* delivers up-to-the minute news on every aspect of the chemical enterprise, from business to government, and research to education. Plus, you get an in-depth reporting of trends that puts it all in perspective.

You'll find practical information that enhances day-to-day business dealings, as well as long-range planning — information you can use to hold a competitive edge.

There's only one sure way to get the comprehensive chemistry news you need. Reading *C&EN* puts you on top. For subscription information, call toll-free:

1-800-333-9511.

Success for your company and your career.

CHEMICAL & ENGINEERING NEWS

C&EN

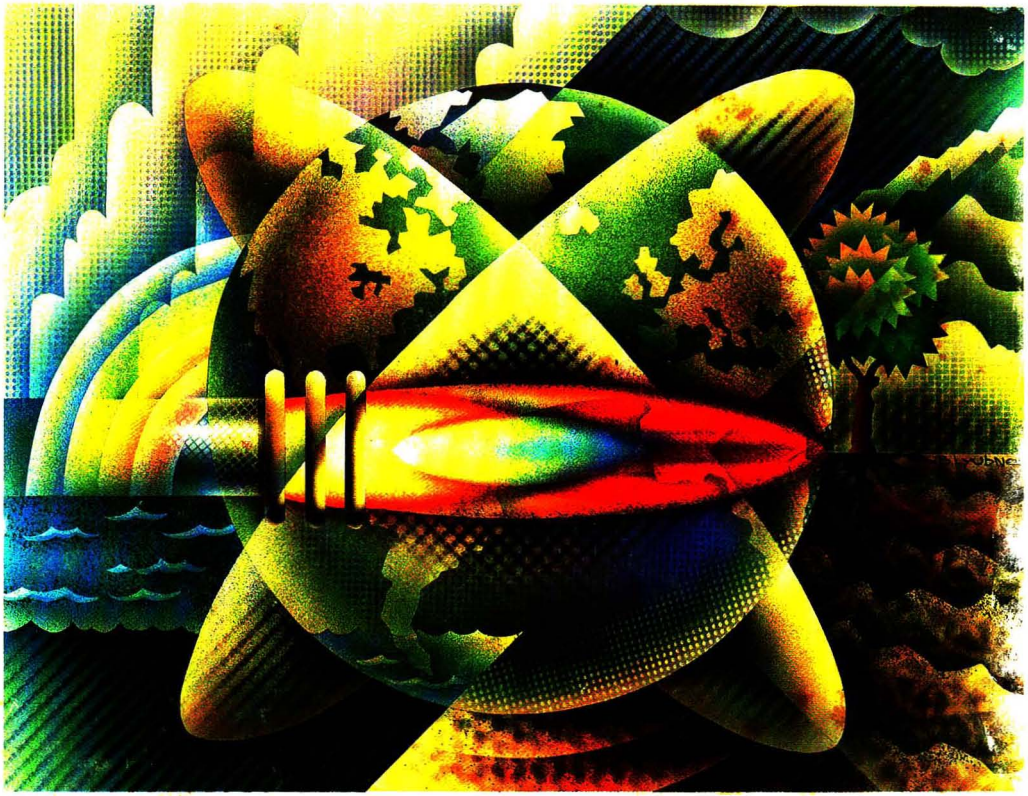

The world leader in inorganic analysis redefines routine ICP-MS.

The new ELAN 6000 ICP-MS System is more compact and easier to use than any other system—yet delivers proven reliability, productivity and analytical performance. The ELAN 6000 follows a tradition of excellence set by PE Sciex. It is the ideal choice for facilities that handle a broad range of challenging samples on a day-to-day basis. Even method compliance becomes routine.

A system tailored to your needs. The ELAN 6000 offers the most extensive line of accessories available: the exclusive flow injection system, electrothermal vaporization and laser sampling, as well as other popular accessories to expand your capabilities.

Answers that work in the real world. From sample preparation and method development to data handling, look to the world leader in inorganic analysis for systems, support and solutions. Perkin-Elmer brings more than 30 years of experience in inorganic analysis to help you deliver quality results as a matter of routine.

ISO 9001 CERTIFIED

Get all the elements you need with one phone call. For sales information or literature in the U.S., call 1-800-762-4000. Outside the U.S., contact your Perkin-Elmer representative.

New ELAN 6000 ICP-MS System

PE SCIEX

The Perkin-Elmer Corporation, 761 Main Avenue, Norwalk, CT 06859-0012, USA
Perkin-Elmer Ltd., Post Office Lane, Beaconsfield, Bucks HP9 1QA, UK; Bodenseewerk Perkin-Elmer GmbH, Postfach 10 17 61, D-88647 Ueberlingen, Germany
All analytical instruments and systems manufactured by Perkin-Elmer are certified under the quality requirements of ISO 9001

Circle No. 2 for Literature only. Circle No. 3 for Literature and Sales Call.